Origin and Characterization of the Local Stress State at Dislocation Channel – Grain Boundary Interaction Sites and its Role in Irradiation Assisted Stress Corrosion Cracking

by

Drew Coulson Johnson

A dissertation submitted in partial fulfillment
of the requirements for the degree of
Doctor of Philosophy
(Nuclear Engineering and Radiological Sciences)
University of Michigan
2020

Doctoral Committee:

Professor Gary S. Was, Chair
Professor Fei Gao
Associate Research Scientist Zhijie Jiao
Professor Amit Misra
Professor Ian M. Robertson

Drew C. Johnson

dcoulson@umich.edu

ORCID ID: 0000-0002-7996-4691

Dedicated to my family in Washington who supported my from thousands of miles away

To my friends in Michigan who kept me sane throughout the years

And to Dr. Was for believing in me when I found it hard to believe in myself

ACKNOWLEDGEMENTS

I would like to start by thanking my advisor, Dr. Gary S. Was, for his support and guidance throughout the entirety of my doctoral program. Without the time and effort he dedicated to assisting me in my growth as a scientist and developing my current research, none of this would have been possible. A special thanks is in order for Dr. Diana Farkas and Dr. Brian Kuhr who assisted me greatly in my research by performing many molecular dynamics simulations to compliment my own experimental finding and provided valuable discourse throughout the length of my tenure in the PhD program. I would also like to thank the members of my dissertation committee, Dr. Fei Gao, Dr. Amit Misra, Dr. Ian Robertson, and Dr. Zhijie (George) Jiao for their willingness to serve on my committee as well as support throughout my research.

I would like to thank my colleagues for their assistance throughout my 11 years at the University of Michigan. I've grown a lot since my freshman year as an undergrad in 2009 and that is in no small part to the wonderful people surrounding me. Encouragement and training provided by Mike McMurtrey, Tyler Moss, Kale Stephenson, Stephen Raimen, Shyam Dwaraknath, Liz Getto, Anthony Monterosa, and Justin Hesterberg was invaluable in entrenching me into the research community. Working alongside David Woodley, Stephen Taller, and Gerrit VanCoevering (a fellow 2009 inductee into the UM family) has been instrumental in my trajectory and growth as a scientist over the years, and their assistance is truly appreciated.

I am grateful for the help I received from Ovidiu Toader, Fabian Naab, and Tom Kubley at the Michigan Ion Beam Laboratory and the support I received from Alex Flick and Connor Shamberger conducting autoclave experiments in the High Temperature Corrosion Laboratory.

Finally I would like to thank my family for trusting me when I set out on this journey over a decade ago. My parents, Gunther and Molly, my grandmother, Margie, as well as my siblings, Jessica Johnston and Anthony Kelly-Glasoe, have shown nothing but unconditional love and patience throughout the years and have never doubted my ability to eventually succeed in my academic pursuits. I want to thank them for their constant encouragement and optimism throughout this endeavor.

This work was supported by the U.S. Department of Energy, Office of Basic Energy Sciences, under grant DE-FG02-08ER46525

TABLE OF CONTENTS

LIST OF TABLES

LIST OF FIGURES

LIST OF APPENDICES

Abstract

The objective of this study was to quantitatively measure the stress state present at the interaction sites between dislocation channels and grain boundaries in irradiated stainless steel. The full geometry of grain boundaries was determined using electron backscatter diffraction and mechanical serial sectioning techniques such that calculated stresses could be resolved in a direction acting normal to the grain boundary plane. The full stress tensor surrounding dislocation channel – grain boundary interaction sites were calculated prior to straining in a high temperature aqueous environment

Grain boundary susceptibility to intergranular fracture was characterized based on boundary misorientation, offset angle with respect to the loading axis, Schmid Factor, and stress magnitude acting at the point of intersection between individual dislocation channels and grain boundaries. Results show that the magnitude of the tensile stress acting perpendicular to the grain boundary is strongly correlated with the cracking susceptibility of the boundary, however a complete picture of the mechanisms responsible for irradiation stress corrosion cracking is still unknown.

Molecular dynamics simulations and a discrete dislocation array model were used to benchmark the calculated stress values made using cross correlation at individual dislocation channel – grain boundary interaction sites. Both models, while approaching the problem using different methods and length scales, were able to accurately describe the stresses that were observed experimentally at both discontinuous and continuous channel interaction sites.

Discontinuous channel interactions were observed to generate a large stress field at the grain boundary, while a similar stress amplification was not observed at continuous channel sites.

Comparing the cross correlation stress measurements with cracking behavior after straining in a simulated reactor environment allowed for the direct linkage of tensile and shear stress magnitude with crack initiation, which is a first of a kind measurement. This work was able to determine a pseudo-threshold for crack initiation in a Fe13Cr15Ni alloy, where below this stress no cracks were observed. Above this threshold, cracks were observed to form and the cracking fraction of analyzed sites increased as the total stress acting normal to the grain boundary increased. The findings of this work indicate that the stress acting normal to the grain boundary, which is caused by both the impinging dislocation channel and the applied stress during deformation, drives the crack initiation process as long as the material is subjected to a high temperature corrosive environment. This helps provide additional insight into the mechanisms which are fundamental to the IASCC process.

Chapter 1 - Introduction

The energy produced by nuclear plants continues to be an important component of the energy portfolio in the United States and many other countries across the world. The US Nuclear Regulatory Commission (NRC) reported in 2014 that 100 licensed reactors in the US generate approximately 20% of the total electricity in the country [1]. These reactors were originally licensed to operate for 40 years, but with current regulation several reactors have been awarded extensions to continue operation for an additional 20 years. As the current reactor fleet continues to age, with 60% of US reactors operating for 35 years or more, it is becoming increasingly important to understand how the materials in these reactor will degrade over lifetimes potentially up to 80 years for current generation reactors. Along with maintaining the current reactor fleet, several concepts are being developed for the next generation of reactors, denoted as "Gen IV" reactors. These next generation reactors will potentially run for longer lifetimes, operate at higher temperatures, and subject materials to more corrosive environments. These new harsher operating parameters put even more focus on the materials with which we build these reactors and emphasize the necessity to understand the mechanisms by which these materials can fail prematurely. Material failures can be a safety hazard and can cause incredibly expensive reactor downtimes as maintenance is performed.

Austenitic stainless steel is used for many core internal components for current generation light water reactors, and is a prime candidate to be used in future reactor design

concepts. This material was chosen initially due to its sufficient resistance to general corrosion, good mechanical properties, and relative abundance which makes it cost effective to use as a structural material. While this material has many attractive attributes, there are still well known issues with its performance in an irradiation environment as irradiation can have a significant effect on the material microstructure. Radiation induced segregation of elemental species to and away from grain boundaries, production of defect clusters, loop formation, precipitate formation and dissolution, and stacking fault tetrahedra formation all occur dynamically during the reactor lifetime of a component [2-6]. The complexities of these simultaneous processes make it incredibly difficult to isolate the root causes and fundamental mechanisms behind the potential failure modes of material under irradiation in a corrosive environment.

One of the main mechanisms of failure in irradiated austenitic stainless steels is irradiation assisted stress corrosion cracking (IASCC) [7-9]. As the name implies, a material must be subjected to both a corrosive environment as well as mechanical stresses while under irradiation at elevated temperature. Although this phenomenon was discovered several decades ago, an exact mechanism behind IASCC is not fully understood. Several studies have looked at the microstructural progression of key material features like radiation induced segregation of chromium away from the grain boundaries, radiation hardening, etc. but none of these individual factors appear to correlate well with the material susceptibility to IASCC [10-12]. In recent years, localized deformation has emerged as a potentially key factor in the IASCC initiation process [13,14]. The multitude of defects which are produced during irradiation act as barriers to dislocation motion in the steel. This dislocation motion is the primary mode by which strain is accommodated in the material. If the magnitude of stress acting on the material reaches high enough levels (above the critically resolved shear stress), dislocations will be pushed through this

array of newly produced defects. As these dislocations interact with the defect microstructure, they will partially annihilate the defects which are present on the same slip plane in which the dislocation is moving. In the wake of these first dislocations is a region which has been partially cleared of defects and has lower resistance to subsequent dislocation motion. The result is that a majority of the deformation in these materials is confined to a very narrow band of slip planes, which is referred to as a dislocation channel. These dislocation channels typically consist of a collection of parallel slip planes roughly 100nm in width, and are spaced on the order of 5 microns apart [15]. The dislocations which are present within these channels eventually reach a grain boundary, and interact in two main ways. The first interaction type is for slip to be transmitted into the adjacent grain along a favorably oriented slip system. This type of interaction is referred to as a continuous dislocation channel, as the trace of the channel appears to be continuous on the sample surface as you move into the neighboring grain. The second interaction is for the dislocations within the channel to be completely arrested at the intersection of the channel with the grain boundary. Slip is not transmitted into the adjacent grain with the large population of dislocations piling up at the grain boundary, and the channel trace on the surface of the material appears to terminate at the grain boundary. Channels showing this behavior are referred to as discontinuous channels. Previous studies have showed a correlation between the type of dislocation channel interaction at the grain boundary (either continuous or discontinuous) and the susceptibility of that boundary to cracking [16]. There appears to be a clear connection between the dislocation channels and intergranular crack initiation, but an underlying mechanism or predictive model for crack initiation cannot be generated from these generalized correlations.

One theory on why discontinuous channels correlate with cracking is that there is a large stress build-up at the grain boundary caused by the pile-up of dislocations [17,18] and that this stress can induce fracture. If this is true, then the probably of fracture should scale with the magnitude of the stress. Further, nature of the stress responsible for fracture should be determinable as well. Due to the difficulty of the measurements and limitations of technology, getting accurate measurements of the stresses acting in the immediate vicinity surrounding these dislocation channel – grain boundary interaction sites has been exceedingly difficult. Recent development of high resolution electron backscatter diffraction (HREBSD) by Wilkinson, Meaden, and Dingley [19-22] has made quantitative measurements of residual elastic stresses at appropriate length scales for investigation of dislocation channel – grain boundary interactions. During typical EBSD analysis, Kikuchi patterns are collected on an electron sensitive phosphor detector by satisfying Bragg diffraction conditions on the sample surface with the SEM electron beam. These patterns will distort slightly in the presence of residual elastic strain, like the regions around a dislocation channel. Through HREBSD, it is possible to quantitatively measure the elastic strain field present around dislocation channel – grain boundary interaction sites by using the image correlation software package CrossCourt. Offline analysis of the saved Kikuchi patterns can detect small changes in the band structure, and calculate a full strain tensor. Using material appropriate elasticity coefficients, this strain tensor can be used to calculate a full stress tensor for each point in the EBSD scan. By combining the quantitative measurement of stresses at specific dislocation channel-grain boundary interaction sites with slow constant extension rate tensile (CERT) tests in simulated reactor water conditions, it was possible for the first time to directly link the stress acting normal to the grain boundary with the cracking susceptibility of the material.

The primary focus of this thesis will be to quantitatively characterize the stresses present at dislocation channel – grain boundary interaction sites, and determine the nature and role of grain boundary stress on IASCC. Chapter 2 of this thesis describes relevant background information, in particular general irradiation effects, deformation in irradiated stainless steel, and IASCC. Chapter 3 summarizes the objective of this thesis and the approach taken to realize that objective. Chapter 4 describes the experimental procedures and the systems/techniques that are used in this study. Chapter 5 contains the results of the stress analysis and cracking experiments performed to achieve the thesis objective. Chapter 6 is the discussion of the results presented in chapter 5, focusing on the quantitative relationship between stress and cracking susceptibility. Chapter 7 ends this thesis with the conclusions of this study and suggests possible future work to enhance the understanding to the mechanisms controlling the crack initiation process is irradiated austenitic stainless steels.

Chapter 2 - Background

Before a proper discussion can be had about the underlying mechanisms that drive crack initiation in irradiated stainless steels, it is first necessary to present a review of published literature surrounding austenitic stainless steel and their deformation under reactor relevant conditions. The production and evolution of defects during irradiation will be discussed including their effect on the microstructure, mechanical properties, and deformation mode. A thorough section focused on irradiation assisted stress corrosion cracking (IASCC) is presented with particular emphasis on correlations between microstructural evolution and localized deformation with crack initiation.

2.1 Properties of Austenitic Stainless Steel

Steel is an iron based alloy which has been developed and used for countless applications due to its abundance, mechanical strength, and machineability. The primary phases present in steel are austenite, ferrite, and martensite with the fraction of each present dependent on both the composition of the base alloy as well as the heat treatment and processing steps followed during fabrication [23-25].

2.1.1 Composition and Phase Structure

Pure iron is stable in a body-centered cubic (BCC) atomic stacking configuration up to 1180K [26], but additions of other atomic species can help stabilize the austenitic phase which has a face-centered cubic (FCC) stacking structure. This stacking structure is displayed in figure 2.1 and shows the repetition of stacking in 3 sequential positions referred to as A, B, and C. The unit cell for the FCC structure is presented in figure 2.1.

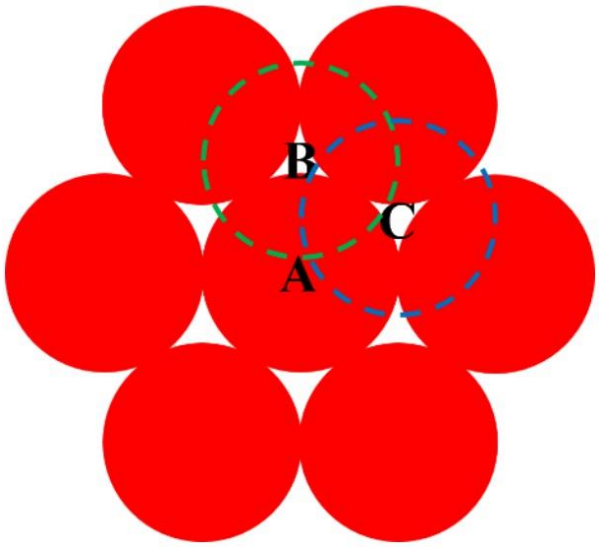

Figure 2.1. Diagram of close packed {111} planes in an FCC crystal

Nickel is often added to stainless steel alloys in order to stabilize the austenite phase. The addition of nickel can have a small effect on the overall SCC susceptibility of the alloy, but this effect appears to be very minimal relative to the effect of chromium additions [27,28]. Carbon, nitrogen, and manganese can also act to stabilize the austenite phase, but are all typically only found as trace elements.

2.1.2 Effect of Carbon Addition

On an atom percent basis, carbon has a factor of 30 more influence than nickel in stabilizing the FCC phase [29], however the carbon content is typically kept very low in order to prevent the formation of carbides either in grain interiors or at grain boundaries. The most commonly found carbides which precipitate in austenitic stainless steels are $M_{23}C_6$ carbides where M represents iron, molybdenum, chromium, and nickel [30]. These carbides are typically chromium rich, and therefore consume a significant amount of chromium in the local regions where they are formed. Since chromium is added to support the production of a passivating oxide layer, loss of chromium to carbides will diminish the efficacy of chromium diffusion to the metal/water interface and will result in a less protective oxide. $M_{23}C_6$ carbides form an FCC structure with a lattice parameter roughly 3 times that of the austenite phase, and preferentially form along high angle grain boundaries where the grain orientation mismatch better allows for the larger carbide structure [31]. Presence of carbides in the material can cause increased intergranular corrosion, decreased ductility, and decreased toughness which are all typically viewed as detrimental to the material performance [32-35]. This process of carbide formation on grain boundaries which decreases the resistance to intergranular failure is commonly referred to as sensitization. There is some evidence that carbides can impede deformation by grain boundary sliding and improve resistance to creep, but the negatives due to carbide formation outweigh this benefit for most structural applications.

2.1.3 Effect of Chromium Addition

What makes a steel “stainless”, is the addition of chromium. This addition to the alloy causes the formation of a chromium rich inner oxide layer which impedes oxygen diffusion and thus restricts further aqueous corrosion in a high temperature water environment [36,37]. A more complete description of the oxidation process in high temperature water environment will be presented in a later section. While the addition of chromium is beneficial to the oxidation behavior of the base metal, it reduces the stability of the austenite phase and favors the BCC orientation of the ferrite phase [38]. Molybdenum, silicon, and niobium also stabilize the BCC phase, and their effect can be seen in the Schaeffler diagram shown in figure 2.2. The presence of the BCC phase results in an increase in the overall yield stress of the material, but a decrease to overall corrosion resistance which makes it less viable in the high temperature water environment surrounding the reactor core [39].

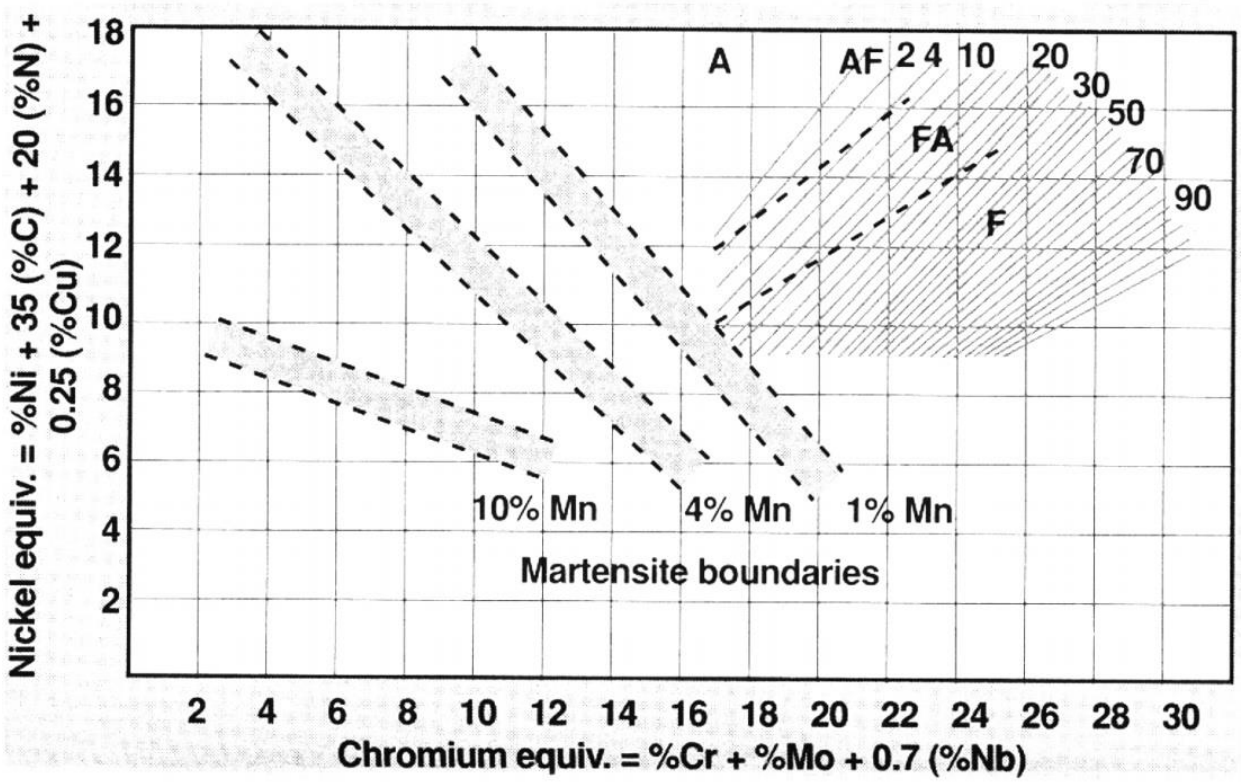

Figure 2.2. Schaeffler diagram showing percent austenite, ferrite, and martensite based on steel composition [29]

2.2 Deformation in Crystalline Materials

Deformation in crystalline materials occurs primarily through crystallographic slip along the most densely packed planes and directions in the lattice. This is true for both single and polycrystalline solids, with the latter adding additional restrains to accommodate for the deformation of adjacent grain orientations. For an FCC material, like austenitic stainless steel, dislocations are typically generated on {111} crystallographic planes and move in the <110> close packed direction [40,41]. For FCC crystal structures there are a total of 12 variant of this orientation relationship where dislocations can glide. While slip is possible on several slip systems, there will be certain combinations of close packed planes and directions which will be

favored given an externally applied load. In order to predict the slip system which is most likely to activate within a given stress field, Schmid factors are widely used [42].

2.2.1 Schmid Factor Analysis

Within an applied stress field, a shear component of that stress can be resolved such that it is acting on each of the planes in the slip system. As the externally applied load is increased, so is the resolved shear stress (τ_{RSS}). The requirement for dislocations to start moving through the lattice and induce permanent shape change is when this resolved shear stress reaches some critically resolved shear stress. This is known as Schmid's Law,

$$\tau_{RSS} = \tau_{CRSS} \tag{2.1}$$

or

$$\tau_{CRSS} = \sigma \cos\lambda \cos\varphi, \tag{2.2}$$

where σ is the yield stress, λ is the angle between the slip direction and the tensile axis, and φ is the angle between the slip plane normal and the tensile axis as shown in figure 2.3. Due to these geometric constraints, the values of λ and φ range between 0 and 90 degrees. The maximum value for the resolved shear stress occurs when $\cos\lambda\cos\varphi$ is maximized, which occurs when both λ and φ are 45 degrees resulting in a maximum value for the resolved shear stress of $\sigma/2$. The Schmid factor, m, is equal to the quantity $\cos\lambda\cos\varphi$.

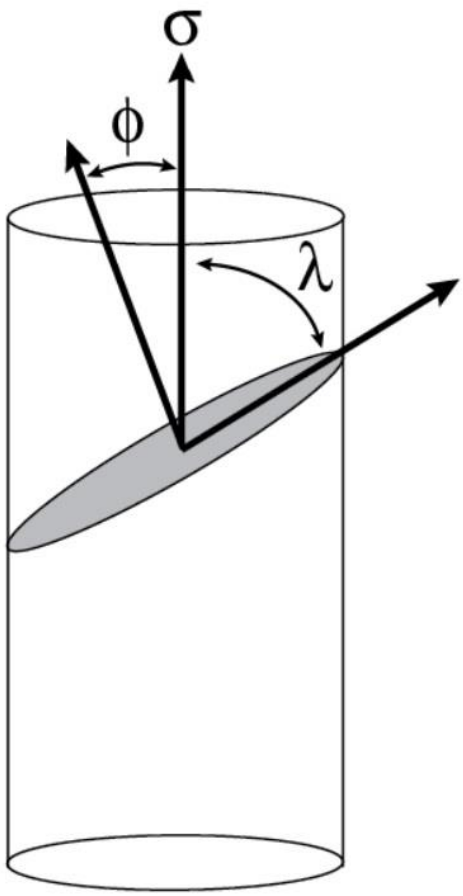

Figure 2.3. Illustration of variables in Schmid factor calculation for a crystal in uniaxial tension

Each crystallographic slip system has its own Schmid factor based on its orientation relative to the applied stress, but if only a single value is reported it is for the most favorably oriented slip system for this is the one that will require the least amount of applied stress in order to initiate slip. Figure 2.4 shows the relationship between the orientation of the tensile axis and Schmid factor for FCC systems.

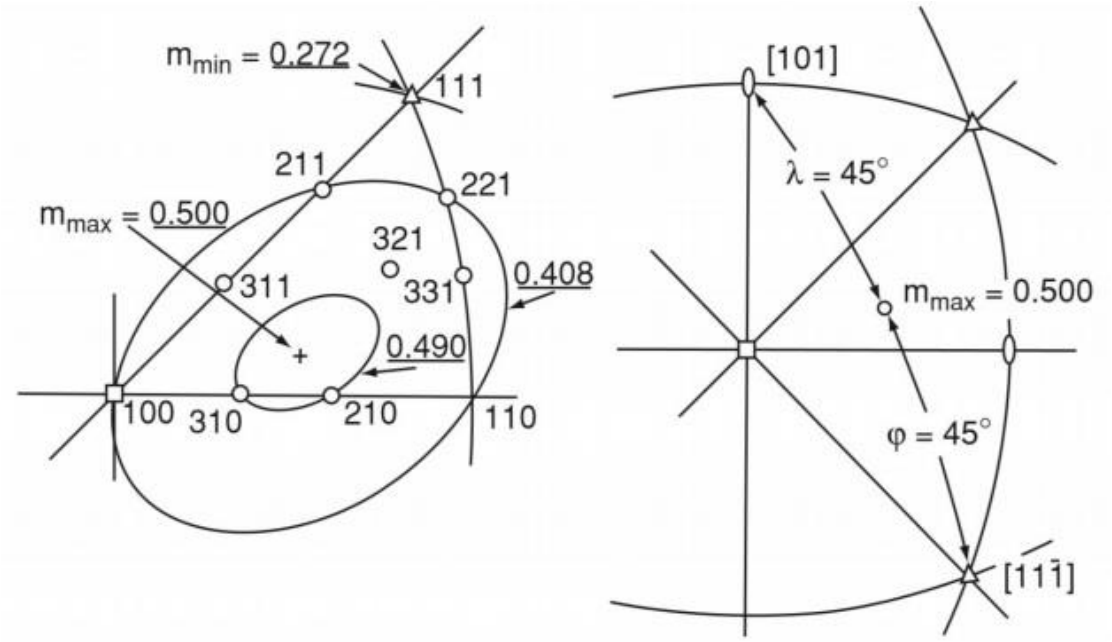

Figure 2.4. Calculation of Schmid factor base on FCC crystal orientation [43]

2.2.2 Taylor Factor Analysis

Taylor's plasticity analysis has four key assumptions,

(1) All crystals undergo the same shape change as the entire polycrystalline aggregate

(2) Five slip systems are active in each crystal to accommodate the necessary shape change

(3) The critically resolved shear stress is the same for all active slip systems

(4) All deformation is the result of dislocation production/slip

The five slip systems chosen for inclusion in the Taylor model were done so to minimize the sum of shear strains required to meet the overall shape change of the grain, and the other seven slip systems undergo no deformation whatsoever [44].

When an external uniaxial tensile stress is applied to the crystal aggregate, the deformation in each individual grain is driven by the shear stresses so it is convenient to represent the external normal ($d\varepsilon_{xx}$, $d\varepsilon_{yy,}$ $d\varepsilon_{zz}$) and shear ($d\gamma_{yz}$, $d\gamma_{zx,}$ $d\gamma_{xy}$) strains in relation to the three cubic axes of the crystal $d\varepsilon_{1,}$ $d\varepsilon_{2,}$ $d\varepsilon_{3,}$ $d\gamma_{23,}$ $d\gamma_{31,}$ $d\gamma_{12}$. The shape change of the individual grains can then be described by the shear strains from the crystal reference frame and the orientation of the specimen axes can be related to the crystal axes by two angles, ψ and χ, as shown in figure 2.5.

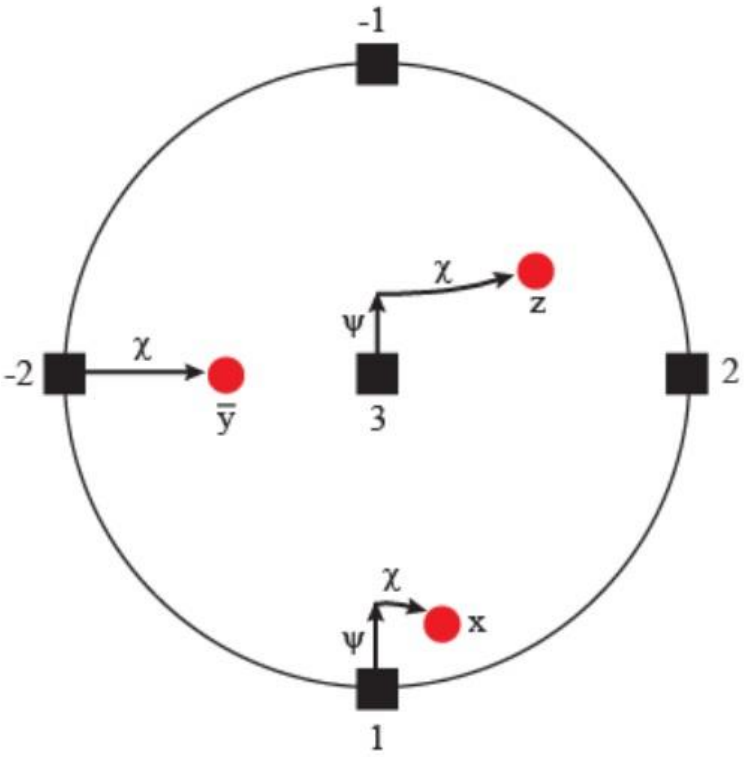

Figure 2.5. Stereographic diagram relating the specimen axes x, y, and z (red dots) to the crystallographic axes 1, 2, and 3 (black squares) [45]

Taylor's model assumes that crystallographic slip would proceed in a way that minimizes the energy required to achieve the necessary deformation. The incremental work caused by slip (dw) in a given grain is defined as

$$dw = \sum \tau_i d\gamma_i \tag{2.3}$$

where τ_i is the shear stress required for slip to occur in slip system i, and γ_i is the shear strain in that slip system. Based on the third of Taylor's assumptions stated previously, τ_i is the same for all slip systems and therefore can be moved outside the summation. Due to this, minimizing the work necessary to accommodate the shape change is equivalent to minimizing the total amount of shear strain, which is represented by

$$d\gamma = \sum \left| d\gamma_i \right| . \tag{2.4}$$

The incremental work expressed in terms of the externally applied tensile stress, σ_x, and strain along the tensile axis, ε_x, is given by the equation

$$dw = \sigma_x d\varepsilon_x , \tag{2.5}$$

and is equivalent to the work performed by the individual grains expressed as

$$\sigma_x d\varepsilon_x = \tau d\gamma . \tag{2.6}$$

The Taylor factor (M) is defined as

$$M = d\gamma / d\varepsilon_x = \sigma_x / \tau . \tag{2.7}$$

The Taylor factor describes the amount of shear strain required to match the overall shape change of the crystal aggregate. Larger values for the Taylor factor imply that large amounts of shear strain is required to deform the grain, and therefore more energy is required to accomplish this task. For the FCC crystal structure, Taylor factors range between 2.449 and 3.674 depending on the orientation of each individual grain.

2.2.3 Lattice Rotation

Previous analyses of crystal deformation try primarily to link the deformation of the crystal aggregate with the deformation of individual grains. However, this type of analysis neglects certain restraints to crystal deformation imposed by the presence of neighboring grains. Without constrains, in response to an applied uniaxial tensile stress a grain will elongate without changes to the slip plane and direction, but the orientation of the tensile axis changes with respect to the crystal orientation. If constraints are placed on the orientation of the loading axis, the crystal will again elongate from the applied stress, but elements within the crystal are forced to rotate with respect to the loading axis. This is illustrated in figure 2.6.

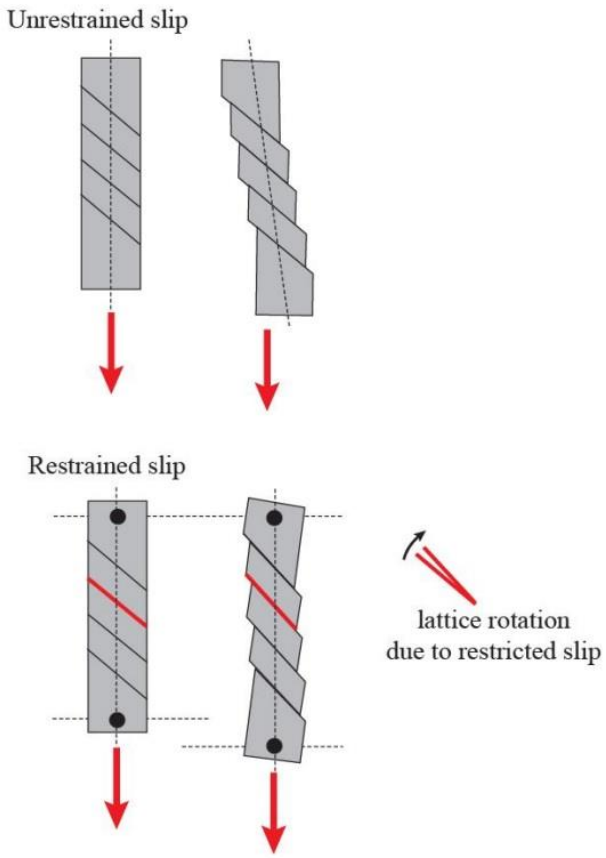

Figure 2.6. Unrestrained slip versus restrained slip behavior detailing necessary lattice rotation

The normal (ε_{xx}, ε_{yy}, ε_{zz}) and shear displacements (ε_{xy}, ε_{yx}, ε_{xz}, ε_{zx}, ε_{yz}, ε_{zy}) for macroscopic deformation can be expressed in tensor form [46]. In the limit of very small strains, the normal and shear displacements may be expressed in partial derivative form

$$\begin{vmatrix} \varepsilon_{xx} & \varepsilon_{xy} & \varepsilon_{xz} \\ \varepsilon_{yx} & \varepsilon_{yy} & \varepsilon_{yz} \\ \varepsilon_{zx} & \varepsilon_{zy} & \varepsilon_{zz} \end{vmatrix} = \begin{vmatrix} \frac{\partial u}{\partial x} & \frac{\partial u}{\partial y} & \frac{\partial u}{\partial z} \\ \frac{\partial v}{\partial x} & \frac{\partial v}{\partial y} & \frac{\partial v}{\partial z} \\ \frac{\partial w}{\partial x} & \frac{\partial w}{\partial y} & \frac{\partial w}{\partial z} \end{vmatrix}, \tag{2.8}$$

where the mathematical shear displacements are equal to half of the engineering shear displacements, γ_{ij}

$$\begin{aligned} \varepsilon_{yz} &= \varepsilon_{zy} = \frac{1}{2}\gamma_{yz} = \frac{1}{2}\left(\frac{\partial v}{\partial z} + \frac{\partial w}{\partial y}\right) \\ \varepsilon_{zx} &= \varepsilon_{xz} = \frac{1}{2}\gamma_{zx} = \frac{1}{2}\left(\frac{\partial w}{\partial x} + \frac{\partial u}{\partial z}\right) \\ \varepsilon_{xy} &= \varepsilon_{yx} = \frac{1}{2}\gamma_{xy} = \frac{1}{2}\left(\frac{\partial u}{\partial y} + \frac{\partial v}{\partial x}\right) \end{aligned}. \tag{2.9}$$

The shear displacements here lead to both strain as well as rigid body rotation while the normal displacements result purely in strain. Since the shear displacements can have both strain and rotational elements, it is helpful to separate the displacement tensor into a strain tensor, ε_{ij}, and a rotation tensor, ω_{ij}

$$\varepsilon_{ij} = \begin{vmatrix} \varepsilon_{xx} & \varepsilon_{xy} & \varepsilon_{xz} \\ \varepsilon_{yx} & \varepsilon_{yy} & \varepsilon_{yz} \\ \varepsilon_{zx} & \varepsilon_{zy} & \varepsilon_{zz} \end{vmatrix} = \begin{vmatrix} \dfrac{\partial u}{\partial x} & \dfrac{1}{2}\left(\dfrac{\partial u}{\partial y}+\dfrac{\partial v}{\partial x}\right) & \dfrac{1}{2}\left(\dfrac{\partial u}{\partial z}+\dfrac{\partial w}{\partial x}\right) \\ \dfrac{1}{2}\left(\dfrac{\partial u}{\partial y}+\dfrac{\partial v}{\partial x}\right) & \dfrac{\partial v}{\partial y} & \dfrac{1}{2}\left(\dfrac{\partial v}{\partial z}+\dfrac{\partial w}{\partial y}\right) \\ \dfrac{1}{2}\left(\dfrac{\partial u}{\partial z}+\dfrac{\partial w}{\partial x}\right) & \dfrac{1}{2}\left(\dfrac{\partial v}{\partial z}+\dfrac{\partial w}{\partial y}\right) & \dfrac{\partial w}{\partial z} \end{vmatrix}, \tag{2.10}$$

$$\omega_{ij} = \begin{vmatrix} \omega_{xx} & \omega_{xy} & \omega_{xz} \\ \omega_{yx} & \omega_{yy} & \omega_{yz} \\ \omega_{zx} & \omega_{zy} & \omega_{zz} \end{vmatrix} = \begin{vmatrix} 0 & \dfrac{1}{2}\left(\dfrac{\partial u}{\partial y}-\dfrac{\partial v}{\partial x}\right) & \dfrac{1}{2}\left(\dfrac{\partial u}{\partial z}-\dfrac{\partial w}{\partial x}\right) \\ \dfrac{1}{2}\left(\dfrac{\partial v}{\partial x}-\dfrac{\partial u}{\partial y}\right) & 0 & \dfrac{1}{2}\left(\dfrac{\partial v}{\partial z}-\dfrac{\partial w}{\partial y}\right) \\ \dfrac{1}{2}\left(\dfrac{\partial w}{\partial x}-\dfrac{\partial u}{\partial z}\right) & \dfrac{1}{2}\left(\dfrac{\partial w}{\partial y}-\dfrac{\partial v}{\partial z}\right) & 0 \end{vmatrix}. \tag{2.11}$$

Whenever corresponding displacement gradients are not equal, rigid body rotation will occur about the perpendicular axis. This rotation would cause the primary slip direction to rotate relative to the loading direction. These rotations are restricted due to the physical constraints of neighboring grains, but can occur heterogeneously throughout individual grains, with orientation gradients typically developing where the imposed constraints are the stiffest, i.e. near grain boundaries.

2.2.4 Grain Boundary Geometry

The previous sections focused on the deformation of individual grains within an aggregate cluster. However, it is equally important to study the effects which are present only at

the boundary between individual grains. A grain boundary is the region adjoining two adjacent crystal lattices with dissimilar crystallographic orientations. Due to the imperfect union between two grains, excess free volume is present in this region which is not found anywhere in the grain interior. Presence of this excess free volume changes the properties of the grain boundary relative to the unperturbed matrix, and the magnitude of these changes depends of the order of mismatch between the two adjoining grains [47,48]. The degree of mismatch between grains, also referred to as misorientation, can affect diffusion, elemental segregation, accommodation of defects and strain, and nucleation phenomena [49-52].

2.2.5 Grain Misorientation

Misorientation is often represented as either an angle/axis pair, or with a misorientation matrix. For the angle/axis pair, an axis of misorientation (UWV) and a misorientation angle, θ, must be defined [53]. A diagram representation showing an arbitrary angle/axis pair is presented in figure 2.7.

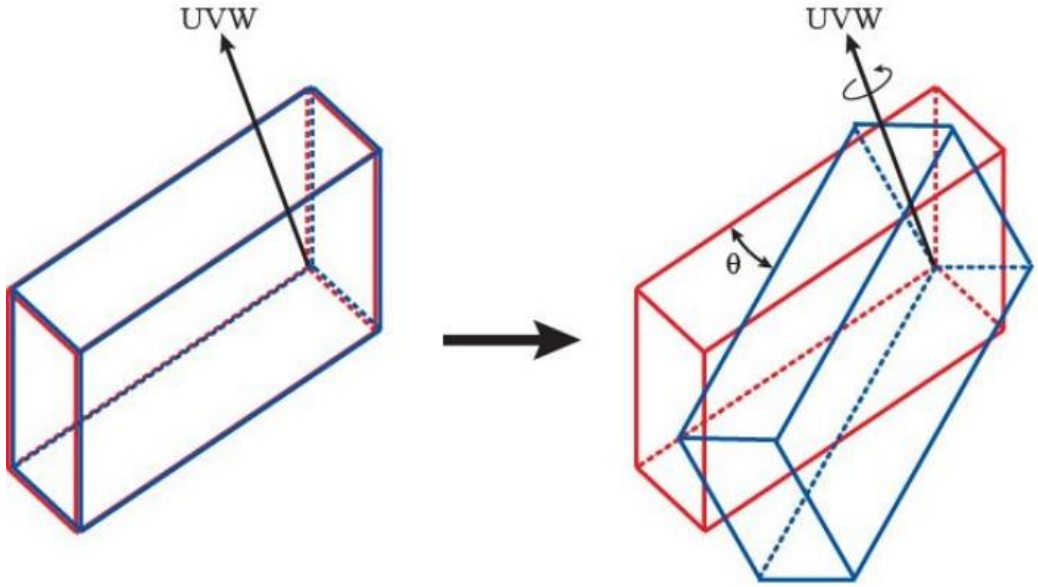

Figure 2.7. A misorientation between two lattices as described by an angle/axis pair

While more difficult to visualize, misorientation matrices are more typically used for misorientation calculations. The orientation of a grain relative to its neighbor can be expressed through three sequential rotations about specified axes. Two arbitrary, yet distinctly different, crystal orientations are presented in figure 2.8 with their axes given by $x_1y_1z_1$ and $x_2y_2z_2$. The three rotations required to make the second crystal coincide with the first are

(1) Crystal 2 must be rotated by angle φ_1 about axis z_2

(2) Crystal 2 must be rotated by angle φ_2 about axis x'_2

(3) Crystal 2 must be rotated by angle φ_3 about axis z_1

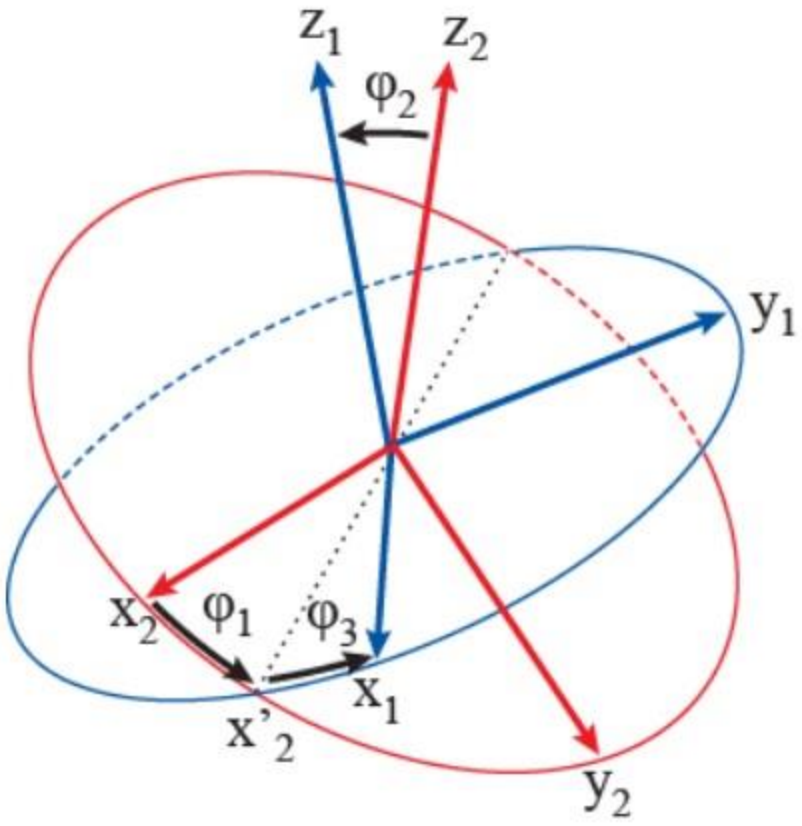

Figure 2.8. Illustration of Euler angles describing the misorientation between two crystal lattices [54]

Each of these rotations can be expressed in the form of a matrix, m_1, m_2, m_3, and the final misorientation matrix can be expressed as

$$M_M = m_3 m_2 m_1 = \begin{vmatrix} a_{11} & a_{12} & a_{13} \\ a_{21} & a_{22} & a_{23} \\ a_{31} & a_{32} & a_{33} \end{vmatrix}, \tag{2.12}$$

or in terms of Euler angles as

$$M_M = \begin{vmatrix} \cos\varphi_1 \cos\varphi_3 - \sin\varphi_1 \cos\varphi_2 \sin\varphi_3 & \sin\varphi_1 \cos\varphi_3 + \cos\varphi_1 \cos\varphi_2 \sin\varphi_3 & \sin\varphi_2 \sin\varphi_3 \\ -\cos\varphi_1 \sin\varphi 3 - \sin\varphi_1 \cos\varphi_2 \cos\varphi_3 & -\sin\varphi_1 \sin\varphi_3 + \cos\varphi_1 \cos\varphi_2 \cos\varphi_3 & \sin\varphi_2 \cos\varphi_3 \\ \sin\varphi_1 \sin\varphi_2 & -\cos\varphi_1 \sin\varphi_2 & \cos\varphi_2 \end{vmatrix}. \quad (2.13)$$

Due to crystal symmetry in cubic systems, like FCC, there are 24 different routes to achieve the same misorientation. The misorientation matrix typically used is therefore the one which corresponds to the smallest value of θ taken from the angle/axis pair method.

2.2.6 Coincident Site Lattice Boundaries (CSLBs)

The misorientation values as defined in the previous section can be used to better describe the character of specific grain boundaries and assist in predicting the response of these boundaries given an external load. Low angle boundaries (LABs) are defined as those which have a misorientation angle, as defined by the angle/axis pair method, less than 15˚ [55]. Boundaries with a misorientation greater than 15˚ are referred to as high angle boundaries (HABs). A special subclass of boundaries were classified by Kronberg and Wilson [56] after noticing that specific misorientations result in a high degree of alignment between the lattices of the adjacent grains. These boundaries are called coincident site lattice (CSL) boundaries. To emphasize the overlap of lattice positions, the atomic positions of two grains are overlapped in figure 2.9. This example is of a Σ5 boundary, with the value of Σ representing the reciprocal of the ratio of the number of coincident sites to all lattice sites(e.g. for Σ5, one in five lattice sites are coincident between the two grains).

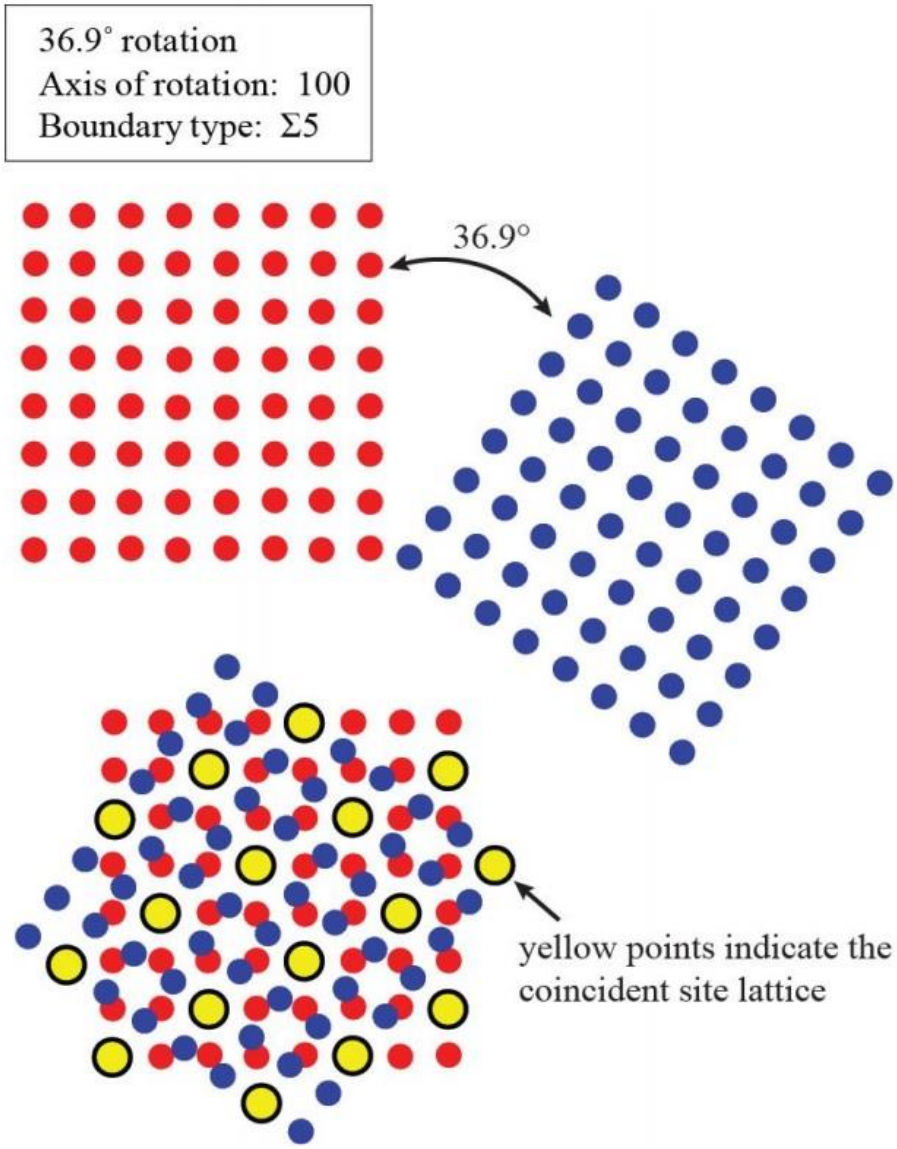

Figure 2.9. Illustration of the coincident sites which line up after a 36.9˚ rotation about the 100 axis in a Σ5 CSL boundary

Many different orientations result in different values of Σ, and CSL boundaries for Σ≤35 are listed in table 2.1. It is unlikely that misorientation between adjacent grains will exactly fit the values listed in table 2.1 so a degree of tolerance for allowable deviation is assigned for classifying CSL type boundaries. The Brandon criterion [57] is often used which states that

$$\nu_m = \nu_0 \Sigma^{-1/2} \tag{2.14}$$

where ν_m is the maximum allowed deviation from exact coincidence and ν_0 is a proportionality constant equal to the maximum allowed deviation for a Σ1 boundary, 15˚. By this relationship the allowable deviation from pure coincidence decreases with increasing values of Σ.

Table 2.1 Disorientation angle/axis pairs for CSLs with reciprocal densities up to 35 [58]

Σ	θ	UVW	Σ	θ	UVW
3	60	111	23	40.5	311
5	36.9	100	25a	16.3	100
7	38.2	111	25b	51.7	331
9	38.9	110	27a	31.6	110
11	50.5	110	27b	35.4	210
13a	22.6	100	29a	46.3	100
13b	27.8	111	29b	46.4	221
15	48.2	210	31a	17.9	111
17a	28.1	100	31b	52.2	211
17b	61.9	221	33a	20.1	110
19a	26.5	110	33b	33.6	311
19b	46.8	111	33c	59	110
21a	21.8	111	35a	34	211
21b	44.4	211	35b	43.2	331

These CSL boundaries are of particular importance due to the difference in interfacial energy for these boundaries relative to other RHABs. This is especially true for Σ3, or twin boundaries. Interfacial energies for a number of CSL boundaries are shown in figure 2.10.

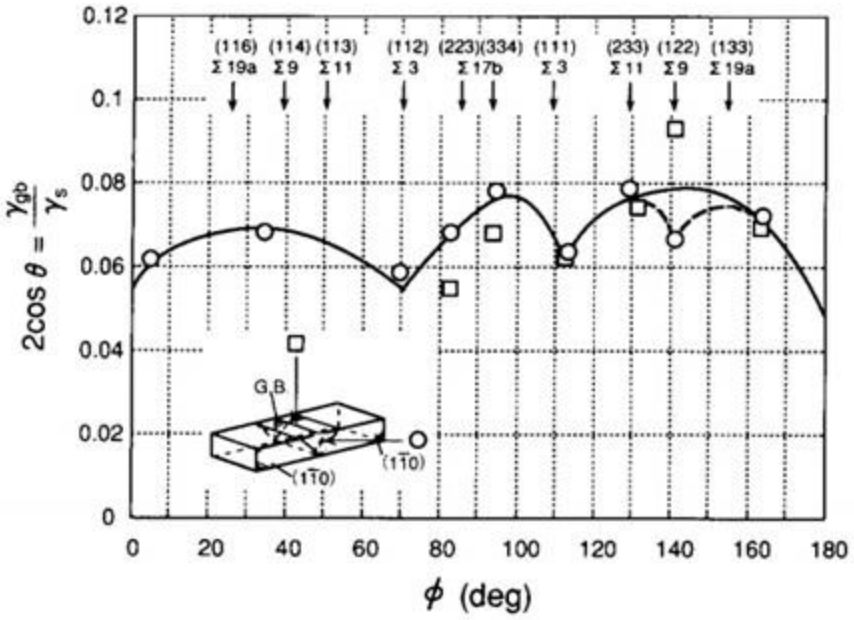

Figure 2.10. Misorientation dependence of the relative grain boundary energy [59]

The increase in coincident sites leads to better cohesion at the grain boundary, ultimately decreasing the amount of excess volume at the interface. This increase in cohesive strength is a prime argument for why these CSL boundaries exhibit significantly less susceptibility to intergranular fracture, which will be discussed in a later section.

2.2.7 Dislocations in FCC polycrystalline material

Permanent shape change within metals is typically facilitated the production and subsequent motion of dislocations through the crystal lattice. These dislocations are defined by the proportion of their edge and screw characteristics. In the case of a pure edge type dislocation, it acts as an extra half plane of atoms within the crystal and produces slip in the direction that the dislocation moves. The magnitude and direction of the distortion in the lattice caused by the

dislocation is represented by the Burgers vector, b. For edge dislocations this Burgers vector points in a direction perpendicular to the dislocation line, and for screw dislocations it points in a direction parallel to the dislocation. For austenitic stainless steel and the FCC crystal system, the primary dislocation type generated is the edge type dislocation.

In FCC systems, perfect dislocations can dissociate into two Shockley partial dislocations, leaving a stacking fault between the two partials [60]. An equilibrium separation between the two partials can be determined by a balance between the repulsive forces of the two partials and the attractive forces due to the stacking fault energy. A diagram detailing the geometry of these Shockley partials is shown in figure 2.11. Without an applied external stress this separation distance can be on the order of 10 nm for alloys with small stacking fault energies on the order of 10 mJ/m^2 [61]. This separation increases with decreasing SFE. In low SFE alloys, because the separation of two partial dislocations is large, the gliding dislocations are confined to a thin slip band and show a banded linear array microstructure. This planar dislocations slip can easily form twins and induces martensitic transformation [62,63]. For high SFE material, the stacking fault separation is small allowing for cross slipping and climbing. This mobility eventually results in the dislocations a tangled array of dislocation cells. The tendency for materials to form these stacking fault structures is dependent on the deformation conditions and the hardness of the material being deformed [64-66]. Stacking fault formation is enhanced at low temperatures and high strain rates, and also increases in the presence of irradiation [67].

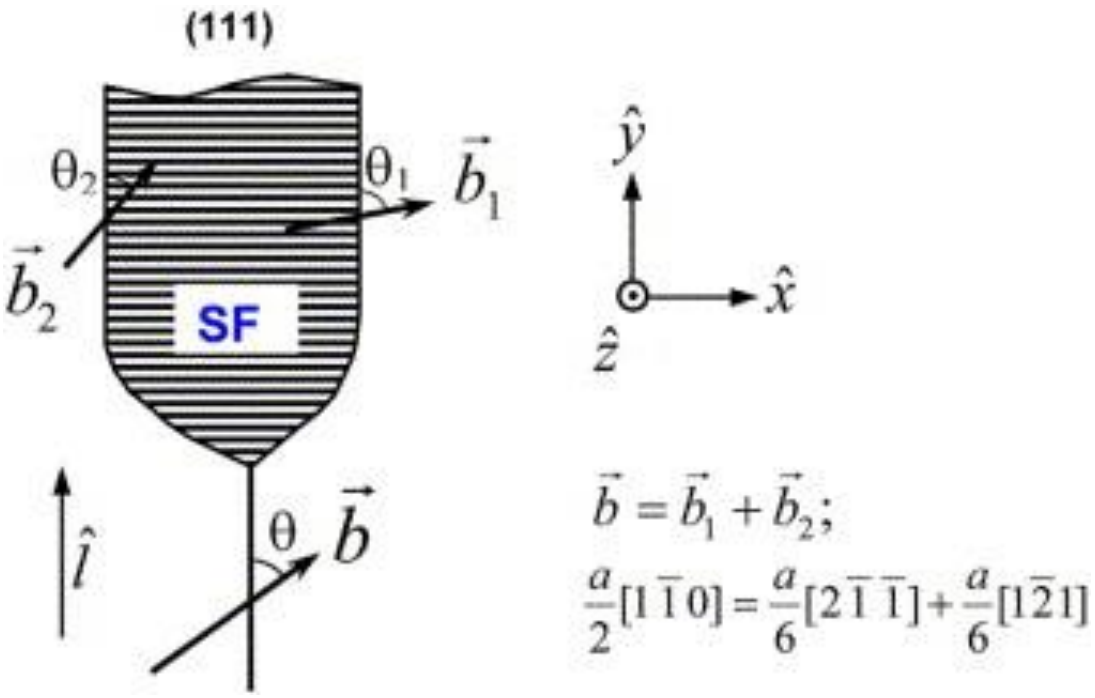

Figure 2.11. Diagram illustrating the geometry of Shockley partial dislocations

The magnitude of the SFE is related to the elemental composition of the material[68]. Empirical correlations have been developed to give a general idea of the SFE of a given alloy, however the errors in these formulas can be large meaning they are typically only useful for relative approximations. Each empirical formula takes the general form of

$$SFE\left(mJ/m^2\right) = X_{const} + \sum_i X_i C_i \tag{2.15}$$

where the values of X are determined empirically and the concentrations (C) of the alloying elements are known beforehand. Table 2.2 lists the constants from three different models.

Table 2.2. Empirical derived constants for Pickering, Schramm, and Rhodes SFE derivation based on alloy composition

	X_{const}	X_{Cr}	X_{Ni}	X_{Mn}	X_{Mo}	X_{Si}	X_{C}	X_{N}
Pickering [96]	25.7	-0.9	2.0	-1.2	NA	-13.0	410.0	-77.0
Schramm [97]	-53.0	0.7	6.2	3.2	9.3	NA	NA	NA
Rhodes [98]	1.2	0.6	1.4	17.7	NA	-44.70	NA	NA

2.2.8 Dislocation interaction at grain boundaries

Dislocation motion within a grain is determined by the resolved shear stress acting on the specific slip system which contains the dislocation. Once the critically resolved shear stress is reached, the dislocation will propagate, but there are several features which at as barriers to this dislocation motion. A primary barrier to the continued slip of a dislocation is its interaction with grain boundaries. When a dislocation encounters a grain boundary, there are multiple interactions which may occur. These interactions are typically divided into two categories: (1) discontinuous slip and (2) continuous slip. In the first case, dislocation motion is completely arrested at the grain boundary and no further slip occurs. For the continuous case dislocations may directly transmit across the grain boundary , cross slip onto a different slip system within the same grain, be absorbed by the grain boundary, or nucleate additional dislocations within the adjacent grain to alleviate the stress field generated by the dislocation near the boundary. Figure 2.12 presents a diagram with these different types of interactions.

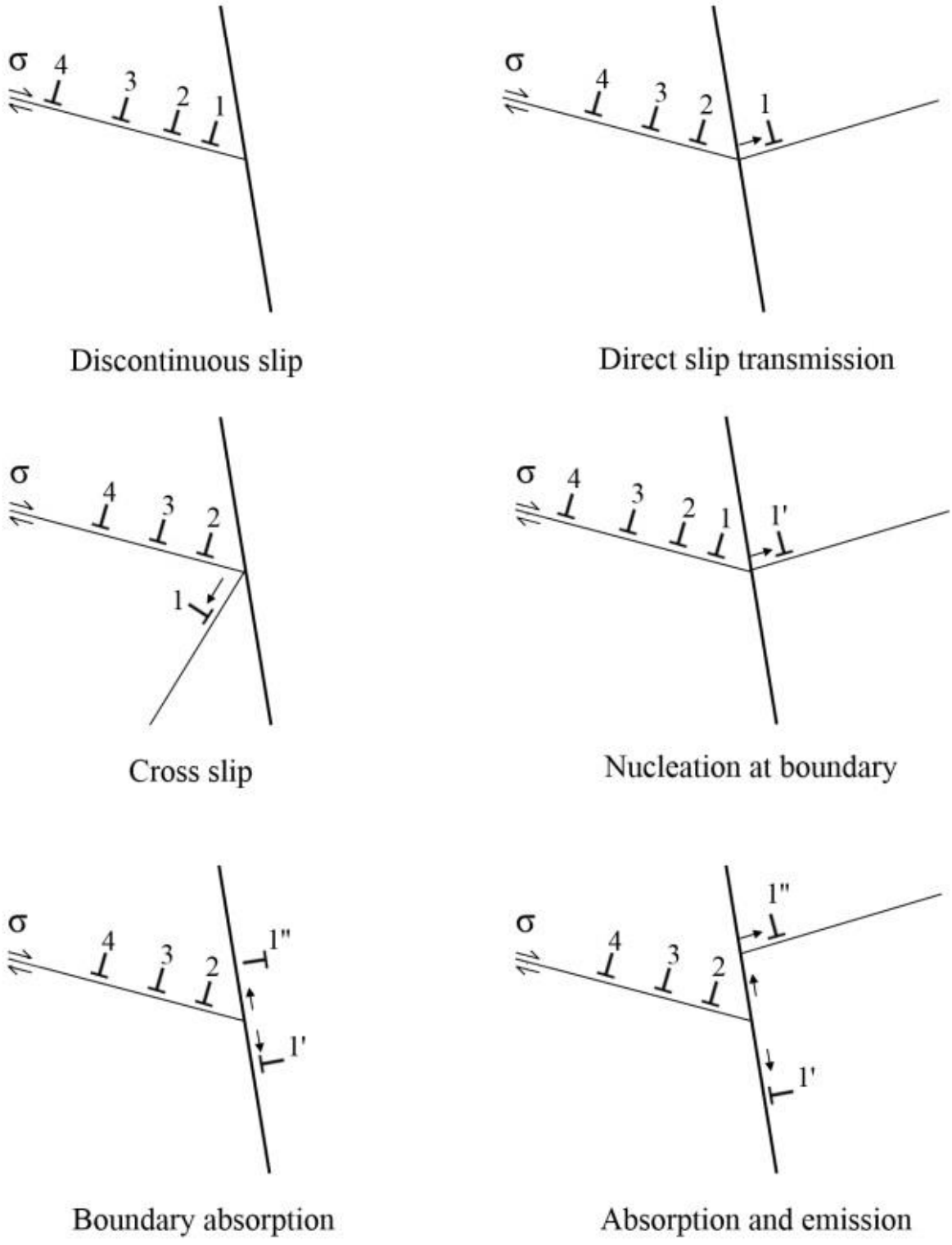

Figure 2.12. Methods of slip accommodation at grain boundary interaction sites [69,70]

The factors which govern which type of interaction is most favorable have been studies by several groups [71-76]. Robertson et al. [77] recently determined three factors which govern which slip system in an adjacent grain will activate based on a set of incoming dislocations. These factors include

(1) The angle between the lines of intersection of the incoming and outgoing slip planes relative to the grain boundary should be minimized
(2) The resolved shear stress on the outgoing slip system should be maximized
(3) The Burgers vector of the residual dislocation left in the grain boundary after the emission of a dislocation into the adjoining grain should be minimized

Factor 3 has been observed to be the most impactful on the transmission process.

While these factors were developed for non-irradiated material and the modest accumulation of dislocations piling up at the grain boundary prior to slip transmission, they are still applicable to irradiated material. The primary effect of irradiation in this sense is that the defect matrix creates a significantly higher barrier to dislocation motion compared to non-irradiated material. For a dislocation channel, the stress required to propagate dislocations is much higher, but once a critical resolved shear stress value is reached dislocations will move throughout the irradiated matrix, as in a non-irradiated matrix. The hardened matrix will pin a greater number of dislocations at the grain boundary, but the considerations for slip transmission are unchanged. If there exists a slip system that is well oriented in the adjacent grain, as defined by the three criteria above then slip transmission will occur and the channel will appear continuous. If slip systems are poorly aligned then the stress required for transmission is much higher, and the channel has a significantly higher probability of remaining discontinuous. Given

enough stress, discontinuous channels will convert to continuous channels as long as the stress required to do this is less than the fracture strength of the boundary.

2.2.9 Deformation twinning

The primary deformation mode in FCC metals is crystallographic slip, however it is possible for deformation by twinning to occur if certain criteria are met. In order for this to occur, the critically resolved shear stress, which is the value needed to propagate dislocations in the solid, must be greater than the stress required to form twins. In low SFE materials like austenitic stainless steels, mechanical twinning can be enhanced at both low temperatures and high strain rates [78,79]. The twins which form tend to do so on {111} planes oriented such that the shear stress resolved onto the lattice plane is maximized [80]. FCC metals were previously thought to not undergo deformation by twinning, however this phenomenon was first observed by straining FCC copper at liquid helium temperatures [81]. Since then, deformation twinning has also been observed in austenitic stainless steels in temperature ranges between 0 and 100 degrees Celsius [82-85]. The stress required to initiate twinning does not vary significantly with temperature, however the yield stress of the material increases dramatically at lower temperatures which can result in the stress required to move dislocations increasing beyond the twinning stress [86].

2.3 Effects of irradiation on Austenitic Stainless Steel

In the presence of radiation, energetic particles (e.g. neutrons, protons, heavy ions, etc.) transfer energy through collisions with the material lattice [86]. These interactions displace atoms from their original lattice positions creating vacancies and interstitial point defects and can result in the formation and growth of many features. Defect formation will depend on several factors including particle energy and particle species. As these defects accumulate in the material several changes will occur at the macroscopic level, making it important to track and understand the changes happening at the microstructural level.

2.3.1 Point defect formation

Initially, vacancy and interstitial populations increase due to their relatively low concentrations. As time progresses at reactor relevant temperatures, different competing processes determine the equilibrium concentration of each species. Due to the increased diffusivity of interstitials, they have the ability to propagate and annihilate at sinks such as grain boundaries, dislocations, and free surfaces leading to a relatively higher fraction of vacancies in the system [87-89]. The recombination of vacancies and interstitials is another process which acts to decrease the total number of defects in the system. Surviving interstitials and vacancies can form small defect clusters on the order of 0.5 nm or smaller [90]. In austenitic stainless steels these small defect clusters are thought to be faulted interstitial loops and vacancy clusters [91,92]. TEM analysis analysis by many groups have confirmed the identity of the defect clusters to be faulted interstitial type dislocation loops [92-95].

2.3.2 Dislocation Loops

Dislocation loops may form during the recombination phase immediately following the initial damage cascade [96]. Since these loops act as a sink to point defects, they can nucleate and grow due to the enhanced mobility of interstitials over vacancies. The growth of these loops can continue until an equilibrium is reached with the vacancy and interstitial populations. Evolution of the loop density and size with dose for an austenitic stainless steel at a reactor relevant temperature of 288 ˚C is shown in figure 2.13. Dislocation loop size and density has been experimentally measured for austenitic stainless steels operating in light water reactor (LWR) conditions [97-100] and were observed to match the theoretical behavior [101].

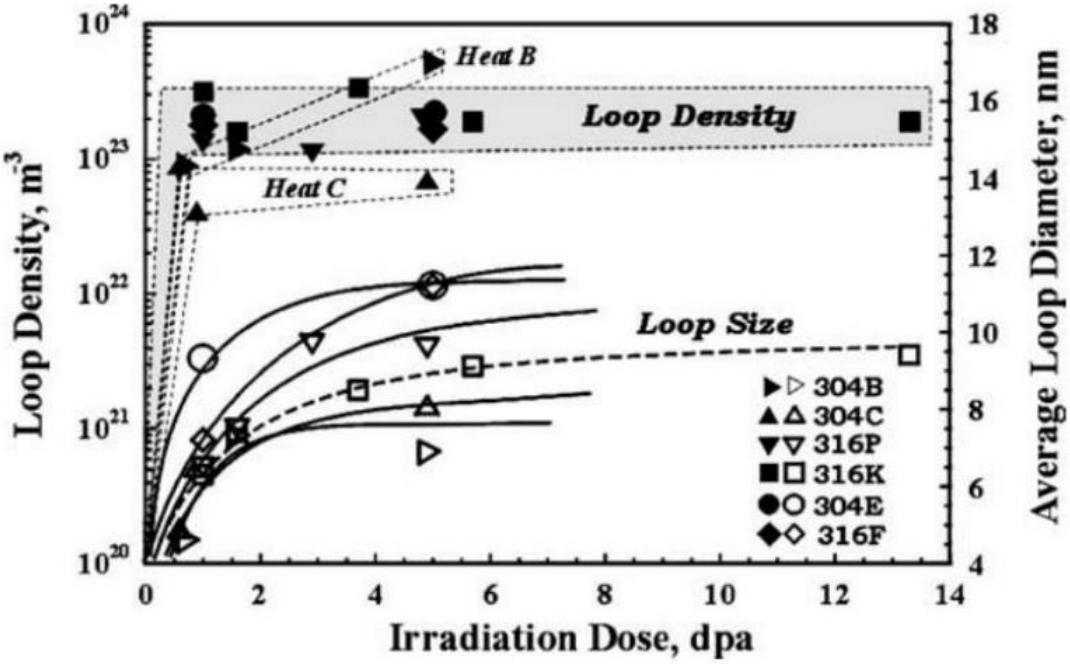

Figure 2.13. Average size and density of dislocation looks in an austenitic stainless steel as a function of irradiation dose after 275 ˚C irradiation

2.3.3 Voids, Cavities, and Bubbles

The term void refers to the larger defect cluster generated by the coalescence of vacancies into a stable structure. Under irradiation, helium is generated as a transmutation product [102] and hydrogen is absorbed from the water environment. As these gas atoms diffuse within the material system, then can find their way into voids, turning them into cavities. When the amount of gas accumulates to a level where the gas pressure is in mechanical equilibrium with the matrix, the defect is referred to as a bubble. Since the formation and growth of these features is dependent on the ability for vacancies to diffuse in the solid, temperatures responsible for generating these defects are typically above those observed in traditional light water reactor system (i.e. <300 ˚C). However, gamma heating within core internal components can significantly increase local temperature [103] resulting in the observation of cavities/bubbles in stainless steels after operation in LWRs, especially at high doses. Although these defects have been observed, the point defect and loop microstructure will dominate material performance in austenitic stainless steels during operation in light water reactor systems [104].

2.3.4 Radiation Hardening

Previous discussion revolved around the initiation of dislocation motion within a perfect lattice. Due to the rapidly changing microstructure during irradiation, the addition of point defects, loops, precipitates, and voids make the crystal lattice far from perfect. Each of these defects present a barrier which needs to be overcome by the dislocation in order to continue propagation. At damage levels 5-10 dpa, the yield stress of the material can reach levels multiple times that of the non-irradiated material [105]. A typical method for determining the change in

the yield stress of a material is to use the dispersed barrier hardening (DBH) model [106]. This model states that the change in the yield stress will be proportional to the size and density of defects present following the equation

$$\Delta\sigma_{y,x} = \alpha_x M \mu b \sqrt{N_x d_x} \tag{2.16}$$

where $\Delta\sigma_y$ is the change in yield stress, α is the barrier strength of the defect, d is the size of the defect, and N is the defect density. The barrier strength, α, varies from 0-1 with 1 representing a perfectly hard barrier. M, μ, and b are the material parameters Taylor factor, shear modulus, and magnitude of the Burgers vector respectively. This base formula can be expanded to include the influence of multiple defect populations either by linear superposition

$$\Delta\sigma_y = \alpha_A M \mu b \sqrt{N_A d_A} + \alpha_B M \mu b \sqrt{N_B d_B} \tag{2.17}$$

or by square superposition

$$\left(\Delta\sigma_y\right)^2 = \left(\alpha_A M \mu b \sqrt{N_A d_A}\right)^2 + \left(\alpha_B M \mu b \sqrt{N_B d_B}\right)^2 \tag{2.18}$$

Linear superposition tends to be more accurate when combining defects which have dramatically different barrier strength, while square superposition is used when similar barrier strengths in the defects are observed. Barrier strength values for faulted loops are generally reported to be between 0.2 and 0.5 [107] while values for precipitate tend to be higher, although those values are greatly dependent on their size and coherency with the matrix.

2.3.5 Radiation Induced Segregation (RIS)

The mobile point defects which are produced during irradiation have the ability to transport specific atomic species. As vacancies move, atoms are moving in the opposite direction whereas interstitial motion is in the same direction as atomic movement. The mechanism by which local microchemistry changes based on the preferential diffusion mechanism is called the inverse Kirkendall effect [108]. If an element has a tendency to diffuse more easily by way of interstitial migration or by vacancy migration, elements can enrich or deplete at defect sinks where significant defect diffusion is present like near grain boundaries or larger defects. Multiple sources show chromium depletion as the significant player in IASCC [109,110]. A nominal chromium content of 13 at% is required for an austenitic stainless steel to maintain its corrosion resistance. Many times RIS profiles around grain boundaries on differ within ~5nm of the grain boundary, making accurate measurements difficult [111]. Observations around faulted loops and voids sometimes reach 10s of nanometers, but this is generally as wide as the profiles come when it comes to RIS. Therefore proper calibration and use of the TEM is required in order to see quantitatively the redistribution of solute atoms.

Many studies have shown Nickel segregating towards the defect sink and Cr segregating away from the sink[112-117]. Typical RIS profiles are shown in figure 2.14. Grain boundaries are not the only defect sinks where RIS is observed. Faulted dislocation loops also act as large enough sinks to cause RIS effects in samples investigated under TEM[118]. Nickel and silicon are enriched at loops where chromium and iron are depleted. The magnitude of the composition change is noteworthy as sometimes the dominant element in the matrix can become secondary to another element in the vicinity next to a faulted loop. It has been observed that nickel concentrations can exceed that of iron in a Fe-15Cr-16Ni alloy in a range of 10nm from the grain

boundary. This RIS behavior is a strong function of the loop size. Consider for a factor of 4 increase in size, 16 times more point defects are required to annihilate at the larger dislocation loop, which should in theory transport 16 times more solute atoms.

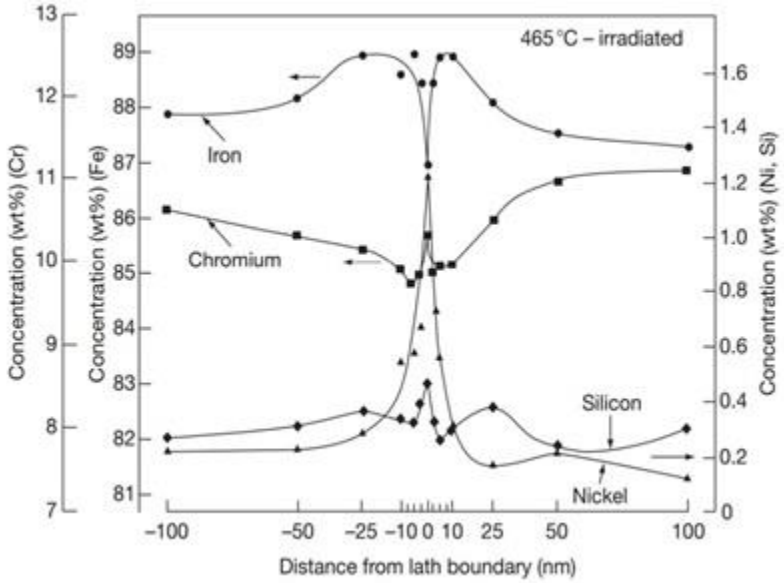

Figure 2.14. Concentration profiles of Cr, Ni, Si, and Fe in 12% Cr martensitic steel after irradiation to 46 dpa at 465 ˚C [119]

Larger loops also have a different defect bias factor when compared to smaller loops. Small loops are strong preferential sinks for interstitials, but as the diameter of the loop increases the interstitial capture efficiency (which can be on the order of 30 when the loop is small[120]) decreases substantially. If the vacancy mechanism for RIS is dominant over the interstitial mechanism, then RIS would be biased towards later loop life when they have grown to appreciable size such that vacancy migration to the loop can have an appreciable effect on the RIS behavior[121].

The main reason chromium depletion (and depletion of other major and minor elements) has been investigated to such a large extend has to do with the apparent correlation between the magnitude and drop-off of the chromium content near grain boundaries and the IASCC

susceptibility with respect to total neutron fluence. Chromium has a very similar dependence on irradiation dose compared to the susceptibility of stainless steels to IASCC [122] and is shown in figure 2.15. It has also been observed in thermally segregated alloys (used to isolate the effects of segregation apart from irradiation induced defects) and proton irradiated SS that there exists a threshold for the amount of chromium present at the grain boundary before IASCC begins to appear. For thermally segregated alloys, this threshold appears to be around 14 wt% and for irradiated samples the threshold appears to increase to 16 wt%.

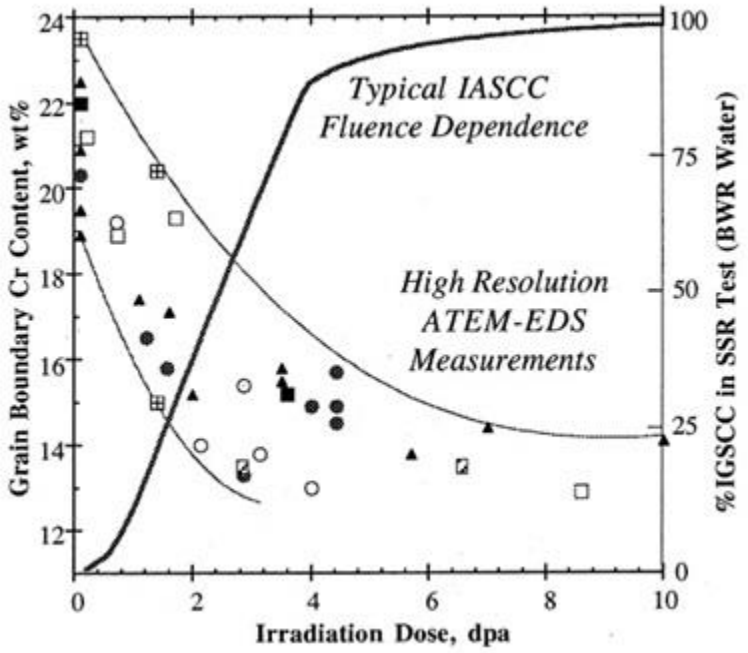

Figure 2.15. RIS of Cr as a function of neutron dose in comparison to typical IG cracking of 304ss

At first glance the correlation between chromium content and IASCC looks promising, but much literature has been written which shows a much more complicated picture. Systematic studies trying to pinpoint the primary mechanism by which IASCC occurs have looked at the factors giving rise to chromium segregation. Extreme chromium depletion is predicted to occur

at lower damage rates and at higher temperatures, where conditions are favorable for defect survival (unfavorable for mutual recombination) [123]. However, even in some instances where the chromium depletion has been very severe (down to 12 wt% [124]) these alloys have shown higher resistances to IASCC when compared to other alloys of very similar composition but with lower levels of chromium depletion. Therefore this paints a picture of chromium segregation not being the primary mechanism for the initiation of IASCC. Additional research which casts doubt onto chromium segregation being a primary mechanism for IASCC was carried out by Busby et al. using post irradiation annealing to preferentially anneal away matrix damage caused by proton irradiation while leaving the generated RIS profiles largely unaltered. In this way, the effect of matrix damage and solute segregation could be largely decoupled. This set of experiments showed that for a given set of parameters, matrix damage (faulted loops) could be annealed away to values less than 10% of their initial value while maintaining 90% of the RIS profile produced through irradiation [125]. Annealing in this way decreased IASCC susceptibility dramatically while keeping a majority of the RIS intact.

2.3.6 Localized Deformation and Dislocation Channeling

Upon irradiation, the primary deformation mode in austenitic stainless steels gradually transforms from homogeneous slip to heterogeneous dislocation channeling. This heterogeneity causes very large deformation values in very localized areas, while other areas remain virtually unstrained. The degree of localization is often expressed as a ratio between the strain measured in these highly localized regions and the macroscopic axial plastic strains. It has been observed using both atomic force microscopy (AFM) [126] and in situ TEM experiments [127,128] that

this ratio can be upwards of 10. The actual regions where deformation localization occurs is in defect-reduced channels called either dislocation channels or sometimes “clear bands”[129].

It has been mentioned before and observed many times that the point defects, and larger agglomerations of defects, act as barriers for mobile dislocations in the matrix. Through in-situ TEM observations by Briceno [130], dislocations were shown to be halted by the presence of point defects. This was achieved by first straining a TEM sample to produce mobile dislocations, and then irradiating that same sample with 1 MeV krypton ions. Although the dislocations were able to be generated and move through the matrix in the pre-irradiated matrix, their movement was supremely stunted upon subsequent straining. The point defects were assumed to be the reason for this stalled motion, because the dislocations were trapped even though there weren’t any large identifiable obstacle preventing the dislocations from moving [131-133]. A secondary indication of the point defect effects on dislocation motion came from the in situ TEM images through continual straining. The motion of the active slip band moved in a discontinuous/jerky manner, which is consistent with isolated segments of the dislocation breaking free from obstacles at different times. This was to be expected since the point defect barriers are not expected to provide a uniform resistance to the entire dislocation. The dislocation motion was also witnessed as being non-uniform as a function of time. Periods of inactivity would be followed by periods of relatively large dislocation motion. As time increased, the total amount of dislocation motion increased. This is consistent with the mobile dislocations being able to decrease the barrier strength by either annihilating the defect or reducing its size thereby making an easier glide path.

As a result, subsequent dislocations moving through this region would face a smaller barrier and glide easier. This is fundamentally what gives rise to the dislocation channels. The

motion of mobile dislocations annihilates defects, producing a relatively defect free path for other dislocations to glide easily through while taking out additional defects along the way. Detailed work has shown the progression of deformation from homogenous toward heterogeneous deformation [134], and have observed that dislocation channeling along with micro twinning are the primary deformation modes for stainless steel irradiated to levels greater than 0.1 dpa. Beyond this damage level, the degree of localization as measured by channel height and channel spacing is observed to increase [135].

2.4 Irradiation Assisted Stress Corrosion Cracking

Intergranular fracture has been observed in irradiated austenitic stainless steels at strains and in environments that would not typically result in failure. This premature degradation and ultimate failure of components in the presence of ionizing radiation is referred to as Irradiation Assisted Stress Corrosion Cracking (IASCC). This phenomenon was initially observed several decades ago and in the years since many review articles have been written on the subject [136-138]. Although a lot of time and effort has been devoted to this specific problem, the exact mechanisms which drive crack initiation in reactor environments is still not fully understood. As the name implies, IASCC requires the combination of an applied stress, a corrosive environment, and a susceptible material. Radiation in this context acts to complicate the underlying mechanisms since it has the ability to change both the material susceptibility and the properties of the corrosive environment. A list of historically observed incidents of IASCC in BWRs is presented in table 2.3.

Table 2.3. History of observations of stress corrosion cracking in BWR environments [139]

Event	Year of detection
Fuel Cladding IGSCC	Late 1950s and early 1960s
IGSCC of 304 during construction	Late 1960s
IGSCC of furnace sensitized 304 during operation	Late 1960s
IGSCC of welded small diameter piping	Mid 1970s
IGSCC of large diameter 304 piping	Late 1970s
Crevice-induced cracking of 304L and 316L	Mid 1980s
Cracking of low carbon and stabilized stainless steels in vessel locations	Late 1980s to present

2.4.1 Environmental Effects

It is important to emphasize that the corrosive environment in which the material is present plays a significant role in IASCC. Without a corrosive environment there cannot be stress corrosion cracking. In this context water chemistry refers to the feed water which is in direct contact with the reactor core and all structural core components. For BWR systems there are two distinct water chemistries use. These are normal water chemistry (NWC) and hydrogen water chemistry (HWC). A detailed description of the main differences between NWC and HWC is presented in Table 2.4. The main difference separating these two water chemistries is the amount of dissolved oxygen in the water [140]. Increasing the dissolved oxygen content of the

water has been shown to increase the electrochemical potential (ECP) which makes for a more corrosive environment [141]. Increasing the ECP results in reduced strain to failure and increases the intergranular cracking fraction of irradiated stainless steel measured post straining in constant extension rate tensile tests [142]. The addition of hydrogen in HWC is done in an effort to capture free oxygen radicals, thus decreasing the dissolved oxygen content and therefore decreasing the ECP [143]. Addition factors may be introduced through the addition of hydrogen into the feed water such as changing specific oxide stability and increasing radiation fields [144].

Table 2.4. Water chemistry parameters for commercial light water reactors

Environmental Parameters	BWR-NWC	BWR-HWC	PWR
Coolant Temp (°C)	288	288	320
Coolant Pressure (psig)	1020	1020	2420
pH (at 25°C)	6.0	6.0	7.0-7.2
Oxygen (ppb)	300-2000	<10	<5
Hydrogen (ppm)		0.4-3	3-5 (35 cc/kg)
ECP (mV_{SHE})	+150	<-230	-770
Conductivity (μS/cm)	<0.1	<0.1	20.5
B content (ppm)			1000
Li content (ppm)			2-3
SO_{4}- content (ppb)	<3	<3	<3
Cl^- content (ppb)	<1	<1	<1

Radiolysis, the process by which new oxidizing species are produced through the dissociation of water during irradiation, can also have a large effect on the ECP and therefore the aggressiveness of the water environment. The population of radiolytic products is estimated to be proportional to the square root of the radiation flux for pure water [145]. These products can have a noticeable effect on the ECP in NWC where the population of reducing agents is

relatively low compared to HWC. Experiments in the present study have all been conducted in a simulated NWC water environment without the presence of a radiation field as the full influence of radiolysis on crack initiation is outside the scope of this project.

2.4.2 Microstructural Effects

The change in IASCC susceptibility is known to change dramatically as the microstructure evolves with increasing dose through a reactor's lifetime. These microstructural changes effect the physical properties of the material, mainly the yield stress and hardness, and have a dramatic effect on the preferred modes of deformation. Although the microstructural evolution can account for the hardening of the material, it does not directly correlate with the IASCC susceptibility [146]. West et al. showed that hardening, dislocation loops, and void distributions could not fully account for the differences observed in IASCC susceptibility in both Fe based and Ni based alloys [147]. There is also a considerable amount of data present showing a large discrepancy in the observed %IG cracking fractions observed in high yield strength material, pointing to the importance of additional factors driving IASCC.

Similarly, hardness alone does not correlate with material susceptibility. Comparing commercial purity 304 stainless steel with different levels of cold work and irradiation to produce the same hardness value, Hash et al. was able to show that only the samples with the greatest amount of irradiation damage were susceptible to intergranular fracture [148]. Thus, the source of hardening plays an important role, and irradiation is a necessary step for inducing this type of failure mode.

2.4.3 Localized Deformation Effects

As dislocation channels impinge upon a grain boundary, several different interactions may occur. (1) The dislocation channel can slip transfer into an adjacent grain. This shows up as a simple point-wise change in the propagation direction of the dislocation channel. This is typically observed when there is a low angle misorientation between the affected grains. (2) The dislocation channel will experience cross-slip within the same grain. (3) The grain boundary will begin to absorb dislocations from the channel which ultimately leads to grain boundary sliding. (4) Dislocations from the channel build up at the grain boundary interface resulting in a stress concentration at the intersection. This has been studied both through experimental work and through a vast computational effort [149-154]. As stated previously, when the dislocation channel interacts with a grain boundary a step is formed which is on the order of tens to hundreds of nanometers. The larger step heights cannot always be accommodated by the grain boundary and when they fail to do so they must find some other mechanism to relieve the stress which includes cracking.

Recently, the effect of these DC-GB interaction geometries have been studies in detail to illuminate their roles in grain boundary cracking behavior. Through a combination of EBSD grain boundary orientation mapping SEM image correlation, specific interaction types were investigated for their cracking susceptibility [155-158]. Throughout this study there were two main categories of interaction. There was either continuous slip, where the dislocation was accommodated in some way by the grain boundary by either propagating along the grain boundary itself or traversing the grain boundary and continuing to propagate at a different angle in the adjacent grain, or there was discontinuous slip, where mobility of the dislocation channel was blocked by the grain boundary. Several key results came from this study. The first result

compared the cracking susceptibility to the orientation of the grain boundary. It was shown that random high angle boundaries (RHAB) were more than 4 times as likely to experience cracking than low angle or twin boundaries. These results were consistent with other intergranular corrosion studies of austenitic alloys [159,160]. As for the special boundaries, they have high levels of symmetry, smaller changes in atomic spacing from the normal lattice, and less open volume. The susceptibility of RHAB is two-fold seeing as they are less likely to transmit strain across the boundary and they have a lower cohesion strength than the special boundaries. It was also observed that boundaries which made traces on the surface at angles greater than 70 degrees to the tensile direction showed a much higher susceptibility to cracking. This makes sense based on the work done by West and Was [46] which gives compelling evidence that there is a minimum threshold for intergranular cracking in irradiated materials and these grain boundaries lined up normal to the tensile stress direction will reach this threshold first. The cracking fraction as a function of grain boundary trace angle observed in this study is shown in figure 2.16.

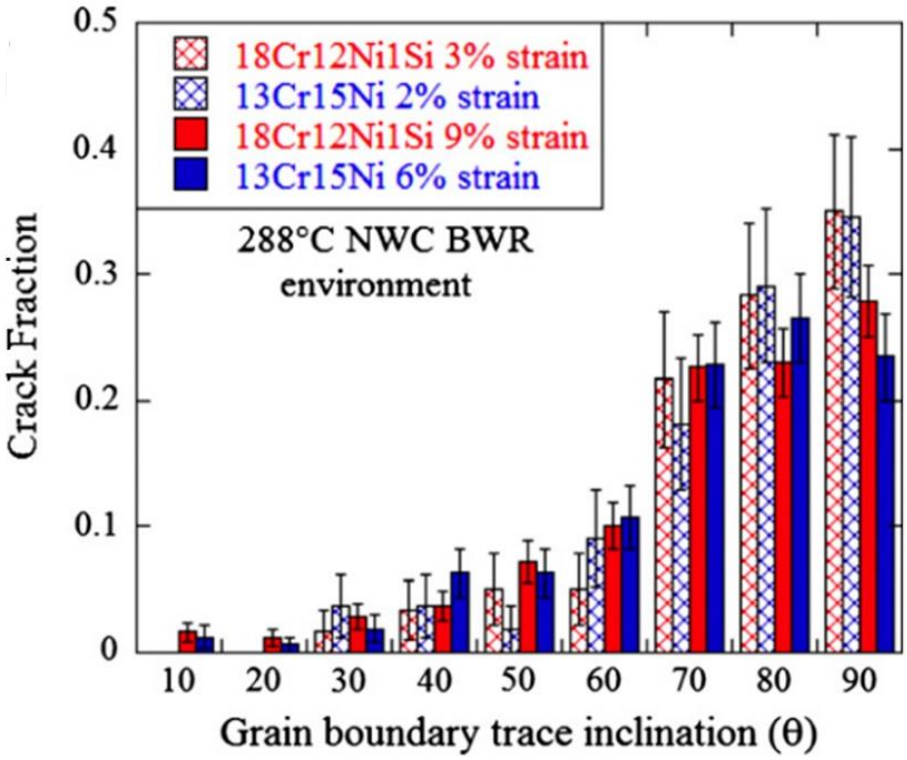

Figure 2.16. Cracking fraction at varying grain boundary surface trace angles for two alloys irradiated to 5 dpa at 360 ˚C and strained to two levels of plastic strain in simulated BWR-NWC at 288 ˚C

The most striking result of this study was the correlation between the type of interaction of the channel at the grain boundary (continuous or discontinuous) and cracking susceptibility. The cracking susceptibility at discontinuous channel sites was a factor of six greater than continuous channel sites, which is believed to be caused by the high local tensile stress generated by the pile-up of dislocations at the boundary.

2.4.4 Stress Threshold for IASCC

Much of the testing for IASCC, especially crack initiation and failure mechanics, is done using slow rate tensile tests. Another branch of tensile stress experiments have been performed in recent years, opting for a constant load and dynamic strain rather than constant strain rate and

dynamic loading. The main purpose of this style of static loading experiment is to determine both the amount of stress which is required to observe failure of irradiated components as well as the amount of time at a constant load necessary to cause failure. Bosch et al [161] compiled the available testing data on constant load tests on irradiated material while including more data points at very high dpa values (up to 80 dpa). The dataset as a whole now covers 10-80 dpa for small variations in PWR water chemistry. The trend shows that at about 10 dpa, the amount of stress which is necessary to cause failure of stainless steel components decreases steadily with increasing dpa up until 40 dpa. At this point the amount of stress (recorded as percent of the macroscopic yield stress) remains constant with increasing dose up to 80 dpa. This threshold appears to be at 40-50% of the yield stress. The results of the constant load experiments are shown in figure 2.17.

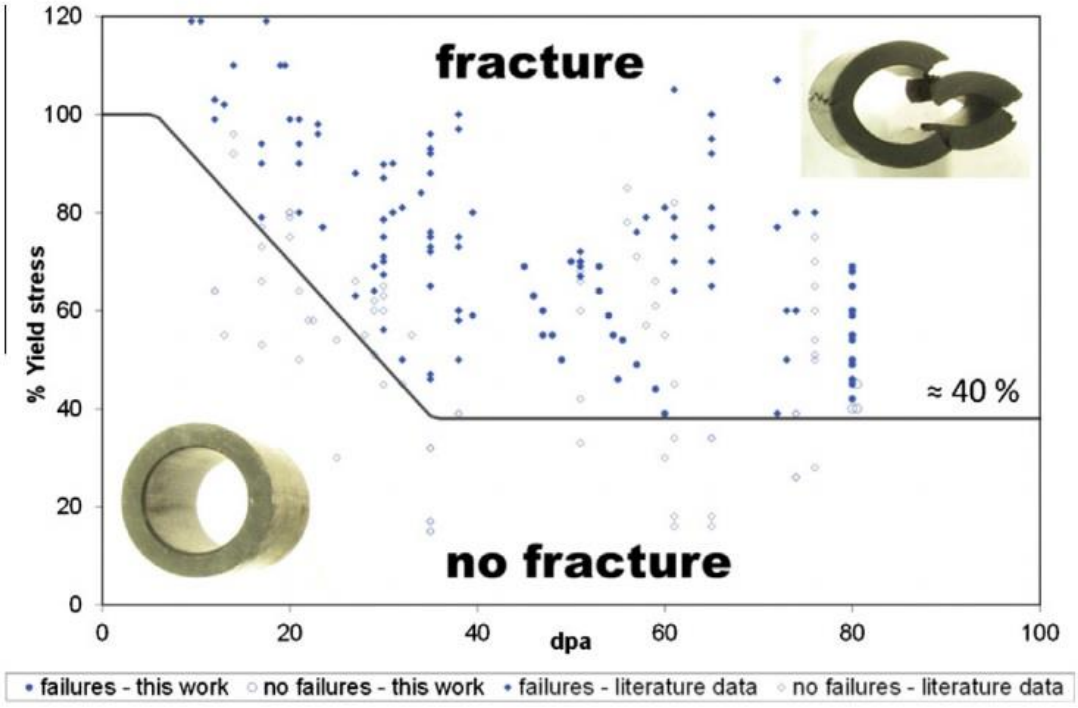

Figure 2.17. Compiled data of constant load testing of O-ring specimens in simulated PWR conditions

In certain regions, due to grain orientation and stress concentrators, the yield stress can be exceeded locally giving rise to deformation before the material as a whole begins to yield. Below this stress value there is no observed cracking of irradiated components for testing times up to 6 months. For failed components during the Bosch study, the fracture plane was analyzed to determine the mode of failure. It was clearly evident from the available SEM images that the cracking was intergranular in nature. In other constant load studies [162] the total percentage of intergranular cracking decreased with increasing stress amount. The samples of this study were tensile bar samples, so as the crack began to propagate the cross section of the sample was diminished. Using the cross sectional area of the ductile fracture region the true stress at failure was determined for the failed samples to correlate well with the initial yield strength of the material. Therefore, for the case of tensile bar samples tested the failure resulted from initiation and propagation of IASCC which then transitioned to ductile failure when the cross sectional area was reduced to levels where the macroscopic yield stress was eclipsed. The uniaxial constant load experiments showed a lower threshold of 400 MPa (~0.4 yield strength) for sample failure in a PWR environment. Similar values of 400-500 MPa for IASCC initiation were reported in highly irradiated CW316SS under slow strain rate tensile conditions [163,164].

The observed IASCC initiation at stresses much below the yield strength is likely due to local high stresses near grain boundaries and heterogeneous channel deformation. Although the macroscopic tensile stress applied to the specimen is half the yield strength, high local stresses likely occur because of a non-uniform stress distribution due to the anisotropy of elasticity of each grain in a polycrystalline body. Kamaya et al [165] reported that local stresses near grain boundaries and triple points can reach about twice (x2.22) the macroscopic stress based on the results of FEA of a random polycrystalline SS body with elastic anisotropy. This suggests that

local stresses of 1000 MPa could be generated from an applied tensile stress of 400 MPa. These localized stresses would then be high enough to induce channel formation, which would then interact with grain boundaries to produce their own localized increase in stress, eventually resulting in crack initiation and propagation.

Along with primary cracks, which were observed at the positions of highest stress based on FEA models, secondary cracks were also visible in regions away from these maximum stress values. These cracks were observed to run in a parallel direction with the primary failure crack, pointing towards a similar mechanism of cracking in these secondary cracks. This again can give insight into the stress threshold for cracking. The cracking region of the thimble tube specimens had a width of 1.2 mm, correlating with stress values between 545 MPa and 400 MPa based on the FEA model. This was also shown to correspond to a stress threshold between 40-45% of the yield stress. It is also important to note that parallel experiments were run in an inert argon atmosphere for samples of 80 dpa. After six months, with stress values ranging from from 45-69% of the yield stress, zero failures were observed highlighting the importance of environment on the cracking phenomenon. Therefore deformation or other purely mechanical processes cannot be linked directly to the cracking behavior.

2.4.5 Dislocation Pile-up in Irradiated Steel

Through the use of HREBSD, all six components of the stress tensor are available to analyze in terms of magnitude and behavior as you move away from the interaction site between the dislocation channel and the grain boundary into the adjacent grain. Theoretical work by Eshelby et al. [68] produced an analytical solution to the pile-up of dislocations at an immovable barrier, similar to the case here in which dislocations within a channel are blocked by a grain

boundary. In the Eshelby model, the number of dislocations, *n*, are constrained to lie in the same slip plane under the combined action of their mutual repulsion and the force of an applied stress. For an infinitely long dislocation of mixed character, the non-zero components of stress acting on a slip plane can be defined based on the distance between the dislocation core and a point of interest. The stress value based on a single dislocation is defined as *p*.

$$p = \frac{A}{x - x_i}, \tag{2.19}$$

where *A* is constant that depends on the edge/screw character of the dislocation, x is the location of the first dislocation, and xi describes the location of all other dislocations in the system. In order for a dislocation to be in a stable position, the component of the traction in the direction of the Burgers vector on the slip plane due to all other dislocations and applied stresses must be equal to zero. Therefore:

$$\sum_{\substack{i=1 \\ i \neq j}}^{n} \frac{A}{x_j - x_i} + P\left(x_j\right) = 0; \;\; j = 1, 2, \ldots, n. \tag{2.20}$$

The first component in the summation accounts for the individual stress contributions of all the dislocations other than one specific dislocation of interest acting at the position of the specific dislocation, $P(x)$ accounts for any applied stresses acting at the position of the specific dislocation, an *n* gives the total number of dislocations participating in the pile-up event. This condition must hold for every dislocation in the system. A function, *f*, is defined such that the logarithmic derivative equates to the stress due to all dislocations:

$$f = \prod_{i=1}^{n} \frac{A}{x - x_i}, \tag{2.21}$$

$$\frac{f'}{f} = \sum_{i=1}^{n} \frac{A}{x - x_i}. \tag{2.22}$$

By solving for the zeroes of this function, it is possible to arrive at an analytic solution for the positions of each dislocation resting on a single slip plane. For a large number of dislocations the stress acting in the adjacent grain ahead of the pileup can be reduced to the simplified form:

$$\sigma = A\sqrt{\frac{n}{x}}. \tag{2.23}$$

The resulting stress field on the other side of the stationary barrier was found to be closely approximated by $r^{-1/2}$ dependence, where r is the distance from the dislocation pile-up. A fully detailed derivation of equation 5.5 is given in [68]. If the Eshelby model is an appropriate theory to apply to the HREBSD data, then the stresses observed should follow a similar $r^{-1/2}$ trend. A least squares fitting algorithm was applied to each of the HREBSD scans with a functional form of:

$$\sigma_N = A + \frac{K}{\sqrt{r + B}} [\text{GPa}], \tag{2.24}$$

where σ_N denotes the grain boundary normal stress and *K* is the stress intensity factor that describes the resistance to slip transfer of this specific grain boundary. It is important to note that the stress in this equation is due to the pile-up of dislocations and does not account for external stresses that may be applied to the system. Since the HREBSD technique itself relies on the selection of a reference pattern to act as its zero stress state, the *A* parameter is added to account for the small stress that is acting on the reference pattern which makes it deviate from a truly relaxed Kikuchi band structure. For reasonable agreement with the data the magnitude of *A* should be less than the fluctuation of stresses observed far from any features in the grain which could potentially amplify the recorded stress (grain boundaries, channels, precipitates, etc). The value of this fluctuation is typically on the order of 0.15 GPa in the Fe13Cr15Ni sample. The analytic solution is well defined at all points where the distance from the dislocation pile-up is greater than zero, however by nature of the discrete data points collected during EBSD it is impossible to determine the exact location of the grain boundary. The fitting parameter *B* is added to the equation to account for the unknown location of the grain boundary under the resolution of the EBSD step size, which was 100 nm for all data presented in this work. Therefore, for good agreement between the fit and the data, the value of B should be less than the step size used of 100 nm. A majority of the calculated fitting parameters fall within the physical boundaries outlined above, and result in the Eshelby analysis to be a good fit for describing the interaction between discontinuous dislocation channels and grain boundaries. When the *K* parameter from this study is compared to experimentally calculated values in non-irradiated titanium [87], it is seen that the values in this study are considerably higher with some fitting parameters of *K* reaching values 70% higher than ones observed in titanium. As this fitting parameter *K* is related to the resistance to slip transfer at the grain boundary, much higher values

are expected in irradiated materials since the defect microstructure inhibits the production and propagation of dislocations. Therefore the elevated values of *K* observed in this study are reasonable.

Chapter 3 – Experimental Procedures and Methods

The primary aim of this study is to quantitatively understand the stress state present near dislocation channel – grain boundary interaction sites and have those specific stresses influence the crack initiation process. This was accomplished by first performing a set of experiments to quantitatively calculate the stress tensor present with sub-micron resolution at different dislocation channel – grain boundary interaction sites in a set of proton irradiated samples. In a separate set of experiments, the pre-characterized samples were strained in a simulated BWR water environment to initiate small cracks on the sample surface. The strain tensors at each site were compared with crack initiation data in an attempt to link the local stress state with cracking susceptibility.

3.1 Alloy description and specimen preparation

3.1.1 Alloy composition and heat treatment

Two austenitic stainless steels were used in this study with compositions as listed in table 3.1. The first alloy composition, Fe-13Cr-15Ni, was selected due to its moderate susceptibility to cracking. Several other studies have used this composition of material and have shown that it is susceptible to IASCC [78]. This will be used as the baseline for this study to understand how local stresses influence the cracking susceptibility of the material. The second alloy, Fe-21Cr-

32Ni, was selected due to its relatively high resistance to crack initiation and to potentially determine specific material properties which mitigate intergranular fracture which might deepen the understanding of the entire IASCC mechanism.

Table 3.1. Composition (wt%) of alloys used during this study

Material designation	Fe	Cr	Ni	Mn	Si	P	C
Fe-13Cr-15Ni	Bal.	13.41	15.04	1.03	0.1	0.011	0.016
Fe-21Cr-32Ni	Bal.	20.73	31.16	0.94	0.1	0.014	0.014

3.1.2 Tensile sample fabrication and preparation

Tensile bar samples were machined using electrical discharge machining (EDM). An engineering drawing showing the tensile bar geometry are shown in Figure 3.1. As shown, the samples have a 2 mm x 2 mm cross section and a gauge length of 21 mm. EDM was used as the primary fabrication method to reduce the zone affected by mechanical damage. Since a majority of the analysis performed in this study involves calculating stresses on the sample surface, the residual stresses induced through fabrication need to be kept to a minimum. Each of the tensile bars were cut such that their length was parallel to the rolling direction of the base block of material.

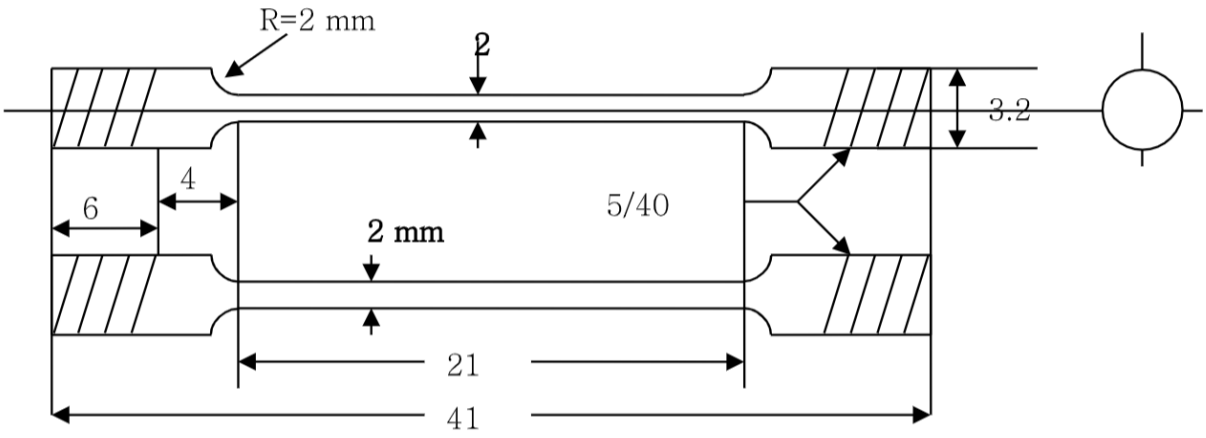

Figure 3.1 Tensile bar sample geometry

After tensile bar samples were EDM cut, they were mechanically polished using successively higher grits of silicon carbide paper. Grits of 200, 400, 600, 800, and 1000 were used with the final mechanical polishing SiC paper having a median particle of 2.5 μm. To remove induced stresses from mechanical polishing, each tensile bar sample was electropolished. Electropolishing was performed in a solution of 10% perchloric acid and 90% methanol cooled to -40 ˚C. A 30V potential was applied to each sample and polished for 60 seconds. During polishing a current between 0.1 and 0.2 A were achieved using a stainless steel cathode. After electropolishing, samples had a mirror-like finish without any visible residual scratches from the mechanical polishing step.

3.1.3 Orientation Imaging Microscopy (OIM) analysis

To facilitate analysis of the irradiated section of the tensile bar gauge length, hardness indents were used to mark rectangular regions on the sample surface. Indents were made with a spacing of 1.5 mm by 0.7 mm and an indenter gram force of 200 g to make 10 distinct regions. A

diagram showing the placement of indents is shown in figure 3.2. These indents were made to assist in relocating specific grain boundaries for analysis.

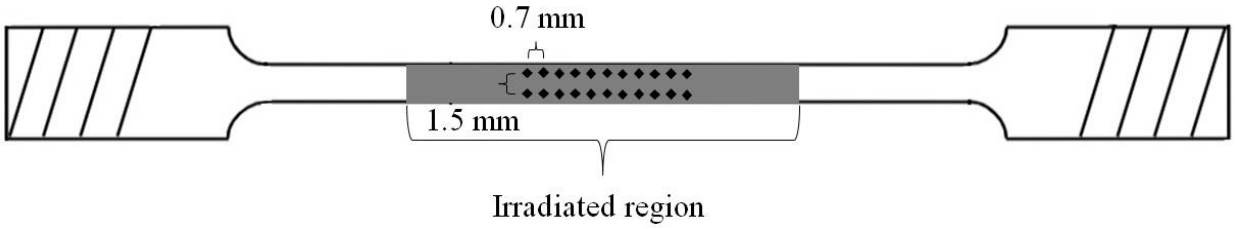

Figure 3.2 Hardness indent geometry to mark out distinct regions within the irradiated area

Electron backscatter diffraction (EBSD) was used as the primary method for characterizing the grain sizes, orientations, and grain boundary types (i.e. RHAB, RLAB, CSL). EBSD analysis was performed at the Michigan Center for Materials Characterization using both a Philips XL30 FEG SEM and a Tescan MIRA-3 SEM. A schematic of the EBSD setup is shown in Figure 3.3. Tensile bar samples were first attached to Ted Pella SEM stubs using a colloidal graphite solution. The sample is left to dry under a heating lamp for 20 minutes to make sure the colloidal graphite has solidified. This helps to significantly reduce the amount of sample drift during analysis. Once loaded in the SEM, samples are tilted to 70˚ relative to the electron beam. Electrons from the SEM will scatter off the sample surface both elastically and inelastically in all directions. A fraction of the inelastically scattered electrons will satisfy Bragg diffraction conditions. The Bragg diffraction criterion relates the electron wavelength with the atomic spacing of the material and the incoming direction of the electrons. The Bragg diffraction condition is presented as:

$$\lambda = 2d \sin\theta, \tag{3.1}$$

where λ is the electron wavelength, d is the spacing between atomic planes in the material, and θ is the angle between the sample surface and the incident electron beam. Electrons satisfying this criterion are scattered in the direction of a phosphor screen which produce photons collected by a CCD camera. Inelastically scattered electrons move in all directions, so the subsequent elastic scattering creates a cone shape. Since only a portion of this cone intersects the detector, it appears as a straight line which is referred to as a Kikuchi band. Each band that appears on the detector is associated with the specific lattice plane where the Bragg diffraction conditions were met.

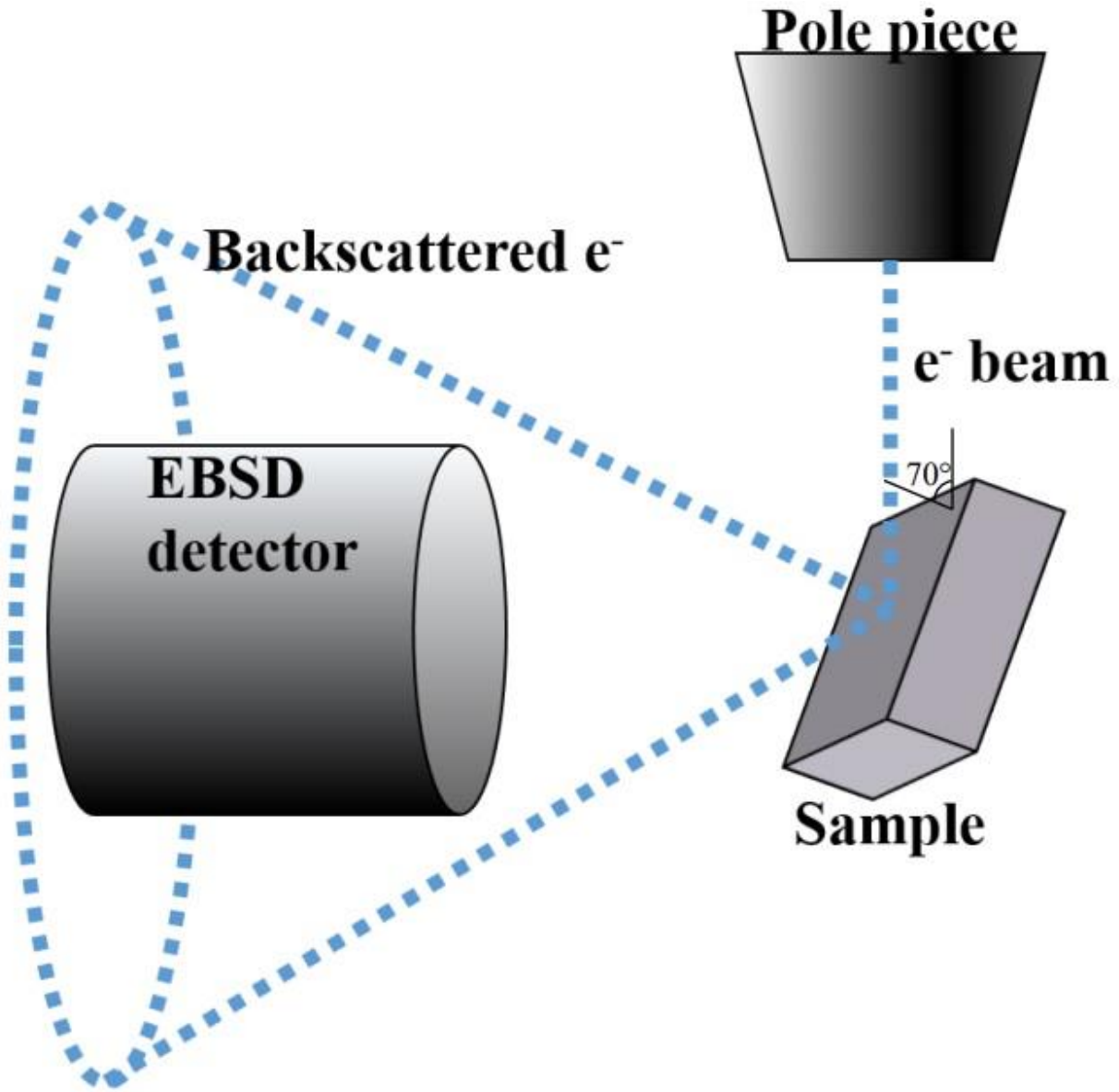

Figure 3.3 EBSD configuration inside of SEM

EBSD Kikuchi band patterns were collected using a step size of 1 μm over the entire area marked out by the hardness indents. At each point, TSL OIM data collection software automatically indexes the Kikuchi band structure and determines the Euler angles of the lattice. Orientation maps are then generated based on this collection of Euler angles. An inverse pole figure can then be created by coding a color to a pole figure with each color referencing a

particular crystal orientation. These collections of orientations are also used in order to determine grain boundary types (RHAB, RLAB, CSL), Schmid factors, and Taylor factors. Since each slip system present in a grain has its own Schmid factor, the highest value is reported since this is the particular system which is most likely to activate first during deformation.

EBSD analysis is inherently a surface technique since the penetration depth of the electrons is only on the order of a few 10's of nanometers. This means that no information about subsurface morphology of the grains can be acquired from a single scan. In order to gain information about the grain boundary plane, a serial sectioning and rescanning technique is performed. After the orientations of all grains in the area outlined by the hardness indents have been measured, 20 nm colloidal silica solution was used to remove ~5 microns from the sample surface. The actual amount of material removed from the surface was measured by scanning each hardness indent with an Olympus LEXT confocal microscope before and after the polishing to determine the change in depth of the indent. The amount of material removed from a single section of the gauge length was determined to be the average change in depth of the four indents which marked the region. Since the centroid of the indent location is unaffected by surface polishing, the exact same regions can be analyzed using EBSD in the same way as mentioned previously within this section. The EBSD inverse pole figures were then aligned using the centroid of the hardness indents, and the shift of individual grain boundaries could be observed. The angle the grain boundary makes relative to the sample surface could then be easily determined from the amount of material removed from the sample surface and the lateral movement of the grain boundary.

3.1.4 Proton Irradiation

All samples were irradiated using the 1.7 MV Tandem accelerator at the Michigan Ion Beam Laboratory, located at the University of Michigan. Temperature of the samples was monitored during the irradiation with a FLIR two-dimensional infrared thermal imager. Three areas of interest (AOIs) were tracked on each bar to ensure temperature uniformity across the samples. Temperature on the sample surface controlled by balancing the influence of an electrical heater and constant air flow, both located behind the irradiation stage.

Samples were irradiated to 5 dpa with 2 MeV protons at 360 °C at a rate of ~$1x10^{-5}$ dpa/s. This proton energy corresponds to a damage depth of roughly 20 microns. The damage profile, as shown in figure 3.4, was calculated using the Stopping and Range of Ions in Matter (SRIM) code. Protons exhibit a relatively flat damage profile, but for consistency the actual damage rate used was taken at a depth that was 60% of the Bragg peak depth. For these samples, this depth was 12 μm from the surface.

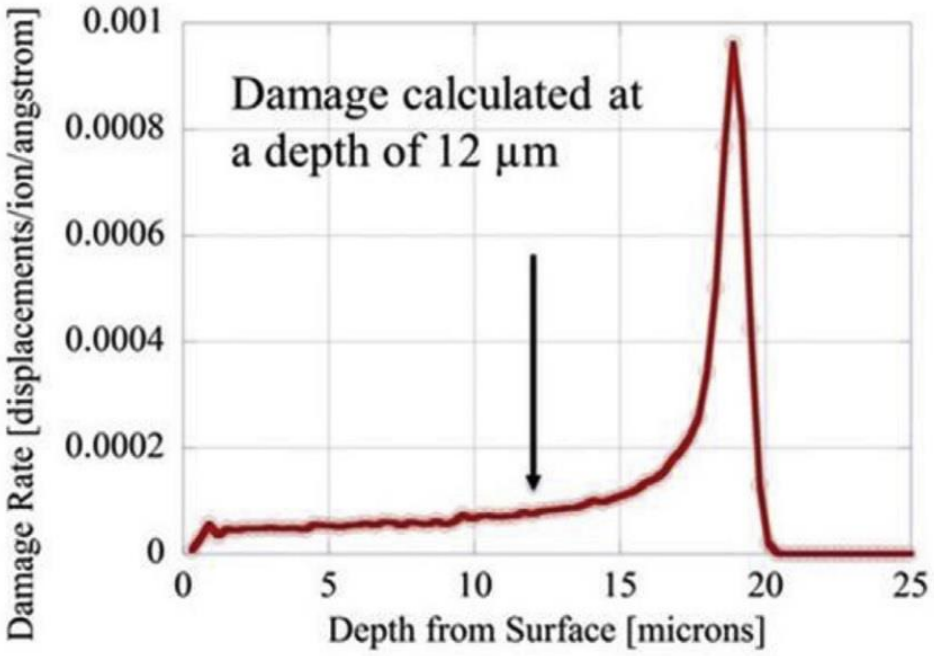

Figure 3.4 Damage rate depth profile for austenitic stainless steel irradiated with 2 MeV protons

Damage was calculated based on the measured current of the proton beam hitting the sample surface and the displacement rate calculated from SRIM.

3.2 Autoclave System and Testing Conditions

All constant extension rate tensile (CERT) tests were performed in the High Temperature Corrosion Laboratory at the University of Michigan. Tests were performed in autoclaves where the environment could be closely controlled and monitored. A single moveable crosshead was attached to the tensile samples through pull rods, and the displacement was measured using a linear variable differential transformer (LVDT). A general depiction of these systems is shown in figure 3.5. For this study, two environments were used: an inert argon environment, and a simulated BWR NWC environment.

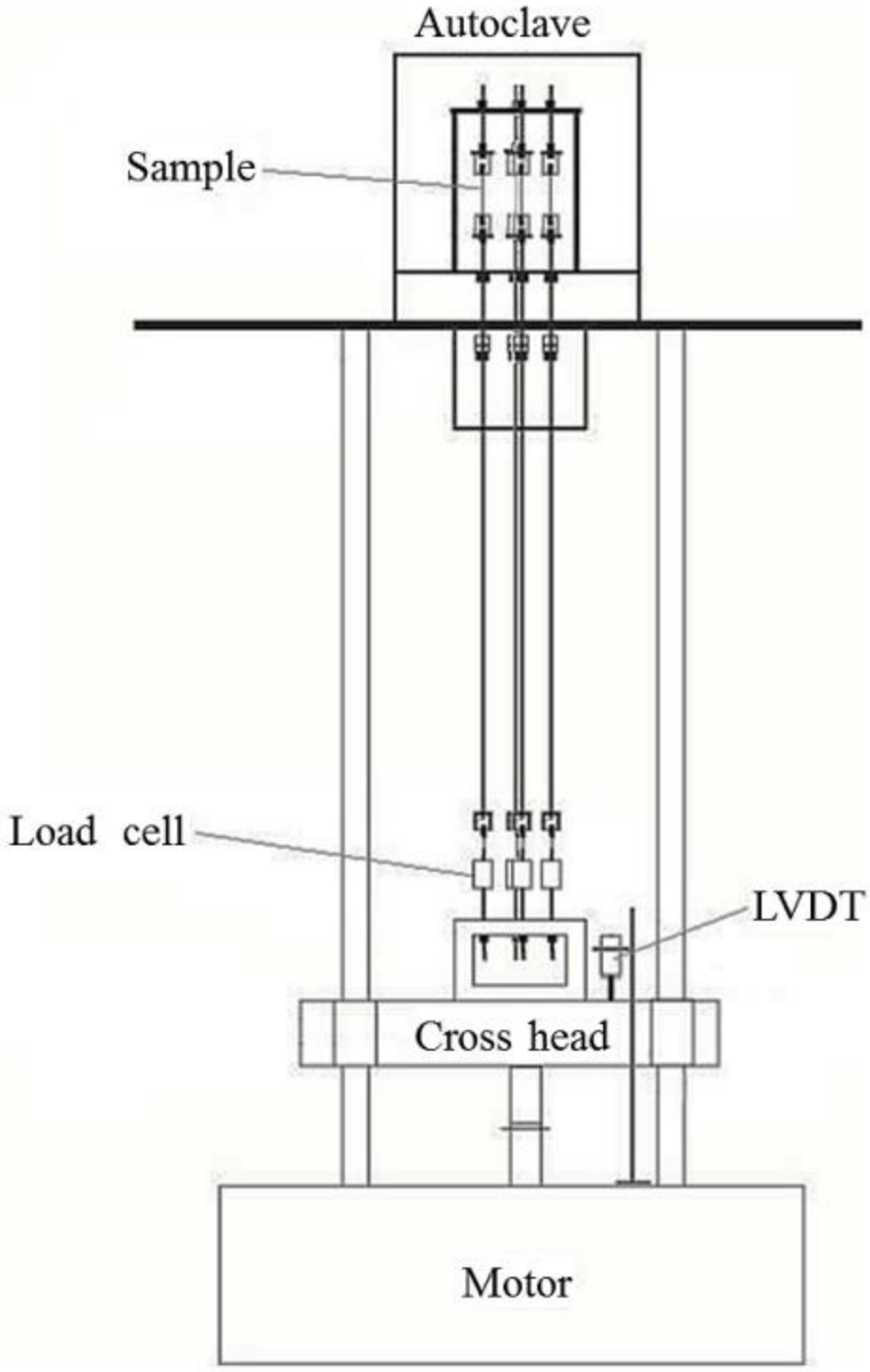

Figure 3.5 Schematic for CERT testing apparatus

3.2.1 Argon CERT Tests

Samples were first strained in an inert argon environment to avoid the influence of oxidation and cracking. Tests were performed at 288 °C as to simulate the deformation response under typical reactor conditions. Initial argon purity was 99.999% and was purified further using a 27601-U Supelco purifier up to 99.99999% purity. This helped to remove any trace water and oxygen from the system which could potentially oxidize the samples during straining.

Samples were strained using a strain rate of $3.5x10^{-7}$ s^{-1} as measured from the LVDT attached to the system crosshead up to 4.5% plastic strain. This amount of straining resulted in the formation of many dislocation channels on the sample surface, which interacted with grain boundaries in a multitude of ways. However, since the material wasn't in a corrosive environment, no cracking was observed either inside or outside of the irradiated area.

3.2.2 Simulated BWR NWC CERT Testing

To initiate cracks, samples were strained in a simulated boiling water reactor normal water chemistry environment consisting of 288 °C water with a dissolved oxygen concentration of 2000 ppb. Conductivity of the water was controlled closely through the addition of 10^{-6} molar sulfuric acid to bring the conductivity of the water up to 0.2 µS/cm. Water was pressurized using a Pulsafeeder high pressure pump which flows at 200 mL/min through the autoclave. Temperature was maintained using two 1800 W Watlow heating bands which are attached to the surface of the autoclave. Water exiting the pre-heats the inlet water stream by flowing through a tube-in-tube heat exchanger and is then cooled using a second tube-in-tube heat exchanger connected to a chiller system before returning to the primary water column. Pressure during

experiments was maintained at 1500 psi with a Tescom back pressure regulator. A K-type thermocouple positioned near the center of the autoclave is used to monitor and control the temperature of the water. Dissolved oxygen and conductivity are monitored continuously using Orbisphere 31110 oxygen sensors and conductivity sensors. Samples were strained using a strain rate of $3.5x10^{-7}$ s^{-1} as measured from the LVDT attached to the system crosshead and the stress applied to the sample was measured using a Transducer Techniques 1000 lbf load cell. The general water loop system is shown in Figure 3.6. All data was recorded every 5 seconds using a LabView data acquisition program. All BWR NWC CERT experiments were conducted after an initial argon straining step. For the 13Cr15Ni sample a single straining increment was performed, adding an additional 1.5% plastic strain. The 21Cr32Ni sample went through two increments of straining, each adding an additional 1.5% plastic strain.

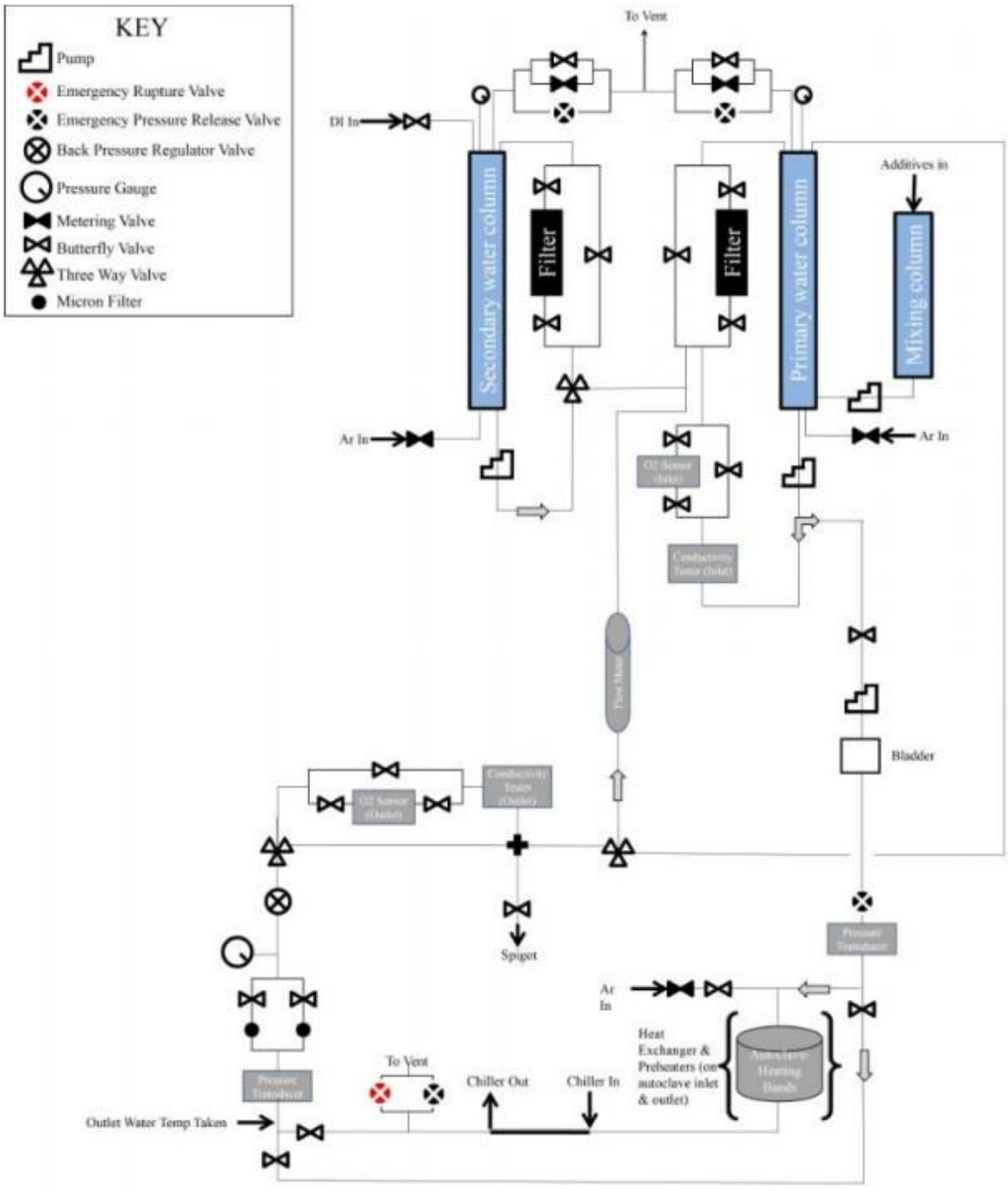

Figure 3.6 Water loop system diagram feeding into autoclave system

3.2.3 Oxide Removal

The amount of strain put into each sample was done to reach a point where cracks are just starting to initiate. Due to this, the cracks can sometimes be very small and obscured by the oxide film which develops during CERT testing in high temperature water. To facilitate finding these small cracks, the oxide was removed following the BWR NWC CERT tests. Removal of the oxide layer was achieved using two water based solutions: 100 g/L sodium hydroxide with 30 g/L potassium permanganate, and 100 g/L ammonium oxalate. Solutions were heated to ~95 °C and samples were first placed into the sodium hydroxide/potassium permanganate solution for 5 minutes, transferred to the ammonium oxalate solution for 5 minutes, and finally sonicated in DI water for 5 minutes. This three step process was repeated until no visible oxide was observed on the sample surface. Typically this required three iterations through the different solutions.

3.2.4 Confocal Microscopy

Topographical maps were taken with the Olympus LEXT laser confocal microscope at the Michigan Lurie Nanofabrication Laboratory. This instrument has a spatial resolution of ~125 nm and a height resolution of ~10 nm. Topographical maps are generated by varying the laser focus between a lower and upper limit as set by the user. Using an aperture to block all light that is out of focus, the microscope can detect which portion of the imaged area is in focus, and can map the height based on when each area comes into focus. These topographical maps allow for the measurement of the step heights produced by dislocation channels after deformation. Wide area maps were taken for each of the 10 OIM regions using a 10x magnification. Certain DC-GB

interaction sites of interest were scanned using a 50x zoom to increase the resolution of the step height measurement. With information about the orientation of each grain, the active slip system can be estimated based on which system has the highest Schmid factor. This slip system can be confirmed by looking at the trace angle (the angle of the dislocation channel with respect to the sample reference frame) and making sure that slip system is consistent with the one selected using Schmid factor analysis. With the slip system determined, an estimate for the number of dislocations passing through the dislocation channel can be made from the channel step height measured with the confocal microscope and the Burgers vector of the selected slip system.

3.3 Elastic strain/stress measurements

Elastic strain is difficult to measure do to the fact that it does not depend on the creation and subsequent motion of dislocations which cause permanent deformation to the crystal lattice. An increase in the tensile stress acting on a crystal will increase spacing between individual atoms, or the lattice parameter and compressive stress will decrease the lattice parameter. Since the diffraction of electrons during EBSD analysis is related to the spacing of crystallographic planes, residual elastic strains will distort the Kikuchi band structure relative to the pristine crystal structure.

Wilkinson et al. [118] was able to show that these small changes in the Kikuchi band structure could be used to measure the elastic strain tensor by relating the diffraction patterns of the deformed crystal to a reference pattern which is assumed to have no residual strain. This can be shown first by looking at the relationship between the shift in the EBSD pattern (q_i), as

measured perpendicular to the direction (r_i) along some selected feature of the Kikuchi structure (e.g. a zone axis), and the displacement gradient tensor:

$$q_i = \frac{\partial u_i}{\partial x_j} r_i - \left(\frac{\partial u_i}{\partial x_j} r_i \bullet r_k \right) r_i \ , \tag{3.2}$$

where

$$\frac{\partial u_i}{\partial x_j} r_i = \begin{pmatrix} \frac{\partial u_1}{\partial x_1} & \frac{\partial u_1}{\partial x_2} & \frac{\partial u_1}{\partial x_3} \\ \frac{\partial u_2}{\partial x_1} & \frac{\partial u_2}{\partial x_2} & \frac{\partial u_2}{\partial x_3} \\ \frac{\partial u_3}{\partial x_1} & \frac{\partial u_3}{\partial x_2} & \frac{\partial u_3}{\partial x_3} \end{pmatrix} \begin{pmatrix} r_1 \\ r_2 \\ r_3 \end{pmatrix} , \tag{3.3}$$

and u_i is the displacement tensor at some position x_i, and r_i is a unit vector. By combining equations for individual components of q_i, it is possible to eliminate $\frac{\partial u_i}{\partial x_j} r_i \bullet r_k$ with two simultaneous equations derived from (3.2)

$$r_1 r_3 \left[\frac{\partial u_1}{\partial x_1} - \frac{\partial u_3}{\partial x_3} \right] + r_2 r_3 \frac{\partial u_1}{\partial x_2} + r_3^2 \frac{\partial u_1}{\partial x_3} - r_1^2 \frac{\partial u_3}{\partial x_1} - r_1 r_2 \frac{\partial u_3}{\partial x_2} = r_3 q_1 - r_1 q_3 \tag{3.4}$$

and

$$r_2 r_3 \left[\frac{\partial u_2}{\partial x_2} - \frac{\partial u_3}{\partial x_3} \right] + r_1 r_3 \frac{\partial u_2}{\partial x_1} + r_3^2 \frac{\partial u_2}{\partial x_3} - r_1 r_2 \frac{\partial u_3}{\partial x_1} - r_2^2 \frac{\partial u_3}{\partial x_2} = r_3 q_2 - r_2 q_3 \tag{3.5}$$

To solve this system of equations, this shift in the EBSD pattern (q_i) must be measured in at least four distinct regions of the pattern with each region having a unique r_i. Without this last restriction the system of equations become singular. Additional shifts can be measured above the

required value of 4. If the number of shifts is increased, a solution for the distortion tensor is calculated for all different permutations of four distinct shifts. After all distortion tensors are calculated, an average best fit distortion tensor is made, improving the statistical errors in the measurement. Increasing the number of shifts used in this analysis increases the computational resources and time for analysis by a factor of N^2, so that number of analyzed points cannot be arbitrarily inflated. For this study, 50 regions were used to determine the best fit distortion tensor.

The distortion tensor is comprised of two components, the elastic strain tensor (ε_{ij}) and the rotation tensor (ω_{ij}). Since the component of the distortion gradient tensor necessary for calculating the local stress state in the material is the elastic strain tensor, the rotation tensor must be separated out. The rotation tensor and the elastic strain tensor can be calculated separately as:

$$\varepsilon_{ij} = \frac{1}{2}\left(\frac{\partial u_i}{\partial x_j} + \frac{\partial u_j}{\partial x_i} \right), \tag{3.6}$$

and

$$\omega_{ij} = \frac{1}{2}\left(\frac{\partial u_i}{\partial x_j} - \frac{\partial u_j}{\partial x_i} \right). \tag{3.7}$$

The rotation tensor may be used to determine the number of geometrically necessary dislocations required in order to cause the curvature of the crystal lattice, but this value will significantly underestimate the number of dislocations present in the crystal since dislocations of opposite sign will act to cancel out the crystal rotation. Due to this, the rotation tensor does a poor job estimating the plastic strain in the system and therefore is not fit for determining the number of

statistically necessary dislocations which make up a large fraction of the dislocations generated through plastic deformation. The primary purpose of separating the rotation tensor is to isolate the true elastic strain.

Elastic stress measurements can be calculated from the elastic strain tensor by using a simple form of Hooke's law:

$$\sigma_{ij} = c_{ijkl}\varepsilon_{kl}, \tag{3.8}$$

where σ_{ij} is the stress tensor, ε_{kl} is the elastic strain tensor, and c_{ijkl} is the fourth order tensor describing the relationship between stress and strain tensors. This fourth order tensor is also referred to as the stiffness tensor. The stiffness tensor is defined using the elastic modulus (E) and Poisson's ratio (ν) of the material. These values have been measured in multiple studies for austenitic stainless steels [119-121]. Hooke's law can then be expressed as:

$$\begin{bmatrix} \sigma_{11} \\ \sigma_{22} \\ \sigma_{33} \\ \sigma_{23} \\ \sigma_{31} \\ \sigma_{12} \end{bmatrix} = \frac{E}{(1+\nu)(1-2\nu)} \begin{bmatrix} 1-\nu & \nu & \nu & 0 & 0 & 0 \\ \nu & 1-\nu & \nu & 0 & 0 & 0 \\ \nu & \nu & 1-\nu & 0 & 0 & 0 \\ 0 & 0 & 0 & (1-2\nu)/2 & 0 & 0 \\ 0 & 0 & 0 & 0 & (1-2\nu)/2 & 0 \\ 0 & 0 & 0 & 0 & 0 & (1-2\nu)/2 \end{bmatrix} \begin{bmatrix} \varepsilon_{11} \\ \varepsilon_{22} \\ \varepsilon_{33} \\ 2\varepsilon_{23} \\ 2\varepsilon_{31} \\ 2\varepsilon_{12} \end{bmatrix}. \tag{3.9}$$

If the elastic strain tensor can be measured, then the stress tensor can be calculated using the appropriate elasticity coefficients at any given point in the material as long an EBSD pattern has been taken at that point.

Calculation of the elastic strain tensor and subsequent stress tensor was performed using BLG CrossCourt4 analysis software offline following EBSD analysis. This specific style of

analysis is referred to as high resolution EBSD, or HREBSD. The high resolution in this case does not refer at all to the spatial resolution, but the ability of the software to distinguish very small differences in the angular resolution of the collected EBSD patterns. At specific DC-GB interaction sites, a ~20 μm x 20 μm area was scanned using a low current electron beam with an energy of 30 kV. This energy allowed for analysis just below the sample surface and limited the amount of pattern distortion that could be caused by any residual contamination on the surface or any lingering residual stresses caused by the polishing procedure. Since the analysis procedure is dramatically influenced by the quality of the EBSD patterns collected, large dwell times at low current were used to collect crisp patterns. An exposure time of 2 seconds was used at each point in the scan which consisted of a rectangular array of points spaced 100 nm apart.

After analysis, all points with a calculated mean angular error in the distortion tensor above 10^{-3} rad were removed from analysis since these errors resulted in very large error in the stress calculation. This was often a result of partially sampling the pattern coming from the adjacent grain at scan points very close to the grain boundary which caused significant changes in the base EBSD pattern. A reference pattern was selected as a "zero stress" reference case. Since the vast majority of deformation is isolated to the dislocation channels, the material in between these channels is left somewhat unaffected by the deformation. It is assumed that patterns coming from these regions away from any potential stress concentrators (e.g. channels or grain boundaries) are relatively stress free. A pattern near the grain center away from potential stress concentrators with a high image quality is selected to act as the "zero stress" reference state. The default calculation of the stress tensor in the CrossCourt software is made in the sample reference frame. However, for this study the stresses which are of the most importance are those which are acting parallel to a specific grain boundary normal vector. Since previous

analysis allowed for the determination of the full 5-factor grain boundary geometry, the stress tensor calculated by the CrossCourt4 software package is then resolved such that the principle tensile stress, σ_{11}, is pointing parallel to the grain boundary normal and σ_{22} is aligned parallel to the grain boundary trace. With two axes defined, the third axis is calculated from the cross product of these two vectors.

3.4 Cracking Analysis

As discussed previously, samples that have undergone deformation in a high temperature inert argon environment and subsequent analysis with HREBSD undergo straining in a simulated BWR NWC water environment in order to induce intergranular cracks on the sample surface. These cracks are generally quite small, ranging from 2-20 μm and are generally isolated to a single grain boundary facet. Images were taken using an SEM across each of the OIM regions defined above at a base magnification of 1000x. From these images, if a potential crack was visible, additional high magnification images up to 15,000x were taken to determine whether or not these observed features were indeed intergranular cracks. Once cracks were identified, it was possible to determine the crystallographic orientation from EBSD patterns and geometric orientation of the boundary from the serial sectioning procedure.

Samples were examined for cracking in a JOEL JSM-6480 SEM. Once cracks were located, they were characterized by their grain boundary type, Schmid factors of the two grains, and the geometric orientation of the grain boundary. Special emphasis was made for grain boundaries which had been previously analyzed with HREBSD. The presence of dislocation channels and their interactions with the grain boundaries were also taken into account. The

location of each crack (e.g. mid boundary or at triple junction), and angle of the cracked boundary with respect to the loading axis were measured directly in the SEM.

Chapter 4 – Results

This chapter summarizes the results of CERT experiments on proton irradiated austenitic stainless steel in both an inert environment and in simulated BWR NWC. First, data is provided characterizing the two alloys studied extensively during this work for the purpose of comparing their deformation and cracking behavior. Data for each alloy is presented including HREBSD analysis at specific dislocation channel – grain boundary interaction sites calculated after straining in an inert environment and observation of crack initiation sites after straining in high temperature water. Significant results include the stress state observed at the interaction site between different types of dislocation channels and grain boundaries and model results for stresses on the grain boundary due to multiple parallel slip planes.

4.1 Pre-characterization of Fe-13Cr-15Ni and Fe-21Cr-32Ni

The two alloys used in this study were selected based on the differences in their material properties and the differences in their respective susceptibility to intergranular fracture in a high temperature water environment. One key material property where the two alloys differ is in the stacking fault energy, which was calculated for these two alloys using the methods described in the background section chapter of this thesis and presented in Table 4.1. Since empirical formulas are used for this calculation, they are generally only an estimate of the actual SFE of the alloys. However, the difference in this value is large enough to ensure reasonable confidence

that the difference in the SFE energies of these two alloys is statistically significant. For comparison, stacking fault energies are also calculated for a commercial purity 304 stainless steel due to its prevalence throughout the nuclear industry as a structural material.

Table 4.1. Calculated stacking fault energies using empirical methods

	CP304	Fe13Cr15Ni	Fe21Cr32Ni
Pickering	40.6	49.0	73.8
Schramm	23.0	53.9	158.6
Rhodes	47.2	48.5	73.3

Both alloys investigated here were lab purity alloys produced by General Electric Global Research and had chemical compositions as listed in Table 4.3. Composition analysis was performed by Element Materials Technology using a LECO GDS-850A glow discharge atomic emission spectrometer. During the production of the bulk material, alternating steps of cold rolling and annealing heat treatments (1200 C for 2 hours) were performed in order to produce a flat sheet. A final homogenization annealing treatment was done at 950 C for 1 hour to reach a final average grain size of 30 μm. The dimensions of the bulk Fe13Cr15Ni material was 28.1 cm x 6.8 cm x 0.35 cm with the longest dimension extending parallel to the rolling direction. Bulk Fe21Cr32Ni material was 11.6 cm x 8.3 cm x 0.42 cm. Several samples were created from these bulk pieces of material and analyzed during the course of this research. Table 4.2 lists the samples IDs as well as the irradiation damage of the samples studied as well as the geometry of the sample.

Table 4.2. Sample identifications and irradiation damage level for studied material

Sample ID	Heat	Base Composition	Sample Type	Irradiation Damage [KP]
BSCC1	2192	21Cr32Ni	Tensile Bar	0 dpa
BSCC2	2192	21Cr32Ni	Tensile Bar	5 dpa
BTEM1	2192	21Cr32Ni	TEM bar	5 dpa
ASCC1	PV5119	13Cr15Ni	Tensile Bar	0 dpa
ASCC2	PV5119	13Cr15Ni	Tensile Bar	5 dpa
ASCC3	PV5119	13Cr15Ni	Tensile Bar	0.5 dpa
ATEM1	PV5119	13Cr15Ni	TEM bar	5 dpa

Figure 4.1 shows a collection of inverse pole figures generated from EBSD maps taken over a large area of the ASCC1 Fe13Cr15Ni 0 dpa tensile bar sample which had been electropolished. As irradiation does not have an effect on the grain size or orientation, these are representative of grains in each of the Fe13Cr15Ni samples. Three separate maps are shown, taken from the left hand side, center, and right hand side of the gauge section on the tensile bar to show uniformity of the grain morphology across samples. Figure 4.2 plots a histogram of 3,188 measured grain sizes taken from the same ASCC1 Fe13Cr15Ni sample and shows a calculated average grain size of 28.36 μm. Each plot is taken in the same sample orientation, with the rolling direction of the bulk sample aligned horizontal to the given IPFs. Figure 4.3 and Figure 4.4 show the results taken from the BSCC1 Fe21Cr32Ni 0 dpa sample and shows an average grain size of 31.73 μm. A full collection of inverse pole figures taken for the Fe13Cr15Ni and Fe21Cr32Ni samples are presented in Appendix A.

Table 4.3. Bulk Chemical Compositions for Investigated Steels [wt%]

Alloy	**Cr**	**Ni**	**C**	**Mn**	**S**	**P**	**Si**	**Al**	**Cu**
Fe13Cr15Ni	13.41	15.53	0.011	1.01	<0.005	0.011	0.13	<0.005	<0.01
Fe21Cr32Ni	20.73	31.16	0.014	0.94	<0.005	0.014	0.11	<0.01	<0.01

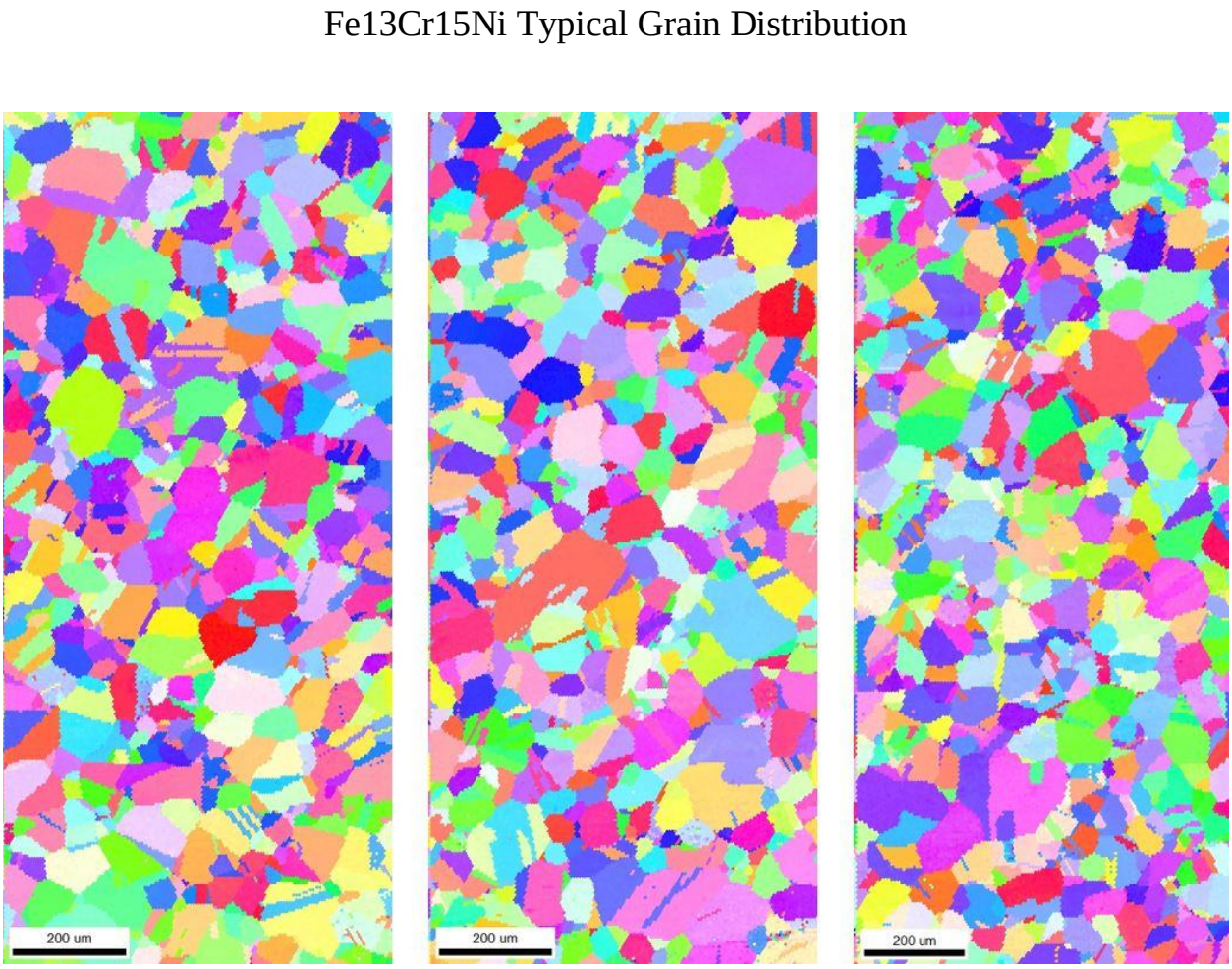

Figure 4.1: Inverse Pole Figure (IPF) taken from EBSD analysis on ASCC1 Fe13Cr15Ni 0 dpa sample showing typical grain structure and orientation at the left hand side, center, and right hand side of the gauge section. Rolling direction of bulk material is aligned horizontally to each of the IPFs.

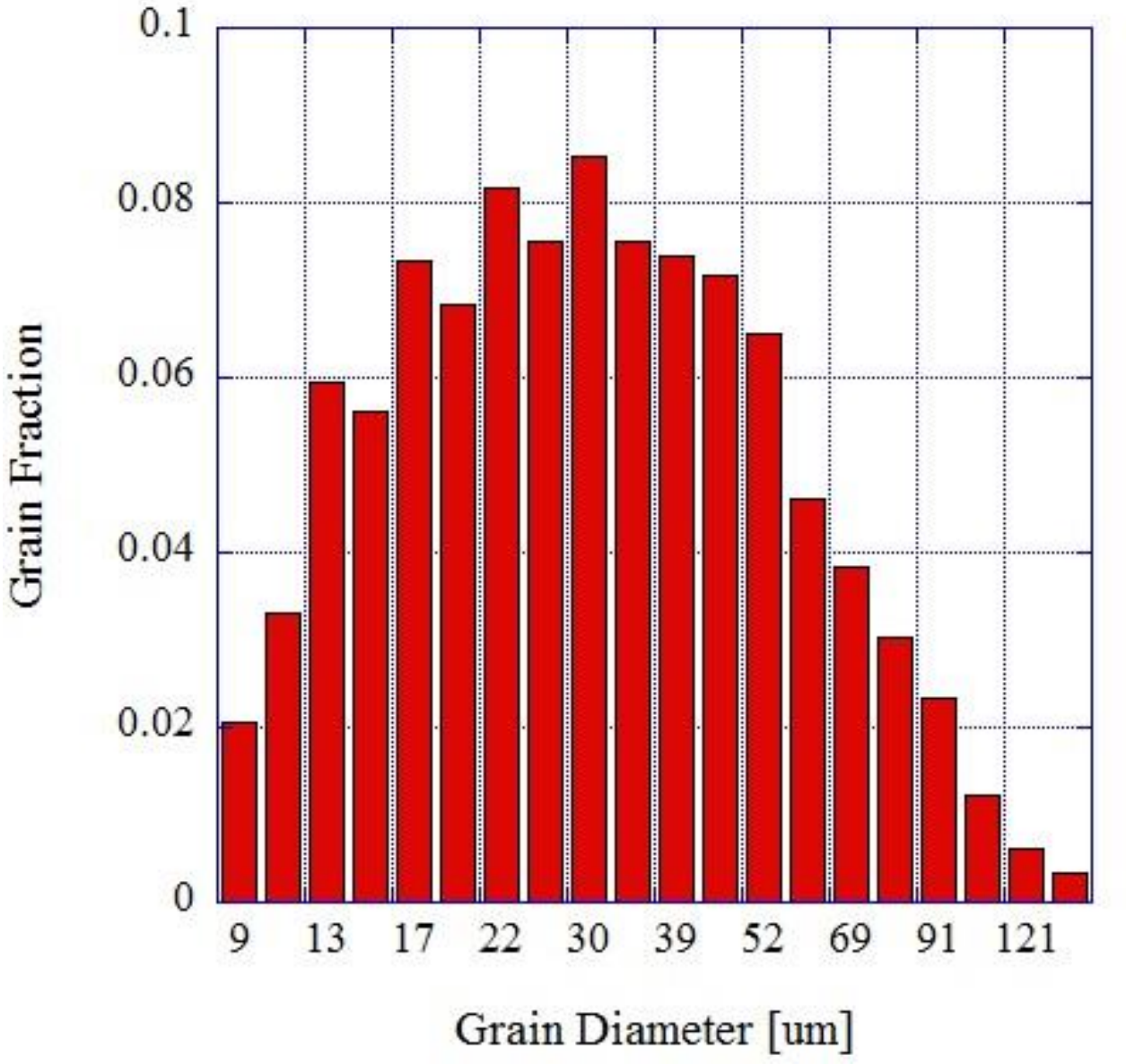

Figure 4.2: Distribution of grain sizes in the ASCC1 Fe13Cr15Ni 0 dpa tensile bar sample.

Fe21Cr32Ni Typical Grain Distribution

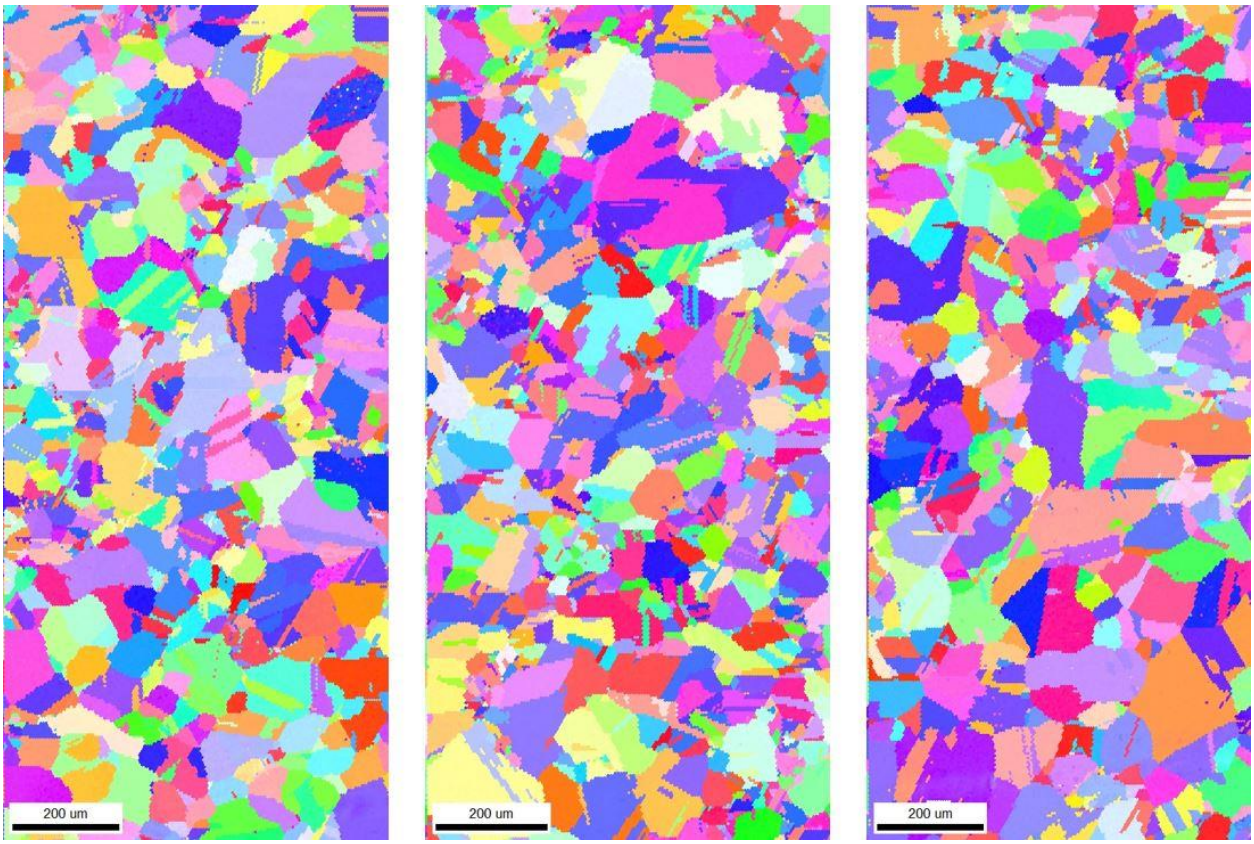

Figure 4.3: Inverse Pole Figure (IPF) taken from EBSD analysis on the BSCC1 Fe21Cr32Ni 0 dpa sample showing typical grain structure and orientation at the left hand side, center, and right hand side of the gauge section. Rolling direction of bulk material is aligned horizontally to each of the IPFs.

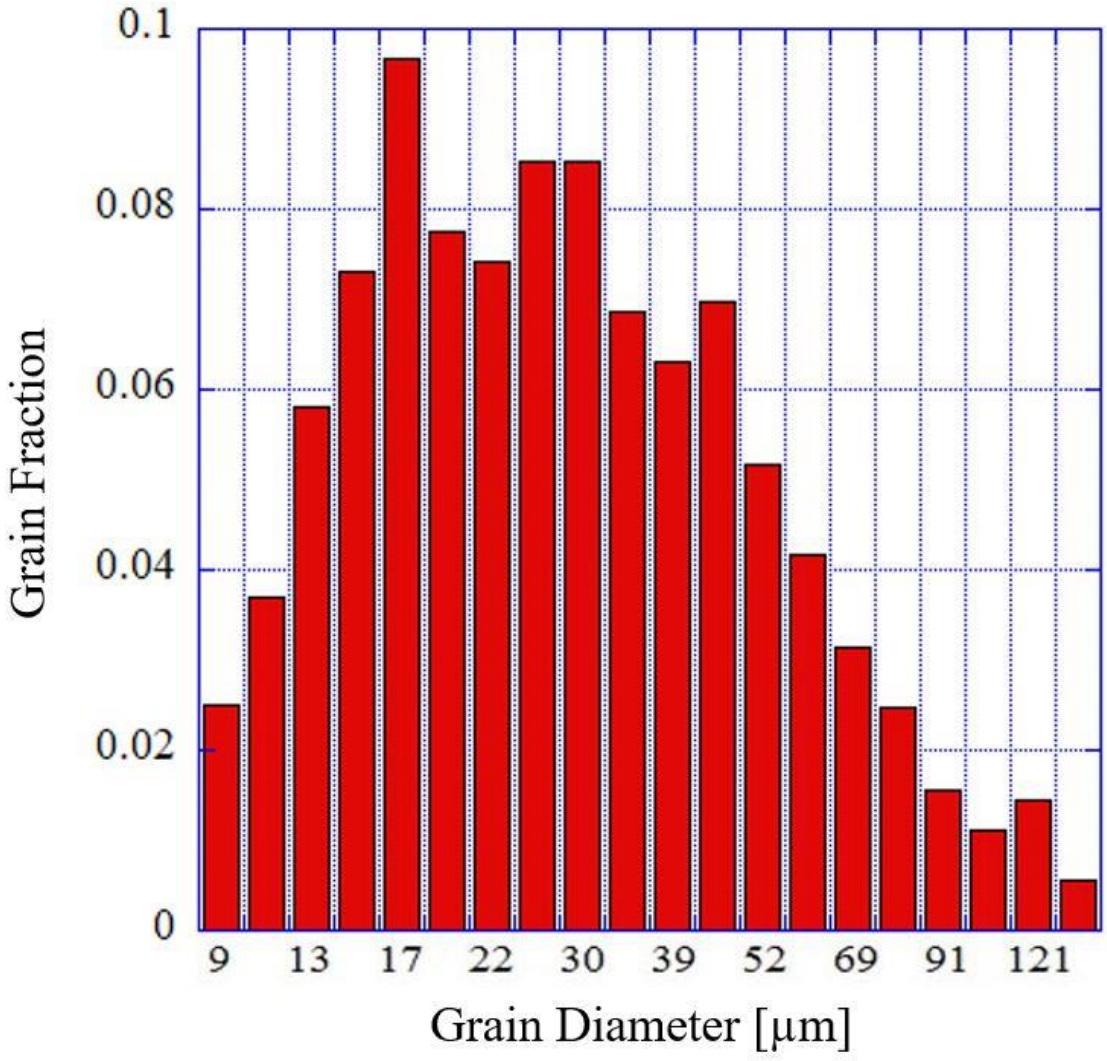

Figure 4.4: Distribution of grain sizes in the BSCC1 Fe21Cr32Ni 0 dpa tensile bar sample.

Since the main focus of this study revolves around the behavior of grain boundaries, it was necessary to understand the character and distribution of certain grain boundary types as well as grain orientations prior to any experiments. This included specific CSL boundaries, grain orientations, Schmid factors, and Taylor factors which were all described in detail in the background chapter of this thesis. A table comparing the bulk properties of these two alloys is presented in table 4.4. It is important to note that the vast majority of grain boundaries in these

materials are random high angle boundaries, although a decent fraction of CSL boundaries, like the Σ3 twin boundary, are observed. The distribution of grain boundary types was homogeneous throughout both materials. A bar graph showing the distribution of all CSL boundary types up to Σ29 is presented in Figure 4.5 and Figure 4.6 for Fe13Cr15Ni and Fe21Cr32Ni, respectively. The data presented here was taken from the ASCC1 and BSCC1 non-irradiated samples.

Table 4.4. Number and percentage of boundaries of each type in Fe13Cr15Ni and Fe21Cr32Ni, as measured by EBSD.

		13Cr15Ni [#]	13Cr15Ni Fraction	21Cr32Ni [#]	21Cr32Ni Fraction
Number of boundary types in a random sampling	RHABs	16762	0.51	21125	0.61
	LABs	3287	0.10	1997	0.06
	Σ3	8217	0.25	6956	0.20
	Σ5	1316	0.04	1016	0.03
	Σ9	1418	0.04	1332	0.04
	Σ27	393	0.01	921	0.03
	CLSs	1485	0.05	1510	0.04
Number of grains with a given Taylor Factor	2.37	151	0.05	99	0.03
	2.5	291	0.09	208	0.06
	2.63	267	0.08	306	0.09
	2.76	189	0.06	262	0.08
	2.89	305	0.09	290	0.09
	3.02	331	0.10	338	0.10
	3.15	290	0.09	349	0.11
	3.28	388	0.12	312	0.09
	3.41	356	0.11	403	0.12
	3.54	328	0.10	360	0.11
	3.67	370	0.11	334	0.10
Number of grains with a given Schmid factor	0.29	8	0.01	11	0.01
	0.32	39	0.02	44	0.02
	0.35	107	0.04	96	0.04
	0.38	226	0.08	184	0.07
	0.41	208	0.08	288	0.10
	0.44	533	0.20	589	0.21
	0.47	864	0.32	761	0.27

	0.5	729	0.27	810	0.29

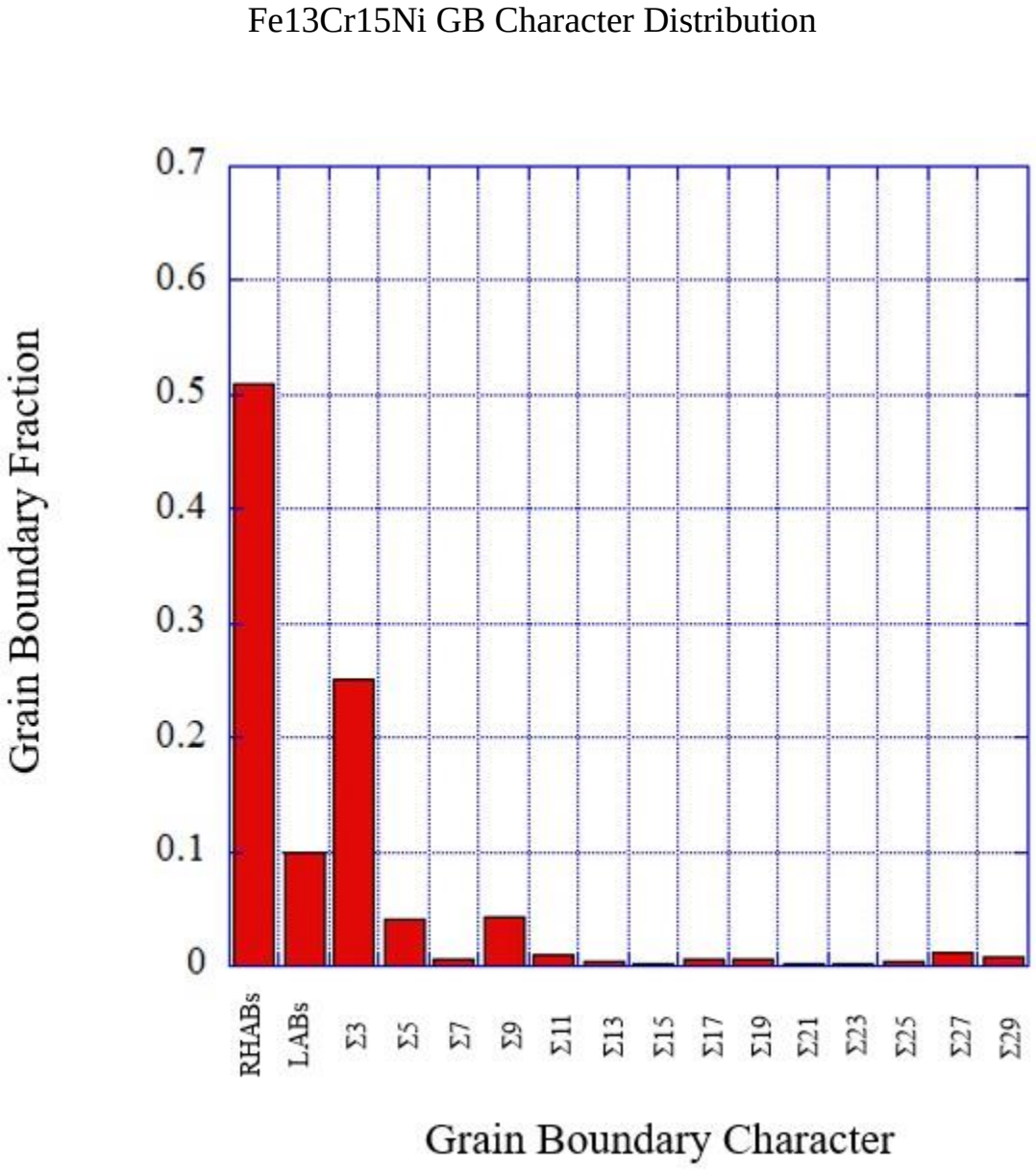

Figure 4.5:Distribution of Fe13Cr15Ni grain boundary character including CSL boundaries up to Σ29 taken from EBSD analysis of the ASCC1 0 dpa tensile bar sample.

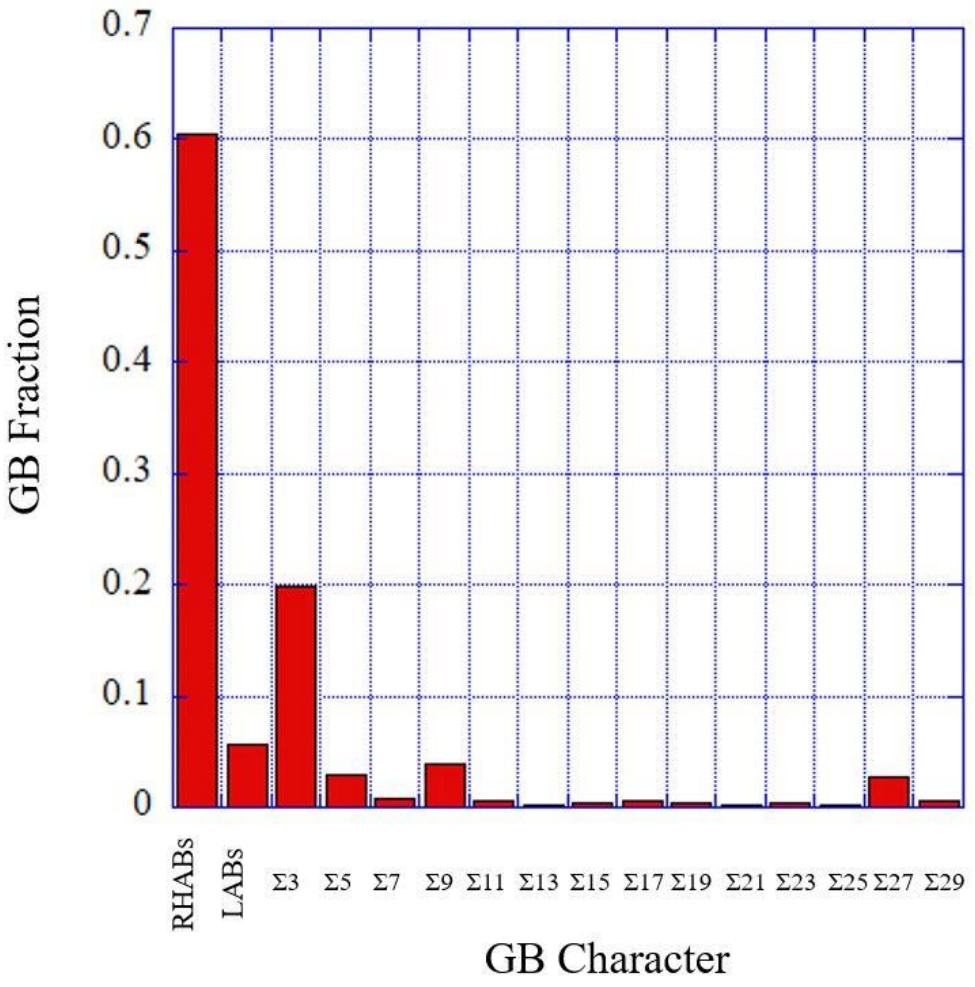

Figure 4.6: Distribution of Fe21Cr32Ni grain boundary character including CSL boundaries up to Σ29 taken from EBSD analysis of the BSCC1 0 dpa tensile bar sample.

Proton irradiation of these austenitic stainless steels results in microchemical changes due to radiation induced segregation and these changes to the grain boundary chemistry are observed throughout the samples at random high angle boundaries. TEM analysis performed by He et al. [35] shows the distribution of iron, nickel, and chromium at different sites along a single grain boundary in a Fe13Cr15Ni heat similar to the one used in the present study. Figure 4.7 shows line scan profiles taken from two separate lift-outs either near the water-metal interface and several microns below the surface.

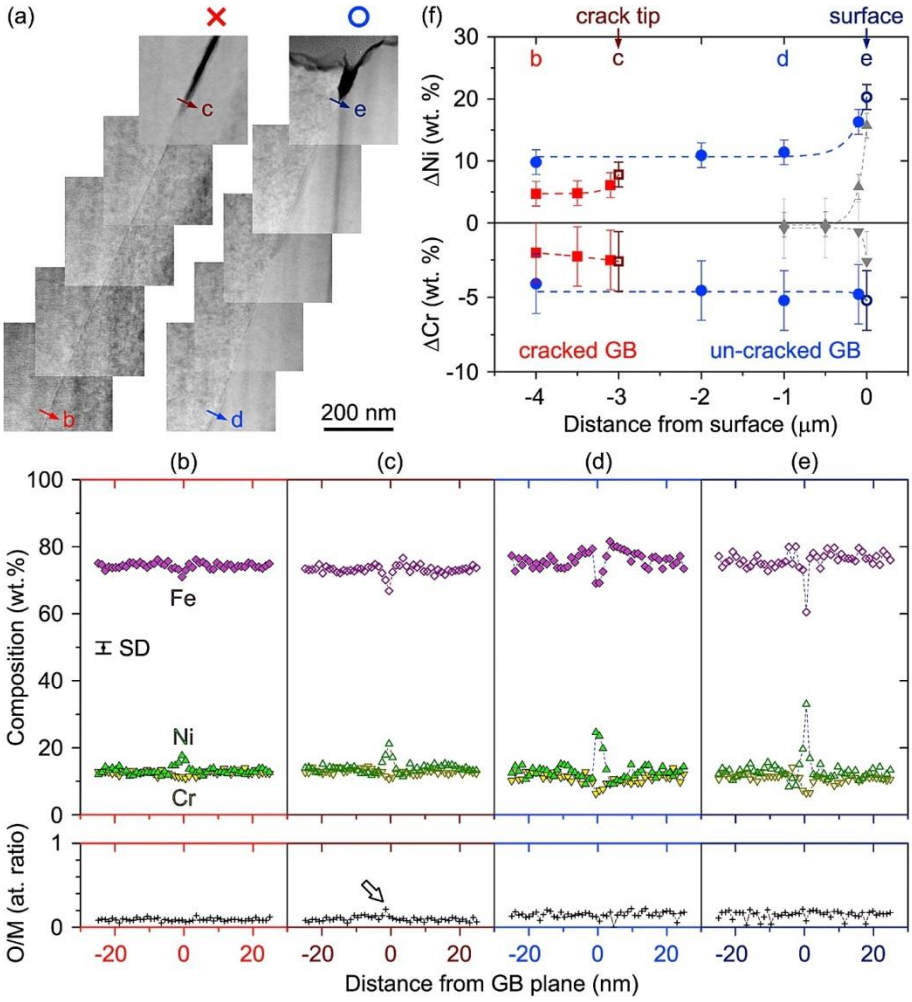

Figure 4.7: Representative measurements of GB composition. (a) GBs under the cracked (left) and un-cracked (right) sites, respectively. Both GB sites are viewed edge-on. (b–e) EDS line-scan profiles along arrows b-e in (a): c is beyond crack tip, e is under un-cracked surface (c is indeed ~3 μm deeper than e); b and d are ~1 μm deeper than c and e, respectively. Error bar shows standard deviation (SD) at each measurement point. (f) Changes in GB composition, i.e., enrichment of Ni (upper half) and depletion of Cr (lower half), as a function of distance from the un-cracked surface in (a). All curves are fit with an exponential function, which is arbitrarily used to sketch the enhanced variation in the vicinity of reaction front. Change of GB composition near the surface of un-irradiated samples is represented by grey symbols.Taken from [35]

At a position far from the sample surface, the grain boundary chemistry is representative of chemistry that develops due to the proton irradiation of the material. This effect is beyond the hardening of the sample matrix, and is limited to a very small region on either side of the grain boundary. From these scans it is observed that chromium is depleted up to 5% while nickel is enriched to between 5-10% depending on the specific location along the grain boundary. The magnitude of depletion/enrichment and the length scale for these microchemical changes (2-3 nm on either side of the GB) are consistent with typical RIS

profiles. Since the alloys being used in this study are lab purity alloys with very low carbon content, there isn't a significant source of carbon or other impurities to create secondary phases on or near the grain boundary which could act as stress concentrators or preferential sites for cracking the boundary.

4.2 Grain Boundary Plane Determination

One feature of the current work compared to previous studies is that additional work was performed to determine the grain boundary plane angle relative to the sample surface so that the full grain boundary orientation could be determined in the sample reference frame. This was performed through a process of serial sectioning and EBSD analysis as outlined in Chapter 3. In order to determine the grain boundary plane angle through serial sectioning, two things are needed; the thickness of material removed from the sample surface and the perpendicular distance between the grain boundary location before and after polishing. A simple diagram outlining this calculation is presented in Figure 4.8.

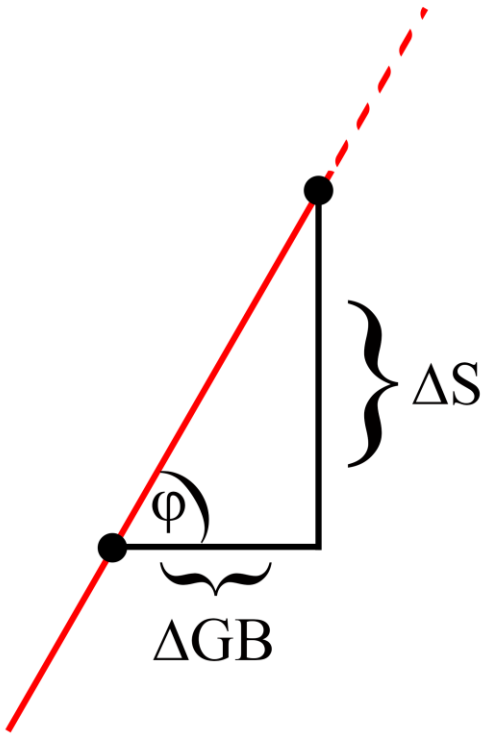

Figure 4.8:Diagram showing the calculation of the grain boundary plane angle using serial sectioning and EBSD

ΔS is thickness of material removed from the sample surface, ΔGB is the change in location of the specific grain boundary, and φ is defined as the grain boundary plane angle which is calculated from the formula:

$$\varphi = \tan^{-1}\left(\frac{\Delta S}{\Delta GB}\right). \qquad (4.1)$$

Mechanical polishing was selected due to the fact that chemical polishing would decrease the accuracy to which the thickness of material removed from the surface could be calculated. Chemical polishing is sensitive to the local geometry of the sample, and will attack the areas

around hardness indents and the edges of the tensile bar samples at a different rate compared to the central flat region of the gauge section. Thickness removal would then be estimated using a polishing for either the Fe13Cr15Ni or Fe13Cr15Ni. Since controlling the exact conditions during electropolishing or other forms of chemical polishing is difficult, the errors on the amount of material removed during this process can be high especially when there isn't a direct measurement being made to determine the height of material being removed. With chemical polishing methods, it is also difficult to determine if the thickness of material removed is uniform across the gauge length of the tensile bar samples. Since the calculated value of φ is sensitive to small changes in ΔS, variation of the removed thickness would have a large effect on the calculated grain boundary plane angles if local variations are not accounted for in the calculation of φ. Hardness indents that were initially placed on the sample surface to mark specific regions for EBSD analysis were used to track the thickness of material removed from the sample. Since the mechanical polish with 20 nm colloidal silica does not remove material from the bottom of the indent, the change in depth of the indent before and after polishing gives a reasonable value for the thickness removed. Figure 4.9 shows a line scan performed across the center of an indent on the ASCC2 Fe13Cr15Ni 5 dpa sample and the subsequent height profile as measured before and after mechanical polishing.

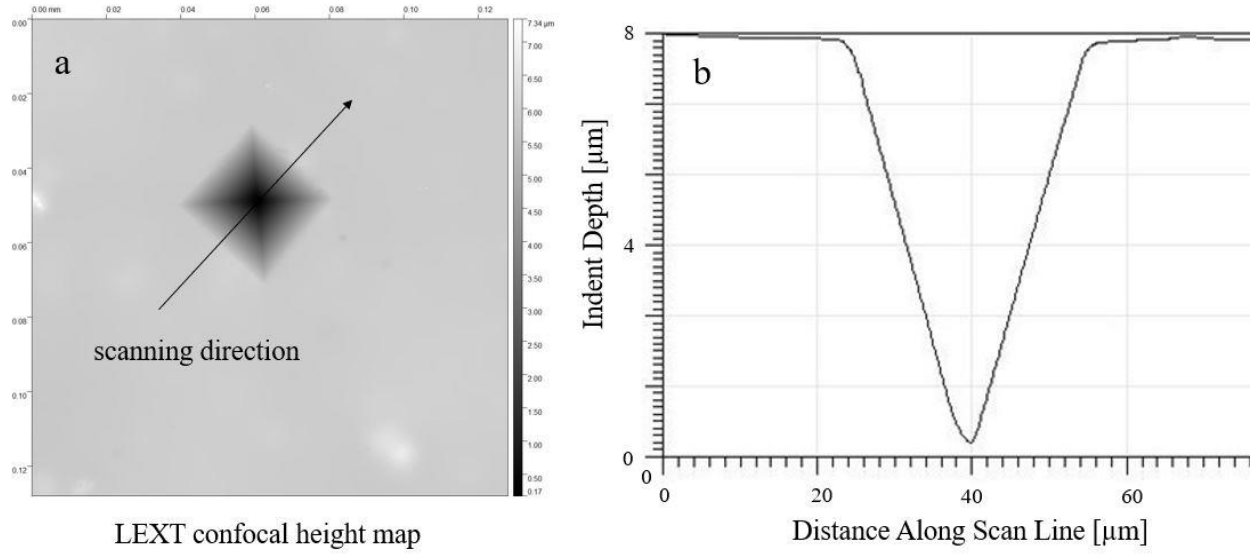

Figure 4.9: Representative LEXT confocal laser measurement for a) the 2D depth distribution of a hardness indent and b) the line scan profile to determine the depth of the indent in the ASCC2 Fe13Cr15Ni 5 dpa sample.

To ensure that detectable amounts of grain boundary translation, ~5µm of material was removed from the sample surface. The amount of material removed from the sample surface did show small amounts of variation across the gauge section of the tensile bar. Figure 4.10 shows the indent height measurements before and after polishing along the full length of the EBSD analyzed gauge length for the ASCC2 Fe13Cr15Ni 5 dpa tensile bar sample.

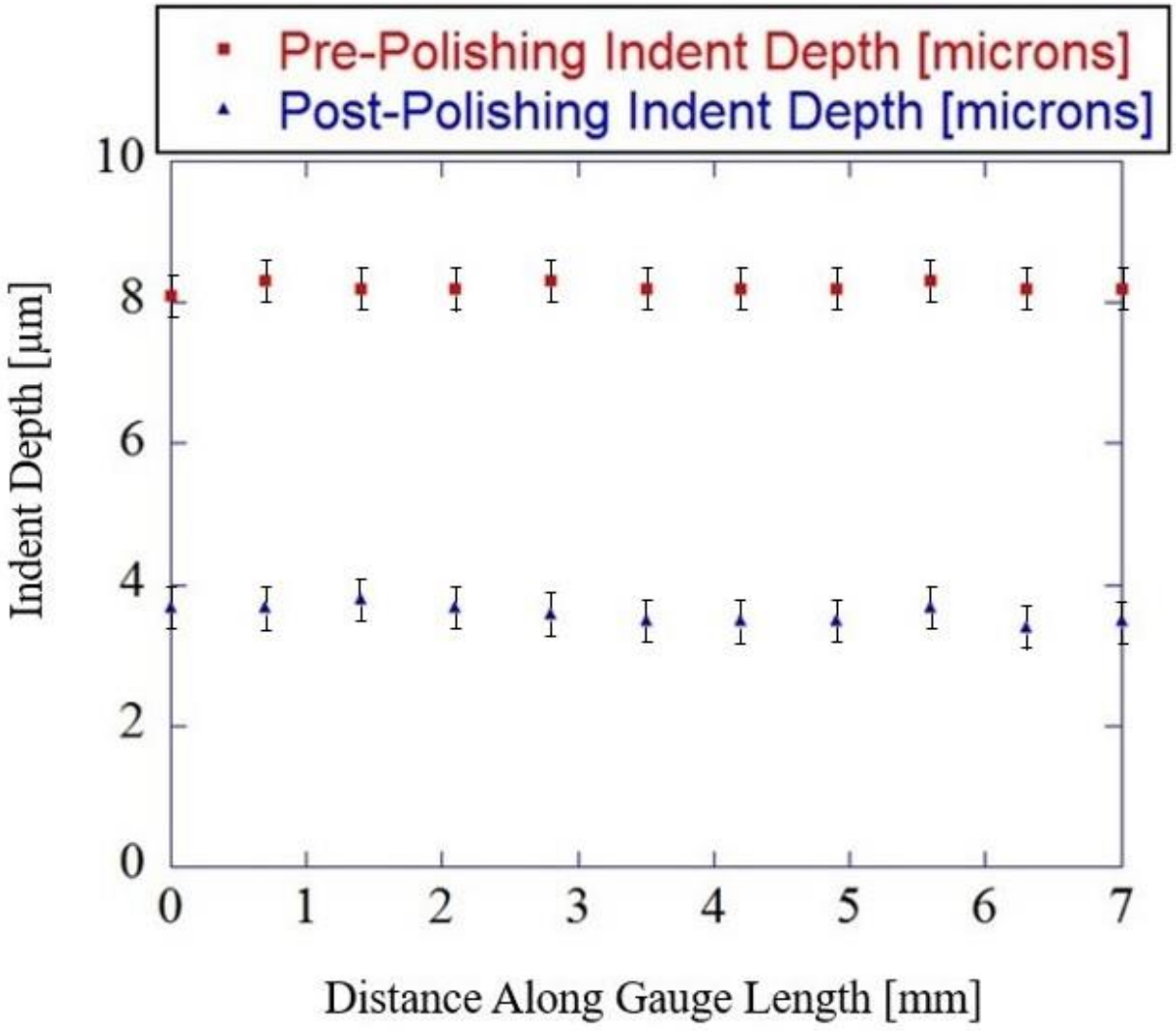

Figure 4.10: Measurements of indent depth over the tensile bar gauge length before and after mechanically polishing with 20 nm colloidal silica in the ASCC2 Fe13Cr15Ni 5 dpa tensile bar.

The variation observed was less than 10% and the grain boundary plane measurements were made using the indent height measurements closest to the EBSD scanned region in order to decrease the errors in these measurements.

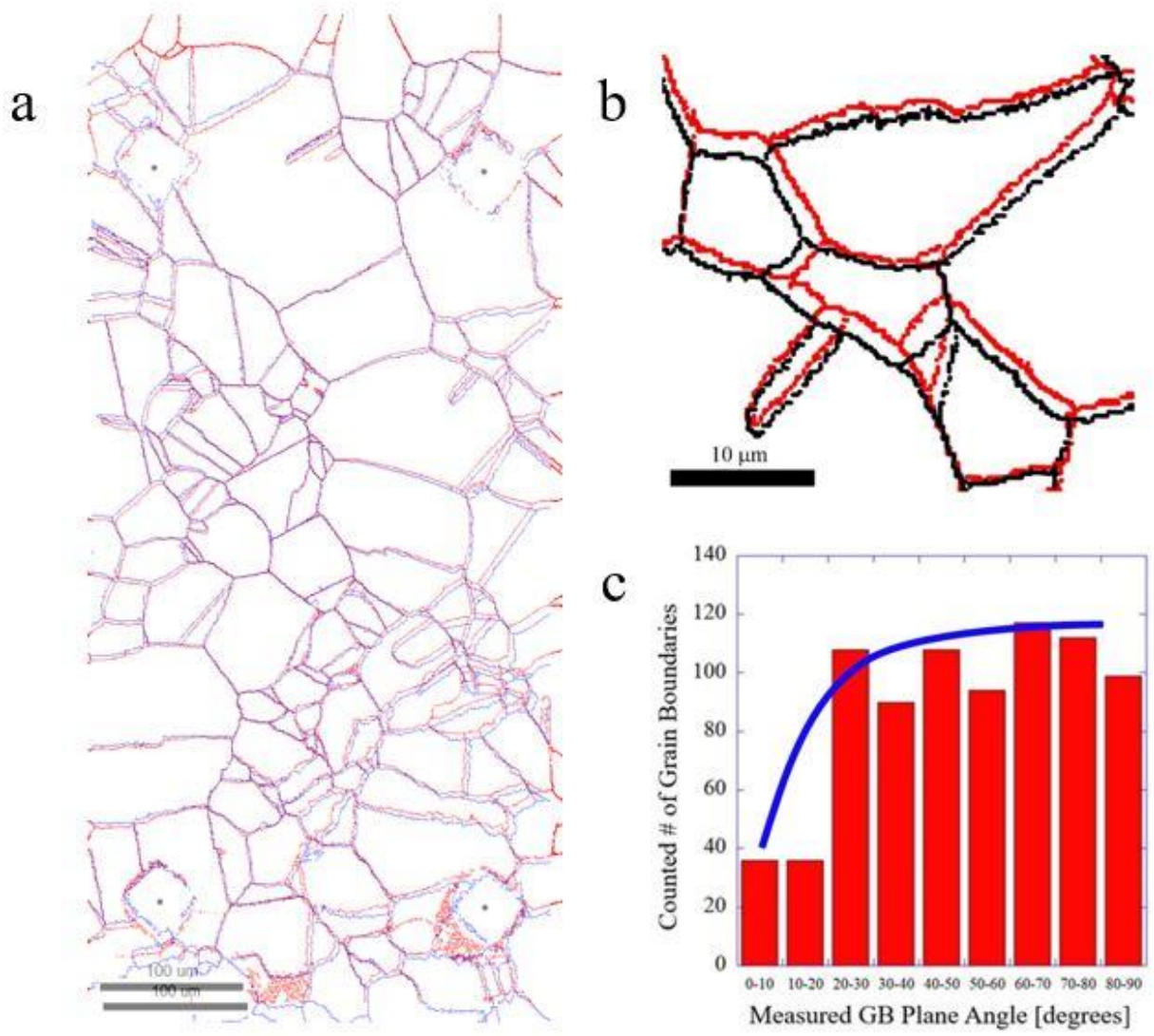

Figure 4.11:a) Superimposed grain boundary maps used for determining grain boundary plane angles including b) a close up cluster of grains for visualizing the movement of individual bounadries and c) the distribution of measured grain boundary plane angles in the ASCC2 Fe13Cr15Ni Tensile bar sample

Figure 4.11a shows a large area scan and Figure 4.11b shows a magnified region with EBSD grain boundary maps after polishing superimposed on those prior to polishing. Clear translation of the grain boundary location is observed between the two maps. Not every orientation of grain boundary plane angle is equally likely to intersect the sample surface. As the grain boundary plane angle φ as defined above decreases, the grain boundary becomes more parallel with the

sample surface. Since the current measurement technique is looking at two distinct slices in the material, a grain boundary plane oriented nearly parallel to the sample surface has a very low likelihood of intersecting the surface during one or both of the EBSD scans. The probability of a discrete slice through the material intersecting a specific grain boundary plane orientation is thus related to the projected height of the grain boundary, which is proportional to the cosine of the grain boundary plane angle, φ. Figure 4.12 shows a diagram of three grain boundaries of equal length, but varying grain boundary plane angles.

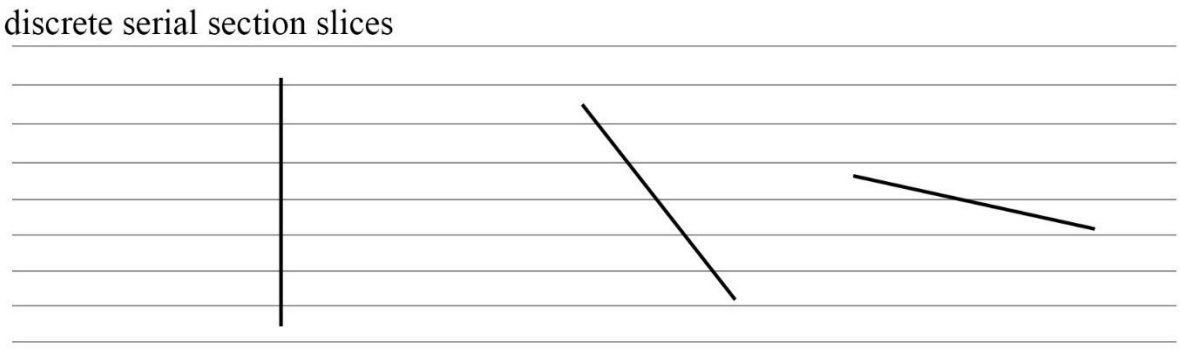

Figure 4.12: Diagram showing the intersection of discrete serial section slices intersecting a grain boundary at 3 different grain boundary plane angles.

This is equivalent to keeping the size and shape of a grain constant while only changing its orientation relative to the sample surface. Although each orientation of the grain is equally probable, the probability of intersecting that specific grain boundary with a discrete slice through the material is orientation dependent. If the slice thickness was made to be infinitesimally small, then the distribution of grain boundary plane angles would be uniform since there is no preferential orientations for the grains. Changes to this uniform distribution are due to the fact that coarse serial section slices are made during analysis. Therefore when measuring the grain boundary plane angles across a large area of the sample surface, the number of measurements

made at very shallow plane angles should be significantly less than the number measured close to perpendicular. Figure 4.11c shows the measured distribution of grain boundary plane angles from the ASCC2 Fe13Cr15Ni 5 dpa tensile bar sample. As expected, the number of measurements made at low plane angles is much less than the number of measurements at high plane angles. The theoretical distribution of plane angle measurements, which follows a cosine of the grain boundary plane angle, is superimposed in blue and fits the data well. A full collection of grain boundary maps used to determine grain boundary plane angles is presented in Appendix C.

4.3 Deformation in an Inert Environment

CERT tests were performed in 288 ˚C argon to compare the relative deformation response without the influence of a corrosive environment. All tests performed in argon were conducted at the same strain rate of $3x10^{-7}$ s^{-1}. To produce quantifiable residual stresses in the material, samples were deformed under uniaxial load up to 4.5% plastic strain. The stress-strain diagram for the tested Fe13Cr15Ni tensile bar is shown in Figure 4.13 and the total elapsed time spent at 288 ˚C was 68 hours.

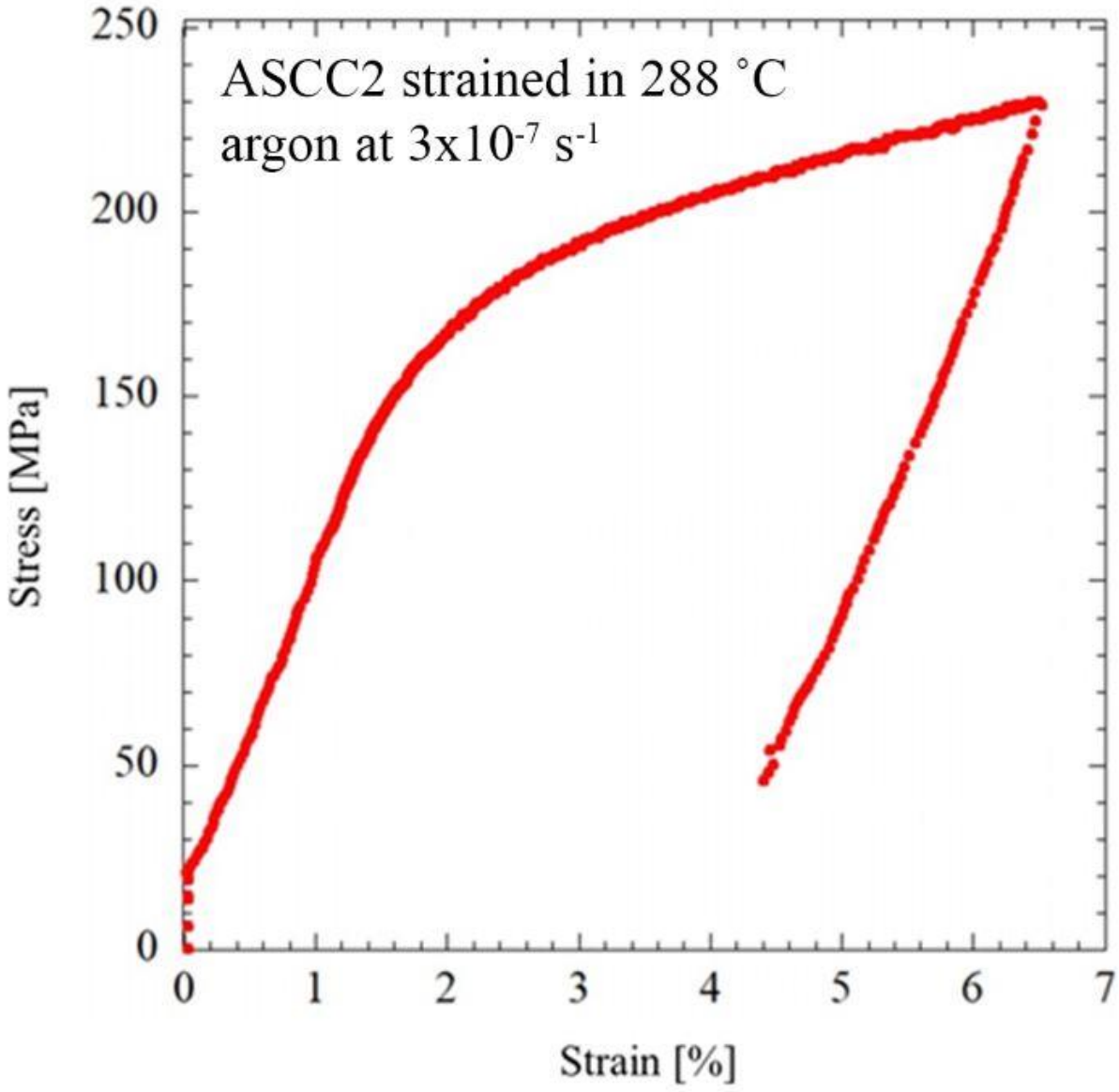

Figure 4.13: Stress-strain diagram for ASCC2 Fe13Cr15Ni 5 dpa tensile bar sample strained in uniaxial tension at 288 ˚C in an inert argon environment from 0% to 4.5% plastic strain at a strain rate of $3x10^{-7}$ s^{-1}.

Since only a small fraction of the tensile bar sample is irradiated, the macroscopically observed stress-strain behavior is the same as that of the non-irradiated metal. Uniform elongation was observed up to a value of ~1.5% prior to the onset of plastic deformation. The sample experienced strain hardening, with the engineering stress increasing during the entirety of the experiment. Both the irradiated and non-irradiated sections of the tensile bar were checked for

any potential crack initiation sites. However, no grain boundary fracture was observed after the inert environment straining, as expected. A very clear division was observable between the irradiated and non-irradiated sections of the tensile bar after this initial straining in an inert environment. The non-irradiated section favored homogeneous slip as its microstructure did not contain many of the defects which obstruct dislocation motion in the irradiated zone. Figure 4.14 is taken using the LEXT confocal laser microscope, described earlier in the methods chapter, at the interface between the irradiated and non-irradiated regions on the sample surface after straining in high temperature argon. Even at lower magnification (10x) the dislocation channels are visible in the irradiated zone, while distinct lines of much closer spacing are only seen on a couple grains in the non-irradiated zone. The surface of the non-irradiated region appears to have significantly more variation in the topography which is evidence of grain rotation. The lack of appreciable defect population in the non-irradiated region allows for more freedom in how clusters of grains accommodate strain. The harder irradiated region has more constraints for deformation and therefore the same topography is not observed in the irradiated section of the tensile bar.

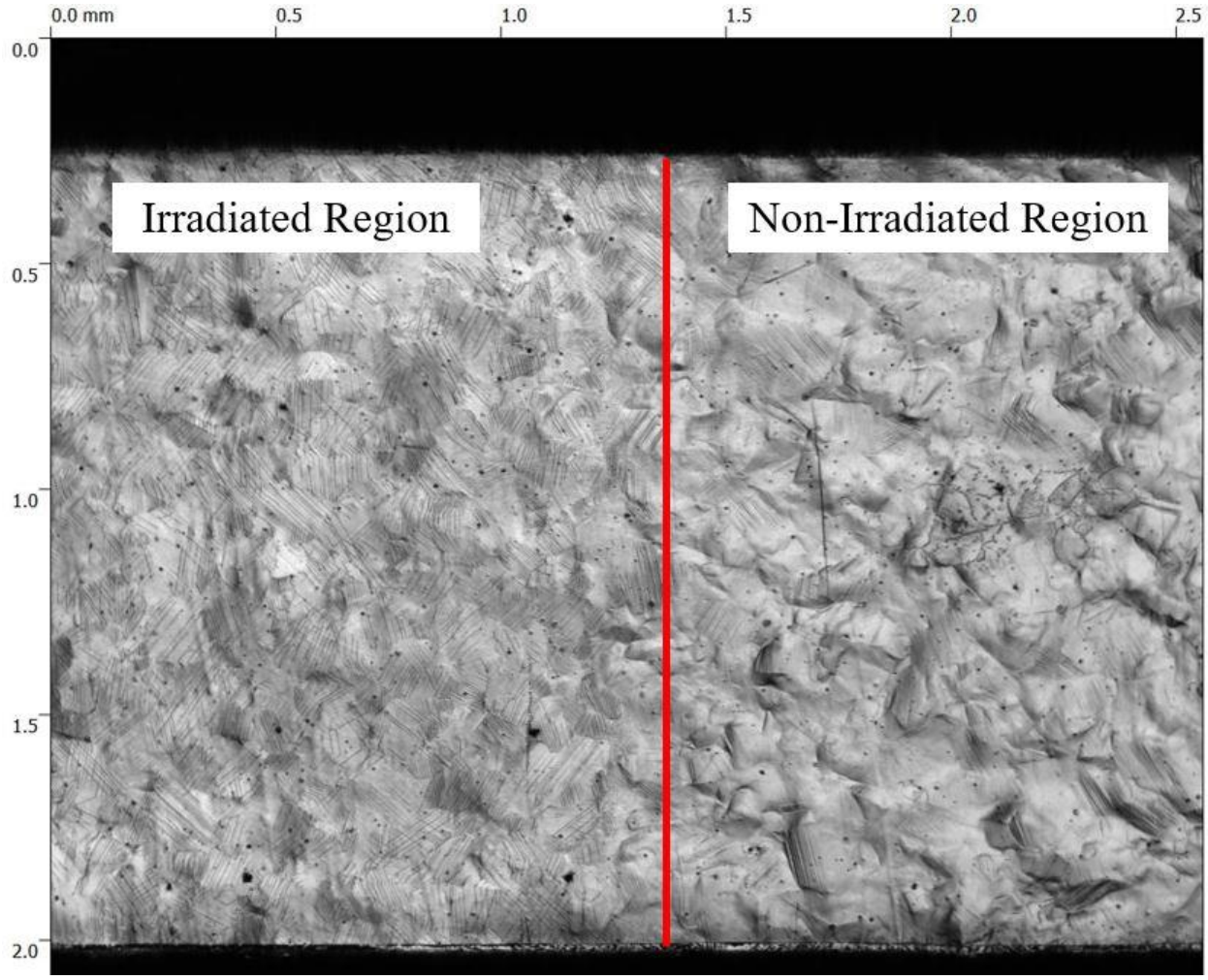

Figure 4.14: LEXT laser confocal image taken at 10x at the interface between the irradiated and non-irradiated regions of the ASCC2 Fe13Cr15Ni 5dpa tensile bar after 4.5% plastic strain in 288 ºC argon at $3x10^{-7}$ s^{-1}.

Dislocation channeling was characterized for both alloys after the same amount of plastic deformation. After 4.5% plastic strain in 288 ˚C argon, special attention was paid to the number of slip systems that were activated in each grain as well as the behavior of the channel once it intersected a grain boundary. An active slip system was defined by the visible channels on the sample surface, with each slip system having a unique orientation with respect to the loading axis. Different slip directions on the same plane could not be distinguished, nor could slip systems that did not contain an appreciable component of their Burgers vector normal to the

sample surface. Slip systems with a Burgers vector oriented nearly parallel with the sample surface would not generate a distinguishable step height on the sample surface and therefore would not show up as a distinct line in SEM images. To be counted as an active slip system, more than one channel attributed to that system must be visible, which appears as parallel lines on the sample surface. The number of active slip systems per grain for the two alloys is presented in Table 4.5 for the same number of randomly sampled grains near the center point of their respective irradiated regions. For this characterization, dislocation channel traces on the sample surface were observed in both SEM and confocal laser microscopes and each distinct set of parallel lines was assumed to be a separate slip system. Representative images for differing numbers of active slip systems are shown in Figure 4.15. For the purpose of comparison, the same number of grains were analyzed from both the ASCC2 and BSCC2 tensile bar samples after a 4.5% straining increment in 288 °C at $3x10^{-7}$ s^{-1}.

Table 4.5. Number of active slip systems in Fe13Cr15Ni and Fe21Cr32Ni after 4.5% plastic strain in 288 ˚C argon at $3x10^{-7}$ s^{-1}.

Number of active slip systems	Fe13Cr15Ni [ASCC2]	Fe21Cr32Ni [BSCC2]
0	88	69
1	359	296
2	301	341
3	57	99
Total	805	805

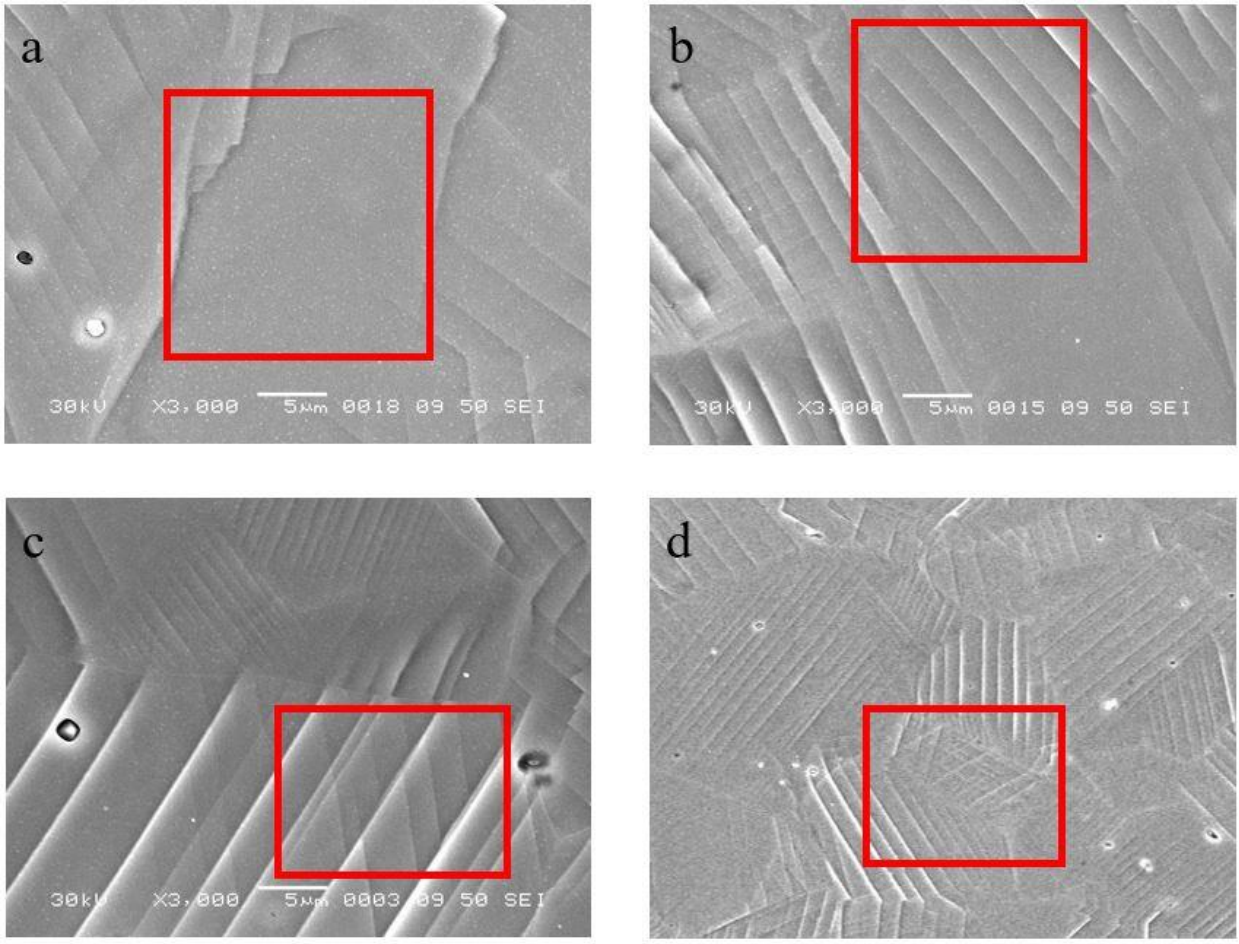

Figure 4.15: SEM images from ASCC2 Fe13Cr15Ni 5 dpa tensile bar sample irradiated region showing representative examples of (a) 0 active slip systems (b) 1 active slip system (c) 2 active slip systems and (d) 3 active slip systems

Grain boundaries were characterized as either allowing slip, which resulted in a continuous channel across the grain boundary, or as discontinuous if the channel happened to be visibly arrested at the grain boundary. It is possible that some deformation could progress along the grain boundary itself, but from the definition provided here these boundaries would be categorized as discontinuous. Figure 4.16 depicts a collection of representative SEM images showing continuous channels taken from the ASCC2 Fe13Cr15Ni sample after argon straining and Figure 4.17 shows a collection of discontinuous channels taken from the same sample. Red

boxes in Figures 4.15 and 4.16 are placed to draw attention to a specific grain boundary or region of the micrograph.

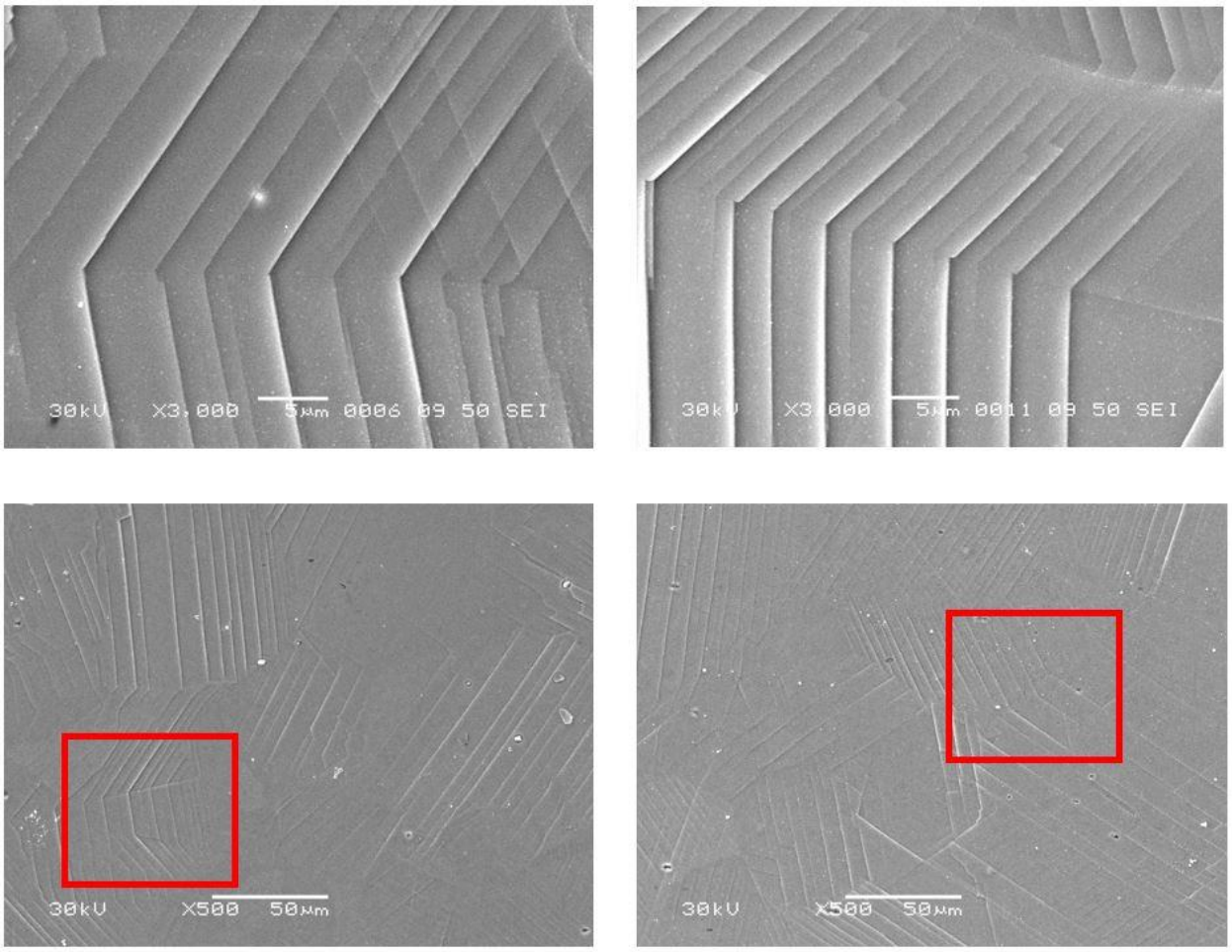

Figure 4.16: Representative SEM images taken from ASCC2 Fe13Cr15Ni 5 dpa tensile bar sample after 4.5% plastic strain in 288 ºC argon at $3x10^{-7}$ s^{-1} showing continuous dislocation channels.

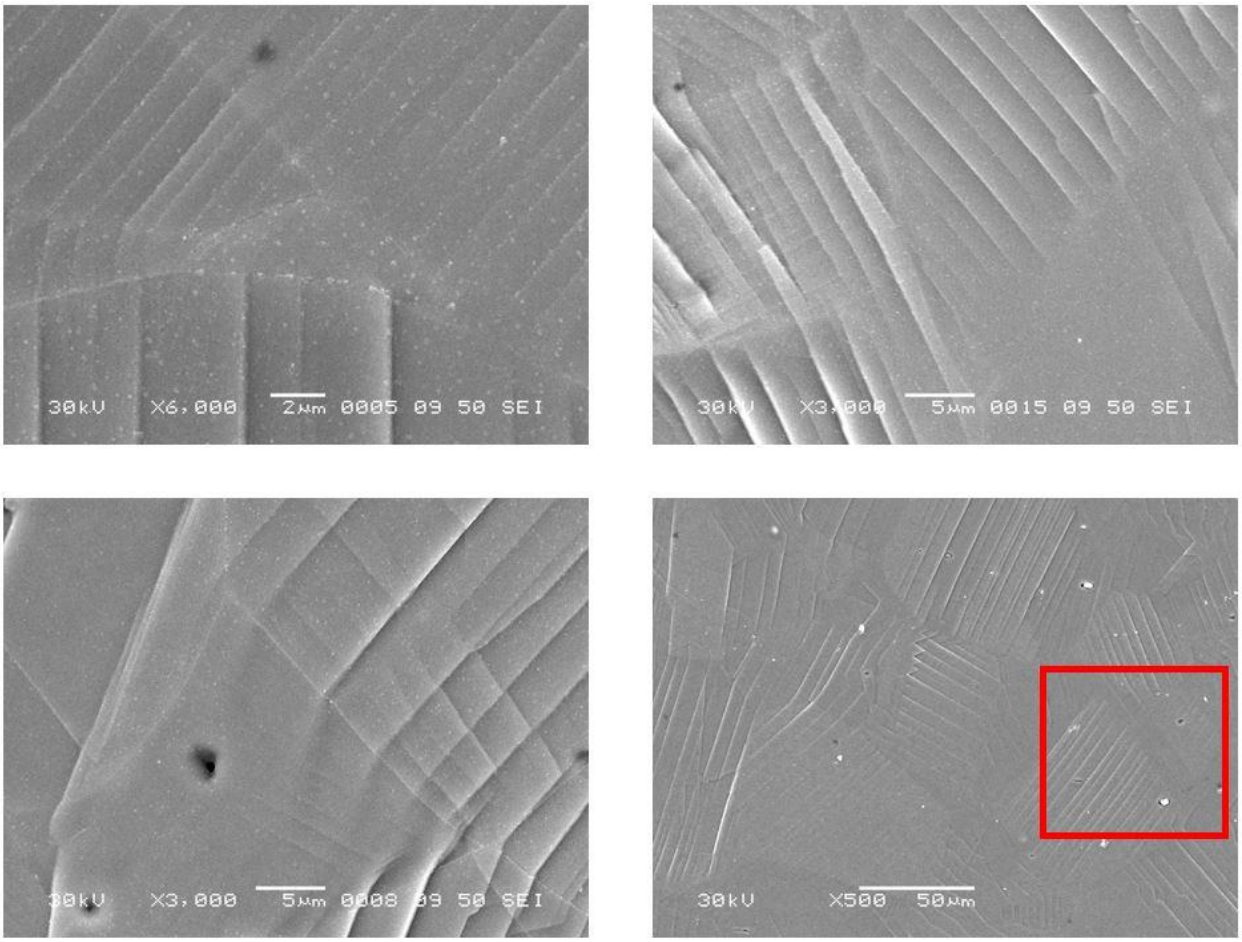

Figure 4.17:Representative SEM images taken from ASCC2 Fe13Cr15Ni 5 dpa sample after 4.5% plastic strain in 288 °C argon at $3x10^{-7}$ s^{-1} showing discontinuous dislocation channels.

Data on general slip continuity of both alloys is presented in Table 4.6. These results were taken after both alloys were strained to 4.5% plastic stain in an inert argon environment at 288 ˚C at a strain rate of $3x10^{-7}$ s^{-1}. It is important to note here that after 4.5% plastic strain, the dominant interaction type of dislocation channels at the grain boundary is continuous in nature. Through subsequent straining, it is possible for dislocation channels which were previously classified as discontinuous to become continuous. However, the fraction of channels that change after this initial level of straining is small and does not dramatically change the ratio of continuous to discontinuous interaction sites. It is also possible for a single boundary to exhibit both

continuous and discontinuous channels along the same boundary. To eliminate any confusion, these heterogeneous slip transfer boundaries were neglected for this part of the study.

Table 4.6. Slip continuity at dislocation channel – grain boundary interaction sites

	Fe13Cr15Ni [ASCC2]	Fe21Cr32Ni [BSCC2]
Continuous Slip	406	388
Discontinuous Slip	94	112
Total	500	500

Imaging and identification of the slip channels was facilitated by the use of a confocal laser microscope, since dislocation channels made clearly visible height changes across the sample surface. The Gwyddion scanning probe microscopy data visualization and analysis software was utilized to calculate the step heights of specific channels. A magnification of 100x and a working distance of 0.35 mm was used for each of the measurements. An intensity map was produced for each scan which uses the amount of reflected laser light to determine the distance between the light source and features on the sample surface. Figure 4.17 shows an optical image generated from the LEXT confocal microscope and the accompanying height profile.

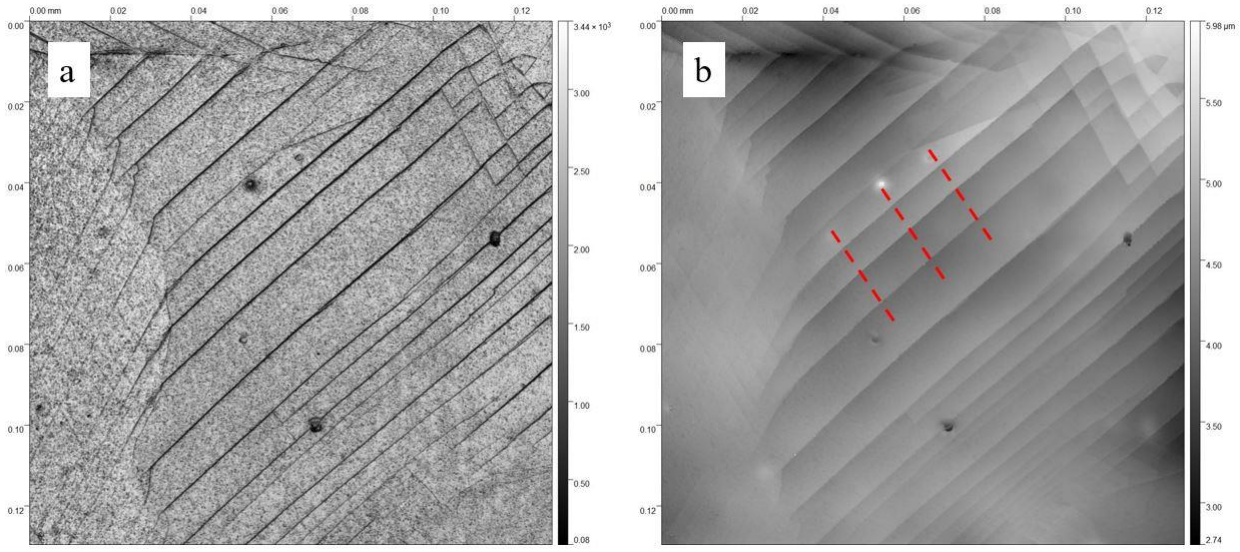

Figure 4.18:LEXT confocal images taken from a working distance of 0.35mm and 100x on the surface of the ASCC2 Fe13Cr15Ni 5 dpa sample after 4.5% strain at $3x10^{-7}$ s^{-1} showing a) an optical micrograph and b) the generated height distribution map. Dashed red lines denote the location of height profile line scans

Channel heights are measured three times in different places along the channel to capture any variation in the height within the grain. Each scan line has a width of 5 pixels to assist in getting an accurate value for the average step height in the grain. The three locations of the height measurement scans are shown as dashed red lines in the intensity map in Figure 4.18 and the step height profiles shown in Figure 4.19. This shows a generalized result for step height measurement, but the collection of scans made for determining channel step height distribution are presented in appendix B.

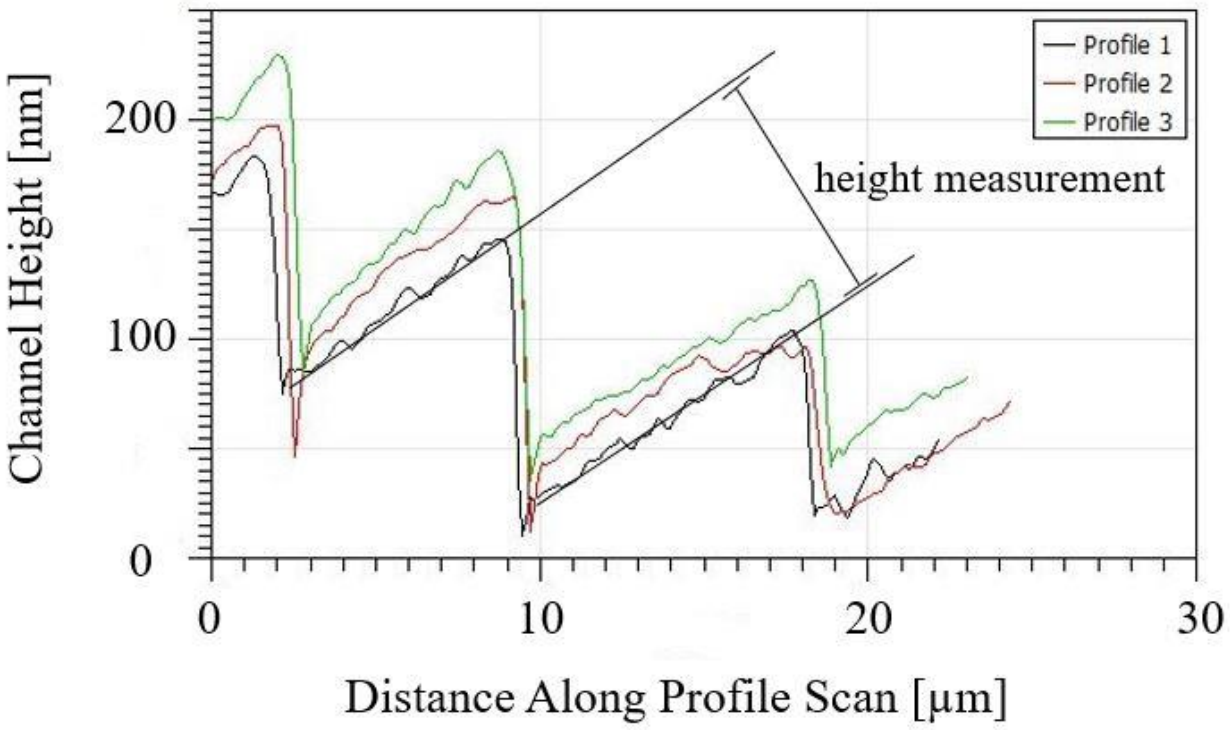

Figure 4.19: Step height profile line scan taken from LEXT confocal laser microscope (Figure 4.18) showing the step height measurement of a single channel in the ASCC2 Fe13Cr15Ni tensile bar sample.

The out of plane deformation measurements ranged from 38 nm to 690 nm of total displacement. The distribution of these channel heights is presented in Figure 4.20. From here it is observed that the majority of step heights fall within the range of 100-200 nm.

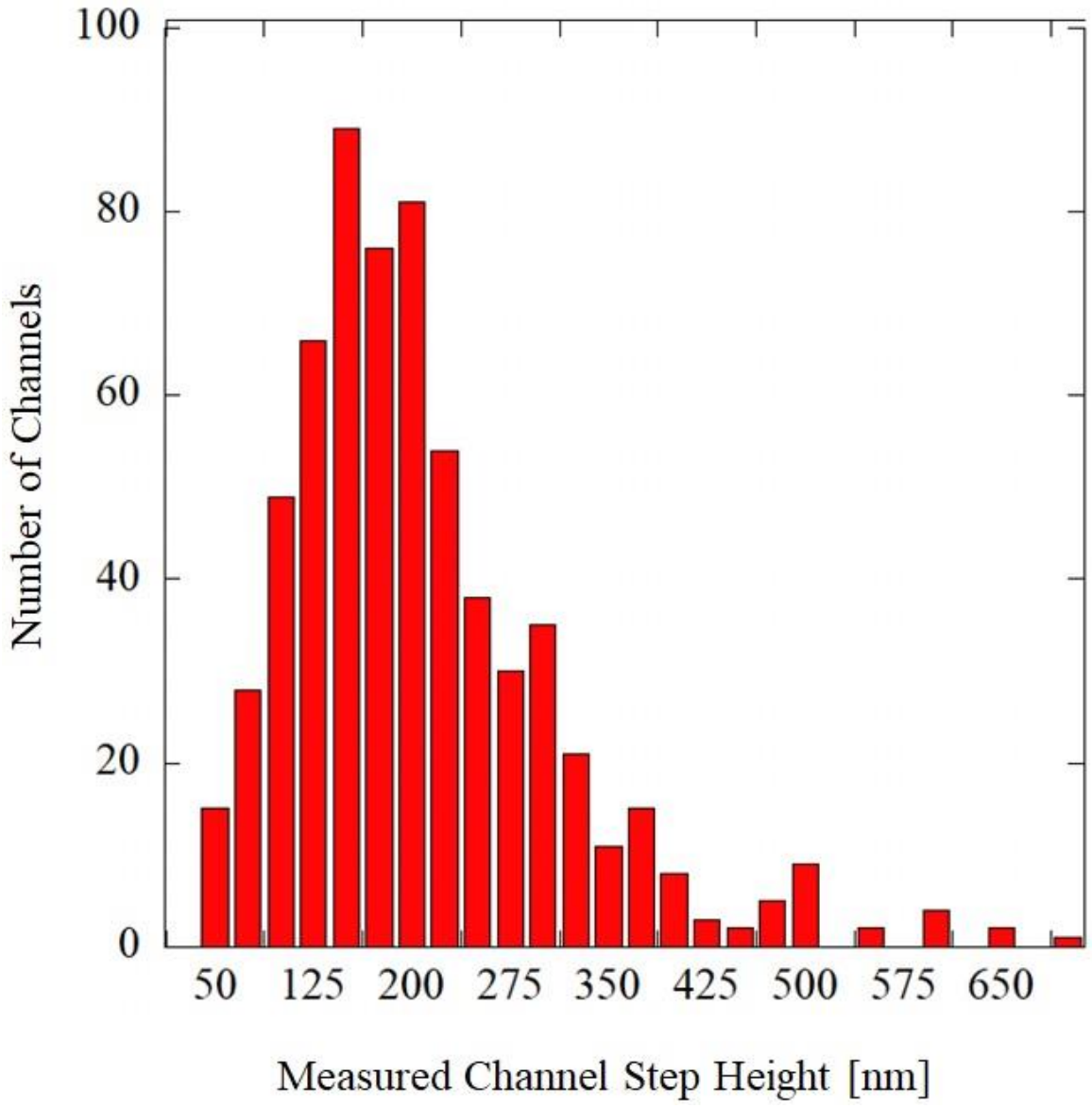

Figure 4.20: Distribution of dislocation channel heights measured by confocal laser microscope in ASCC2 Fe13Cr15Ni 5 dpa tensile bar sample after 4.5 % plastic strain in 288 °C argon at $3x10^{-7}$ s^{-1}.

As the number of dislocations passing through a channel increases, so does the step height. However this process doesn't happen endlessly. As certain obstacles are encountered by glissile dislocations, the activity of specific slip systems will be halted. Increased stresses could continue the motion of dislocations within the channel, but these higher stresses tend to activate secondary channels belonging to the same slip system rather than continuing to deform in the initial channel

or have the ability to activate a completely new slip system as is seen in Figure 4.15 where multiple slip systems are visible within a single grain. There is variation in the channel step heights within a single grain since all of the channels form at different times during the deformation process, but these differences are not typically dramatic.

4.4 HREBSD site selection

While HREBSD is a valuable tool for investigating the stress state near dislocation channel – grain boundary interaction sites, the data collection and subsequent analysis is very labor intensive. Due to this, only a small subset of the grains present in the material can be analyzed. For the ASCC2 Fe13Cr15Ni 5 dpa sample, 75 grain boundaries were selected for analysis with HREBSD with each of these grain boundaries displaying a discontinuous channel impinging on the boundary. From the EBSD analysis and serial section technique presented previously in this section, both the geometric orientation of the grain boundary and the crystallographic orientation of each grain is known. Previous studies have been able to correlate the grain boundary trace angle with intergranular fracture under the assumption that these grain boundaries had a large component of tensile stress acting normal to the grain boundary. Since the grain boundary normal is known, the offset between the grain boundary normal and the loading axis can be used as a metric for how well aligned a specific grain boundary is with the uniaxial tensile stress being applied externally during slow strain rate tensile testing. Figure 4.21 shows a diagram of the grain boundary normal offset angle, α, with respect to the loading axis.

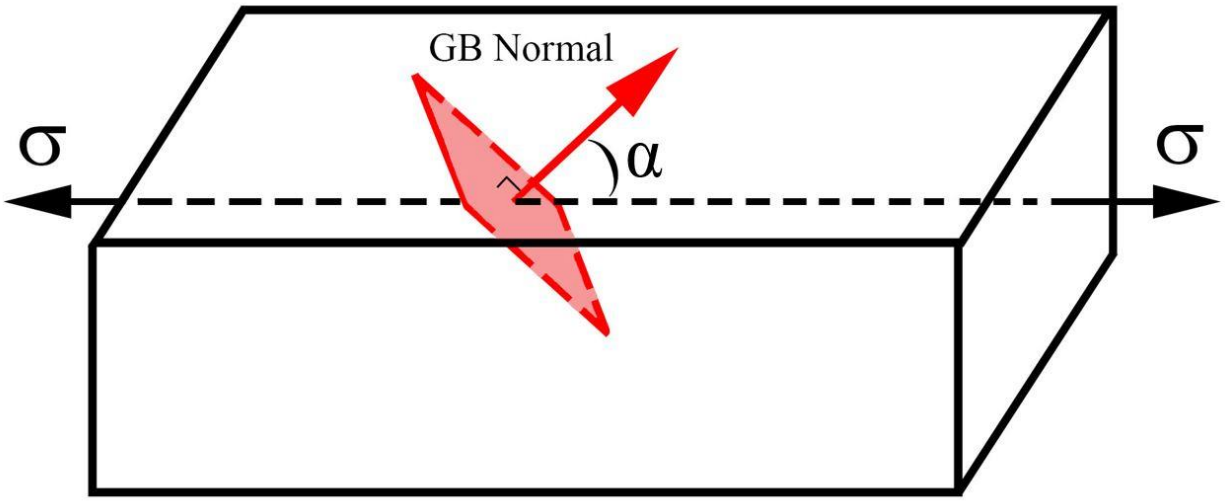

Figure 4.21: Diagram detailing the grain boundary normal offset angle, α, with respect to the loading axis

To incorporate information about the active slip system that is generating the dislocation channels, the Schmid factor is used. With a larger Schmid factor, the grain has a slip system oriented with respect to the loading axis such that the resolved shear stress is high. With a high resolved shear stress on this slip system there is a greater driving force to generate dislocations and push them through the irradiation damage defect matrix. This should result in a larger number of dislocations participating in the pile-up event at the intersection between the grain boundary and discontinuous channels. A new value, the Orientation Factor, is used to incorporate both the geometric orientation of the grain boundary and the crystallographic orientation of the deforming grain. The Orientation Factor is defined by:

$$Orientation\ Factor = Schmid\ Factor * Cos(\alpha). \quad (4.2)$$

For high values of the Orientation factor the grain boundary will be oriented close to perpendicular to the loading axis and the slip system responsible for generating the dislocation channel is also favorably oriented with respect to the applied load. Theoretically sites that have a

large Orientation Factor should have a large component of stress acting perpendicular to that specific grain boundary. The 75 grain boundaries selected from the ASCC2 Fe13Cr15Ni 5 dpa tensile bar sample were split into two separate categories; well oriented and poorly oriented grain boundaries based on the calculated Orientation Factor. Well oriented boundaries were those that had an Orientation Factor greater 0.35. To understand the effect of both types of orientation on the behavior of the material, boundaries were selected uniformly across the orientation space such that the number of sites with preferable orientations (those with an Orientation Factor greater than 0.35) was roughly equal to the number of analyzed sites with poor orientations. Table 4.7 lists the geometric and crystallographic orientations of selected sites that were analyzed by HREBSD.

Table 4.7. Grain boundary geometric and crystallographic orientations for HREBSD selected sites in ASCC2 Fe13Cr15Ni 5 dpa tensile bar sample

Grain Boundary ID	GB Offset [Cos (α)]	Schmid Factor	Orientation Factor
ASCC2-1	0.90	0.49	0.44
ASCC2-2	0.83	0.45	0.37
ASCC2-3	0.95	0.49	0.47
ASCC2-4	0.86	0.45	0.39
ASCC2-5	0.83	0.48	0.40
ASCC2-6	0.89	0.42	0.38
ASCC2-7	0.96	0.47	0.45
ASCC2-8	0.85	0.41	0.35
ASCC2-9	0.90	0.45	0.41
ASCC2-10	0.86	0.45	0.39
ASCC2-11	0.98	0.4	0.39
ASCC2-12	0.87	0.39	0.34
ASCC2-13	0.86	0.43	0.37
ASCC2-14	0.95	0.44	0.42
ASCC2-15	0.89	0.47	0.42
ASCC2-16	0.87	0.46	0.40
ASCC2-17	0.85	0.46	0.39
ASCC2-18	0.80	0.46	0.37
ASCC2-19	0.88	0.38	0.34

ASCC2-20	0.92	0.43	0.39
ASCC2-21	0.85	0.44	0.38
ASCC2-22	0.79	0.4	0.32
ASCC2-23	0.82	0.48	0.39
ASCC2-24	0.83	0.45	0.37
ASCC2-25	0.86	0.43	0.37
ASCC2-26	0.86	0.47	0.40
ASCC2-27	0.85	0.42	0.36
ASCC2-28	0.83	0.39	0.33
ASCC2-29	0.86	0.41	0.35
ASCC2-30	0.82	0.47	0.39
ASCC2-31	0.94	0.45	0.42
ASCC2-32	0.87	0.46	0.40
ASCC2-33	0.93	0.45	0.42
ASCC2-34	0.83	0.44	0.36
ASCC2-35	0.91	0.45	0.41
ASCC2-36	0.81	0.46	0.37
ASCC2-37	0.96	0.46	0.44
ASCC2-38	0.94	0.47	0.44
ASCC2-39	0.87	0.4	0.35
ASCC2-40	0.85	0.48	0.41
ASCC2-41	0.92	0.47	0.43
ASCC2-42	0.97	0.49	0.47
ASCC2-43	0.93	0.45	0.42
ASCC2-44	0.96	0.43	0.41
ASCC2-45	0.98	0.47	0.46
ASCC2-46	0.95	0.47	0.45
ASCC2-47	0.87	0.4	0.35
ASCC2-48	0.92	0.4	0.37
ASCC2-49	0.89	0.43	0.38
ASCC2-50	0.90	0.39	0.35
ASCC2-51	0.71	0.43	0.30
ASCC2-52	0.65	0.39	0.25
ASCC2-53	0.60	0.45	0.27
ASCC2-54	0.59	0.42	0.25
ASCC2-55	0.70	0.47	0.33
ASCC2-56	0.67	0.48	0.32
ASCC2-57	0.62	0.42	0.26
ASCC2-58	0.58	0.39	0.23
ASCC2-59	0.64	0.46	0.30
ASCC2-60	0.62	0.47	0.29

ASCC2-61	0.68	0.44	0.30
ASCC2-62	0.61	0.42	0.26
ASCC2-63	0.65	0.5	0.32
ASCC2-64	0.70	0.45	0.31
ASCC2-65	0.61	0.39	0.24
ASCC2-66	0.67	0.43	0.29
ASCC2-67	0.60	0.48	0.29
ASCC2-68	0.58	0.41	0.24
ASCC2-69	0.60	0.41	0.24
ASCC2-70	0.68	0.44	0.30
ASCC2-71	0.66	0.46	0.30
ASCC2-72	0.64	0.41	0.26
ASCC2-73	0.62	0.47	0.29
ASCC2-74	0.58	0.45	0.26
ASCC2-75	0.71	0.48	0.34

Fe21Cr32Ni has been previously studied and has been shown to have low cracking susceptibility. In order to increase the chances of analyzing a site which ultimately cracks during subsequent straining in high temperature water, only sites which were well oriented for cracking were selected for analysis. In total 40 sites were characterized using HREBSD and the orientations of the selected sites are listed in Table 4.8.

Table 4.8 Grain boundary geometric and crystallographic orientations for HREBSD selected sites in BSCC2 Fe21Cr32Ni 5 dpa tensile bar sample

Grain Boundary ID	**GB Offset [Cos(α)]**	**Schmid Factor**	**Orientation Factor**
BSCC2-1	0.85	0.41	0.35
BSCC2-2	0.9	0.45	0.41
BSCC2-3	0.86	0.45	0.39
BSCC2-4	0.98	0.4	0.39
BSCC2-5	0.87	0.39	0.34
BSCC2-6	0.86	0.43	0.37
BSCC2-7	0.95	0.44	0.42
BSCC2-8	0.89	0.47	0.42
BSCC2-9	0.87	0.46	0.4

BSCC2-10	0.85	0.46	0.39
BSCC2-11	0.97	0.38	0.37
BSCC2-12	0.78	0.43	0.35
BSCC2-13	0.9	0.44	0.39
BSCC2-14	0.94	0.4	0.38
BSCC2-15	0.66	0.48	0.32
BSCC2-16	0.87	0.45	0.39
BSCC2-17	0.76	0.49	0.37
BSCC2-18	0.82	0.45	0.37
BSCC2-19	0.84	0.48	0.4
BSCC2-20	0.85	0.42	0.36
BSCC2-21	0.78	0.47	0.36
BSCC2-22	0.99	0.41	0.41
BSCC2-23	0.83	0.45	0.37
BSCC2-24	0.96	0.46	0.44
BSCC2-25	0.96	0.46	0.44
BSCC2-26	0.76	0.46	0.35
BSCC2-27	0.95	0.43	0.41
BSCC2-28	0.94	0.46	0.43
BSCC2-29	0.97	0.49	0.47
BSCC2-30	0.93	0.45	0.42
BSCC2-31	0.86	0.48	0.41
BSCC2-32	0.94	0.49	0.46
BSCC2-33	0.99	0.45	0.45
BSCC2-34	0.86	0.45	0.39
BSCC2-35	0.88	0.48	0.42
BSCC2-36	0.89	0.45	0.4
BSCC2-37	0.87	0.48	0.42
BSCC2-38	0.87	0.42	0.36
BSCC2-39	0.87	0.47	0.41
BSCC2-40	0.91	0.41	0.37

Figure 4.22 shows the overlapping histograms based on the Orientation Factor for the sites selected for HREBSD analysis in both the ASCC2 and BSCC2 samples.

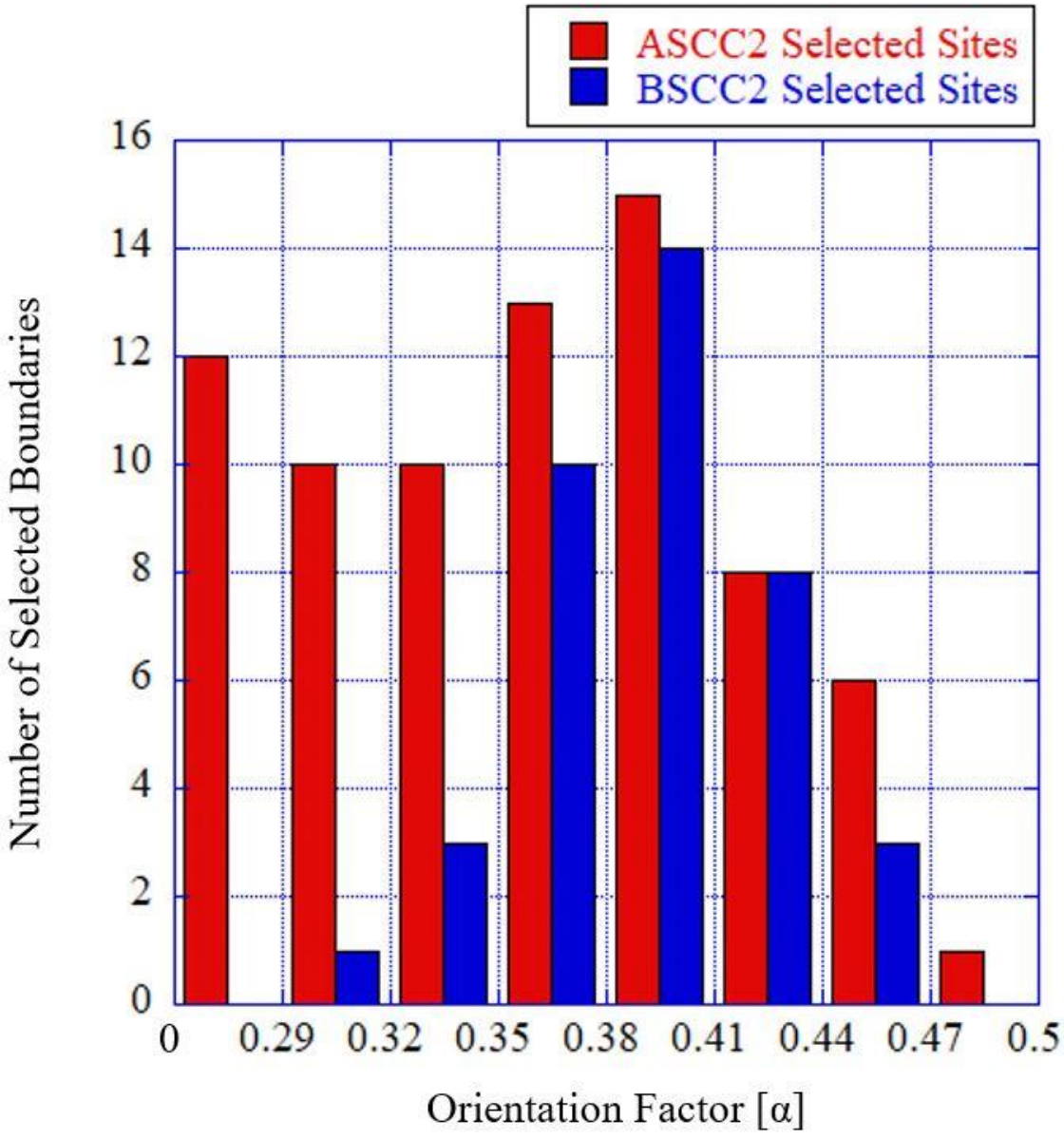

Figure 4.22: Distribution of Orientation Factors for sites selected for HREBSD analysis for both the ASCC2 Fe13Cr15Ni tensile bar sample (red) and the BSCC2 Fe21Cr32Ni 5 dpa tensile bar sample (blue).

4.5 HREBSD Stress Measurements

Measurements taken using HREBSD are typically made in the sample reference frame. Since the actual orientation of the grain boundary relative to the loading axis is known, the

principle σ_{11} tensile stress can be resolved such that it points parallel to the grain boundary normal. An example of the stress tensor generated at a discontinuous DC-GB interaction site is shown in Figure 4.22. Therefore the stress observed is the tensile stress which is acting to separate the two halves of the grain boundary. The y-axis is defined such that it runs parallel to the grain boundary trace observed in the SEM image.

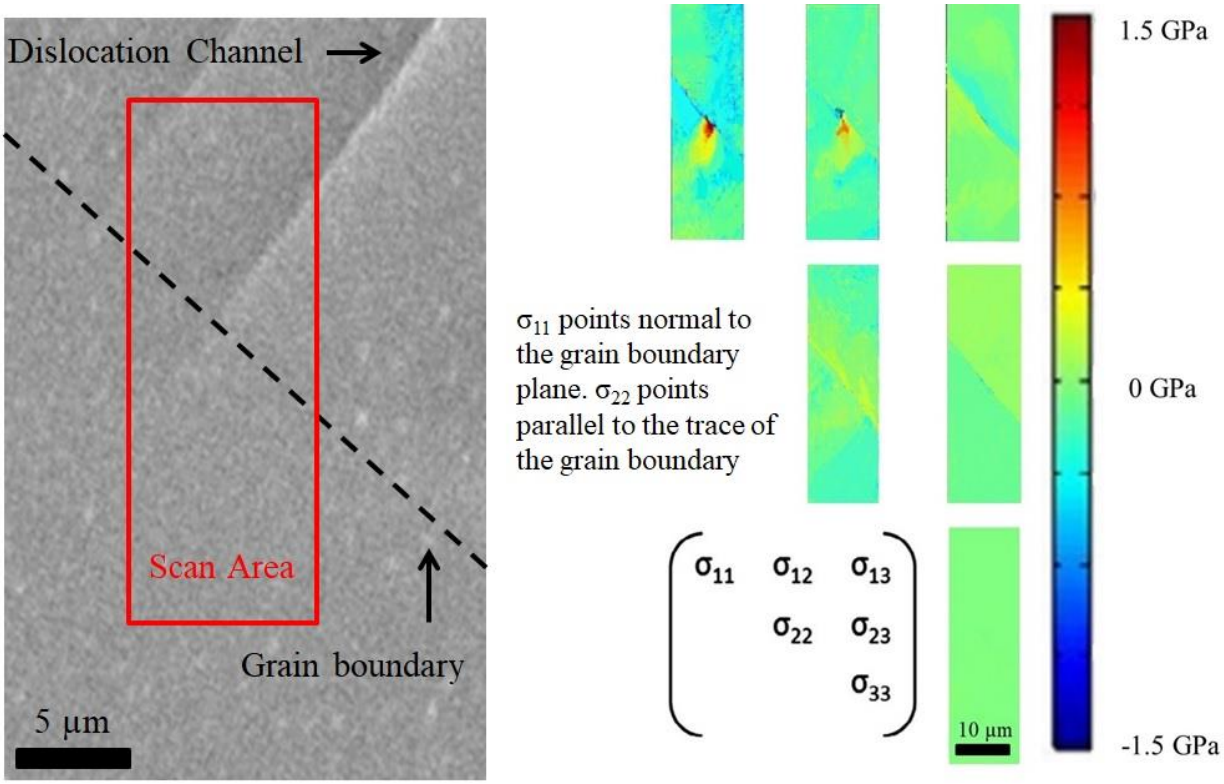

Figure 4.23: Example output of HREBSD residual stress tensor calculation resolved normal to grain boundary normal

For all of the investigated DC-GB interaction sites, an increase in tensile stress was observed at the point of interaction with the peak magnitude of stress occurring very close to the grain boundary. An enlarged version of the σ_{11} stress component from Figure 4.23 is shown below in Figure 4.24.

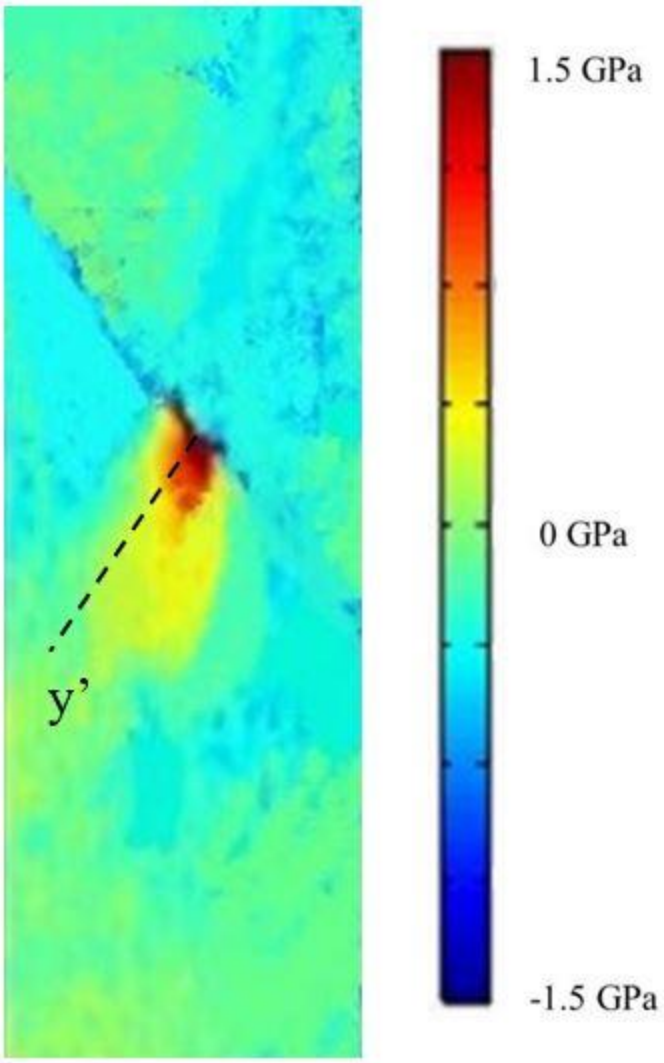

Figure 4.24: 2D σ_{11} stress component map from HREBSD analyzed site ASCC2-32. Line y' (black dashed line) extends perpendicular to the grain boundary trace.

A coordinate system has been superimposed on this figure such that the line y’ (black dashed line) starts at the DC-GB interaction site and extends in a direction perpendicular to the grain boundary trace. Figure 4.25 shows the stress profile moving out from the point of intersection into the non-deforming grain. The raw calculated values of stress are shown in blue and a least squares trend fit with a $r^{-1/2}$ dependence has been applied and plotted in red.

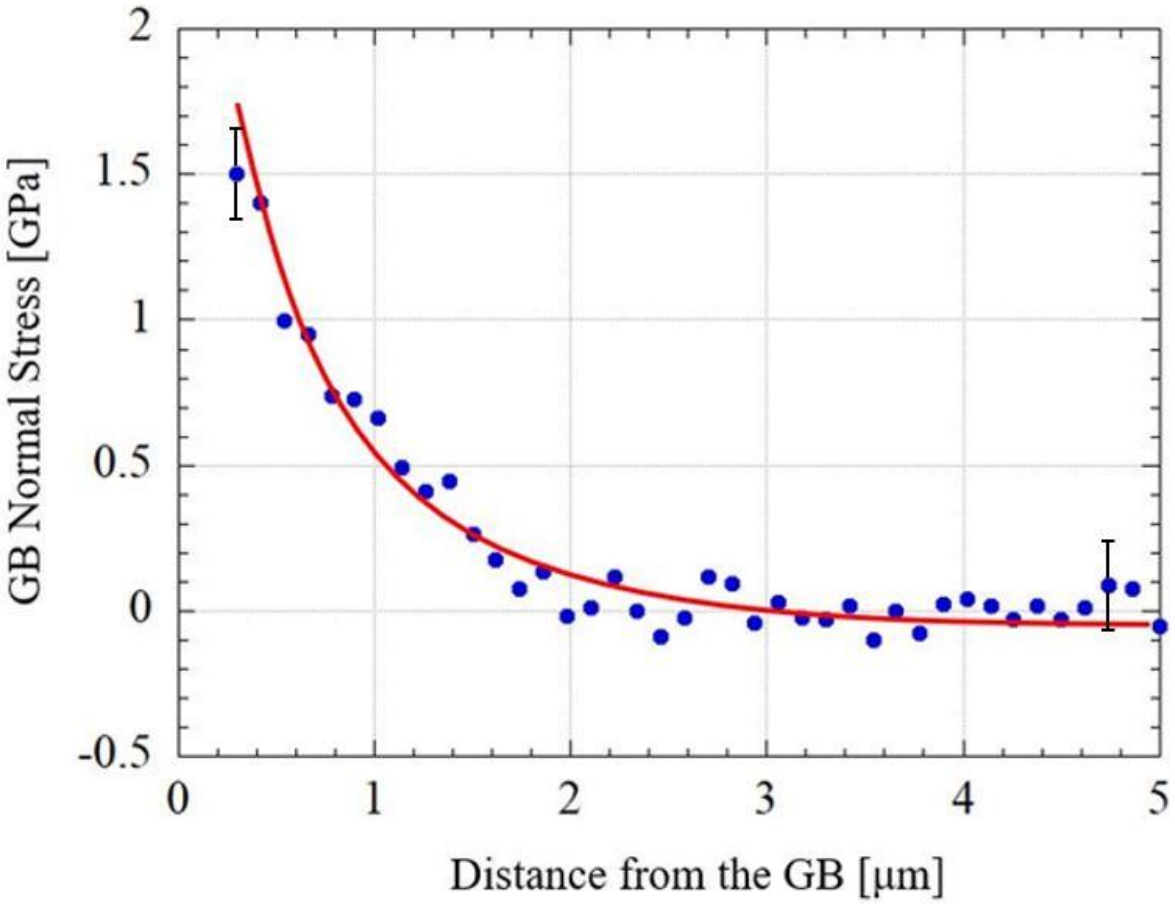

Figure 4.25: Grain boundary normal stress (σ_{11}) profile as a function of distance from the grain boundary at site ASCC2-32 along y'; perpendicular to the observed grain boundary trace.

The peak magnitude in stress is observed at the closest point to the grain boundary and decreases rapidly over the first two microns into the adjacent grain. The first data point used in the plot is taken at a distance roughly 200 nm from the grain boundary to eliminate calculation errors which arise from EBSD pattern overlap when the interaction volume samples from both grains simultaneously.

Although high tensile stresses are observed, the stress field surrounding the DC-GB interaction site cannot be purely positive. Force equilibrium must be maintained in the solid

considering the HREBSD measurements are made in a static environment without any externally applied forces. If the measurements made using HREBSD do not show a certain degree of force equilibrium, it decreases the validity of the measurements being made. In order to evaluate the degree to which force equilibrium is maintained in the HREBSD scans, a radial mesh was applied to the 2D tensile and shear stress map shown in Figure 4.24. An initial circle with a radius of 200 nm was placed at the intersection point between the dislocation channel and the grain boundary. Data points within this circle were not analyzed due to the large errors associated with these values discussed earlier, which are produced by pattern overlap during EBSD analysis. Successively larger circle radii were used to define discrete areas of points within the scan and an average stress value for the annulus of points radiating outwards from the initial circle center was determined. Since the values of stress in the HREBSD scan are taken at discrete locations during the SEM scan, points are only counted within a specific radius if the center of the scan point falls between the bounds of the inner and outer radii. A diagram showing the criteria for points used for calculations within a certain annulus is shown in Figure 4.26.

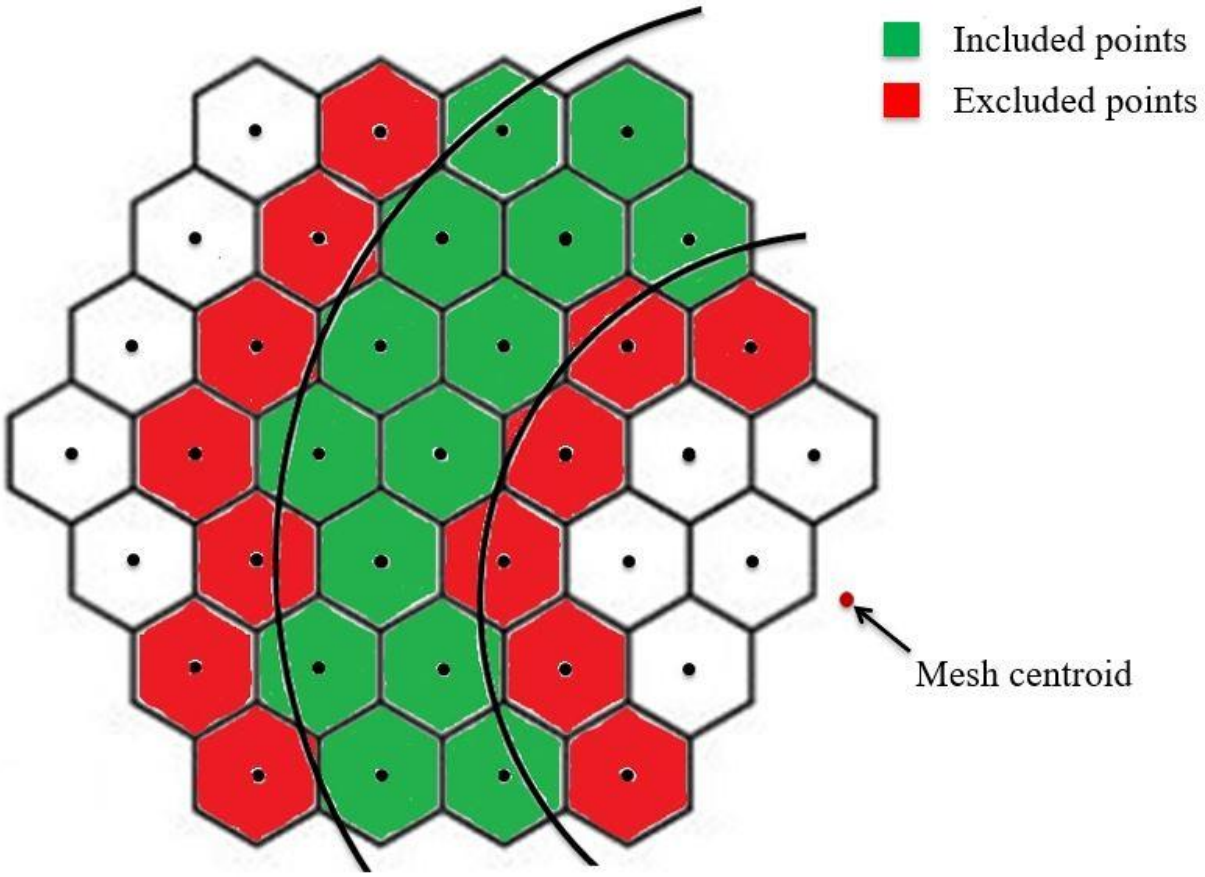

Figure 4.26: Diagram of grid used for EBSD data collection. For radial mesh analysis, green points denote points which are counted for this mesh step while red points are not.

Here the green points are used during the average stress value calculation and the red points are excluded. To account for the fact that as the mesh radius increases more points are used in determining the average stress value present within that annulus, the average stress value is weighted by a factor W which is defined as:

$$W = \frac{A_x}{A_0} \tag{4.9}$$

Where A_x is the area of the current annulus with a defined mesh radius and A_0 is the area of the smallest annulus closest to the GB-DC interaction point. With this setup, the total summed stress

in the region defined by the radial mesh is the area under the generated curve shown in Figure 4.27.

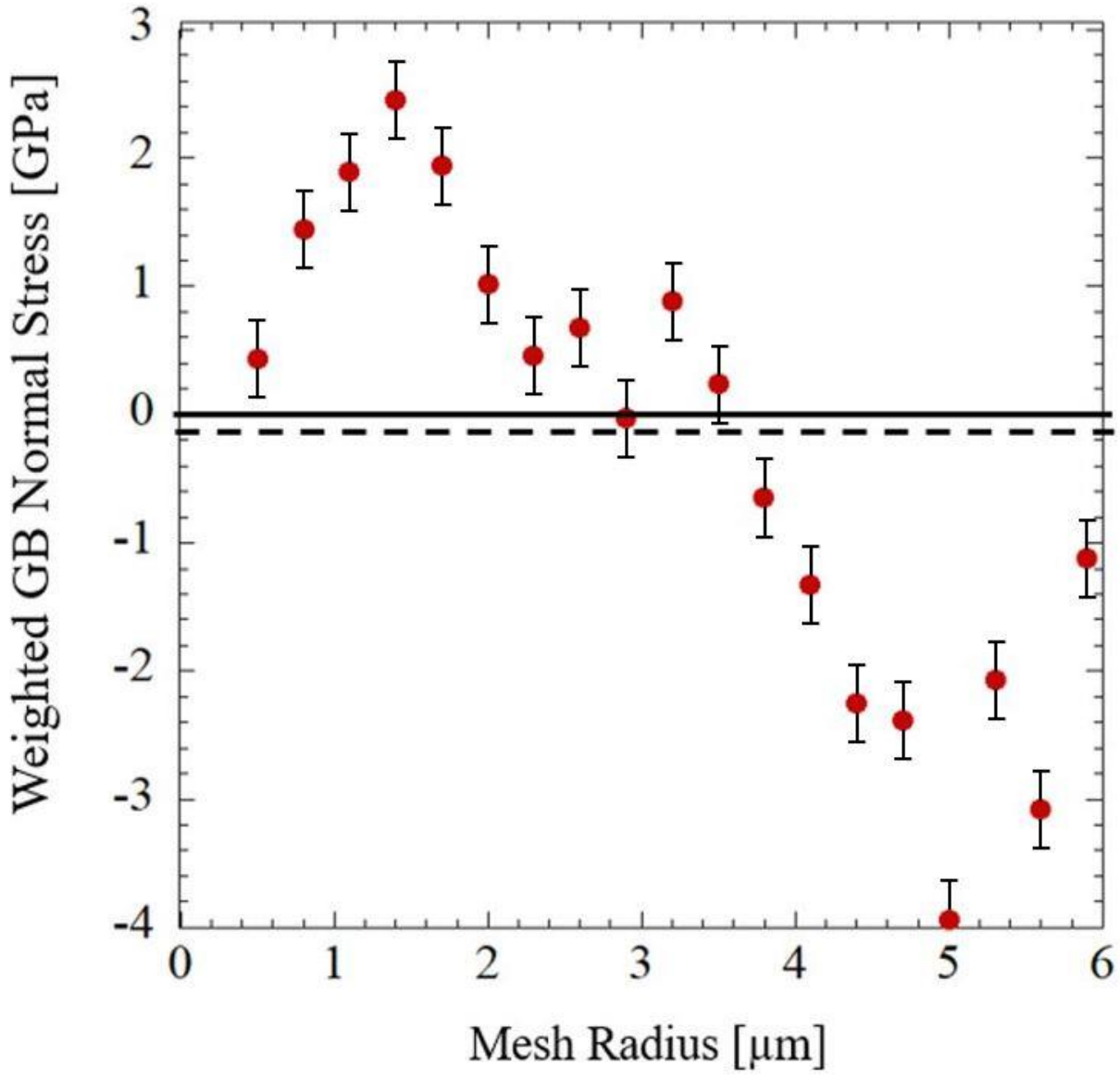

Figure 4.27: Weighted grain boundary normal stress average taken as a function of radial mesh size for ASCC2-32 DC-GB interaction site analyzed by HREBSD. The black dashed line denotes the shifted baseline required to ensure force equilibrium surrounding the interaction site.

For the tensile components of the stress measured by HREBSD, the absolute value of the total stress of the scan was found to exceed 0 GPa, meaning that force equilibrium was not being maintained. Since force equilibrium is a requirement, all points within the scan had a static stress

added such that the summation over all points in the scan would net to zero. This modification of the baseline stress value would be similar to using a different reference image for the HREBSD analysis and calculations which had a slightly different initial orientation. The magnitude of stress offset required to establish force equilibrium for the tensile stress distribution measured by HREBSD was calculated to be 0.093 GPa. This value is below the error observed in these HREBSD measurements, which is typically on the order of 0.15 GPa which means that by changing the value of the baseline stress for each component in the selected HREBSD scan by a value that is within the error of the original baseline measurement, force equilibrium can be maintained which increases the validity of the stresses calculated from HREBSD. The dashed line in Figure 4.26 shows the change in the baseline stress value required to establish force equilibrium in the HREBSD scan. Stress tensors and grain boundary normal stress profiles for all selected sites are presented in Appendix D.

Peak grain boundary normal stresses are plotted as a function of the Orientation Factor in Figure 4.28 for both the ASCC2 Fe13Cr15Ni 5 dpa and BSCC2 Fe21Cr32Ni 5 dpa tensile bar samples. The raw data contained in Figure 4.28 is shown in Table 4.9.

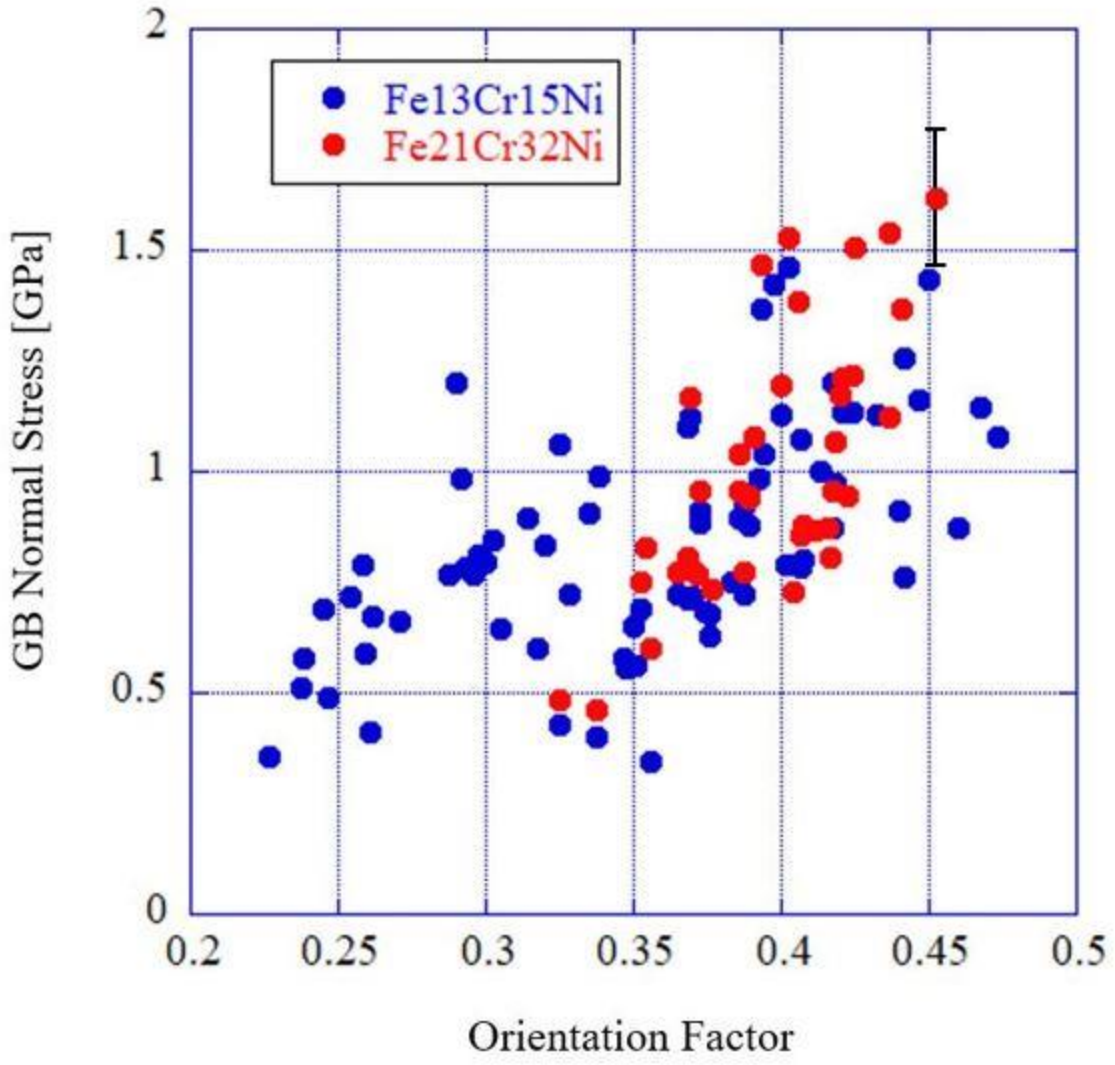

Figure 4.28: Peak grain boundary normal stress measured 200nm from the grain boundary as a function of the Orientation Factor for both Fe13Cr15Ni and Fe21Cr32Ni tensile bar samples

A general trend of increasing grain boundary normal stress is observed with increasing values of the Orientation Factor, which is to be expected. There is considerable overlap between the peak tensile stresses observed in the ASCC2 Fe13Cr15Ni and BSCC2 Fe21Cr32Ni samples which have both been strained to 4.5% plastic strain in 288 °C argon at $3x10^{-7}$ s^{-1}, which underlines the fact that the difference in observed cracking behavior is not purely a mechanical response.

Table 4.9 Peak grain boundary normal stress as a function of Orientation Factor for both Fe13Cr15Ni and Fe21Cr32Ni measured 200 nm from the grain boundary

Grain Boundary ID	Orientation Factor	Peak GB Normal Stress [GPa]
ASCC2-1	0.44	1.25
ASCC2-2	0.37	0.88
ASCC2-3	0.47	1.14
ASCC2-4	0.39	0.92
ASCC2-5	0.40	1.43
ASCC2-6	0.38	0.63
ASCC2-7	0.45	1.44
ASCC2-8	0.35	0.56
ASCC2-9	0.41	0.78
ASCC2-10	0.39	0.89
ASCC2-11	0.39	1.37
ASCC2-12	0.34	0.40
ASCC2-13	0.37	0.72
ASCC2-14	0.42	0.98
ASCC2-15	0.42	1.14
ASCC2-16	0.40	1.13
ASCC2-17	0.39	0.88
ASCC2-18	0.37	1.12
ASCC2-19	0.34	0.91
ASCC2-20	0.39	1.04
ASCC2-21	0.38	0.68
ASCC2-22	0.32	0.60
ASCC2-23	0.39	0.98
ASCC2-24	0.37	0.68
ASCC2-25	0.37	1.10
ASCC2-26	0.40	0.79
ASCC2-27	0.36	0.34
ASCC2-28	0.33	0.43
ASCC2-29	0.35	0.69
ASCC2-30	0.39	0.72
ASCC2-31	0.42	1.13
ASCC2-32	0.40	1.46
ASCC2-33	0.42	0.87
ASCC2-34	0.36	0.72
ASCC2-35	0.41	0.80
ASCC2-36	0.37	0.91

ASCC2-37	0.44	0.91
ASCC2-38	0.44	0.76
ASCC2-39	0.35	0.65
ASCC2-40	0.41	1.07
ASCC2-41	0.43	1.13
ASCC2-42	0.47	1.08
ASCC2-43	0.42	1.20
ASCC2-44	0.41	1.00
ASCC2-45	0.46	0.87
ASCC2-46	0.45	1.16
ASCC2-47	0.35	0.58
ASCC2-48	0.37	0.71
ASCC2-49	0.38	0.75
ASCC2-50	0.35	0.56
ASCC2-51	0.30	0.64
ASCC2-52	0.25	0.72
ASCC2-53	0.27	0.66
ASCC2-54	0.25	0.49
ASCC2-55	0.33	0.72
ASCC2-56	0.32	0.84
ASCC2-57	0.26	0.59
ASCC2-58	0.23	0.36
ASCC2-59	0.30	0.77
ASCC2-60	0.29	0.98
ASCC2-61	0.30	0.81
ASCC2-62	0.26	0.79
ASCC2-63	0.32	1.06
ASCC2-64	0.31	0.89
ASCC2-65	0.24	0.58
ASCC2-66	0.29	0.77
ASCC2-67	0.29	1.20
ASCC2-68	0.24	0.51
ASCC2-69	0.24	0.69
ASCC2-70	0.30	0.80
ASCC2-71	0.30	0.84
ASCC2-72	0.26	0.68
ASCC2-73	0.29	0.79
ASCC2-74	0.26	0.41
ASCC2-75	0.34	0.99
BSCC2-1	0.35	0.83
BSCC2-2	0.36	0.63

BSCC2-3	0.37	0.81
BSCC2-4	0.37	0.77
BSCC2-5	0.38	0.73
BSCC2-6	0.39	1.04
BSCC2-7	0.39	0.94
BSCC2-8	0.39	1.08
BSCC2-9	0.40	0.73
BSCC2-10	0.41	1.39
BSCC2-11	0.41	0.87
BSCC2-12	0.42	0.87
BSCC2-13	0.42	0.81
BSCC2-14	0.42	1.17
BSCC2-15	0.42	0.94
BSCC2-16	0.42	1.50
BSCC2-17	0.43	1.19
BSCC2-18	0.44	1.12
BSCC2-19	0.44	1.54
BSCC2-20	0.44	1.37
BSCC2-21	0.45	1.62
BSCC2-22	0.41	0.86
BSCC2-23	0.39	0.96
BSCC2-24	0.39	1.47
BSCC2-25	0.34	0.46
BSCC2-26	0.37	0.78
BSCC2-27	0.42	1.07
BSCC2-28	0.42	1.21
BSCC2-29	0.40	1.19
BSCC2-30	0.39	0.94
BSCC2-31	0.37	1.17
BSCC2-32	0.36	0.40
BSCC2-33	0.33	0.48
BSCC2-34	0.35	0.75
BSCC2-35	0.39	0.78
BSCC2-36	0.42	1.22
BSCC2-37	0.40	1.53
BSCC2-38	0.42	0.95
BSCC2-39	0.36	0.77
BSCC2-40	0.41	0.88

Similar attention has been paid to the other components of the stress tensor as they might also contribute to cracking in the material. An enlarged version of the σ_{12} 2D stress map presented in Figure 4.23 is presented here in Figure 4.29. Again, a coordinated system is superimposed such that y' (black dashed line) extends perpendicular to the grain boundary trace into the non-deforming grain and the same color axis for stress as the σ_{11} component is used. It is important to note that the shear stress shown here is acting parallel to the plane of the grain boundary based on the established coordinate system and they do not provide any information on the shear stresses acting on specific slip systems within the pair of grains investigated.

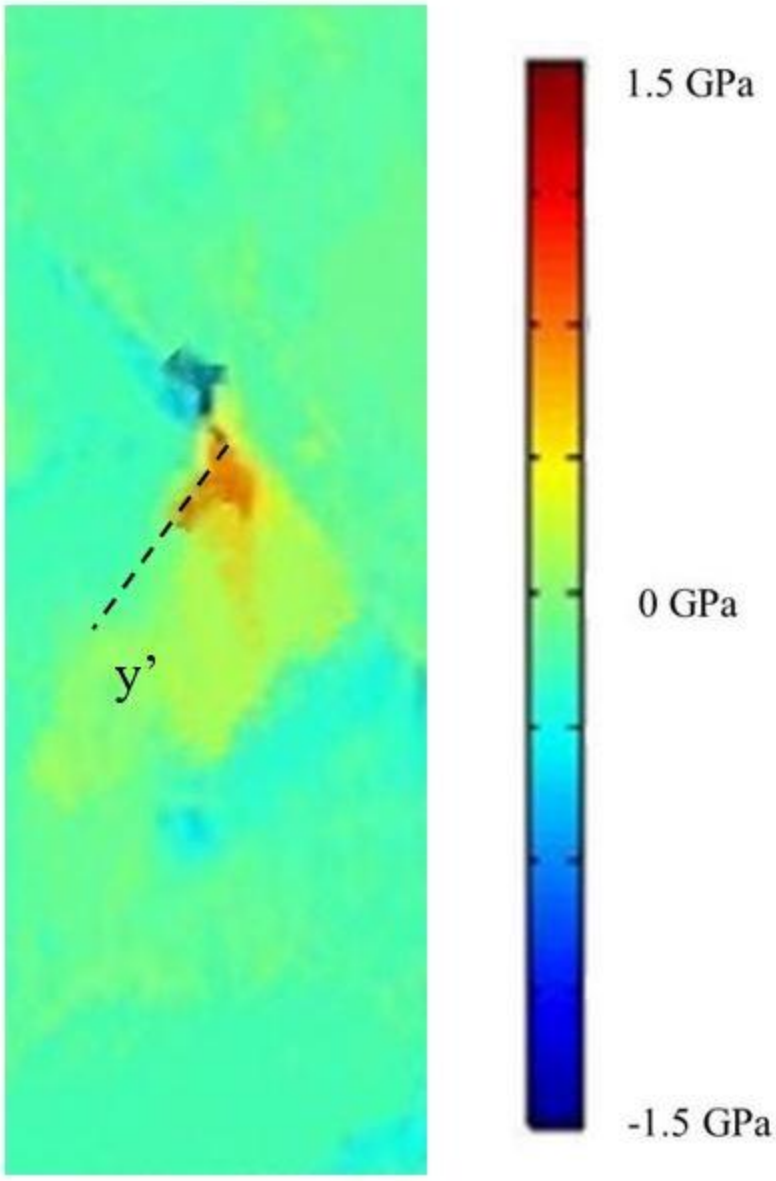

Figure 4.29: 2D σ_{12} stress component map from HREBSD analyzed site ASCC2-32. Line y' (black dashed line) extends perpendicular to the grain boundary trace.

Increased shear stresses are observed at the DC-GB interaction site, however the magnitude observed is significantly less than the tensile stresses. Plotting the magnitude of the shear stress as a function of distance away from the DC-GB interaction site along y’ produces a shape, with the peak stress occurring at the interaction site and a rapid decrease in the stress over the first 2 microns. This is shown in Figure 4.30.

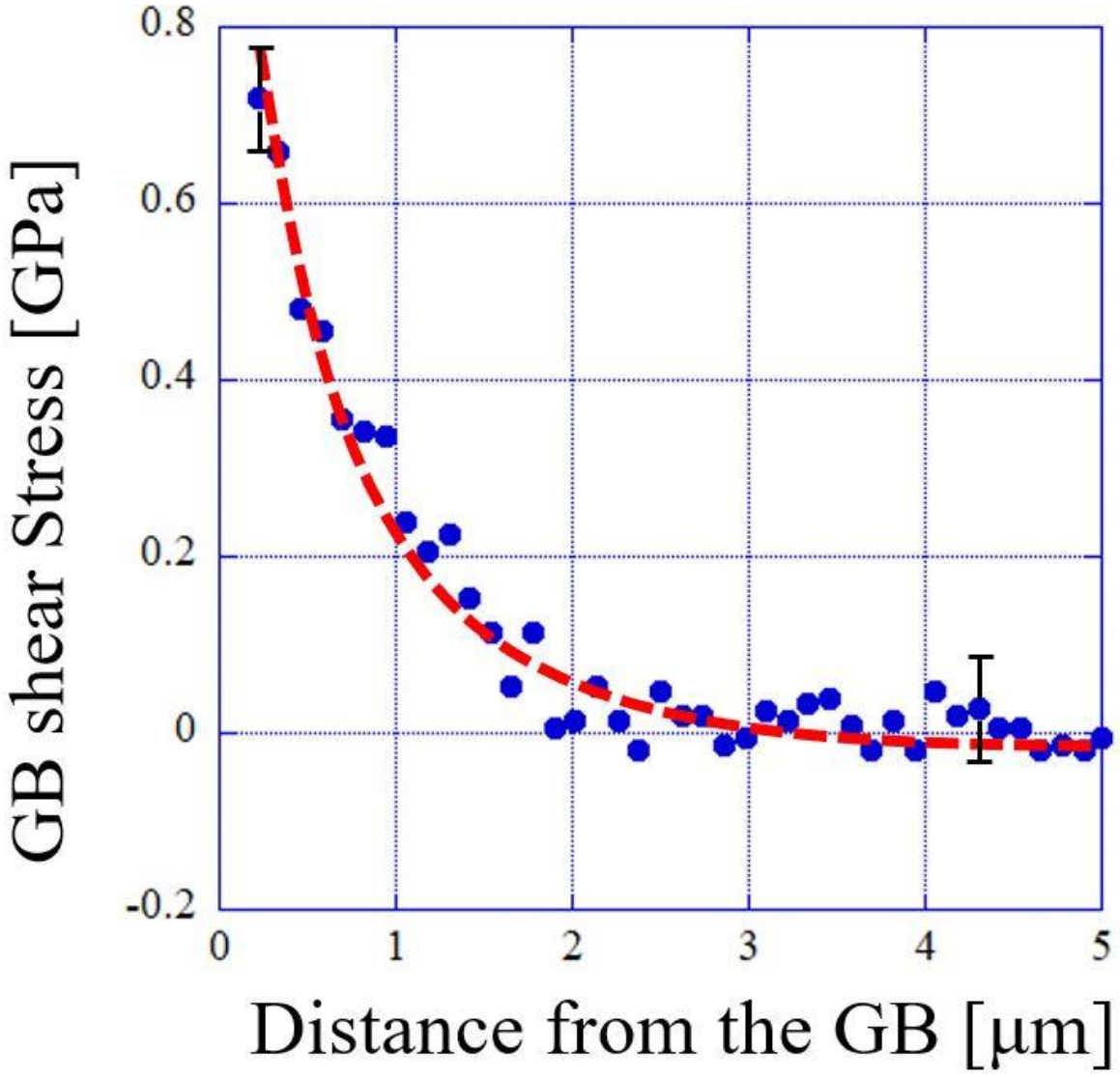

Figure 4.30: Grain boundary shear stress (σ12) profile as a function of distance from the grain boundary at site ASCC2-32 along y'; perpendicular to the observed grain boundary trace.

The same radial mesh procedure was performed for the 2D shear stress map and is plotted in Figure 4.31. In order to reach stress equilibrium, the zero-point stress value needed to be shifted by 0.078 GPa, which is within the error of the HREBSD measurement. The smaller value for the shift in the shear stress case most likely comes from the fact that the magnitudes of the shear stresses calculated using HREBSD are smaller than the tensile stresses.

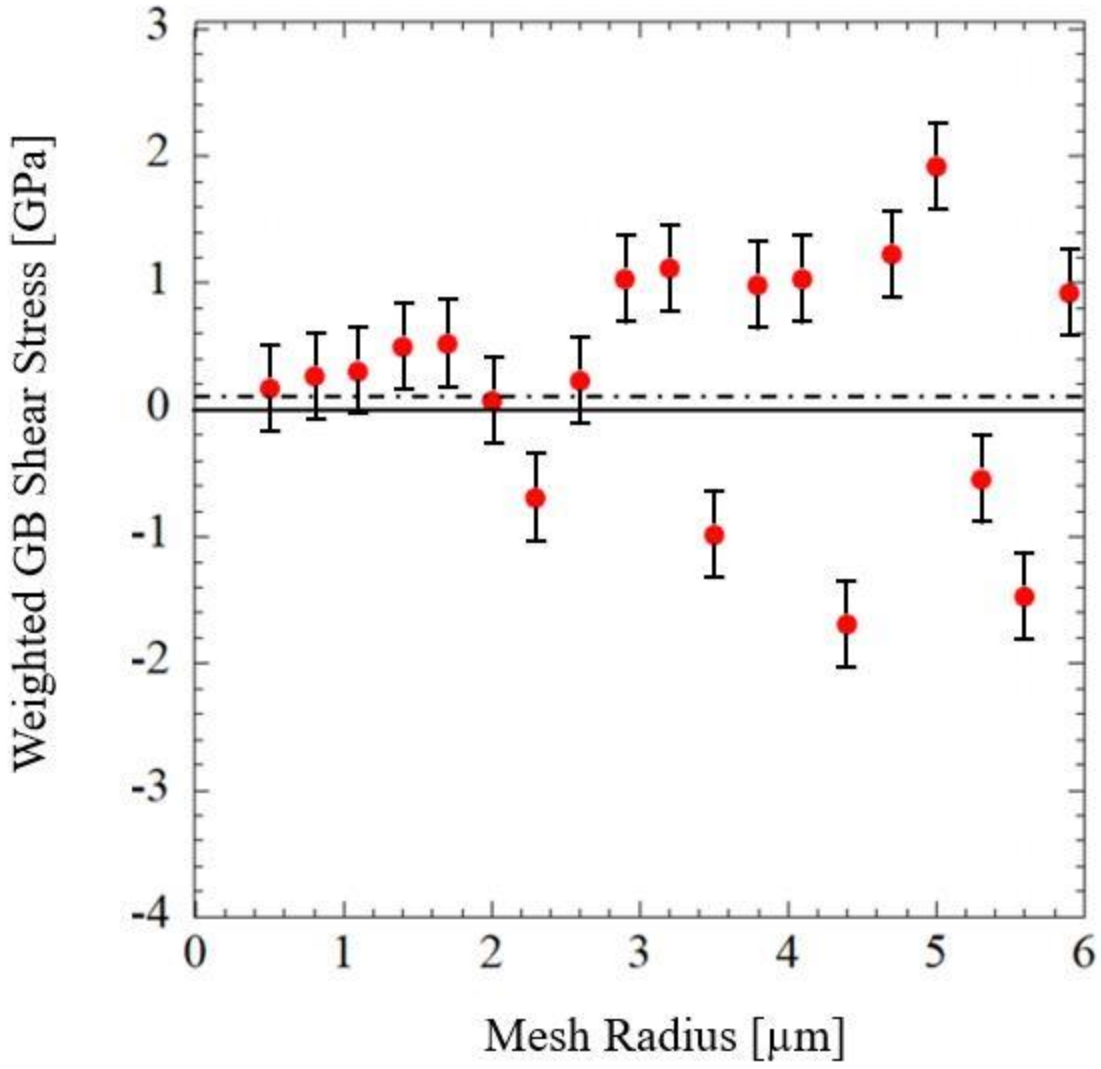

Figure 4.31:Weighted grain boundary shear stress average taken as a function of radial mesh size for ASCC2-32 DC-GB interaction site analyzed by HREBSD. The black dashed line denotes the shifted baseline required to ensure force equilibrium surrounding the interaction site.

The 2D stress maps generated using HREBSD did not show substantial stresses in the σ_{13}, σ_{22}, or σ_{23} plots near the DC-GB interaction site, and therefore a trendline similar to the ones presented in Figure 4.25 and Figure 4.30 could not be generated and the peak stresses reached here were only on the order of 20-30% of the tensile stresses. For the purpose of calculations in the image cross correlation software, the stress acting normal to the sample surface is treated as a

free surface with a negligible stress component. Although the σ_{33} component for the HREBSD analysis presented in Figure 4.23 is not aligned perfectly with the sample surface, it is still pointing in a direction close to this free surface and shows a magnitude of stress near zero for the entire scanned area. For comparison, the peak magnitude for each stress component in the HREBSD calculated stress tensor is given in Table 4.8.

Table 4.10 Peak stresses calculated by HREBSD for each component of the stress tensor for analyzed sites in ASCC2 and BSCC2 tensile bar samples

Grain Boundary ID	Peak σ11	Peak σ12	Peak σ13	Peak σ22	Peak σ23	Peak σ33
ASCC2-1	1.25	0.48	0.30	0.44	0.24	0.10
ASCC2-2	0.88	0.44	0.26	0.38	0.24	0.10
ASCC2-3	1.14	0.63	0.26	0.44	0.28	0.12
ASCC2-4	0.92	0.61	0.27	0.44	0.29	0.11
ASCC2-5	1.43	0.66	0.31	0.36	0.24	0.11
ASCC2-6	0.63	0.48	0.32	0.38	0.24	0.05
ASCC2-7	1.44	0.84	0.26	0.43	0.22	0.08
ASCC2-8	0.56	0.35	0.35	0.49	0.28	0.11
ASCC2-9	0.78	0.40	0.28	0.46	0.26	0.11
ASCC2-10	0.89	0.57	0.31	0.47	0.29	0.06
ASCC2-11	1.37	0.69	0.35	0.41	0.26	0.08
ASCC2-12	0.40	0.23	0.35	0.33	0.28	0.06
ASCC2-13	0.72	0.53	0.33	0.38	0.26	0.06
ASCC2-14	0.98	0.64	0.29	0.47	0.22	0.08
ASCC2-15	1.14	0.45	0.28	0.42	0.27	0.12
ASCC2-16	1.13	0.47	0.28	0.36	0.24	0.10
ASCC2-17	0.88	0.46	0.32	0.44	0.22	0.06
ASCC2-18	1.12	0.53	0.34	0.42	0.24	0.10
ASCC2-19	0.91	0.47	0.34	0.51	0.24	0.07
ASCC2-20	1.04	0.65	0.26	0.46	0.25	0.09
ASCC2-21	0.68	0.48	0.34	0.41	0.27	0.10
ASCC2-22	0.60	0.38	0.29	0.43	0.23	0.12
ASCC2-23	0.98	0.40	0.26	0.48	0.29	0.13
ASCC2-24	0.68	0.35	0.31	0.42	0.22	0.09
ASCC2-25	1.10	0.43	0.26	0.36	0.26	0.10

ASCC2-26	0.79	0.47	0.25	0.40	0.26	0.08
ASCC2-27	0.34	0.22	0.30	0.42	0.27	0.05
ASCC2-28	0.43	0.26	0.25	0.44	0.29	0.05
ASCC2-29	0.69	0.45	0.26	0.45	0.23	0.05
ASCC2-30	0.72	0.38	0.31	0.37	0.25	0.09
ASCC2-31	1.13	0.55	0.35	0.50	0.28	0.12
ASCC2-32	1.46	0.61	0.30	0.44	0.22	0.09
ASCC2-33	0.87	0.38	0.34	0.35	0.25	0.10
ASCC2-34	0.72	0.38	0.26	0.45	0.23	0.08
ASCC2-35	0.80	0.46	0.33	0.36	0.25	0.07
ASCC2-36	0.91	0.38	0.27	0.33	0.25	0.06
ASCC2-37	0.91	0.38	0.31	0.42	0.22	0.13
ASCC2-38	0.76	0.38	0.26	0.47	0.27	0.12
ASCC2-39	0.65	0.40	0.31	0.49	0.29	0.10
ASCC2-40	1.07	0.48	0.27	0.49	0.27	0.09
ASCC2-41	1.13	0.68	0.29	0.45	0.28	0.10
ASCC2-42	1.08	0.74	0.31	0.35	0.25	0.09
ASCC2-43	1.20	0.72	0.28	0.34	0.26	0.07
ASCC2-44	1.00	0.65	0.35	0.43	0.23	0.10
ASCC2-45	0.87	0.40	0.36	0.34	0.24	0.09
ASCC2-46	1.16	0.68	0.29	0.51	0.27	0.12
ASCC2-47	0.58	0.33	0.29	0.47	0.29	0.05
ASCC2-48	0.71	0.49	0.27	0.38	0.25	0.08
ASCC2-49	0.75	0.44	0.31	0.45	0.24	0.12
ASCC2-50	0.56	0.32	0.28	0.44	0.24	0.12
ASCC2-51	0.64	0.42	0.30	0.44	0.24	0.05
ASCC2-52	0.72	0.29	0.35	0.36	0.25	0.09
ASCC2-53	0.66	0.42	0.27	0.43	0.22	0.08
ASCC2-54	0.49	0.21	0.30	0.49	0.28	0.05
ASCC2-55	0.72	0.39	0.30	0.41	0.28	0.11
ASCC2-56	0.84	0.47	0.32	0.44	0.28	0.05
ASCC2-57	0.59	0.33	0.35	0.45	0.25	0.10
ASCC2-58	0.36	0.25	0.31	0.50	0.27	0.12
ASCC2-59	0.77	0.31	0.29	0.47	0.23	0.12
ASCC2-60	0.98	0.59	0.26	0.48	0.27	0.05
ASCC2-61	0.81	0.53	0.31	0.47	0.29	0.12
ASCC2-62	0.79	0.42	0.33	0.49	0.27	0.13
ASCC2-63	1.06	0.54	0.26	0.39	0.29	0.05
ASCC2-64	0.89	0.37	0.27	0.42	0.26	0.10
ASCC2-65	0.58	0.32	0.33	0.34	0.27	0.06
ASCC2-66	0.77	0.31	0.31	0.37	0.28	0.11

ASCC2-67	1.20	0.65	0.28	0.37	0.22	0.07
ASCC2-68	0.51	0.26	0.31	0.51	0.29	0.12
ASCC2-69	0.69	0.34	0.25	0.42	0.22	0.10
ASCC2-70	0.80	0.32	0.30	0.50	0.29	0.05
ASCC2-71	0.84	0.35	0.36	0.39	0.23	0.12
ASCC2-72	0.68	0.31	0.25	0.52	0.24	0.05
ASCC2-73	0.79	0.52	0.30	0.38	0.24	0.13
ASCC2-74	0.41	0.27	0.28	0.38	0.22	0.12
ASCC2-75	0.99	0.51	0.36	0.51	0.22	0.07
BSCC2-1	0.83	0.48	0.33	0.38	0.27	0.07
BSCC2-2	0.63	0.25	0.27	0.47	0.26	0.07
BSCC2-3	0.81	0.32	0.31	0.35	0.26	0.12
BSCC2-4	0.77	0.28	0.30	0.50	0.27	0.12
BSCC2-5	0.73	0.29	0.29	0.49	0.28	0.06
BSCC2-6	1.04	0.57	0.27	0.43	0.25	0.10
BSCC2-7	0.94	0.56	0.27	0.40	0.27	0.10
BSCC2-8	1.08	0.62	0.34	0.42	0.26	0.11
BSCC2-9	0.73	0.39	0.32	0.45	0.29	0.05
BSCC2-10	1.39	0.79	0.31	0.37	0.29	0.08
BSCC2-11	0.87	0.32	0.36	0.37	0.23	0.12
BSCC2-12	0.87	0.40	0.29	0.43	0.25	0.09
BSCC2-13	0.81	0.33	0.30	0.42	0.25	0.08
BSCC2-14	1.17	0.67	0.26	0.34	0.27	0.09
BSCC2-15	0.94	0.37	0.27	0.50	0.22	0.08
BSCC2-16	1.50	0.66	0.30	0.45	0.25	0.12
BSCC2-17	1.19	0.67	0.27	0.52	0.27	0.10
BSCC2-18	1.12	0.61	0.36	0.35	0.22	0.09
BSCC2-19	1.54	0.60	0.33	0.48	0.28	0.06
BSCC2-20	1.37	0.56	0.30	0.46	0.22	0.13
BSCC2-21	1.62	0.92	0.36	0.40	0.25	0.13
BSCC2-22	0.86	0.33	0.26	0.46	0.23	0.10
BSCC2-23	0.96	0.37	0.34	0.48	0.29	0.08
BSCC2-24	1.47	0.65	0.26	0.34	0.28	0.09
BSCC2-25	0.46	0.24	0.34	0.45	0.22	0.05
BSCC2-26	0.78	0.44	0.31	0.45	0.27	0.10
BSCC2-27	1.07	0.60	0.31	0.47	0.26	0.09
BSCC2-28	1.21	0.45	0.34	0.35	0.22	0.06
BSCC2-29	1.19	0.61	0.36	0.41	0.26	0.12
BSCC2-30	0.94	0.39	0.32	0.46	0.25	0.05
BSCC2-31	1.17	0.71	0.32	0.50	0.28	0.07
BSCC2-32	0.40	0.18	0.34	0.39	0.23	0.10

BSCC2-33	0.48	0.23	0.25	0.49	0.27	0.11
BSCC2-34	0.75	0.39	0.33	0.34	0.29	0.07
BSCC2-35	0.78	0.38	0.35	0.38	0.22	0.13
BSCC2-36	1.22	0.60	0.29	0.52	0.28	0.13
BSCC2-37	1.53	0.73	0.30	0.41	0.27	0.10
BSCC2-38	0.95	0.56	0.27	0.46	0.29	0.07
BSCC2-39	0.77	0.46	0.29	0.43	0.26	0.05
BSCC2-40	0.88	0.42	0.26	0.52	0.25	0.09

4.6 High temperature water stress-strain behavior and crack initiation

Slow strain rate tensile tests were performed in simulated BWR-NWC at 288 °C with a nominal strain rate of $3x10^{-7}$ s^{-1} to induce cracks in tensile bar samples which had been previously characterized with HREBSD at specific DC-GB interaction sites. The target water chemistry conditions are listed in Table 4.11. Conductivity of the water was controlled through addition of $3x10^{-6}$ M sulfuric acid into the primary water feed.

Table 4.11 Water Chemistry for Simulated BWR-NWC

Controlled Water Chemistry Variable	Target Value
Autoclave Pressure	1500 psi
Autoclave Temperature	288 ºC
Dissolved Oxygen	2 ppm
Water Conductivity	0.2 µS/cm

Figure 4.32 shows the controlled water chemistry values during the course of a 1.5% plastic strain increment and Figure 4.33 shows the stress-strain behavior of the Fe13Cr15Ni sample which had been previously strained to 4.5% plastic in 288 ºC Argon. Table 4.12 details the strain increment history of the tensile bar samples which had been previously characterized by HREBSD.

Table 4.12 Strain history for samples analyzed with HREBSD prior to straining in simulated BWR-NWC conditions

Sample ID	Strain Increment (Total)
ASCC2	Argon 4.5% (4.5%) BWR-NWC 1.5% (6%)
BSCC2	Argon 4.5% (4.5%) BWR-NWC 1.5% (6%) BWR-NWC 1.5% (7.5%)

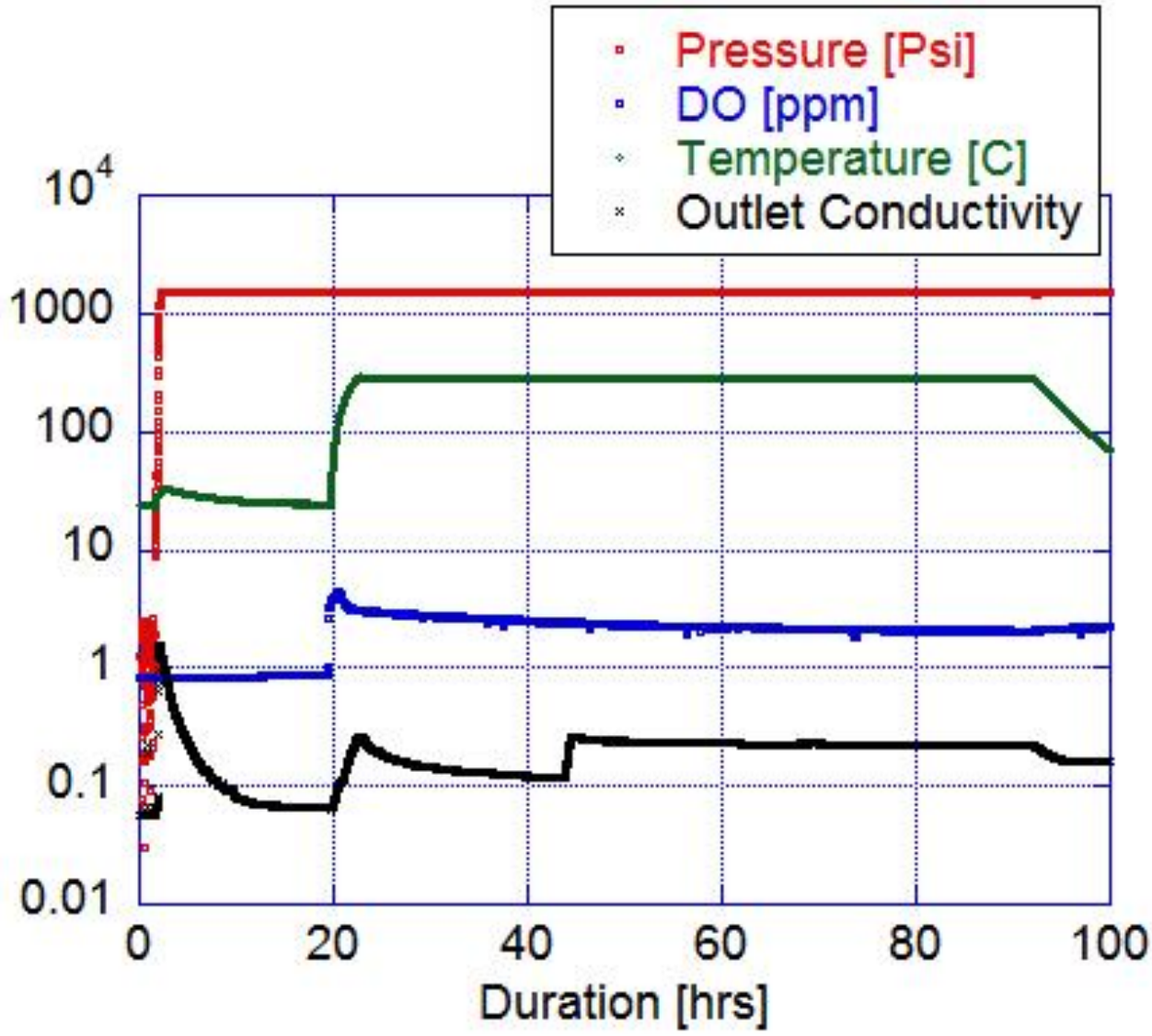

Figure 4.32: BWR-NWC controlled parameters during 1.5% strain increment performed on ASCC2 Fe13Cr15Ni 5 dpa tensile bar sample previously strained to 4.5% in high temperature argon at $3x10^{-7}$ s^{-1}.

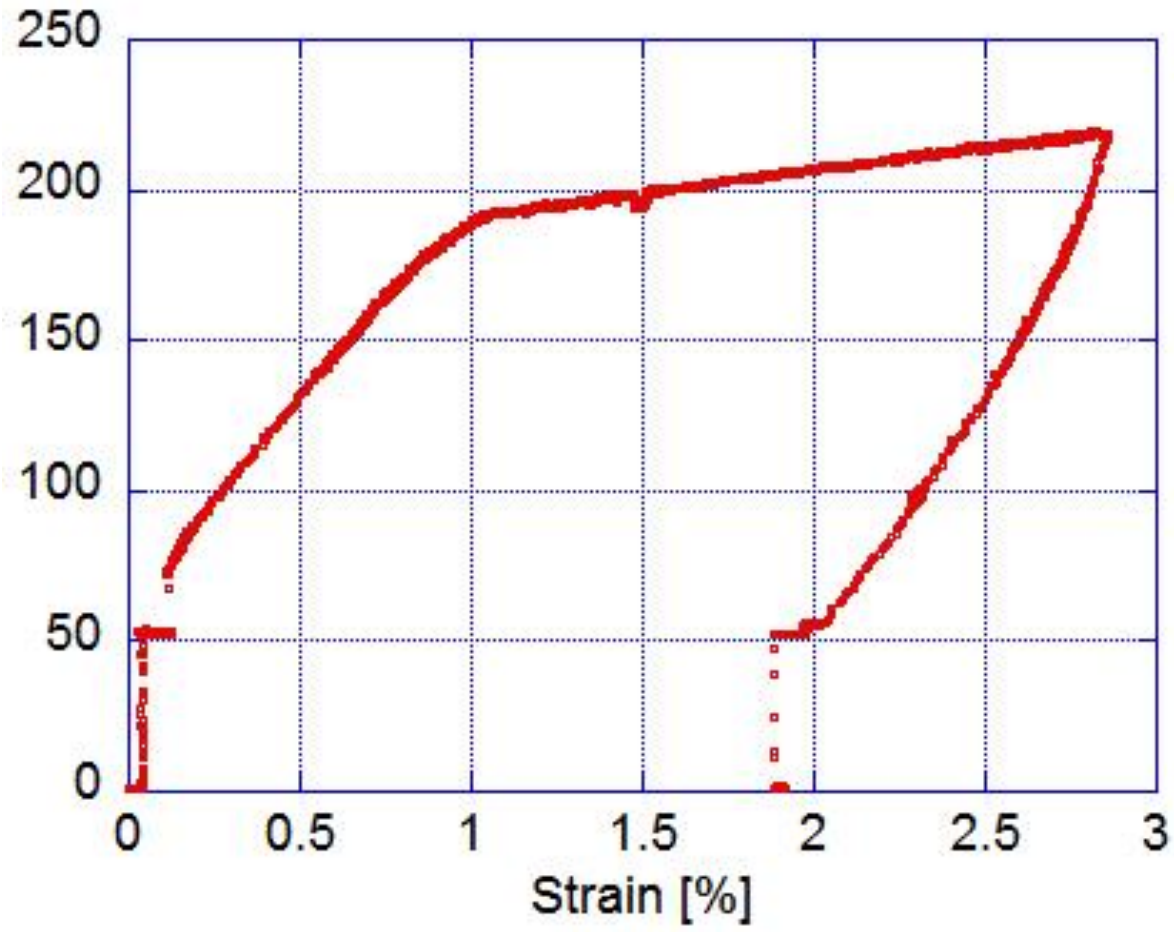

Figure 4.33: Stress-strain behavior for ASCC2 Fe13Cr15Ni 5 dpa tensile bar sample in simulated BWR-NWC to 1.5% plastic strain at $3x10^{-7}$ s^{-1}.

SEM characterization was performed after tensile bar samples were removed from the autoclave and had the oxide removed from the sample surface using the procedure detailed in the methods chapter of this thesis. This was done due to the fact that many of the cracks that developed were small (< 3μm) and were difficult to detect in the SEM without first removing the oxide layer produced through exposure to high temperature water. The 75 boundaries which had been previously characterized using HREBSD were checked again specifically to determine if cracks had initiated at these specific locations. Small cracks were observed in this alloy, and

were found typically in conjunction with discontinuous channels and at triple junctions. Figure 4.34 shows examples cracks which were formed at triple junctions and Figure 4.35 shows cracks which were formed at singular grain boundary facets.

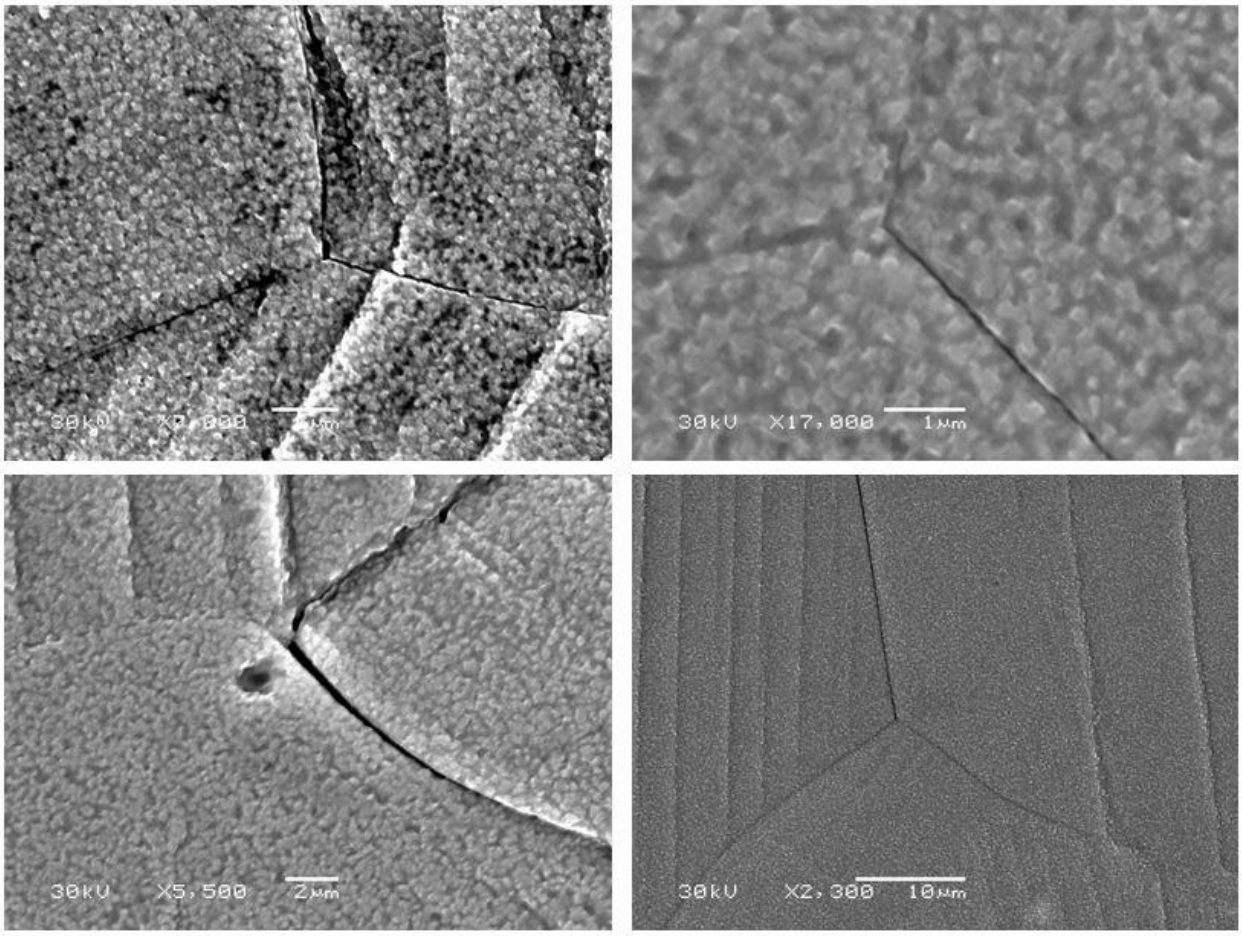

Figure 4.34: Intergranular cracks found in ASCC2 Fe13Cr15Ni 5 dpa tensile bar sample after 1.5% strain increment (6% total) in BWR-NWC at 288 °C at a strain rate of $3x10^{-7}$ s^{-1} that formed at triple junctions.

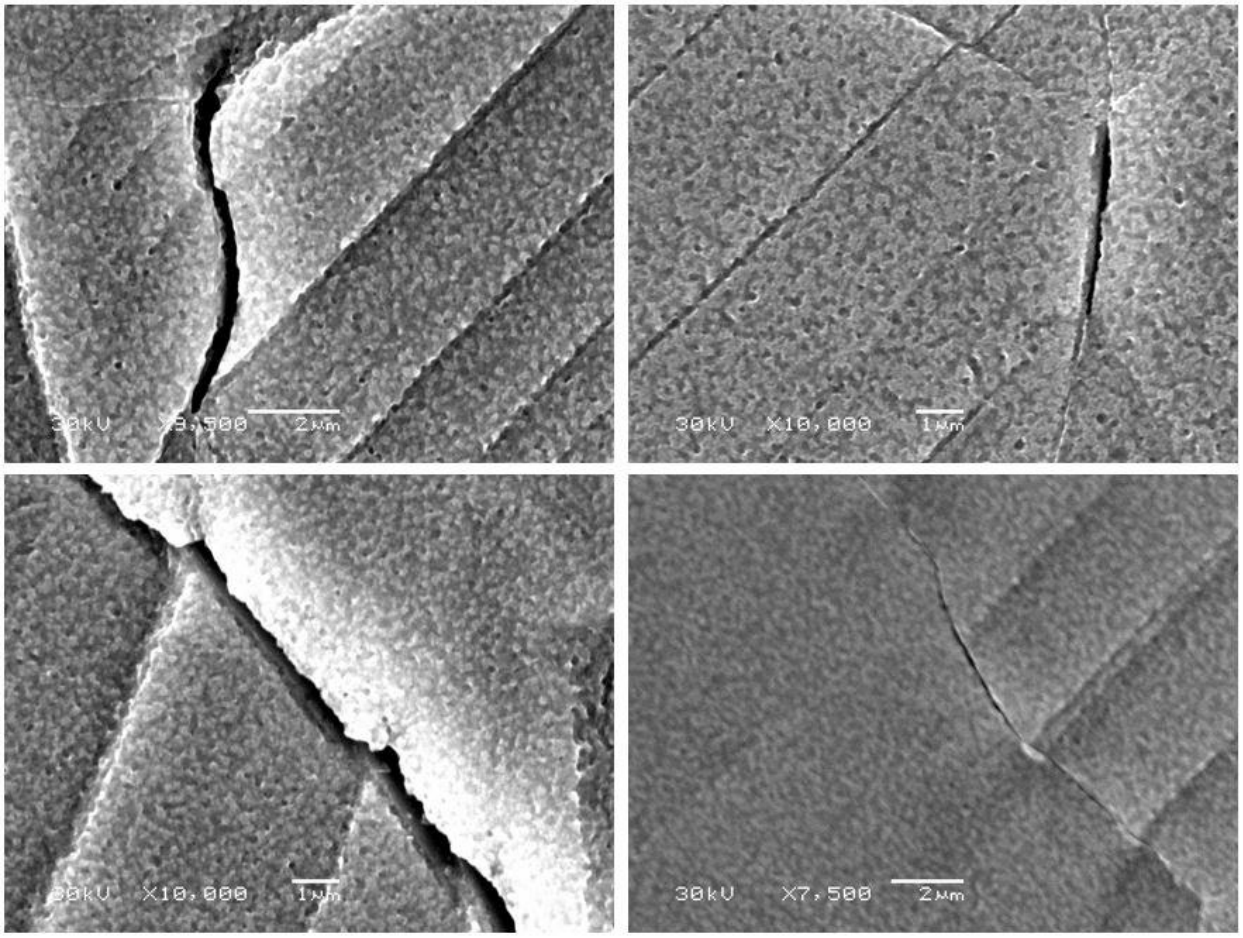

Figure 4.35: Intergranular cracks found in ASCC2 Fe13Cr15Ni 5 dpa tensile bar sample after 1.5% strain increment (6% total) in BWR-NWC at 288 °C at a stain rate of $3x10^{-7}$ s^{-1} that formed along grain facets.

A case of small cracks associated directly with dislocation channeling is shown in Figure 4.36. Of the 75 sites where HREBSD analysis was performed, 26 sites showed evidence of intergranular fracture. All SEM images of the cracks detailed here are shown in Appendix E.

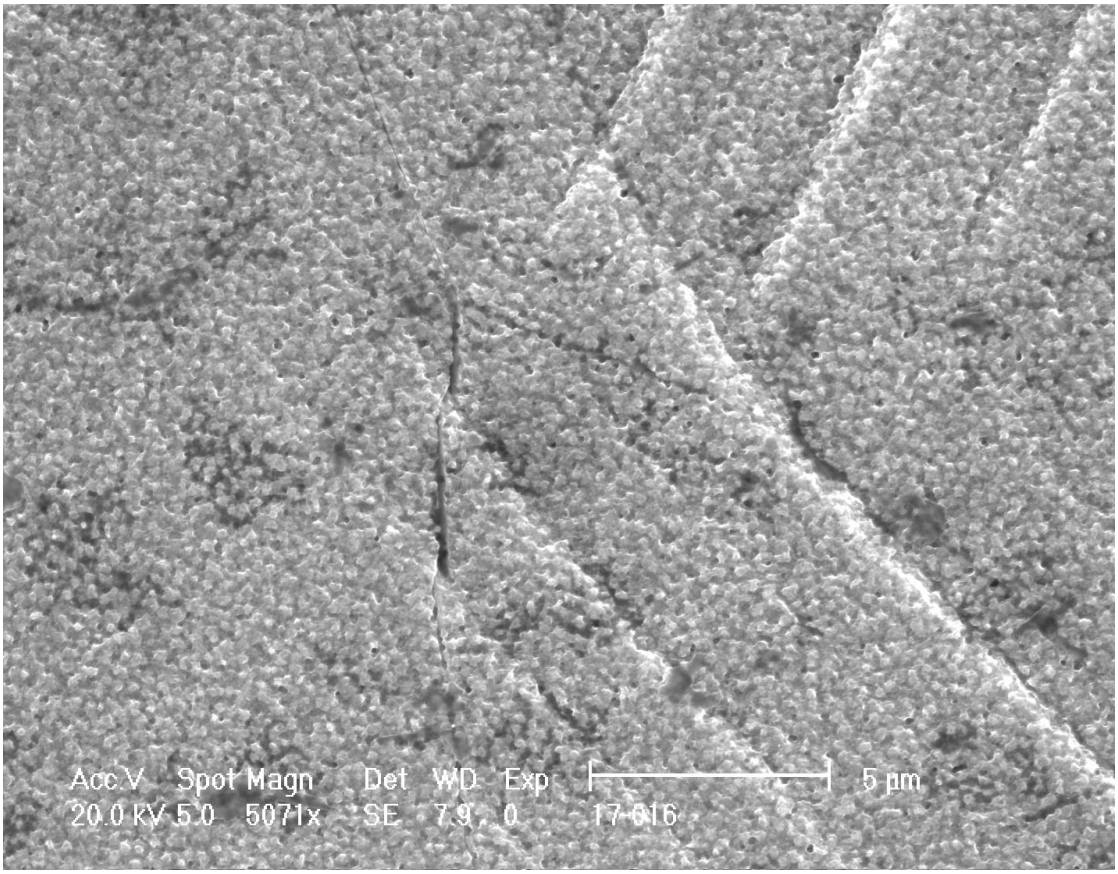

Figure 4.36: Intergranular cracks found in ASCC2 Fe13Cr15Ni 5 dpa tensile bar sample at site ASCC2-13 after 1.5% strain increment (6% total) in BWR-NWC at 288 °C at a strain rate of $3x10^{-7}$ s^{-1} that formed directly at the intersection between dislocation channels and the grain boundary.

During the course of straining in high temperature water, grain boundaries were subjected to both the stresses that were due to the pile-up of dislocations at the boundary as well as those due to the applied load. Therefore, the total grain boundary normal stress was a combination of both stresses. The total GB normal stress is defined as the summation of the elastic stresses generated by the dislocation channel (as measured by HREBSD) and the applied load during tensile testing resolved in a direction normal to the specific grain boundary. The total stress acting on the grain boundary as a function of Orientation Factor is shown in Figure 4.37. The component of stress in this value taken from HREBSD measurements is the peak value of normal stress taken at a point which is 200nm from the grain boundary. This figure also shows

which sites cracked (closed circles) and which sites did not (open circles). Table 4.10 lists the total grain boundary normal stresses and Orientation Factors for the data plotted in Figure 4.29. Since the σ_{12} shear component of stress was also observed to have considerable stress magnitudes near the DC-GB interaction site, the total grain boundary shear stress is also given in Table 4.13.

Table 4.13 Total grain boundary normal stress and shear stress values for HREBSD analyzed DC-GB interaction sites after 6% total strain in ASCC2 Fe13Cr15Ni 5 dpa tensile bar sample

Grain Boundary ID	Orientation Factor	Total GB Normal Stress	Total GB Shear Stress	Cracking (Y/N)
ASCC2-1	0.44	1.53	0.55	N
ASCC2-2	0.37	1.13	0.50	N
ASCC2-3	0.47	1.44	0.72	Y
ASCC2-4	0.39	1.19	0.69	Y
ASCC2-5	0.40	1.68	0.76	Y
ASCC2-6	0.38	0.90	0.54	N
ASCC2-7	0.45	1.73	0.95	Y
ASCC2-8	0.35	0.82	0.40	N
ASCC2-9	0.41	1.06	0.45	N
ASCC2-10	0.39	1.16	0.65	N
ASCC2-11	0.39	1.67	0.78	Y
ASCC2-12	0.34	0.66	0.26	N
ASCC2-13	0.37	0.98	0.60	N
ASCC2-14	0.42	1.27	0.72	N
ASCC2-15	0.42	1.41	0.51	Y
ASCC2-16	0.40	1.39	0.53	Y
ASCC2-17	0.39	1.14	0.52	N
ASCC2-18	0.37	1.37	0.60	Y
ASCC2-19	0.34	1.17	0.53	Y
ASCC2-20	0.39	1.32	0.74	Y
ASCC2-21	0.38	0.94	0.54	Y
ASCC2-22	0.32	0.84	0.43	N
ASCC2-23	0.39	1.23	0.46	N
ASCC2-24	0.37	0.94	0.40	Y
ASCC2-25	0.37	1.36	0.49	Y
ASCC2-26	0.40	1.05	0.54	N

ASCC2-27	0.36	0.60	0.25	N
ASCC2-28	0.33	0.68	0.29	N
ASCC2-29	0.35	0.95	0.51	N
ASCC2-30	0.39	0.98	0.43	Y
ASCC2-31	0.42	1.42	0.62	Y
ASCC2-32	0.40	1.73	0.69	Y
ASCC2-33	0.42	1.15	0.43	N
ASCC2-34	0.36	0.97	0.43	N
ASCC2-35	0.41	1.08	0.52	N
ASCC2-36	0.37	1.16	0.43	N
ASCC2-37	0.44	1.20	0.43	Y
ASCC2-38	0.44	1.05	0.43	Y
ASCC2-39	0.35	0.92	0.45	N
ASCC2-40	0.41	1.33	0.55	N
ASCC2-41	0.43	1.41	0.78	Y
ASCC2-42	0.47	1.38	0.84	Y
ASCC2-43	0.42	1.48	0.82	N
ASCC2-44	0.41	1.29	0.74	N
ASCC2-45	0.46	1.17	0.46	Y
ASCC2-46	0.45	1.45	0.77	N
ASCC2-47	0.35	0.85	0.37	N
ASCC2-48	0.37	0.99	0.56	N
ASCC2-49	0.38	1.02	0.50	Y
ASCC2-50	0.35	0.84	0.36	N
ASCC2-51	0.30	0.86	0.47	N
ASCC2-52	0.25	0.92	0.33	N
ASCC2-53	0.27	0.85	0.47	N
ASCC2-54	0.25	0.67	0.24	N
ASCC2-55	0.33	0.94	0.44	N
ASCC2-56	0.32	1.04	0.53	Y
ASCC2-57	0.26	0.78	0.37	N
ASCC2-58	0.23	0.54	0.28	N
ASCC2-59	0.30	0.96	0.35	N
ASCC2-60	0.29	1.17	0.67	N
ASCC2-61	0.30	1.02	0.60	Y
ASCC2-62	0.26	0.98	0.48	N
ASCC2-63	0.32	1.26	0.62	Y
ASCC2-64	0.31	1.11	0.42	N
ASCC2-65	0.24	0.77	0.37	N
ASCC2-66	0.29	0.97	0.35	N
ASCC2-67	0.29	1.39	0.73	Y

ASCC2-68	0.24	0.69	0.30	N
ASCC2-69	0.24	0.87	0.38	N
ASCC2-70	0.30	1.00	0.36	N
ASCC2-71	0.30	1.05	0.40	N
ASCC2-72	0.26	0.87	0.36	N
ASCC2-73	0.29	0.98	0.60	N
ASCC2-74	0.26	0.59	0.31	N
ASCC2-75	0.34	1.20	0.58	Y

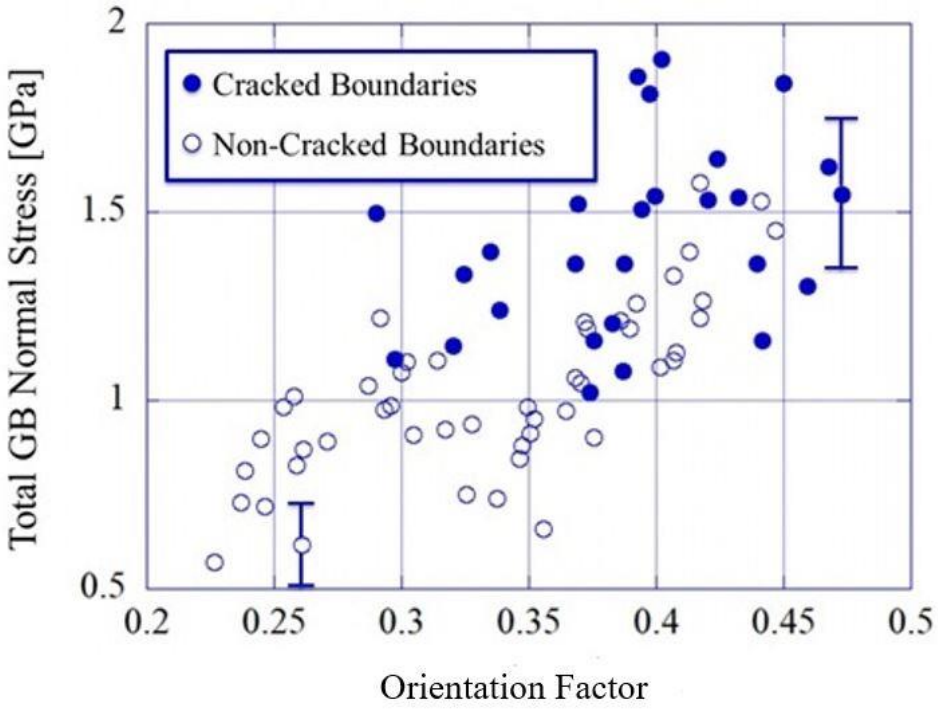

Figure 4.37: Total GB normal stress as a function of Orientation Factor in Fe13Cr15Ni with cracked boundaries highlighted after an additional 1.5% plastic straining step (6% total) in 288 ºC BWR-NWC conditions

Intergranular fracture was not observed in the BSCC2 Fe21Cr32Ni 5 dpa tensile bar sample after 6% total plastic strain. In an attempt to generate cracks, an additional 1.5% plastic strain increment was performed, raising the total strain to 7.5%. Prior to this strain increment, 20 additional HREBSD scans were performed at sites which had been scanned prior to the first BWR-NWC strain increment. Figure 4.38 shows the change in grain boundary normal stress as measured by HREBSD directly after the 4.5% straining step in high temperature argon and after the 6% total strain increment performed in 288 °C BWR-NWC for the BSCC2 Fe21Cr32Ni 5

dpa tensile bar sample. The details of the changes to the total grain boundary normal stress are listed in Table 4.14.

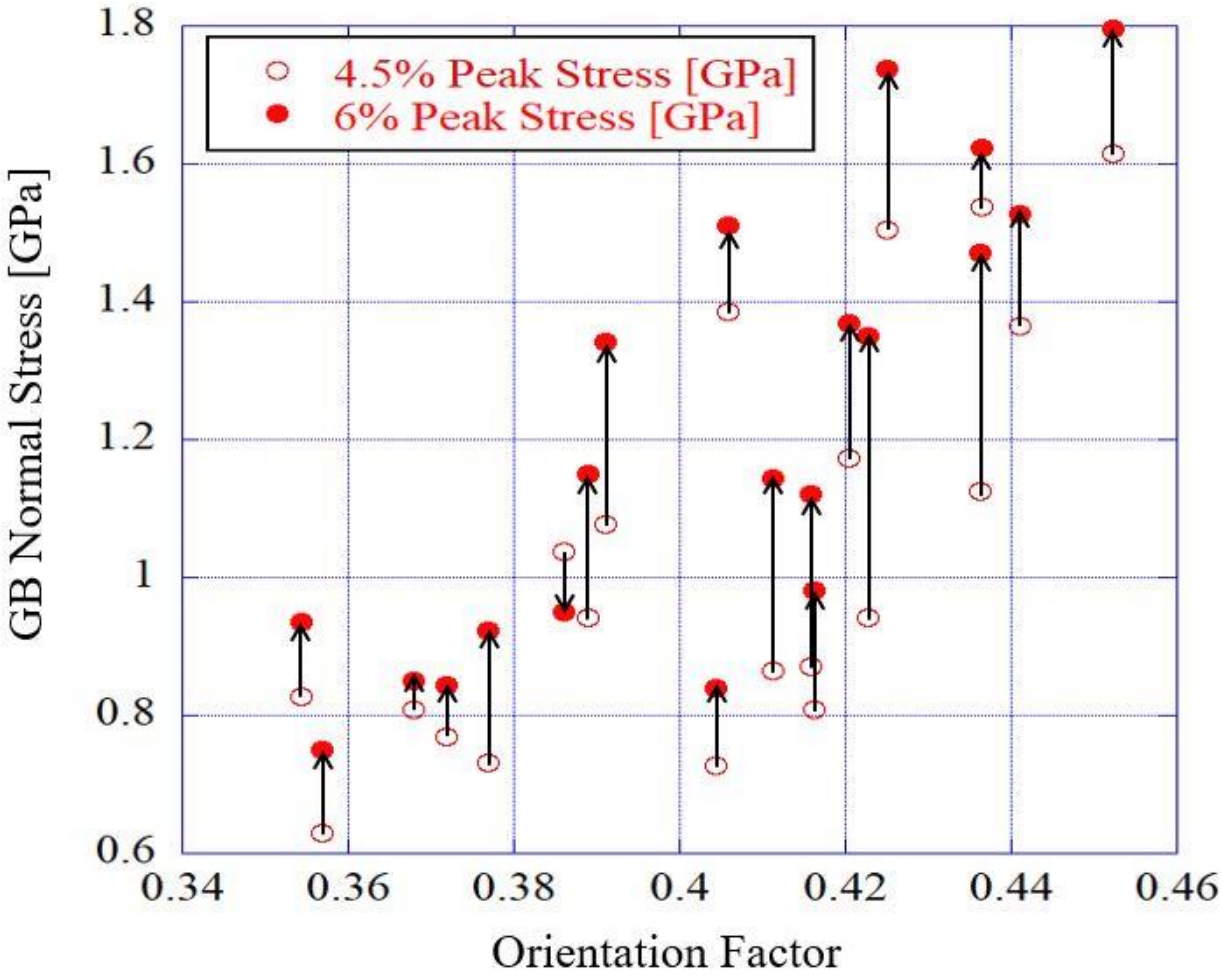

Figure 4.38: Grain boundary normal stress as a function of Orientation Factor calculated from HREBSD after a total of 4.5% plastic strain and 6% plastic strain in BSCC2 Fe21Cr32Ni 5 dpa tensile bar sample.

Table 4.14 Grain boundary normal stress values for HREBSD analyzed DC-GB interaction sites after 4.5% and 6% total strain in Fe21Cr32Ni

Grain Boundary ID	Orientation Factor	4.5% GB Normal Stress [GPa]	6% GB Normal Stress [GPa]	Measured Difference [GPa]	Percent Difference
2192-2	0.36	0.83	0.94	0.11	13.3
2192-3	0.37	0.63	0.75	0.12	19.2
2192-4	0.37	0.81	0.85	0.04	5.3

2192-5	0.38	0.77	0.84	0.08	9.8
2192-6	0.39	0.73	0.92	0.19	26.1
2192-7	0.39	1.04	0.95	-0.09	-8.5
2192-8	0.39	0.94	1.15	0.21	22.1
2192-9	0.40	1.08	1.34	0.27	24.6
2192-10	0.41	0.73	0.84	0.11	15.5
2192-11	0.41	1.39	1.51	0.13	9.1
2192-12	0.42	0.87	1.14	0.28	32.1
2192-13	0.42	0.87	1.12	0.25	28.7
2192-14	0.42	0.81	0.98	0.17	21.4
2192-15	0.42	1.17	1.37	0.20	16.7
2192-16	0.42	0.94	1.35	0.41	43.2
2192-17	0.43	1.50	1.74	0.23	15.6
2192-18	0.44	1.19	1.36	0.17	14.1
2192-19	0.44	1.12	1.47	0.35	30.7
2192-20	0.44	1.54	1.62	0.08	5.5
2192-21	0.45	1.37	1.53	0.16	11.9

The average increase in the stress magnitude after adding an additional 1.5% strain was observed to be 0.176 ±0.132GPa and all sites showed an increase in the grain boundary normal stress except for one site out of the 20.

Chapter 5 - Discussion

This chapter focuses on the stresses generated by dislocation channels when they impinge on a grain boundary, and the effect of these stresses on stress corrosion crack initiation in irradiated steel. Previous chapters showed the presence of a large stress field surrounding the interaction site between dislocation channels and grain boundaries and how samples with observable dislocation channels were susceptible to cracking when exposed to a high temperature aqueous environment. This chapter will discuss the importance of the absolute and relative magnitudes of measurable tensile and shear stresses and their effect on the process of crack initiation.

The chapter will address two major questions, the first of which is the stress state near dislocation channel – grain boundary interaction sites. Stress is a key component to IASCC, and being able to take a quantitative look at the stresses near the grain boundary leading up to crack initiation is important for understanding the overall mechanism and factors which drive the process. The second is the relationship between the experimentally observed stress state and the cracking of specific grain boundaries. The concept of a pseudo threshold for crack initiation in the Fe13Cr15Ni alloy will be discussed along with the effect of crystallographic and grain boundary orientations.

5.1 Model and Measured Local Stresses Near Dislocation Channel – Grain Boundary Interaction Sites

5.1.1 Effect of Multiple Planes on Stress Distribution at Discontinuous Dislocation Channel – Grain Boundary Sites

As discussed in Chapter 2, the Eshelby model is used to describe the pile-up of dislocations on a single slip plane. The dislocation at the head of the pile-up is locked in place due to an impassable barrier, much like a grain boundary. Each dislocation has its own stress field which acts on all other dislocations participating in the pile-up event. A force equilibrium must be maintained for each dislocation. At a given location dislocations closer to the boundary exert a force which pushes back away from the boundary, while dislocations farther away exert a force towards the dislocation pinned at the front of the pile-up. The force equilibrium is given by

$$\sum_{\substack{i=1 \\ i\neq j}}^{n} \frac{A}{x_j - x_i} + P\left(x_j\right) = 0; \;\; j = 1,2,...,n \quad . \tag{5.1}$$

The first component in the summation accounts for the individual stress contributions from all the dislocations other than one specific dislocation of interest acting at the position of the specific dislocation, $P(x)$ accounts for any applied stresses acting at the position of the specific dislocation, and n is the total number of dislocations participating in the pile-up event. Solving for the position terms, (x_j, x_i) such that the force balance is maintained provides the equilibrium position of each dislocation and the magnitude of stress at any position around the pile-up. A major limitation of the Eshelby model is that it relies on distributing a set of dislocations on a single slip plane. While convenient for setting up analytical solutions for the estimated distribution of stress near a pile-up event, it fails to describe the actual geometry of a dislocation

channel. From TEM investigation, it is known that channels are comprised of several parallel slip planes which lead to a channel width on the order of 50-100nm [126-129]. For austenitic stainless steels, this channel width corresponds to 10's of active parallel slip planes in which dislocations can be distributed inhomogeneously. Here is drecribed a discrete dislocation pile-up model was developed to solve for the equilibrium positions of dislocations spread across multiple slip planes and adhering to the geometric constraints of the grain boundary as described in the experimental procedures chapter section 3.4.

As in the Eshelby model, the first dislocation on each slip plane is pinned at the grain boundary. Since the grain boundary plane has a defined geometry relative to both the loading axis and active slip system based on the deforming grain's crystallographic orientation, there is both a vertical and horizontal offset between the first dislocations on each slip plane. This prevents the equilibrium position of all dislocations from aligning in the vertical direction when the same number of dislocations are placed on each of the available slip planes. A simple diagram of the pile-up of dislocations based on the initial geometry of the problem is shown in Figure 5.1 with the vertical and horizontal position differences of the parallel slip planes exaggerated for visualization.

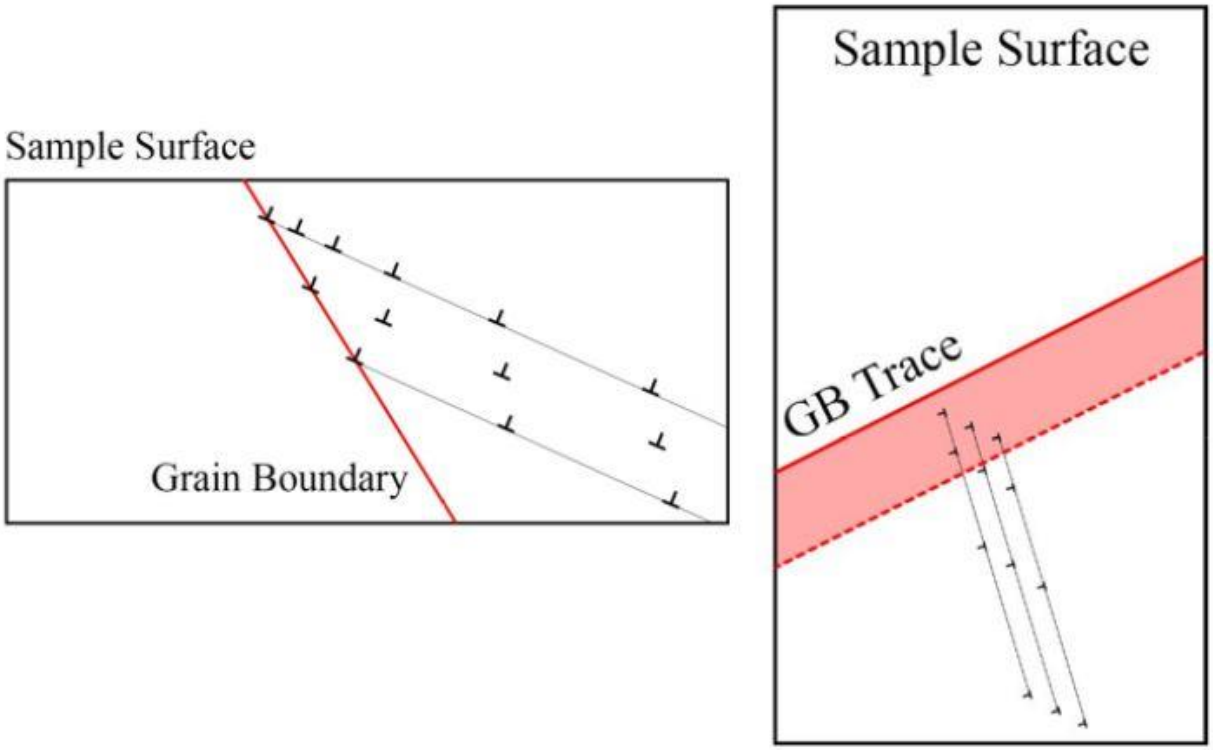

Figure 5.1: Diagram showing the distribution of dislocations on multiple slip systems as viewed from the side (left) and top (right) with respect to the sample geometry

When moving from a single slip plane to several parallel slip planes, the force equilibrium to solve for the position of each dislocation must be modified to account for the vertical separation of the linear arrays of dislocations. Shear stresses that are not acting in the plane of the dislocation will not affect the initial force equilibrium established in equation 5.1. However, since the generalized form of the stress field around an edge type dislocation is a function of both the vertical and horizontal separation between the dislocations, the addition of multiple planes will have a significant effect on the equilibrium location of each dislocation. The generalized form of the stress field around an edge type dislocation used in this analysis is given by:

$$\sigma_{xy} = D * x * \frac{x^2 - y^2}{(x^2 + y^2)^2}, \tag{5.7}$$

$$\sigma_{xx} = -D * y * \frac{3x^2 + y^2}{(x^2 + y^2)^2}, \tag{5.8}$$

$$D = \frac{G * b}{2\pi(1 - \nu)}; \tag{5.9}$$

where x and y are the coordinates of the point of interest away from the individual dislocation, *G* is the material shear modulus, ***b*** is the Burgers vector, and *v* is Poisson's ratio [131]. Since the shear stresses are responsible for dislocation motion on the active slip planes, this stress value is used to establish stress equilibrium while the functional form of the tensile stress is used during analysis once the equilibrium positions of the dislocations have been established. Previous experiments have been able to observe dislocation pile-ups in irradiated materials by performing in-situ straining under direct TEM observation [116,117]. However the dose investigated and total amount of plastic strain were small compared to the parameters in the current study. Due to this, it is difficult to determine the total number of dislocations in the dislocation channels analyzed here. As a first order approximation, the channel height was used to determine the number of dislocations within the channel by dividing the channel step height, as measured by confocal laser microscope, by the component of *b* pointing in the direction perpendicular to the sample surface as described in equation 5.2:

$$n = \frac{Channel\ Height}{b_{\perp}}. \tag{5.2}$$

For comparison with the multi slip plane model, parameters and orientations for the ASCC2-32 channel site were used. HREBSD and confocal laser measurements on the ASCC2 Fe13Cr15Ni 5 dpa sample were performed after a 4.5% straining step in 288 °C argon at a strain rate of $3x10^{-7}$ s^{-1}. The actual channel width is unknown, so a typical value of 85 nm was used based on previous TEM observations [126-129]. The dense dislocation structure following this magnitude of straining makes it impossible to resolve individual dislocations in the channel at the current time, so an approximation must be used. Using equation 5.2, the number of dislocations in this channel was estimated to be 436. In order to maintain symmetry in the distribution of dislocations, 17 dislocations were placed on each of 25 parallel slip planes spaced 1 $\boldsymbol{b}$ apart to create a channel of 85 nm width and containing 425 dislocations. Figure 5.2 shows the 2D tensile stress map generated from the discrete dislocation model and from the experimental measurement using HREBSD.

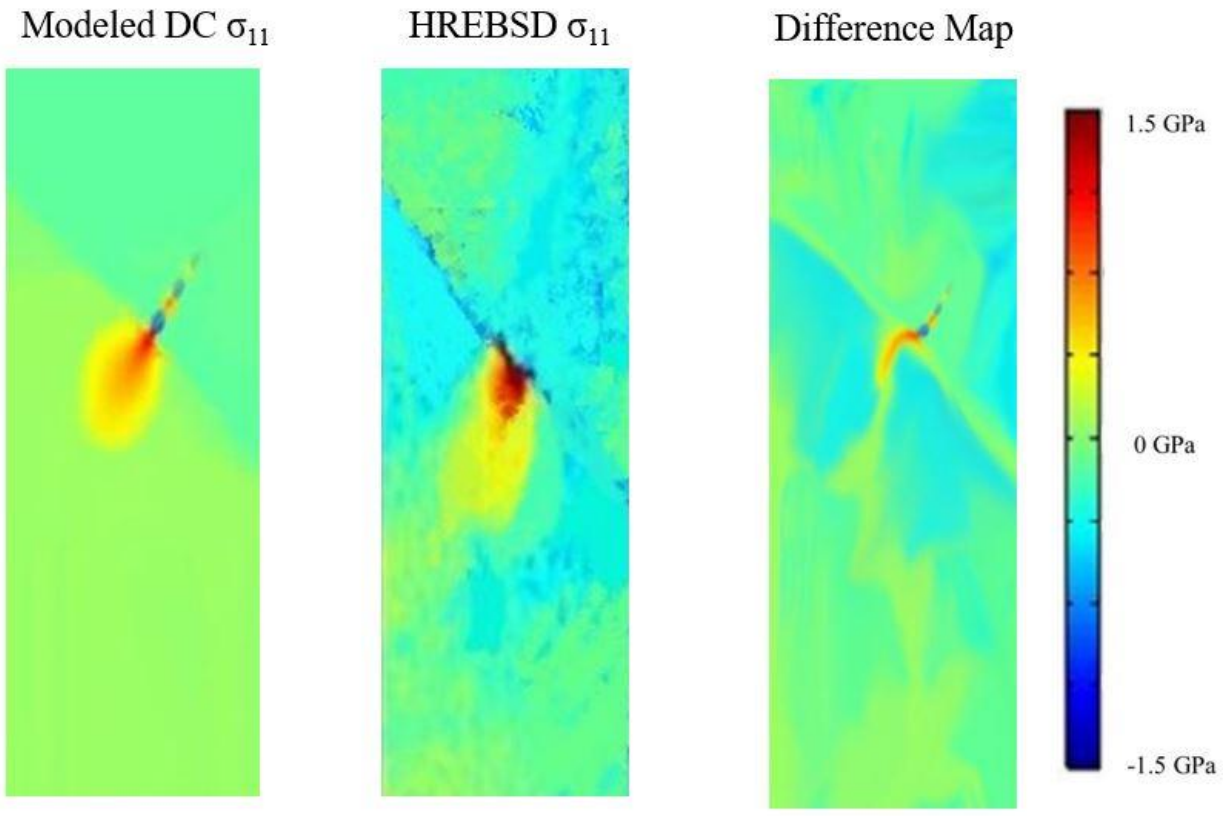

Figure 5.2: 2D tensile stress maps comparing the results from the multi plane discrete dislocation model and the calculated results from HREBSD analysis on channel site ASCC2-32 after 4.5% plastic strain in 288 °C argon at a strain rate of $3x10^{-7}$ s^{-1}.

The general shape and magnitude of the tensile stresses are consistent between the two, which is evident from the difference map provided. Figure 5.3 shows a similar comparison for the calculated 2D shear stress distribution, plotted on the same color scale. While the match between the shear stress is not as close as for the σ_{11} tensile stress component, there are still similarities between the model and HREBSD shear stress distributions with lobes of positive and negative shear stresses present in each.

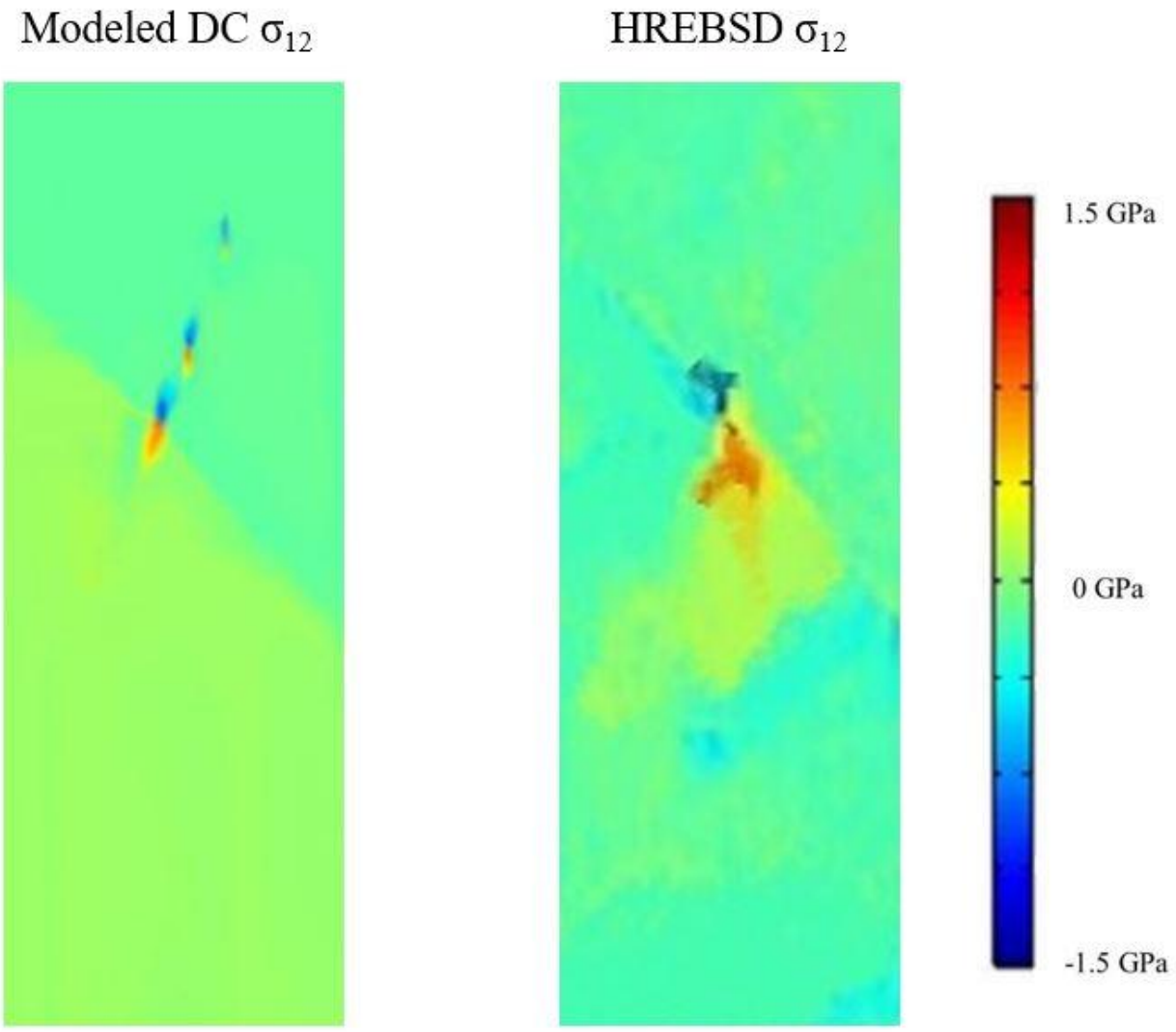

Figure 5.3:2D shear stress maps comparing the results from the multi plane discrete dislocation model and the calculated results from HREBSD analysis on channel site ASCC2-32 after 4.5% plastic strain in 288 °C argon at a strain rate of $3x10^{-7}$ s^{-1}.

Figure 5.4 and Figure 5.5 compare the tensile and shear stresses as a function of distance away from the grain boundary for both the simulated dislocation channel and the HREBSD data respectively. While the stress generated by the simulated dislocation channel decreases more rapidly with distance away from the interaction site, the agreement is reasonable. Considering the level of agreement, it is possible to obtain an estimation of the number of dislocations in a

dislocation channel, without direct TEM observation, which has proven difficult to make with the current level of both irradiation damage and strain in these tensile bar samples.

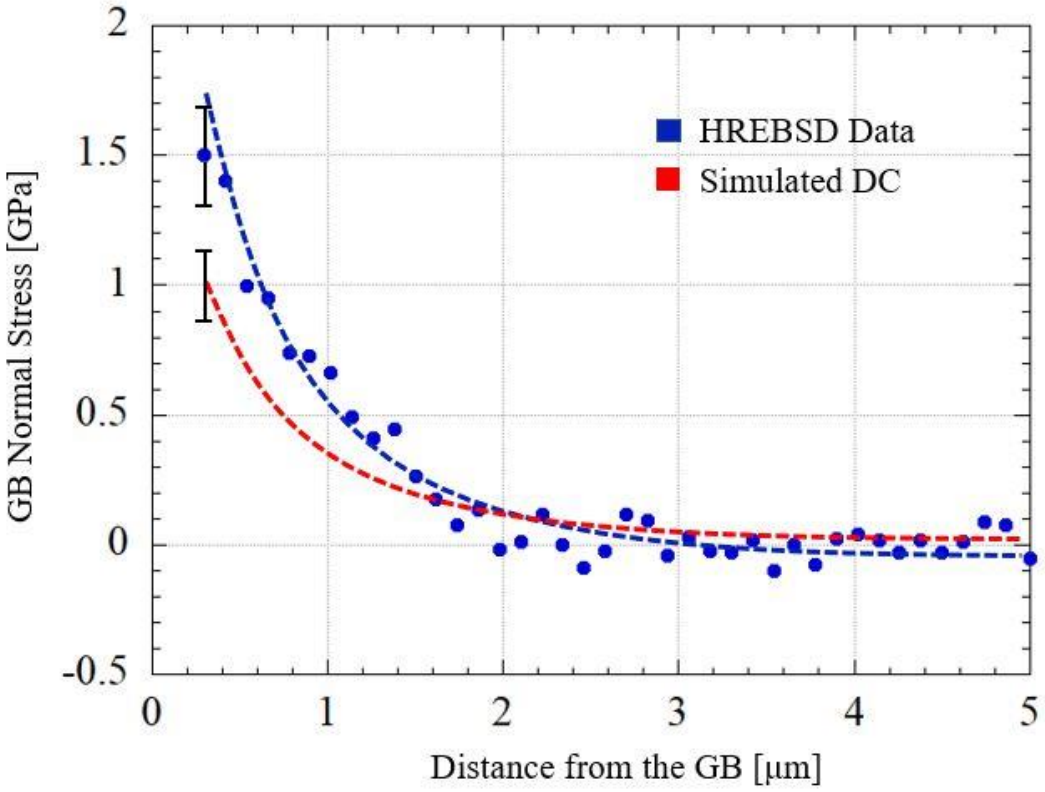

Figure 5.4: Tensile stress profiles as a function of distance from the grain boundary comparing simulated dislocation channels and HREBSD data for site ASCC2-32 5 dpa Fe13Cr15Ni tensile bar sample after 4.5% strain in 288 °C argon at a strain rate of $3x10^{-7}$ s^{-1}.

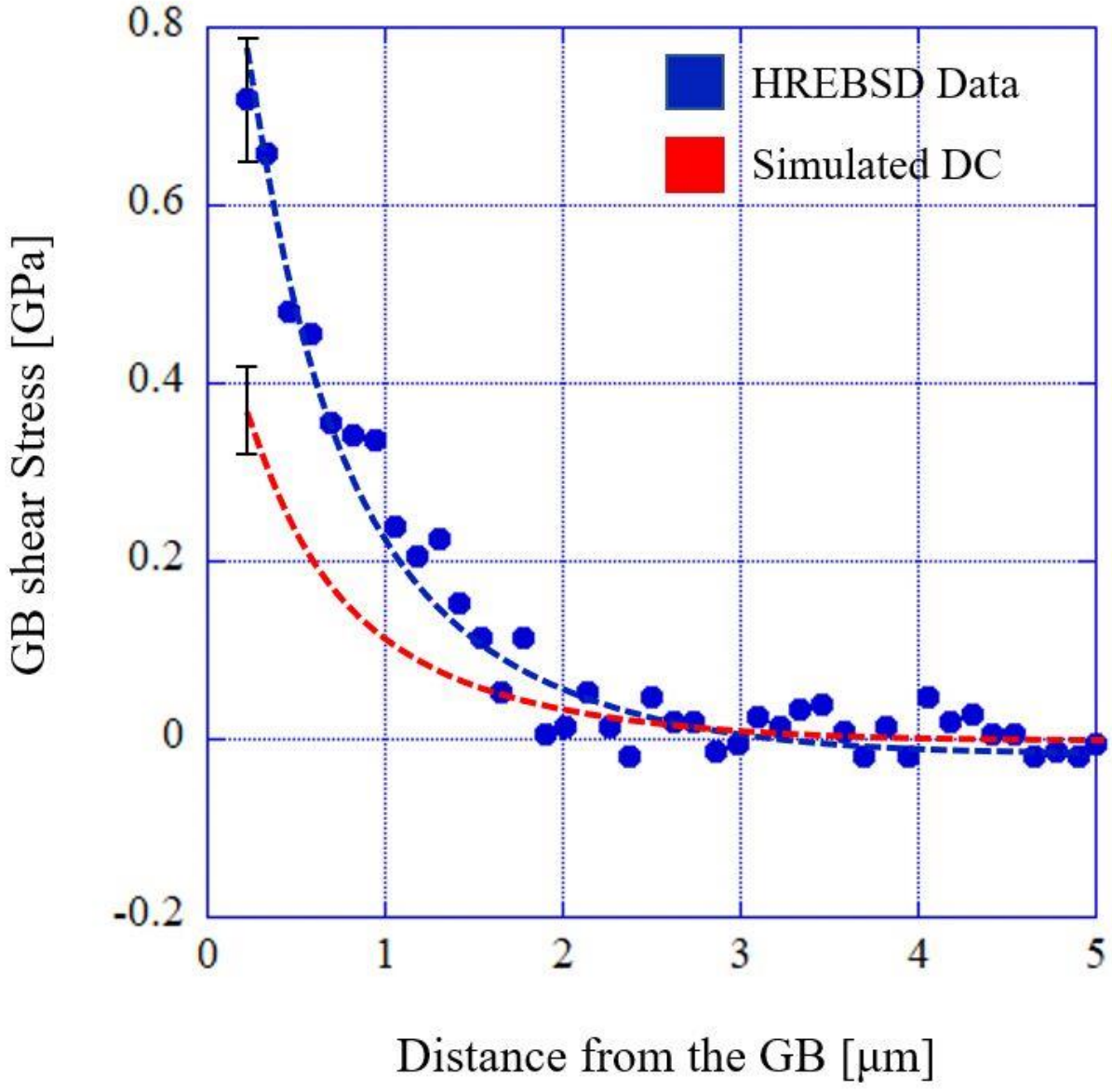

Figure5.5: Shear stress profiles as a function of distance from the grain boundary comparing simulated dislocation channels and HREBSD data for site ASCC2-32 5 dpa Fe13Cr15Ni tensile bar sample after 4.5% strain in 288 °C argon at a strain rate of $3x10^{-7}$ s^{-1}.

The original analysis of the calculated dislocation model stress only showed that the stress profile generated had the same general form as the observed HREBSD distributions. However it is important to note that the stress plumes in the experimental case were wider than predicted by the model and the magnitude measured by HREBSD was higher than the model

predicted. There are multiple factors which differentiate the experimental system from what was set up in the model. The model used a perfectly flat plane with constant angle relative to the incoming slip system while the grain boundary plane in the experimental case is comprised of the interface between two grains which can have many imperfections and local changes in geometry which would act to alter the distribution of dislocations along the grain boundary. The distribution of dislocations on separate parallel slip planes is also not uniform, as is assumed in the model. These changes to the distribution would result in a generated stress plume which is not entirely symmetrical, and could account partially for the difference in width between the experiment and dislocation model. For both the tensile and shear components of stress, there was no overlap in the error bars of the experiment and the dislocation model. This could potentially be due to that fact that the number of dislocations used in the model were estimated assuming that only a single slip system was active in the deforming grain. TEM observations made by J. Kacher et al. showed that within a small slip band multiple slip systems can be active [148]. In situ strainings were performed after a 304 austenitic stainless steel had been irradiated to 0.14 dpa using 1 MeV krypton ions. This dose would increase the defect population of the matrix and cause a degree of strain localization. If a similar phenomenon were to occur in the ASCC2 Fe13Cr15Ni 5 dpa tensile sample , the contribution of this second active slip system would not be accounted for in the dislocation model. A second active slip system would act to increase the lateral spread of the observed stress plume and would also contribute in increasing the peak stress magnitude observed in the adjacent grain. To confirm this, direct observation of discrete dislocations in the dislocation channel would be necessary, but those observations are not possible at this time.

The analysis presented here assumes that the stresses observed using HREBSD are generated by a large collection of dislocations near the grain boundary in the deforming grain. As stated earlier, the high population of defects in irradiated material and the relatively high strain values reached in this study make it difficult to determine the dislocation content within the individual channels. A recent study by Guo et al. [145] was able to use differential aperture x-ray microscopy (DAXM) to calculate the geometrically necessary dislocation (GND) densities at the interaction sites between slip bands and grain boundaries in commercial purity titanium. Although the samples studied in this work were not irradiated, dislocations were halted at a grain boundary in the same way dislocation motion is arrested in the current material. Figure 5.6 shows an SEM image of the analyzed slip bands in commercial purity titanium and Figure 5.7 shows the GND densities measured at this location using DAXM.

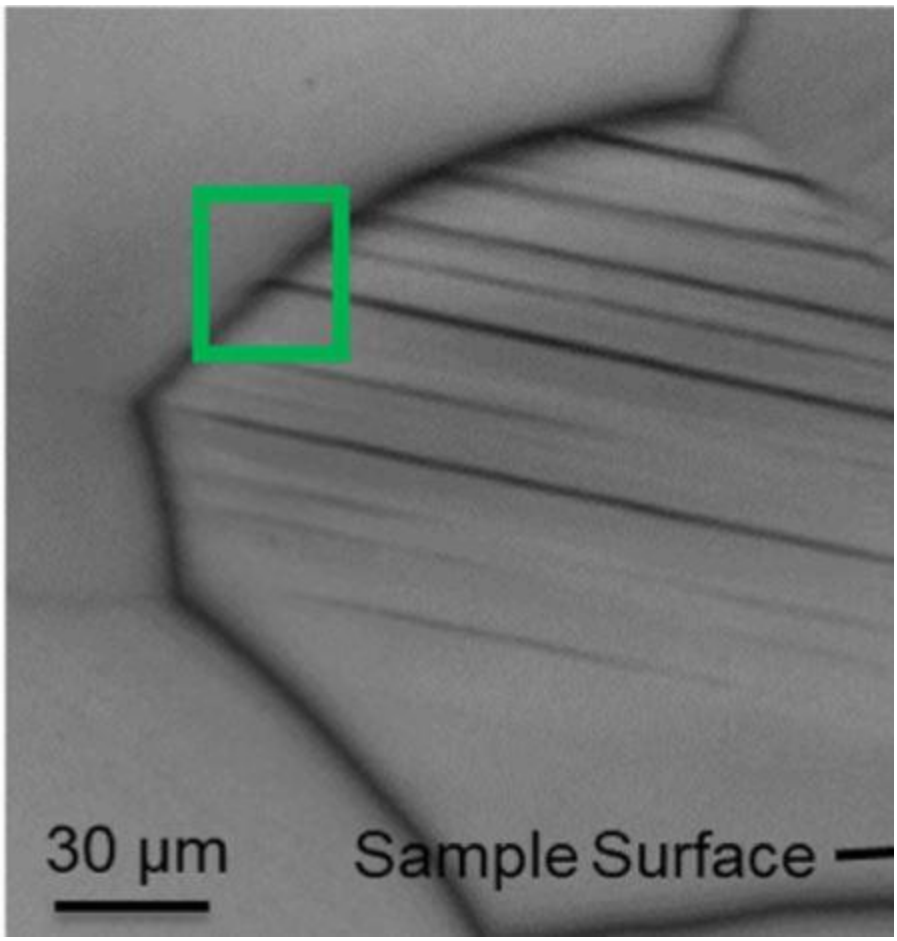

Figure 5.6: SEM image showing the interaction site of a discontinuous slip band with a grain boundary in commercial purity titanium sample [145]

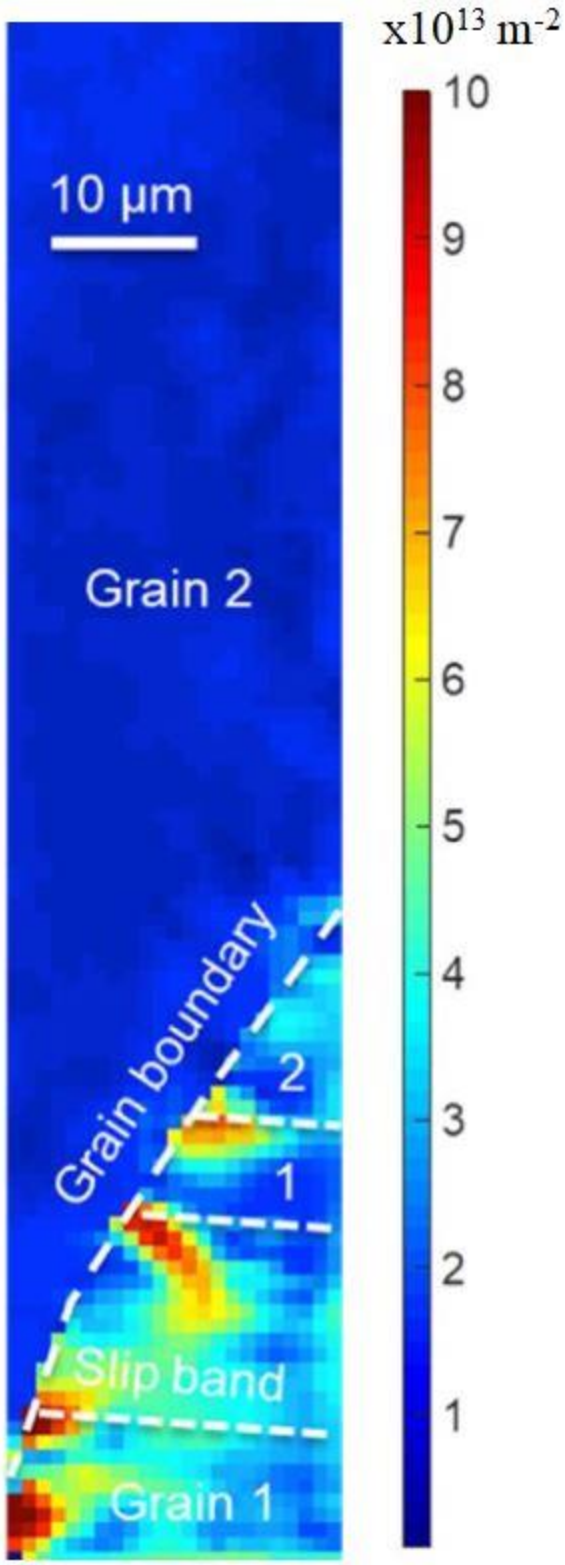

Figure 5.7: GND density map near discontinuous slip band - grain boundary interaction sites measured with DAXM in commercial purity titanium [145]

A high density of dislocations is observed at the point of interaction between the discontinuous slip band and the grain boundary only in the deforming grain. In the adjacent grain, GND densities are calculated to be an order of magnitude smaller. This is all consistent with the setup of the discrete multi plane dislocation model presented above. All dislocations appear to be in the deforming grain, with a majority of them clustered within the first few microns of the grain boundary. The DAXM results also show variation in the GND density between the slip bands contained within a single grain, which could help to explain the presence of both cracked and non-cracked sites along a single boundary observed in proton irradiated austenitic stainless steel by He et al. [35].

Molecular dynamics simulations have also been widely used to study the properties of dislocations in both irradiated and non-irradiated materials [136-138]. The computational limitations of simulation size prevent the modeling of complete dislocation channels, but much can be learned about the stress that develops around dislocations on individual slip planes as they interact with grain boundaries. Johnson et al. [82] used molecular dynamics to investigate the deformation response of a cluster of grains which had been modeled after a similar cluster taken from a tensile bar sample. Tensile stresses measured near both continuous and discontinuous dislocation channel – grain boundary interaction sites using HREBSD in a Fe13Cr15Ni alloy were compared to similar sites in the MD simulation where a small number of dislocations interacted with the grain boundary after several steps of virtual strain. The tensile bar sample used for this study was irradiated to 5 dpa prior to CERT straining to a total plastic strain level of 3% in 288 °C argon at a strain rate of $3x10^{-7}$ s^{-1}. After straining, a cluster of grains in the tensile bar sample was selected which included both continuous and discontinuous dislocation channels. Due to symmetric requirements for the MD boundary conditions, only the central 5 grains could be modeled, and the overall shape of the grains needed to be altered slightly. The average grain size for the MD simulation also needed to be limited to 120 nm to prevent the simulation from

being too computationally expensive. While the geometry of the individual grains needed to be adjusted to allow for MD simulation, the crystallographic orientation of each grain could be matched closely between the experiment and the simulation based on the EBSD analysis performed on the physical sample. Figure 5.8 compares the cluster of grains analyzed using HREBSD with the grains used in the MD simulation.

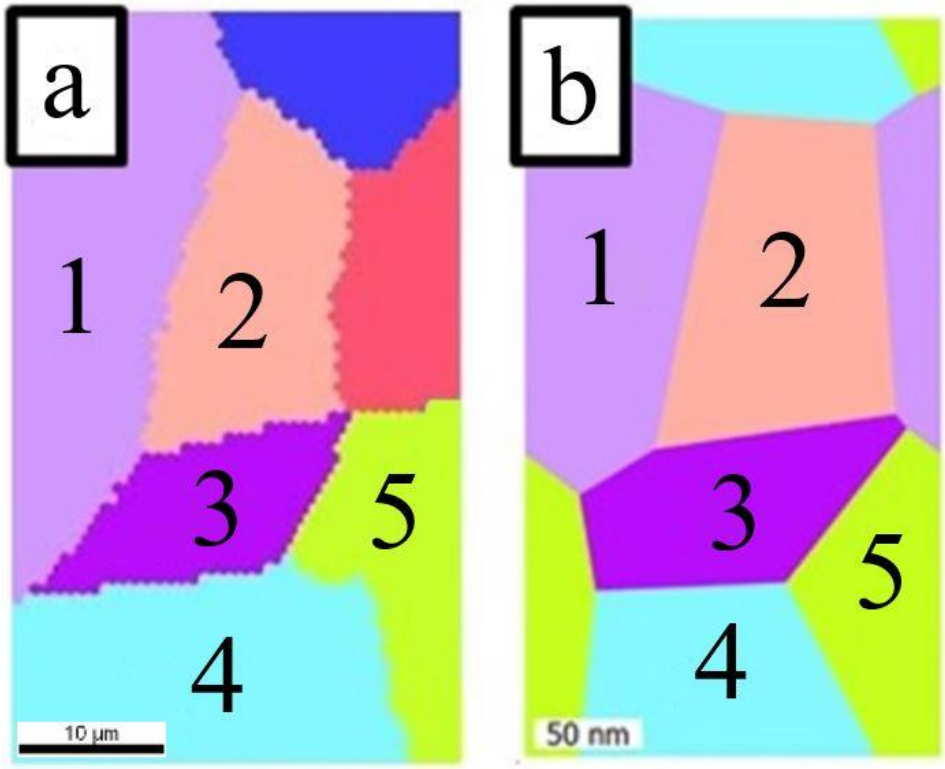

Figure 5.8: (a) Cluster of grains taken from a proton irradiated 5 dpa Fe13Cr15Ni tensile bar sample and (b) the same cluster of grains recreated for MD analysis.

In both the experiment and the MD simulation, only 2D information is known about the grain geometry. In order to simplify the MD simulation and subsequent calculations, the grain boundaries were made to be perpendicular to the sample surface. Due to computational limitations, the thickness of the simulated volume was 9 nm. For the sake of calculations it was also assumed that the grain boundaries in the experimental cluster of grains were perpendicular

to the sample surface. This would effectively provide an upper limit on the stress acting normal to the grain boundary in the experimental cluster of grains. D. Farkas and B. Kuhr performed MD simulations using the LAMMPs code which incorporates the embedded atom method (EAM) interatomic potential that were modified from a FCC nickel potential to simulate the FCC austenitic stainless steel. In this simulation, there is only one type of atomic bond interaction (Ni-Ni), however the differences in interatomic bond strength between iron, nickel, and chromium atoms in a FCC lattice are small, making the nickel interatomic potential an appropriate substitute for including the other atomic species. While this simplifies the bonding structure in the simulation, it also means that complicated interactions between the virtual cluster of grains and the corrosive environment required for IASCC is outside the current capabilities of the model. Deformation of the virtual sample is performed at a considerably higher strain rate of $3x10^8$ s^{-1} at a temperature of 300K. Additional information about the MD simulation can be found in [146] and [147].

These conditions, while different from experimental conditions, are not expected to have a dramatic effect on the behavior of the system in terms of the slip systems activated during virtual straining and setting these parameters to values more in line with the experimental procedures would increase the time required for computation significantly. Following increments of 0.5% strain, the virtual sample was quenched from 300K to 1K in 50 ps to eliminated any remnants of stress caused by thermal fluctuations of individual atom positions and the 6 unique components of the stress tensor was estimated in LAMMPs as a sum of pairwise forces on each atom and using the average volume occupied by a nickel atom in a FCC lattice. The tensile stress field was calculated at the boundary between grains 2 and 3 as labeled in Figure 5.6 in both the experimentally analyzed cluster of grains and the MD simulation after virtual straining to

compare both the magnitude and distribution of the stresses. Since the stress component of interest is the tensile stress acting to pull the grain boundary apart, the stress tensor has been rotated such that the σ_{11} component of stress is pointing in a direction perpendicular to the grain boundary trace. The 2D tensile stress profiles for both the physical and MD simulated samples are presented in Figure 5.9. The stress map used for the MD simulation was taken after a total of 5% plastic strain as measured from the volumetric strain of each atom relative to the original non-deformed configuration. This value increases as neighboring atoms move away from each other due to slip, but are unaffected by uniform atomic displacement.

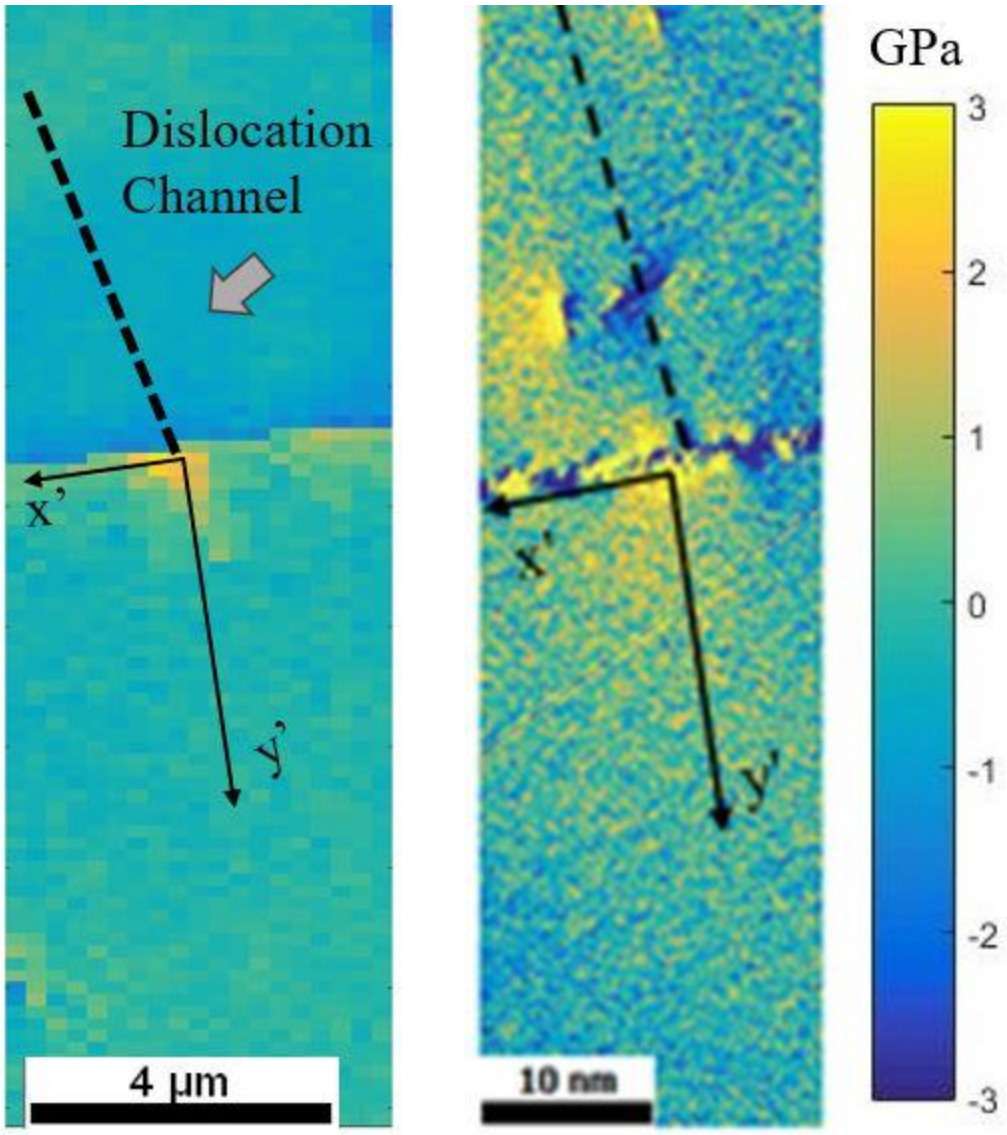

Figure 5.9: Comparison of 2D grain boundary normal stress distributions at the same location for a discontinuous dislocation channel - grain boundary interaction site in a 5 dpa proton irradiated Fe13Cr15Ni alloy strained to 3% plastic strain in 288 ˚C argon at a strain rate of $3x10^{-7}$ s^{-1} (left) and a molecular dynamics simulation of the same grain boundary virtually strained to 5% plastic strain (right).

A substantial increase in stress is observed directly at the intersection between the dislocation channel and the grain boundary, with the peak stress located at the point closest to the boundary for both the physical and simulated cases. For the physical sample, the peak calculated grain boundary normal stress was 2.78 GPa and the peak shear stress was 0.91 GPa. These

values are higher than the ones presented in Chapter 4, but are still reasonable considering that they are an overestimation of the actual stress since the true grain boundary plane angle is not being accounted for in the calculation. For the MD simulation, the peak tensile stress was calculated to be 4.75 GPa, which is significantly more than observed in the physical sample. This is most likely due to the ability of the MD simulation to resolve data points much closer to the actual location of the grain boundary. Shorter pile-up lengths and the close proximity of this site with other grains and dislocations due to the small simulated grain size could possibly explain the observed differences between the experimental and simulated data. Figure 5.10 shows the stress as a function of distance from the grain boundary along the line y' shown in Figure 5.9 for both the experimental and MD simulation. In the MD simulated grains, a 30 atom moving average was taken as a measurement of the local stress since the large variation in the stress state of individual atoms does not give an appropriate depiction of the bulk behavior. In order to account for the large difference in length scale, the distance is normalized by the grain size. Eshelby fits are applied to both data sets based on the least squares fitting procedure outlined in Chapter 4. The $r^{-1/2}$ dependence outlined by Eshelby is able to fit both the experimental and MD results well despite the large difference in sample size and active dislocations in the pile-up event.

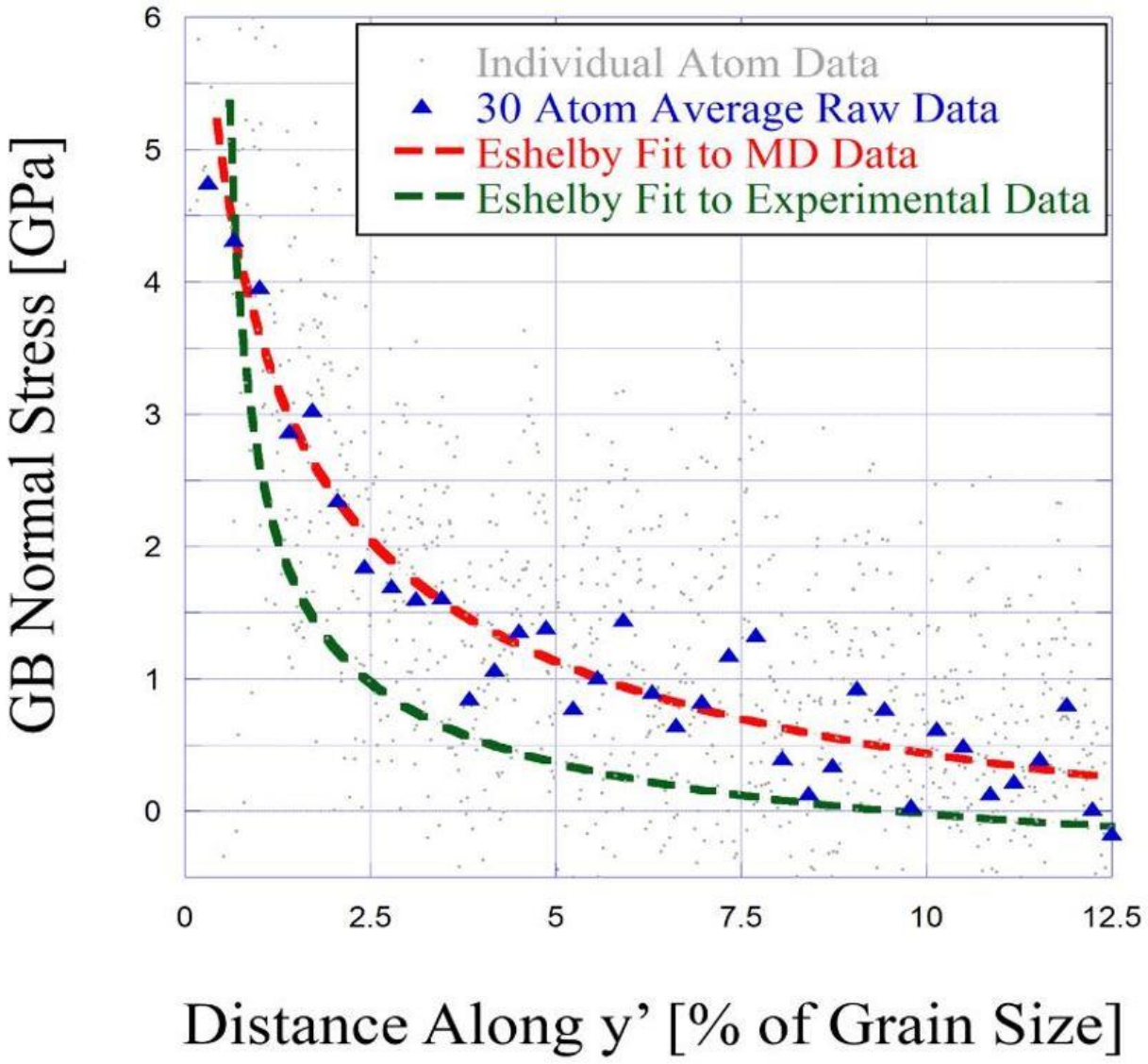

Figure 5.10: Comparison of the grain boundary normal stress as a function of distance away from the grain boundary along y' for a Fe13Cr15Ni 5 dpa proton irradiated tensile bar sample strained to 3% in 288 C argon at a strain rate of $3x10^{-7}$ s^{-1} and an MD simulation of the same grain boundary virtually strained to 5%.

Thus far, MD simulation results have been consistent with those from experiment and from using a discrete dislocation array to describe the behavior of dislocation channels in irradiated steels.

While there are key similarities between the behavior of the molecular dynamics model and experiment, there are crucial differences that must be noted. Ultimately, the MD models are only able to simulate the formation of a few dislocations propagating in the simulated system

even up to several percent of virtual strain. This is important for investigating how dislocations interact with a grain boundary, but does not approach simulating an actual dislocation channel with 10's or 100's of dislocations populating many parallel slip planes. The simulations used in this study also don't account for radiation damage or oxidation in an aqueous environment which are known to be necessary for IASCC. The MD simulations employed here are important for understanding the fundamental mechanisms around pile-up and deformation near grain boundaries, but still lack the complexity to incorporate all of the key features surrounding IASCC so a perfect match between MD simulations and experimental measurements is not expected.

5.1.2 Stress Distribution at Continuous Dislocation – Grain Boundary Interaction Sites

This preceding analysis focused on the ability to explain the stress states that were observed at discontinuous DC-GB interaction sites. Equally important to the understanding of the increased cracking susceptibility at grain boundaries is the ability to understand the stress state present near continuous channel sites. HREBSD analysis has also been performed at continuous DC-GB interaction sites by Johnson et al [83]. Figure 5.11 shows the grain boundary normal stress as a function of distance from the grain boundary near a continuous DC-GB interaction site in a 5 dpa proton irradiated Fe13Cr15Ni tensile bar sample strained in °288 C argon to 4.5% plastic strain at a strain rate of $3x10^{-7}$ s^{-1}. The red dashed lines in this plot show the upper and lower bounds for data points collected across HREBSD scans performed at 15 different continuous DC-GB interaction sites.

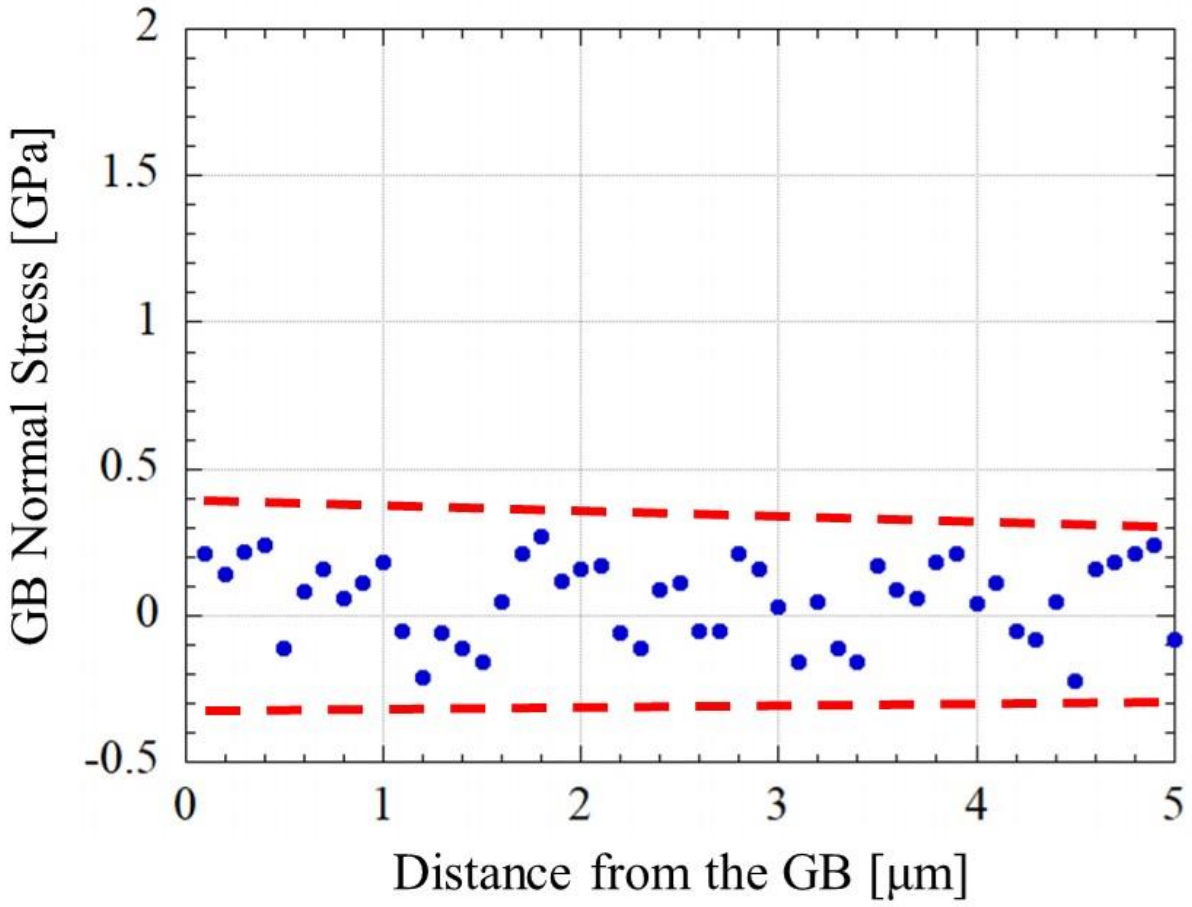

Figure 5.11: HREBSD calculated stress profile at a continuous DC-GB interaction site in 5 dpa proton irradiated Fe13Cr15Ni tensile bar sample strained in 288 °C argon to 4.5% plastic strain at a strain rate of 3x10-7 s-1. Raw calculated data is shown in blue. Dashed lines denote upper and lower bounds observed for the collection of 15 continuous sites analyzed.

From the HREBSD analysis presented in Figure 5.11, no appreciable stress increase was observed near continuous channels. Stress magnitudes remained relatively flat regardless of distance from the grain boundary. Fluctuations in the stress ranged between -0.2 and 0.2 GPa, however these stresses are nearly an order of magnitude lower than the stresses observed at discontinuous DC-GB interaction sites. It is important to note that the HREBSD results are a snapshot of the local stress profile after slip transmission has already occurred. It does not impart any information about the stress state at the grain boundary prior to the transmission event. At these continuous channel sites, slip transmission allows for the relaxation of dislocation pile-ups

and therefore the main component responsible for generating stress at the grain boundary is no longer present. Molecular dynamics simulations allow for the visualization of the pile-up event of dislocations at a much smaller scale and also allows for the visualization of discrete dislocations which is currently not possible in the proton irradiated samples. The progression of stress at a specific dislocation – grain boundary interaction site before and after a slip transmission event was observed by Johnson et al. [83] and followed the same MD setup as presented in [82]. Digitally straining the virtual samples activated dislocation sources, propagating dislocations through the grain until they were arrested at a grain boundary opposite the initial source. At the grain boundaries where dislocation motion was halted, an increase in tensile stress was observed at the interaction site. An example map showing the tensile stress acting normal to the grain boundary of a region near a dislocation-grain boundary interaction site in the MD simulation is presented in Fig. 5.12.

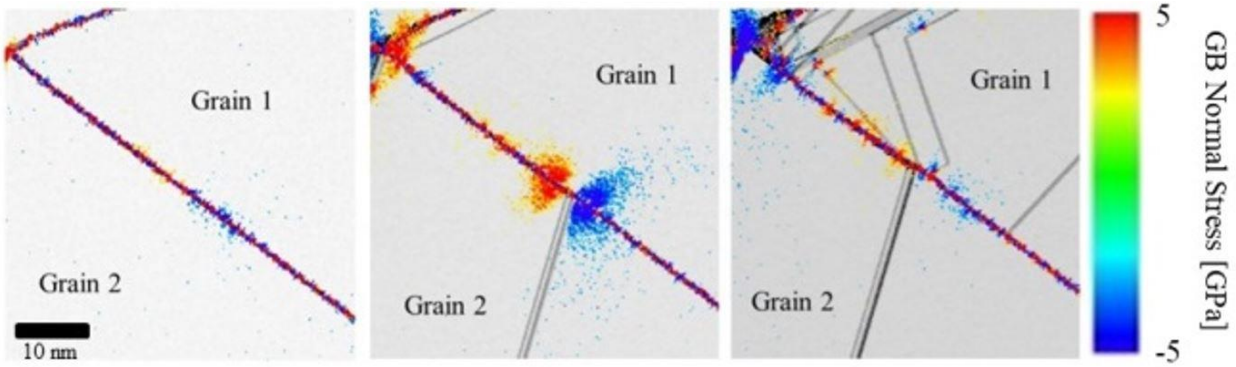

Figure 5.12:MD simulation of dislocation interacting with a grain boundary at 3% virtual strain before the dislocations reach the grain boundary, 4% when the dislocations hit the boundary, and 5.5% virtual strain after slip transmission occurs.

The dislocations generated during this straining were of the Shockley partial type and propagated across grain 2, ultimately reaching the boundary between grains 1 and 2, as outlined in Figure

5.8. The incoming Shockley partials have a Burgers vector of 1/6[121] in the lower grain which had a Schmid factor of 0.38. The partial transmitted into the upper grain had a Burgers vector of 1/6[-211] and a Schmid factor of 0.34. Prior to dislocation interaction with the grain boundary, the local tensile stresses were very low as shown in Fig. 5.4. At levels of strain greater than 4%, slip transmission across the grain boundary was observed. The slip transmission event resulted in significant stress reduction at the grain boundary, returning the stress at the grain boundary back to background levels. These results underline two key points from the experiments. The first is the build-up of stress as dislocation motion is halted at the grain boundary. This large increase in stress is similar in morphology of the stress increase observed using HREBSD. The second point is that the stress relaxes after slip has been transmitted into the adjacent grain. Figure 5.10 shows the progression of the GB normal stress as a function of applied virtual strain, measured at a fixed distance of 4 nm from the grain boundary.

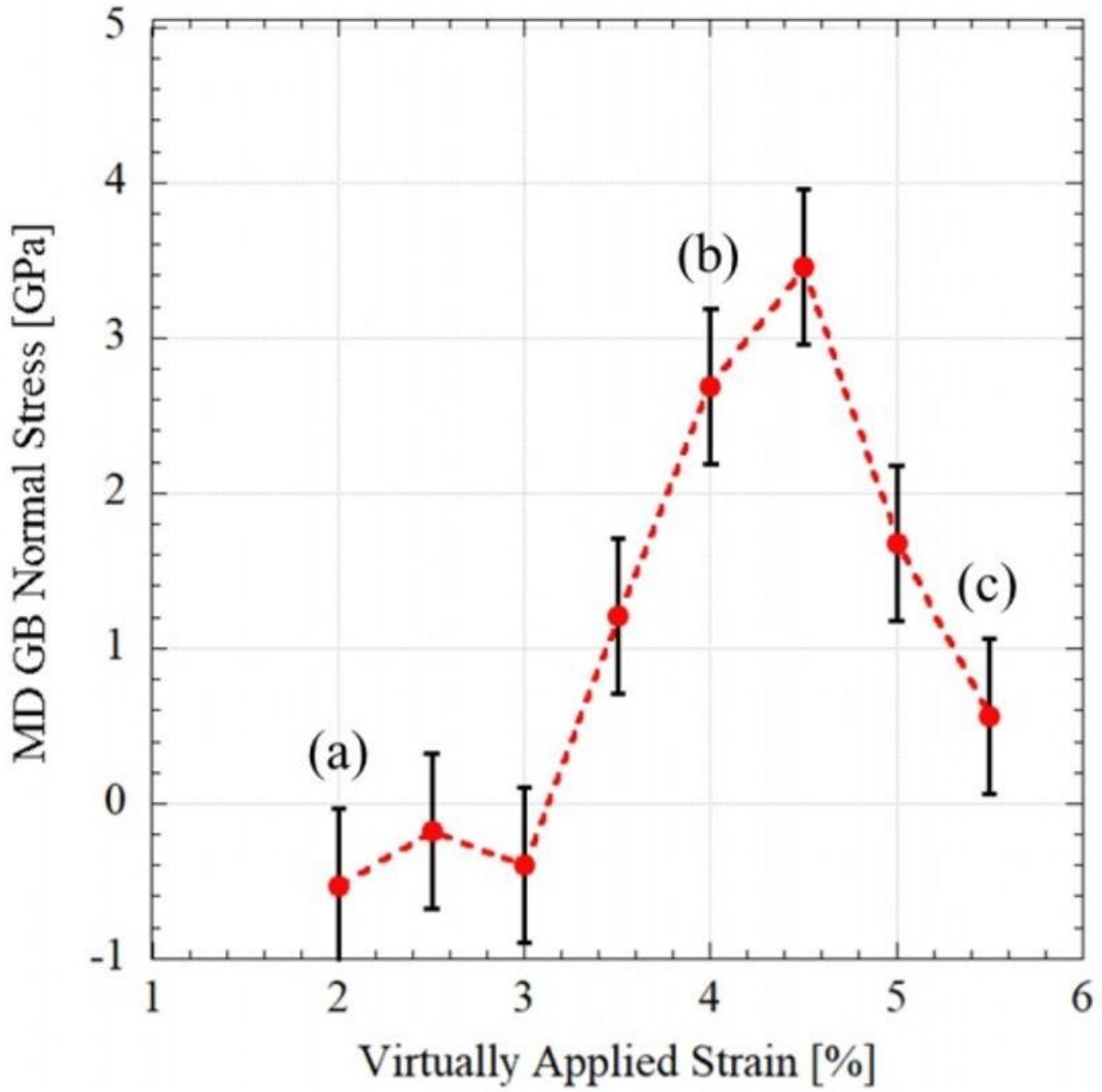

Figure 5.11: Progression of MD calculated grain boundary normal stress at the site of dislocation transmission as a function of the virtually applied strain [96]

After slip transmission, the normal stress acting at the grain boundary is reduced by a factor of 6.2. If this same factor is applied to the HREBSD results, the near GB stress value would drop from 1.5 GPa to 0.24 GPa, which is smaller than the typical errors associated with the HREBSD measurement. This low stress amplification near continuous channels was also observed by Guo

et al. [75] where no stress elevation was observed near slip transmission sites in titanium. This is consistent with the observations made with HREBSD, which show a very low residual stress at locations where slip transmission has occurred. The act of transmitting dislocations into the adjacent grain is a significant stress relief mechanism, resulting in these sites being at a significantly lower level of stress than the discontinuous sites. It is important to emphasize that the transmission event simulated using MD cannot be directly compared to dislocation channels present in physical samples on a quantitative level since only a few dislocations are observed in the MD model propagating on a single slip plane. However, the qualitative behavior of the MD model clearly shows a method for stress relaxation which is consistent with the experimental HREBSD measurements.

The initiation of plasticity at the grain boundary, as seen in the MD simulations, is a mechanism by which the crystal lattice alleviates the stress in the material. Therefore we would not expect that the stress present at an observed discontinuous channel would be the same in cases where dislocations were initiated at the grain boundary and places where the grain boundary completely arrested the motion of dislocations. However, since the dislocation channels were first observed after a 4.5% plastic straining step in 288 ˚C argon, it is not possible to determine whether each dislocation channel originated at the grain boundary, terminated at the grain boundary, or if a dislocation source within the grain interior is responsible for the channel formation.

5.1.3 Force Balance in HREBSD Measurements

As detailed with the discrete dislocation model setup, a force balance must be maintained in the solid under equilibrium conditions. This true for both the model and the measurements

taken using HREBSD. To evaluate the degree to which a force balance is maintained in the HREBSD scans, a radial mesh was applied to the 2D tensile and shear stress maps shown in figures 5.2 and 5.3. An initial circle with a radius of 200 nm was placed at the intersection point between the dislocation channel and the grain boundary. Datapoints within this circle were not analyzed due to the large errors associated with these values and since values in the discrete dislocation model tend toward infinity when the distance from the dislocation drops to zero. Successively larger circle radii were used to define discrete areas of points within the scan and an average stress value for the annulus of points radiating outwards from the initial circle center was determined. Since the values of stress in the HREBSD scan are taken at discrete locations during the SEM scan, points are only counted within a specific radius if the center of the scan point falls between the bounds of the inner and outer radii.

For both the shear and tensile components of the stress measured by HREBSD, the absolute value of the total stress of the scan was found to exceed 0 GPa, meaning that force equilibrium was not being maintained. Since force equilibrium is a requirement, all points within the scan had a static stress added such that the summation over all points in the scan would net to zero. By offsetting each individual data point in the scan by a static value, the baseline stress value is shifted by an amount equal to this offset. This would be similar to using a different reference image for the HREBSD analysis and calculations which had a slightly different initial orientation. Table 5.1 shows the weighted stress values each binning region in the radial mesh for both the analyzed tensile stress and shear stress 2D stress distribution maps. Since the values have already been normalized to account for the different number of data points within each bin, the summation of these points must be equal to zero for equilibrium conditions to be satisfied.

The average offset away from a net zero stress is then the total sum of the weighted stress values divided by the number radial mesh points.

Table 5.1 Weighted average tensile stress and shear stress values for each radial mesh size in scan site ASCC2-32 Fe13Cr15Ni 5 dpa tensile bar sample strained to 4.5% plastic strain in 288 °C argon at a strain rate of $3x10^{-7}$ s^{-1}

Mesh outer radius [um]	Area Ratio [W]	Weighted average tensile stress [GPa]	Weighted average shear Stress [GPa]
0.5	1.00	0.44	0.18
0.8	1.86	1.43	0.25
1.1	2.71	1.88	0.31
1.4	3.57	2.42	0.49
1.7	4.43	1.94	0.51
2	5.29	1.01	0.05
2.3	6.14	0.47	0.69
2.6	7.00	0.66	0.22
2.9	7.86	-0.05	1.03
3.2	8.71	0.88	1.14
3.5	9.57	0.23	-0.99
3.8	10.43	-0.64	0.98
4.1	11.29	-1.34	-2.44
4.4	12.14	-2.22	-1.67
4.7	13.00	-2.39	1.21
5	13.86	-0.2	1.91
5.3	14.71	-2.07	-0.58
5.6	15.57	-3.08	-1.47
5.9	16.43	-1.14	0.92
SUM		-1.77	2.74
Average offset		-0.093	0.144

The magnitude of stress offset required to establish force equilibrium for the tensile stress distribution measured by HREBSD was calculated to be -0.093 GPa and the offset required to establish force equilibrium in the shear stress distribution was 0.144 GPa. Both of these values are below the error which is observed in these HREBSD measurements, which comes from selecting several different reference patterns. By changing the value of the baseline stress for each component in the selected HREBSD scan by a value that is within the error of the original

baseline measurement, force equilibrium can be maintained which increases the validity of the stresses calculated from HREBSD.

Through the use of two different modeling methods, the high tensile stress values observed using HREBSD have been benchmarked against realistic collections of dislocations interacting with a grain boundary. The HREBSD results presented in Chapter 4 can be reasonably described by a collection of edge dislocations distributed across several parallel slip planes. The number and distribution of these dislocations are reasonable based on typical dislocation channel sizes and estimations of the dislocation content of the channel made using confocal laser measurements. The differing behavior between discontinuous and continuous channel interactions with grain boundaries has been accurately reflected in MD simulations. When dislocations are prevented from propagating into an adjacent grain by a boundary, large tensile and shear stresses are observed at the interaction site just like in the experimental results. If slip transmission occurs, there is a sharp decrease in the stress observed at the boundary which is consistent with the experimental observations of low stresses near continuous DC-GB interaction sites. The consistent behavior between models and experiment coupled with maintaining force equilibrium by shifting the baseline stress value by less than the experimental error helps to validate both the HREBSD measurements and the current understanding of dislocation content within channels in the absence of direct observations.

The large difference in the observed stresses between continuous and discontinuous channels could help explain why sites in irradiated materials which have an impinging discontinuous channel show higher susceptibility to crack initiation [62,71,75]. Both the transmission of dislocations and crack initiation offer a way for the crystal system to alleviate the build-up of stresses. Because of this, there is a direct competition between the critical value of

stress necessary to initiate intergranular cracks and the stress required to transmit\nucleate dislocations in the adjacent grain. However, it is difficult at this time to make any definitive statements about the threshold of stress required to propagate dislocations in the irradiated matrix due to the nature of the present study. For this analysis, the stress state in the grain boundary immediately prior to channel nucleation is required, which isn't possible for these finite interrupted straining steps. The stress required to transmit\nucleate dislocations is also going to be a function of the local grain boundary structure and defect microstructure which are both unavailable to the MD and experimental analysis techniques used for this study. For the MD simulations, there is no simulated effect of radiation damage on the dislocation mobility nor are there any effects due to the high temperature water environment which is necessary for any intergranular cracking to occur.

5.2 **Link Between Dislocation Channeling and IASCC**

Although the exact mechanism(s) behind IASCC are not known, most established models describing stress corrosion cracking, like the slip-oxidation model and selective internal oxidation (SIO) model, involve the initiation of a crack after formation of a passive oxide layer during exposure to high temperature water. For slip-oxidation, the oxide layer formed during exposure ruptures and exposes fresh metal to the corrosive environment. Through prolonged cyclical rupturing and dissolution of the grain boundary, an intergranular crack can develop and grow with each successive cycle. In the SIO model, oxidation down the grain boundary affects the mechanical properties of the grain boundary as the formed oxide is significantly more brittle than the bulk alloy. In the context of these models, both the stress and strain could be

responsible for the degradation and cracking of the grain boundary. Large amounts of shear at the grain boundary could cause GB slip, cracking the surface oxide and exposing fresh material to the corrosive environment while tensile stresses at the grain boundary could fracture the grain boundary oxide, providing a pathway down the boundary to further oxidation and fracture. Since dislocation channels impinging on a grain boundary create both significant levels of tensile and shear stresses, it is important to understand their relative magnitudes and whether they can explain the observed cracking behavior.

5.2.1 Relation between Grain Boundary Stress and IASCC

Previous work has shown a strong connection between localized deformation and crack initiation [62,71,75], however, the value of stress needed to initiate a crack has not been determined to date. The question that still remains is whether the primary driving force for crack initiation is the magnitude of the local stresses near points of contact between dislocation channels and the grain boundary, and if so, which stress component is responsible for initiating the crack. The average tensile and shear stresses from the 6% total strain increment in the Fe13Cr15Ni sample as a function of the grain boundary orientation are shown in Figure 5.14. The hashed section denotes the component of the total stress that came from the applied load during CERT testing and the solid regions are due to discontinuous channel-grain boundary interaction. Note that the average tensile component of stress is much larger than that of the shear stress, with the shear component only measuring ~40% of the tensile magnitude.

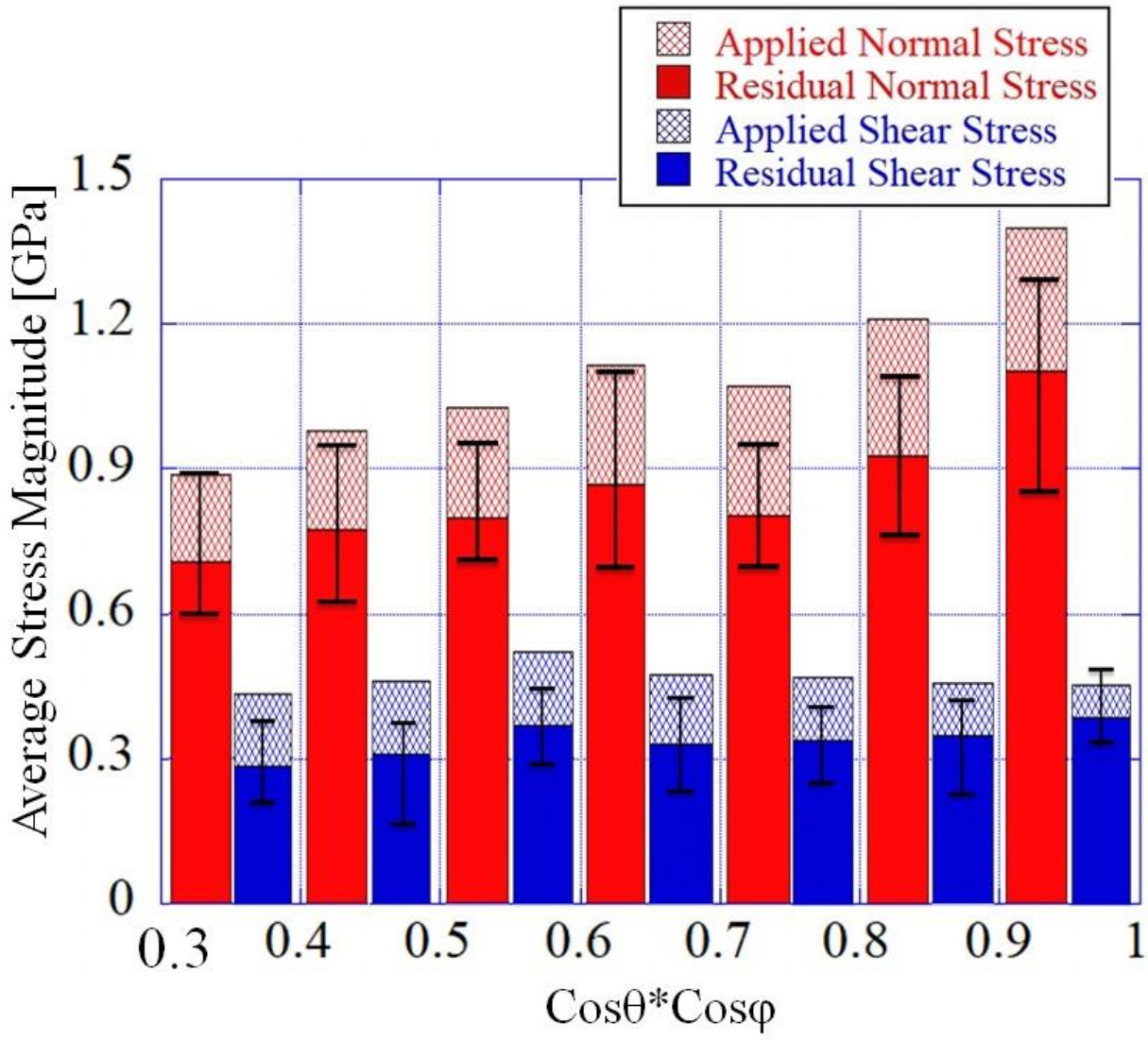

Figure 5.14:Average shear and tensile stress magnitudes measured as a function of grain boundary trace and grain boundary plane angles after 6% total strain in ASSC2 5 dpa Fe13Cr15Ni tensile bar sample. Applied stresses are denoted by the hash marked regions

This ratio of shear to tensile stress magnitudes was also observed by He et al [99] in the same alloy system irradiated to 5 dpa using the TEM ASTAR cross correlation software which is similar in approach as the HREBSD method, but uses differences in diffraction spot positions rather than the Kikuchi band structure. It is also observed in Figure 5.11 that the majority of the total stress is caused by the pile-up of dislocations at the grain boundary. This could potentially

explain the cracking observed during O-ring constant stress tests [91] and interrupted 4-point bend tests [119] that revealed cracking after reaching applied stresses only a fraction of the yield stress of the alloy. During interrupted 4-point bend tests, samples taken up to 50% of their yield stress still exhibited dislocation channel formation and these channels were either observed prior to or simultaneously with the first crack initiation event. Even with a low amount of applied stress, certain grain orientations will undergo yield by formation of dislocation channels that can apply a significant residual stress at the grain boundary, ultimately causing failure of the grain boundary.

With the much larger tensile stresses, there is a larger driving force to cause crack initiation. The dislocation pile-up within the discontinuous channels cause regions of large stress in the underlying metal layer. Stress is transferred to the oxide from the metal substrate via the interface between the two as there is no evidence of delamination of the oxide layer. In this way the stress generated by channels in the bulk has the ability to transfer this stress to the brittle oxide above. The stress does not reach a level high enough to rupture the grain boundary in the underlying metal, otherwise cracking would not require an aggressive environment, and would occur even when the specimens were strained in high temperature argon (an inert environment). Micromechanical testing of oxidized grain boundaries has been conducted by Lozano-Perez et al. [114] and has observed brittle fracture events when testing microcantilever fabricated from alloy 600 coupons exposed to simulated PWR primary water for 2700h using a focused ion beam setup. Non-oxidized grain boundaries taken from the same sample were observed to deform plastically, but never fracture even though the applied stresses between the two types of samples were similar in magnitude. Figure 5.15 shows the load-displacement curve for a cantilever

sample with an oxidized grain boundary. A crack initiated in this sample just after 500 nm of displacement and a load of less than 0.4 mN.

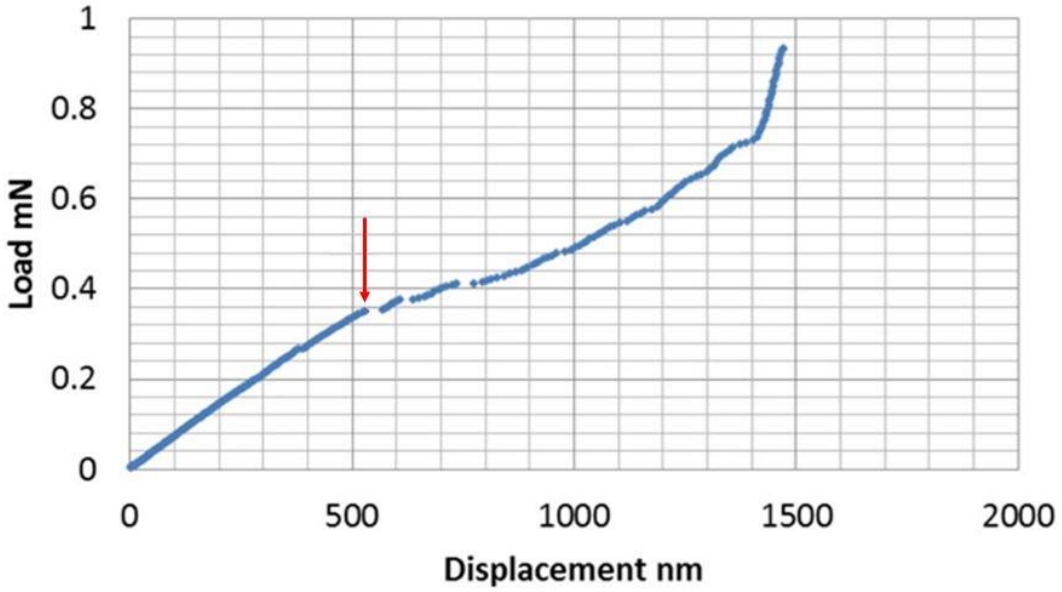

Figure 5.15: Load-displacement curve for an oxidized grain boundary cantilever taken from an alloy 600 sample exposed to simulated PWR primary water for 2700h which exhibited intergranular fracture. The fracture point is marked with a red arrow. [114]

For comparison, several load-displacement curves are shown in figure 5.16 which are taken from tested grain boundaries that were not oxidized.

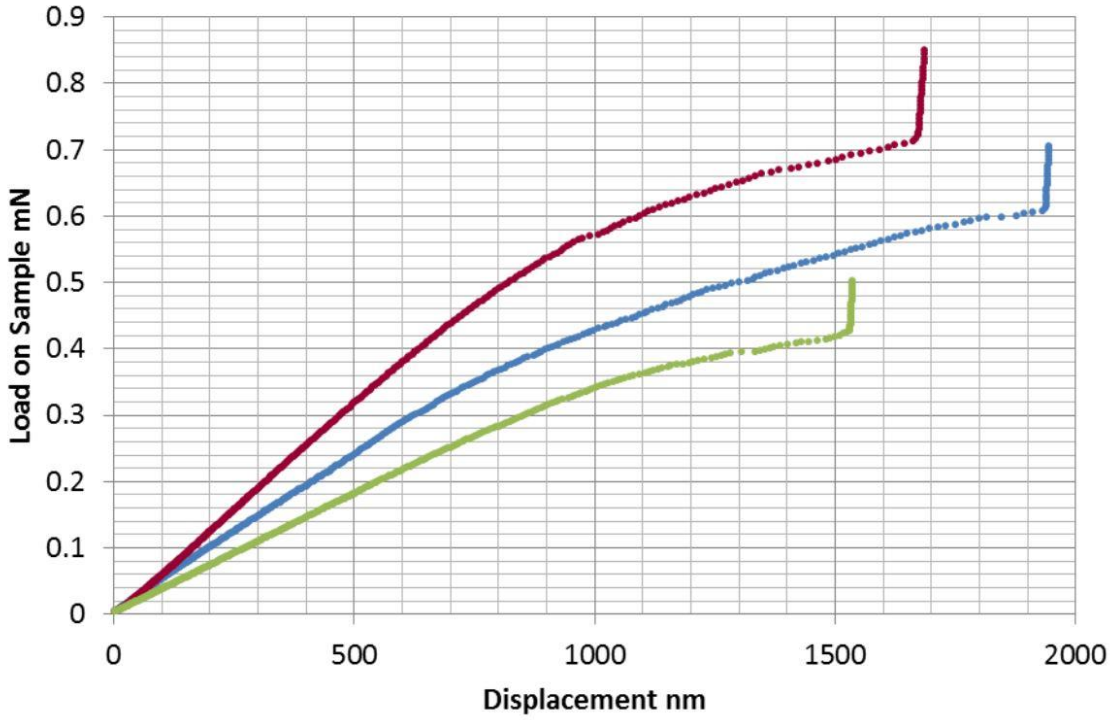

Figure 5.16: Load-displacement curves for multiple cantilever samples taken from an alloy 600 sample exposed to simulated PWR primary water for 2700h which were not oxidized and exhibited plastic deformation and no fracture [114].

Micro tensile tests were also performed on samples made from alloy 600 exposed to simulated PWR primary water by Fuji et al. [133]. Rectangular shaped micro tensile specimens were made using a focused ion beam of 30 kv gallium ions, and contained a single grain boundary. Thermal aging of the material at 1200 °C for 100h developed and average grain size of 1 mm which made collecting only a single grain boundary in each micro tensile sample relatively simple. Three sets of samples were investigated, with the only difference being the time spent in simulated PWR primary water. 4 samples exposed for 1500h and 3 samples exposed for 2700 hours, and 4 samples that were not exposed in high temperature water were straining in uniaxial tension at room temperature, and the load was measured at the point of grain boundary fracture. Each of these grain boundaries fractured in a brittle manner at the grain boundary.

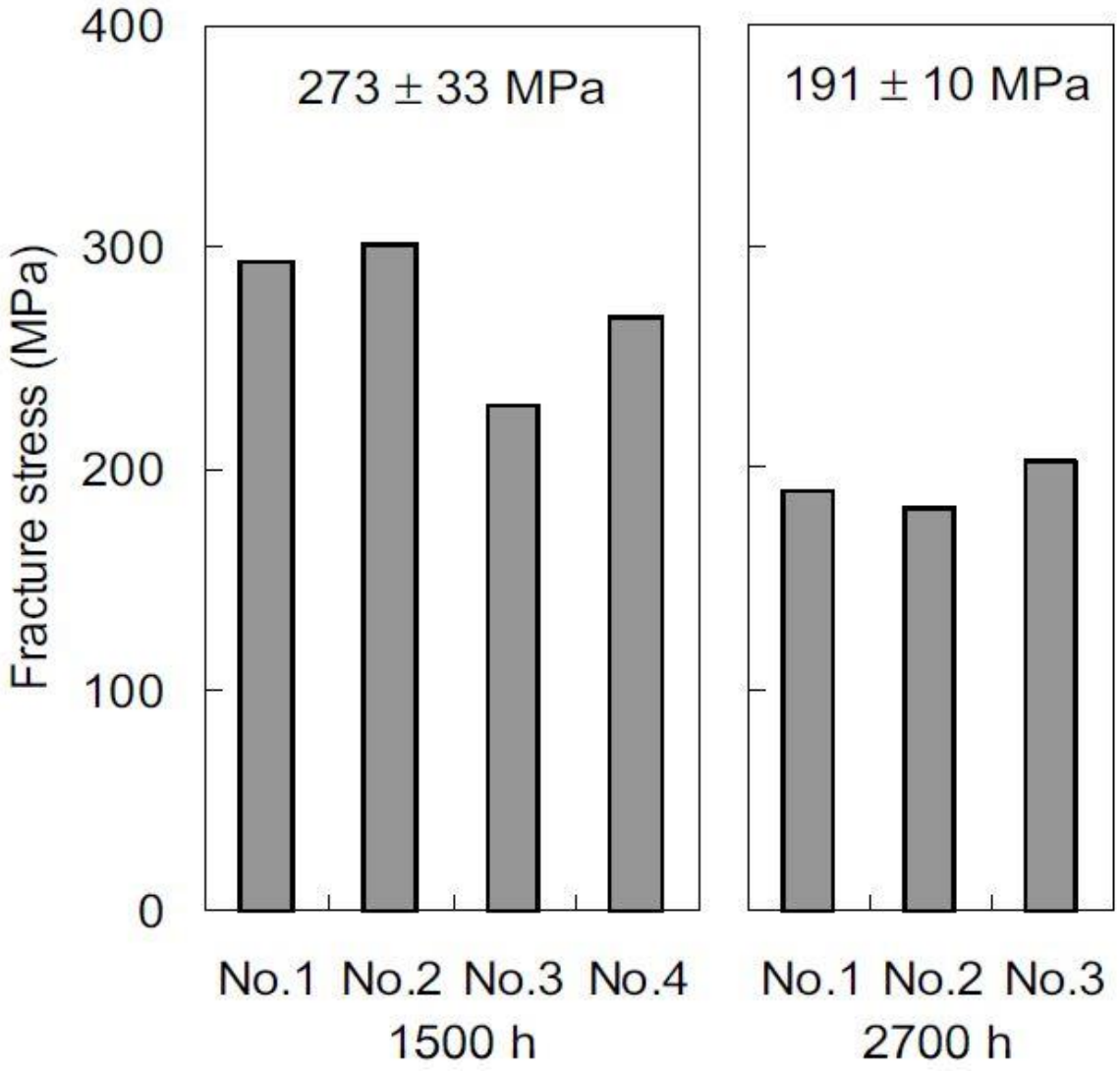

Figure 5.17: Compilation of uniaxial tensile stress required to fracture micro tensile samples made from non-irradiated Alloy 600 exposed in simulated PWR primary water for either 1500h or 2700h [133].

The samples which had been exposed for a longer period of time showed a lower fracture stress, Figure 5.17, which is indicative of increased degradation of the grain boundary cohesive strength with continued oxidation. Non-oxidized grain boundaries were also investigated using the same set-up, and no fracture was observed up to an applied grain boundary normal stress of 1000 MPa. This is consistent with the micro cantilever data and highlights the requirement of an oxidative

environment for IASCC to occur. The decrease in stress required to crack oxidized grain boundaries points toward a cracking mechanism where an oxide phase is first formed in the material in the vicinity of the grain boundary, ultimately reducing the stress threshold required to crack that portion of the grain boundary to expose the underlying material to the surrounding corrosive environment. Alterations to the grain boundary chemistry through the depletion of key elements like chromium during the passivating inner oxide formation can affect the GB cohesive strength slightly, but even when high levels of radiation induced segregation are observed in austenitic stainless steels, cracking is still not observed when straining is performed in an inert environment. If the change in grain boundary chemistry were enough to explain the increase in cracking susceptibility through a change in grain boundary cohesive strength, cracking would be observed in an inert environment when changing the relative values of iron, chromium, and nickel at the grain boundary. Only when the proton irradiated samples are strained in a high temperature water environment is cracking observed.

In this study, the IASCC behavior was assessed from 75 discontinuous channel sites and an analogous set of continuous channel sites in the Fe13Cr15Ni alloy. In the 75 discontinuous sites analyzed using HREBSD, 26 of the boundaries were observed to have cracked after a 1.5% strain increment in BWR NWC conditions, following 4.5% strain in argon. To visualize this cracking data, the cracking fraction was calculated as a function of the total grain boundary normal stress, which is comprised of both the HREBSD calculated value after the 4.5% straining step in argon and the applied stress during the BWR NWC straining step, and plotted in Figure 5.18.

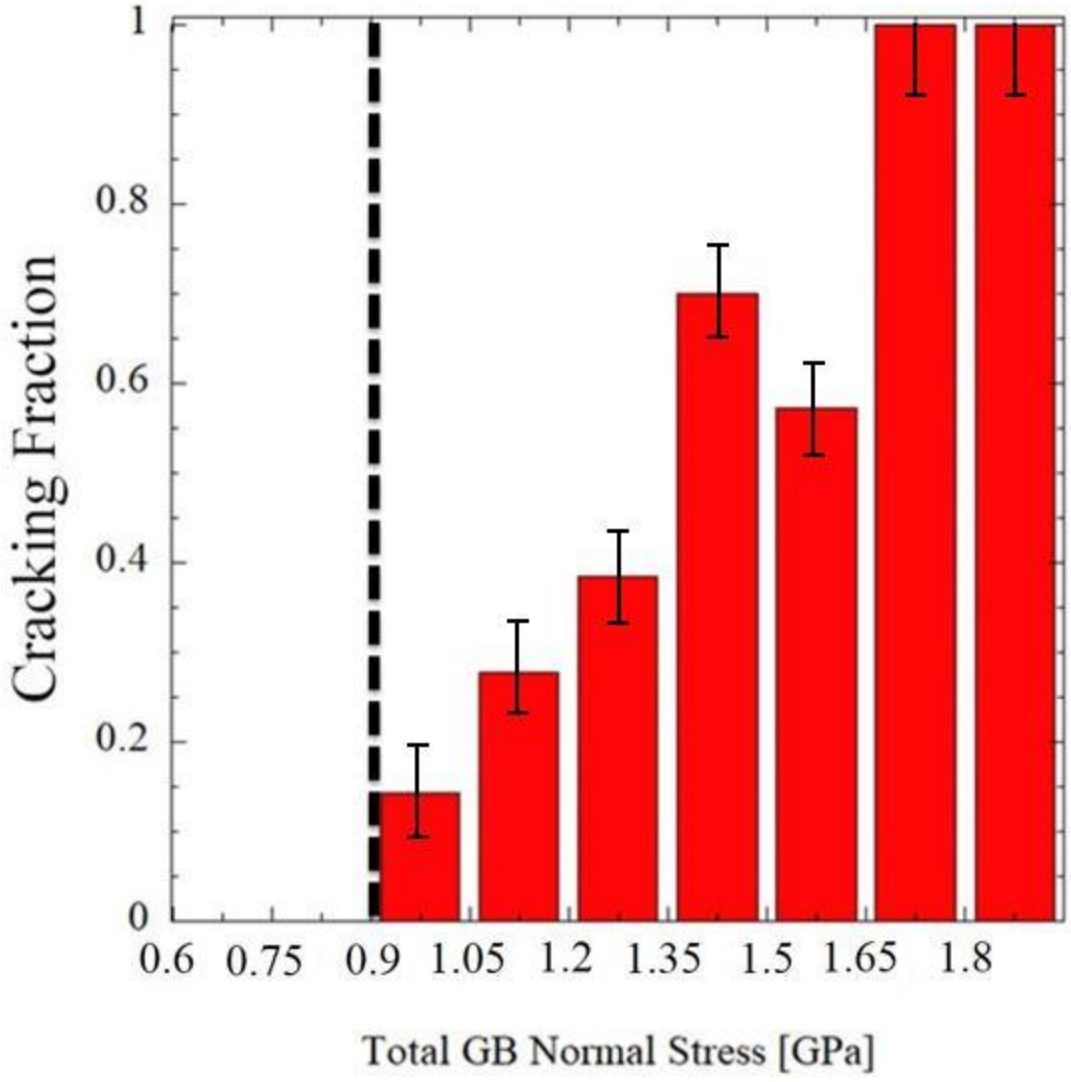

Figure 5.18: Cracking fraction as a function of total grain boundary normal stress for data collected from ASCC2 Fe13Cr15Ni 5 dpa tensile bar sample after 1.5% strain increment (6% total) in simulated BWR-NWC at 288 °C with a strain rate of $3x10^{-7}$ s^{-1}.

Note that there exists a lower bound for crack initiation of about 0.9 GPa. Below this value of GB normal stress, no crack initiation was observed, suggesting that for a given heat there is a minimum value of normal stress on the grain boundary required to initiate cracks. Once above this threshold there is scatter in the data resulting in some locations with higher stresses which do not show any crack initiation. However, as the total stress acting normal to the grain

boundary increases, so does the susceptibility to cracking. Increasing the stress acting on the grain boundary results in a higher probability of cracking, with all sites above 1.65 GPa cracking. Further, the internal stresses are near zero for boundaries with slip continuity and none of these 75 boundaries cracked. This result provides evidence for a strong dependence of cracking susceptibility on the grain boundary normal stress. They also provide a more fundamental explanation of the observations of a "threshold" stress for cracking of irradiated O-ring samples in primary water at 320°C [91] that provide only the time to failure of the O-ring sample and the applied stress resulting in failure. However, they also show a distinct threshold, above which cracking in this environment occurs and below which there is no cracking.

Previous studies have only been able to investigate the cracking fraction as a function on the grain boundary trace angle, since the grain boundary plane angle was unknown. In this study, since the full grain boundary orientation is known, the cracking fraction can be investigated as a function of both the grain boundary trace and grain boundary plane angles. This data is presented in Figure 5.19.

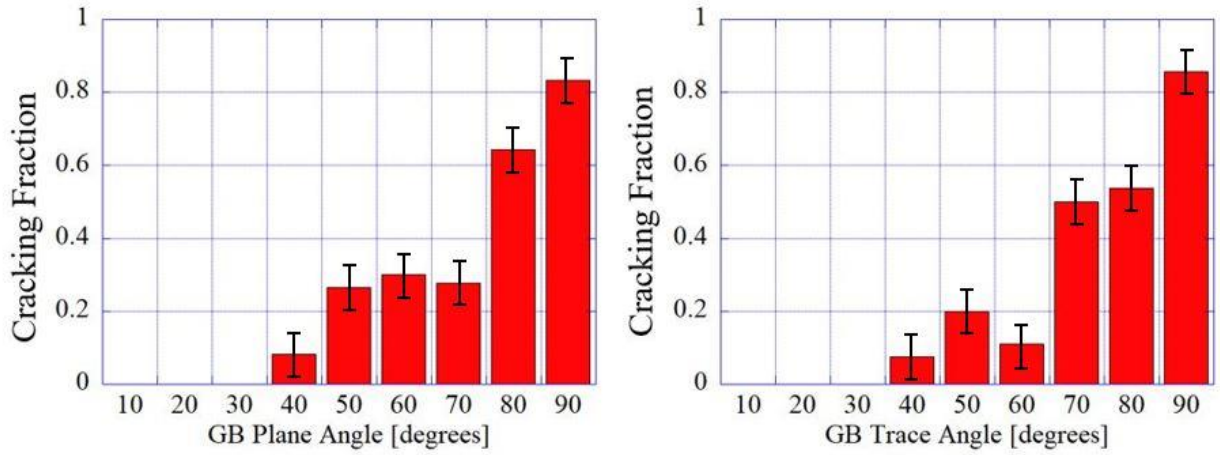

Figure 5.19: Cracking fraction as a function only the grain boundary plane angle (left) and only the grain boundary trace angle (right) in ASCC2 Fe13Cr15Ni 5 dpa tensile bar sample strained 1.5% plastic (6% total) in simulated BWR-NWC at 288 °C with a strain rate of $3x10^{-7}$ s^{-1}.

Both graphs in Figure 5.19 show the same trend with cracking fraction increasing as the trace, or grain boundary plane angle becomes more perpendicular to the loading axis. If one of the two angles, either the trace angle (θ) or plane angle (φ), is kept constant, increasing the other will result in a monotonic increase in the normal stress applied on that grain boundary plane until the angle reaches 90 degrees. This is the same for both the trace angle (θ) and the plane angle (φ). Therefore the trend in cracking fraction as a function of increasing angle should be the same between the two. The cracking fraction can be set as a function of the grain boundary offset angle, α, the angle between the grain boundary normal vector and the loading axis. When the offset angle α is 0, the plane of the grain boundary is perpendicular to the loading axis and the normal stress resolved onto the grain boundary is maximized. The magnitude of the resolved stress varies as a cosine of the offset angle α, and this dependence is superimposed on the cracking fraction plot in Figure 5.20. The cracking fraction plot presented in Figure 5.20 follows the tensile stress distribution closely.

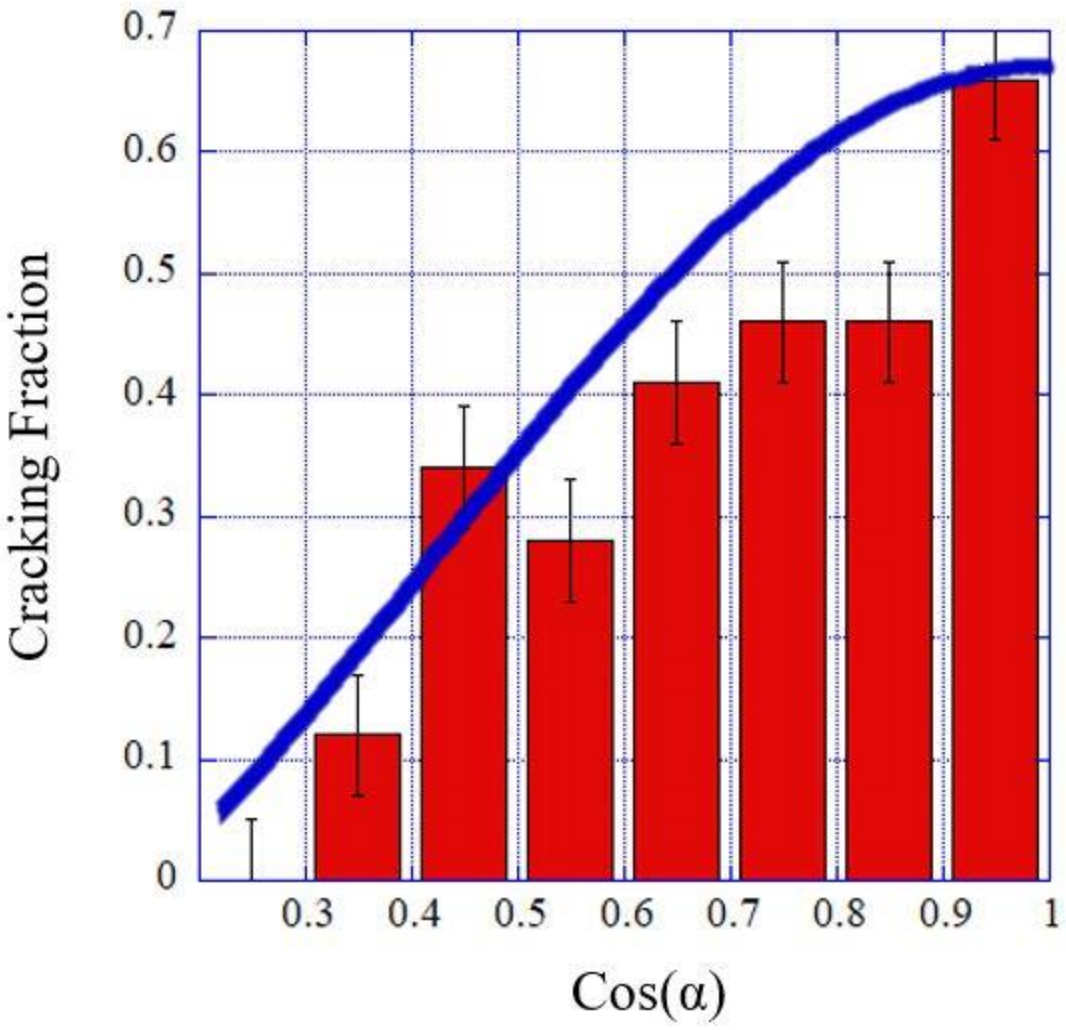

Figure 5.20:Cracking fraction as a function of grain boundary offset angle α for ASCC2 5 dpa Fe13Cr15Ni tensile bar sample strained an additional 1.5% (6% totol) in simulated BWR-NWC at 288 C with a strain rate of 3x10-7 s-1. Normalized theoretical curve for tensile stress magnitude as a function of grain boundary offset angle is shown in blue.

This curve is in stark contrast to the behavior observed in carbon doped nickel based alloy (Ni16Cr9Fe) which was strained to 10% plastic strain at a strain rate of $3x10^{-7}$ s^{-1} in 360 °C water [120]. The cracking fraction as a function of the grain boundary trace angle shows a clear peak in cracking at a grain boundary trace angle of 45 degrees, Figure 5.21. A significant amount of grain boundary sliding was also observed in this nickel based alloy, which is consistent with the apparent shear stress dominated cracking mechanism.

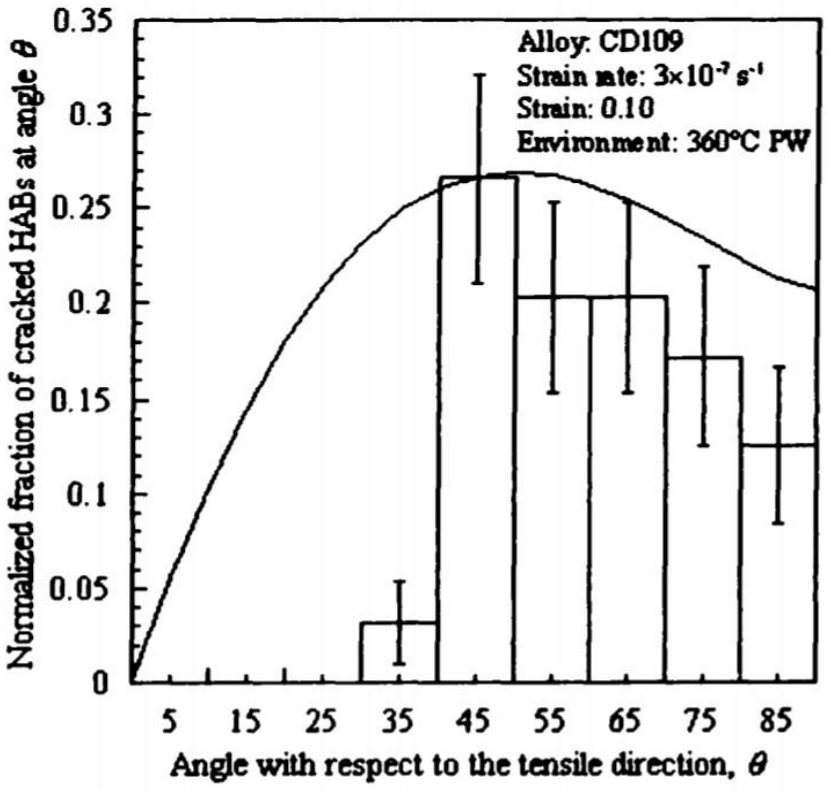

Figure 5.21:Cracking fraction of carbon doped nickel based alloy as a function of grain boundary trace angle after 10% plastic strain in 360 °C water [120]

Beyond the orientation of the grain boundary with respect to the loading axis, additional constraints are in place during the deformation of a crystalline solid. When considering the junction of two grains, austenitic steels are anisotropic and will therefore have slightly different elastic responses based on their differing crystallographic orientations. FEM modeling performed by Meric de Bellefon et al. [93] was used to investigate the stress observed at a grain boundary under uniaxial tension while altering the orientations of the two grains under stress. A result for a single grain coupling with a 300 MPa stress applied is shown in Figure 5.22.

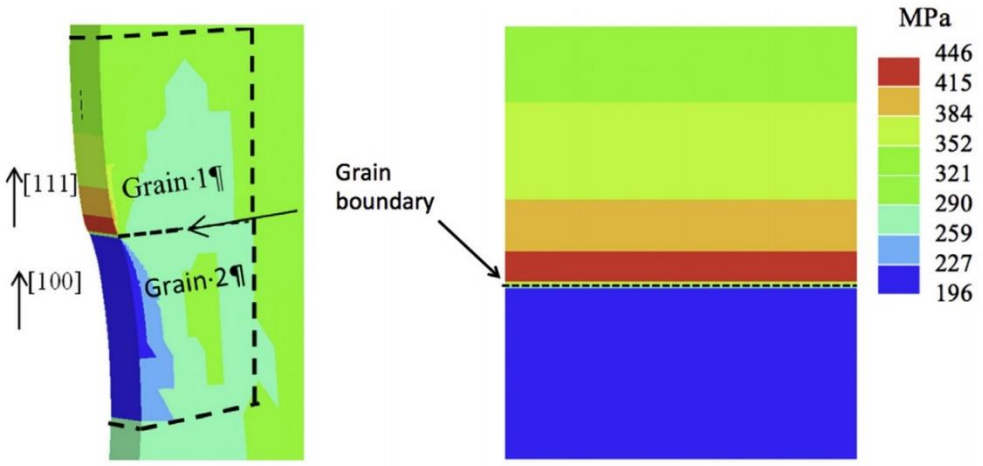

Figure 5.22:FEM results showing the stress distribution across a grain coupling with differing crystallographic orientations and an applied stress of 300 MPa [93].

It was observed that the peak magnitude of the stress local to the grain boundary could be twice that of the applied stress, so to get a more accurate measure of the stress at the grain boundary, crystallographic anisotropy must be incorporated into the total grain boundary normal stress measurement. Figure 5.23 shows the calculated intensity factor (a ratio of the applied stress to the peak observed stress) from the above study as a function of the fitting parameter *P*, defined as:

$$P = \left(\frac{1}{S_{66}^{a}}\right)^{0.1} * \left(\frac{S_{22}^{b}}{S_{22}^{a}}\right) * \left(S_{21}^{a} - S_{21}^{b}\right), \qquad (5.3)$$

where the *S* parameters are taken from the 4th order stiffness tensor calculated from the compliance tensor which is used as an input for the HREBSD calculations. *A* refers to the stiffer grain in the coupling, while *b* denotes the softer grain.

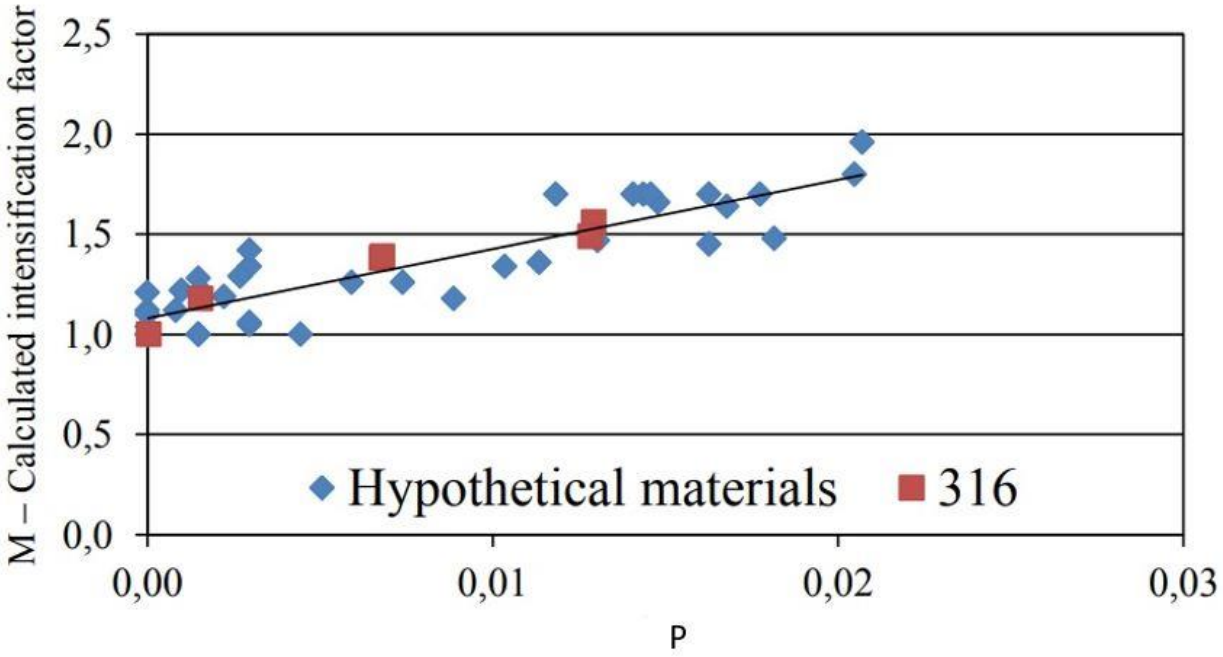

Figure 5.23: Calculated intensification factor as a function of fitting parameter P generated from Meric de Bellefon FEM [93]

By using the trendline established in Figure 5.24, new applied stress components were calculated and are presented along with the initial applied stress measurements in Table 5.2.

Table 5.2 Raw and Anisotropy Modified Applied Stresses During CERT Straining of ASCC2 Fe13Cr15Ni 5 dpa tensile bar sample

Grain Boundary ID	Initial Applied Stress [GPa]	Modified Applied Stress [GPa]	Ratio
ASCC2-1	0.276	0.276	1.00
ASCC2-2	0.254	0.309	1.22
ASCC2-3	0.292	0.476	1.63
ASCC2-4	0.264	0.044	0.17
ASCC2-5	0.253	0.390	1.54
ASCC2-6	0.274	0.274	1.00
ASCC2-7	0.293	0.404	1.38

ASCC2-8	0.260	0.327	1.26
ASCC2-9	0.277	0.326	1.18
ASCC2-10	0.263	0.318	1.21
ASCC2-11	0.301	0.490	1.63
ASCC2-12	0.265	0.342	1.29
ASCC2-13	0.264	0.329	1.25
ASCC2-14	0.291	0.291	1.00
ASCC2-15	0.274	0.397	1.45
ASCC2-16	0.266	0.415	1.56
ASCC2-17	0.259	0.314	1.21
ASCC2-18	0.246	0.401	1.63
ASCC2-19	0.270	0.491	1.82
ASCC2-20	0.281	0.469	1.67
ASCC2-21	0.261	0.481	1.84
ASCC2-22	0.243	0.323	1.33
ASCC2-23	0.250	0.272	1.09
ASCC2-24	0.254	0.341	1.34
ASCC2-25	0.262	0.262	1.00
ASCC2-26	0.262	0.301	1.15
ASCC2-27	0.259	0.316	1.22
ASCC2-28	0.255	0.324	1.27
ASCC2-29	0.263	0.263	1.00
ASCC2-30	0.252	0.355	1.41
ASCC2-31	0.289	0.511	1.77
ASCC2-32	0.268	0.444	1.66
ASCC2-33	0.284	0.349	1.23
ASCC2-34	0.254	0.254	1.00
ASCC2-35	0.277	0.327	1.18
ASCC2-36	0.248	0.300	1.21
ASCC2-37	0.293	0.454	1.55
ASCC2-38	0.288	0.400	1.39
ASCC2-39	0.268	0.335	1.25
ASCC2-40	0.260	0.260	1.00
ASCC2-41	0.282	0.408	1.45
ASCC2-42	0.296	0.467	1.58
ASCC2-43	0.284	0.377	1.33

ASCC2-44	0.294	0.394	1.34
ASCC2-45	0.299	0.434	1.45
ASCC2-46	0.291	0.291	1.00
ASCC2-47	0.265	0.265	1.00
ASCC2-48	0.282	0.349	1.24
ASCC2-49	0.273	0.455	1.67
ASCC2-50	0.275	0.352	1.28
ASCC2-51	0.217	0.265	1.22
ASCC2-52	0.199	0.267	1.34
ASCC2-53	0.184	0.232	1.26
ASCC2-54	0.180	0.232	1.29
ASCC2-55	0.214	0.214	1.00
ASCC2-56	0.204	0.308	1.51
ASCC2-57	0.189	0.238	1.26
ASCC2-58	0.178	0.215	1.21
ASCC2-59	0.197	0.220	1.12
ASCC2-60	0.190	0.235	1.24
ASCC2-61	0.207	0.300	1.45
ASCC2-62	0.188	0.224	1.19
ASCC2-63	0.199	0.274	1.38
ASCC2-64	0.214	0.214	1.00
ASCC2-65	0.187	0.238	1.27
ASCC2-66	0.204	0.274	1.34
ASCC2-67	0.185	0.298	1.61
ASCC2-68	0.177	0.218	1.23
ASCC2-69	0.183	0.208	1.14
ASCC2-70	0.209	0.278	1.33
ASCC2-71	0.201	0.258	1.28
ASCC2-72	0.195	0.195	1.00
ASCC2-73	0.191	0.191	1.00
ASCC2-74	0.177	0.206	1.16
ASCC2-75	0.216	0.250	1.16

Using the modified applied stresses in Table 5.2, the cracking fraction presented in Figure 5.18 was recalculated and plotted in Figure 5.24. as a function of the total grain boundary normal

stress using the anisotropy modified values for the applied stress component. The inclusion of anisotropy does not affect the general trend of increasing susceptibility to intergranular failure with increasing stress, however, the trend is now purely monotonic and shows a more uniform increase in the susceptibility with increasing stress. This provides some additional evidence that the value of the stress acting normal to the grain boundary is very important to crack initiation, and that the pairing of grains which make up the investigated boundary is important since it will otherwise result in an underestimation of the importance of the stress component which is being applied to the system.

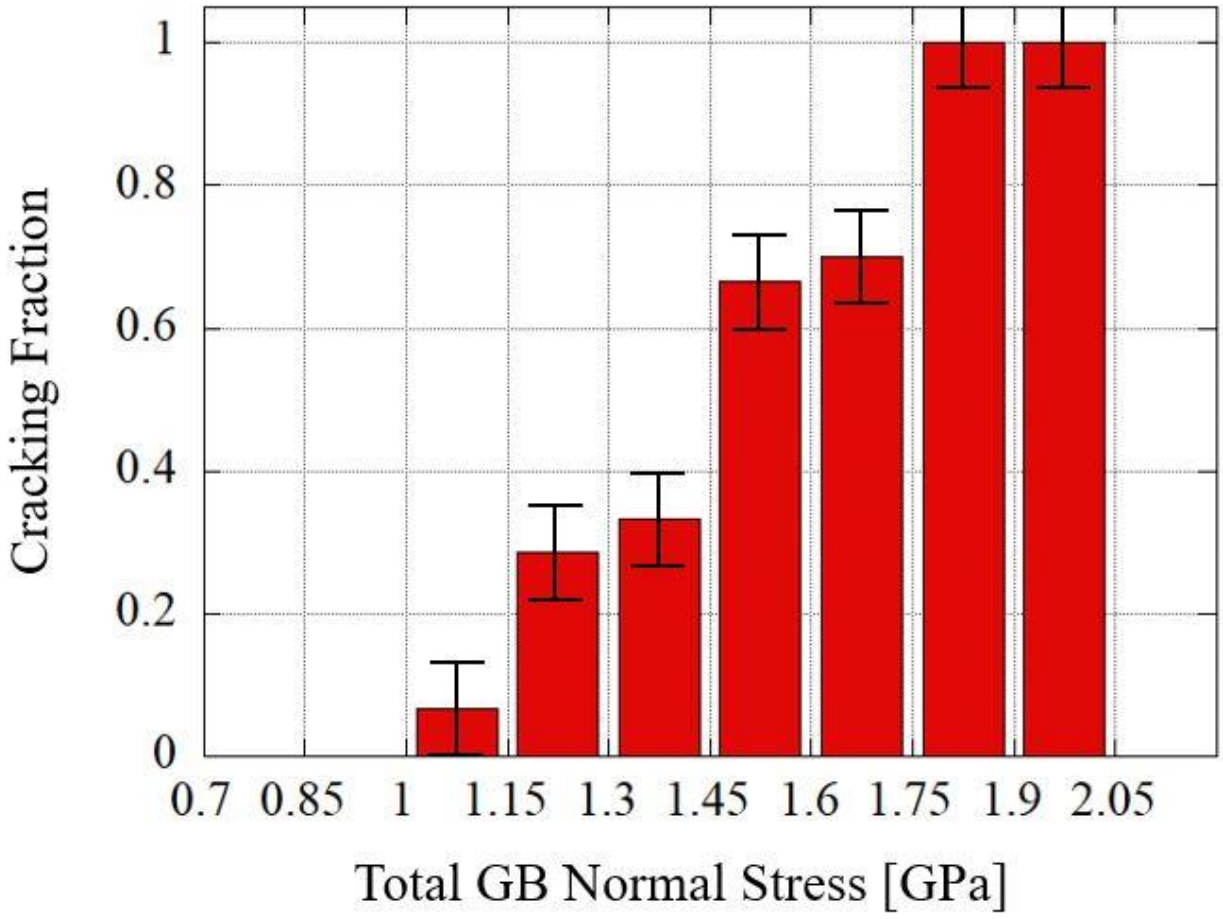

Figure 5.24: Cracking fraction as a function of the anisotropy modified total grain boundary normal stress for ASCC2 5 dpa Fe13Cr15Ni tensile bar sample after 1.5% plastic strain (6% total) in simulated BWR-NWC at 288 °C with a strain rate of $3x10^{-7}$ s^{-1}.

Without the influence of irradiation, deformation in this alloy is limited to more homogeneous planar slip, which results in finely spaced individual slip bands. Tensile bar samples strained in simulated BWR water for this study also included non-irradiated sections along the gauge length adjacent to the irradiated zone. In these non-irradiated regions, dislocation channels did not form, nor was any degree of intergranular crack initiation observed. Similar HREBSD measurements were made in a non-irradiated austenitic stainless steel with similar composition, and showed only moderate increases in stress at slip band – grain boundary interaction sites [51]. Since only GB trace angles were taken into account when resolving the

calculated stresses onto the grain boundary, the stated stresses are overestimated. Even so, the highest observed tensile stress in this study was 0.73 GPa well below the established 0.9 GPa crack initiation threshold observed here. Without the change in microstructure from irradiation and the subsequent change in deformation mode, local stresses high enough to eclipse the lower bound of the crack initiation threshold are not produced. However, it must be emphasized that this is not a purely mechanical problem, and the corrosive water environment in which these experiments take place plays a key role in the IASCC process which cannot be neglected. Additional straining in an inert environment does not produce intergranular fracture, meaning that the high stresses generated by dislocation pile-up at grain boundaries is a necessary, but not sufficient condition to induce intergranular cracking in this alloy. The data in Fig 5.16 shows that there is not a sharp cut-off in the stress for cracking, suggesting that there are other factors that are important in the crack initiation process.

The important link between the CERT testing and constant load testing is getting the material to a place where deformation is possible. Stephenson et al. showed through interrupted 4-point bend tests that crack initiation is observed below the yield stress of neutron irradiated steels. While the stresses applied to these samples were below the yield stress of the material, cracking was only observed after or during the same straining step where plasticity and the formation of dislocation channels where clearly observed. Finite Element models presented by both M. de Bellefon et al. [93] and Kamaya et al. [115] show that local stresses at specific grain boundaries in the material can observe a stress that is much greater than the uniaxial applied tensile stress. For Bellefon the highest fraction observed (GB stress/applied stress) was 1.8 and for Kamaya the highest observed fraction was 2.2. This is very consistent with the onset of deformation and the existence of dislocation channels being a crucial factor in IASCC. If the

applied stress is 40-50% of the yield stress, then the maximum stress observed locally at specific well oriented grain boundaries will exceed the yield stress, resulting in the formation of dislocation channels. These constant load tests do not have local information on the stress at specific grain boundaries or measurements showing the interaction between developed dislocation channels and grain boundaries which makes linking the quantitative results of this study and the constant load experiments difficult at this time.

Measurements of the stress required to initiate cracks in constant load tests were often conducted for hundreds or thousands of hours. During these long exposures passivating oxides form on the surface, significantly slowing down the rate of oxygen diffusion into the metal and the overall oxidation process. While significantly slowed, the oxidation process is not completely stopped. This means that over long exposure times, the effect that corrosion has on the grain boundary strength can continue to increase, ultimately leading to failure, even though the stresses were kept at a constant value. This is consistent with the micro tensile tests performed by Fuji et al. where grain boundaries which had been oxidized for a longer period of time required a lower magnitude of uniaxial tensile stress in order to fracture the boundaries [133]. For the ASCC2 Fe13Cr15Ni 5 dpa tensile bar sample, there are certain grain boundaries which appear to have a residual stress component which is higher than the observed crack initiation threshold. This means that without the application of external stresses, the residual component of stress could be high enough to crack the boundary. However, these slow strain rate tensile tests are performed over a timeframe of less than 100 hours, which is significantly less time than the constant load tests. If the ASCC2 sample were exposed over thousands of hours, it is possible that some sites would fracture without the addition of several hundred MPa which was done in the slow strain rate test.

Local variations in grain boundary chemistry and oxide formation, as observed by Rigen et al. [35], could potentially account for variation in the cracking susceptibility for those boundaries with a moderate level of tensile stress. However, the increase in cracking fraction with tensile stress highlights the importance of stress as the dominant factor driving the crack initiation process, with other factors, like local grain boundary chemistry and aqueous environment, playing a secondary role. When the local stresses reach a high enough magnitude, cracking occurs regardless of local variations in the grain boundary chemistry.

By analyzing the stress field surrounding a DC-GB interaction site prior to straining in a simulated reactor water chemistry environment, it was possible to link the local stress state with the crack initiation behavior of irradiated in a quantitative way that has never been done before. A pseudo threshold for crack initiation was observed, below which no cracking was observed. Above this observed value of 1.0 GPa in the ASCC2 Fe13Cr15Ni 5 dpa tensile bar sample cracks were initiated and the cracking fraction increased as the magnitude of the total grain boundary normal stress increased. This is in stark contrast to other alloys which have been observed to crack where the shear stress acting on the grain boundary is maximized [120]. By incorporating information about the geometric orientation of the grain boundary and the crystallographic orientation of the deforming grains, it is now possible to determine the grain boundaries that are the most susceptible to IASCC.

5.2.2 Competition between Cracking and Deformation for Stress Relaxation

Cracking occurs as a means to relieve stresses in the crystal lattice much in the same way that dislocations are generated and moved in the system to accommodate the bulk shape change and decrease the overall energy in the system. In this way, there is a constant competition

between deformation and cracking at each grain boundary during the process of uniaxial straining. The magnitude of the stresses observed in the HREBSD scans many times are above the yield stress of the material which should theoretically result in a deformation response. This could either be due to a low magnitude of shear stress in the direction of the present slip systems in the grain adjacent to the dislocation pile-up or an overestimation of the stresses being measured by HREBSD. To investigate this issue more closely, the shear stress acting in the direction of available slip systems measured by HREBSD is compared to an estimate for the critically resolved shear stress in the ASCC2 Fe13Cr15Ni tensile bar sample

From Section 2.2.1, the shear stress is maximized when the plane of the grain boundary is inclined 45 degrees relative to the loading axis. This gives a generalized value for the critically resolved shear stress of $\frac{\sigma_{yield}}{2}$. Since only a small portion of the ASCC2 Fe13Cr15Ni 5 dpa tensile bar sample has been irradiated, the yield stress observed during straining in 288 ˚C argon is that of the bulk non-irradiated material rather than the yield stress of the irradiated region. As shown by Busby et al. [133] the yield stress after irradiation can be linearly correlated to the observed change in hardness value for austenitic stainless steels. The change in the yield stress is observed to be

$$\sigma_{yield} = 3.03\Delta Hv \tag{5.4}$$

where the change in yield stress ($\Delta\sigma_{yield}$) is measured in MPa and the change in hardness value (ΔHv) is measured in kg/mm^2. Figure 5.25 shows the hardness profile across the length of the ATEM1 Fe13Cr15Ni 5 dpa sample. The hardness profile begins and ends in regions of the sample which are not irradiated, while the central 10 mm of the bar were irradiated up to 5 dpa. For this Fe13Cr15Ni heat of material, the change in hardness value after 5 dpa is taken to be the

difference between the average hardness value measured in the non-irradiated regions and the average hardness value measured in the irradiated region.

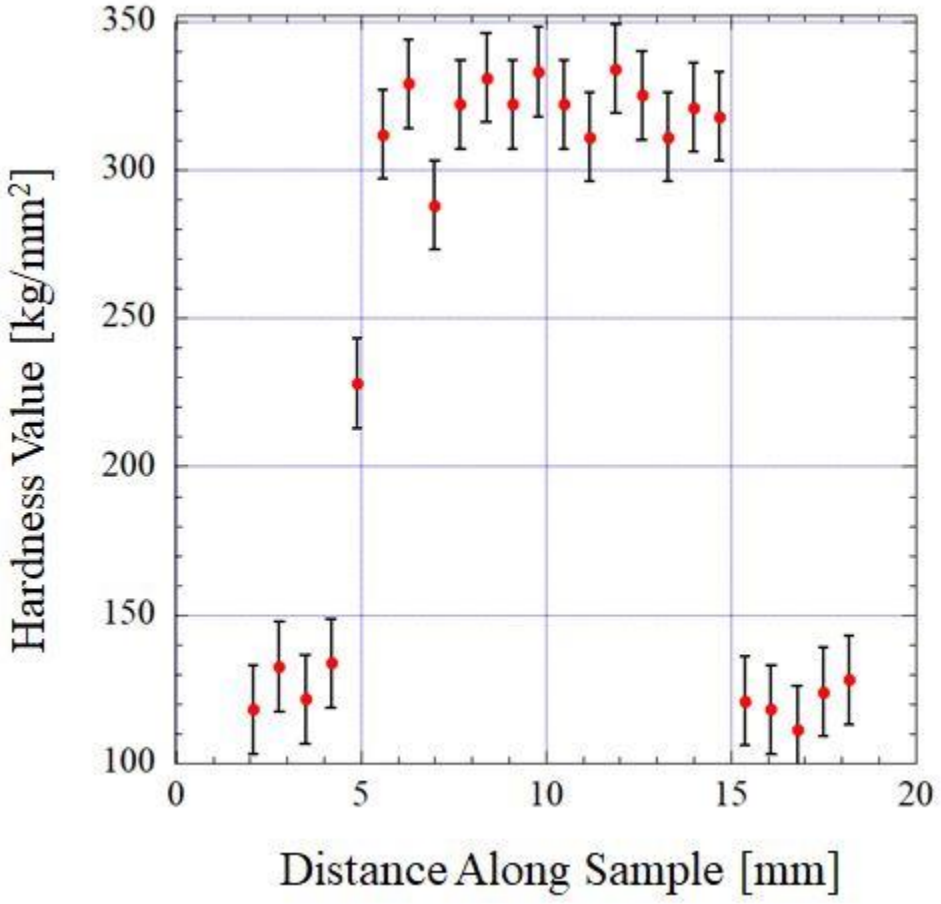

Figure 5.25: Distribution of hardness values measured across the length of ATEM1 Fe13Cr15Ni 5 dpa bar

For the ATEM1 sample, the change in hardness value was measured to be 197 ± 12 kg/mm^2 and the subsequent change in the yield stress was calculated to be 596 ± 37 MPa. Since there are no material differences between the ASCC2 and ATEM1 samples and each was irradiated to the same level of 5 dpa, the estimated change in yield stress calculated from the ATEM1 sample can be used for the ASCC2 sample. The yield stress of non-irradiated Fe13Cr15Ni was 140 ±15 MPa, which results in an estimated yield stress as calculated by equation 5.4 in the irradiated

region of 736 ±39 MPa. In uniaxial tension, the highest shear stress is observed on the plane oriented 45 degrees away from the loading axis. This is also shown in Section 2.2.1. There it is shown that the maximum shear stress on this plane is σ/2. Using the measurements from the ATEM1 sample and equation 5.4, the estimated critically resolved shear stress for the ASCC2 sample is calculated to be 368 ± 21 MPa.

The stress values presented in the previous section were calculated in the reference frame of the grain boundary. The important value for dislocation motion isn't the magnitude of the shear stress in the plane of the boundary, but in the direction of the specific slip system on which the dislocation is propagating. Using the equations presented in 2.2.5 on crystallographic misorientation, the σ_{12} shear stress was calculated in the direction of the slip systems in the grain adjacent to the dislocation pile-up. Since there were no observable dislocation channels in the adjacent grain, it was not possible to determine exactly which slip system would activate during deformation. Therefore shear stress values were taken for each slip system at a distance of 200 nm from the grain boundary and the system which had the highest value (including the contribution from the applied stress) was taken as the preferred slip system for dislocation motion. Figure 5.26 shows the maximum calculated shear stress in the direction of a slip system in the grain adjacent to discontinuous channels for all boundaries in the ASCC2 Fe13Cr15Ni 5 dpa tensile bar sample analyzed with HREBSD as a function of the Orientation Factor. The blue dashed line included is set at the estimated critical resolved shear stress of 368 MPa.

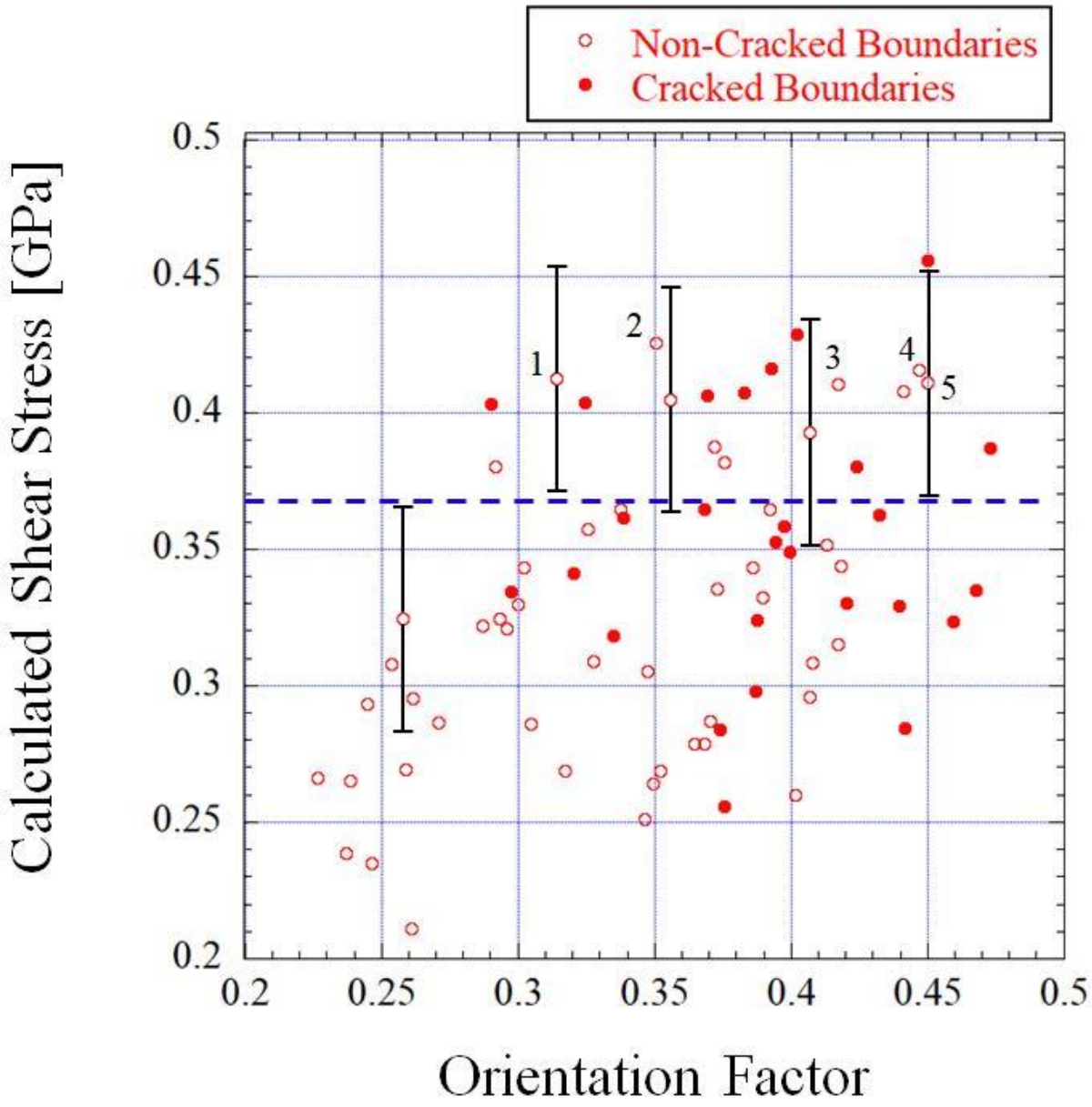

Figure 5.26:Calculated shear stress in ASCC2 Fe13Cr15Ni 5 dpa tensile bar sample acting in the direction of a slip system in the grain adjacent to dislocation pile-up as a function of the Orientation Factor. Blue dashed line denotes the estimated value for the critical resolved shear stress.

It is observed that a majority of points fall below the estimated value for the CRSS, which means that the driving force was not large enough to push dislocations through the radiation hardened matrix and for several of these points cracking occurred as an alternate method to alleviate the

large buildup of stress at the boundary. Of the 75 analyzed points, 5 were observed to exceed the calculated CRSS necessary for deformation by values greater than the error associated with the HREBSD measurement. These points have been labeled 1-5 in Figure 5.26. There are three distinct factors which could account for this discrepancy. The first is that local variations in the grain orientation and defect matrix population could have an effect on the CRSS at the point of intersection between the dislocation channel and the grain boundary which will require a higher stress to induce plasticity. The second involves the estimate of the CRSS. Equation 5.11 taken from Busby et al. fit the experimental data quite well when the yield stress of the material was relatively low (<400 MPa) and when the yield stress of the material was relatively high (>800 MPa). At moderate yield stresses, which is where the estimated yield stress of this material falls, scatter in the data was large. This large scatter in the data could mean that the estimated CRSS value being used for comparison could vary greatly from the actual CRSS of the material. The last factor is the relatively large error associated with the HREBSD measurement. Large errors in the magnitude of the calculated shear stresses makes it difficult at this time to fully analyze the competition between slip activation and cracking at specific grain boundary sites.

Since only a small fraction of the bulk tensile bar samples are irradiated, the stress strain behavior resembles that of the non-irradiated material. However, in order to maintain strain compatibility between the irradiated and non-irradiated regions stresses above the levels measured with the load cells during CERT testing are imparted to the irradiated region. If this were not the case, then deformation would not be observed in the irradiated region at all since the stress levels observed are significantly less than the estimated yield stress of the irradiated matrix. By using the estimated yield stress of the irradiated region presented previously rather

than the load cell value, a new cracking fraction as a function of total grain boundary normal stress can be calculated, which is presented in Figure 5.27.

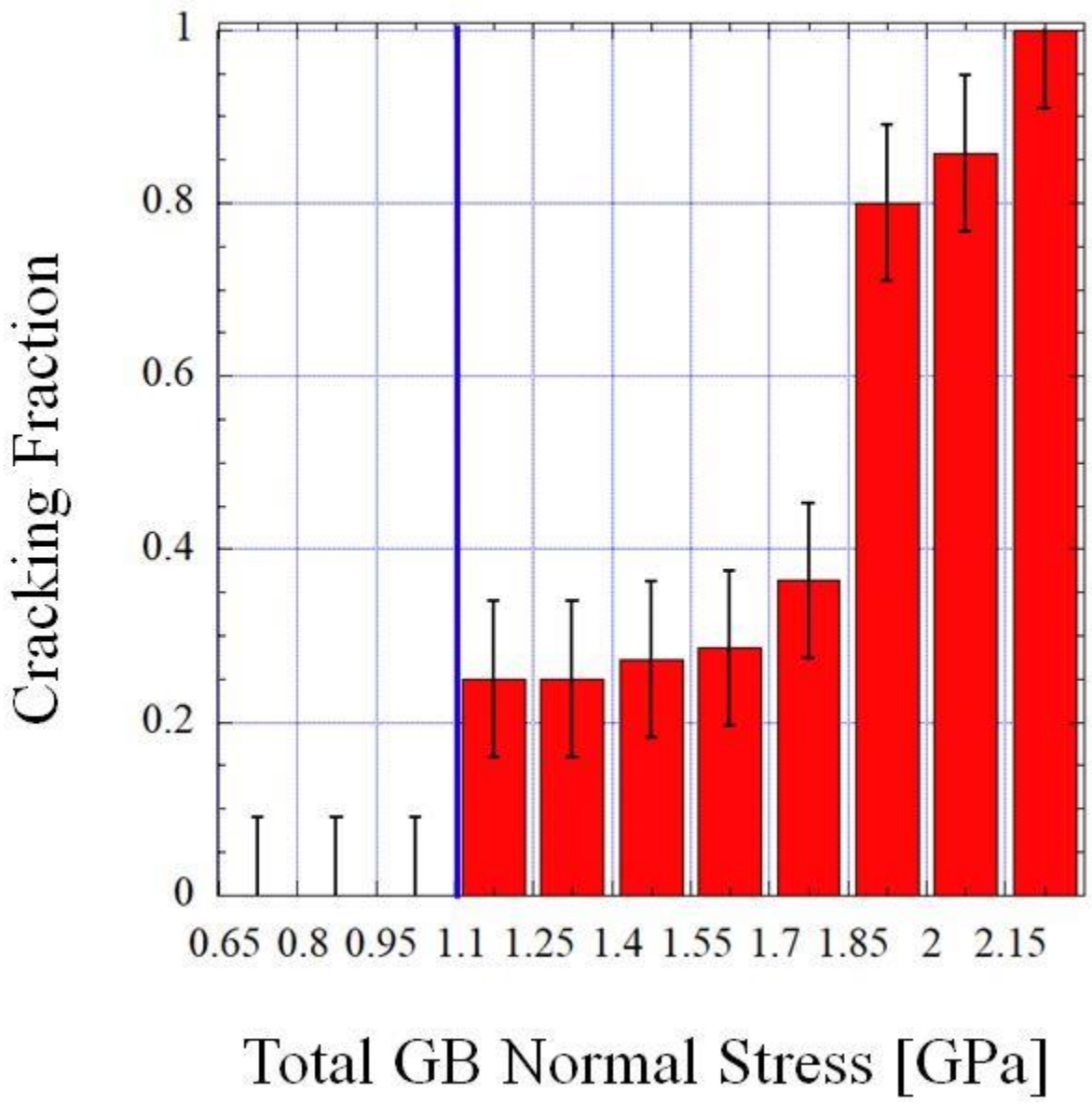

Figure 5.27: Cracking Fraction as a function of total grain boundary normal stress modified to include the effect of stress active in the thin irradiated region in ASCC2 Fe13Cr15Ni 5 dpa tensile bar sample after 1.5% straining increment (6% total) in 288 ˚C simulated BWR-NWC environment at $3x10^{-7}$ s^{-1}.

The results are unchanged from the previous analysis. A cracking threshold is still present and the cracking fraction increases monotonically toward 100% at the highest levels of total grain boundary normal stress. Considering the errors associated with the calculation of the irradiated yield stress and the complexities of stress transfer from the non-irradiated region to the irradiated region, this value for the total grain boundary normal stress is an overestimation and should be treated as an upper bound.

5.2.3 Effect of Alloy Composition on IASCC Susceptibility

While a threshold for crack initiation is observed for the ASCC2 Fe13Cr15Ni sample, this threshold is not universal across all austenitic stainless steels. There are other factors that are crucial to the crack initiation mechanism that are not encompassed by the magnitude of the stress which is present at the grain boundary. Figure 4.37 from Chapter 4 showed the stress present at a selection of boundaries in the BSCC2 Fe21Cr32Ni 5 dpa tensile bar sample after 6% total straining. The magnitude of stress observed here was at the same level or greater than many of the data points collected for the ASCC2 Fe13Cr15Ni 5 dpa tensile bar sample. For the ASCC2 sample, all sites which had a calculated total GB normal stress greater than 1.75 GPa were shown to crack. In the BSCC2 Fe21Cr32Ni 5 dpa tensile bar sample, 18 sites were observed to have a total GB normal stress greater than 1.0 GPa. With this many sites above the pseudo threshold for cracking as established by the ASCC2 Fe13Cr15Ni 5 dpa tensile bar sample, crack initiation would be expect in at least some of these sites if the threshold stress was consistent between the two alloys. In the BSCC2 Fe21Cr32Ni 5 dpa tensile bar sample there were also 5 sites that had a calculated total GB normal stress greater than 1.75. In this stress range, the cracking fraction observed in the ASCC2 sample was 100% while no cracking was observed in the BSCC2

sample. These results underline the importance of factors in the IASCC process which go beyond the mechanical stresses which are present at the grain boundary. With an increased concentration of chromium in the bulk, the BSCC2 Fe21Cr32Ni sample has a larger reservoir of chromium to pull from in order to create a passivating inner oxide layer which could help prevent the continued oxidation and degradation of the grain boundary during exposure to a high temperature corrosive environment.

Chapter 6 – Conclusions and Future Work

6.1 Conclusions

A novel use of high resolution electron backscatter diffraction and serial sectioning was implemented to calculate the local stress tensor near dislocation channel – grain boundary interaction sites in irradiated stainless steel for the purpose of linking local stresses to IASCC susceptibility. Full characterization of the grain boundary geometry, considering both the geometric orientation and the crystallographic orientation of the grains comprising the boundary, was used to resolve the measured stresses onto the boundary, which has previously not been possible. Results from both a molecular dynamics simulation, and a discrete multi-plane dislocation array model compared well with the HRESBD measurements and provided insights into the development of local stresses at either continuous or discontinuous channel-boundary interaction sites. Analysis of specific grain boundaries prior to straining in simulated BWR-NWC at 288 °C allowed for the direct linkage of the stress state at the grain boundary with IASCC crack initiation behavior. Successful HREBSD analysis and subsequent CERT testing of two alloys, Fe13Cr15Ni and Fe21Cr32Ni, has led to the following major conclusions:

- Elevated tensile and shear stresses occur at *discontinuous* channel – grain boundary interaction sites and reach magnitudes of nearly 2 GPa and 1 GPa respectively. These stresses extend over the first few microns into the adjacent grain and decrease with a $r^{-1/2}$

dependence which matches the analytical solution for a linear array of dislocations pinned at an immovable barrier.

- No significant stress increase is observed at *continuous* channel – grain boundary interaction sites, which is in stark contrast to the behavior near discontinuous channels. The low stress amplification near continuous channels is consistent with idea that the high stresses at the grain boundary produced by the pile-up of dislocations are responsible for crack initiation in irradiated stainless steel.
- Extending the traditional Eshelby model for calculating equilibrium positions of a linear array of dislocations to account for reasonable dislocation channel geometry, which includes several parallel slip planes results in a stress profile similar to that observed in experimental HREBSD measurements, providing evidence that the stress state generated at DC-GB interaction sites is primarily caused by the distribution of dislocations which pile up at the grain boundary during plastic deformation.
- The behavior between continuous and discontinuous dislocation channels is also reflected in MD simulations with slip transmission resulting in significant relaxation of the tensile stress at the grain boundary, which helps to explain the difference in cracking susceptibility between these two grain boundary interaction types.
- Cracking was observed in Fe13Cr15Ni irradiated to 5 dpa with the cracking fraction increasing as the total grain boundary normal stress increased. The cracking distribution followed the magnitude of the tensile stress acting normal to the grain boundary rather than the magnitude of the observed shear stresses.
- Accounting for anisotropy between the two grains on either side of the analyzed boundaries had an effect on the distribution of cracks as a function of the total grain

boundary normal stress, which led to a profile which more closely followed the trend of higher GB normal stress resulting in higher IASCC susceptibility.

- A pseudo-threshold for crack initiation was observed in the 5 dpa, Fe13Cr15Ni alloy near 1.0 GPa, providing evidence that while the grain boundary normal stress is a crucial factor in initiating cracks, it needs to reach a critical magnitude before crack initiation will occur.
- Incorporating information about the geometric orientation of the grain boundary and crystallographic orientation of the deforming grains makes it possible to isolate specific grain boundaries which are most susceptible to IASCC.
- The pseudo-threshold for crack initiation established for the ASCC2 Fe13Cr15Ni 5 dpa tensile bar sample is not universal for austenitic steels, and will differ based on the specific alloy composition. Fe21Cr32Ni, with a higher chromium concentration in the bulk, was resistant to crack initiation even in the stress regime that produced many cracks in the ASCC2 sample. This is consistent with a high chromium efficiently supplying chromium to the surface to maintain a protective oxide for the underlying grain boundary.
- The presented data shows a clear correlation between the total GB normal stress and the susceptibility of the GB to IASCC. This is consistent with the model presented in Chapter 5 where rupture of the oxide film was caused by tensile stresses pulling the boundary apart to expose the underlying grain boundary and extend the cracking process.

6.2 Future Work

As this technique for measuring and resolving stresses onto specific grain boundaries is a novel way for analyzing crack initiation in irradiated material, there are many opportunities for future work. A fair amount of mechanical polishing is required throughout the process of ultimately calculating the stress field near a specific DC-GB interaction site which introduces several errors and non-uniformities into the system. This is partially due to the sample geometry, with the outer diameter of the tensile head being larger than the cross section of the gauge section. While this is advantageous for the CERT testing aspect of the experiment, improvements to the accuracy of the GB plane measurement and HREBSD measurements could be made with a different sample geometry.

While this set of experiments focused primarily on the stress fields generated at DC-GB interaction sites in two similar alloys, further investigation into the presence of a crack initiation stress threshold should be made into other alloy systems like commercial purity 304 and alloy 600/690. Experiments should also be run in a simulated PWR environment at 320 C to determine if the same threshold for crack initiation is observable in this water chemistry as well.

The ability to measure the stress at the point of crack initiation is limited by the incremental nature of the CERT experiments. Further work could be done to improve the straining process to limit the uncertainty of the stress that is present at the grain boundary when the crack initially forms. This potentially could be accomplished by moving towards a 4-point bend setup which has been demonstrated to be an effective method for determining a quantitative value for the macroscopic stress needed in order to cause crack initiation. By combining

interrupted 4-point bending with HREBSD analysis it may be possible to further isolate the role of stress on IASCC.

Much more work needs to be performed in order to understand all of the intricate variables surrounding IASCC. This work focused primarily on the role of the stress state generated at the grain boundary due to localized deformation, however there was still a large difference in the cracking susceptibility for the two alloys studied even though similar magnitudes of stress were observed at DC-GB interaction sites in both. The alloy composition and its effect on oxidation are still not well understood in this context and would require much more work before a complete picture for the mechanisms driving IASCC can be determined.

Appendices

APPENDIX A

Inverse Pole Figures (IPFs) Showing Grain Size and Orientation

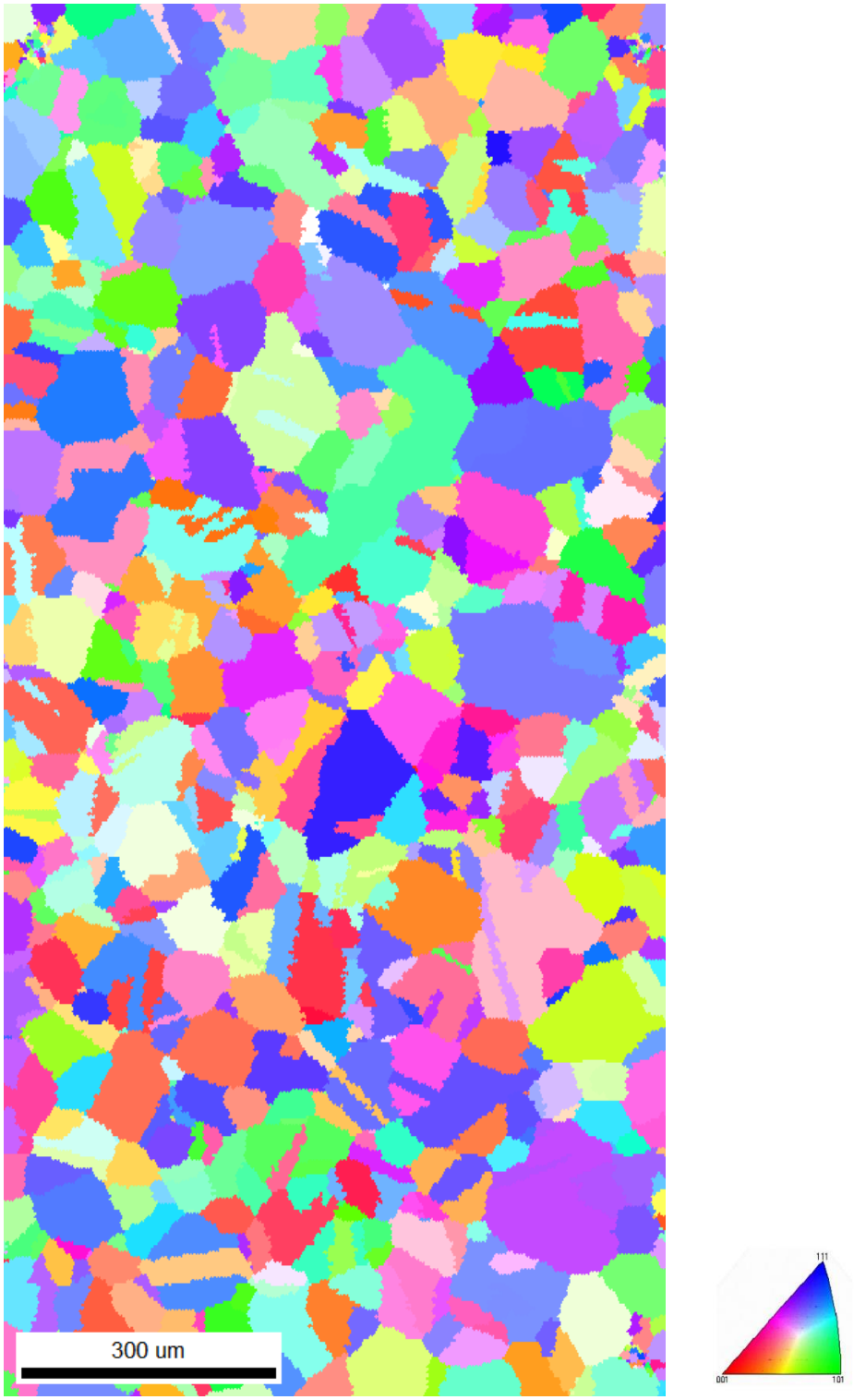

Figure A.1: Inverse pole figure (IPF) taken from ASCC1 Fe13Cr15Ni 0 dpa tensile bar sample OIM region 1 showing grain size and orientation.

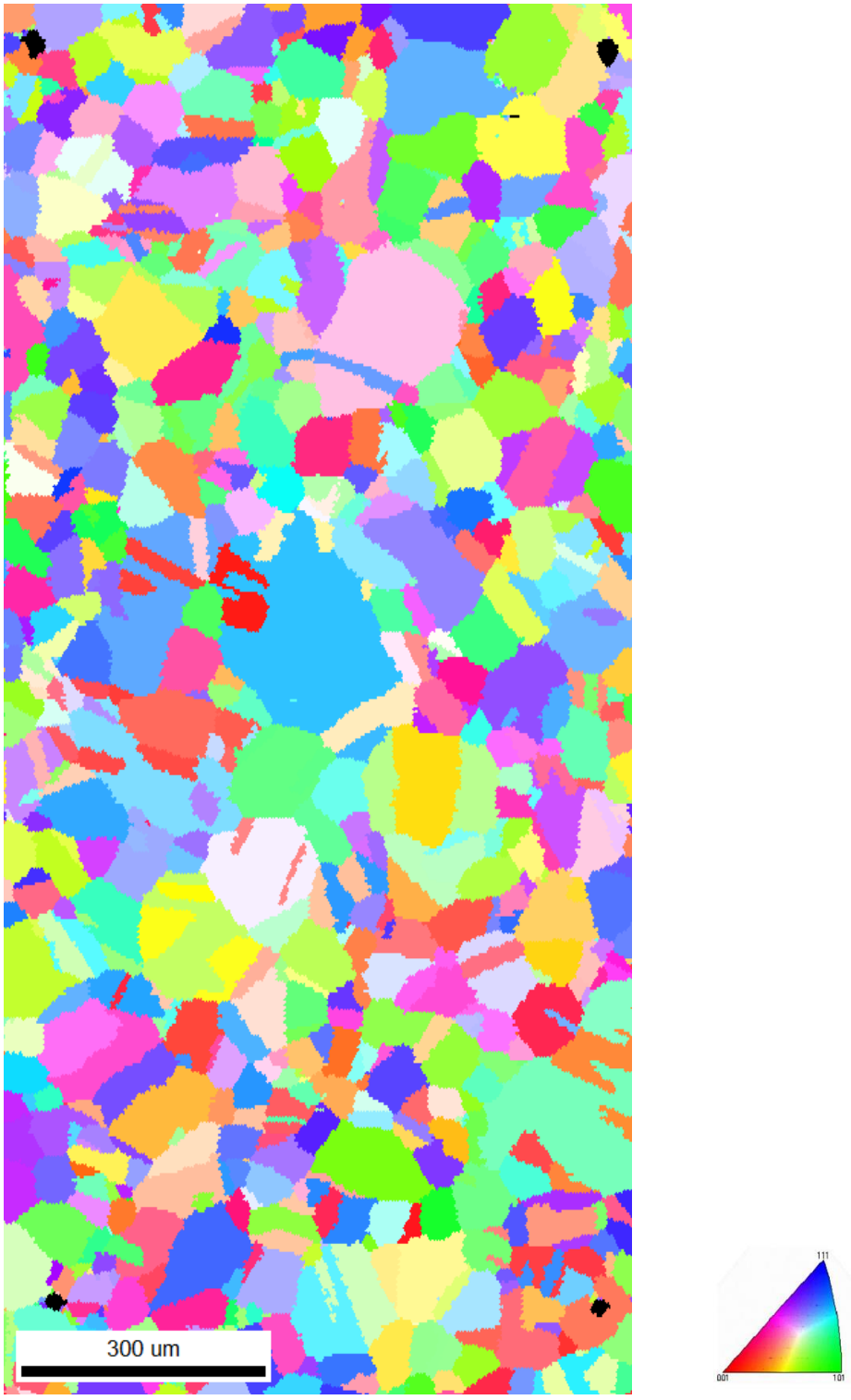

Figure A.239: Inverse pole figure (IPF) taken from ASCC1 Fe13Cr15Ni 0 dpa tensile bar sample OIM region 2 showing grain size and orientation.

Figure A.3: Inverse pole figure (IPF) taken from ASCC1 Fe13Cr15Ni 0 dpa tensile bar sample OIM region 3 showing grain size and orientation.

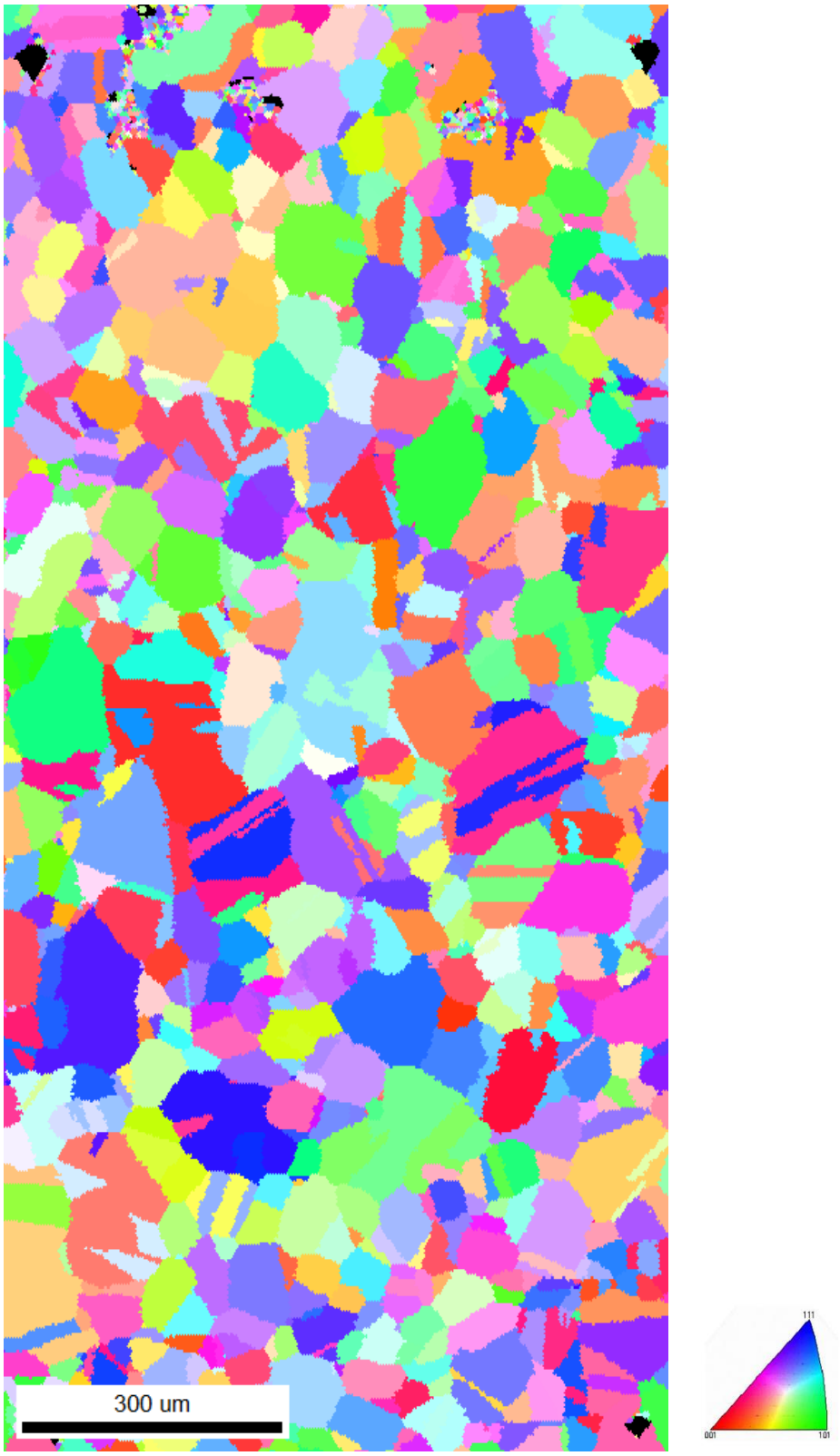

Figure A.440: Inverse pole figure (IPF) taken from ASCC1 Fe13Cr15Ni 0 dpa tensile bar sample OIM region 4 showing grain size and orientation.

Figure A.541: Inverse pole figure (IPF) taken from ASCC1 Fe13Cr15Ni 0 dpa tensile bar sample OIM region 5 showing grain size and orientation.

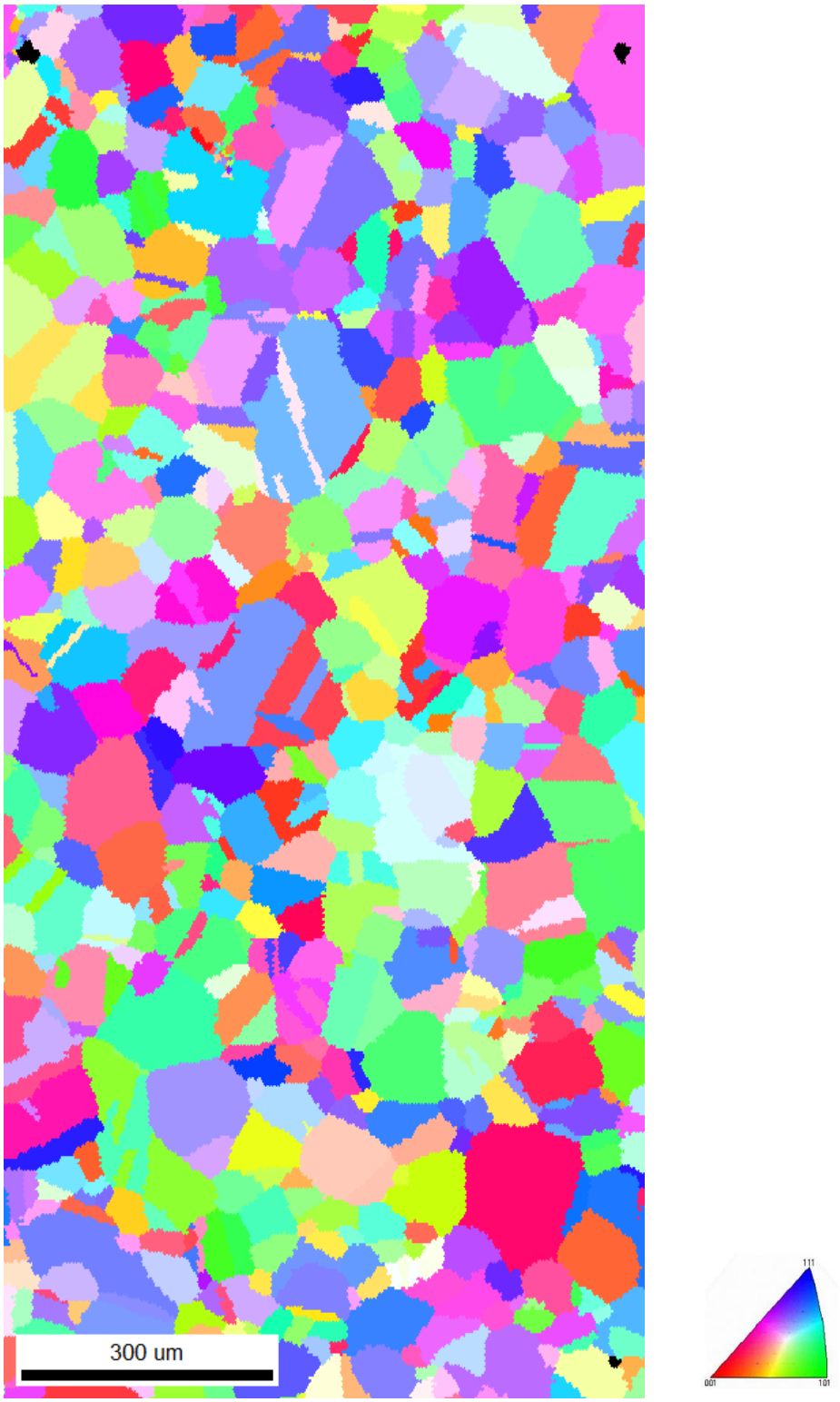

Figure A.642: Inverse pole figure (IPF) taken from ASCC1 Fe13Cr15Ni 0 dpa tensile bar sample OIM region 6 showing grain size and orientation.

Figure A.743: Inverse pole figure (IPF) taken from ASCC1 Fe13Cr15Ni 0 dpa tensile bar sample OIM region 7 showing grain size and orientation.

Figure A.44: Inverse pole figure (IPF) taken from ASCC1 Fe13Cr15Ni 0 dpa tensile bar sample OIM region 8 showing grain size and orientation.

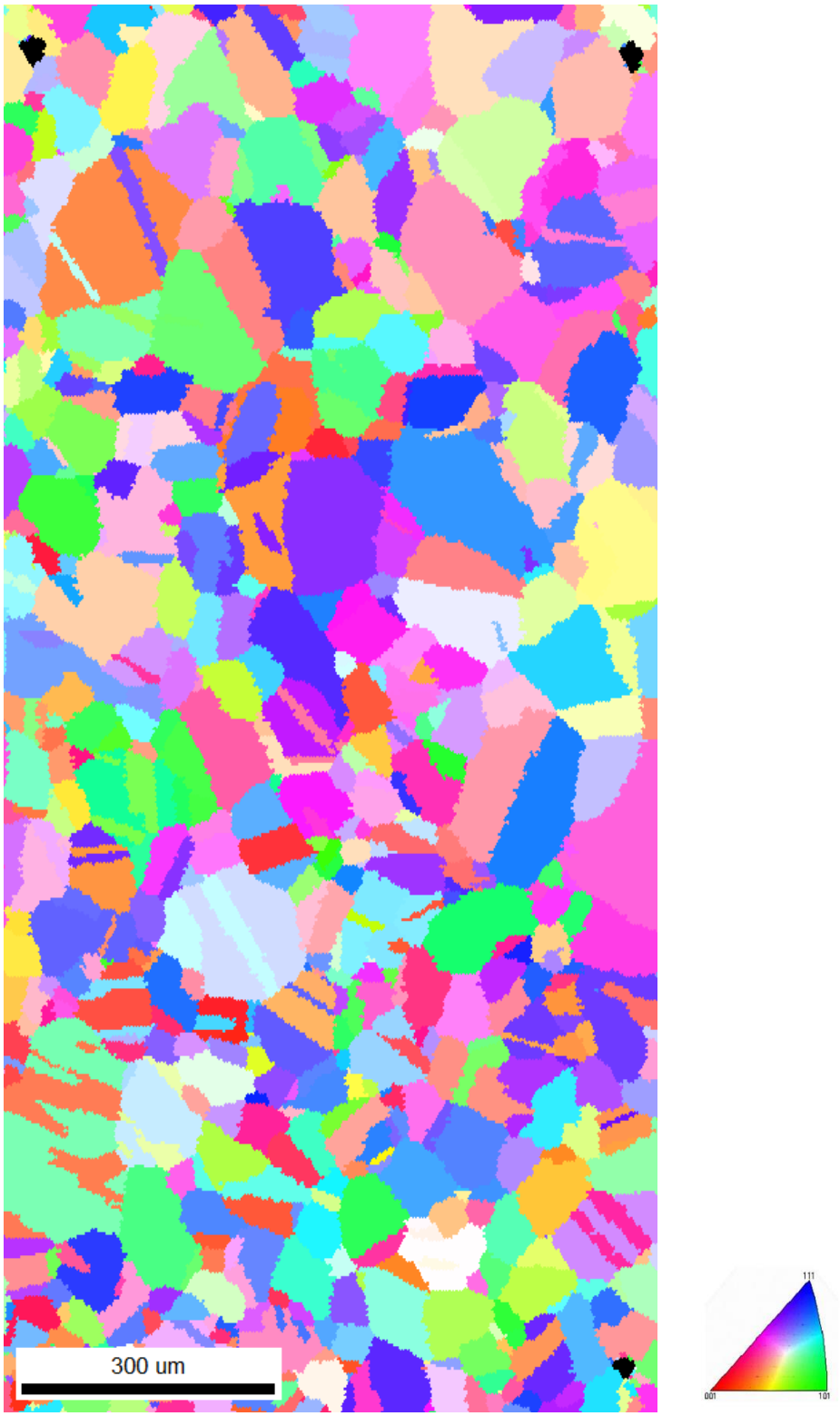

Figure A.9: Inverse pole figure (IPF) taken from ASCC1 Fe13Cr15Ni 0 dpa tensile bar sample OIM region 9 showing grain size and orientation.

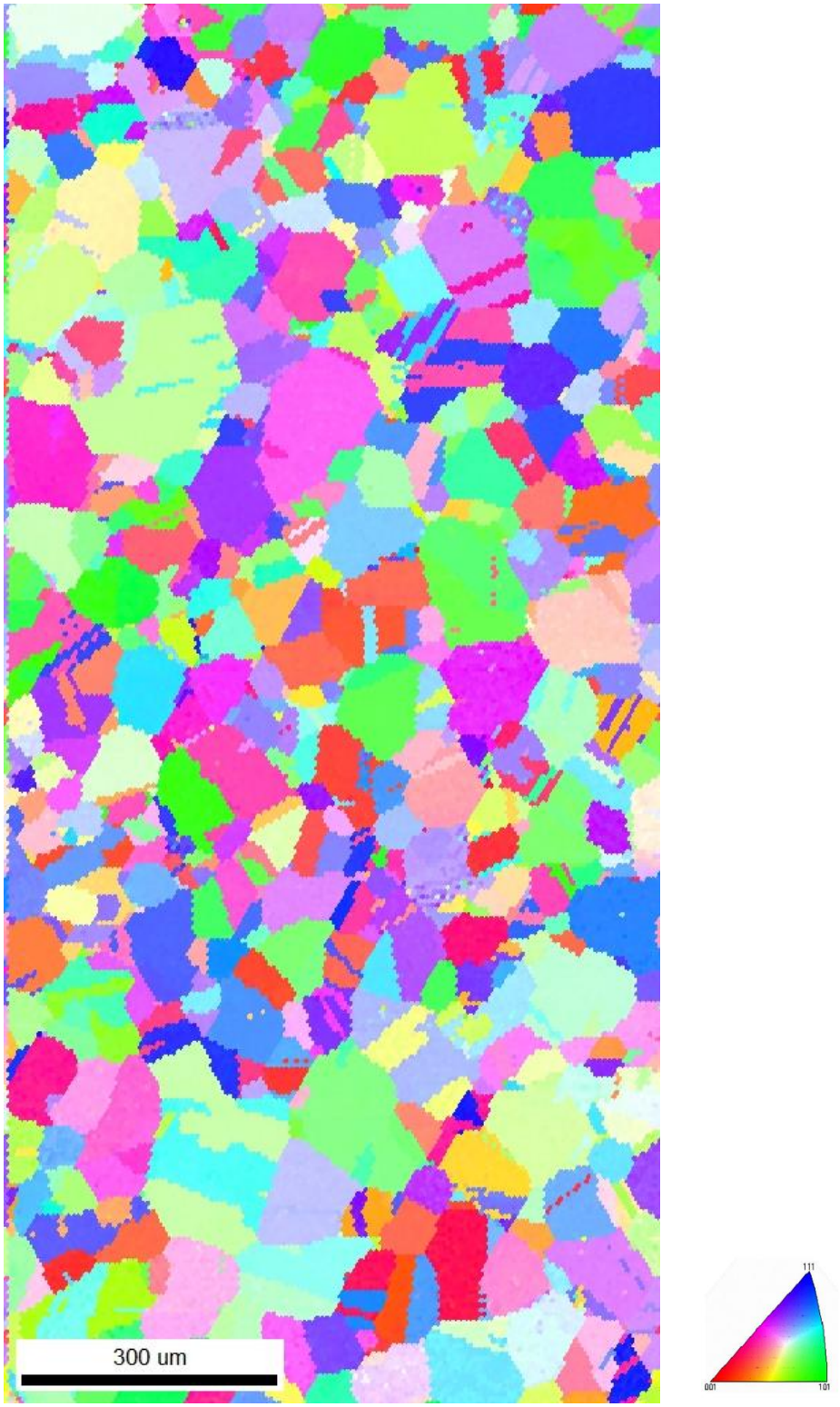

Figure A.1045: Inverse pole figure (IPF) taken from ASCC1 Fe13Cr15Ni 0 dpa tensile bar sample OIM region 10 showing grain size and orientation.

Figure A.11: Inverse pole figure (IPF) taken from ASCC2 Fe13Cr15Ni 5 dpa tensile bar sample OIM region 1 showing grain size and orientation.

Figure A.12: Inverse pole figure (IPF) taken from ASCC2 Fe13Cr15Ni 5 dpa tensile bar sample OIM region 3 showing grain size and orientation.

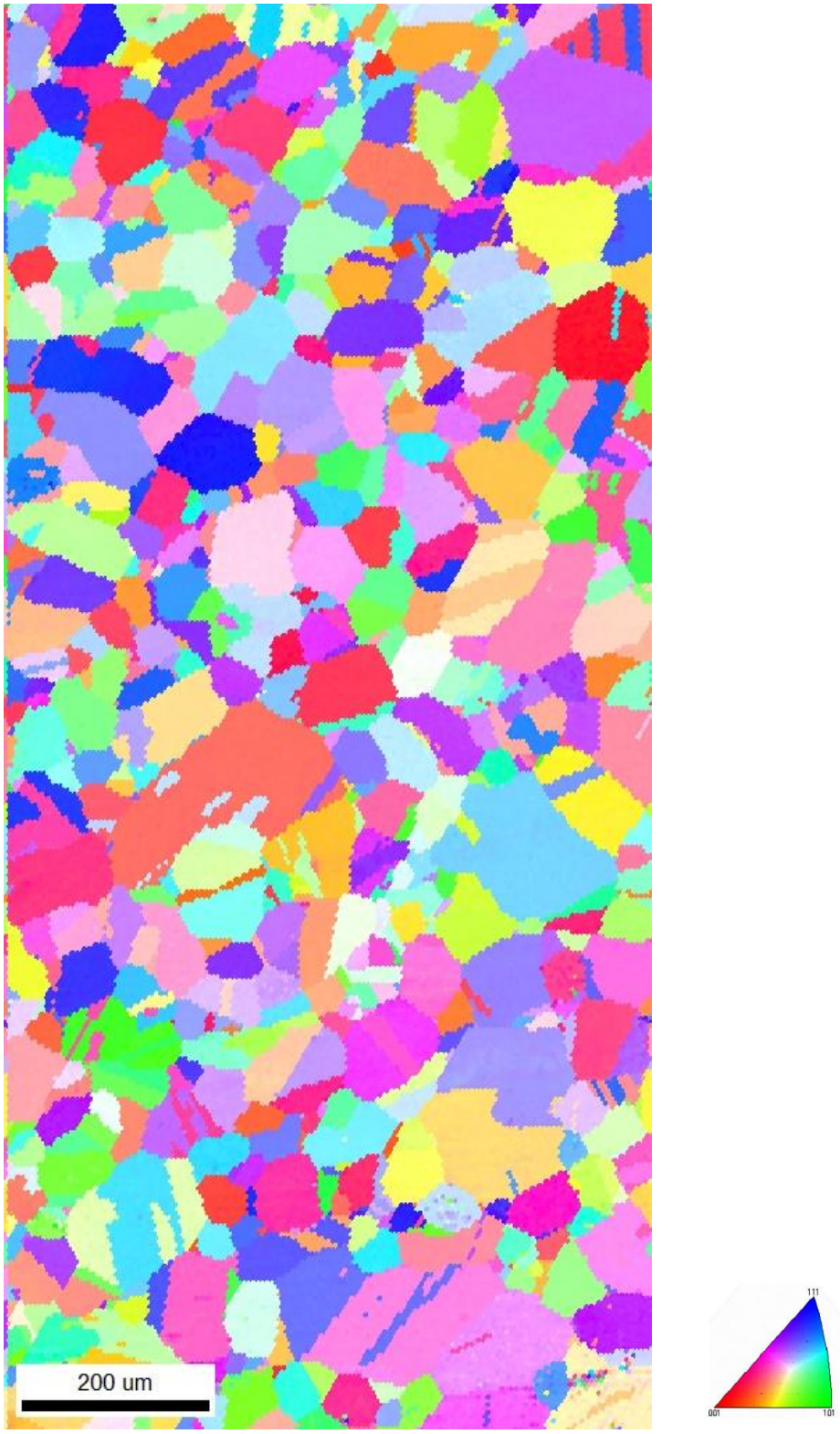

Figure A.1346: Inverse pole figure (IPF) taken from ASCC2 Fe13Cr15Ni 5 dpa tensile bar sample OIM region 5 showing grain size and orientation.

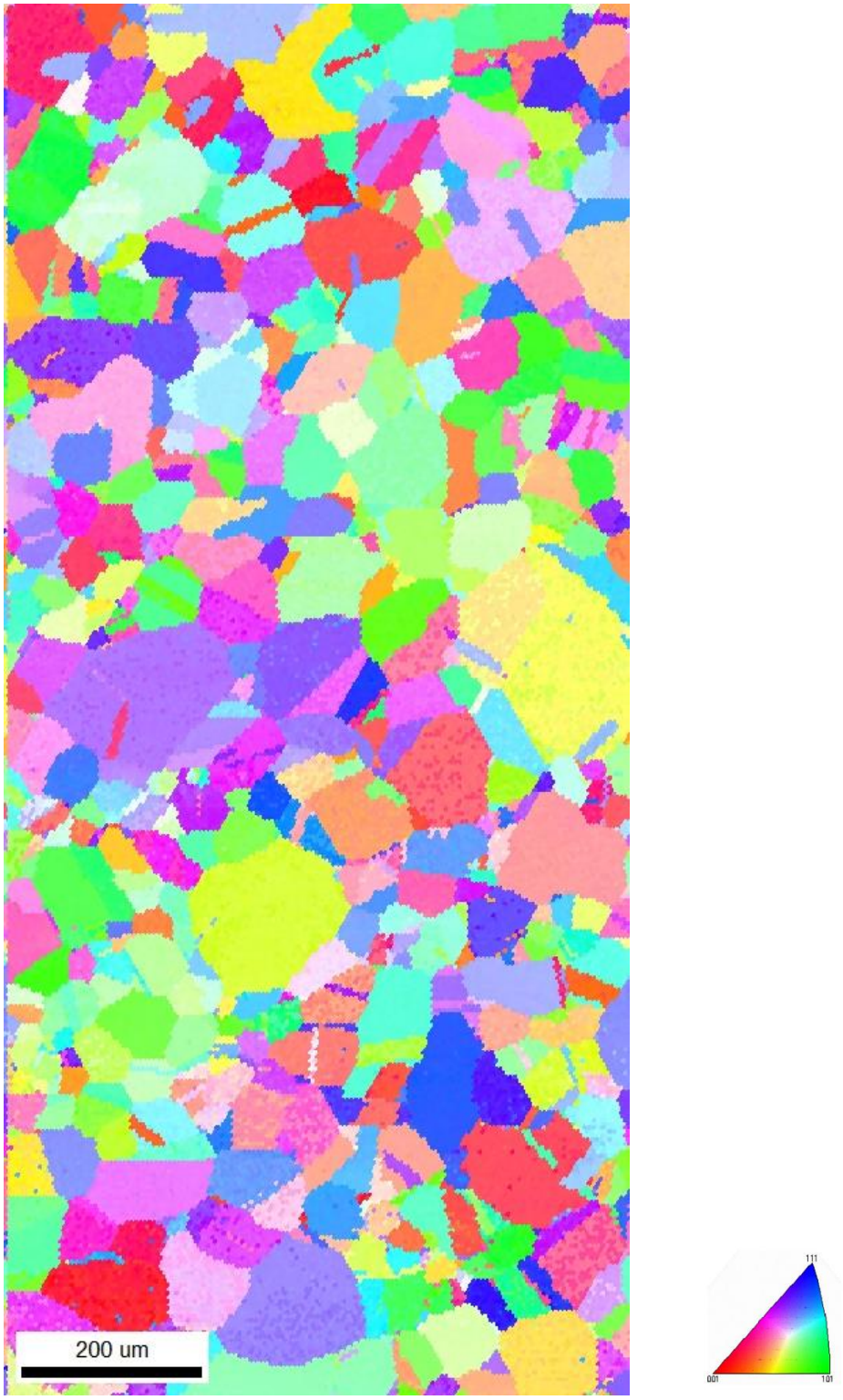

Figure A.1447: Inverse pole figure (IPF) taken from ASCC2 Fe13Cr15Ni 5 dpa tensile bar sample OIM region 7 showing grain size and orientation.

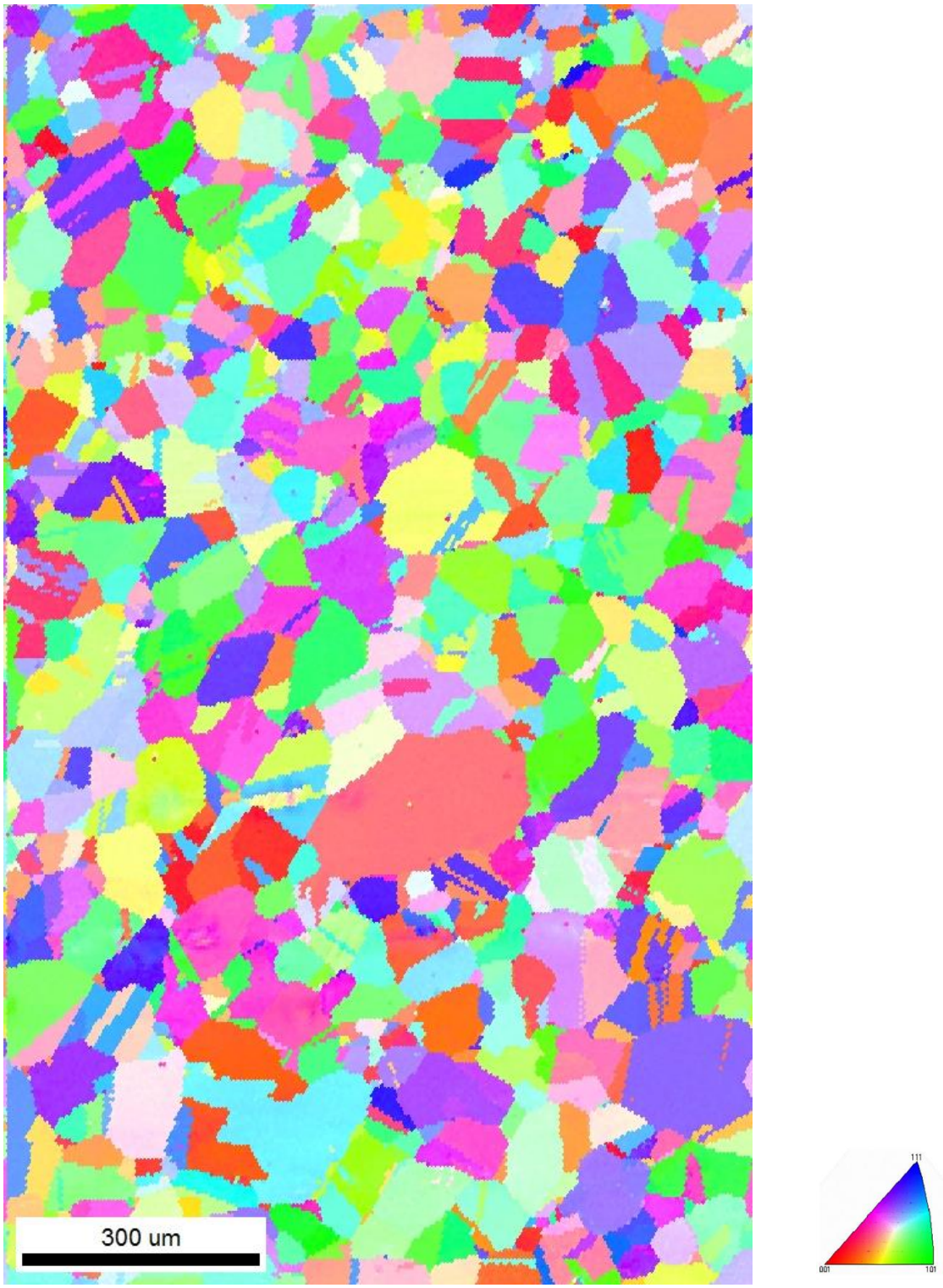

Figure A.15: Inverse pole figure (IPF) taken from ASCC2 Fe13Cr15Ni 5 dpa tensile bar sample OIM region 9 showing grain size and orientation.

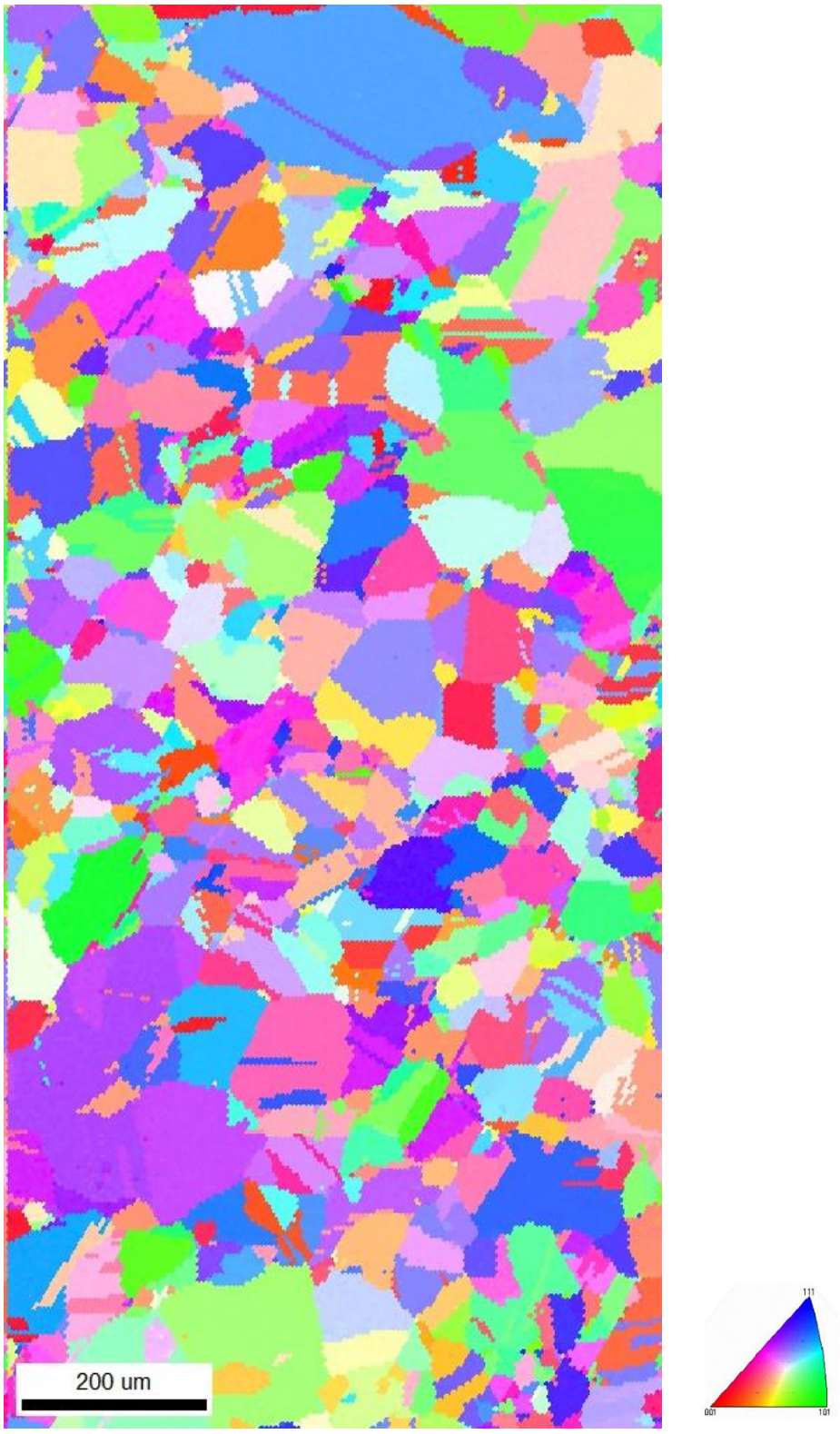

Figure A.1648: Inverse pole figure (IPF) taken from BSCC1 Fe21Cr32Ni 0 dpa tensile bar sample OIM region 1 showing grain size and orientation.

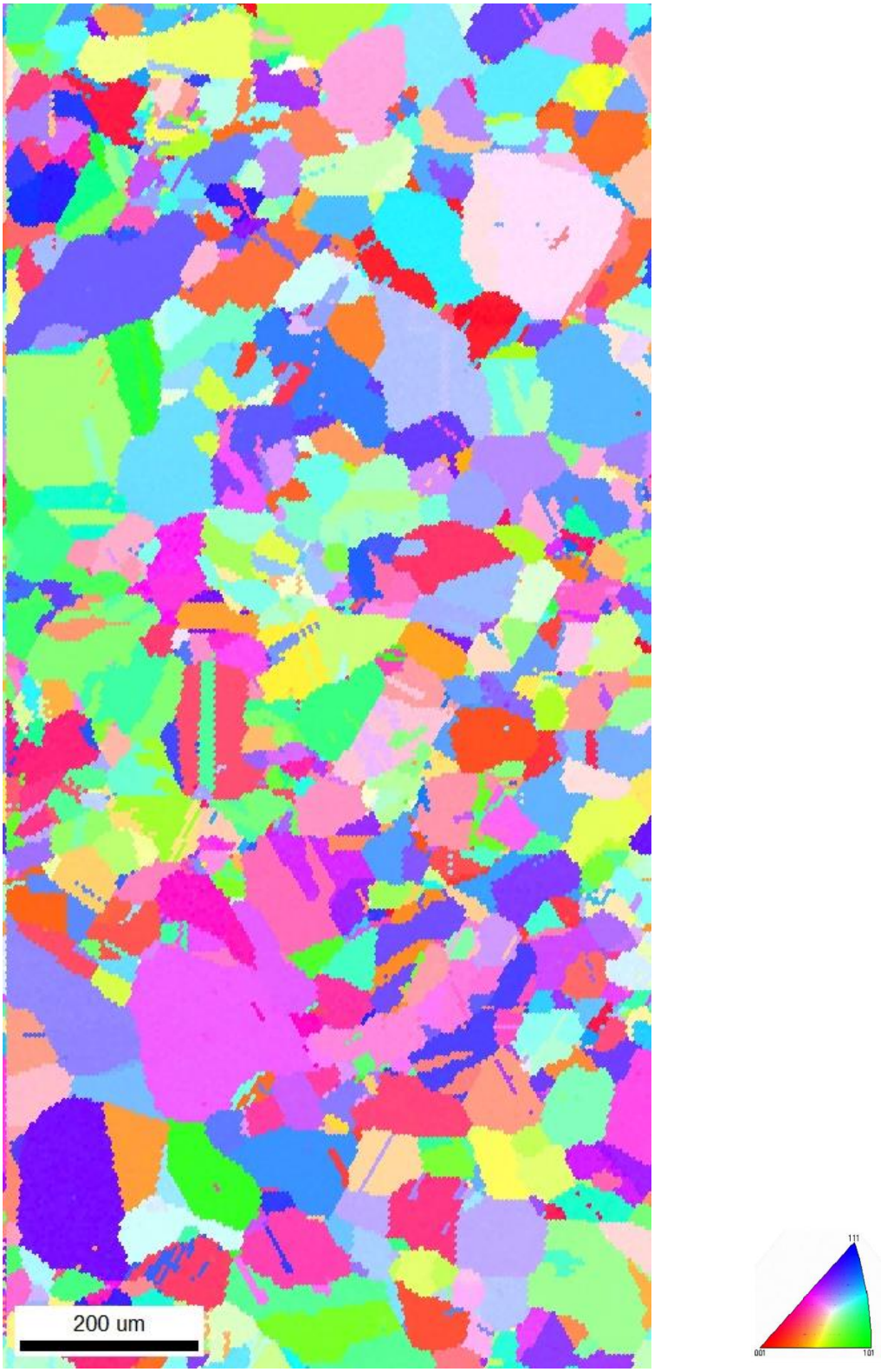

Figure A.17: Inverse pole figure (IPF) taken from BSCC1 Fe21Cr32Ni 0 dpa tensile bar sample OIM region 2 showing grain size and orientation.

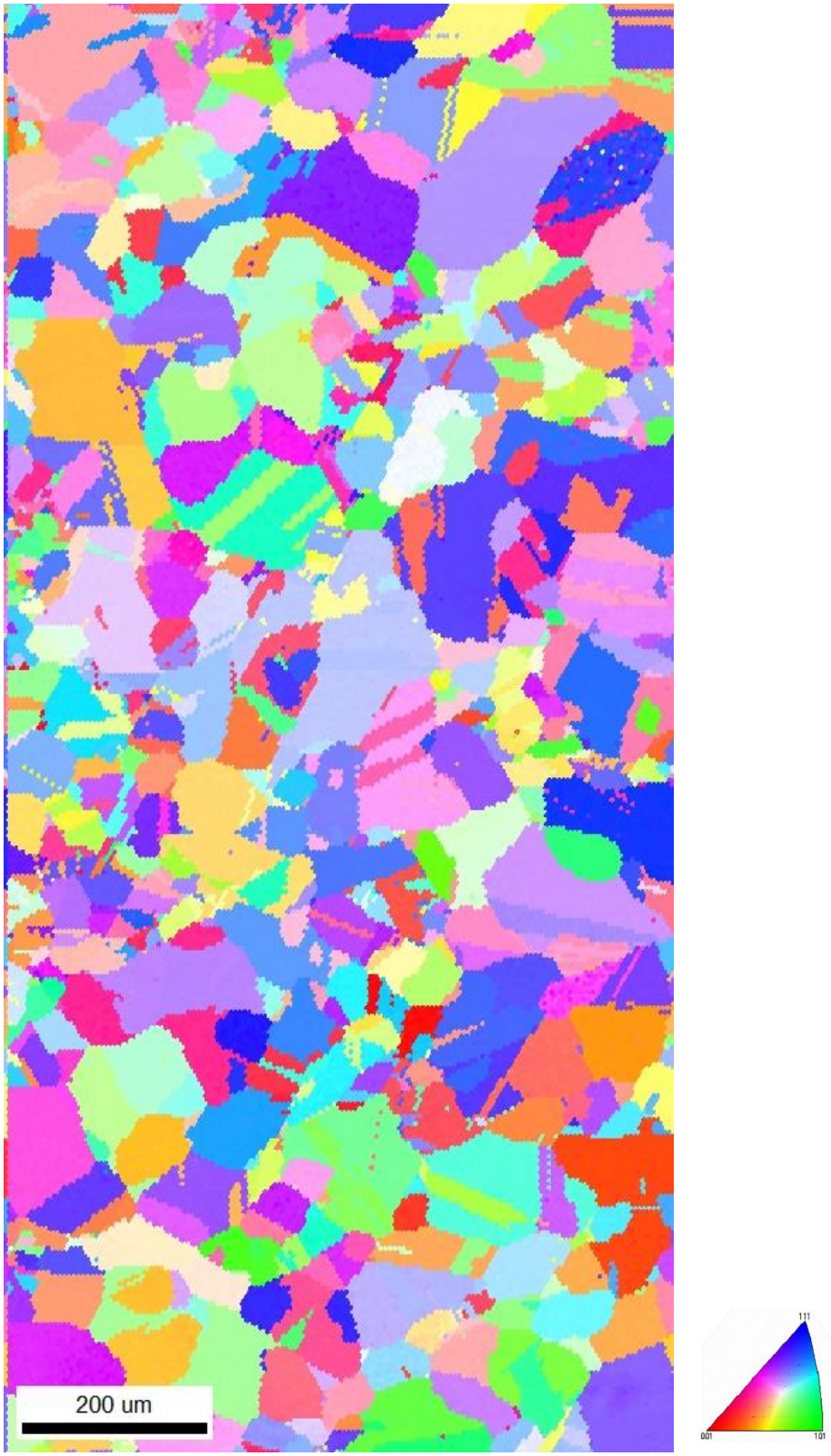

Figure A.1849: Inverse pole figure (IPF) taken from BSCC1 Fe21Cr32Ni 0 dpa tensile bar sample OIM region 3 showing grain size and orientation.

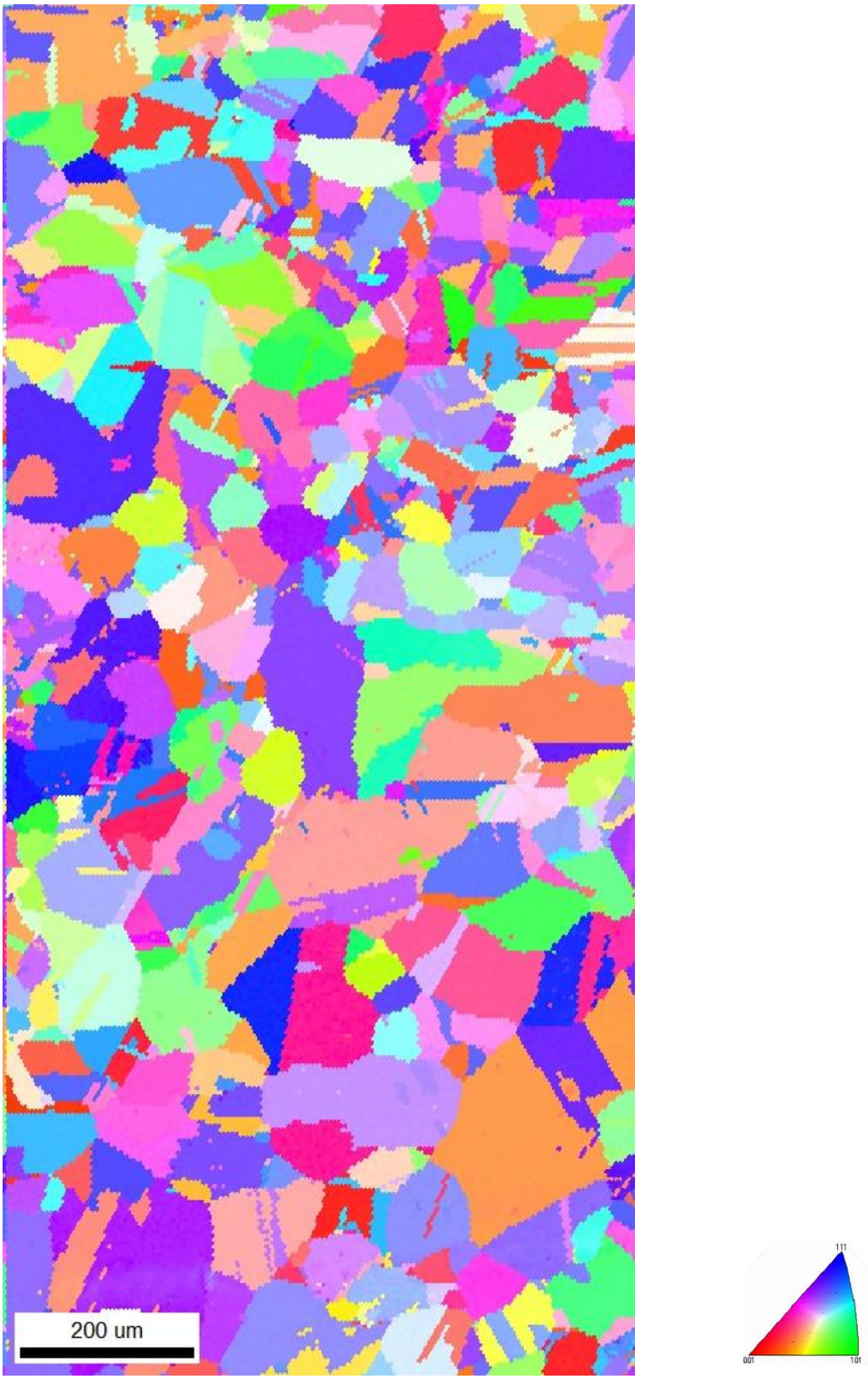

Figure A.1950: Inverse pole figure (IPF) taken from BSCC1 Fe21Cr32Ni 0 dpa tensile bar sample OIM region 4 showing grain size and orientation.

Figure A.2051: Inverse pole figure (IPF) taken from BSCC1 Fe21Cr32Ni 0 dpa tensile bar sample OIM region 5 showing grain size and orientation.

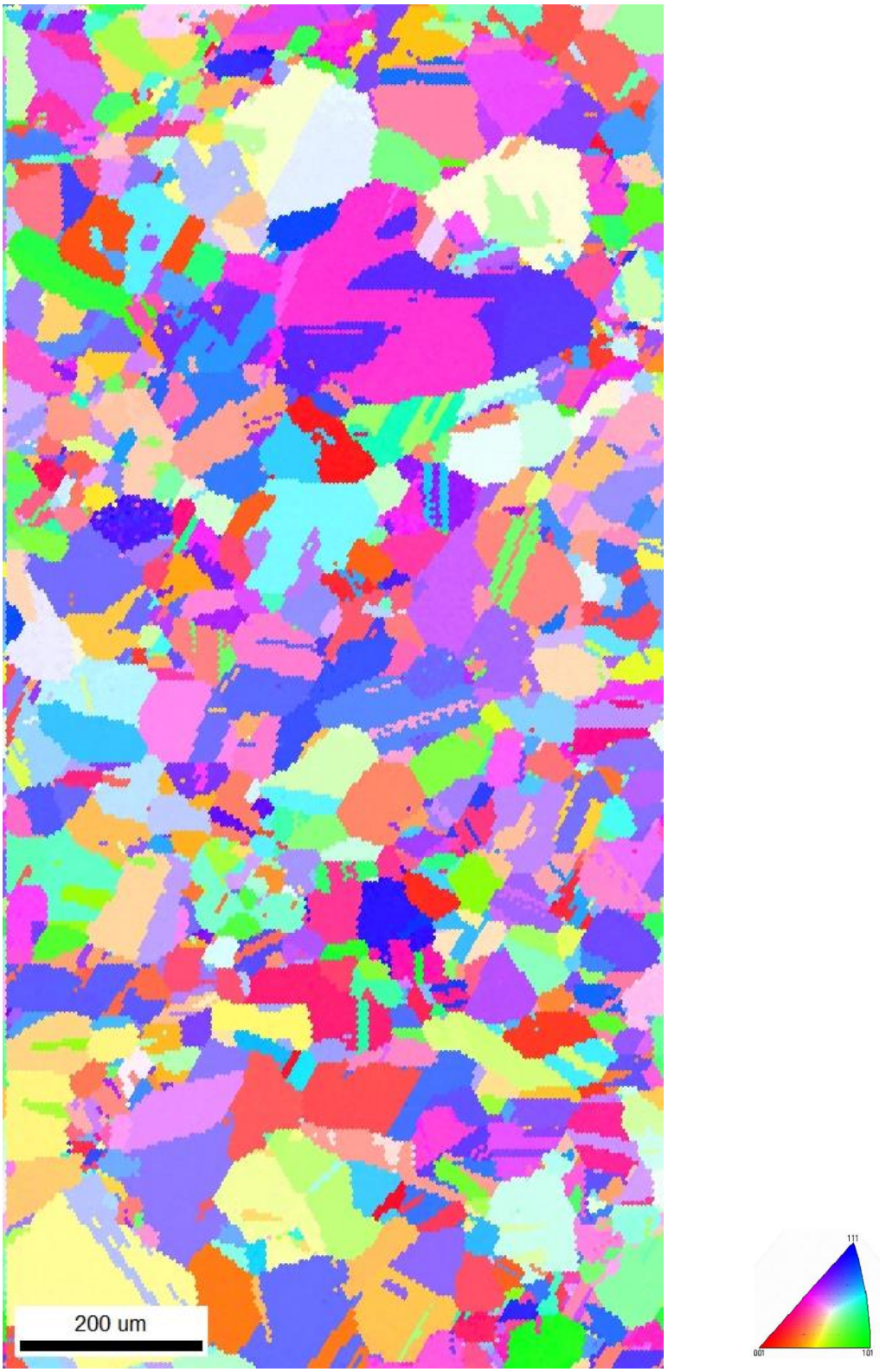

Figure A. 2152: Inverse pole figure (IPF) taken from BSCC1 Fe21Cr32Ni 0 dpa tensile bar sample OIM region 6 showing grain size and orientation.

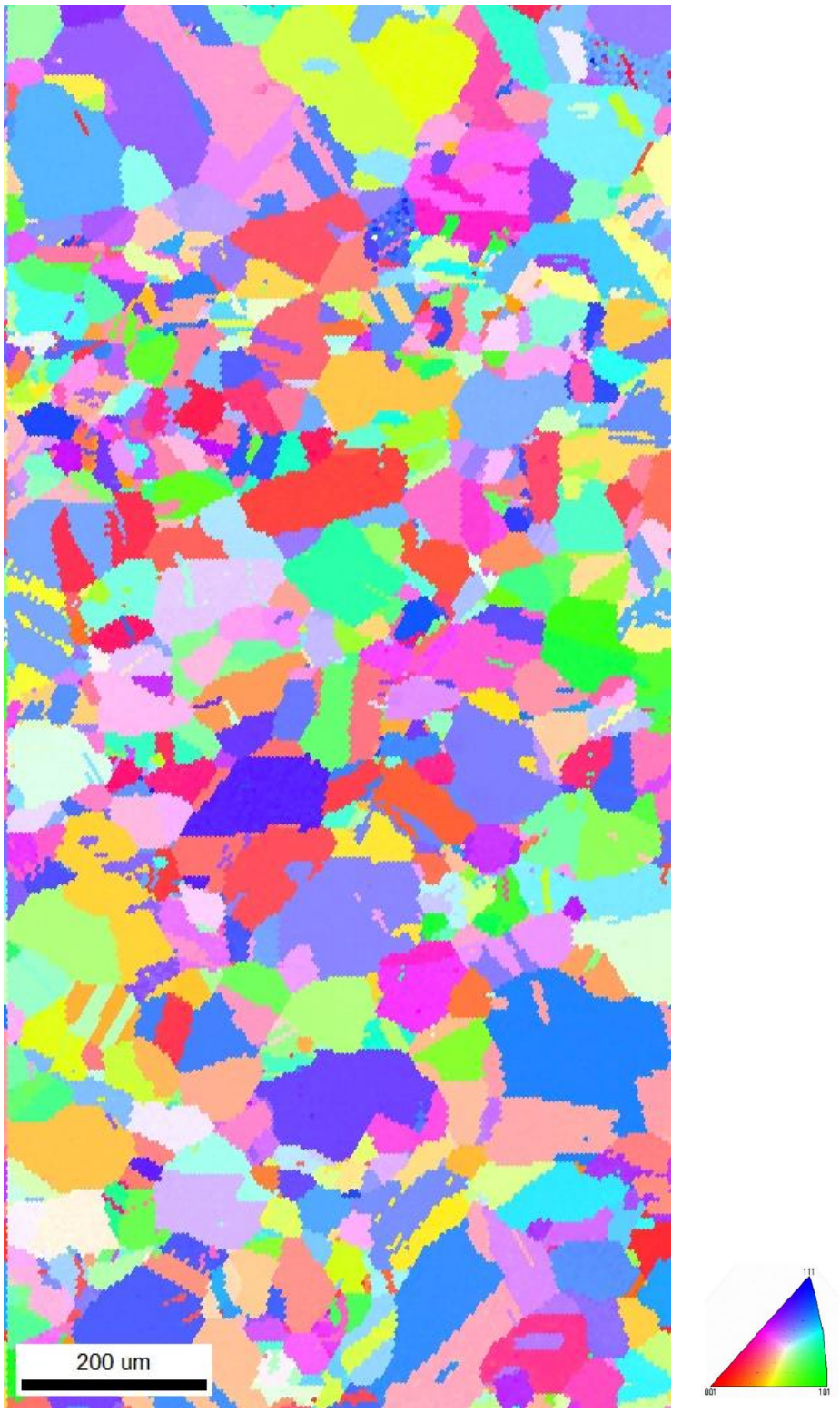

Figure A.2253: Inverse pole figure (IPF) taken from BSCC1 Fe21Cr32Ni 0 dpa tensile bar sample OIM region 7 showing grain size and orientation.

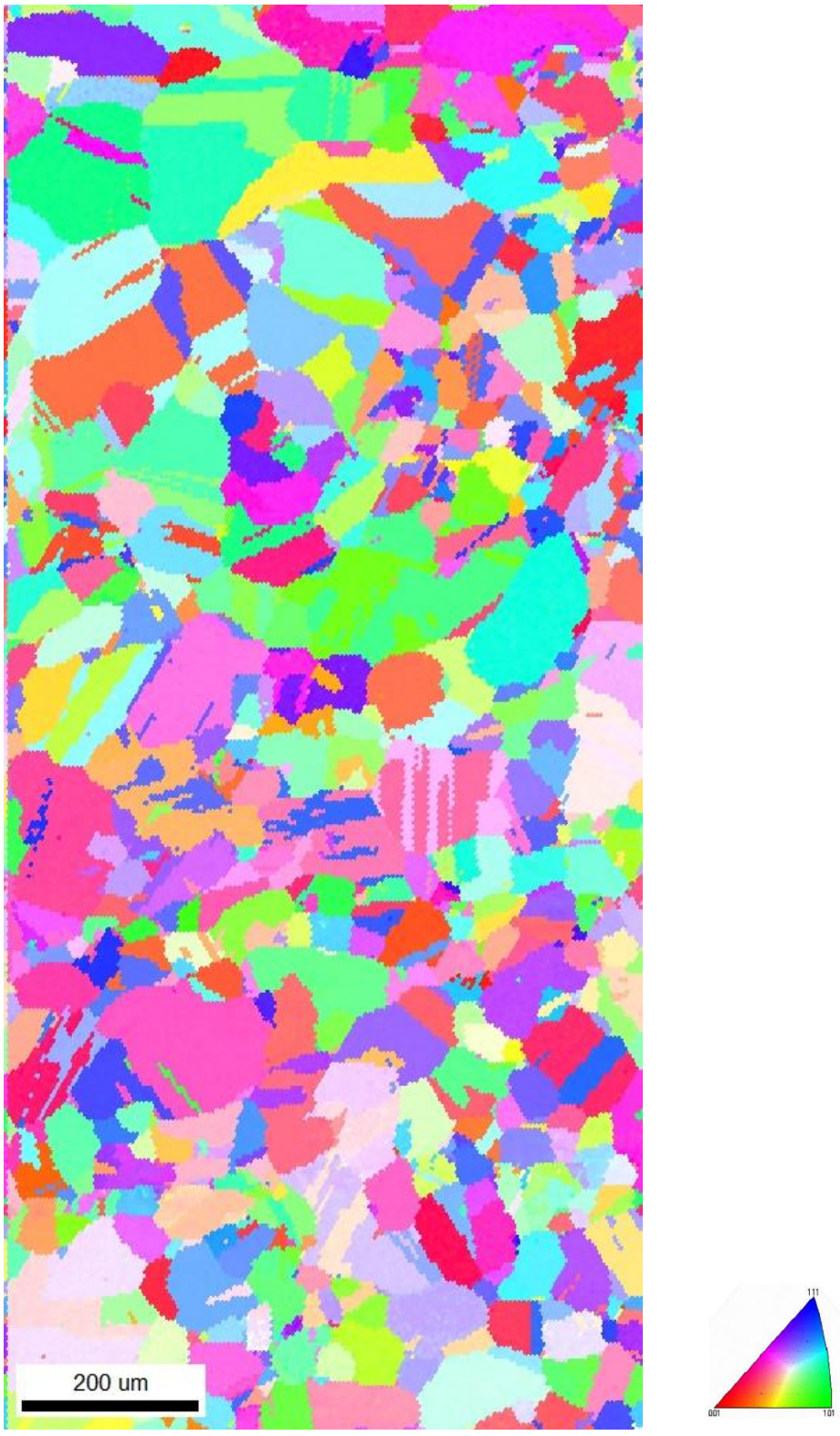

Figure A.23: Inverse pole figure (IPF) taken from BSCC1 Fe21Cr32Ni 0 dpa tensile bar sample OIM region 8 showing grain size and orientation.

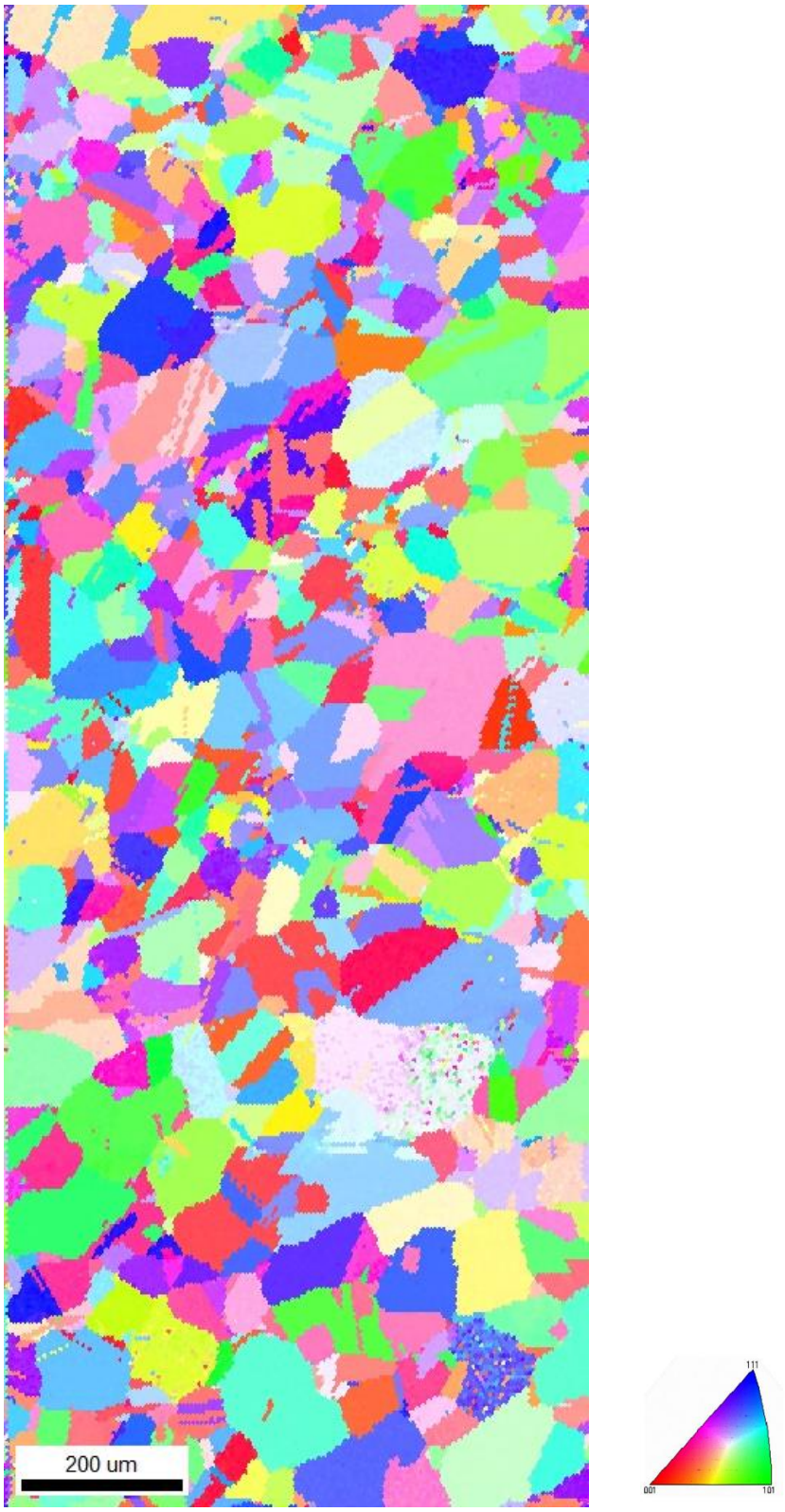

Figure A.24: Inverse pole figure (IPF) taken from BSCC1 Fe21Cr32Ni 0 dpa tensile bar sample OIM region 9 showing grain size and orientation.

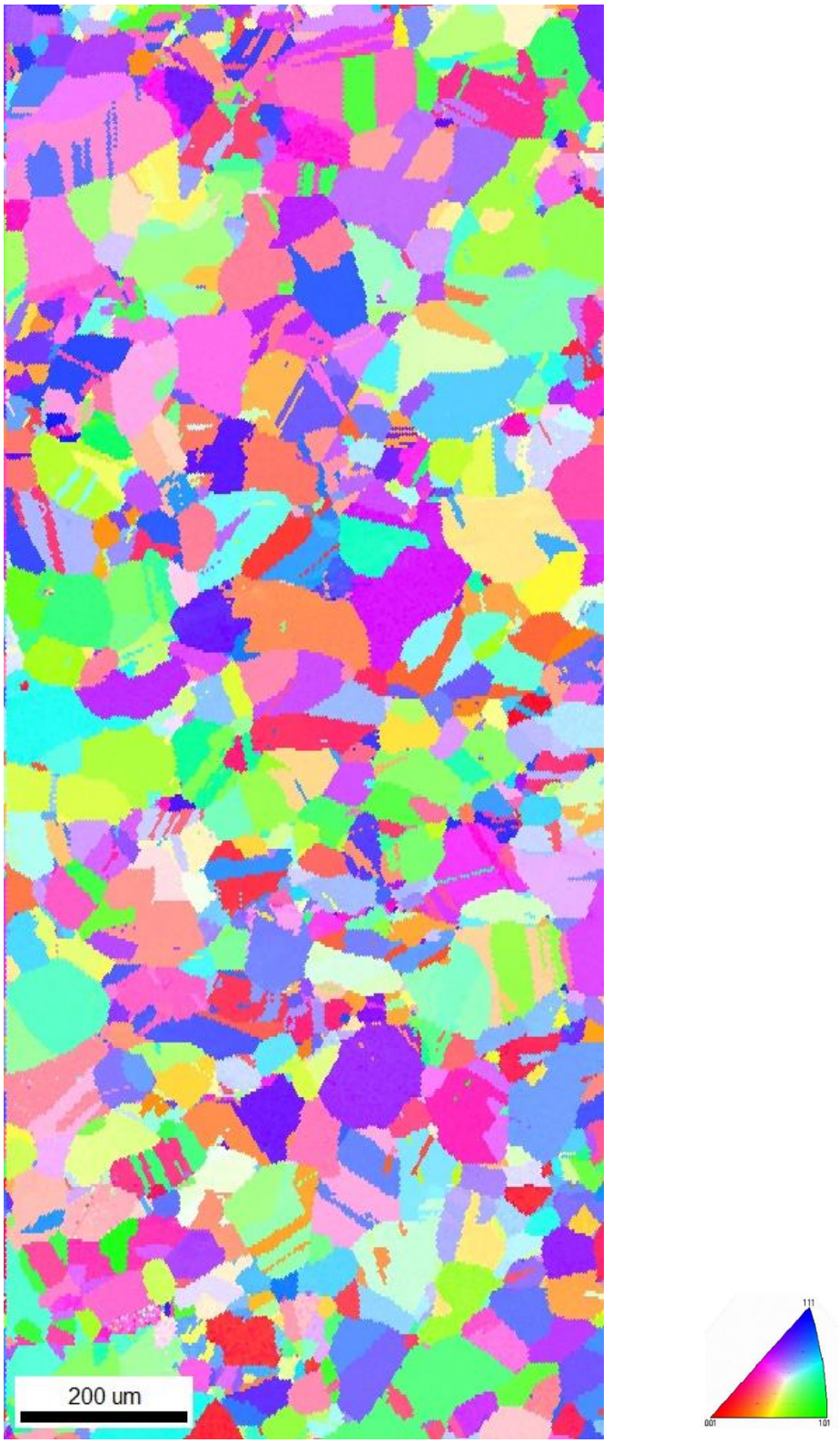

Figure A.25: Inverse pole figure (IPF) taken from BSCC1 Fe21Cr32Ni 0 dpa tensile bar sample OIM region 10 showing grain size and orientation.

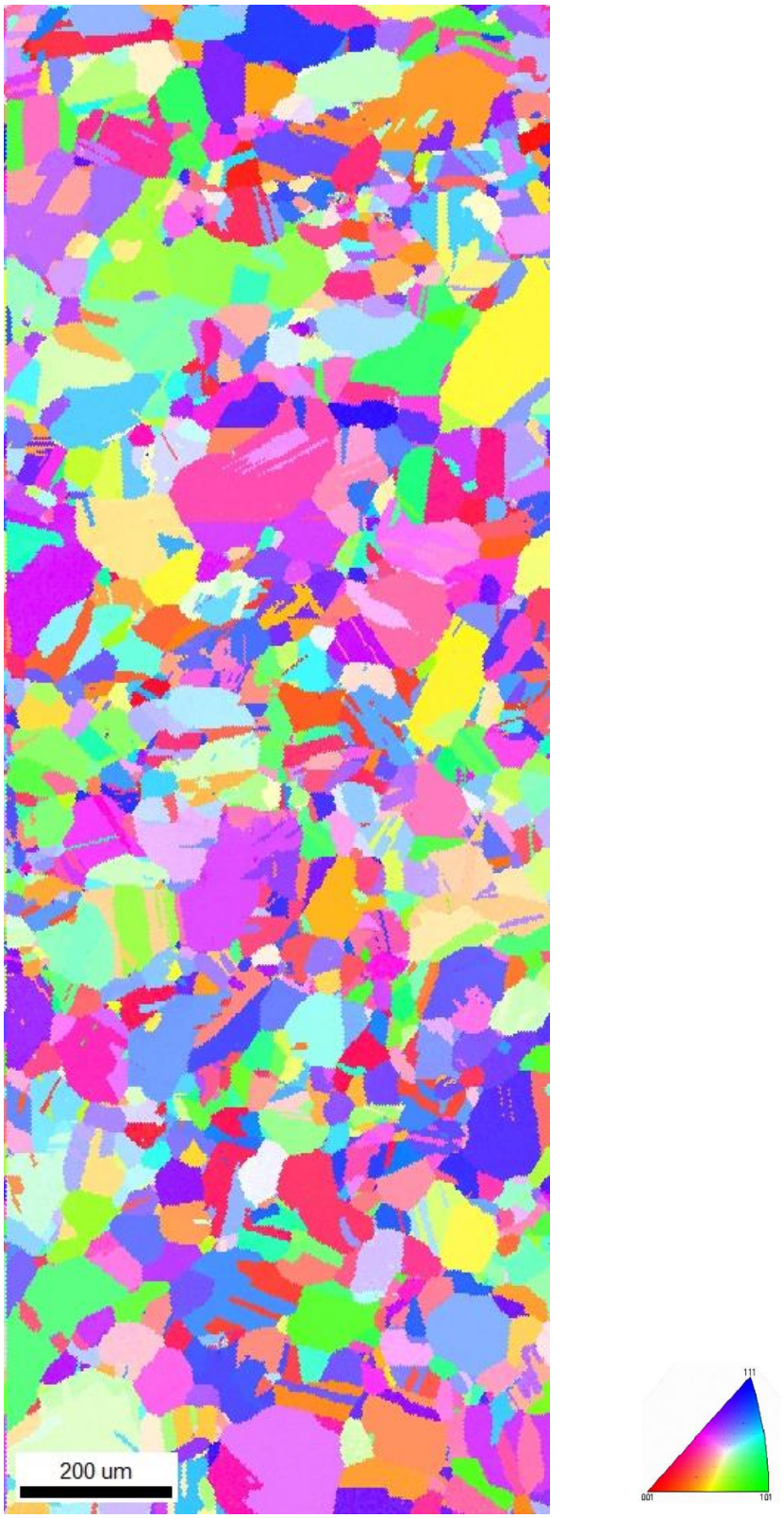

Figure A.26: Inverse pole figure (IPF) taken from BSCC1 Fe21Cr32Ni 0 dpa tensile bar sample OIM region 1 showing grain size and orientation.

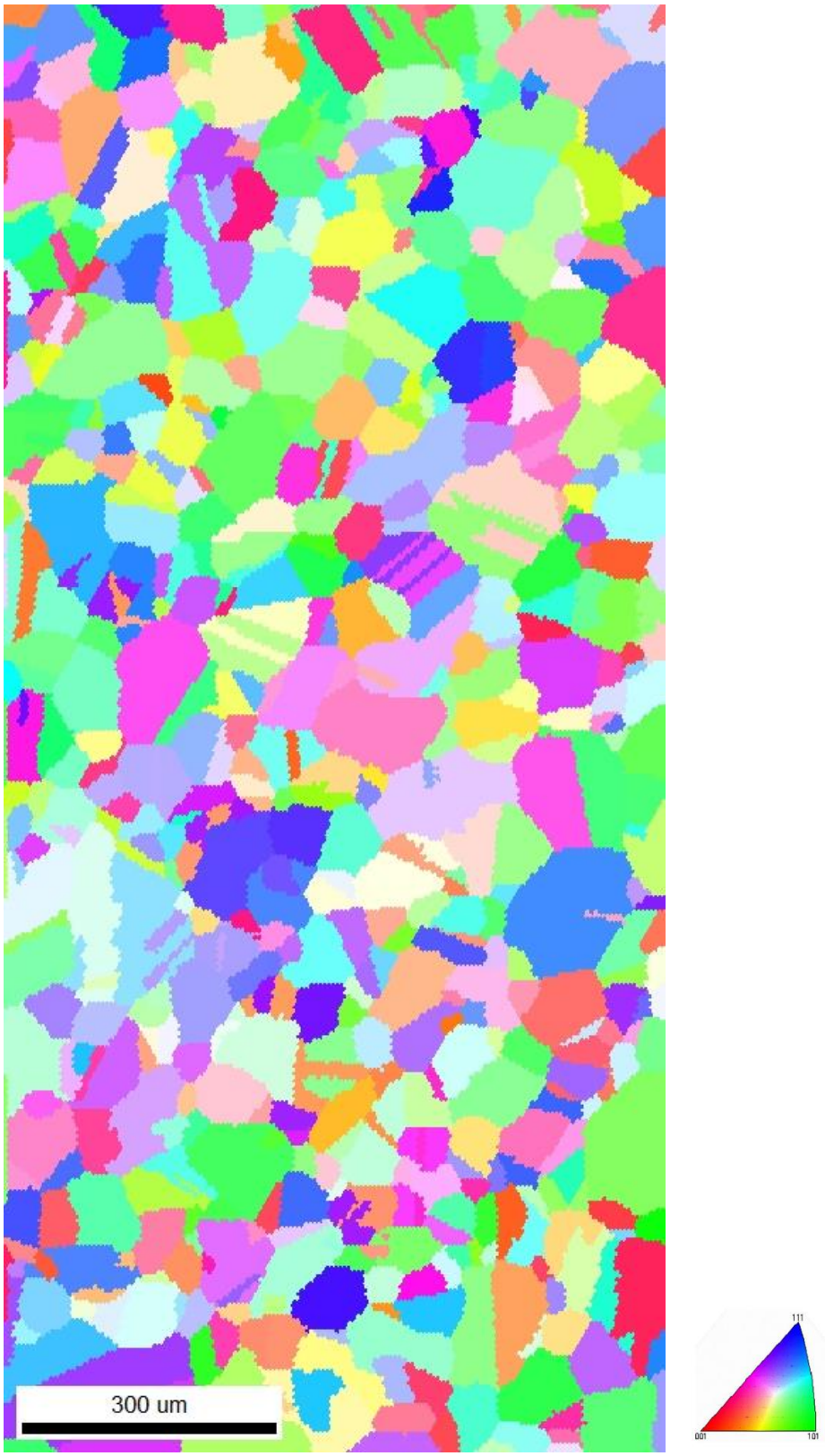

Figure A.27: Inverse pole figure (IPF) taken from BSCC2 Fe21Cr32Ni 5 dpa tensile bar sample OIM region 3 showing grain size and orientation.

Figure A.28: Inverse pole figure (IPF) taken from BSCC2 Fe21Cr32Ni 5 dpa tensile bar sample OIM region 5 showing grain size and orientation.

Figure A.29: Inverse pole figure (IPF) taken from BSCC2 Fe21Cr32Ni 5 dpa tensile bar sample OIM region 7 showing grain size and orientation.

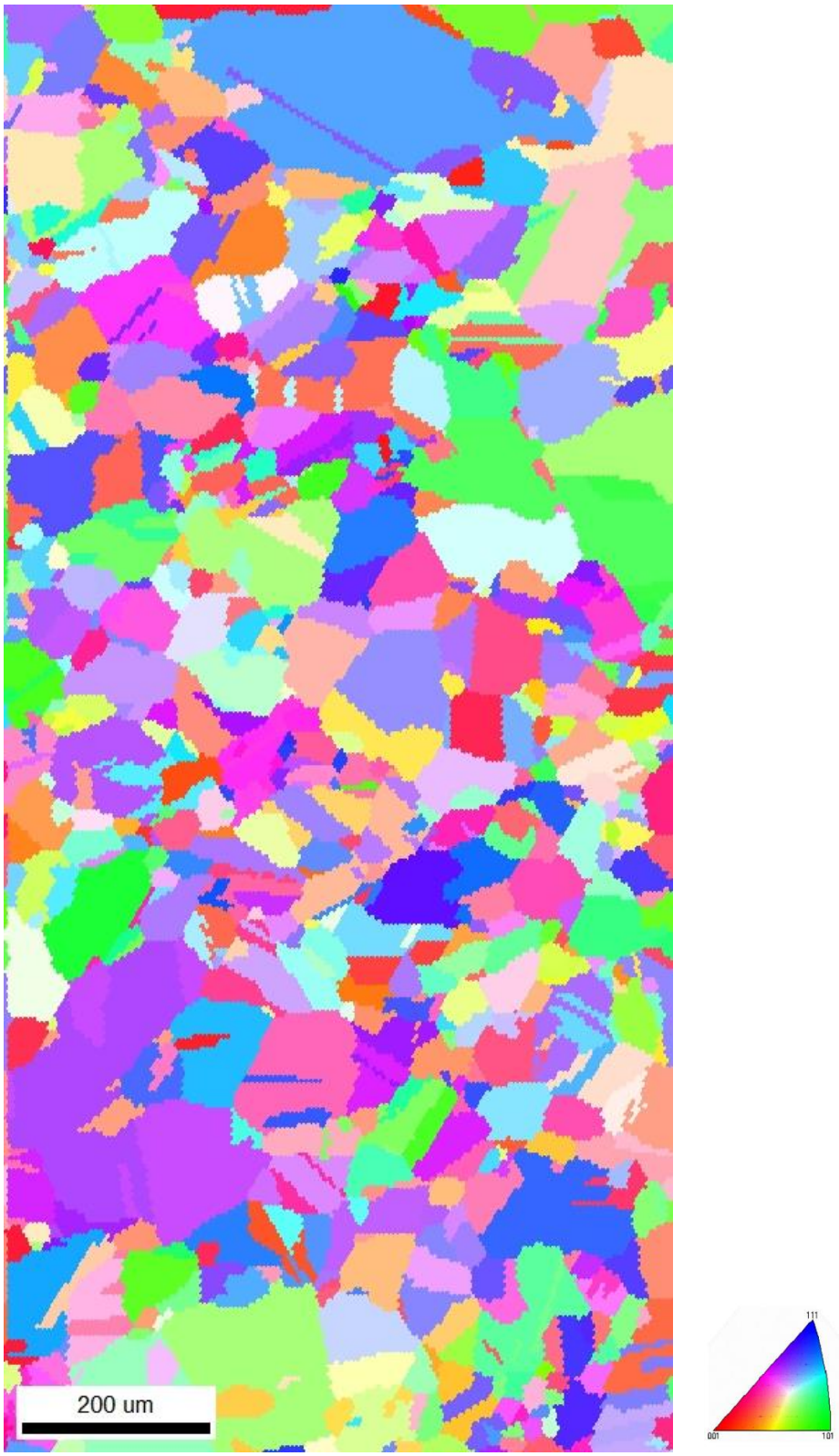

Figure A.30: Inverse pole figure (IPF) taken from BSCC2 Fe21Cr32Ni 5 dpa tensile bar sample OIM region 9 showing grain size and orientation.

APPENDIX B

Grain Maps Before and After Polishing for GB Plane Measurement

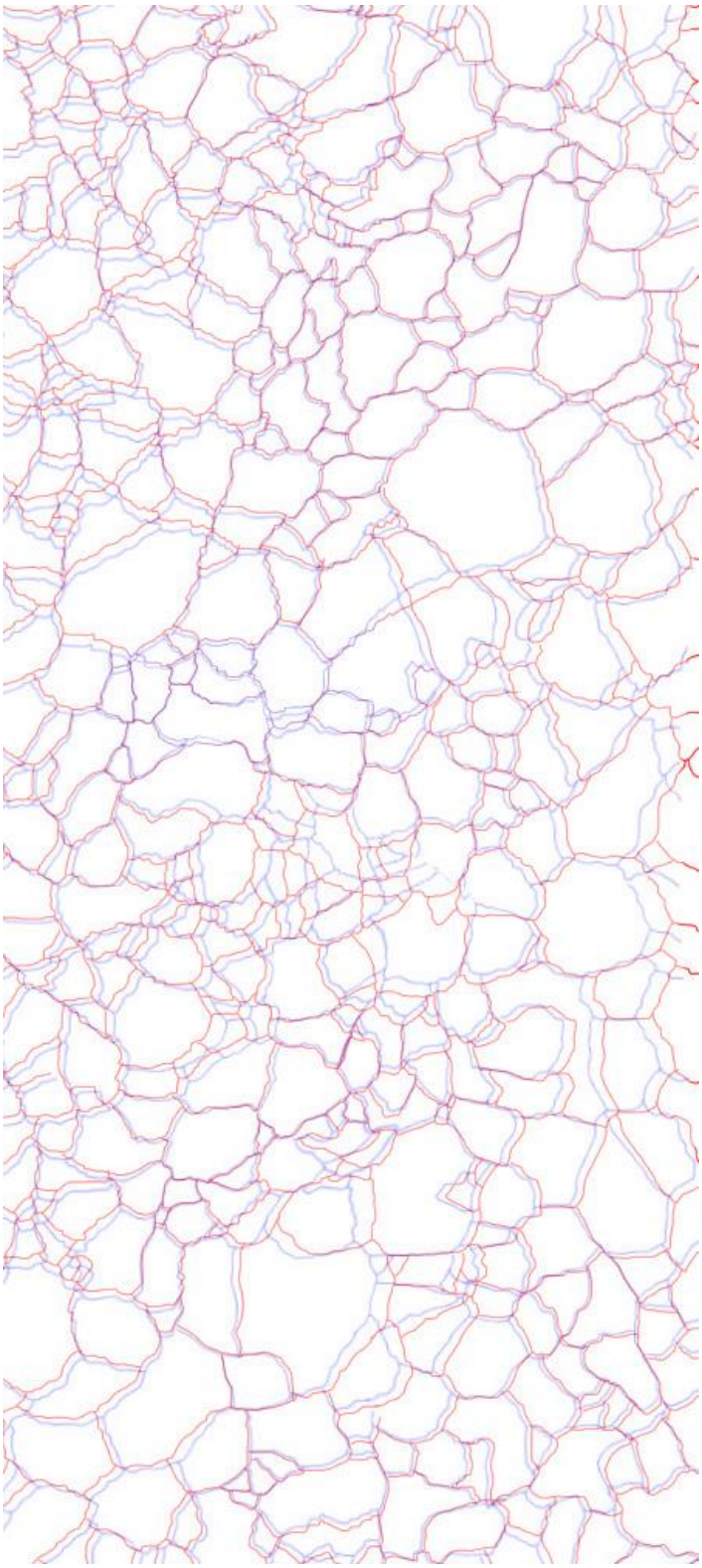

Figure B.1: Overlay of grain boundary maps from ASCC2 Fe13Cr15Ni 5 dpa sample OIM 1 with pre-polish boundaries shown in red and post polish boundaries shown in blue.

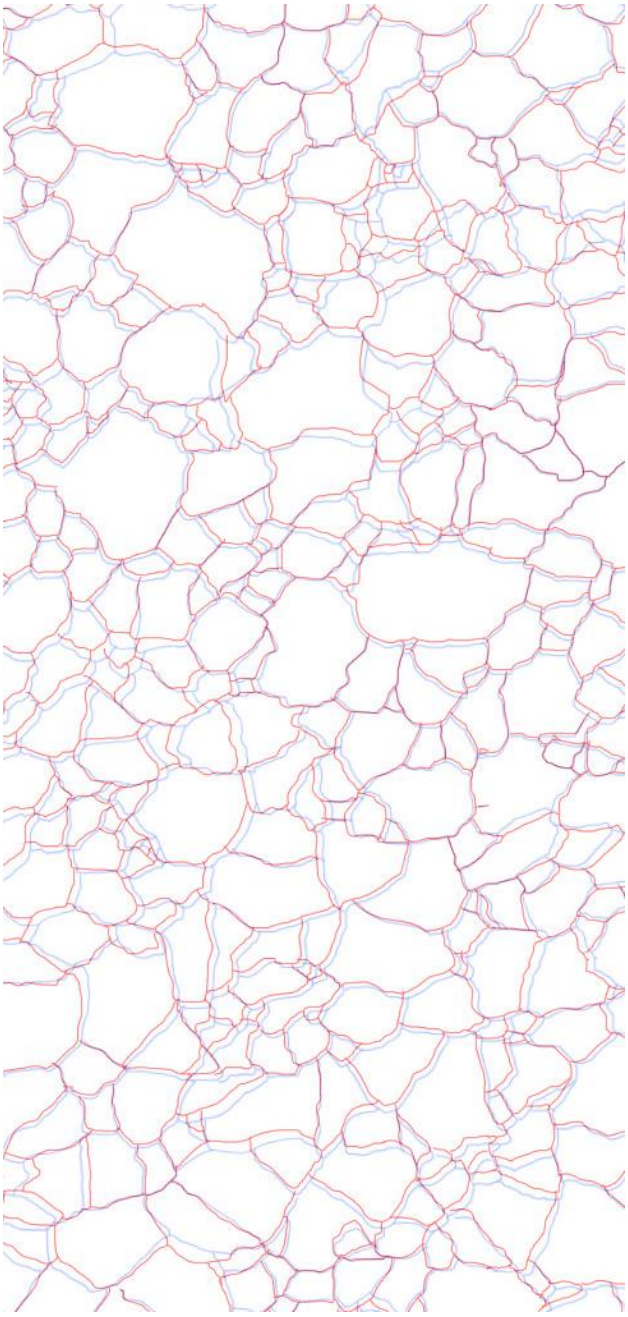

Figure B.2: Overlay of grain boundary maps from ASCC2 Fe13Cr15Ni 5 dpa sample OIM 3 with pre-polish boundaries shown in red and post polish boundaries shown in blue.

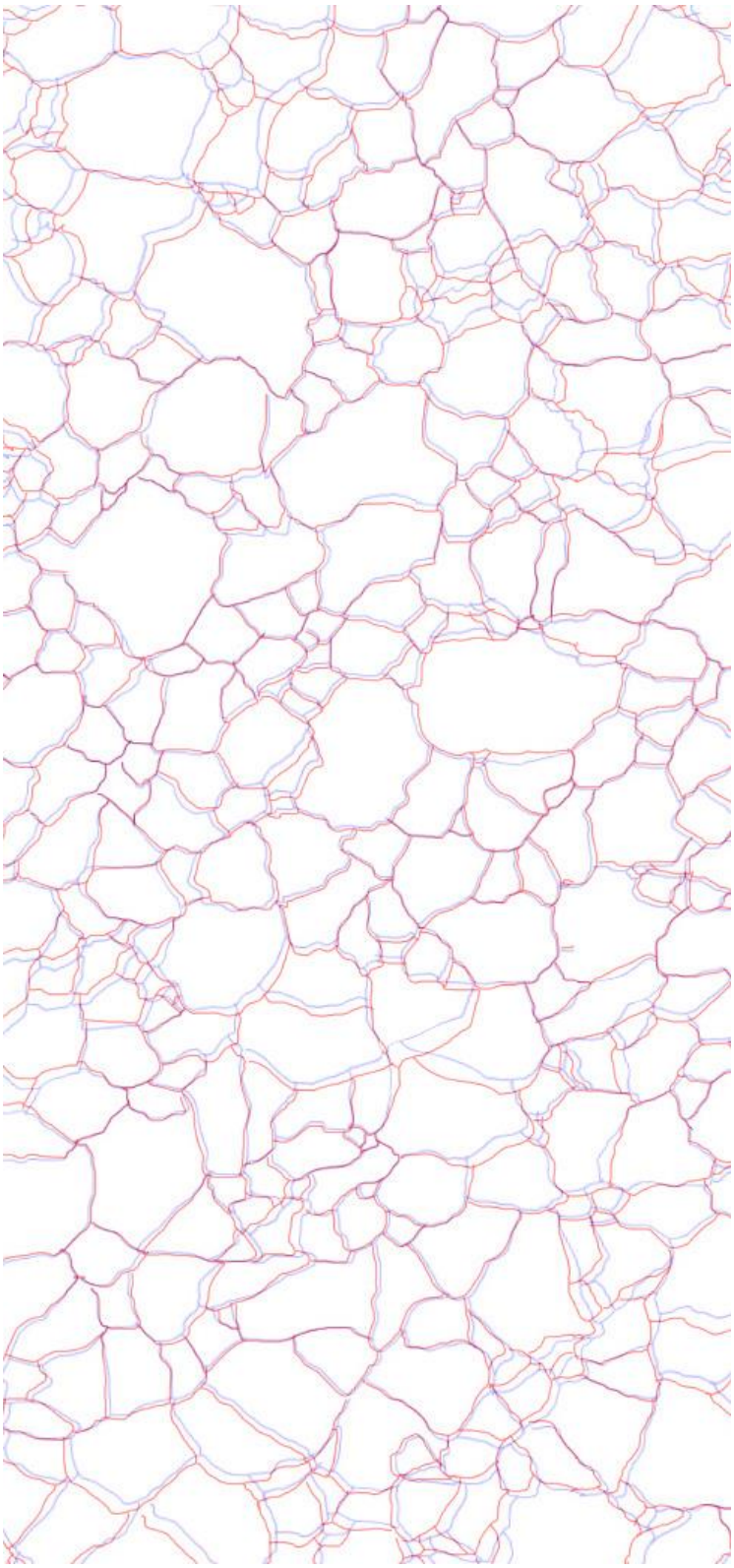

Figure B.3: Overlay of grain boundary maps from ASCC2 Fe13Cr15Ni 5 dpa sample OIM 5 with pre-polish boundaries shown in red and post polish boundaries shown in blue.

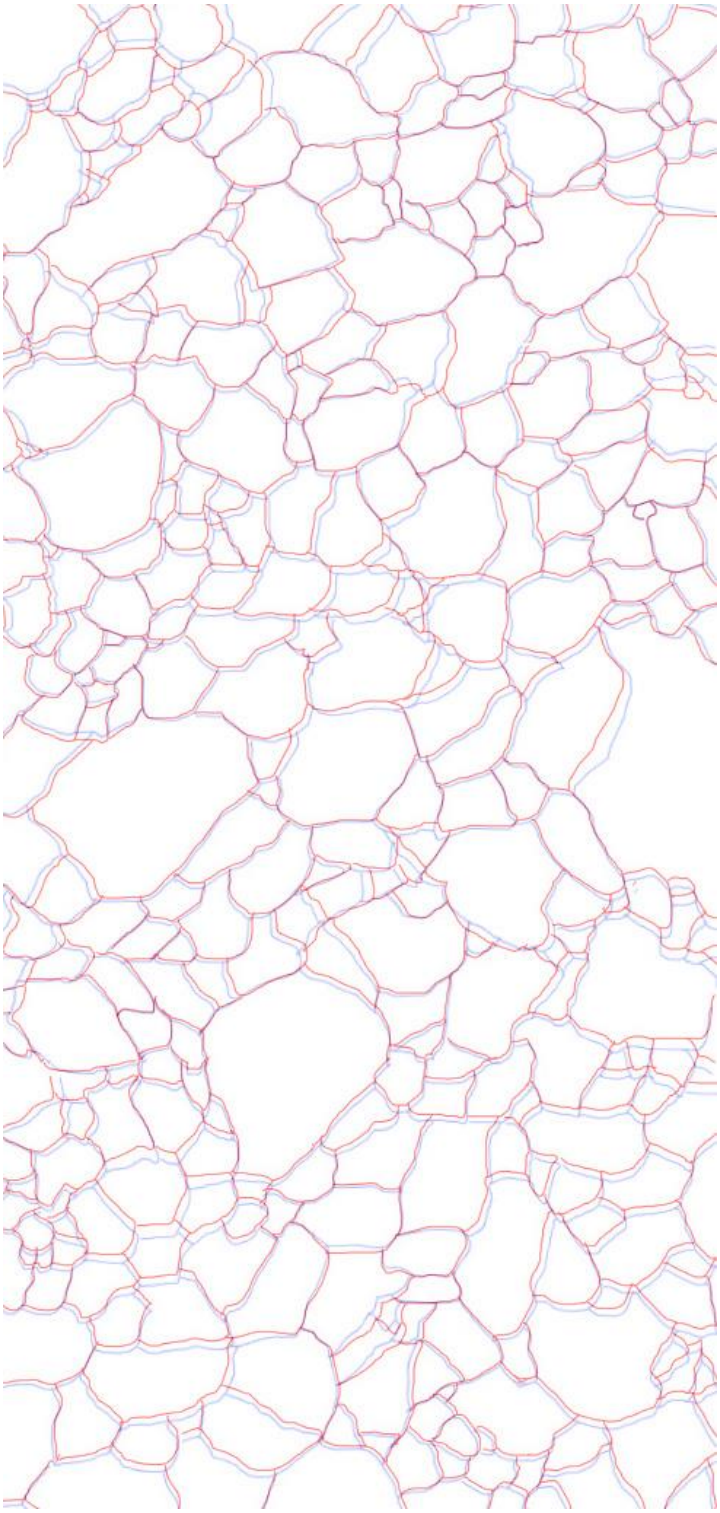

Figure B.4: : Overlay of grain boundary maps from ASCC2 Fe13Cr15Ni 5 dpa sample OIM 7 with pre-polish boundaries shown in red and post polish boundaries shown in blue.

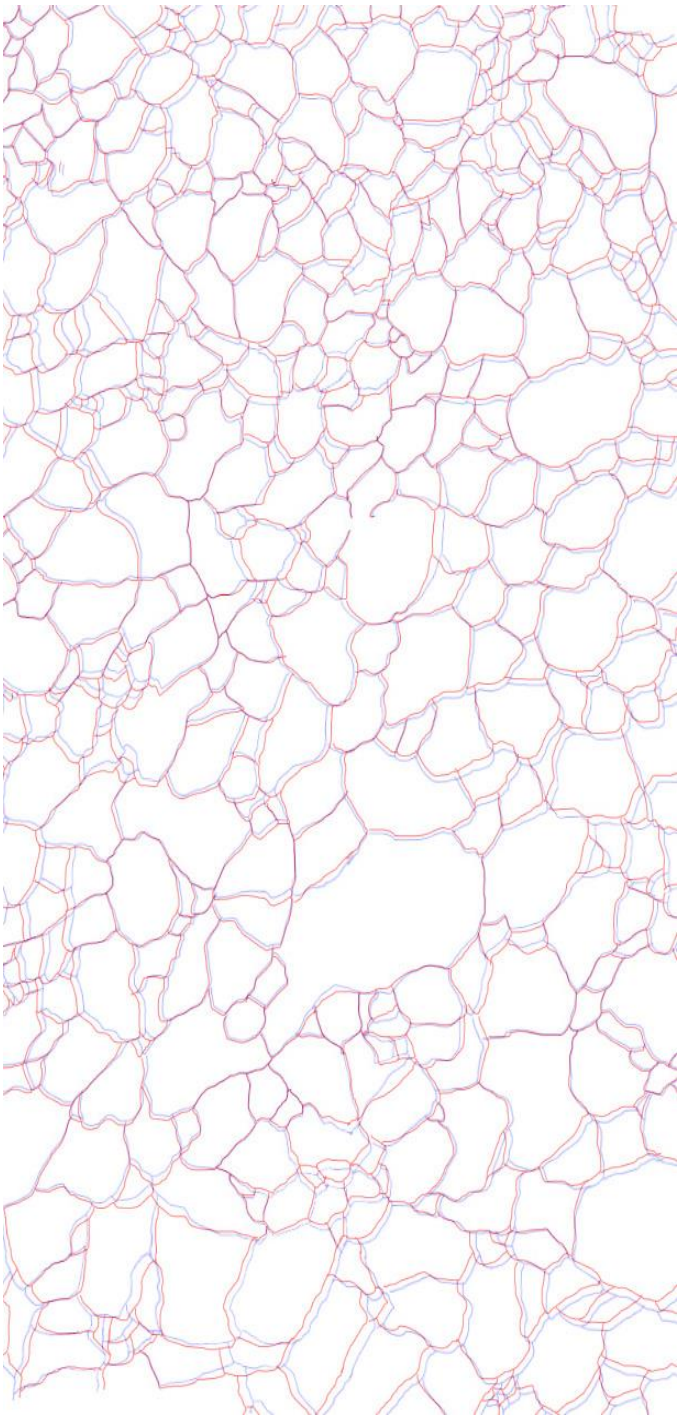

Figure B.5: Overlay of grain boundary maps from ASCC2 Fe13Cr15Ni 5 dpa sample OIM 9 with pre-polish boundaries shown in red and post polish boundaries shown in blue.

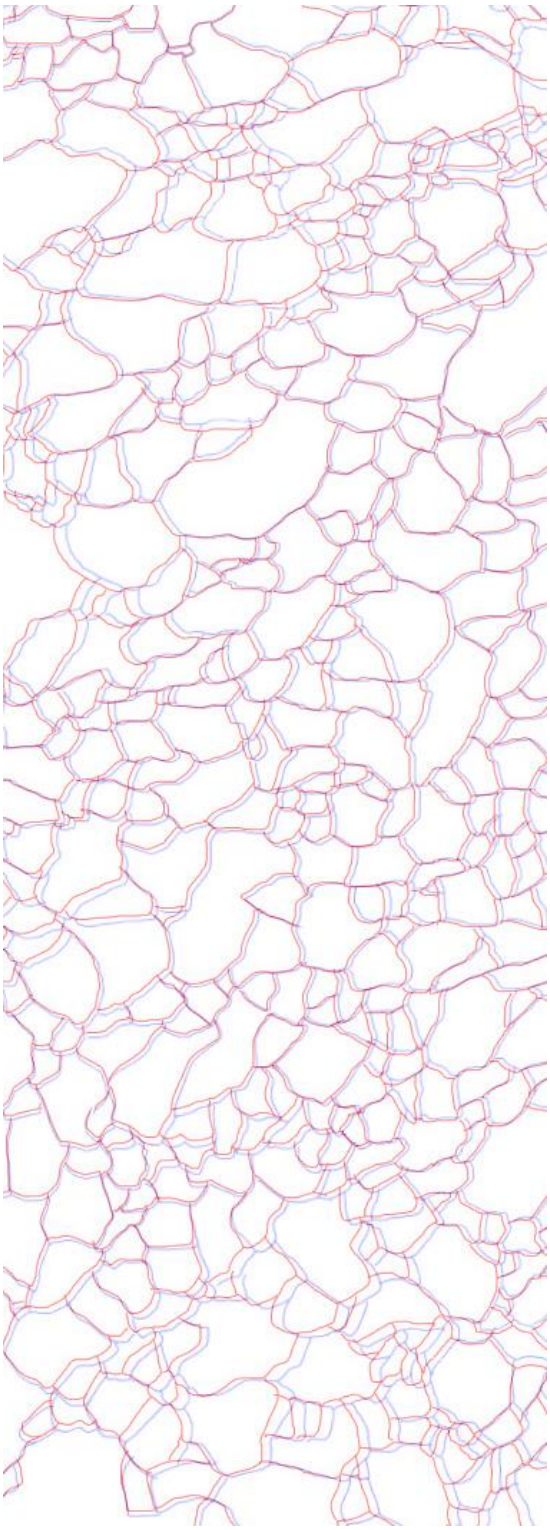

Figure B.6: Overlay of grain boundary maps from BSCC2 Fe21Cr32Ni 5 dpa sample OIM 1 with pre-polish boundaries shown in red and post polish boundaries shown in blue.

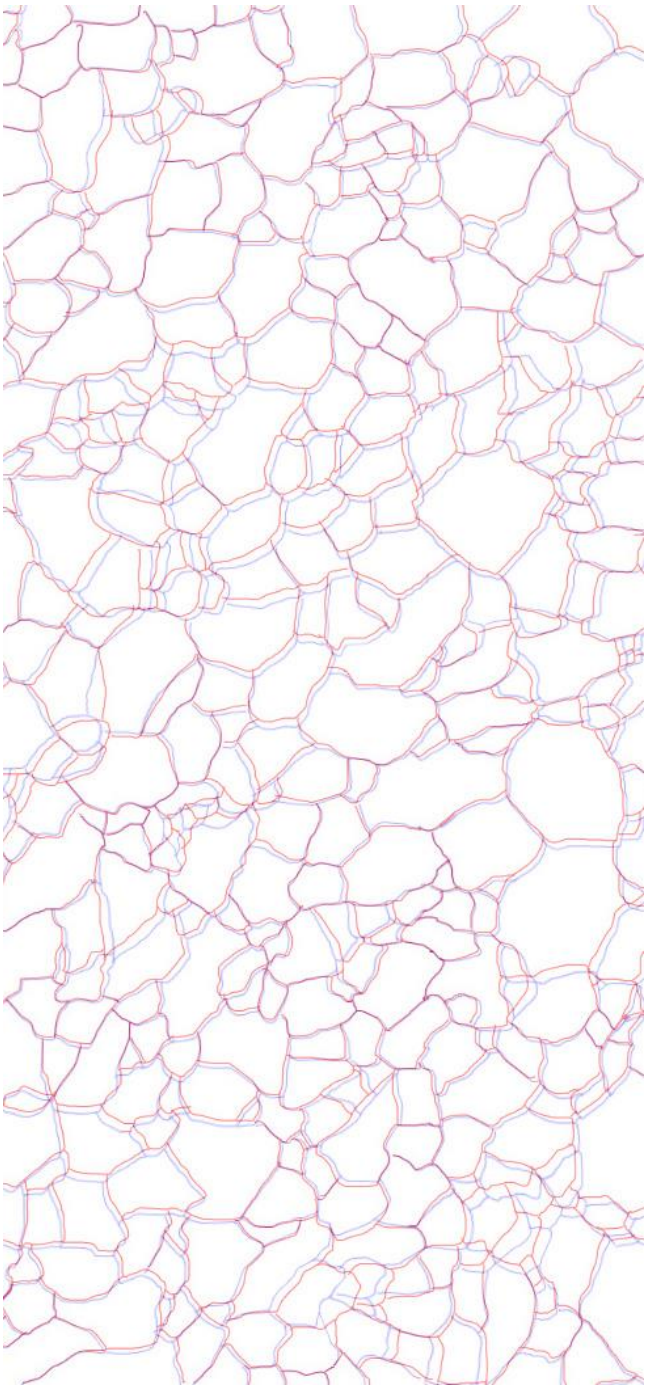

Figure B.7: Overlay of grain boundary maps from BSCC2 Fe21Cr32Ni 5 dpa sample OIM 3 with pre-polish boundaries shown in red and post polish boundaries shown in blue.

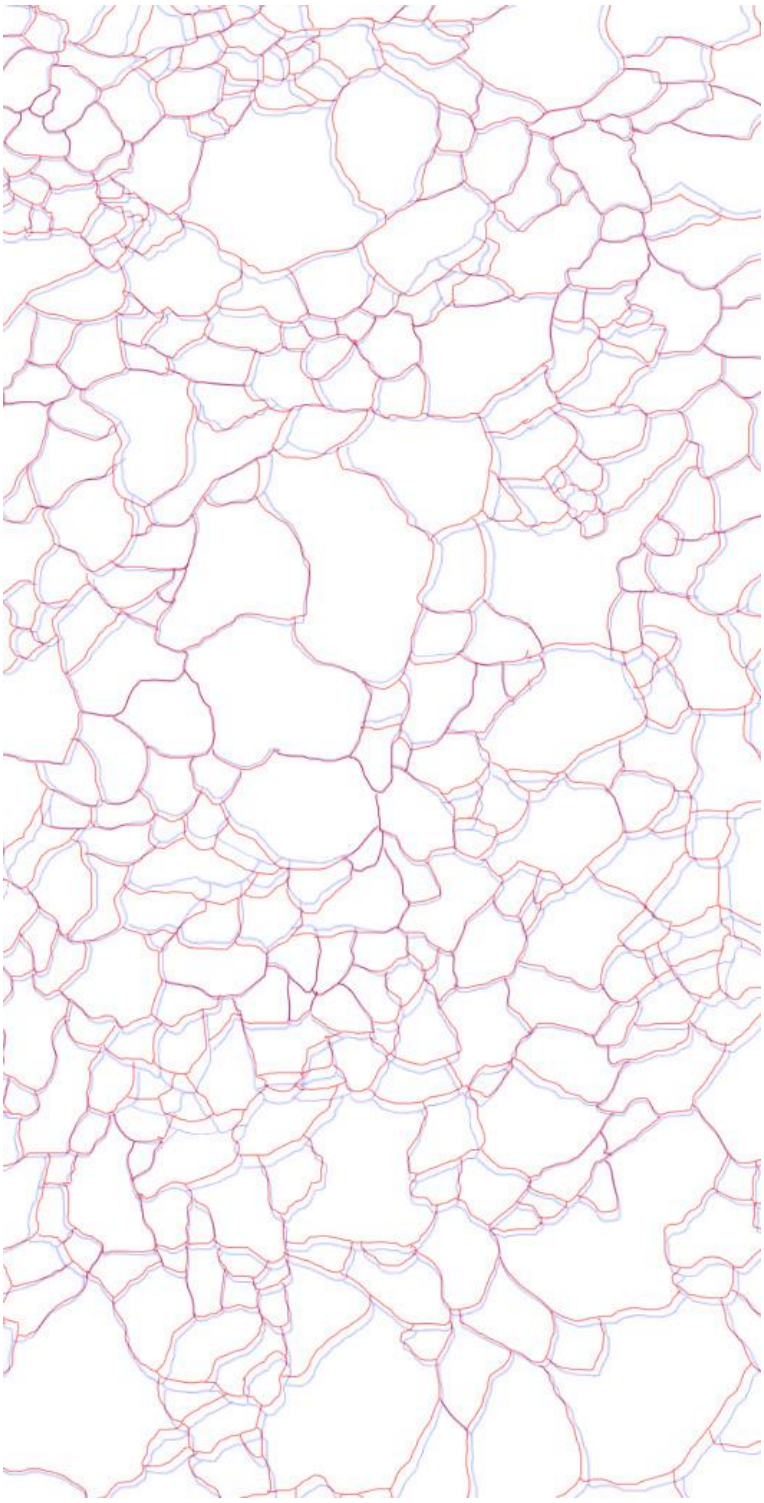

Figure B.8: Overlay of grain boundary maps from BSCC2 Fe21Cr32Ni 5 dpa sample OIM 5 with pre-polish boundaries shown in red and post polish boundaries shown in blue.

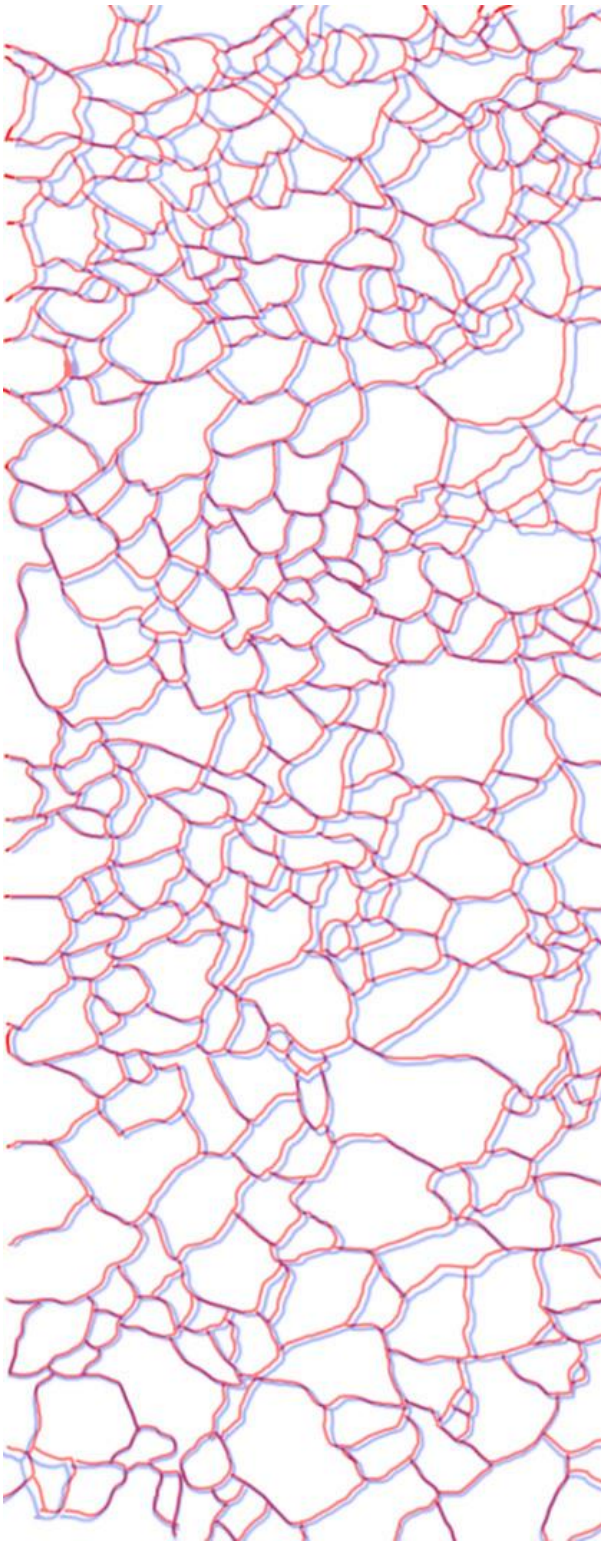

Figure B.9: Overlay of grain boundary maps from BSCC2 Fe21Cr32Ni 5 dpa sample OIM 7 with pre-polish boundaries shown in red and post polish boundaries shown in blue.

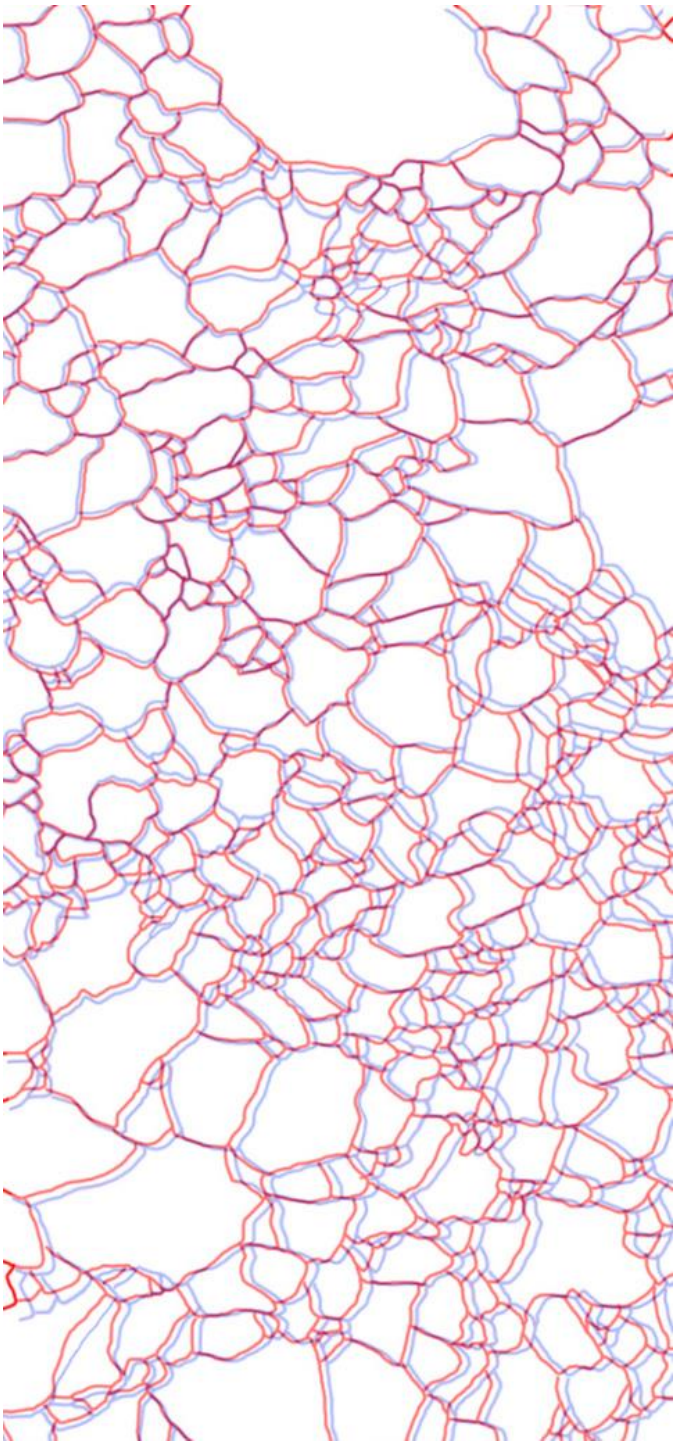

Figure B.10: Overlay of grain boundary maps from BSCC2 Fe21Cr32Ni 5 dpa sample OIM 9 with pre-polish boundaries shown in red and post polish boundaries shown in blue.

APPENDIX C

LEXT Confocal Microscope Surface Images and Channel Height Profiles

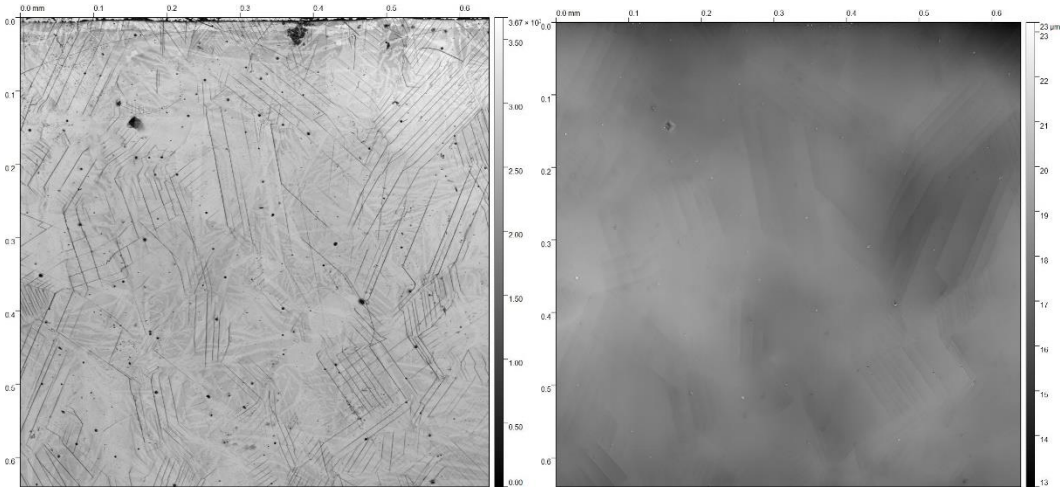

Figure C.1: LEXT confocal microscope large area topography map taken from OIM region 2 on ASCC2 Fe13Cr15Ni 5 dpa tensile bar sample with left hand image showing the sample surface and the right hand image showing the height distribution map

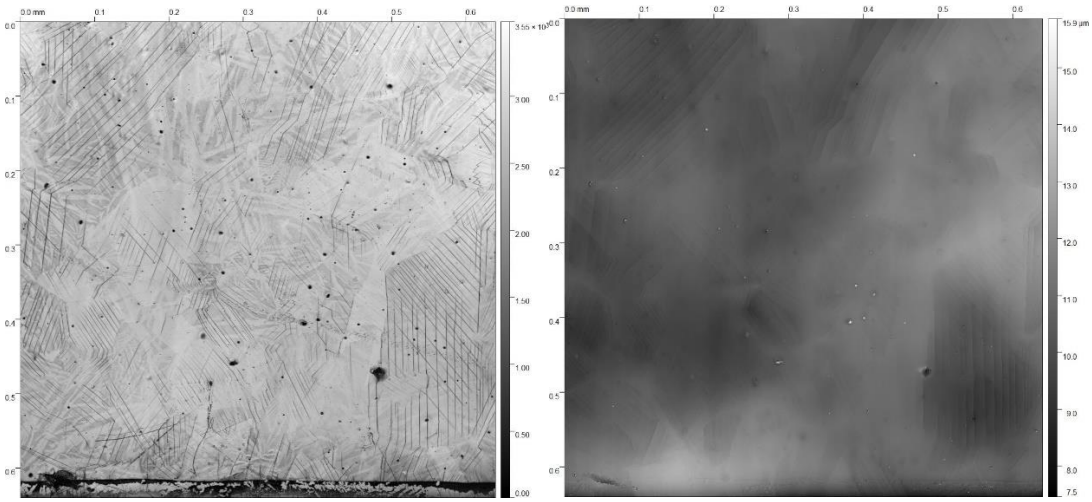

Figure C.2: LEXT confocal microscope large area topography map taken from OIM region 2 on ASCC2 Fe13Cr15Ni 5 dpa tensile bar sample with left hand image showing the sample surface and the right hand image showing the height distribution map

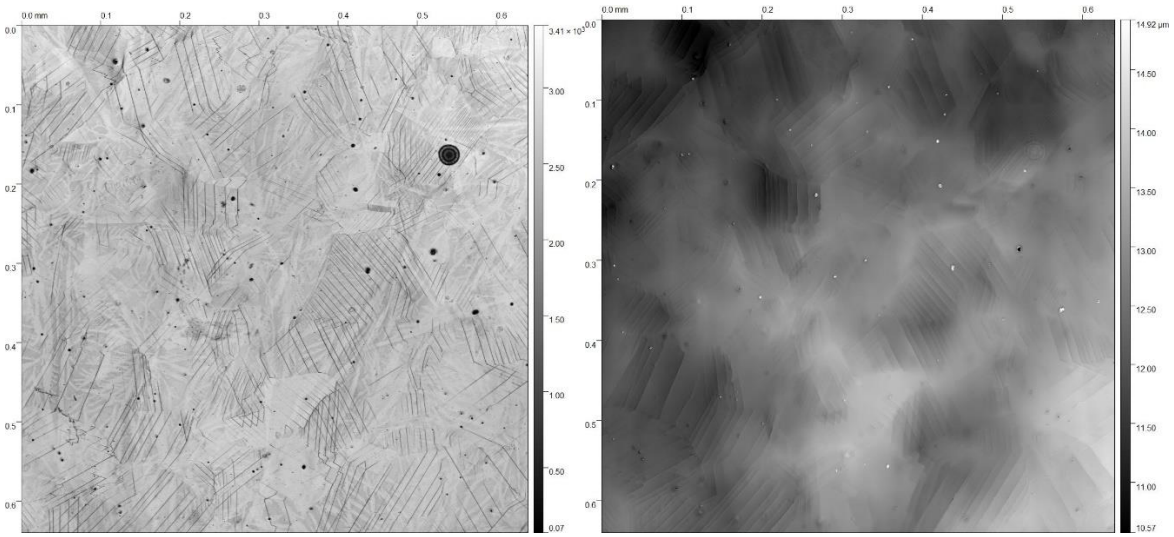

Figure C.3: LEXT confocal microscope large area topography map taken from OIM region 3 on ASCC2 Fe13Cr15Ni 5 dpa tensile bar sample with left hand image showing the sample surface and the right hand image showing the height distribution map

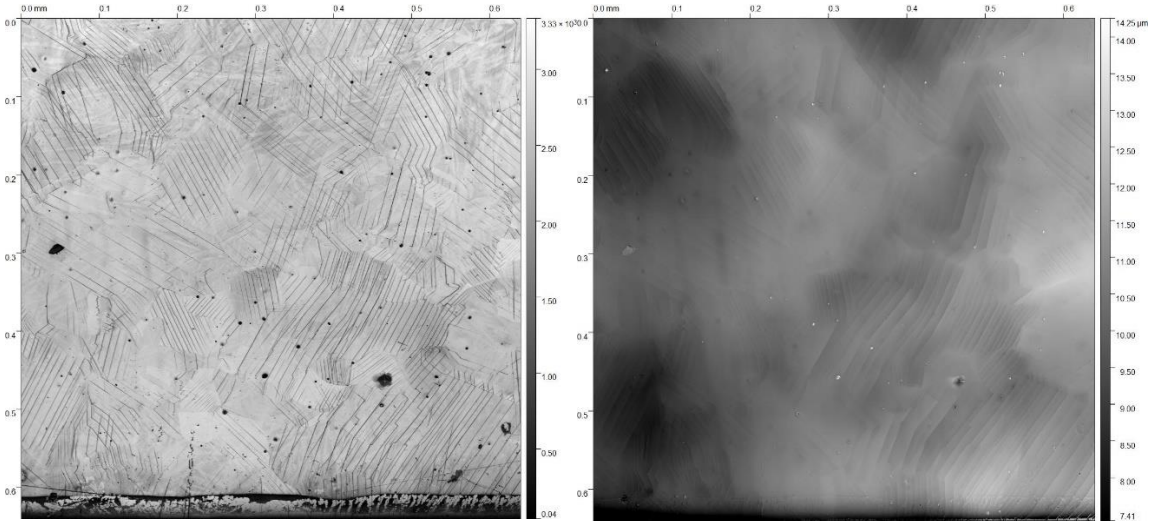

Figure C.4: LEXT confocal microscope large area topography map taken from OIM region 4 on ASCC2 Fe13Cr15Ni 5 dpa tensile bar sample with left hand image showing the sample surface and the right hand image showing the height distribution map

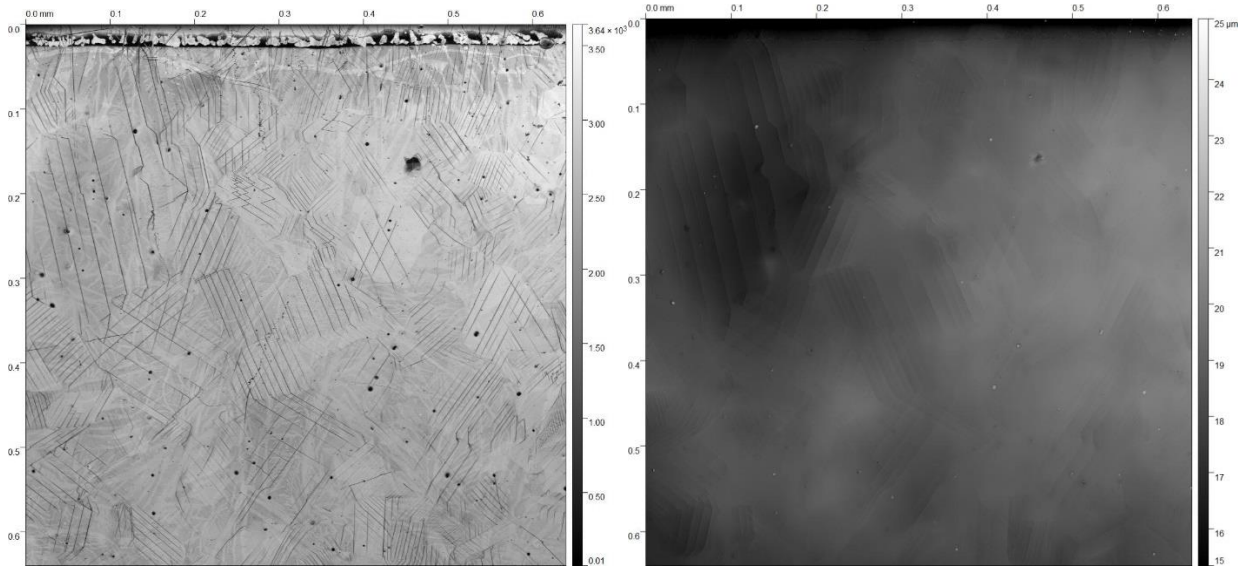

Figure C.5: LEXT confocal microscope large area topography map taken from OIM region 4 on ASCC2 Fe13Cr15Ni 5 dpa tensile bar sample with left hand image showing the sample surface and the right hand image showing the height distribution map

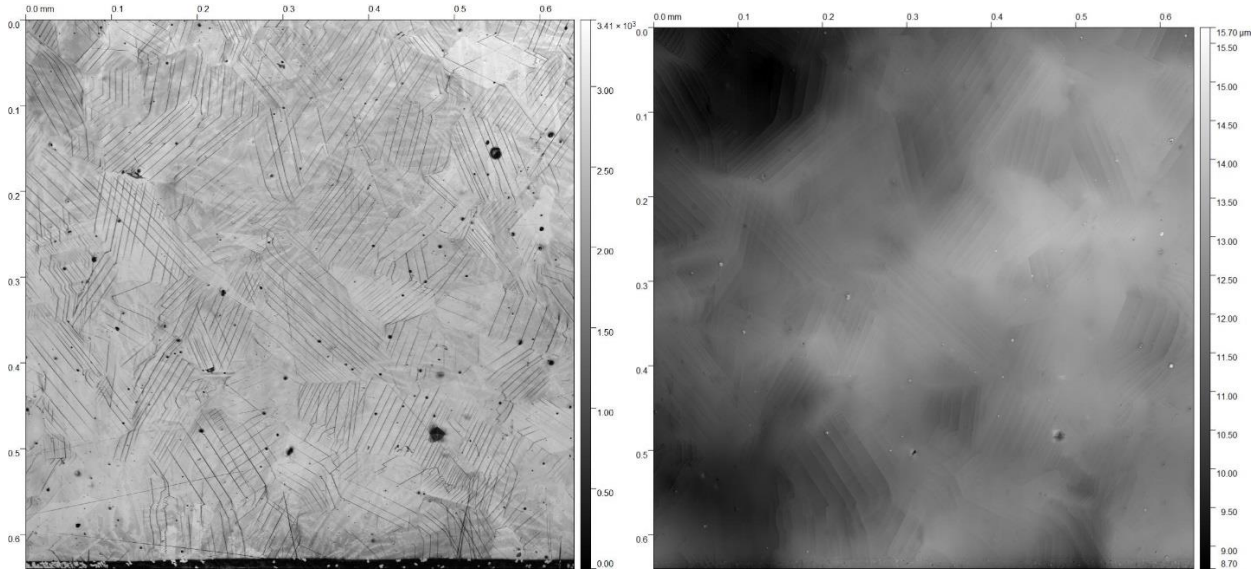

Figure C.6: LEXT confocal microscope large area topography map taken from OIM region 5 on ASCC2 Fe13Cr15Ni 5 dpa tensile bar sample with left hand image showing the sample surface and the right hand image showing the height distribution map

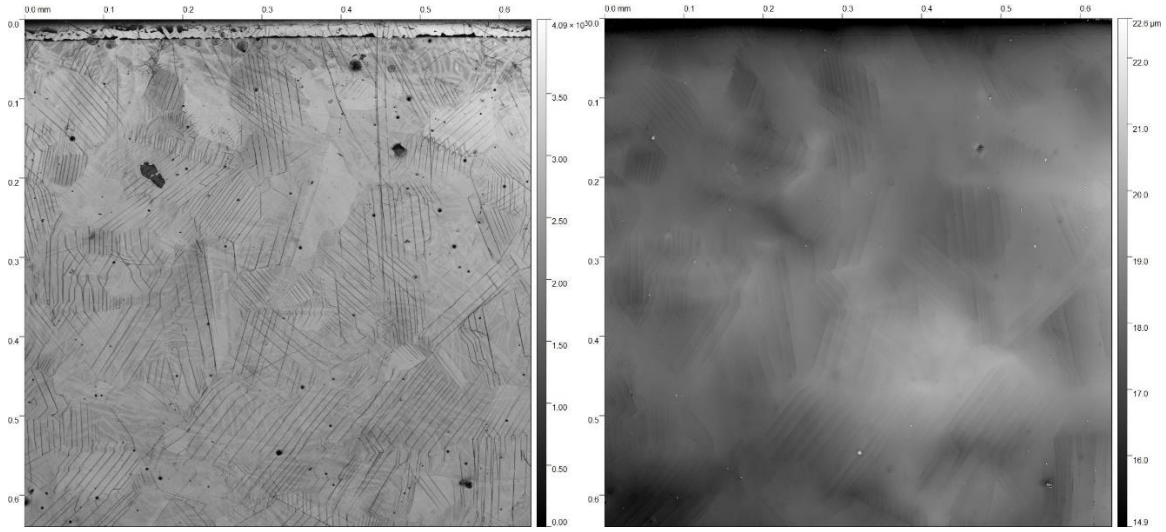

Figure C.7: LEXT confocal microscope large area topography map taken from OIM region 6 on ASCC2 Fe13Cr15Ni 5 dpa tensile bar sample with left hand image showing the sample surface and the right hand image showing the height distribution map

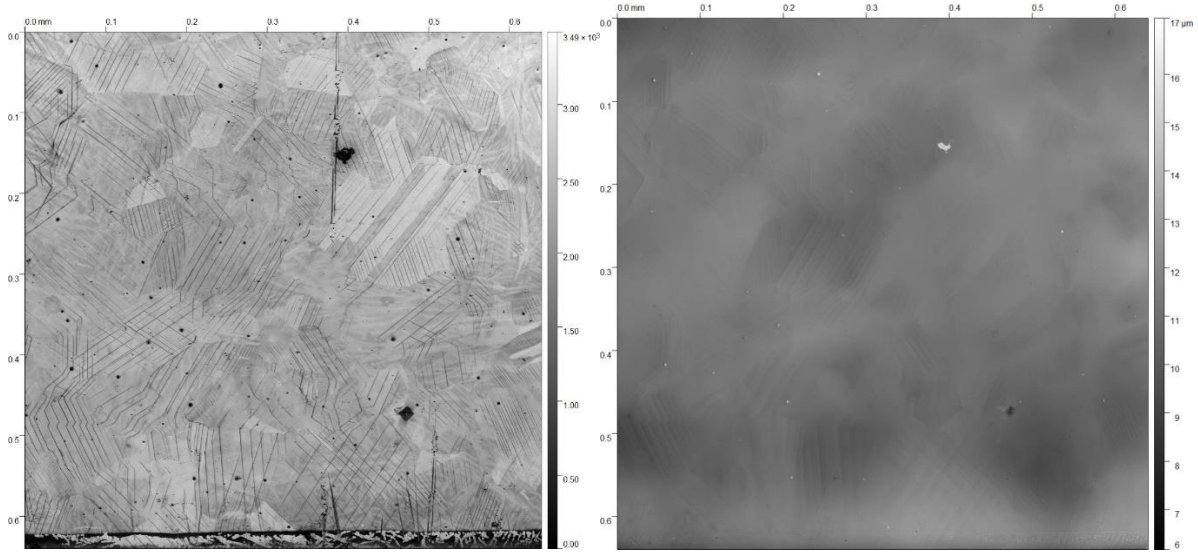

Figure C.854: LEXT confocal microscope large area topography map taken from OIM region 7 on ASCC2 Fe13Cr15Ni 5 dpa tensile bar sample with left hand image showing the sample surface and the right hand image showing the height distribution map

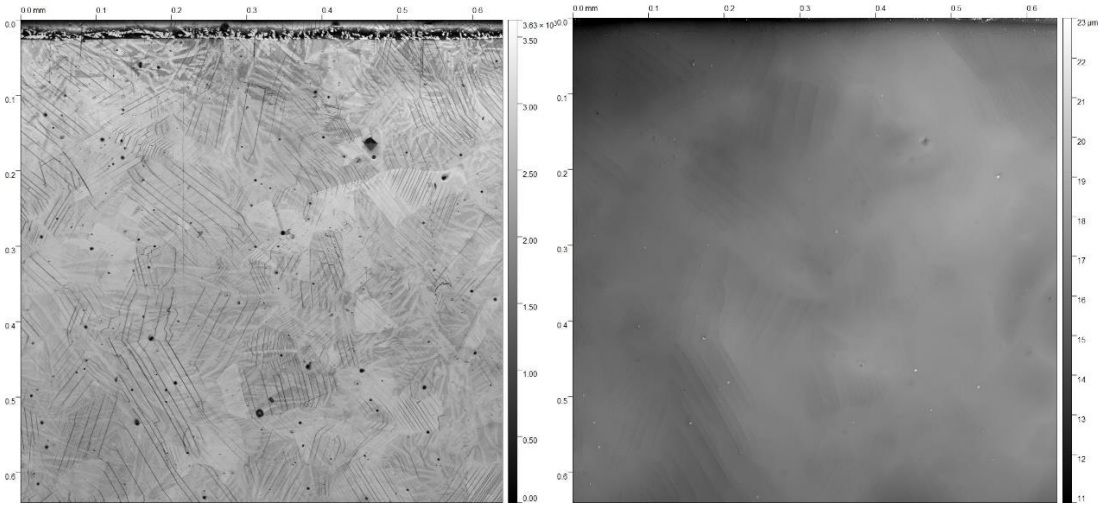

Figure C.9: LEXT confocal microscope large area topography map taken from OIM region 8 on ASCC2 Fe13Cr15Ni 5 dpa tensile bar sample with left hand image showing the sample surface and the right hand image showing the height distribution map

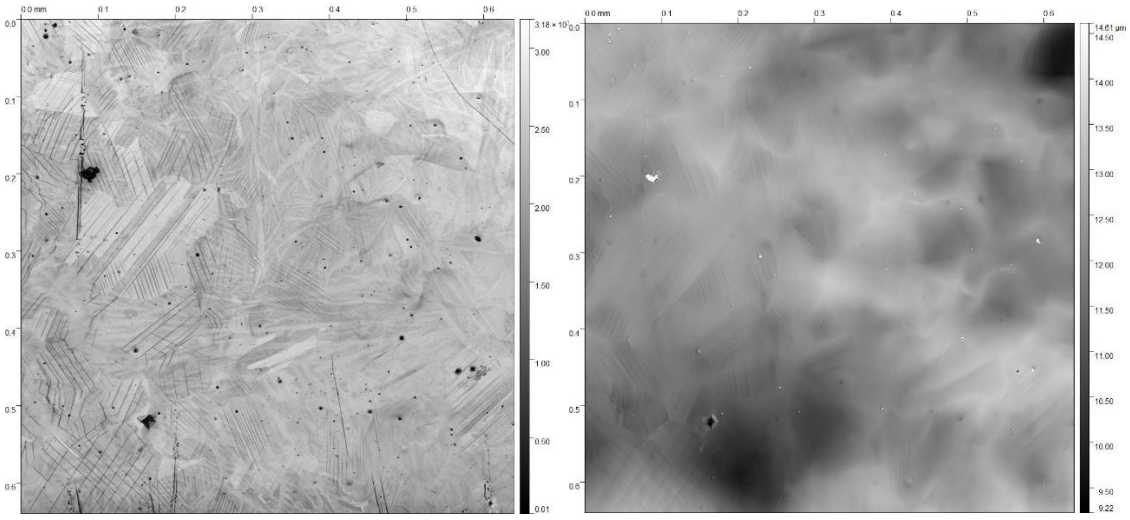

Figure C.10: LEXT confocal microscope large area topography map taken from OIM region 2 on BSCC2 Fe21Cr1532 5 dpa tensile bar sample with left hand image showing the sample surface and the right hand image showing the height distribution map

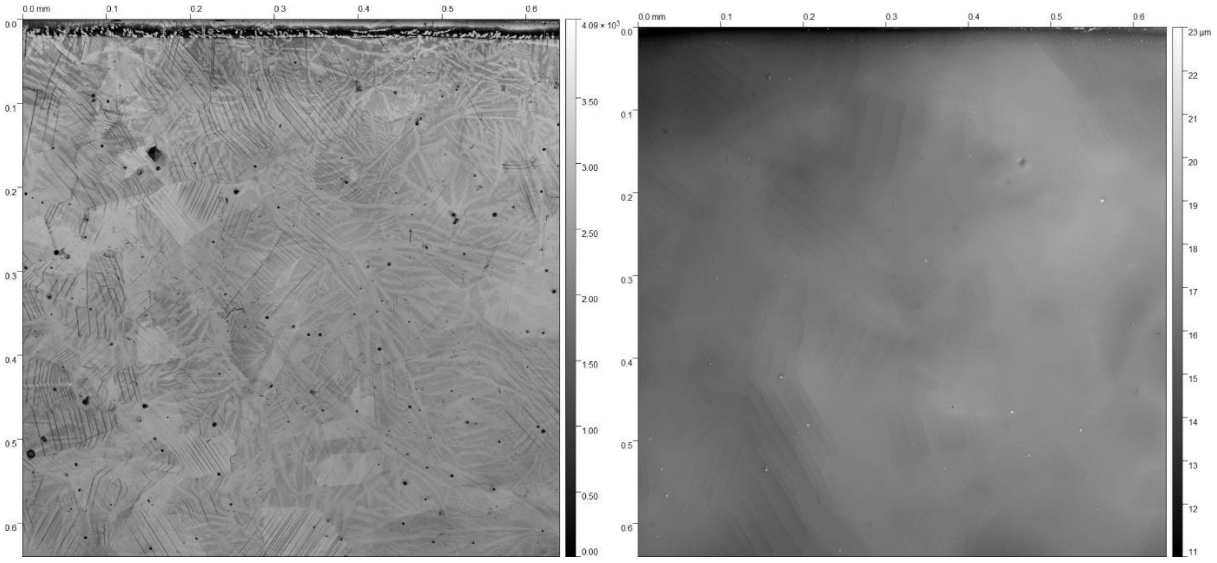

Figure C.11: LEXT confocal microscope large area topography map taken from OIM region 3 on BSCC2 Fe21Cr32Ni 5 dpa tensile bar sample with left hand image showing the sample surface and the right hand image showing the height distribution map

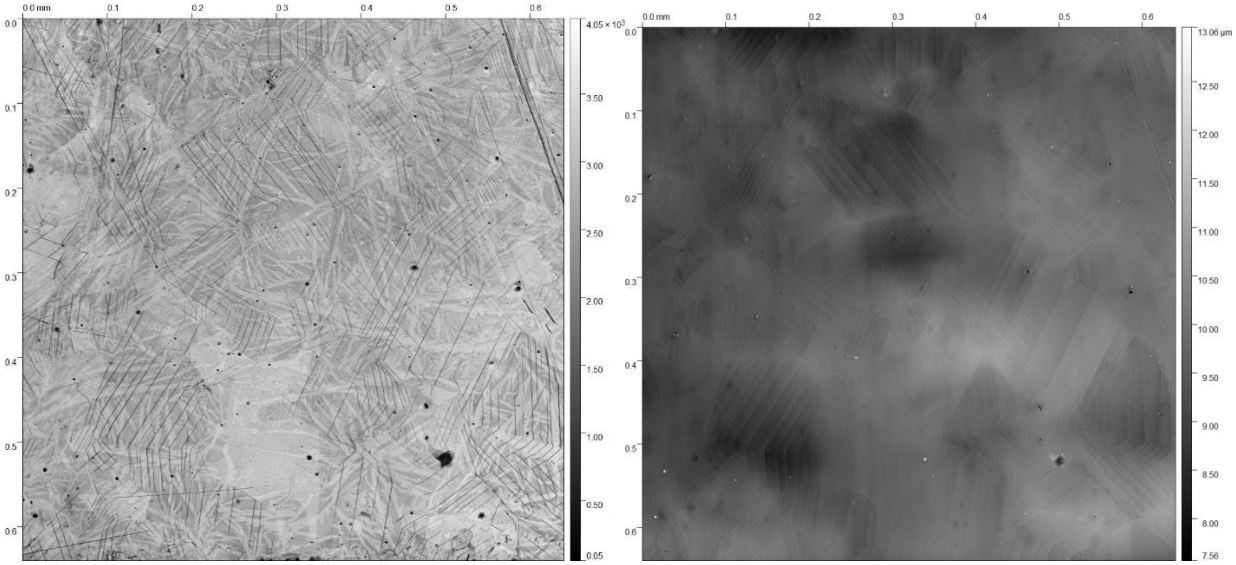

Figure C.12: LEXT confocal microscope large area topography map taken from OIM region 4 on BSCC2 Fe21Cr32Ni 5 dpa tensile bar sample with left hand image showing the sample surface and the right hand image showing the height distribution map

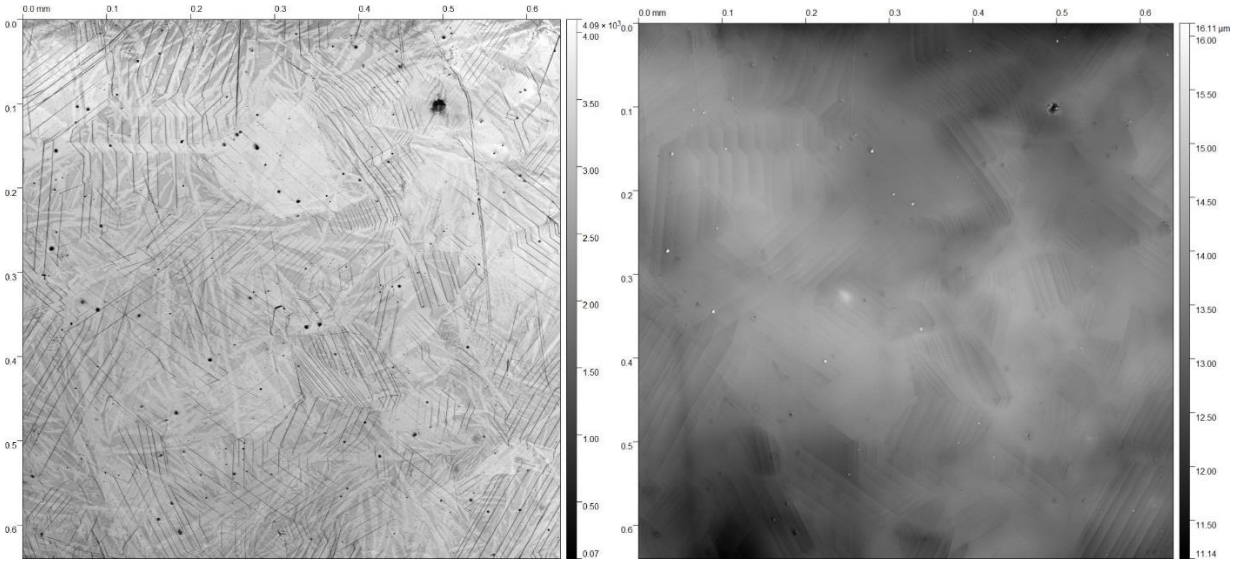

Figure C.13: LEXT confocal microscope large area topography map taken from OIM region 5 on BSCC2 Fe21Cr32Ni 5 dpa tensile bar sample with left hand image showing the sample surface and the right hand image showing the height distribution map

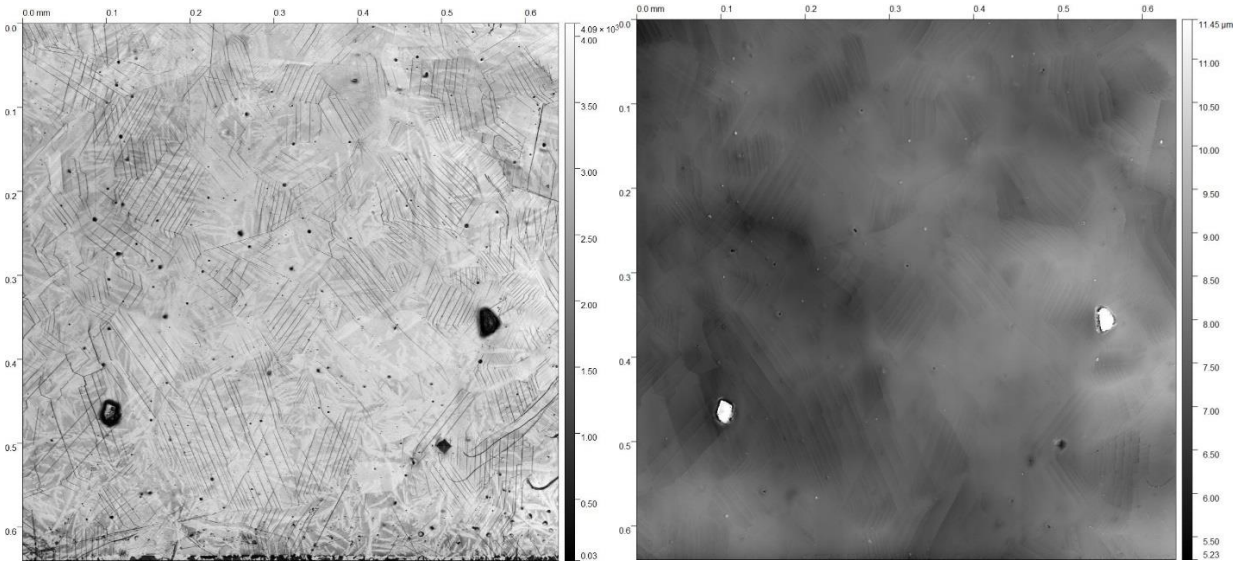

Figure C.14: LEXT confocal microscope large area topography map taken from OIM region 6 on BSCC2 Fe21Cr32Ni 5 dpa tensile bar sample with left hand image showing the sample surface and the right hand image showing the height distribution map

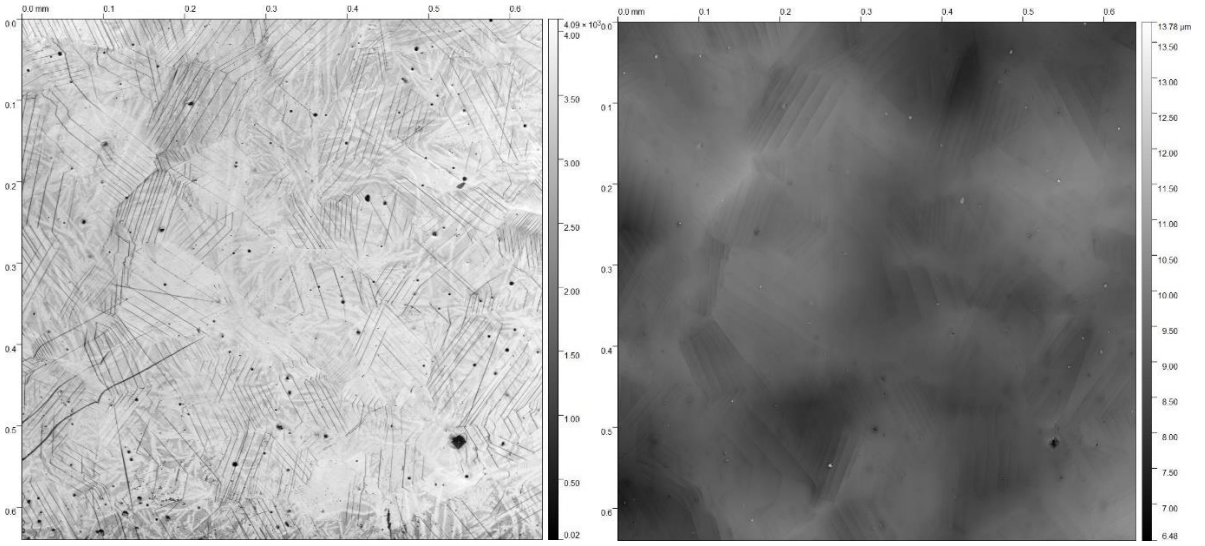

Figure C.15: LEXT confocal microscope large area topography map taken from OIM region 7 on BSCC2 Fe21Cr32Ni 5 dpa tensile bar sample with left hand image showing the sample surface and the right hand image showing the height distribution map

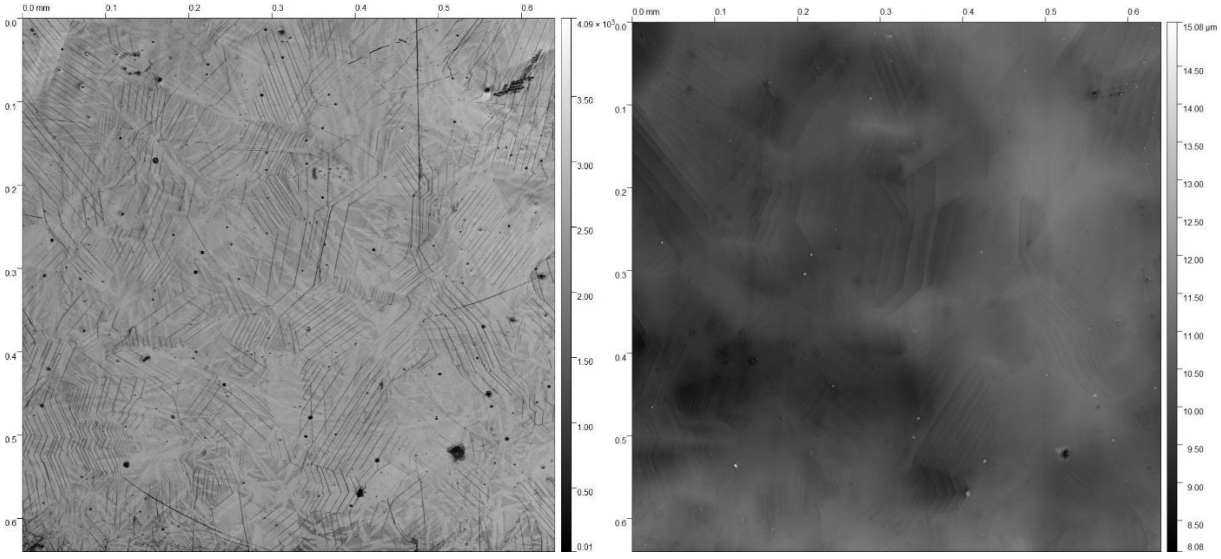

Figure C.16: LEXT confocal microscope large area topography map taken from OIM region 8 on BSCC2 Fe21Cr32Ni 5 dpa tensile bar sample with left hand image showing the sample surface and the right hand image showing the height distribution map

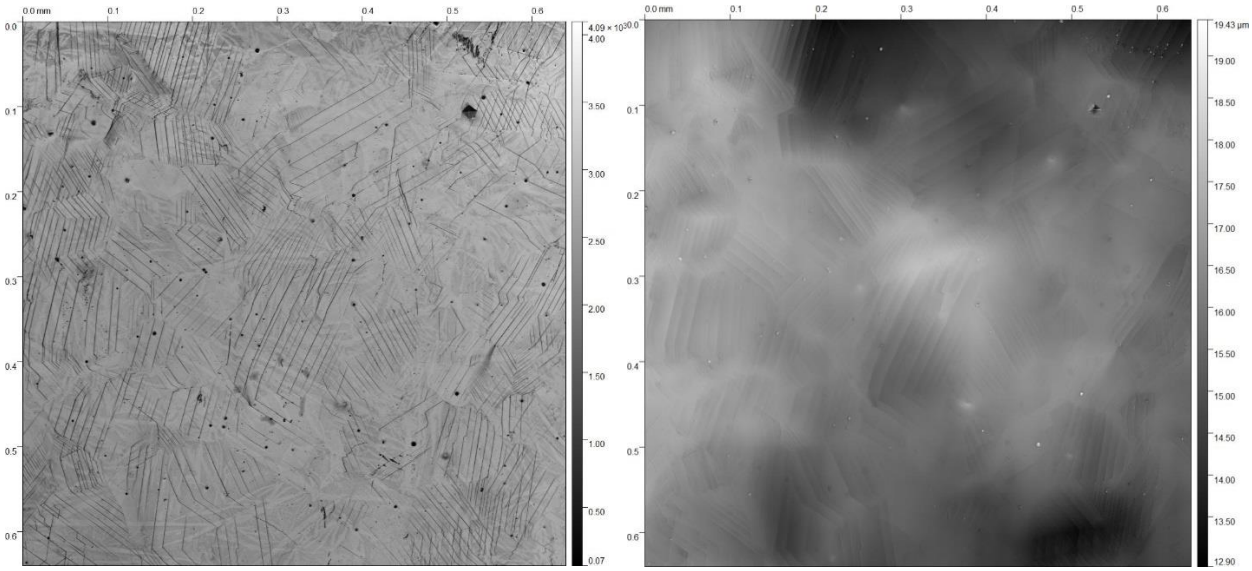

Figure C.17: LEXT confocal microscope large area topography map taken from OIM region 9 on BSCC2 Fe21Cr32Ni 5 dpa tensile bar sample with left hand image showing the sample surface and the right hand image showing the height distribution map

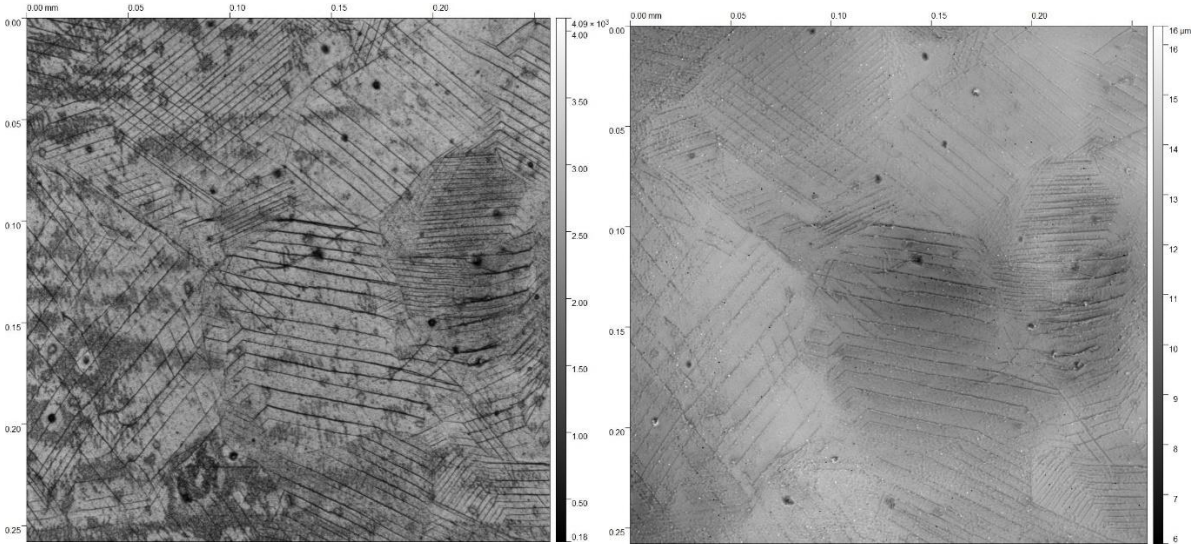

Figure C.18: LEXT confocal microscope 100x mag area topography map taken from OIM region 1 on ASCC2 Fe13Cr15Ni 5 dpa tensile bar sample with left hand image showing the sample surface and the right hand image showing the height distribution map

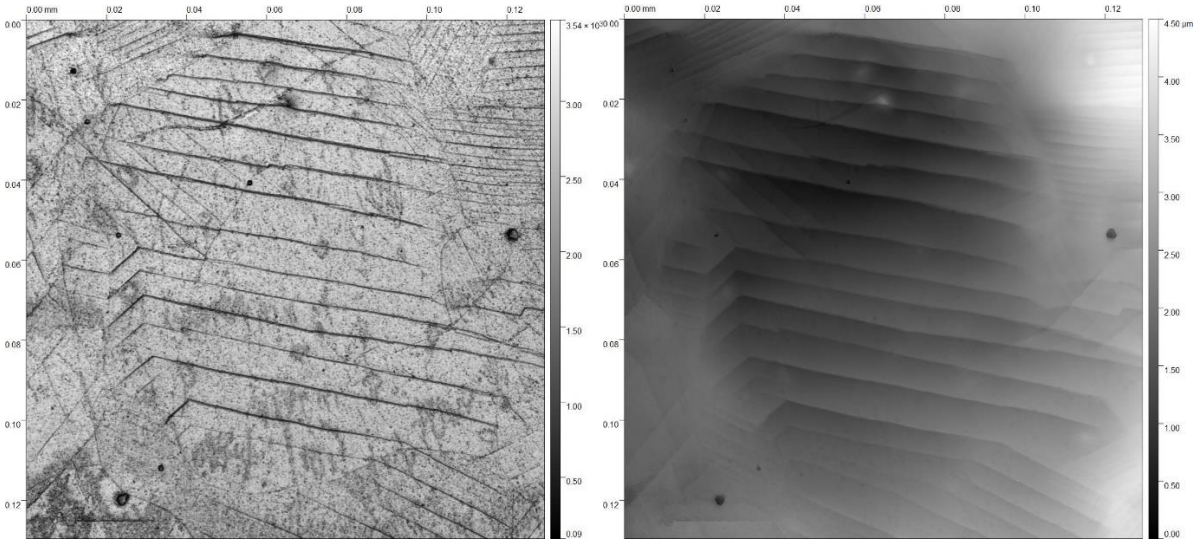

Figure C.19: LEXT confocal microscope 100x mag area topography map taken from OIM region 2 on ASCC2 Fe13Cr15Ni 5 dpa tensile bar sample with left hand image showing the sample surface and the right hand image showing the height distribution map

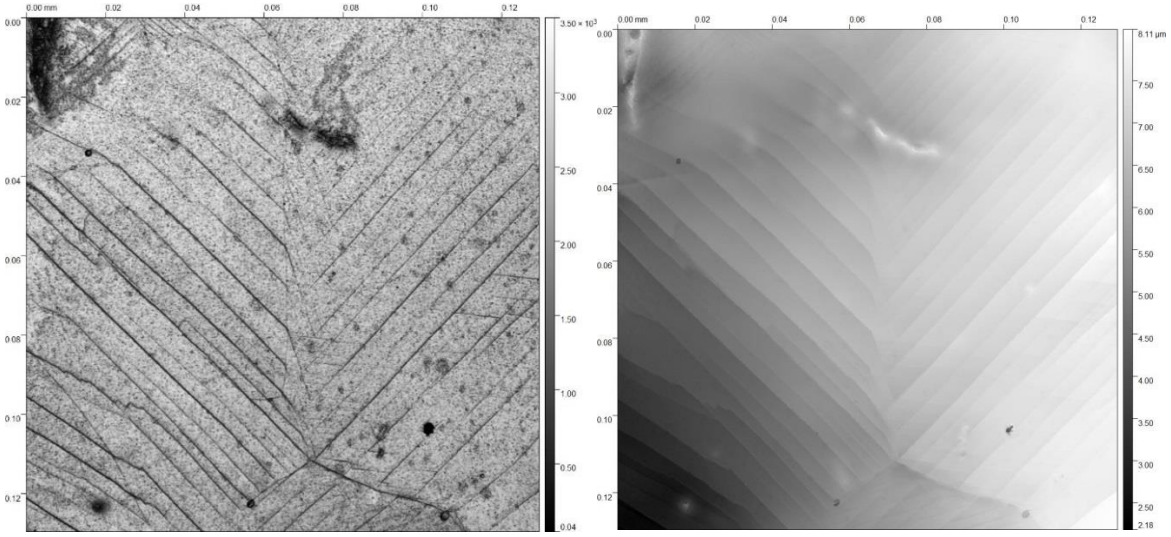

Figure C.20: LEXT confocal microscope 100x mag area topography map taken from OIM region 4 on ASCC2 Fe13Cr15Ni 5 dpa tensile bar sample with left hand image showing the sample surface and the right hand image showing the height distribution map

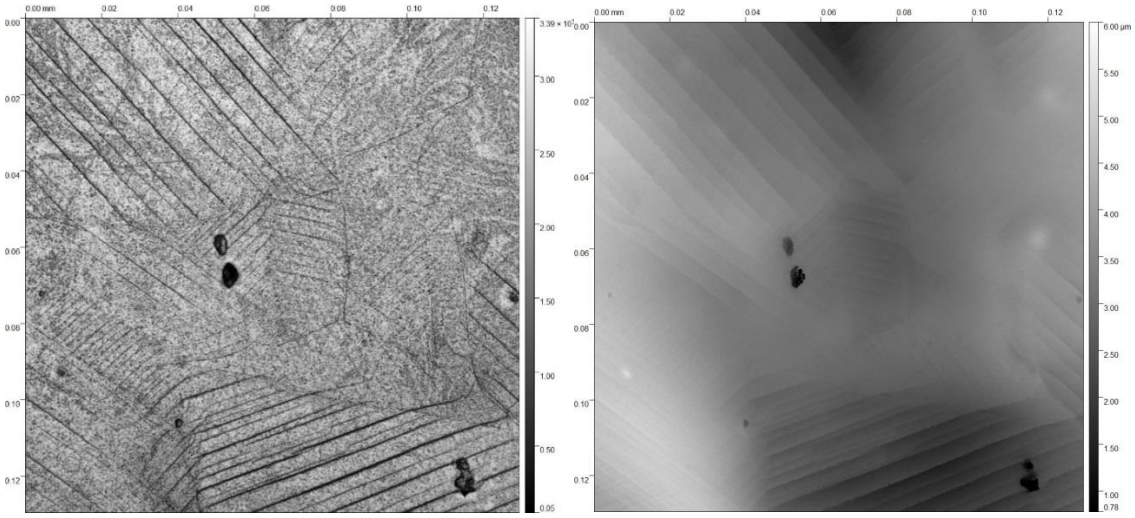

Figure C.21: LEXT confocal microscope 100x mag area topography map taken from OIM region 6 on ASCC2 Fe13Cr15Ni 5 dpa tensile bar sample with left hand image showing the sample surface and the right hand image showing the height distribution map

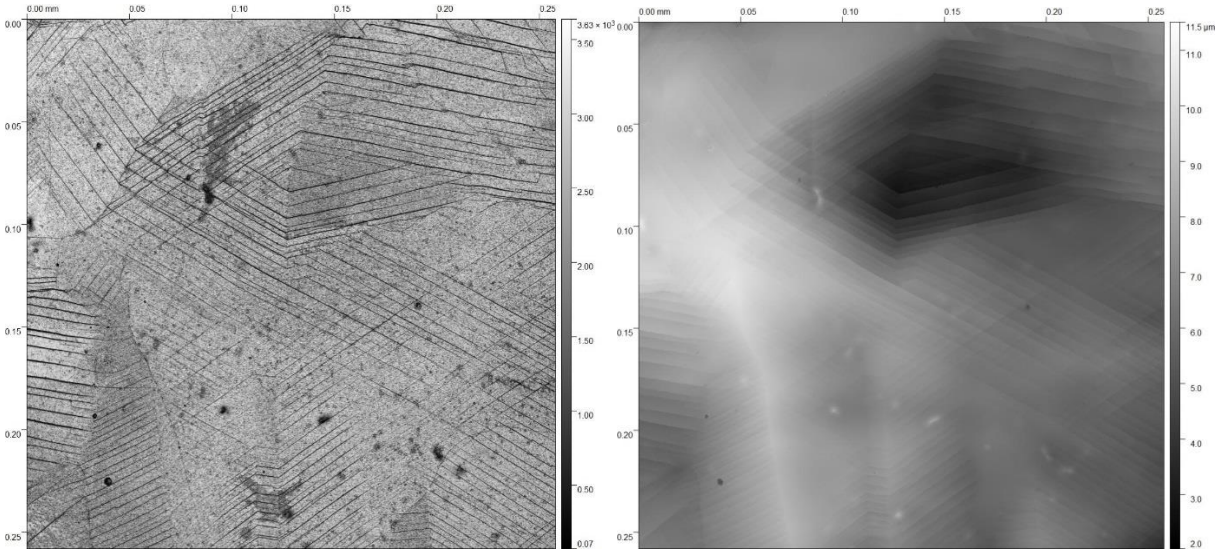

Figure C.22: LEXT confocal microscope 100x mag area topography map taken from OIM region 8 on ASCC2 Fe13Cr15Ni 5 dpa tensile bar sample with left hand image showing the sample surface and the right hand image showing the height distribution map

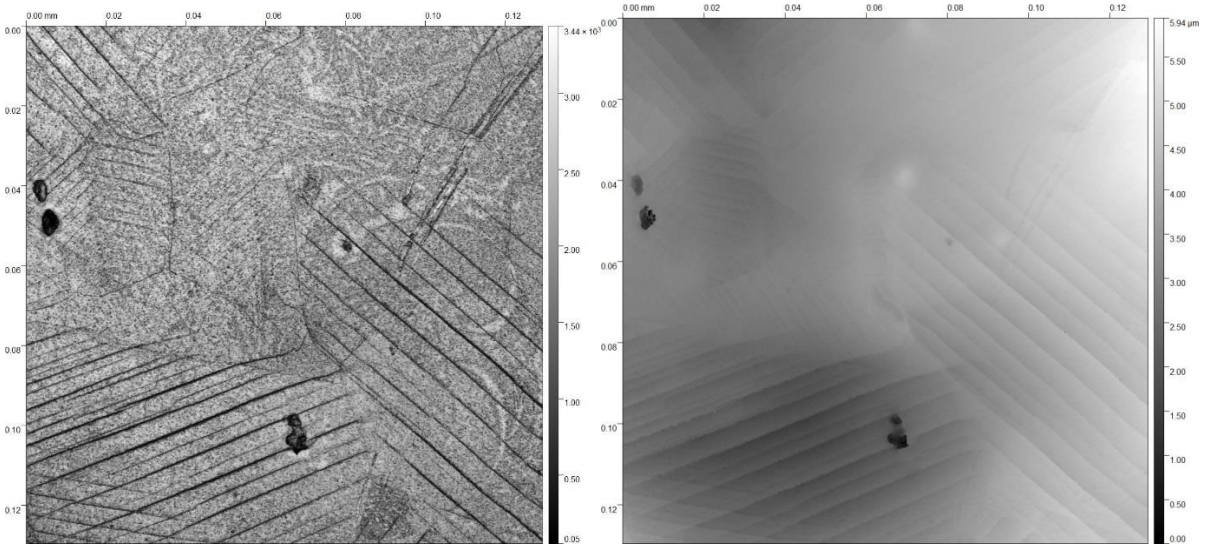

Figure C.23: LEXT confocal microscope 100x mag area topography map taken from OIM region 2 on BSCC2 Fe21Cr32 Ni 5 dpa tensile bar sample with left hand image showing the sample surface and the right hand image showing the height distribution map

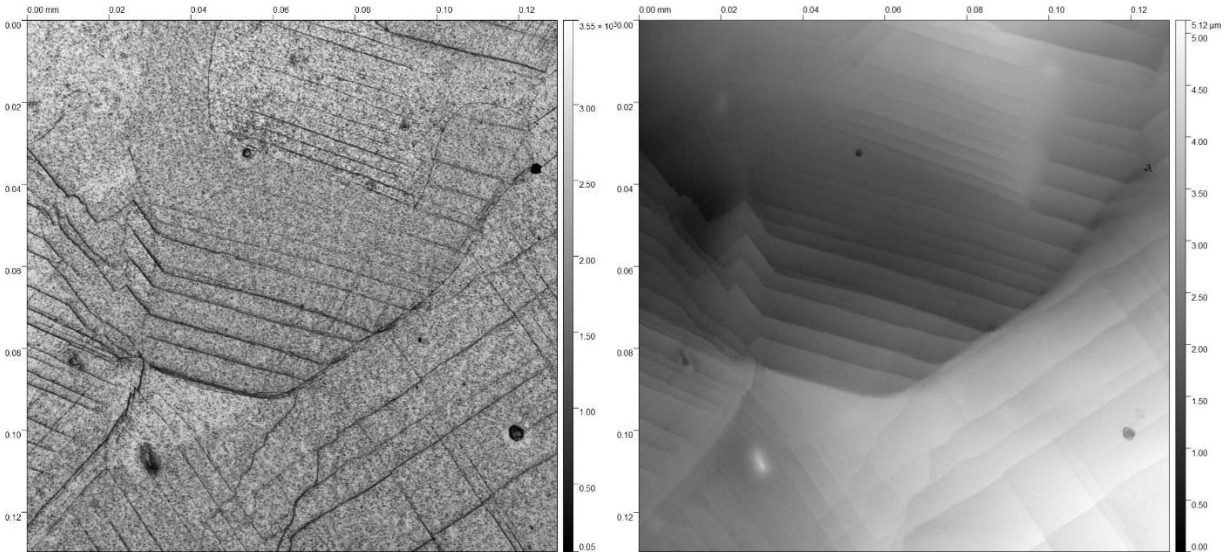

Figure C.24: LEXT confocal microscope 100x mag area topography map taken from OIM region 4 on BSCC2 Fe21Cr32 Ni 5 dpa tensile bar sample with left hand image showing the sample surface and the right hand image showing the height distribution map

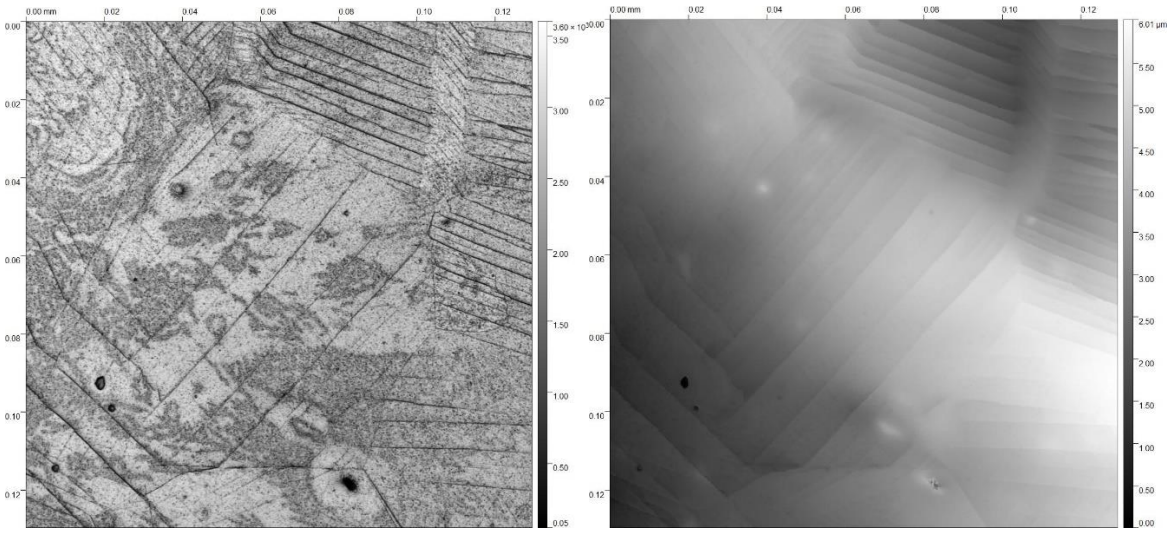

Figure C.25: LEXT confocal microscope 100x mag area topography map taken from OIM region 6 on BSCC2 Fe21Cr32 Ni 5 dpa tensile bar sample with left hand image showing the sample surface and the right hand image showing the height distribution map

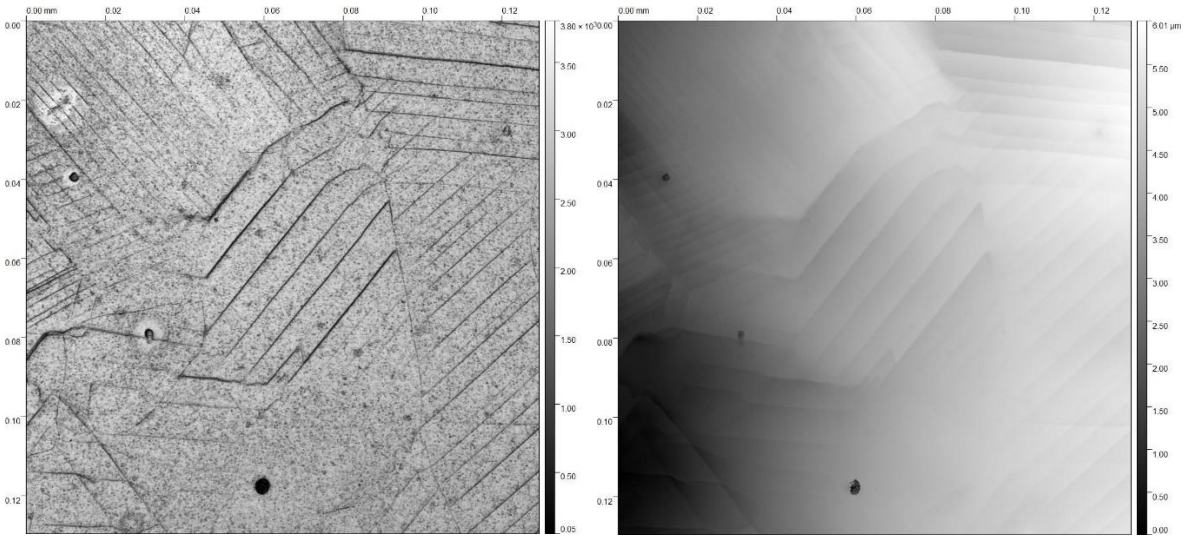

Figure C.26: LEXT confocal microscope 100x mag area topography map taken from OIM region 8 on BSCC2 Fe21Cr32 Ni 5 dpa tensile bar sample with left hand image showing the sample surface and the right hand image showing the height distribution map

APPENDIX D

Raw Stress Profiles Taken from HREBSD Scans

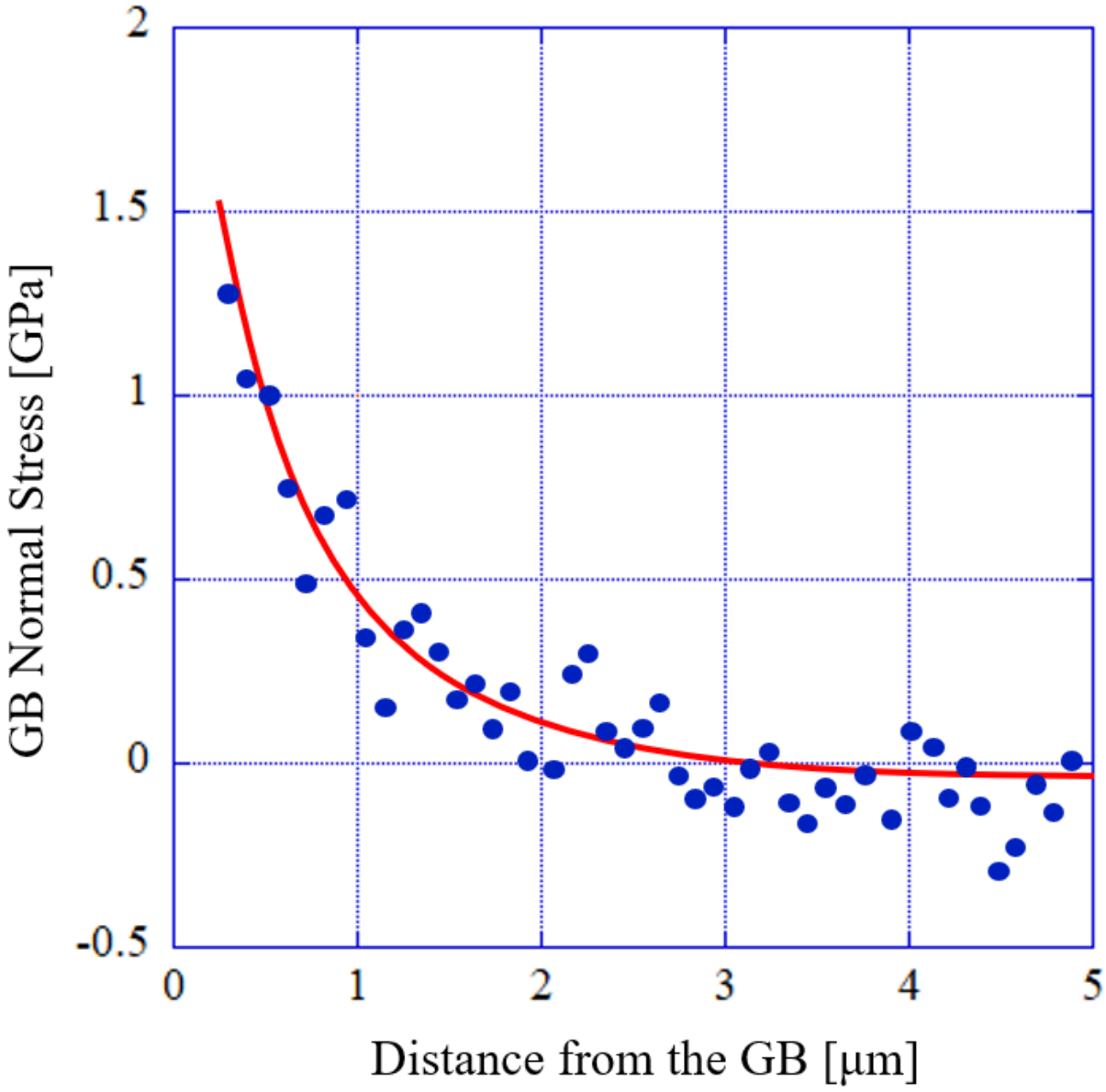

Figure D.1: Tensile stress normal to the grain boundary as a function of distance from the grain boundary in ASCC2 Fe13Cr15Ni 5 dpa tensile bar sample at site ASCC2-1

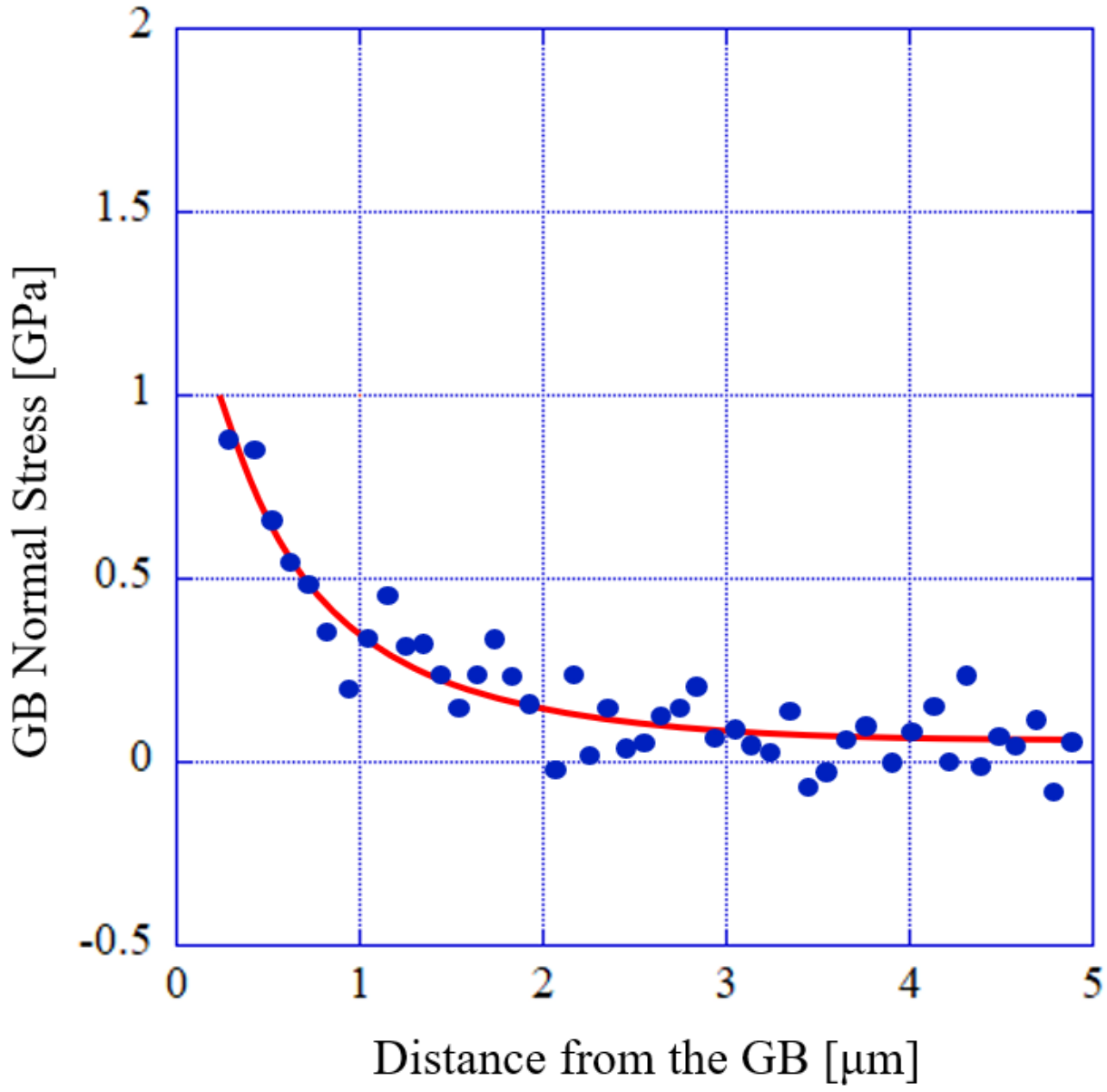

Figure D.2: Tensile stress normal to the grain boundary as a function of distance from the grain boundary in ASCC2 Fe13Cr15Ni 5 dpa tensile bar sample at site ASCC2-2

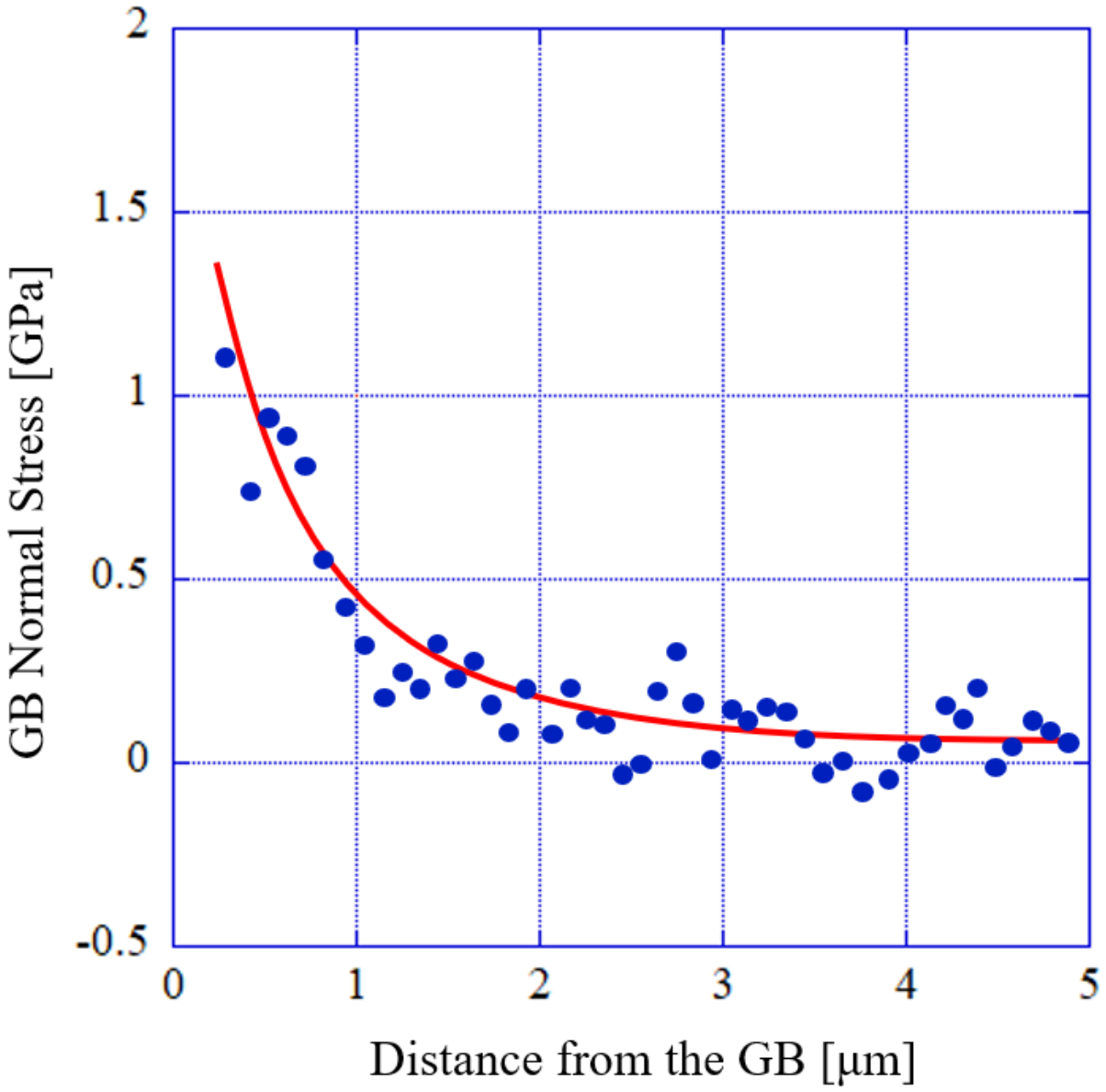

Figure D.3: Tensile stress normal to the grain boundary as a function of distance from the grain boundary in ASCC2 Fe13Cr15Ni 5 dpa tensile bar sample at site ASCC2-3

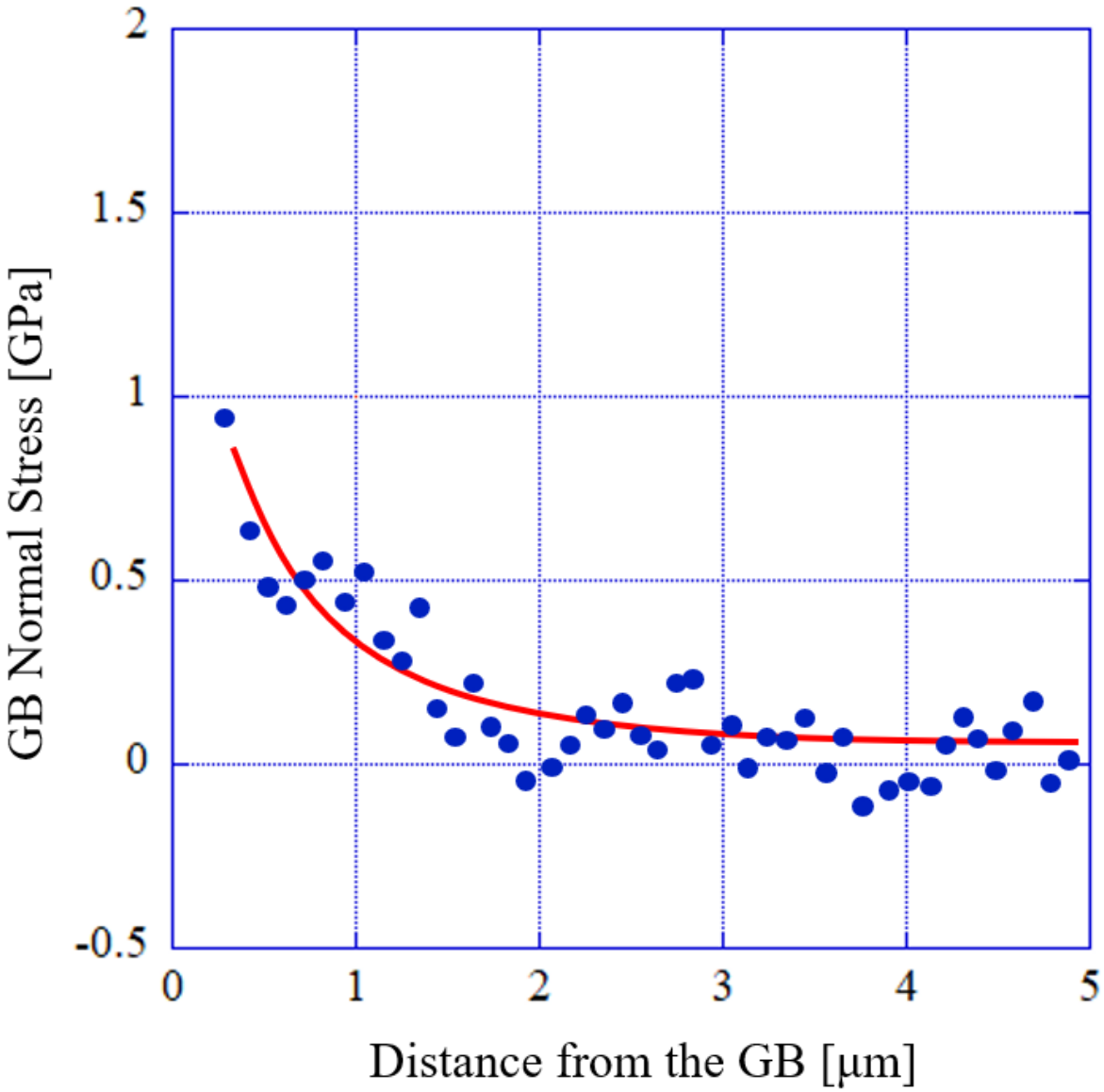

Figure D.4: Tensile stress normal to the grain boundary as a function of distance from the grain boundary in ASCC2 Fe13Cr15Ni 5 dpa tensile bar sample at site ASCC2-4

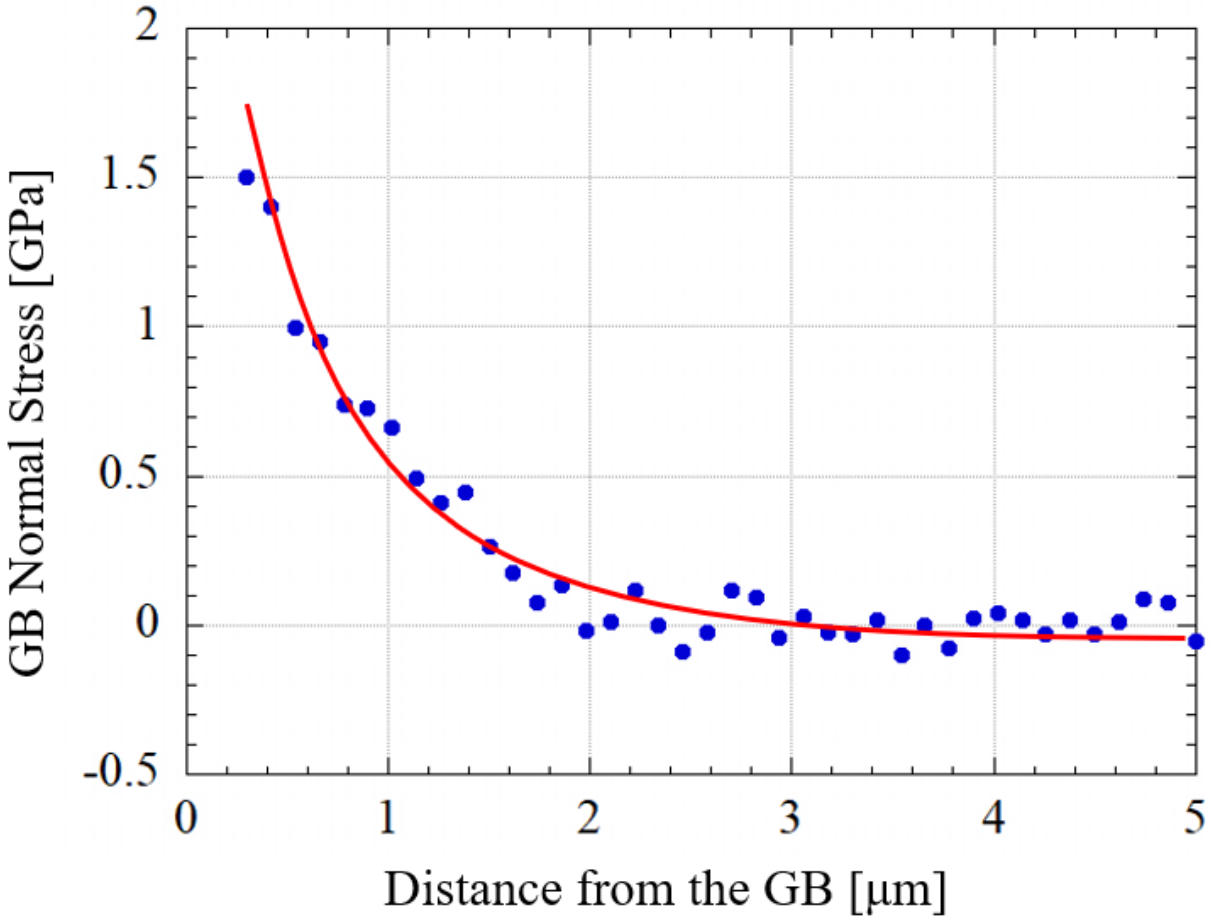

Figure D.5: Tensile stress normal to the grain boundary as a function of distance from the grain boundary in ASCC2 Fe13Cr15Ni 5 dpa tensile bar sample at site ASCC2-5

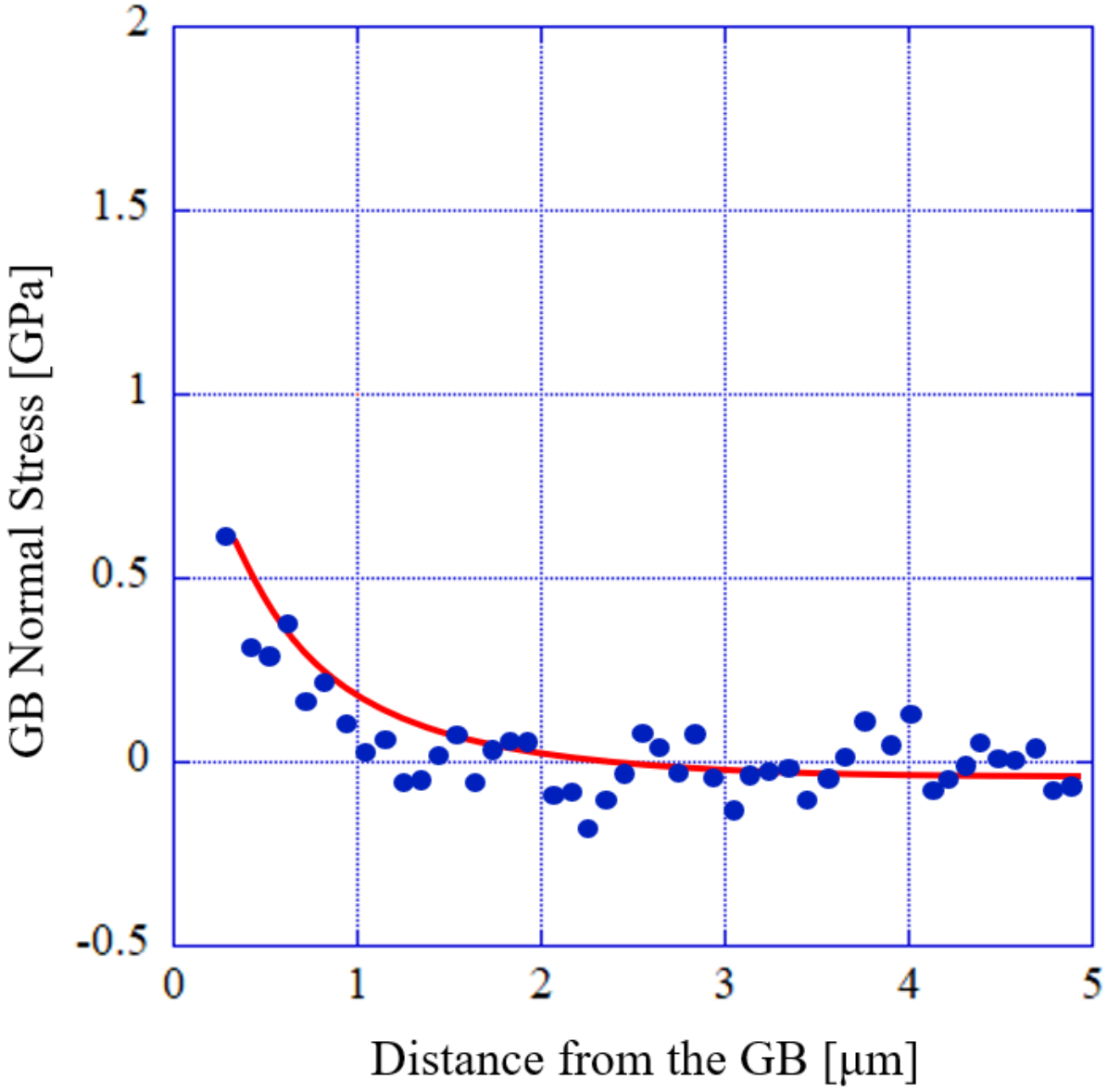

Figure D.6: Tensile stress normal to the grain boundary as a function of distance from the grain boundary in ASCC2 Fe13Cr15Ni 5 dpa tensile bar sample at site ASCC2-6

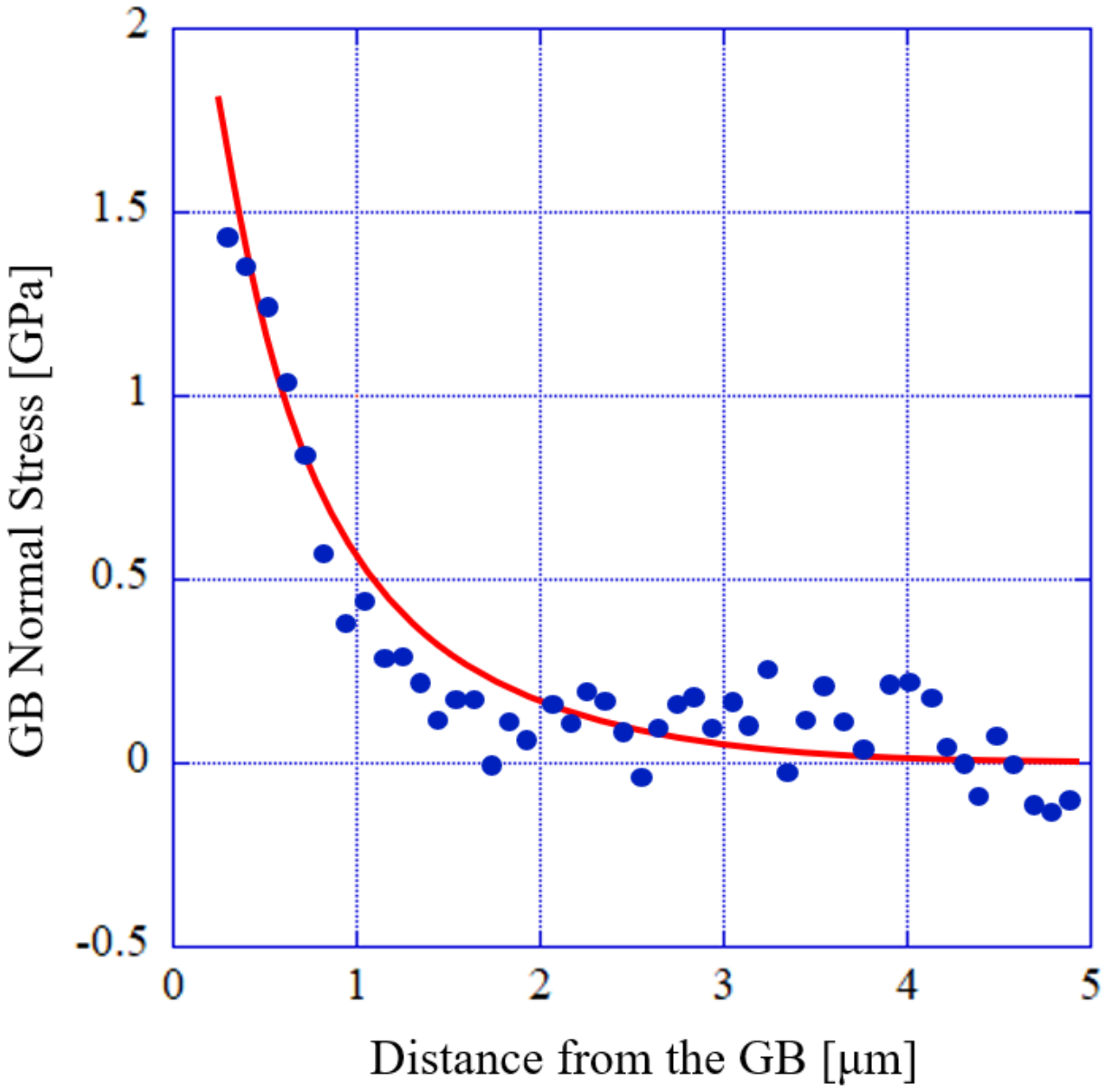

Figure D.7: Tensile stress normal to the grain boundary as a function of distance from the grain boundary in ASCC2 Fe13Cr15Ni 5 dpa tensile bar sample at site ASCC2-7

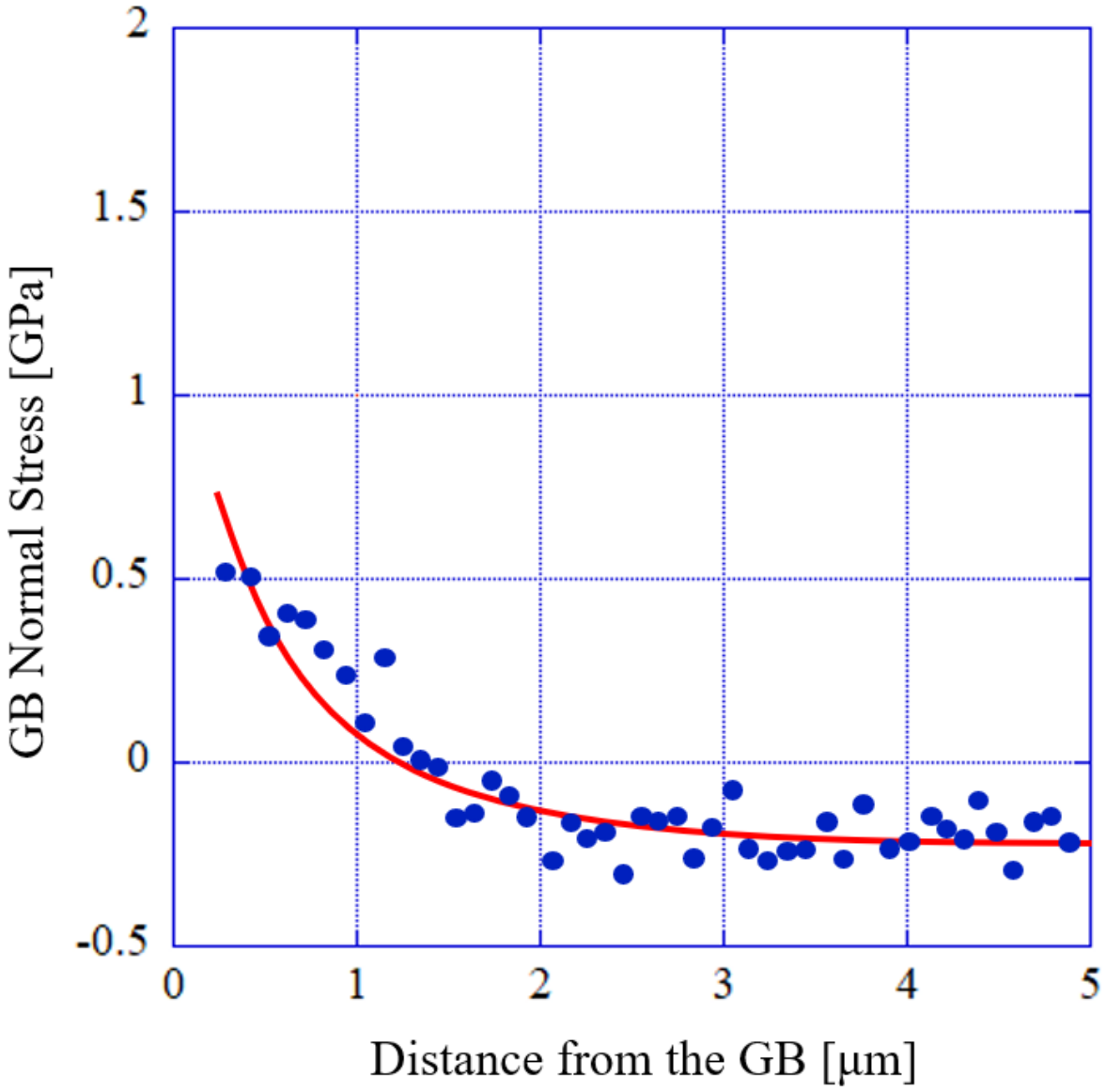

Figure D.8: Tensile stress normal to the grain boundary as a function of distance from the grain boundary in ASCC2 Fe13Cr15Ni 5 dpa tensile bar sample at site ASCC2-8

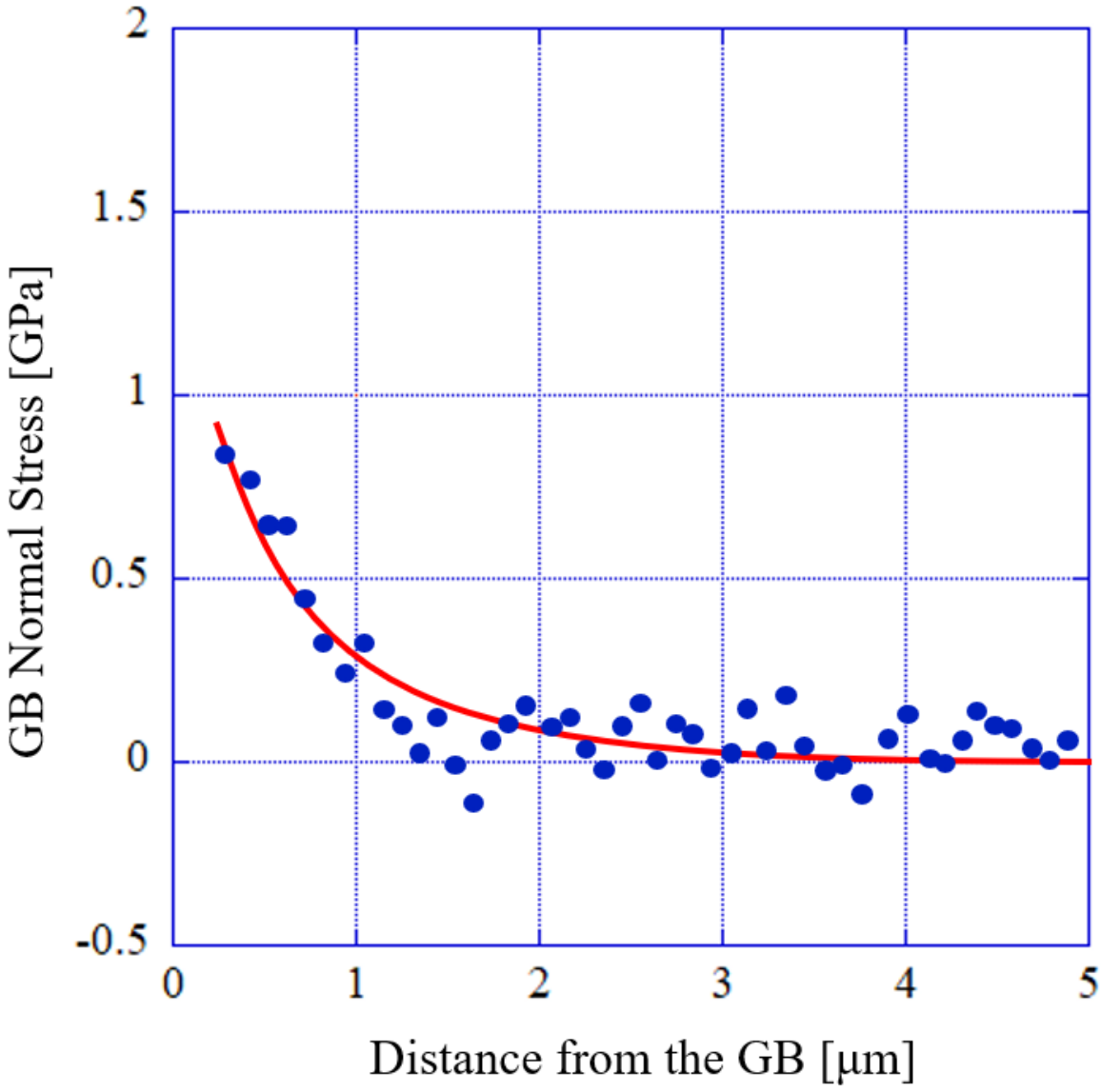

Figure D.9: Tensile stress normal to the grain boundary as a function of distance from the grain boundary in ASCC2 Fe13Cr15Ni 5 dpa tensile bar sample at site ASCC2-9

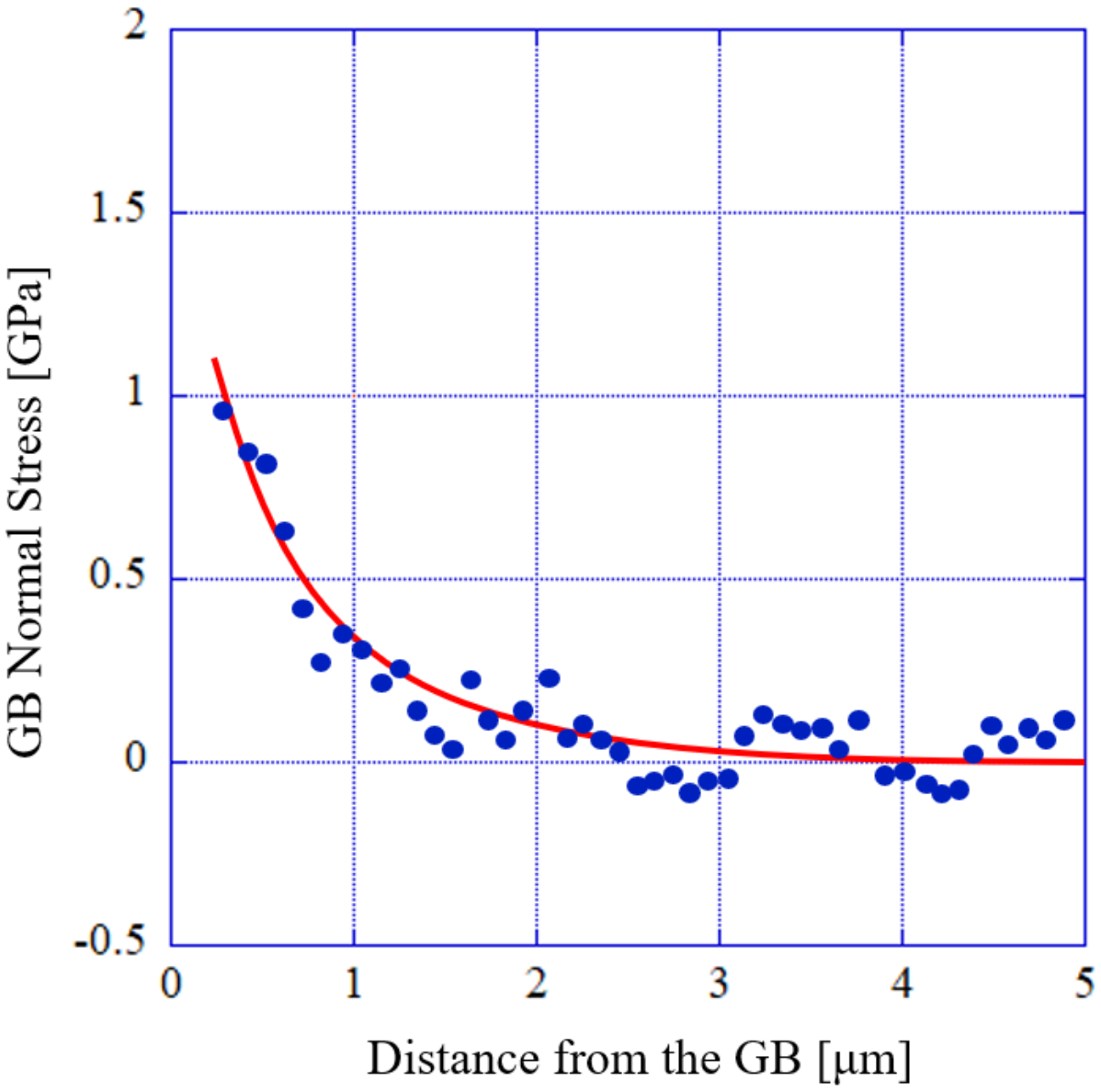

Figure D.10: Tensile stress normal to the grain boundary as a function of distance from the grain boundary in ASCC2 Fe13Cr15Ni 5 dpa tensile bar sample at site ASCC2-10

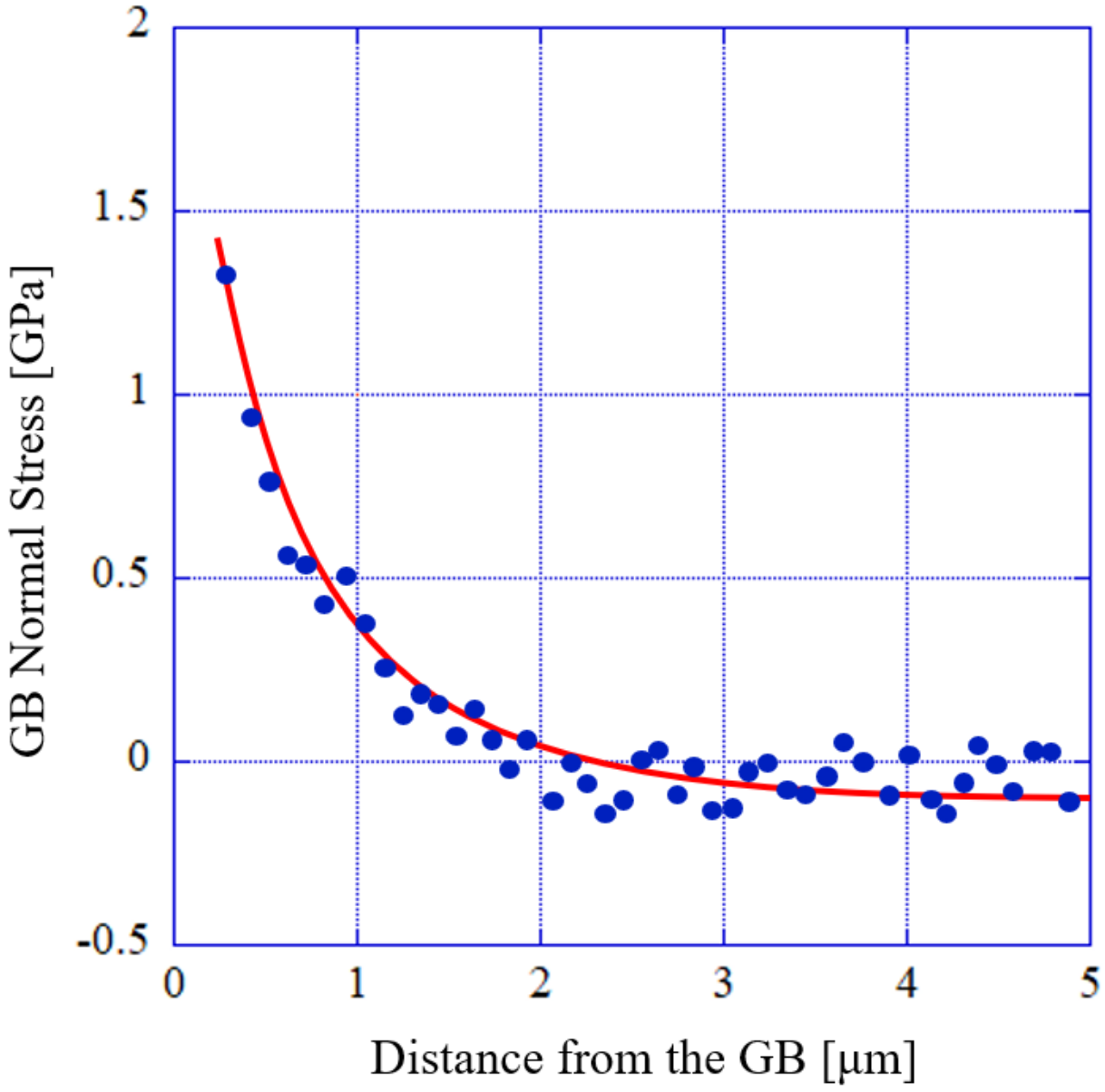

Figure D.11: Tensile stress normal to the grain boundary as a function of distance from the grain boundary in ASCC2 Fe13Cr15Ni 5 dpa tensile bar sample at site ASCC2-11

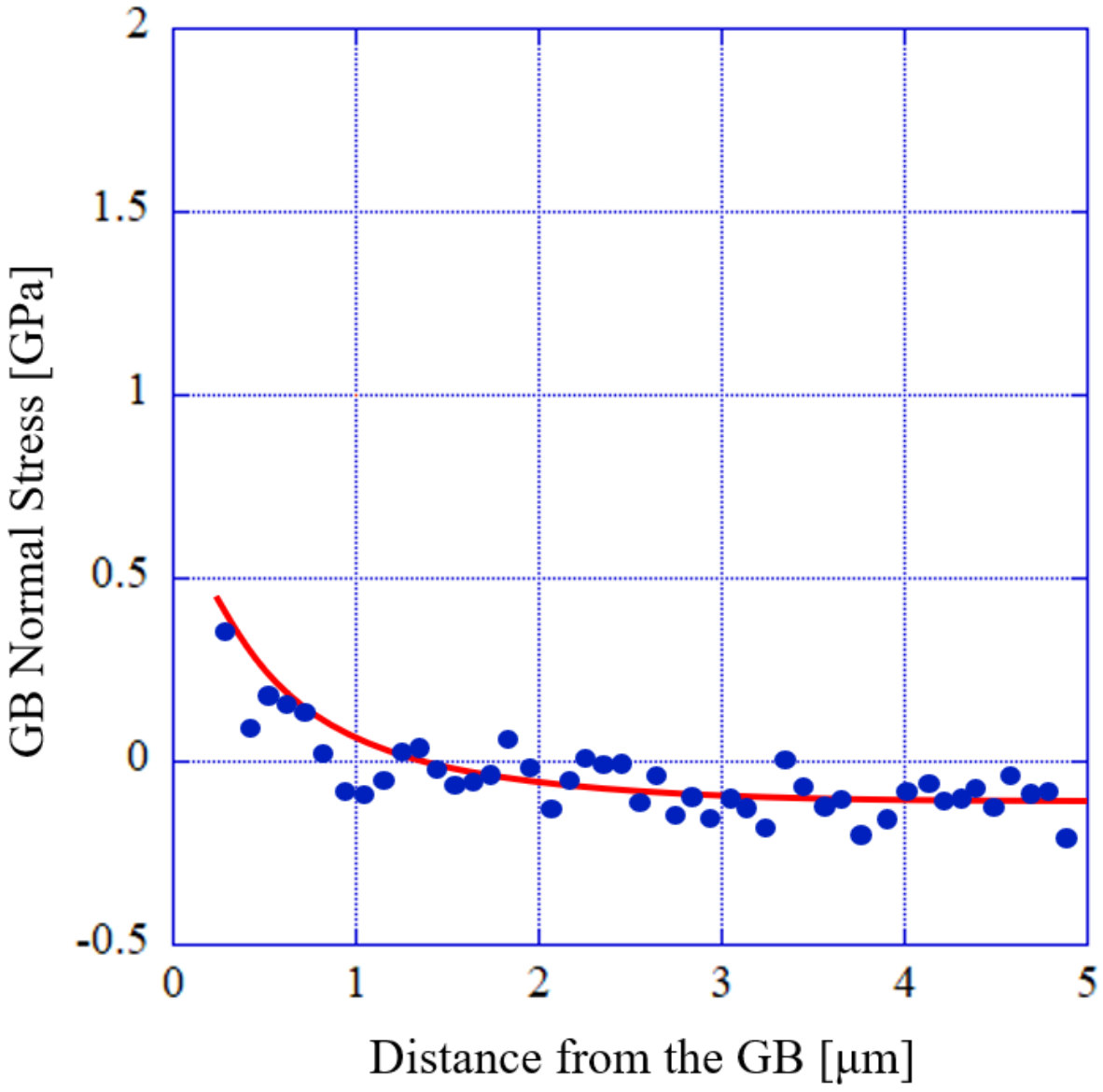

Figure D.12: Tensile stress normal to the grain boundary as a function of distance from the grain boundary in ASCC2 Fe13Cr15Ni 5 dpa tensile bar sample at site ASCC2-12

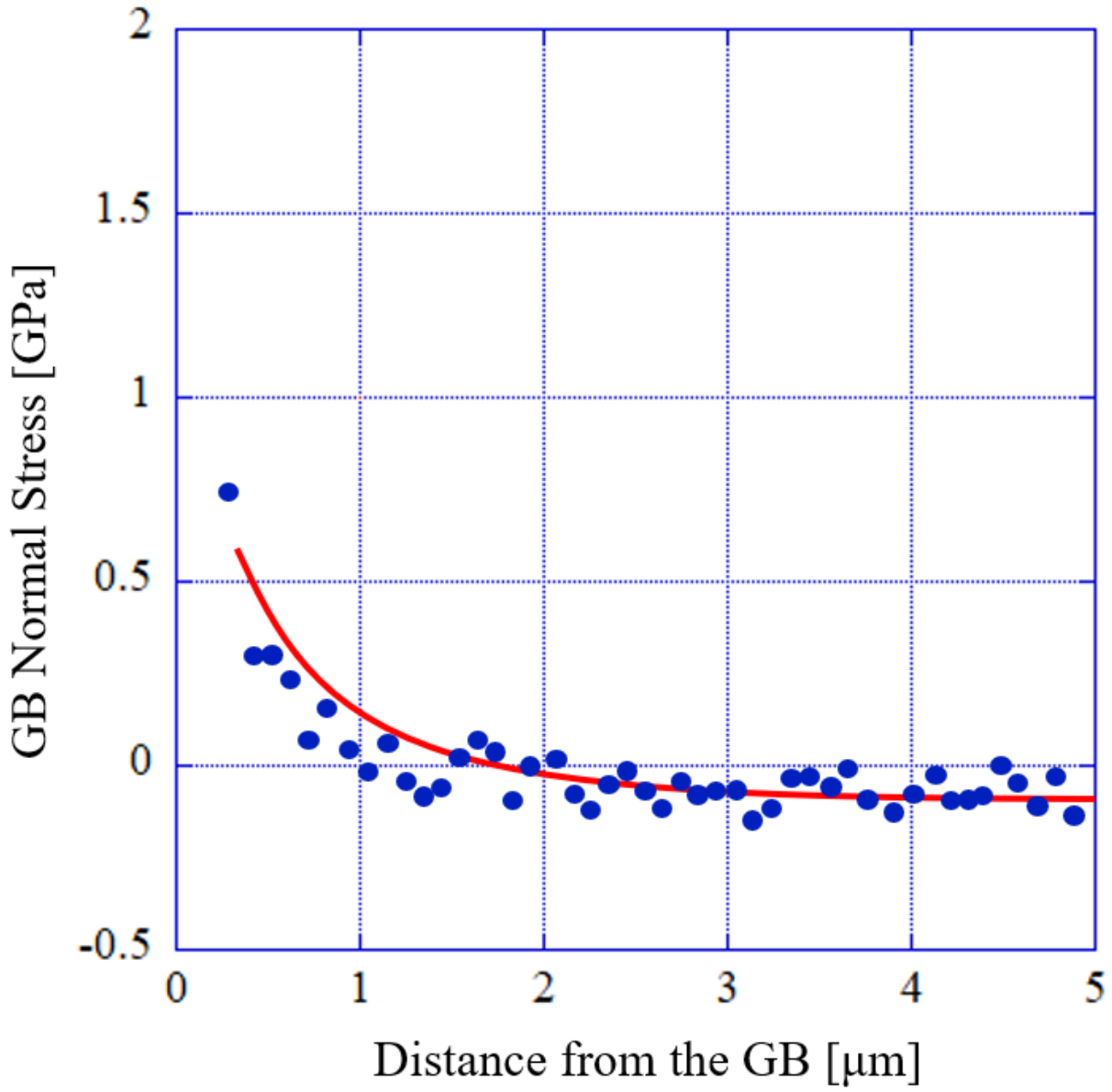

Figure D.13: Tensile stress normal to the grain boundary as a function of distance from the grain boundary in ASCC2 Fe13Cr15Ni 5 dpa tensile bar sample at site ASCC2-13

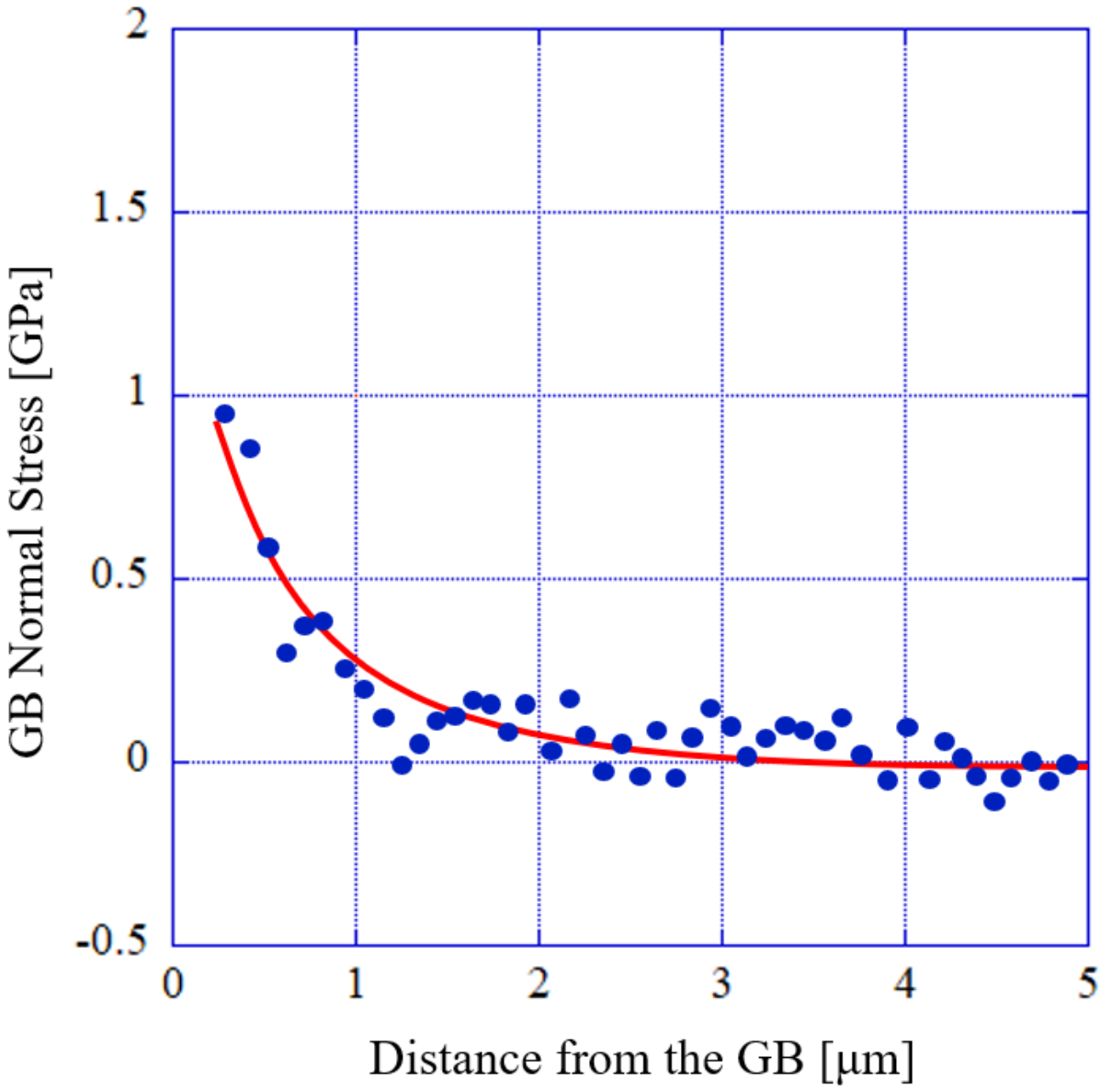

Figure D.14: Tensile stress normal to the grain boundary as a function of distance from the grain boundary in ASCC2 Fe13Cr15Ni 5 dpa tensile bar sample at site ASCC2-14

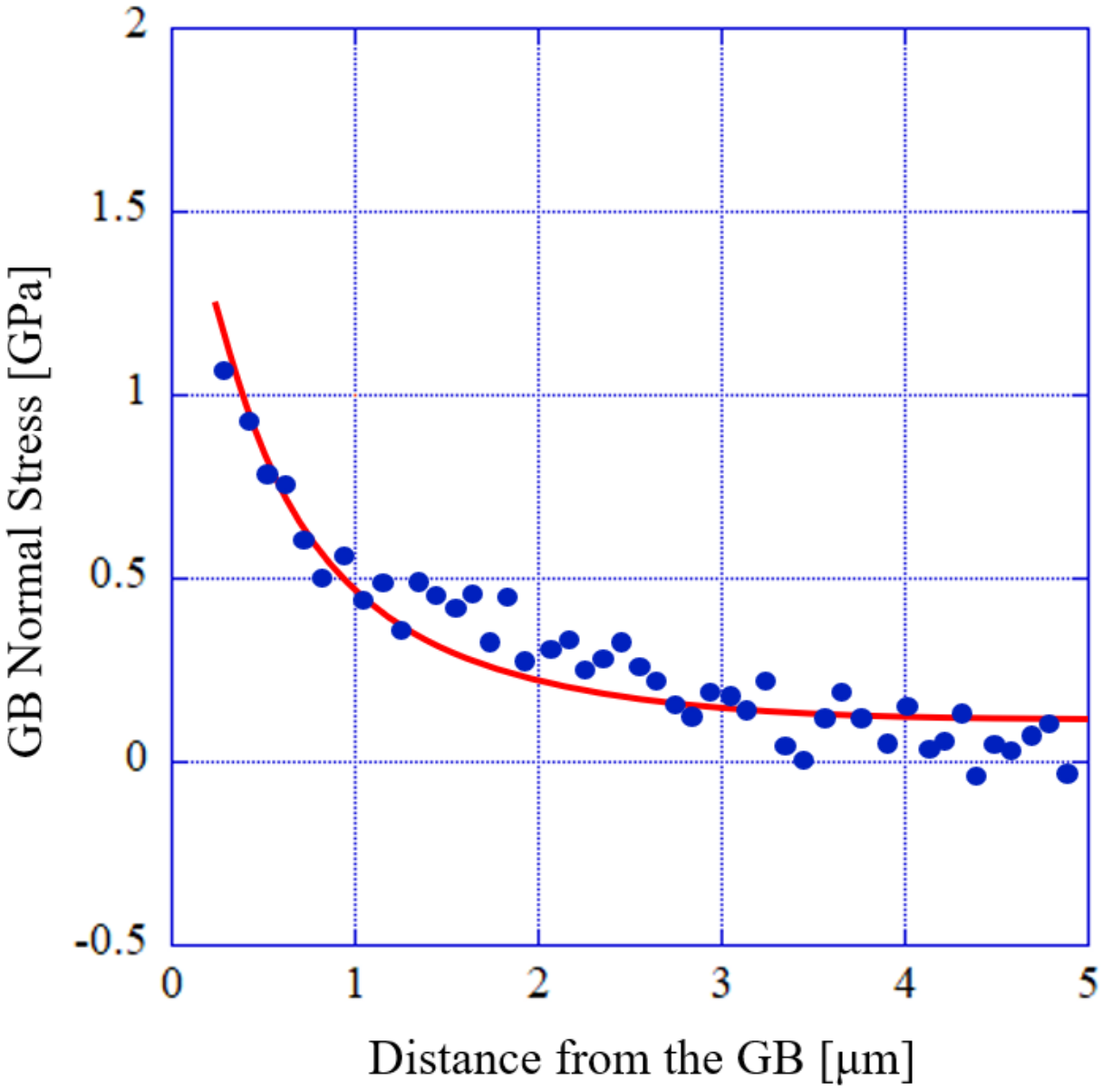

Figure D.15: Tensile stress normal to the grain boundary as a function of distance from the grain boundary in ASCC2 Fe13Cr15Ni 5 dpa tensile bar sample at site ASCC2-15

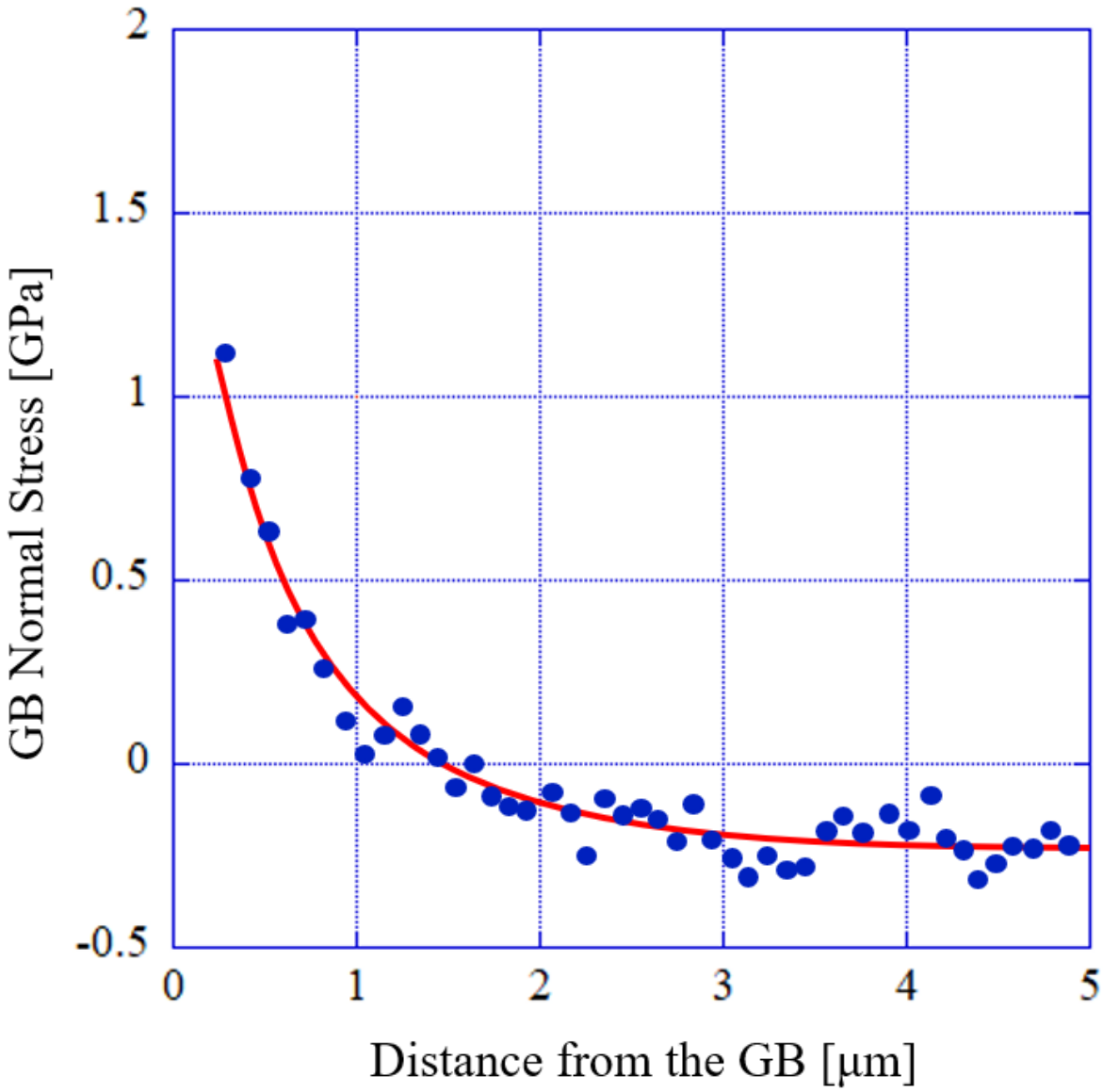

Figure D.16: Tensile stress normal to the grain boundary as a function of distance from the grain boundary in ASCC2 Fe13Cr15Ni 5 dpa tensile bar sample at site ASCC2-16

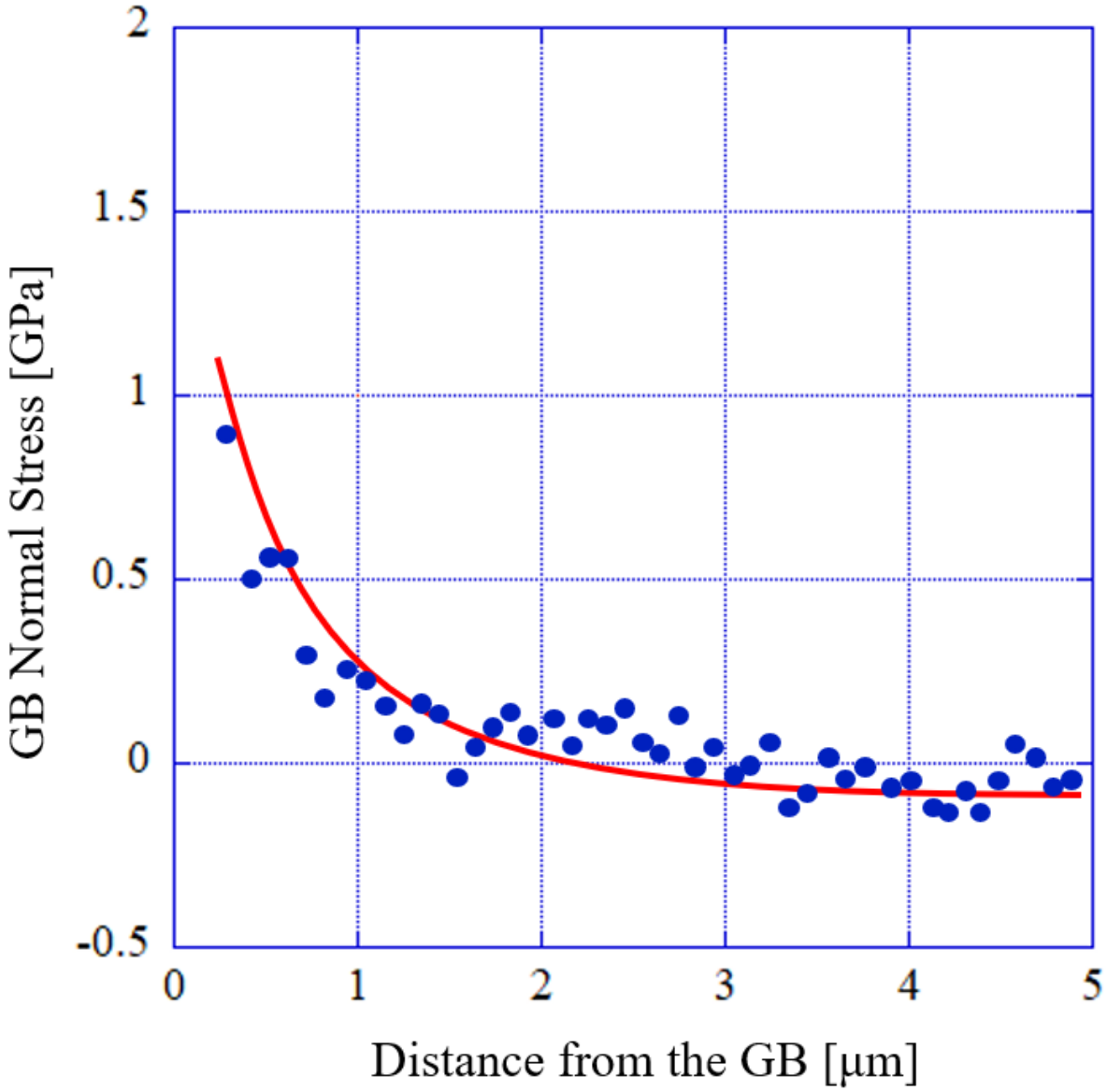

Figure D.17: Tensile stress normal to the grain boundary as a function of distance from the grain boundary in ASCC2 Fe13Cr15Ni 5 dpa tensile bar sample at site ASCC2-17

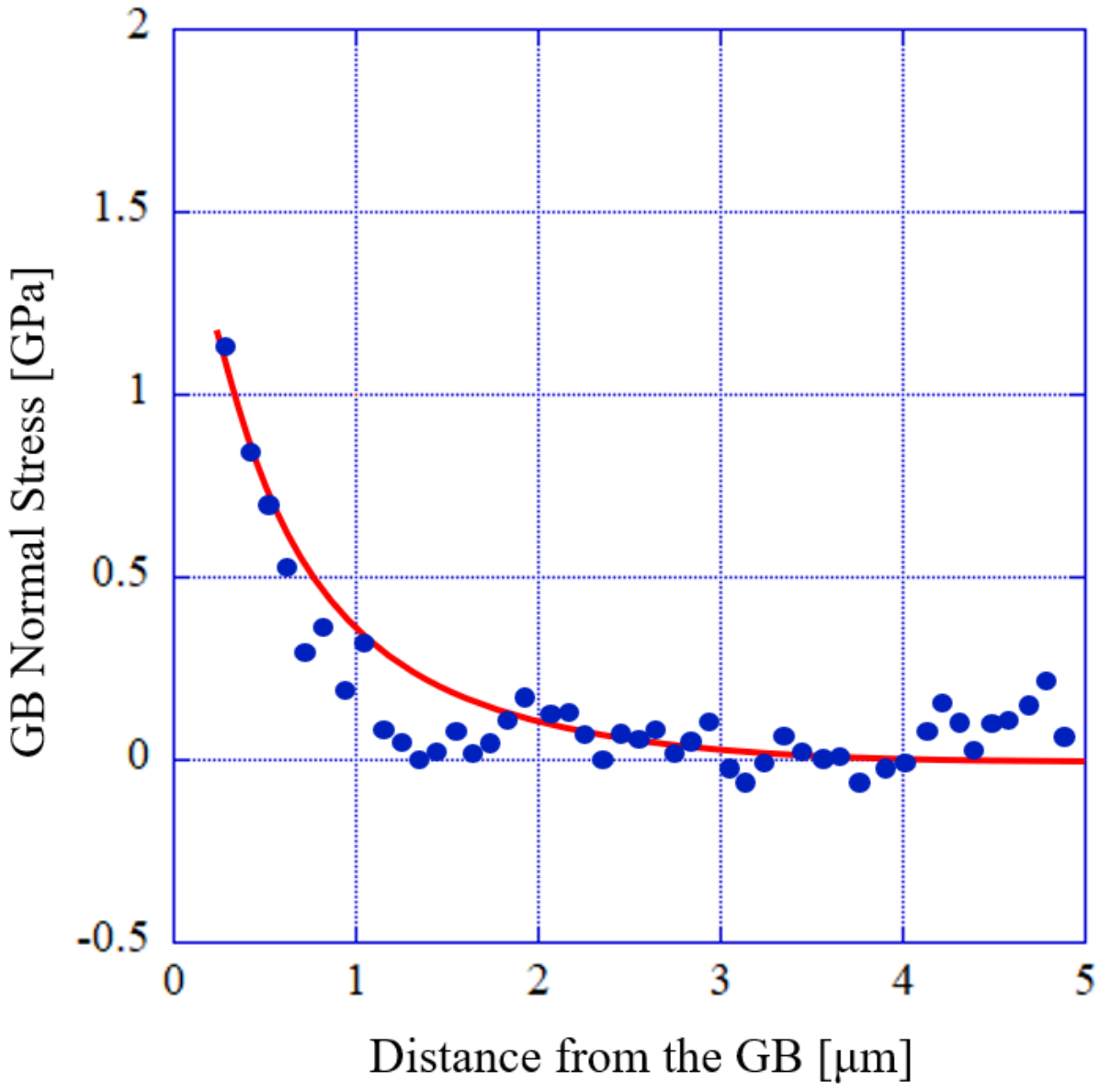

Figure D.18: Tensile stress normal to the grain boundary as a function of distance from the grain boundary in ASCC2 Fe13Cr15Ni 5 dpa tensile bar sample at site ASCC2-18

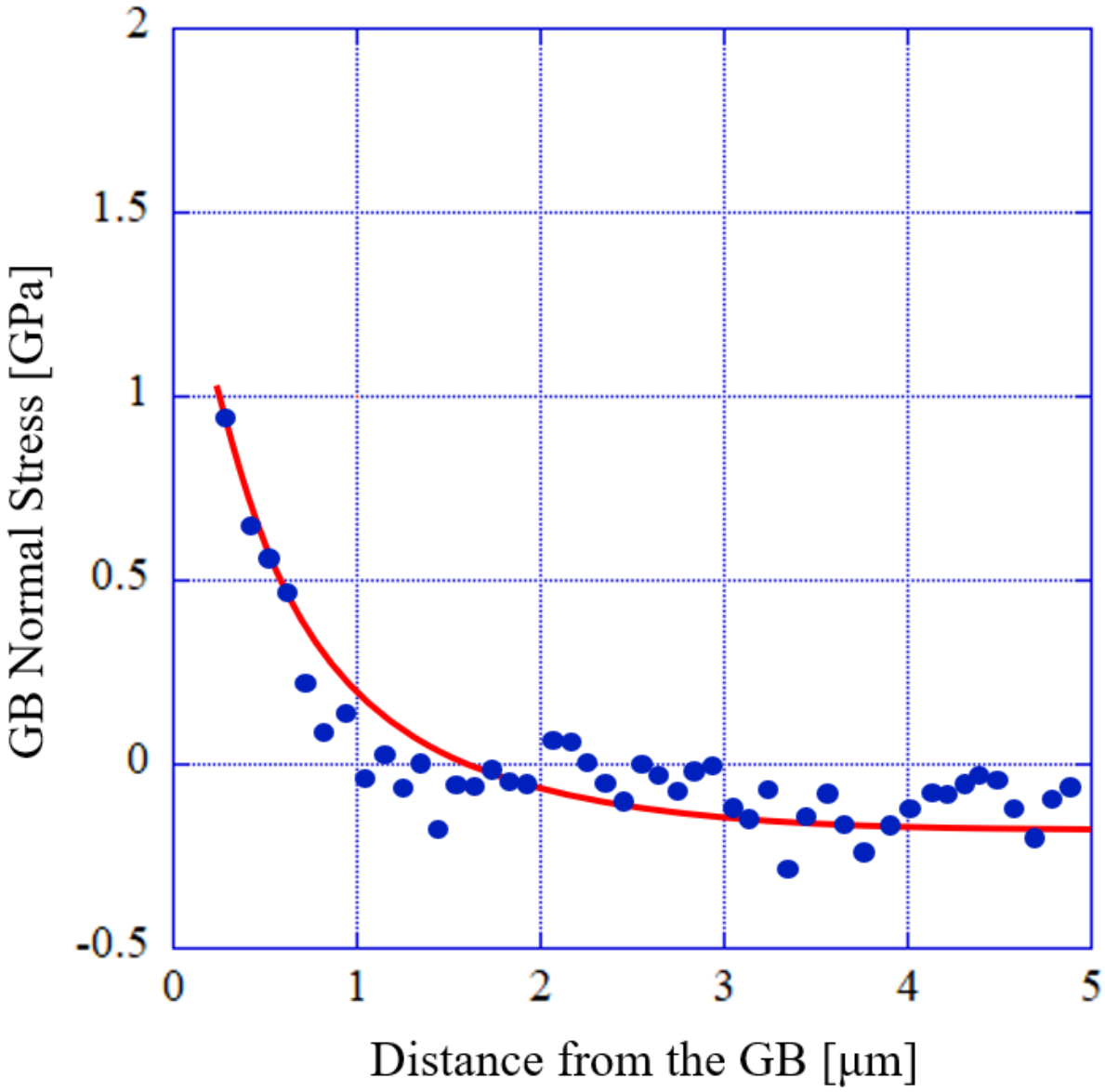

Figure D.19: Tensile stress normal to the grain boundary as a function of distance from the grain boundary in ASCC2 Fe13Cr15Ni 5 dpa tensile bar sample at site ASCC2-19

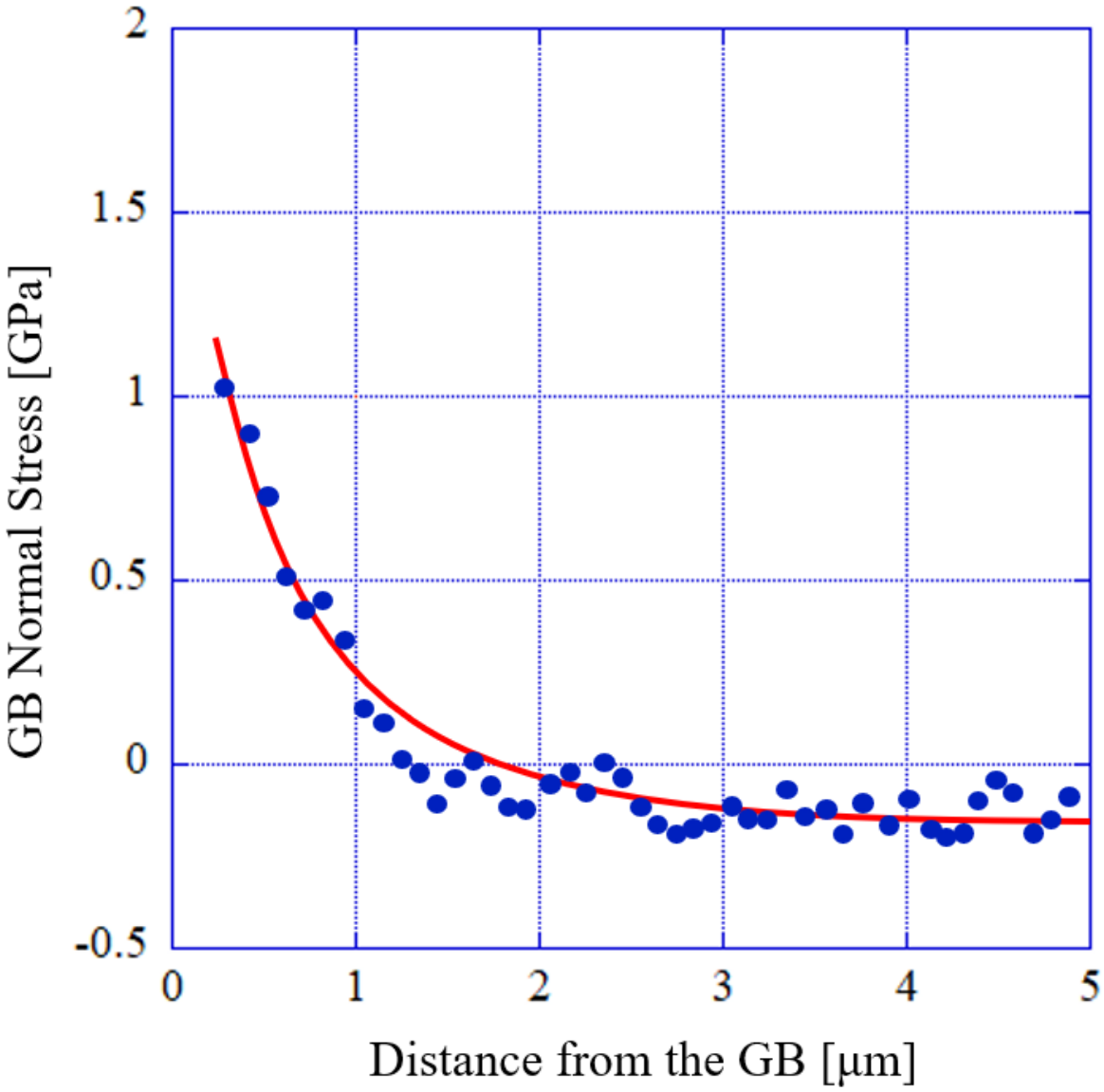

Figure D.20: Tensile stress normal to the grain boundary as a function of distance from the grain boundary in ASCC2 Fe13Cr15Ni 5 dpa tensile bar sample at site ASCC2-20

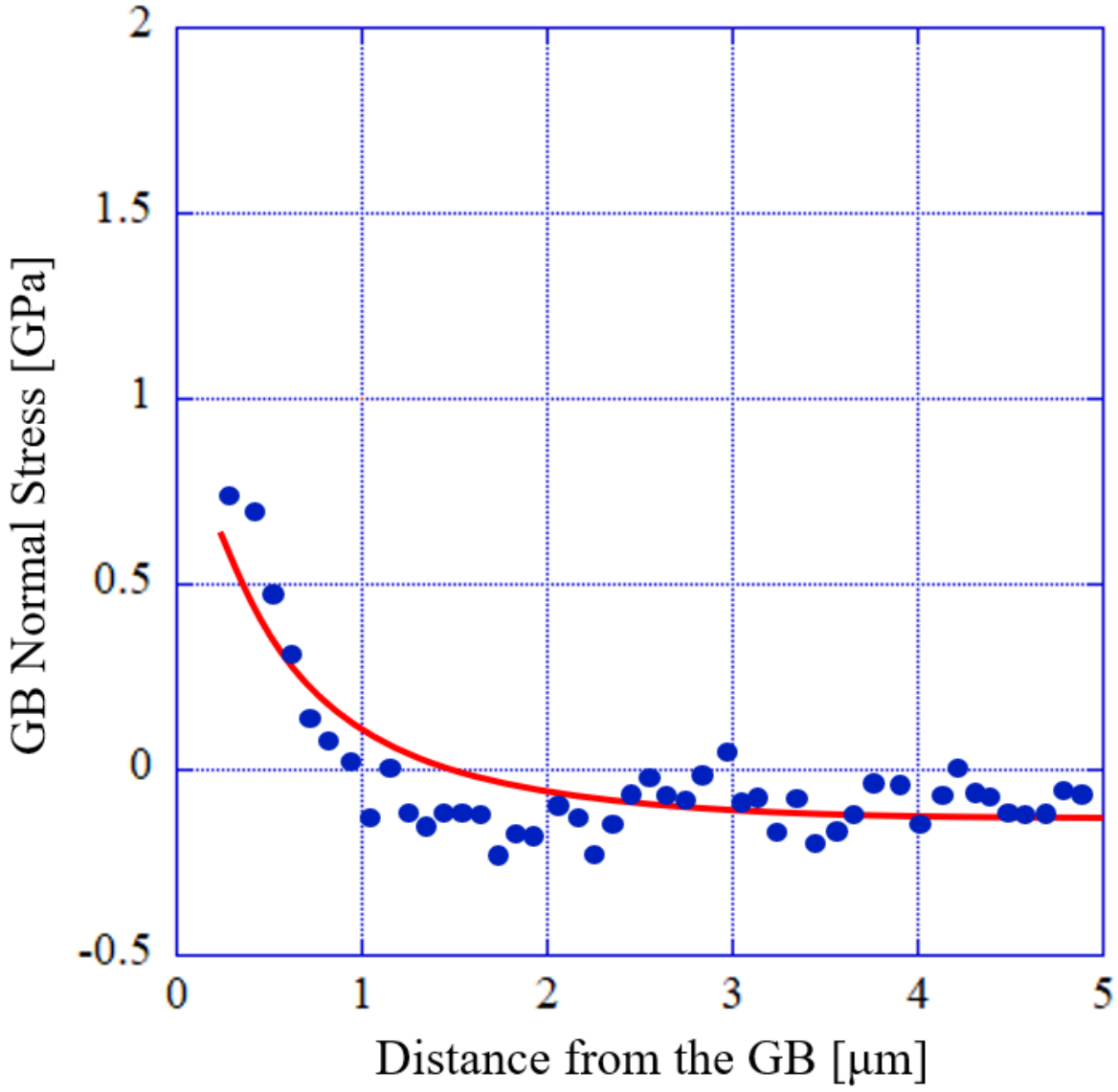

Figure D.21: Tensile stress normal to the grain boundary as a function of distance from the grain boundary in ASCC2 Fe13Cr15Ni 5 dpa tensile bar sample at site ASCC2-21

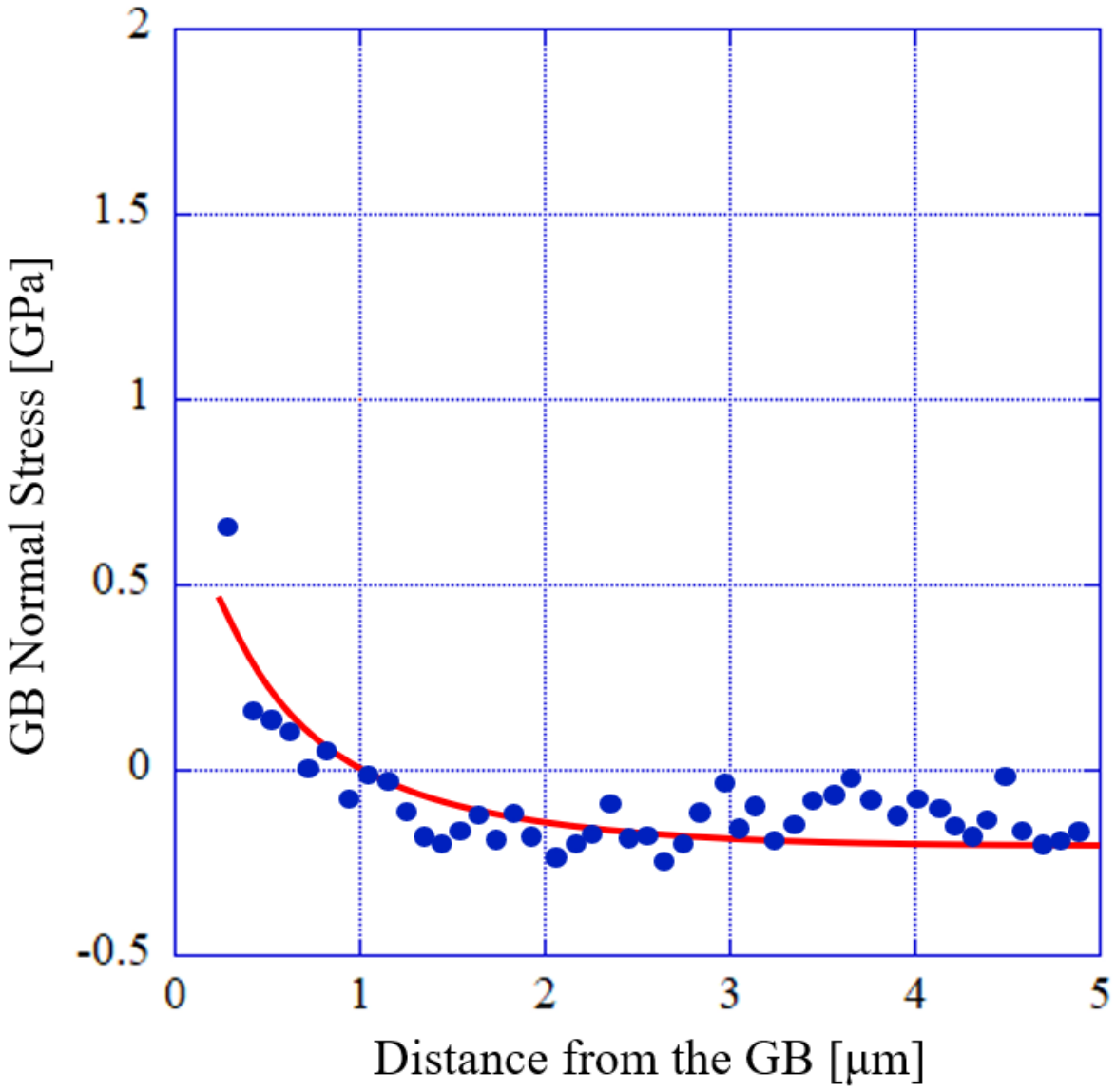

Figure D.22: Tensile stress normal to the grain boundary as a function of distance from the grain boundary in ASCC2 Fe13Cr15Ni 5 dpa tensile bar sample at site ASCC2-22

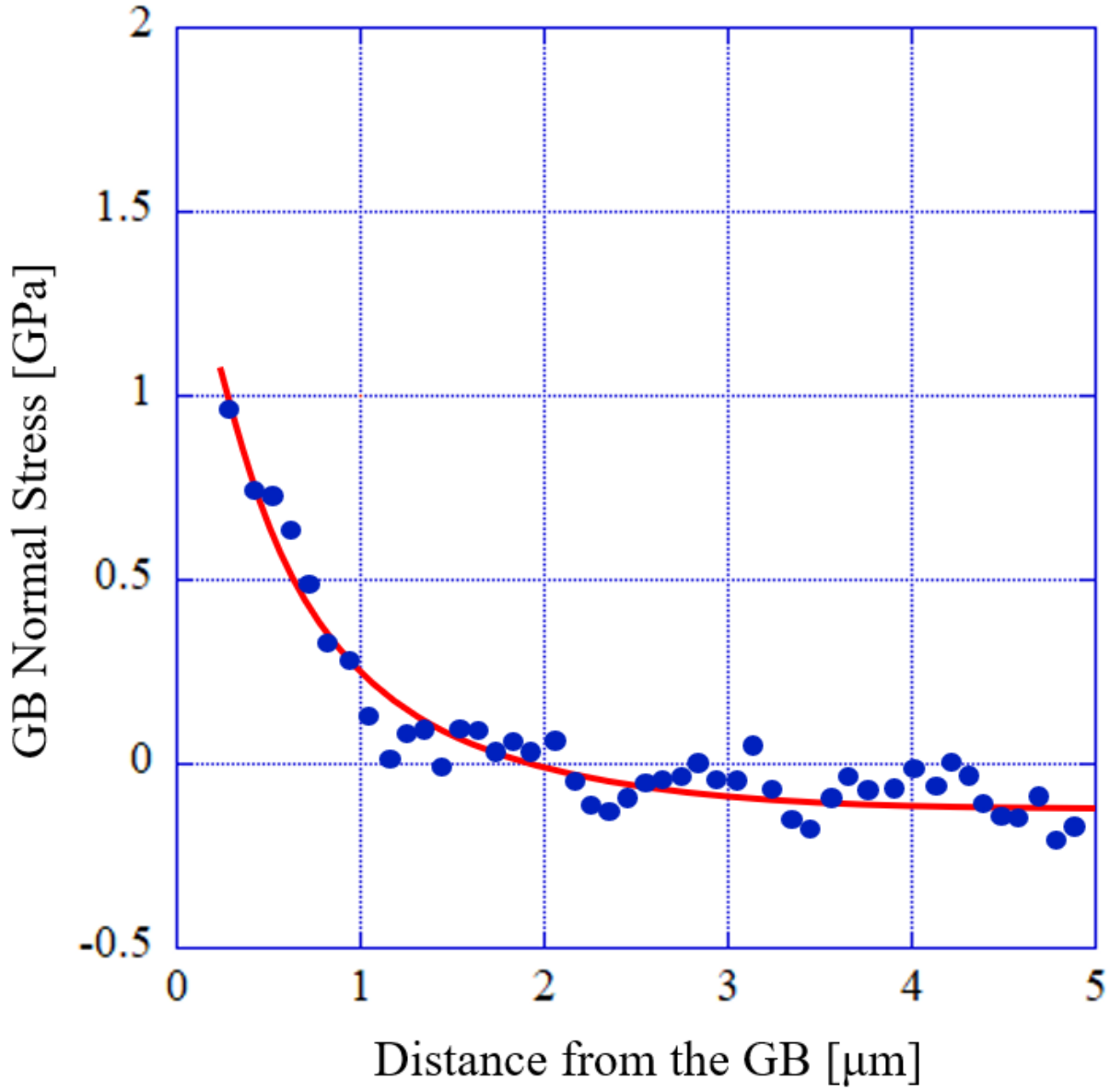

Figure D.23: Tensile stress normal to the grain boundary as a function of distance from the grain boundary in ASCC2 Fe13Cr15Ni 5 dpa tensile bar sample at site ASCC2-23

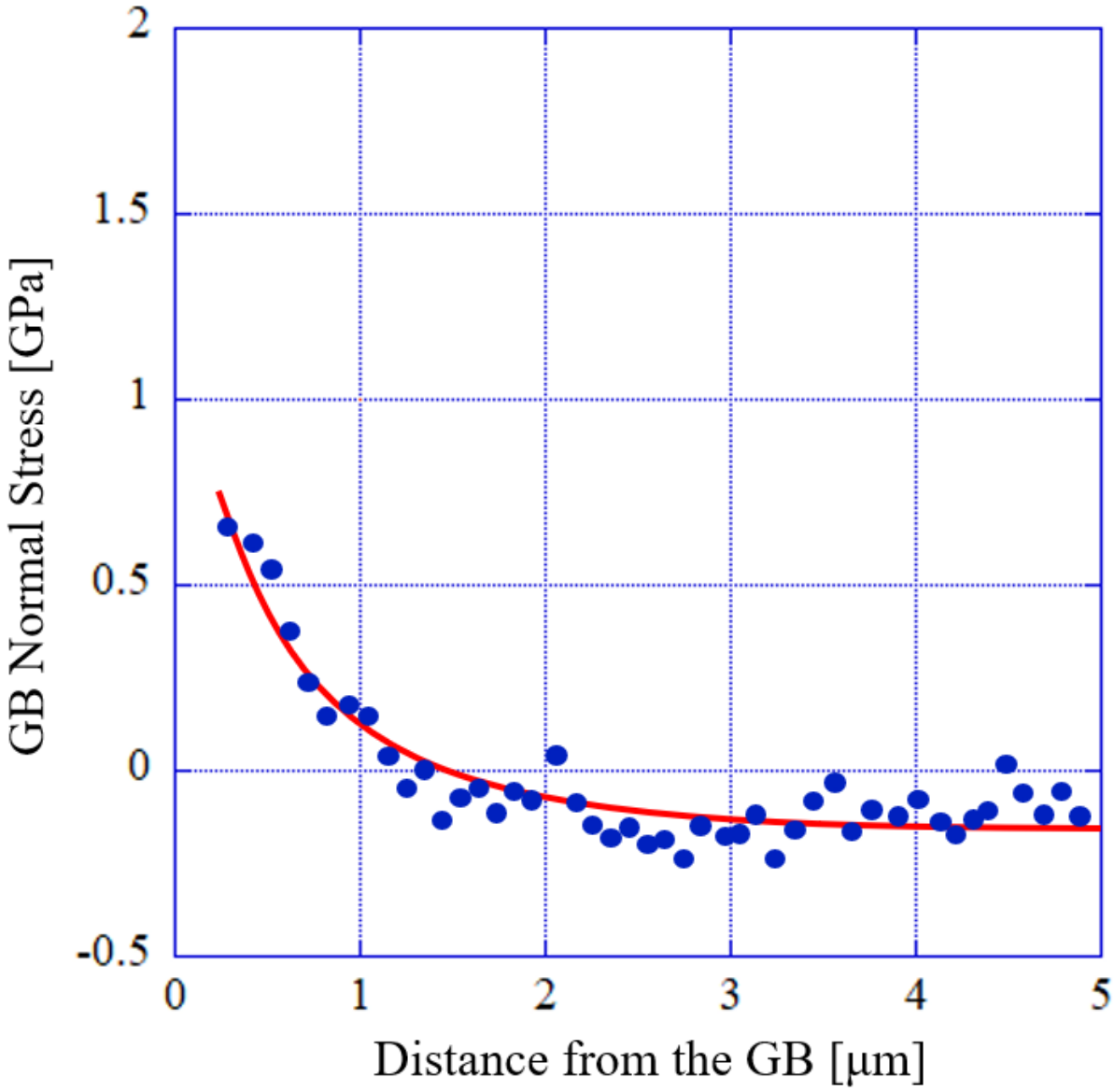

Figure D.24: Tensile stress normal to the grain boundary as a function of distance from the grain boundary in ASCC2 Fe13Cr15Ni 5 dpa tensile bar sample at site ASCC2-24

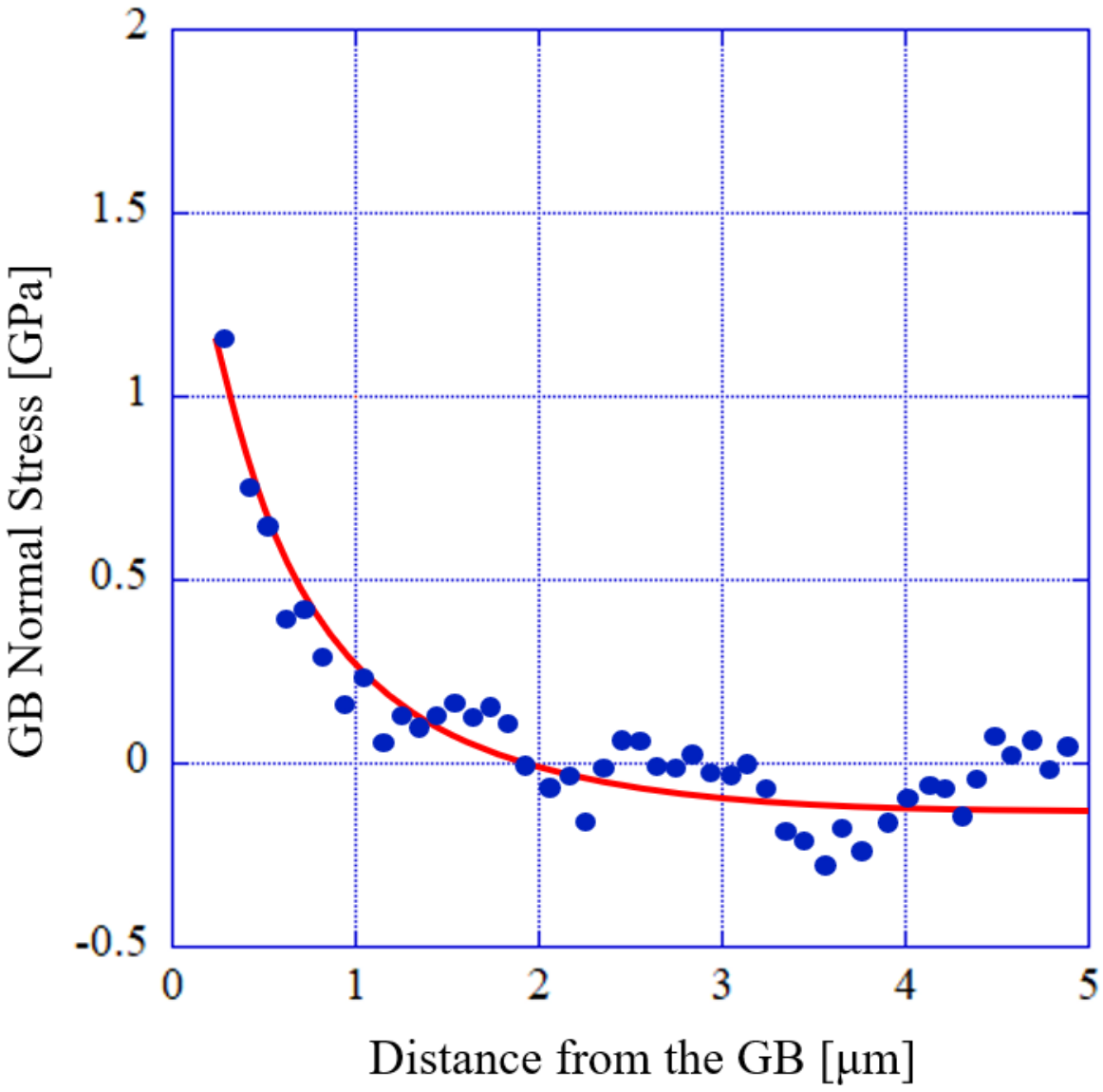

Figure D.25: Tensile stress normal to the grain boundary as a function of distance from the grain boundary in ASCC2 Fe13Cr15Ni 5 dpa tensile bar sample at site ASCC2-25

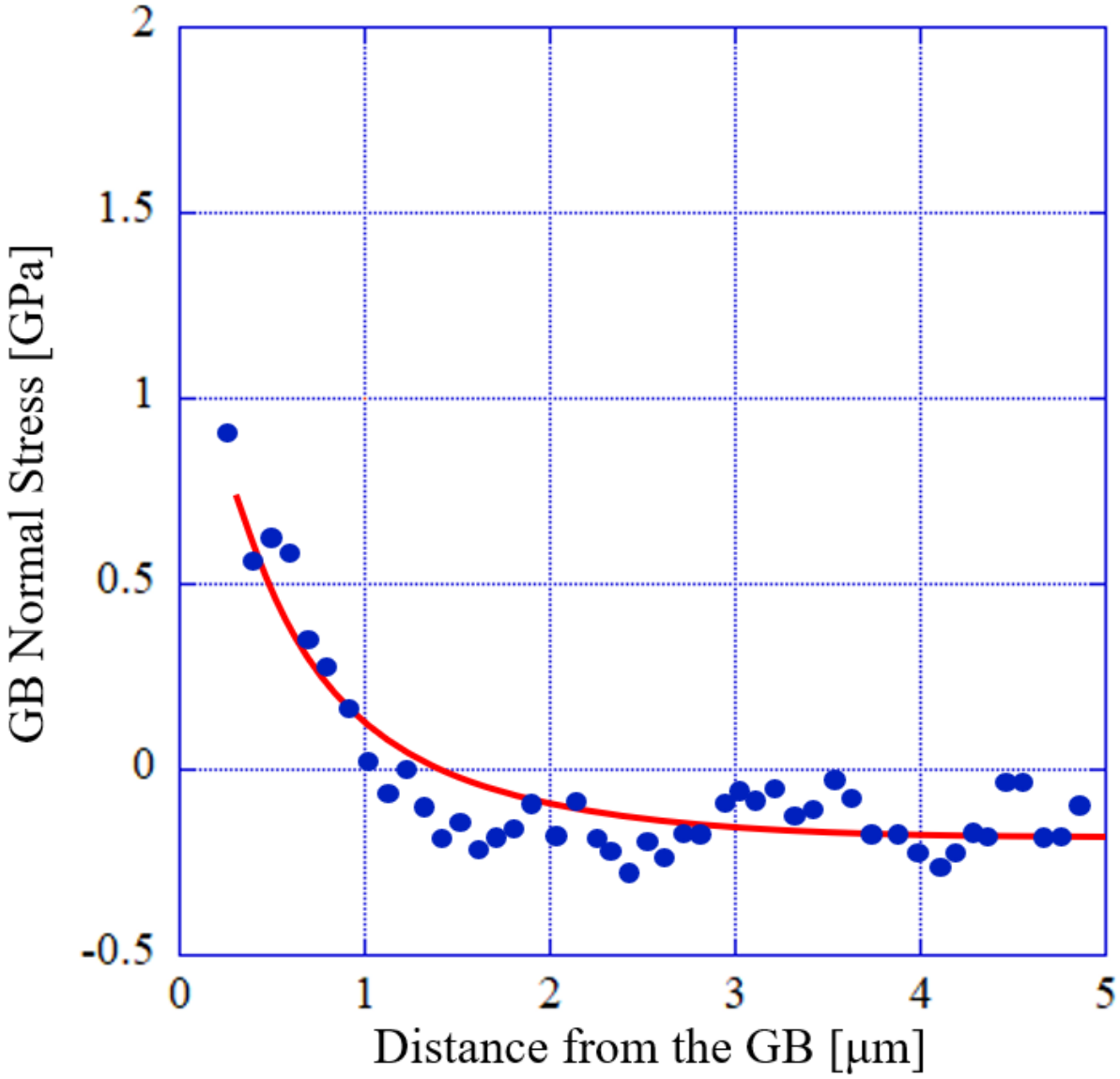

Figure D.26: Tensile stress normal to the grain boundary as a function of distance from the grain boundary in ASCC2 Fe13Cr15Ni 5 dpa tensile bar sample at site ASCC2-26

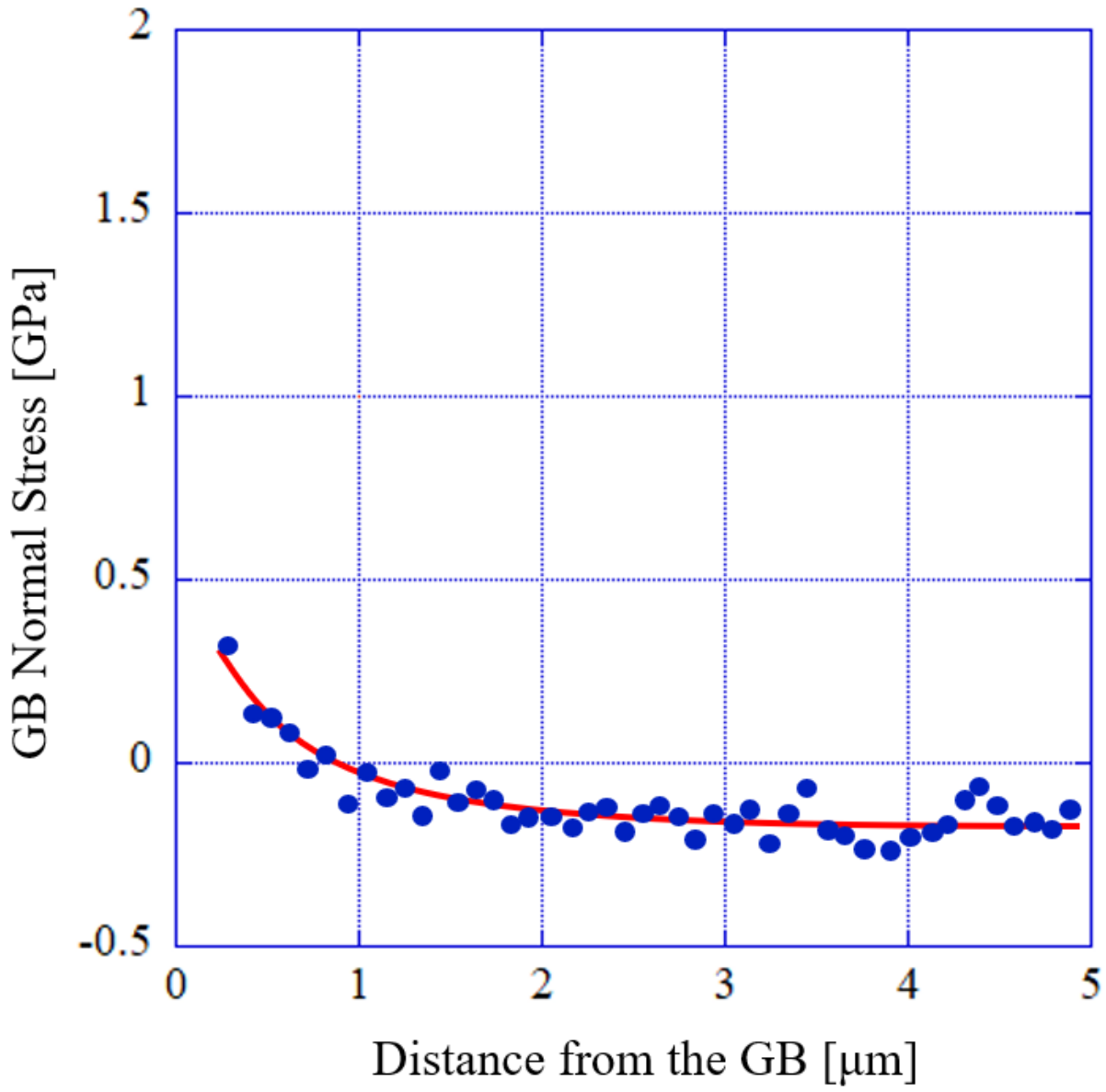

Figure D.27: Tensile stress normal to the grain boundary as a function of distance from the grain boundary in ASCC2 Fe13Cr15Ni 5 dpa tensile bar sample at site ASCC2-27

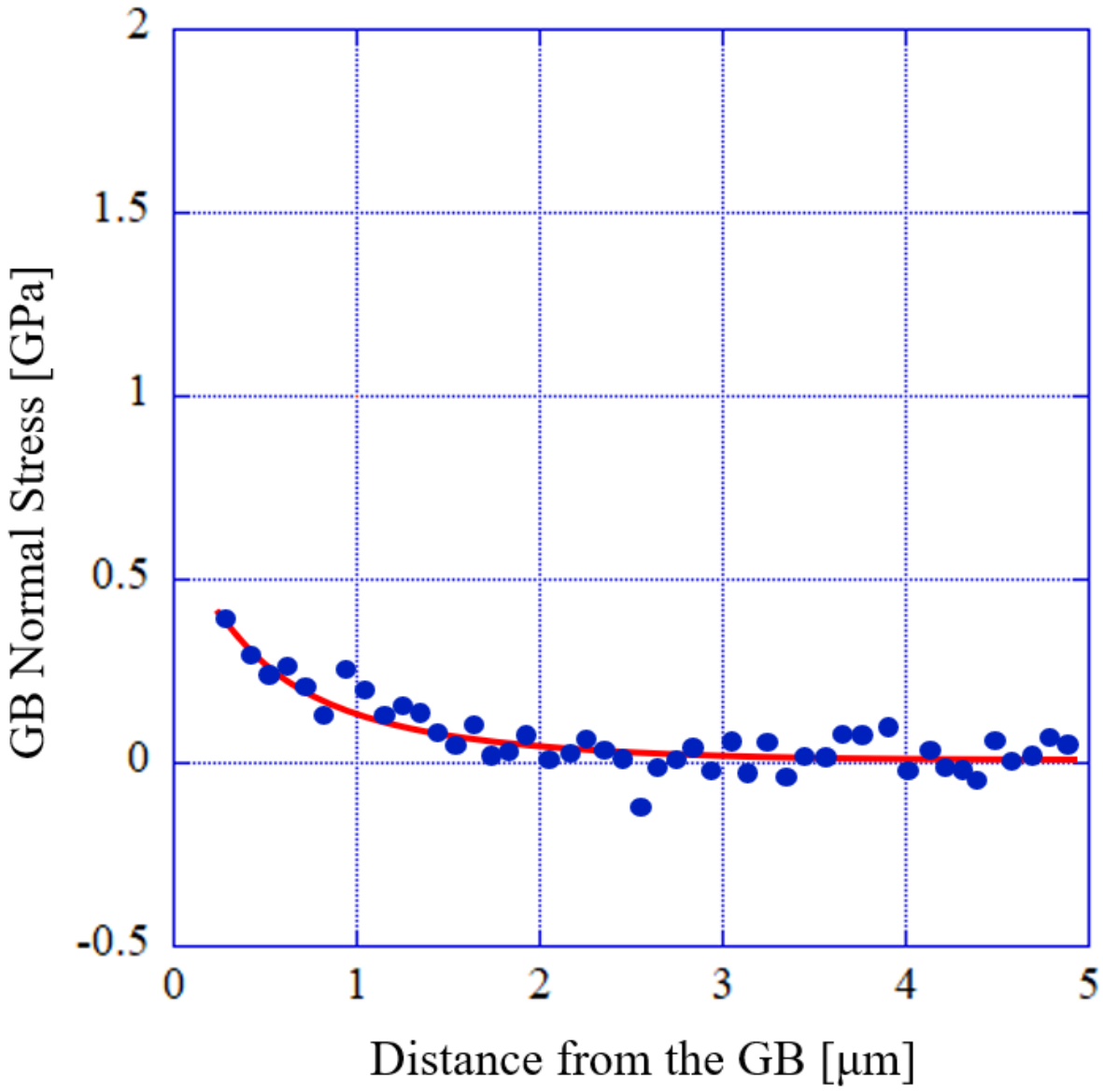

Figure D.28: Tensile stress normal to the grain boundary as a function of distance from the grain boundary in ASCC2 Fe13Cr15Ni 5 dpa tensile bar sample at site ASCC2-28

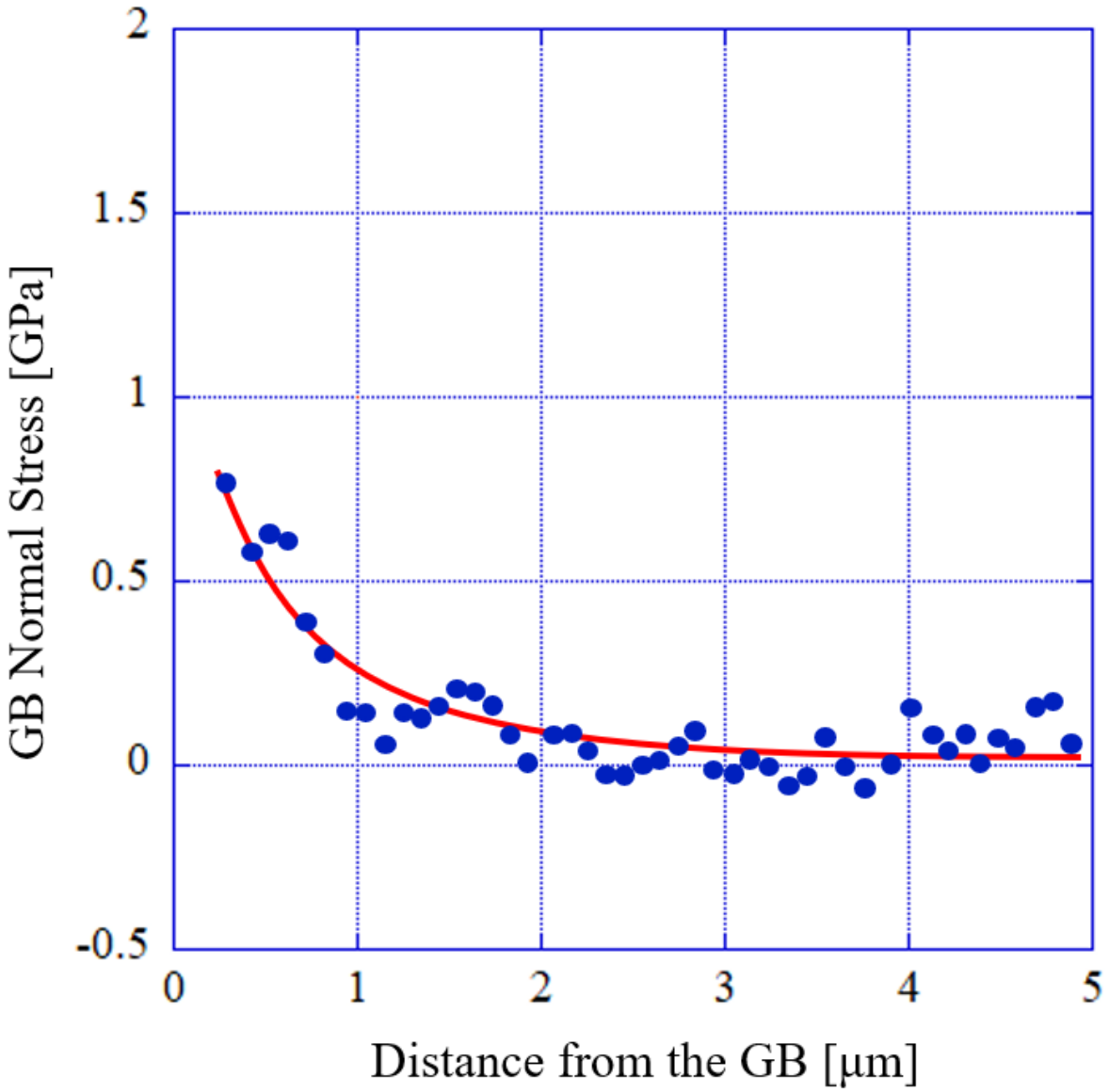

Figure D.29: Tensile stress normal to the grain boundary as a function of distance from the grain boundary in ASCC2 Fe13Cr15Ni 5 dpa tensile bar sample at site ASCC2-29

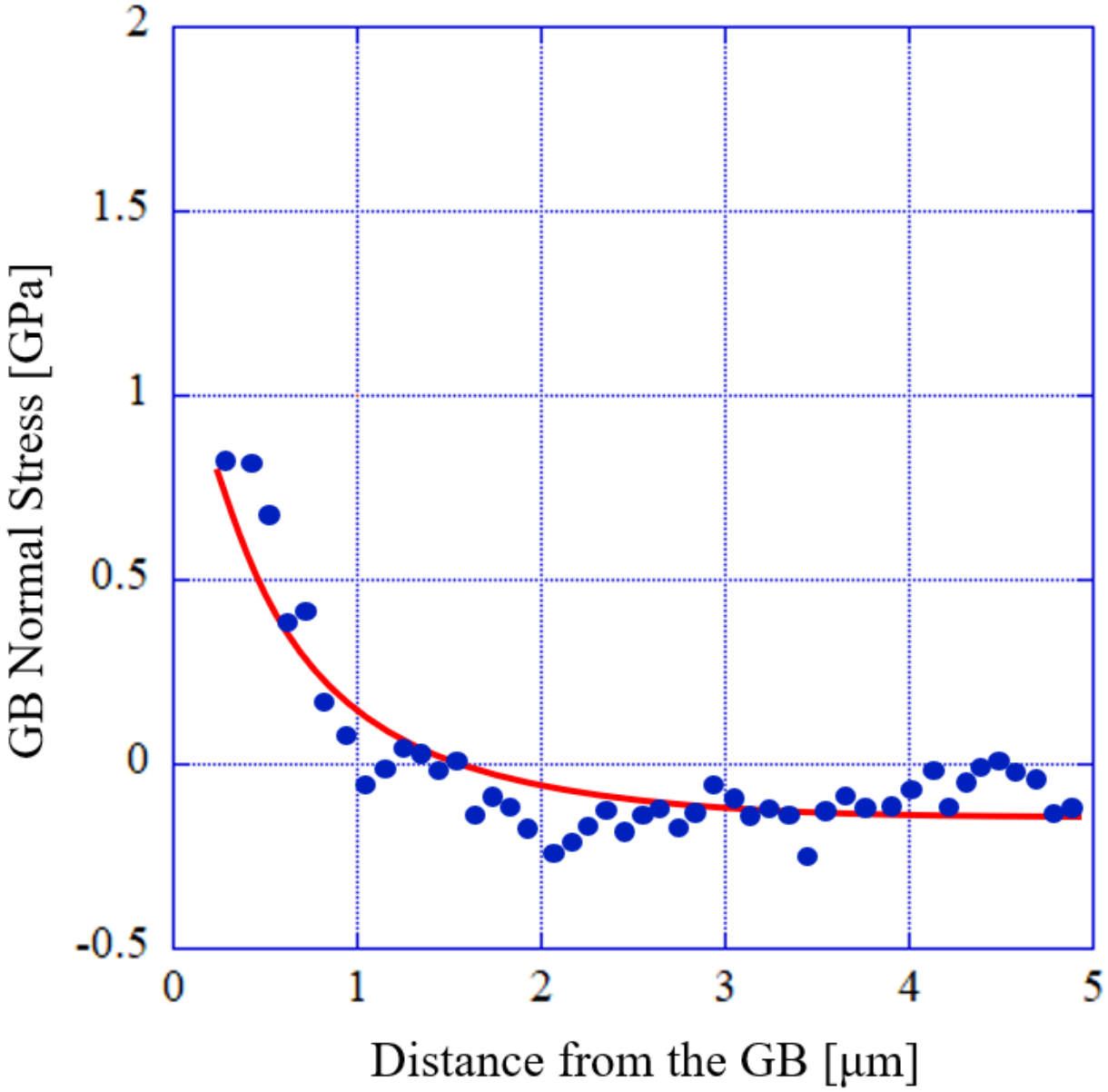

Figure D.30: Tensile stress normal to the grain boundary as a function of distance from the grain boundary in ASCC2 Fe13Cr15Ni 5 dpa tensile bar sample at site ASCC2-30

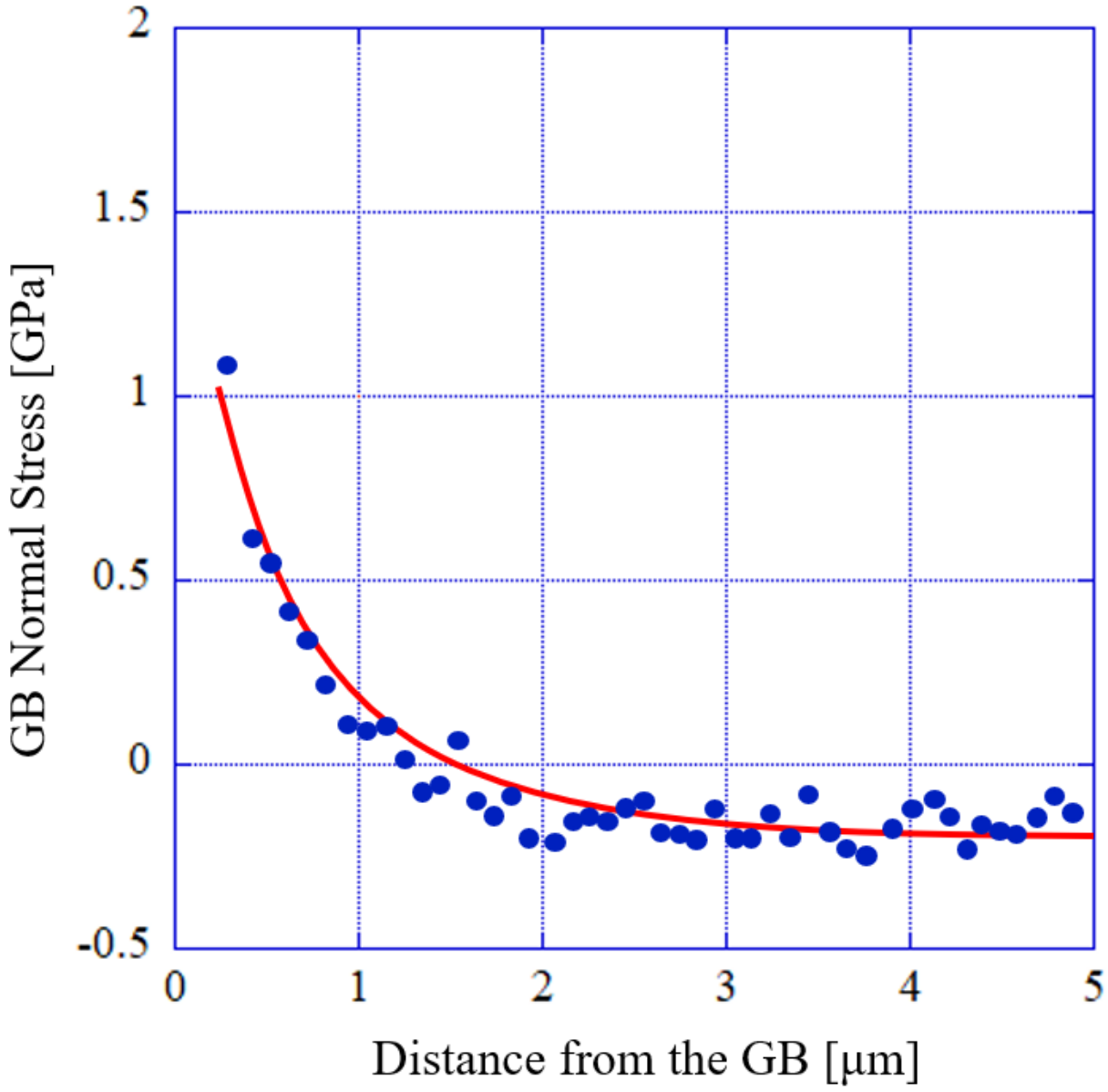

Figure D.31: Tensile stress normal to the grain boundary as a function of distance from the grain boundary in ASCC2 Fe13Cr15Ni 5 dpa tensile bar sample at site ASCC2-31

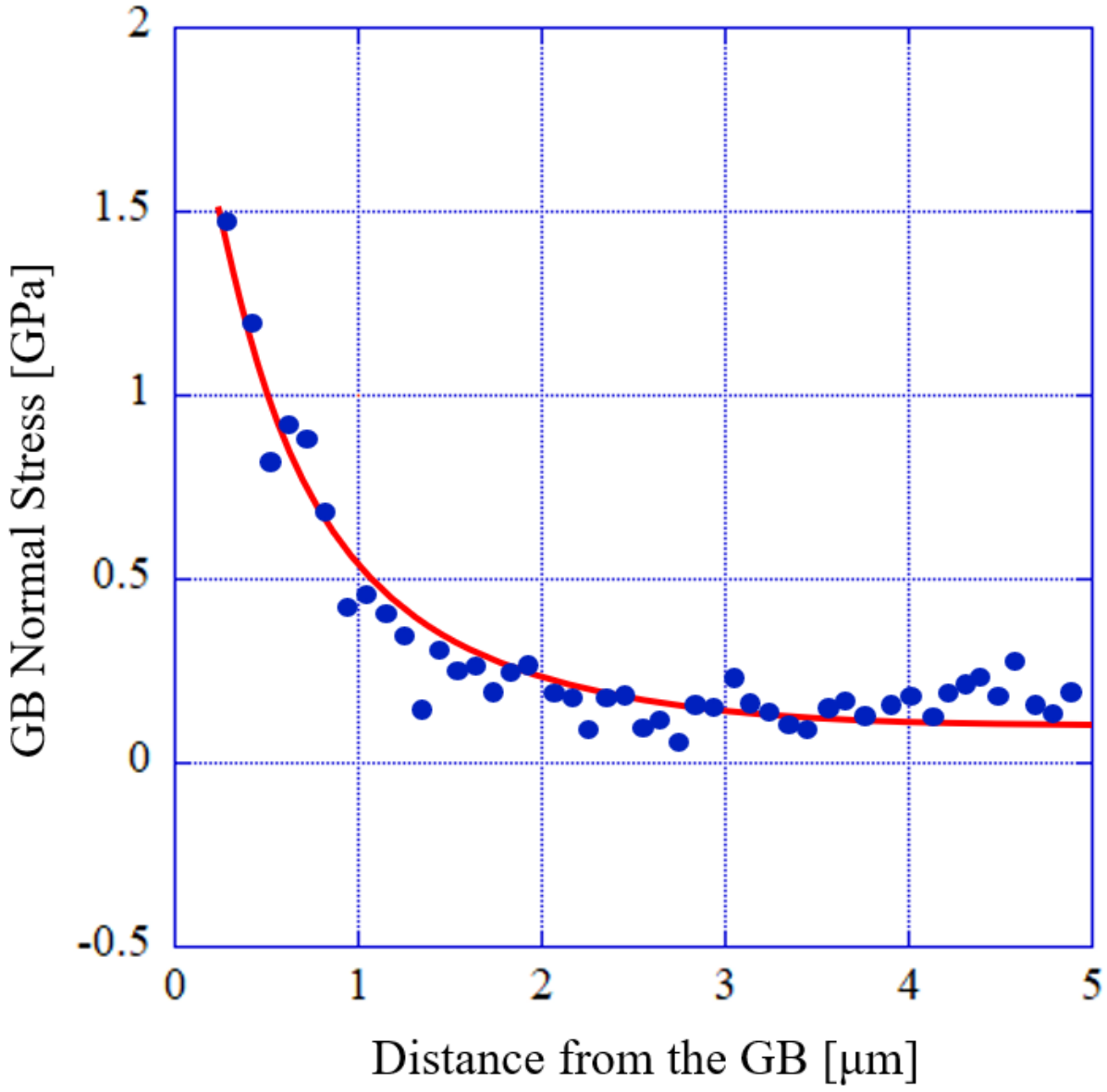

Figure D.32: Tensile stress normal to the grain boundary as a function of distance from the grain boundary in ASCC2 Fe13Cr15Ni 5 dpa tensile bar sample at site ASCC2-32

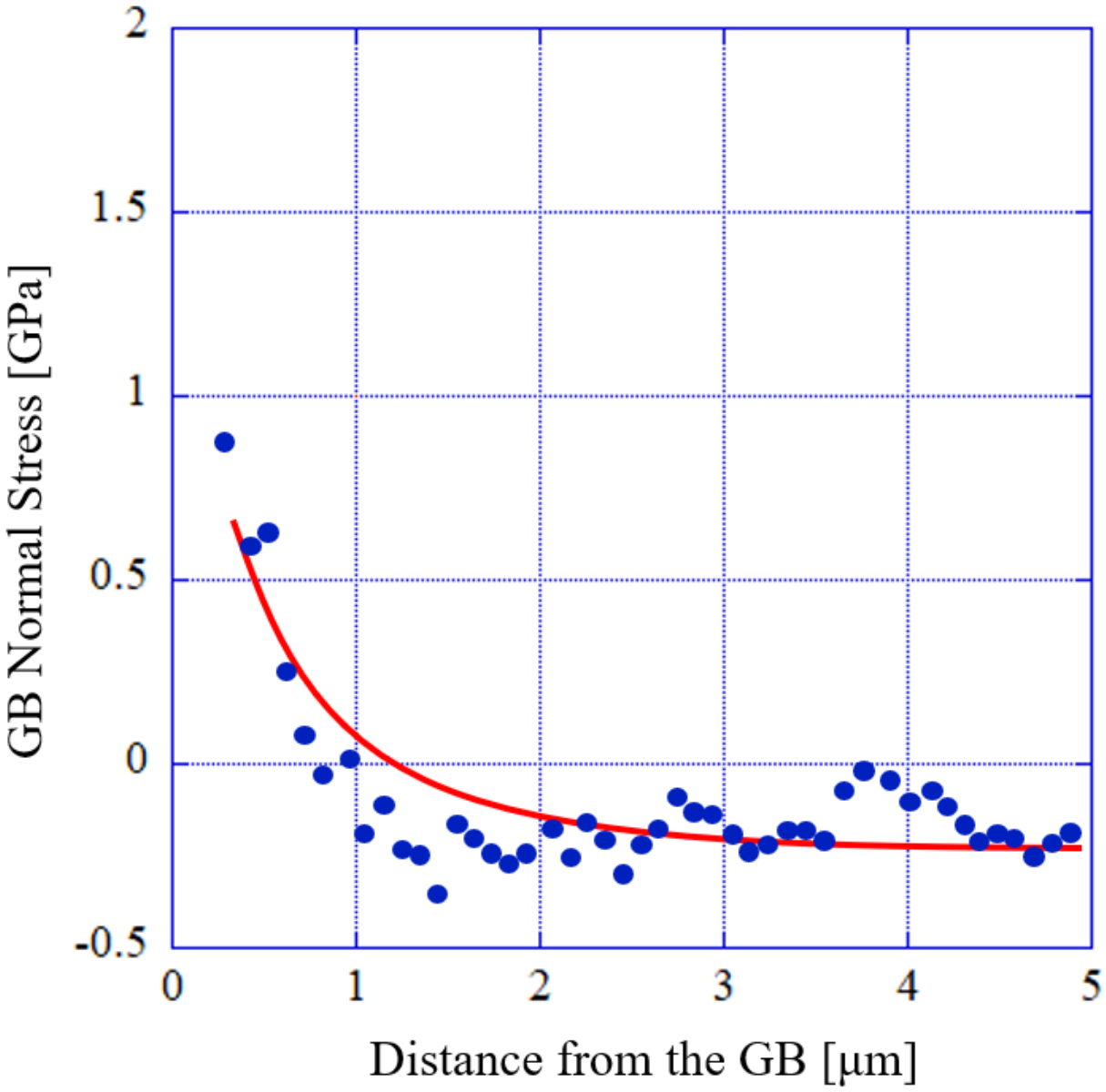

Figure D.33: Tensile stress normal to the grain boundary as a function of distance from the grain boundary in ASCC2 Fe13Cr15Ni 5 dpa tensile bar sample at site ASCC2-33

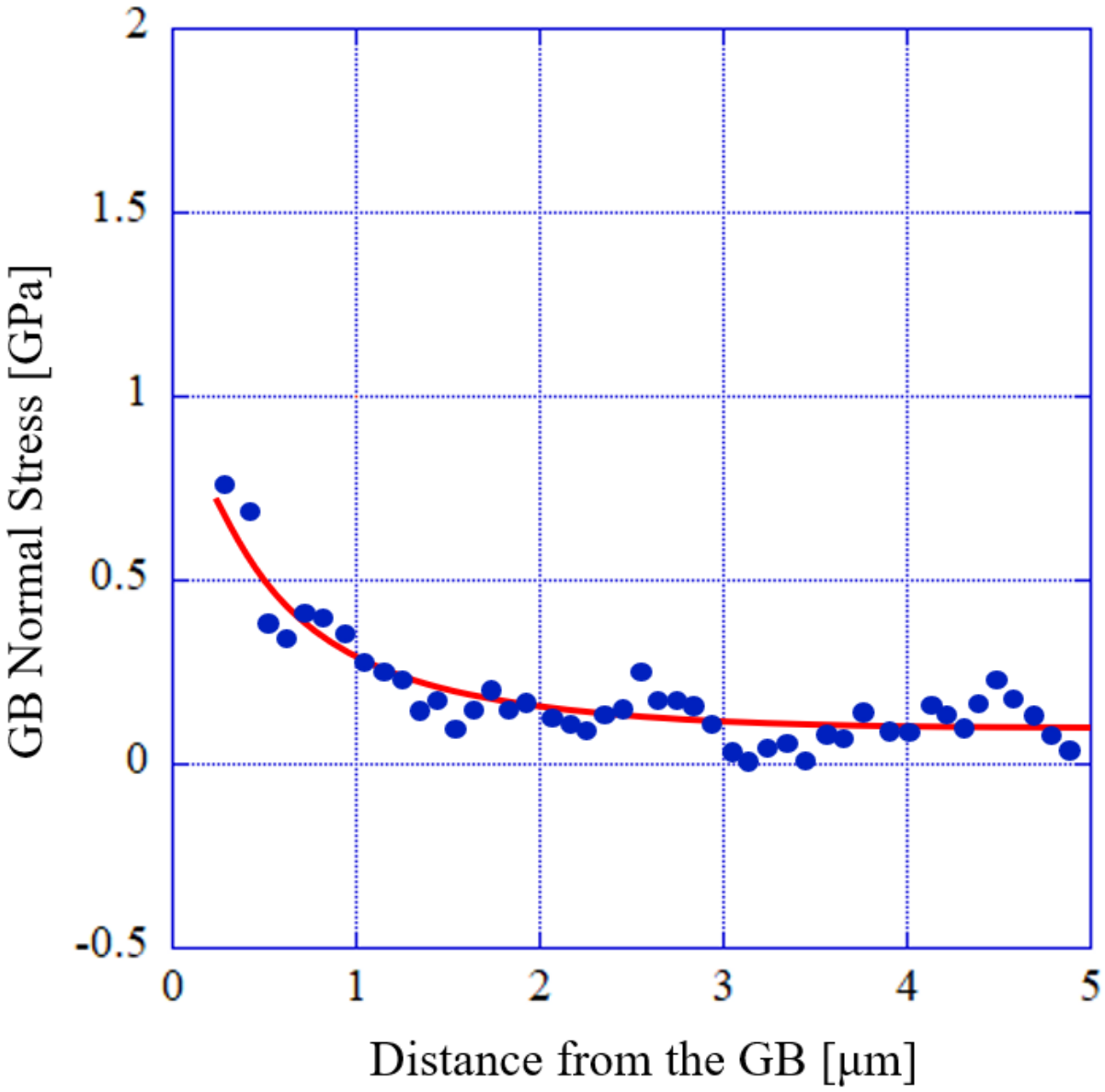

Figure D.34: Tensile stress normal to the grain boundary as a function of distance from the grain boundary in ASCC2 Fe13Cr15Ni 5 dpa tensile bar sample at site ASCC2-34

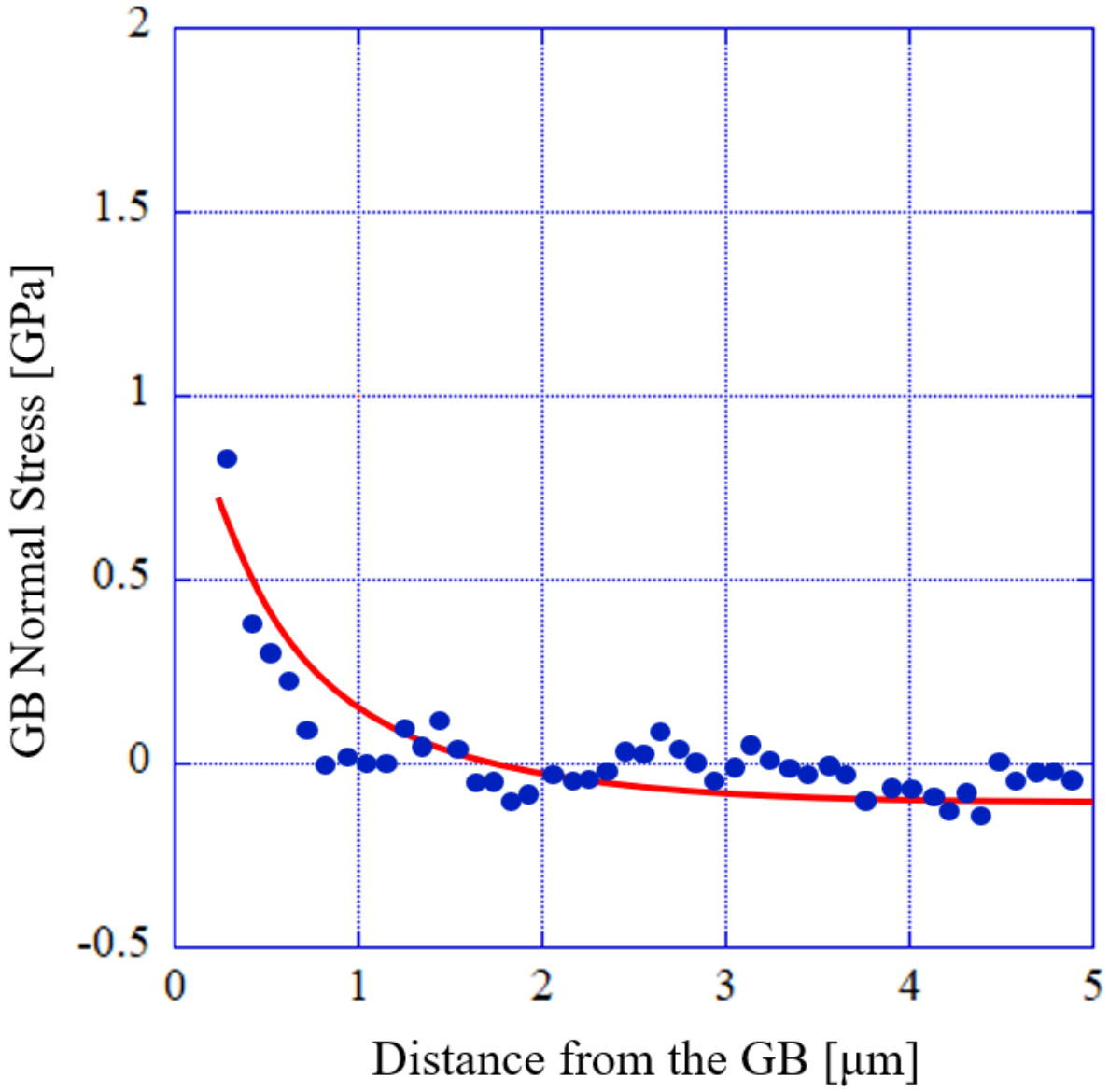

Figure D.35: Tensile stress normal to the grain boundary as a function of distance from the grain boundary in ASCC2 Fe13Cr15Ni 5 dpa tensile bar sample at site ASCC2-35

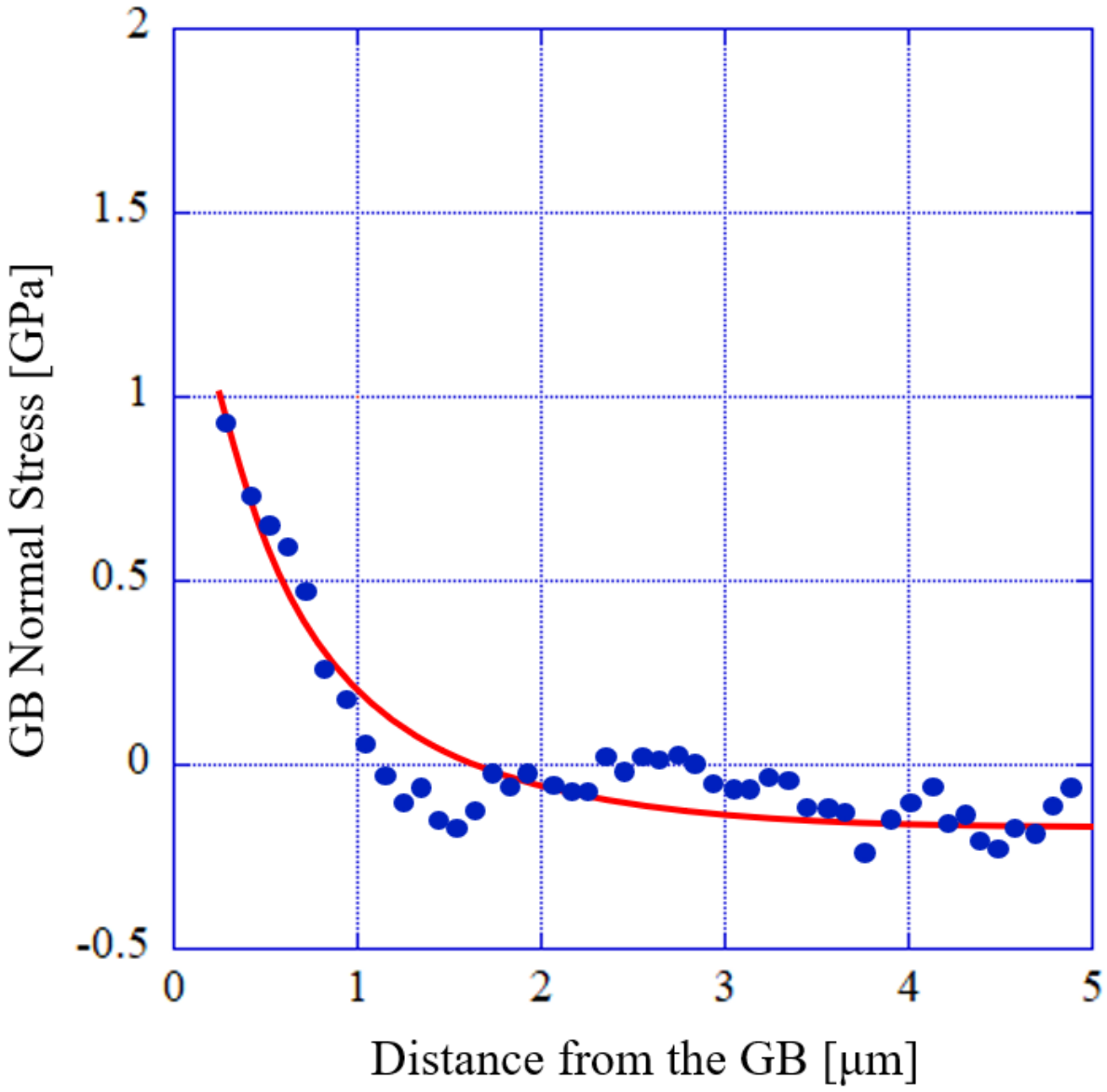

Figure D.36: Tensile stress normal to the grain boundary as a function of distance from the grain boundary in ASCC2 Fe13Cr15Ni 5 dpa tensile bar sample at site ASCC2-36

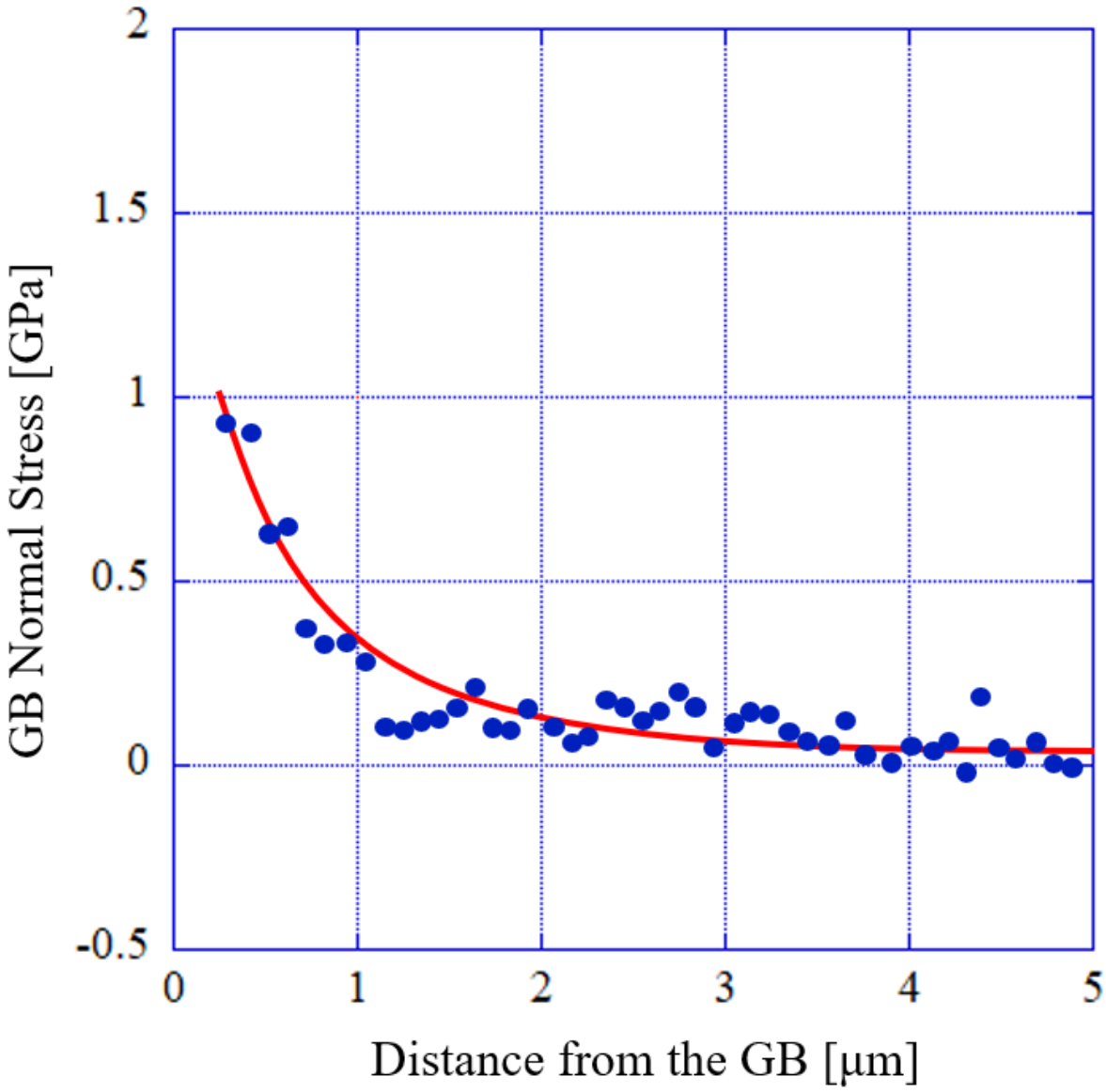

Figure D.37: Tensile stress normal to the grain boundary as a function of distance from the grain boundary in ASCC2 Fe13Cr15Ni 5 dpa tensile bar sample at site ASCC2-37

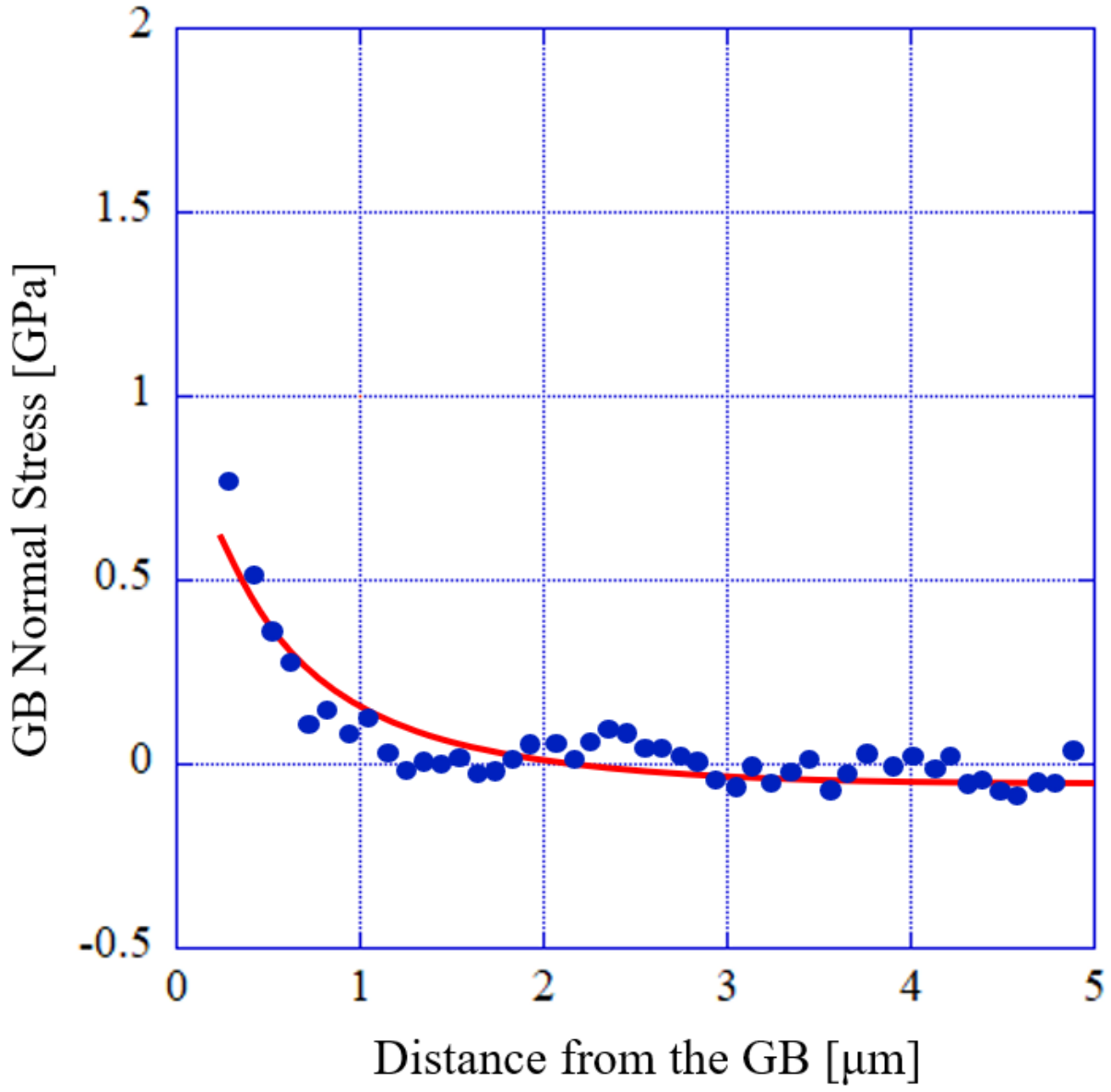

Figure D.38: Tensile stress normal to the grain boundary as a function of distance from the grain boundary in ASCC2 Fe13Cr15Ni 5 dpa tensile bar sample at site ASCC2-38

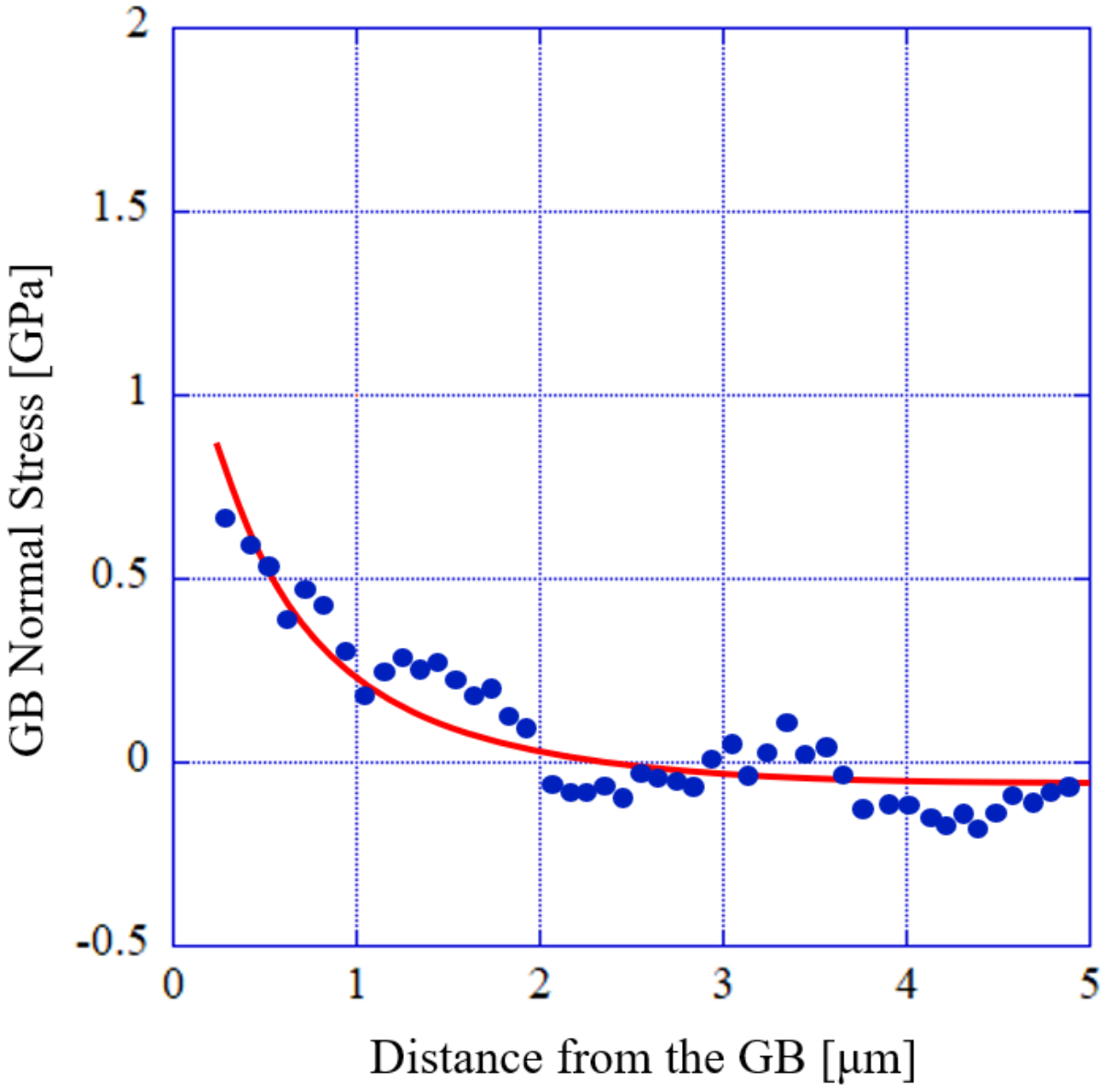

Figure D.39: Tensile stress normal to the grain boundary as a function of distance from the grain boundary in ASCC2 Fe13Cr15Ni 5 dpa tensile bar sample at site ASCC2-39

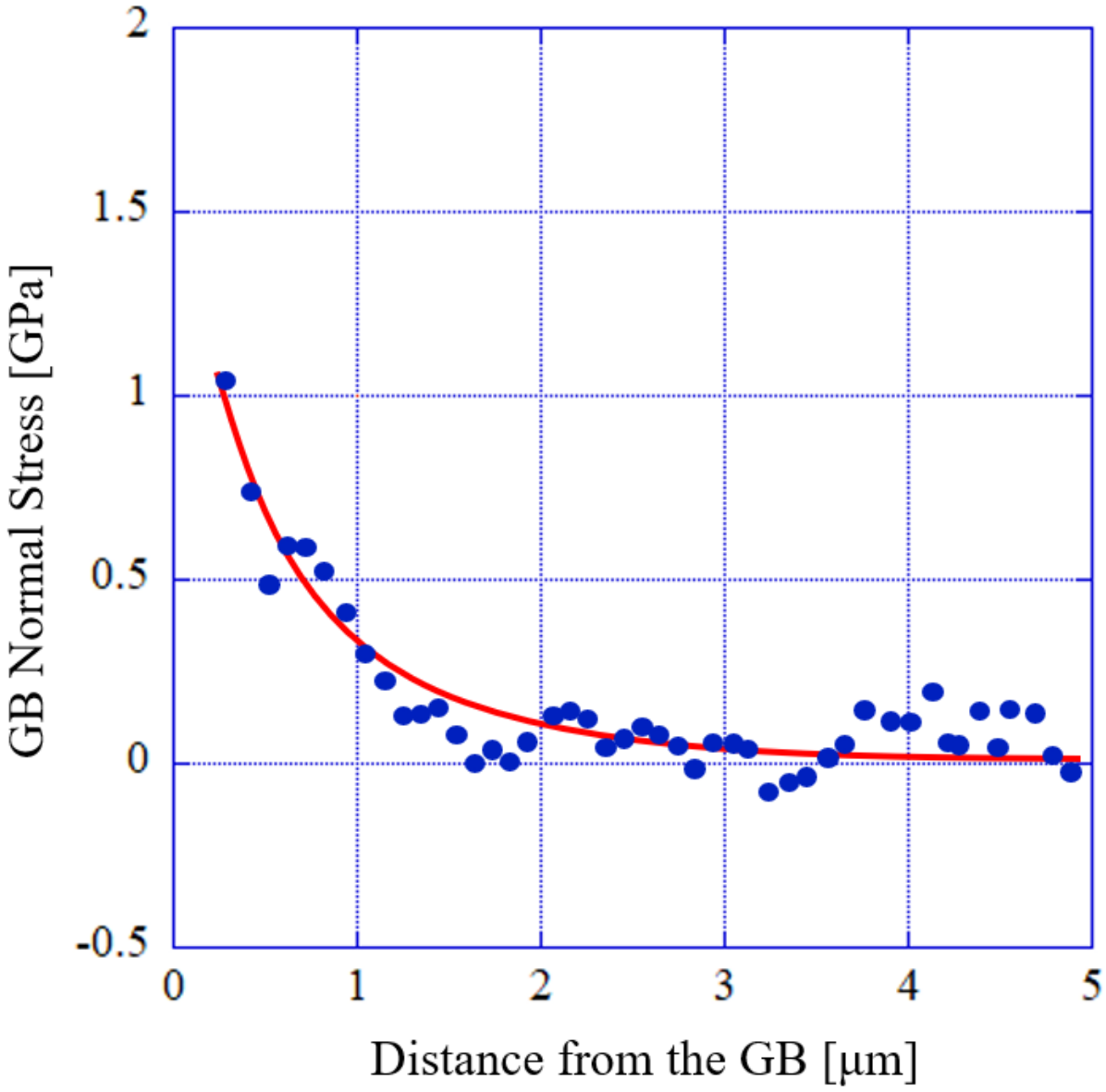

Figure D.40: Tensile stress normal to the grain boundary as a function of distance from the grain boundary in ASCC2 Fe13Cr15Ni 5 dpa tensile bar sample at site ASCC2-40

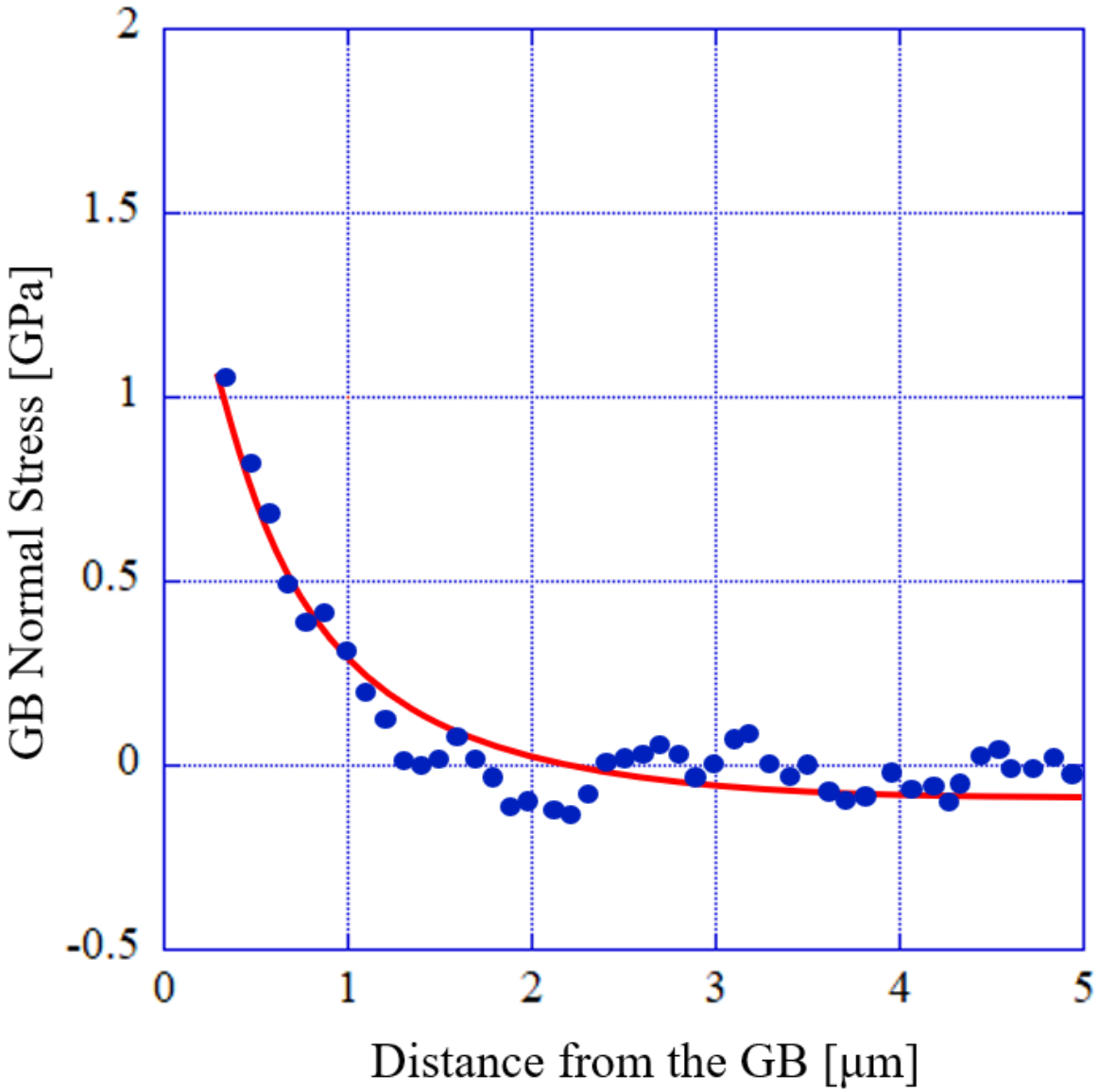

Figure D.41: Tensile stress normal to the grain boundary as a function of distance from the grain boundary in ASCC2 Fe13Cr15Ni 5 dpa tensile bar sample at site ASCC2-41

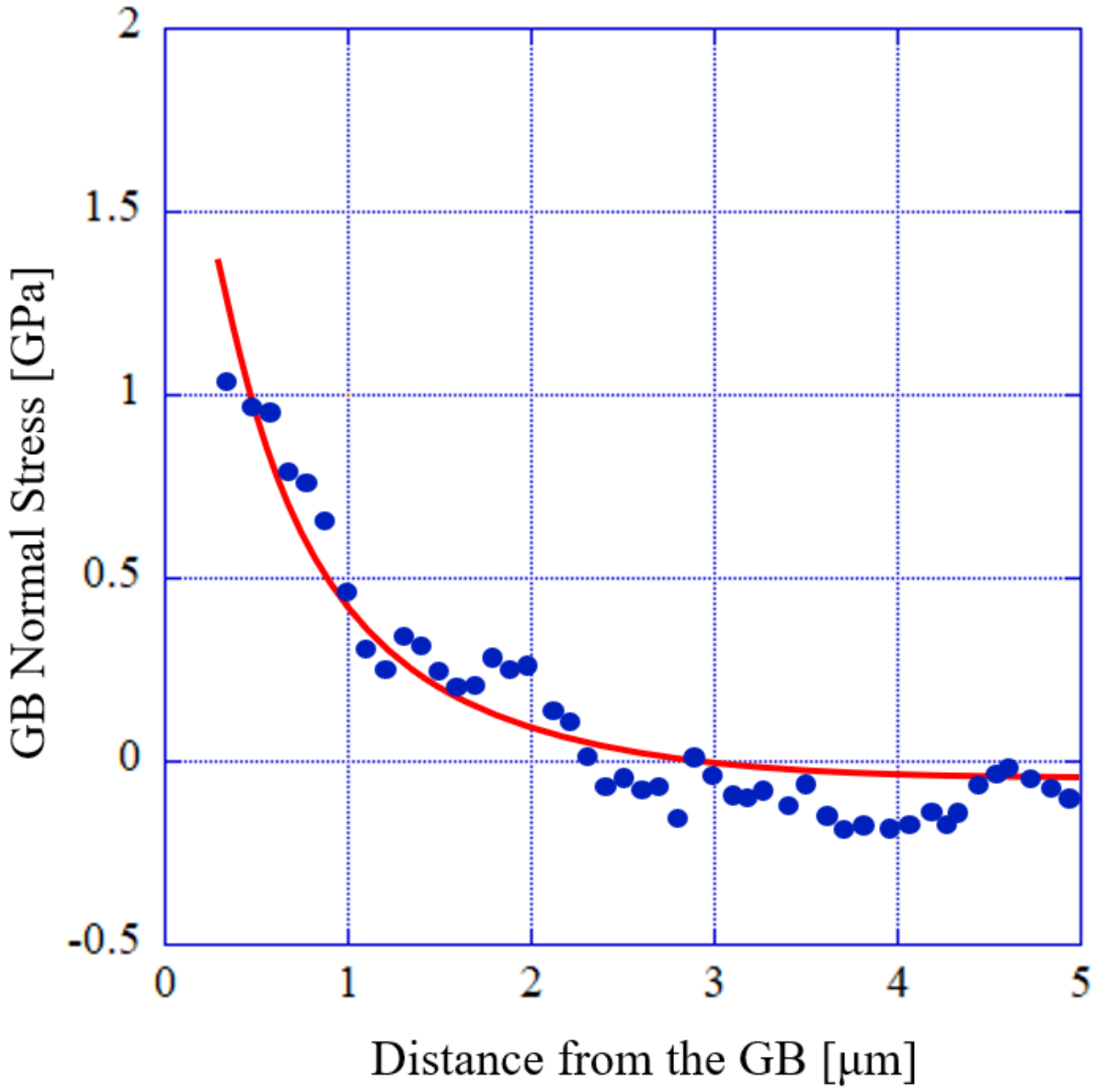

Figure D.42: Tensile stress normal to the grain boundary as a function of distance from the grain boundary in ASCC2 Fe13Cr15Ni 5 dpa tensile bar sample at site ASCC2-42

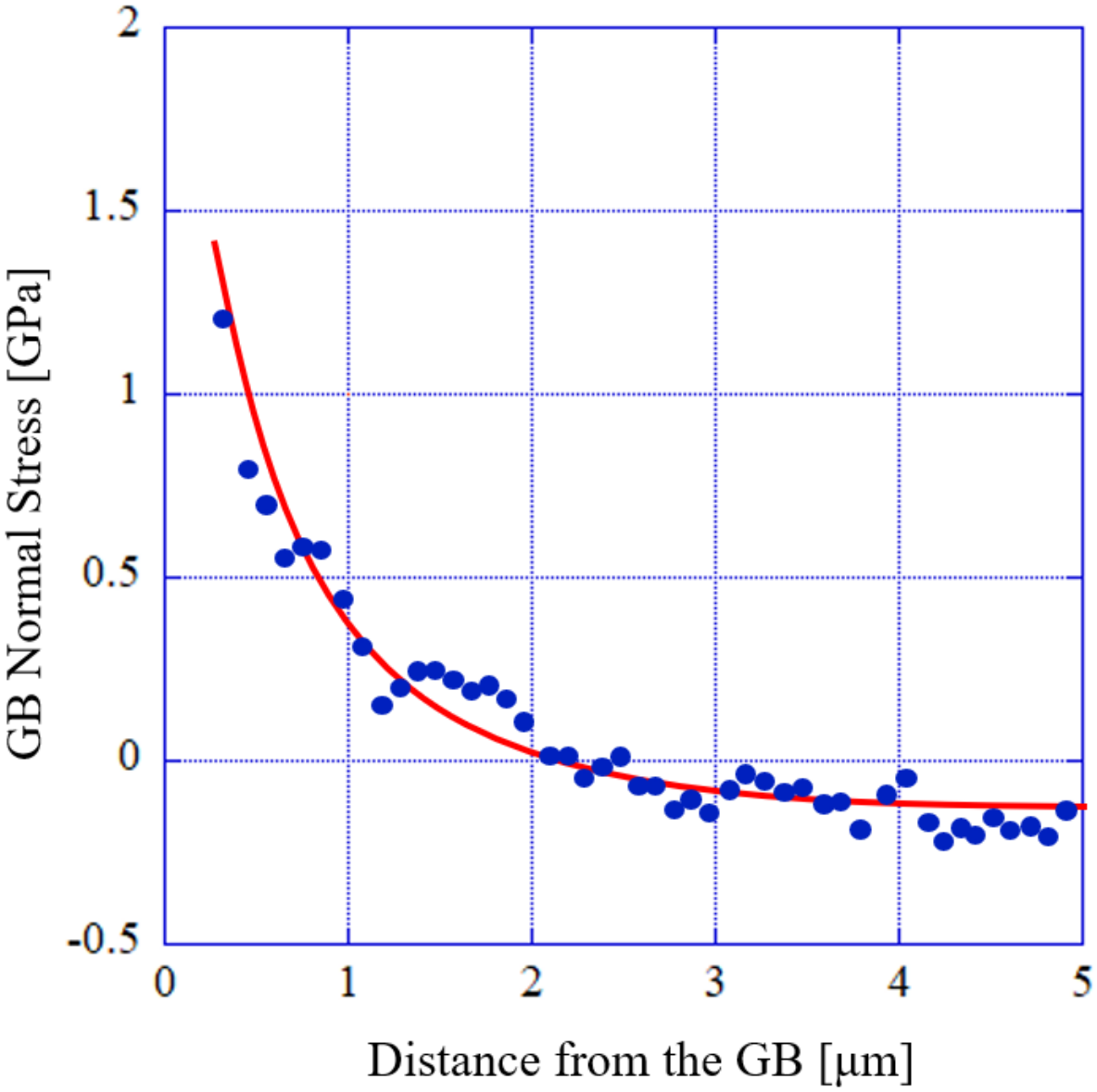

Figure D.43: Tensile stress normal to the grain boundary as a function of distance from the grain boundary in ASCC2 Fe13Cr15Ni 5 dpa tensile bar sample at site ASCC2-43

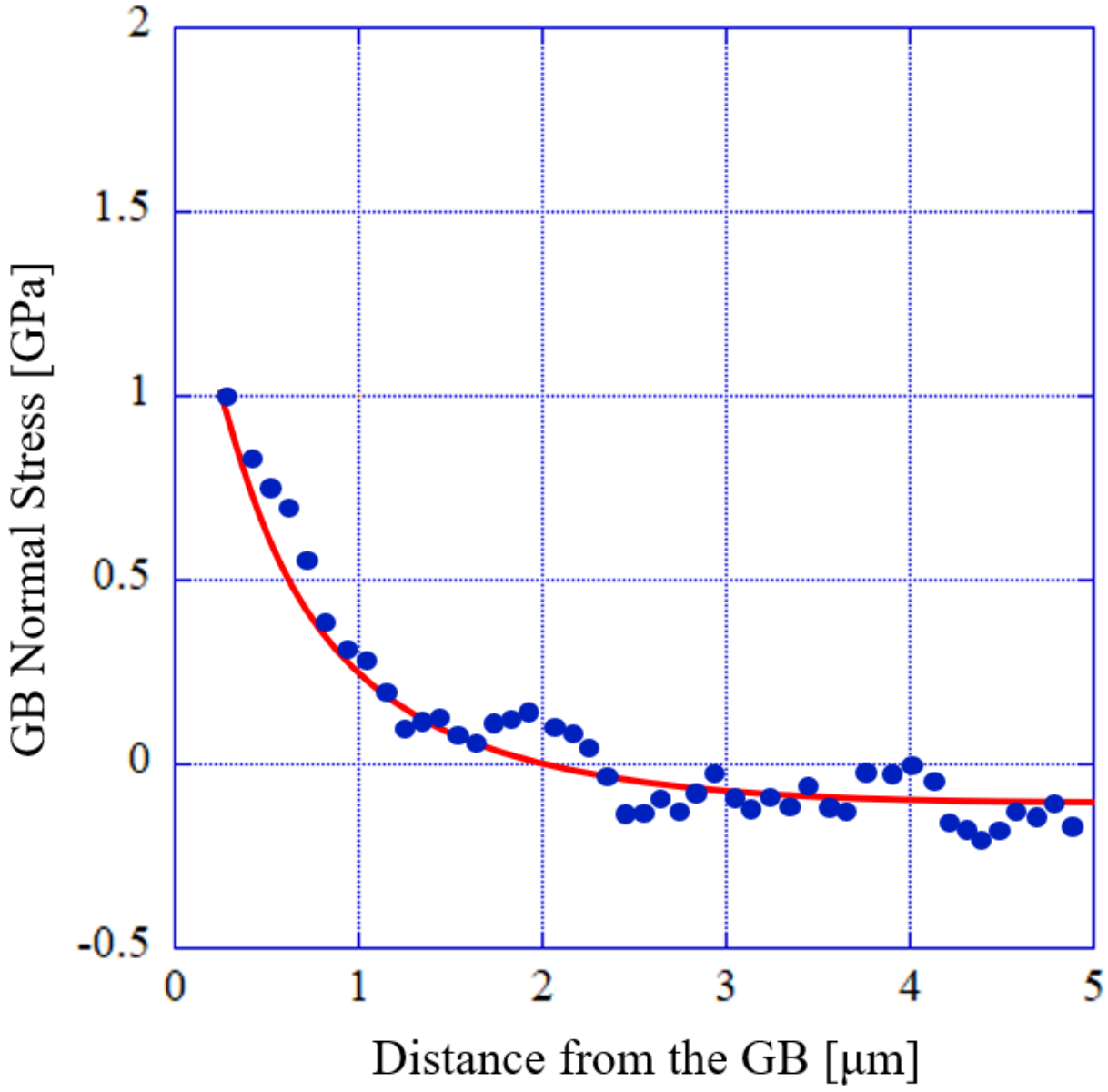

Figure D.44: Tensile stress normal to the grain boundary as a function of distance from the grain boundary in ASCC2 Fe13Cr15Ni 5 dpa tensile bar sample at site ASCC2-44

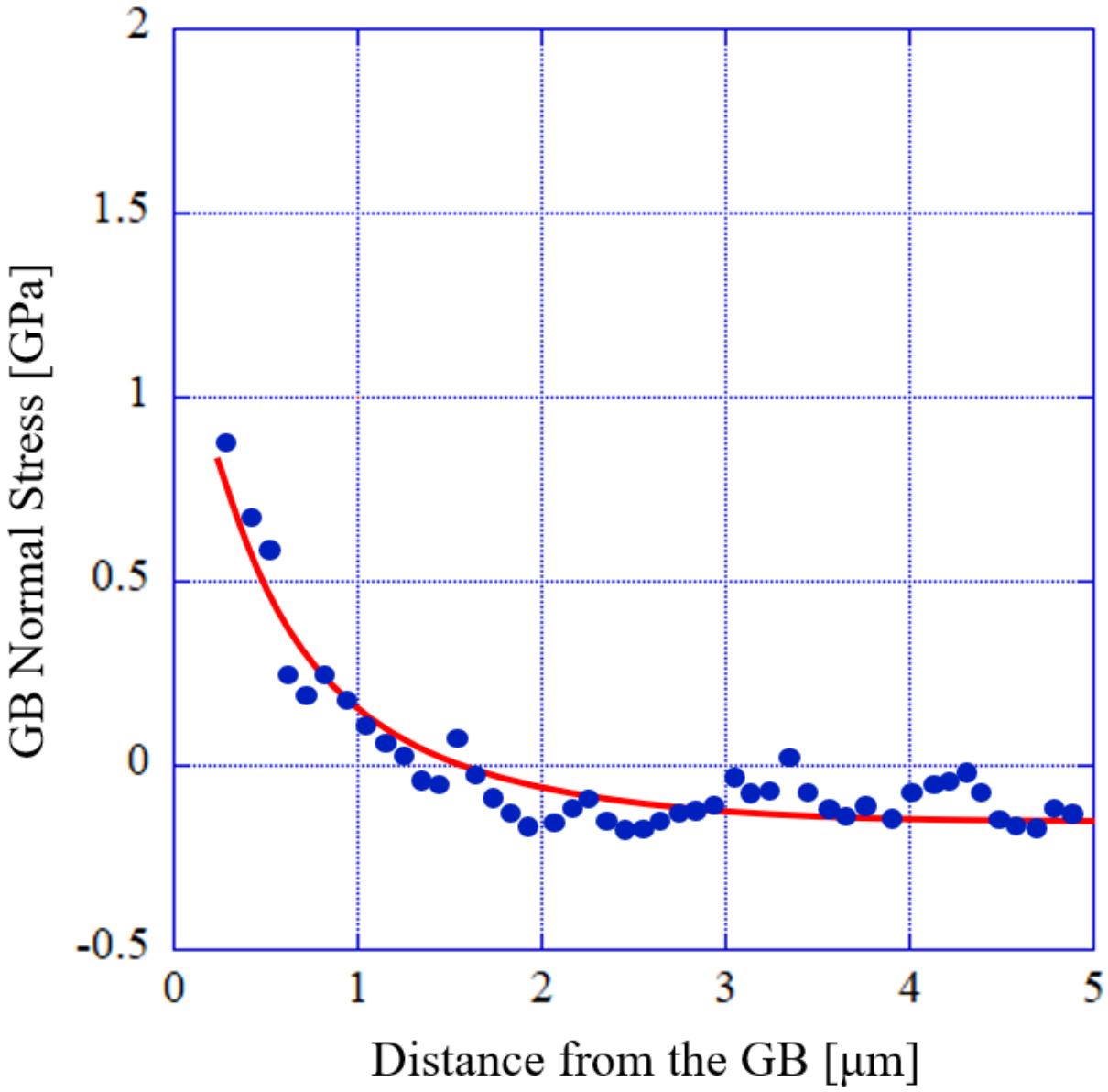

Figure D.45: Tensile stress normal to the grain boundary as a function of distance from the grain boundary in ASCC2 Fe13Cr15Ni 5 dpa tensile bar sample at site ASCC2-45

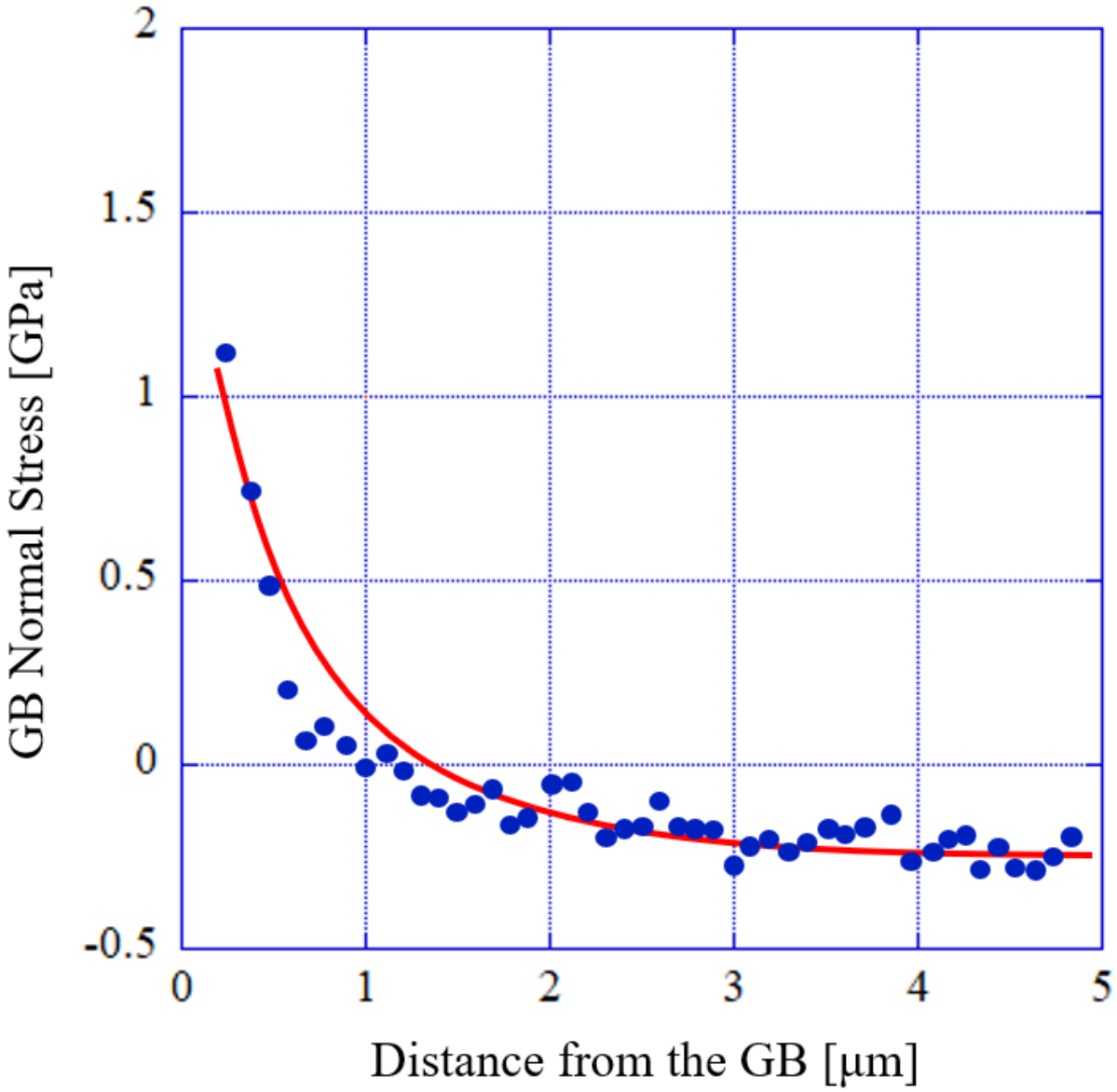

Figure D.46: Tensile stress normal to the grain boundary as a function of distance from the grain boundary in ASCC2 Fe13Cr15Ni 5 dpa tensile bar sample at site ASCC2-46

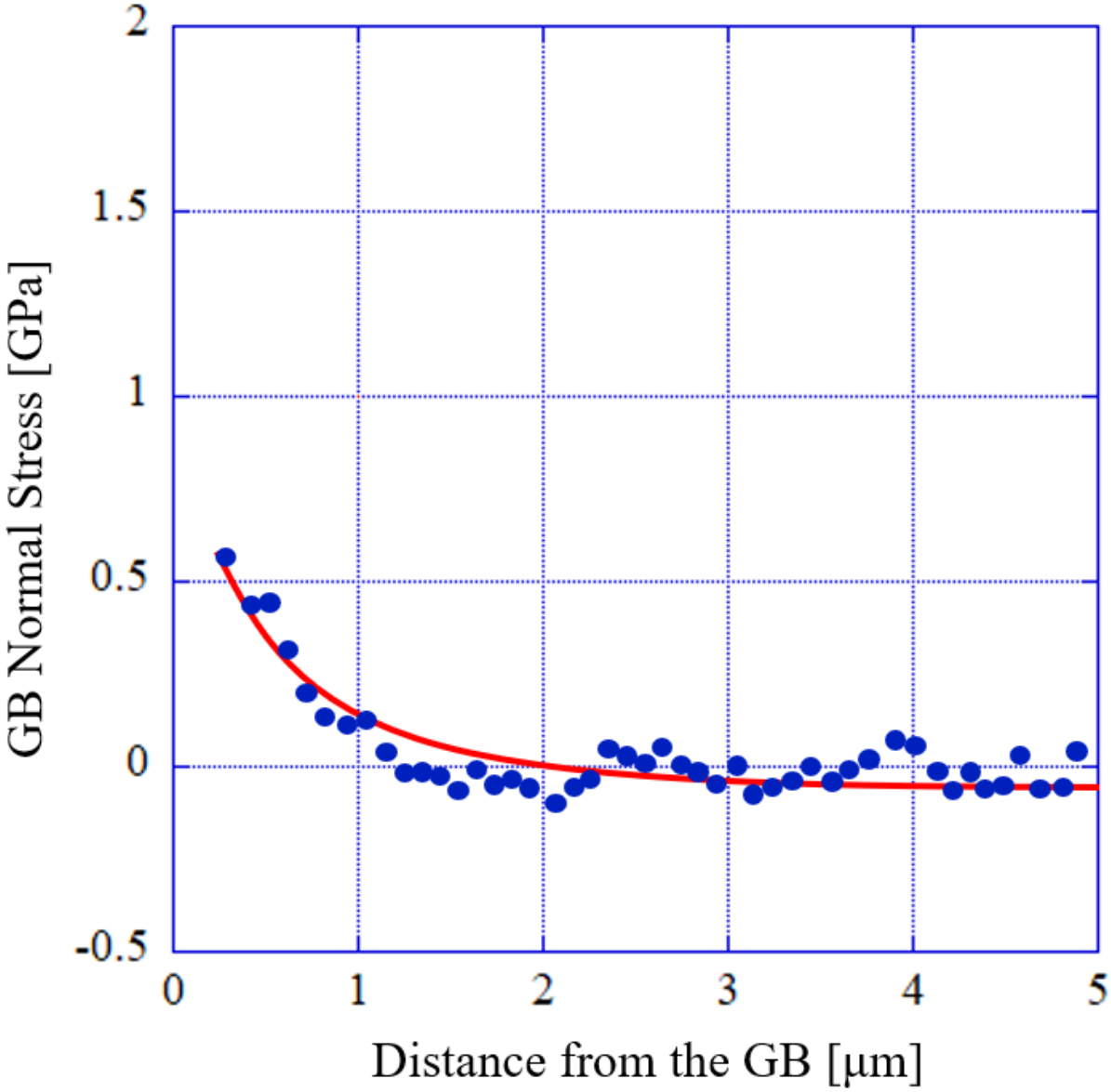

Figure D.47: Tensile stress normal to the grain boundary as a function of distance from the grain boundary in ASCC2 Fe13Cr15Ni 5 dpa tensile bar sample at site ASCC2-47

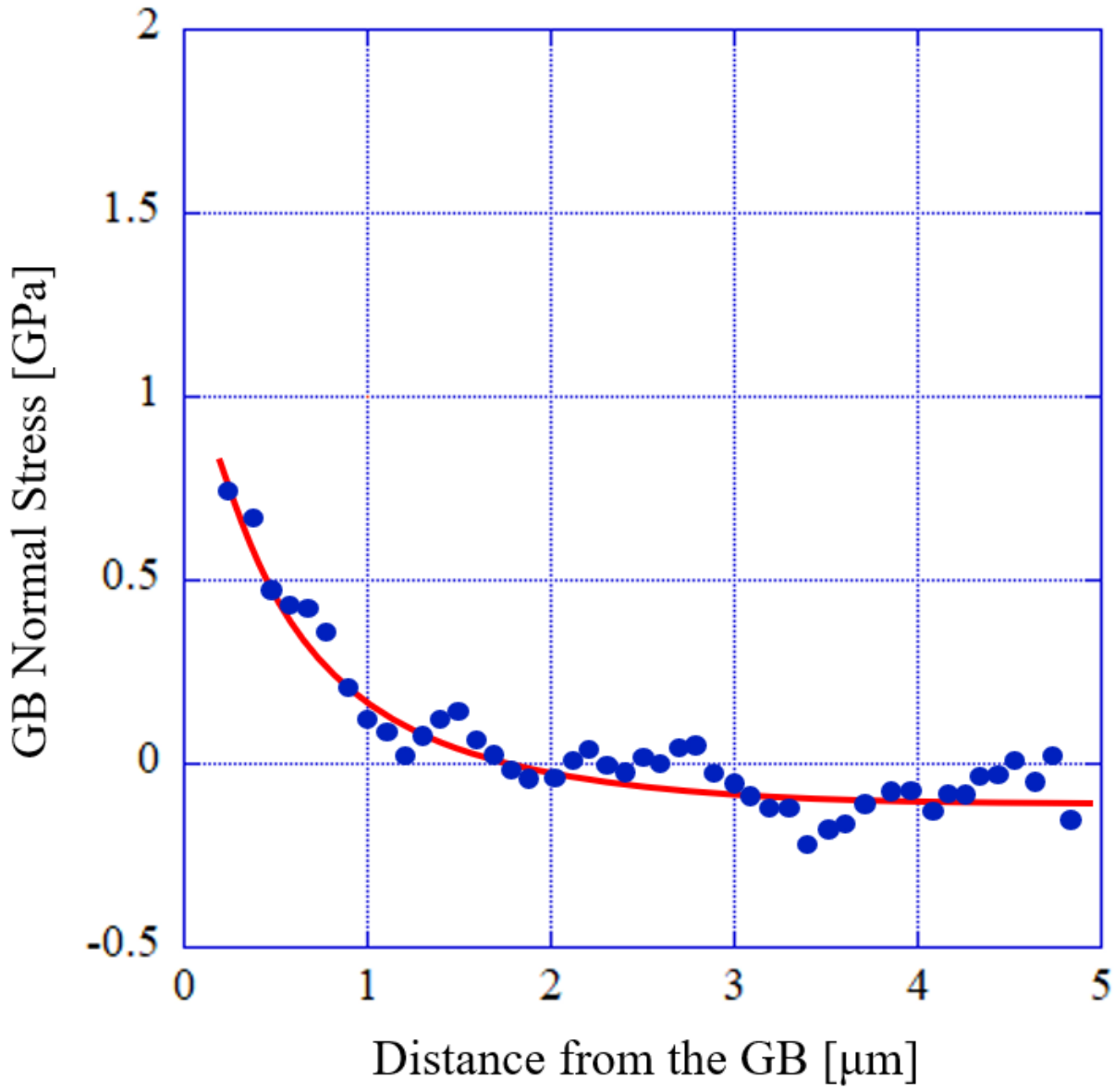

Figure D.48: Tensile stress normal to the grain boundary as a function of distance from the grain boundary in ASCC2 Fe13Cr15Ni 5 dpa tensile bar sample at site ASCC2-48

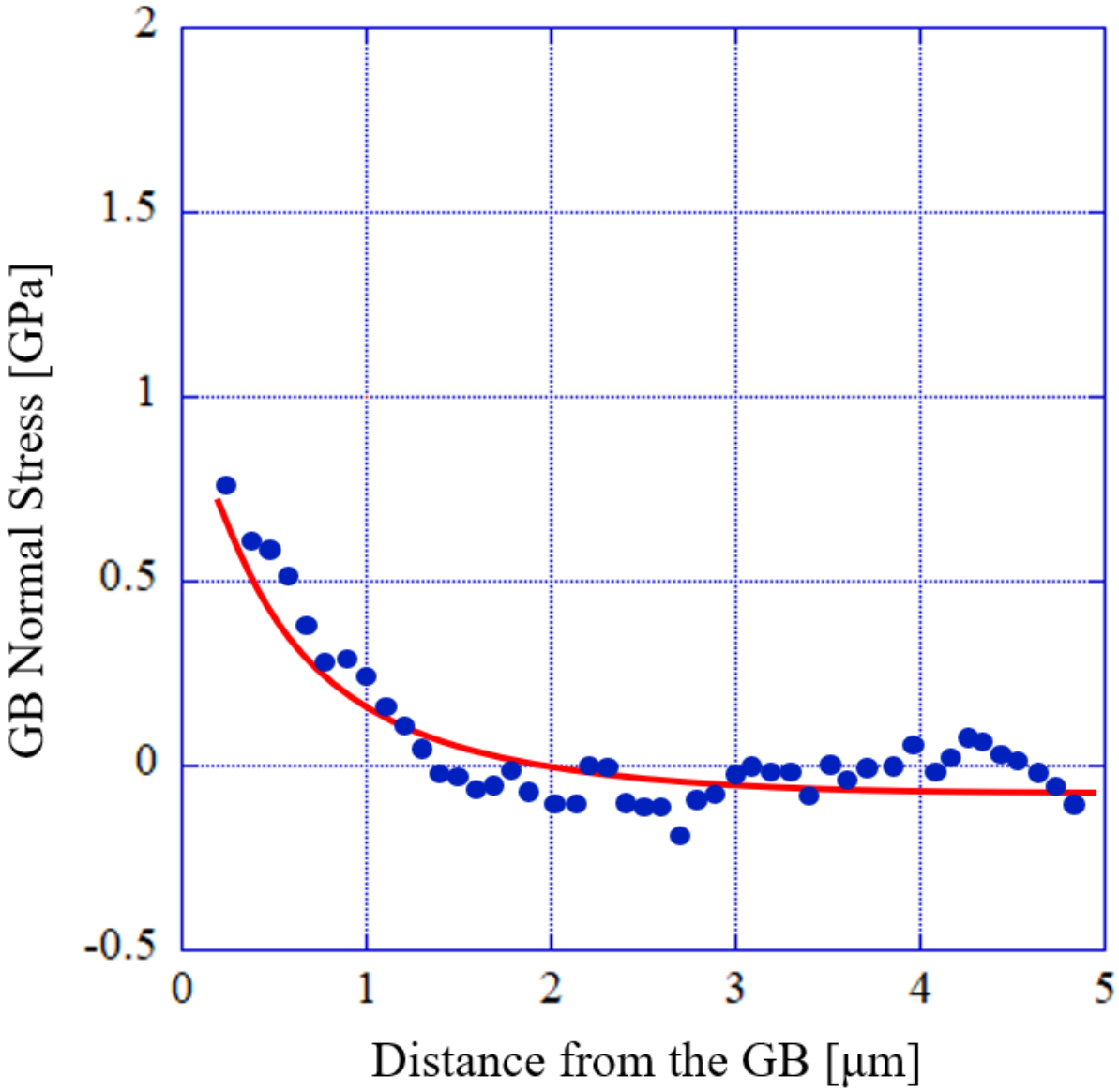

Figure D.49: Tensile stress normal to the grain boundary as a function of distance from the grain boundary in ASCC2 Fe13Cr15Ni 5 dpa tensile bar sample at site ASCC2-49

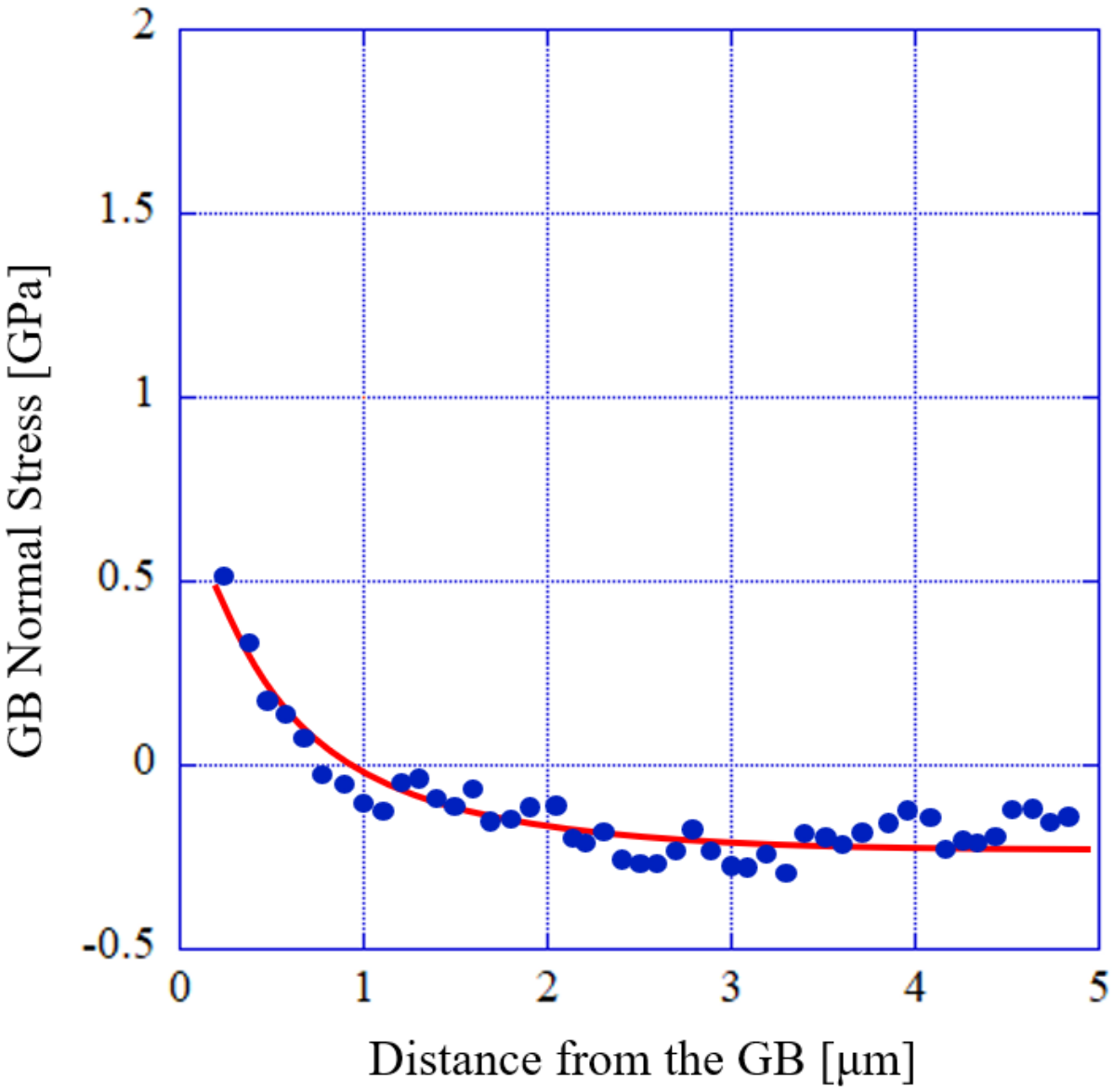

Figure D.50: Tensile stress normal to the grain boundary as a function of distance from the grain boundary in ASCC2 Fe13Cr15Ni 5 dpa tensile bar sample at site ASCC2-50

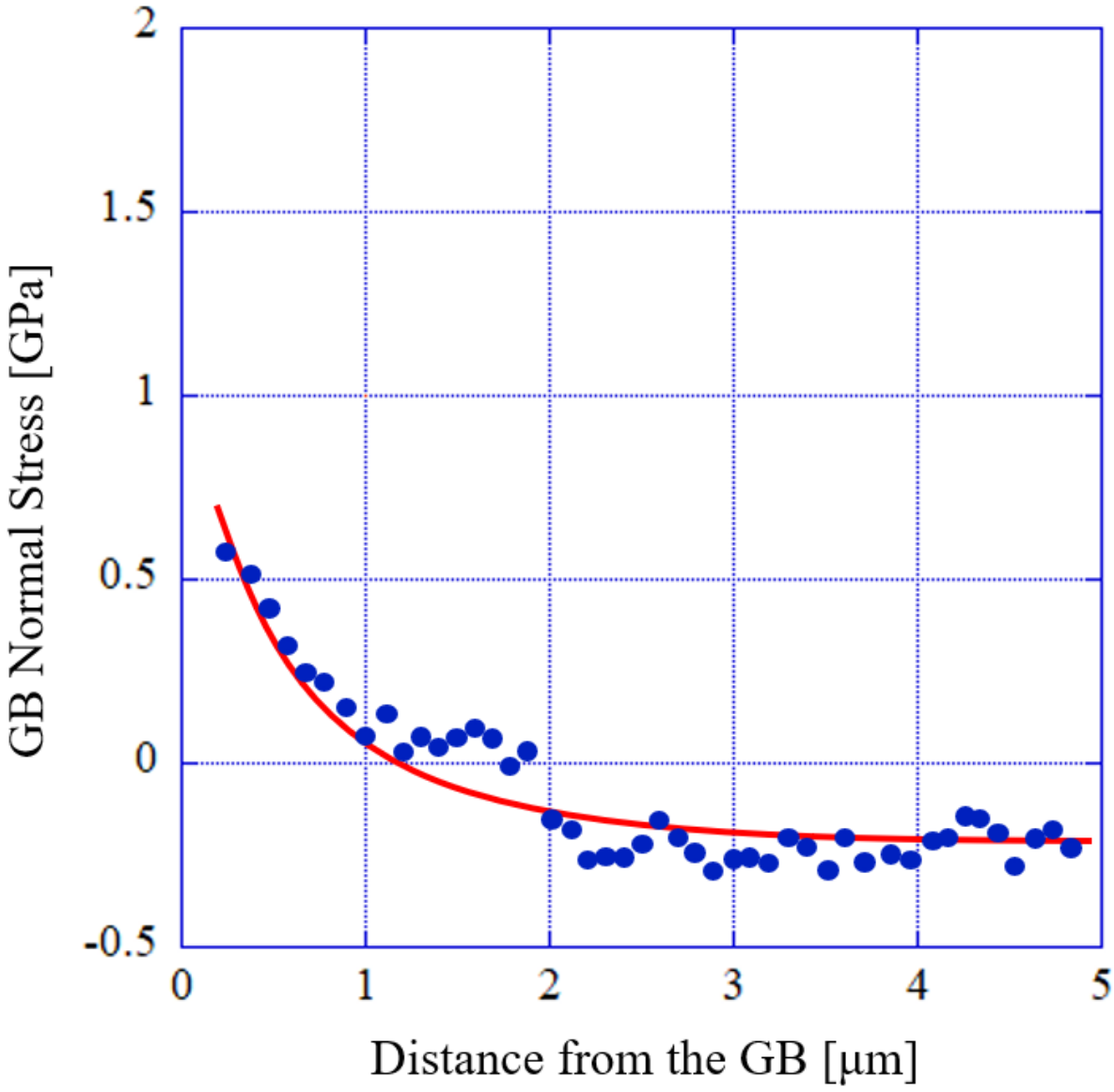

Figure D.51: Tensile stress normal to the grain boundary as a function of distance from the grain boundary in ASCC2 Fe13Cr15Ni 5 dpa tensile bar sample at site ASCC2-51

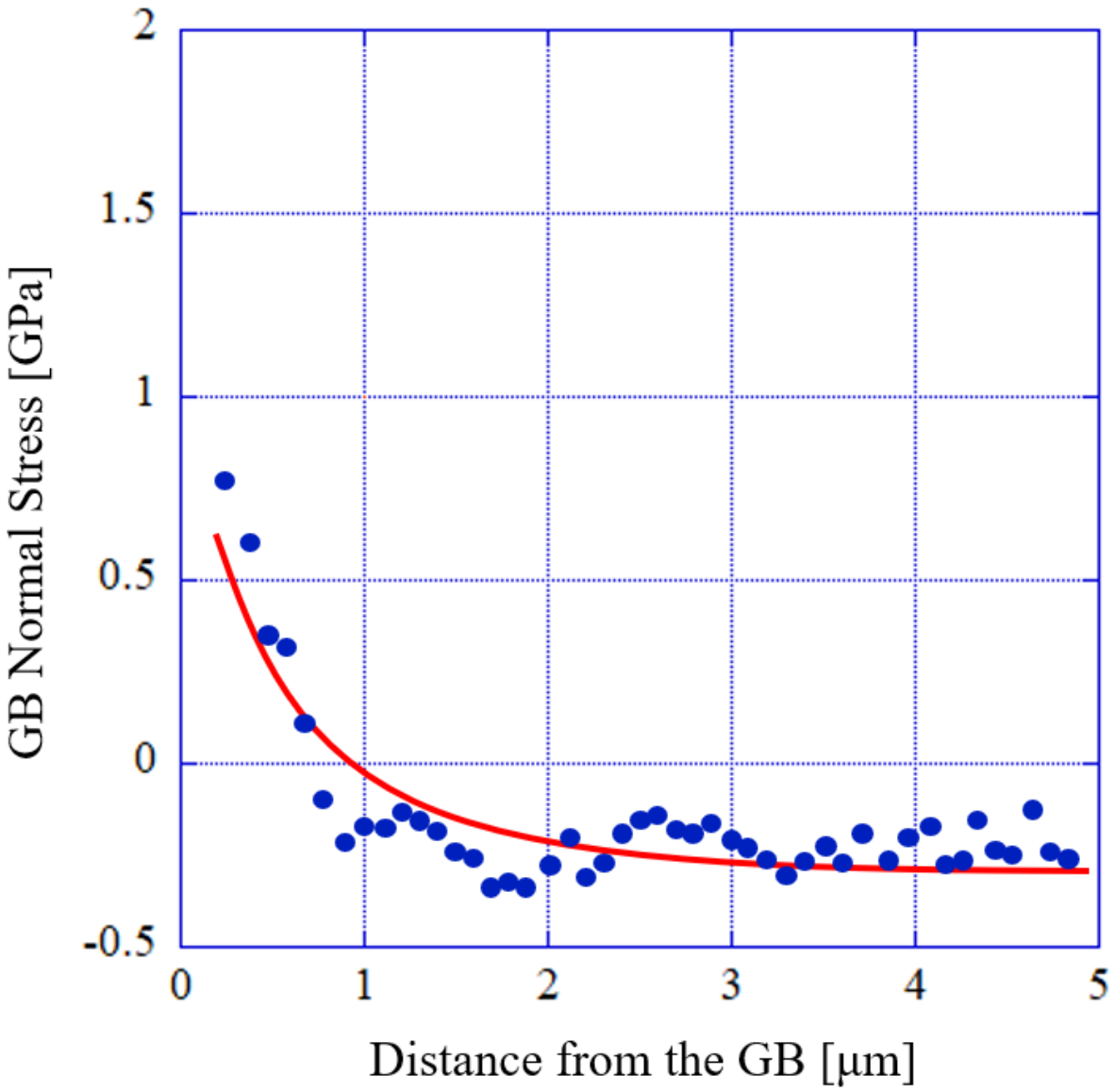

Figure D.52: Tensile stress normal to the grain boundary as a function of distance from the grain boundary in ASCC2 Fe13Cr15Ni 5 dpa tensile bar sample at site ASCC2-52

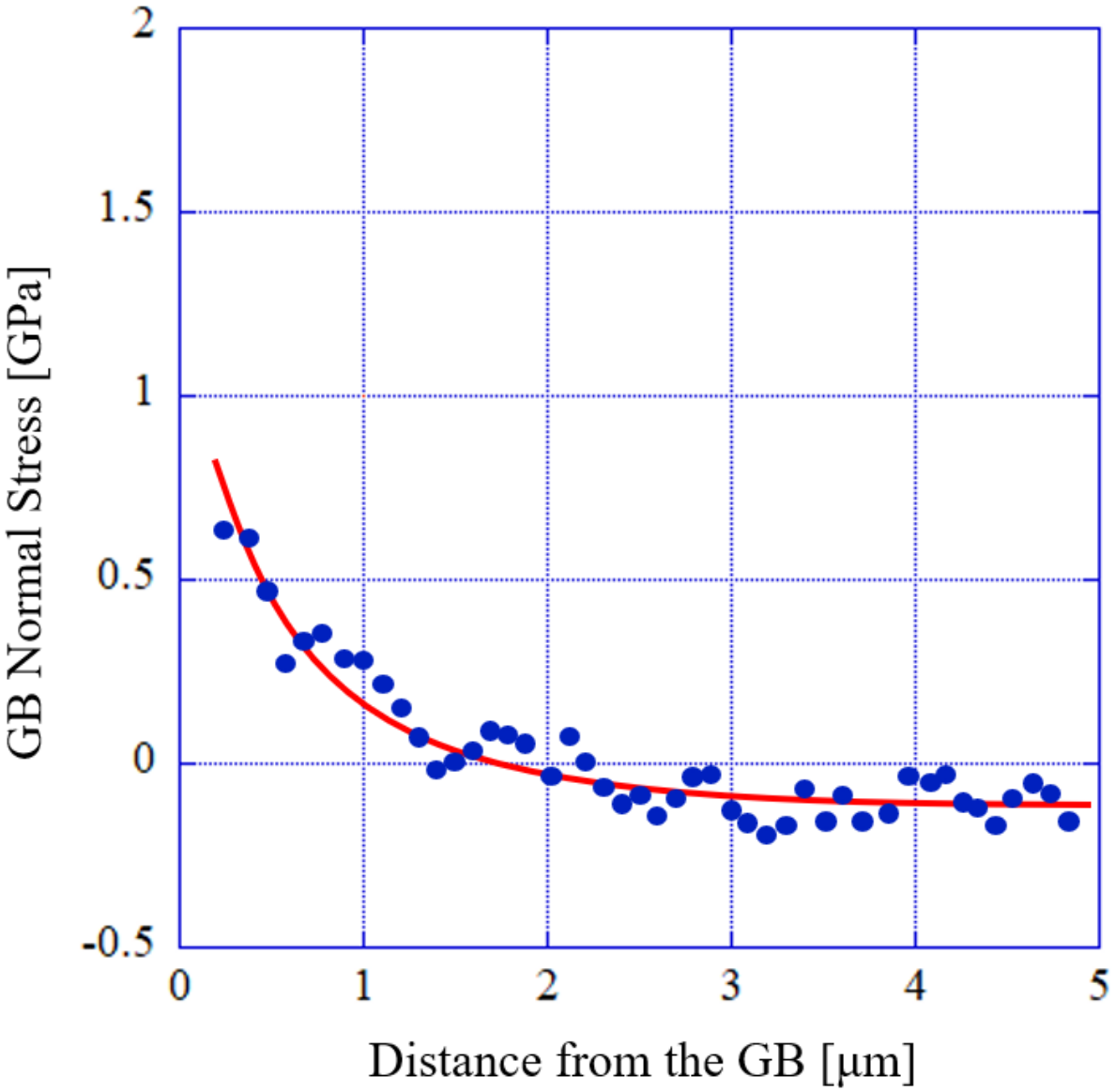

Figure D.53: Tensile stress normal to the grain boundary as a function of distance from the grain boundary in ASCC2 Fe13Cr15Ni 5 dpa tensile bar sample at site ASCC2-53

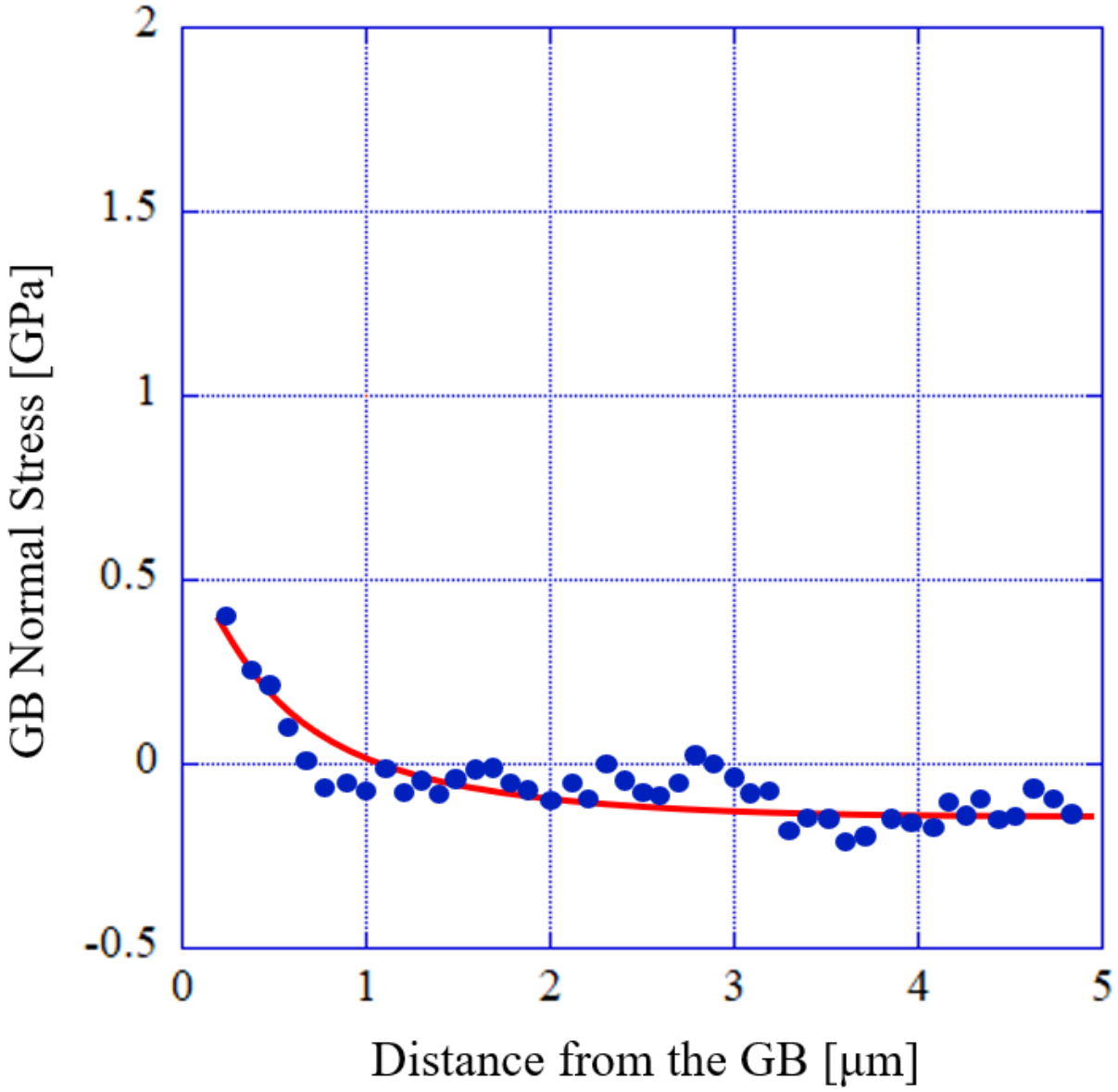

Figure D.54: Tensile stress normal to the grain boundary as a function of distance from the grain boundary in ASCC2 Fe13Cr15Ni 5 dpa tensile bar sample at site ASCC2-54

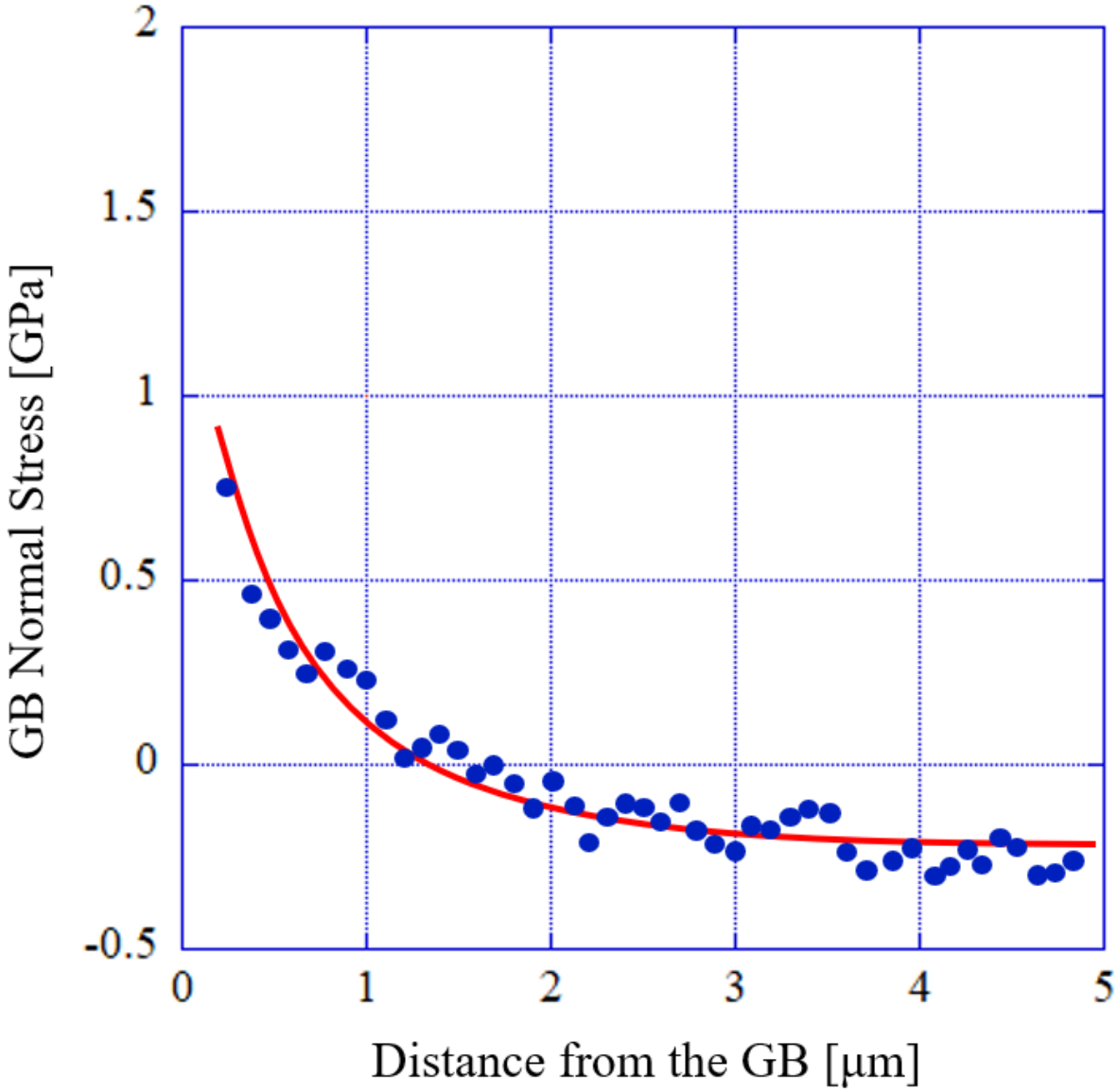

Figure D.55: Tensile stress normal to the grain boundary as a function of distance from the grain boundary in ASCC2 Fe13Cr15Ni 5 dpa tensile bar sample at site ASCC2-55

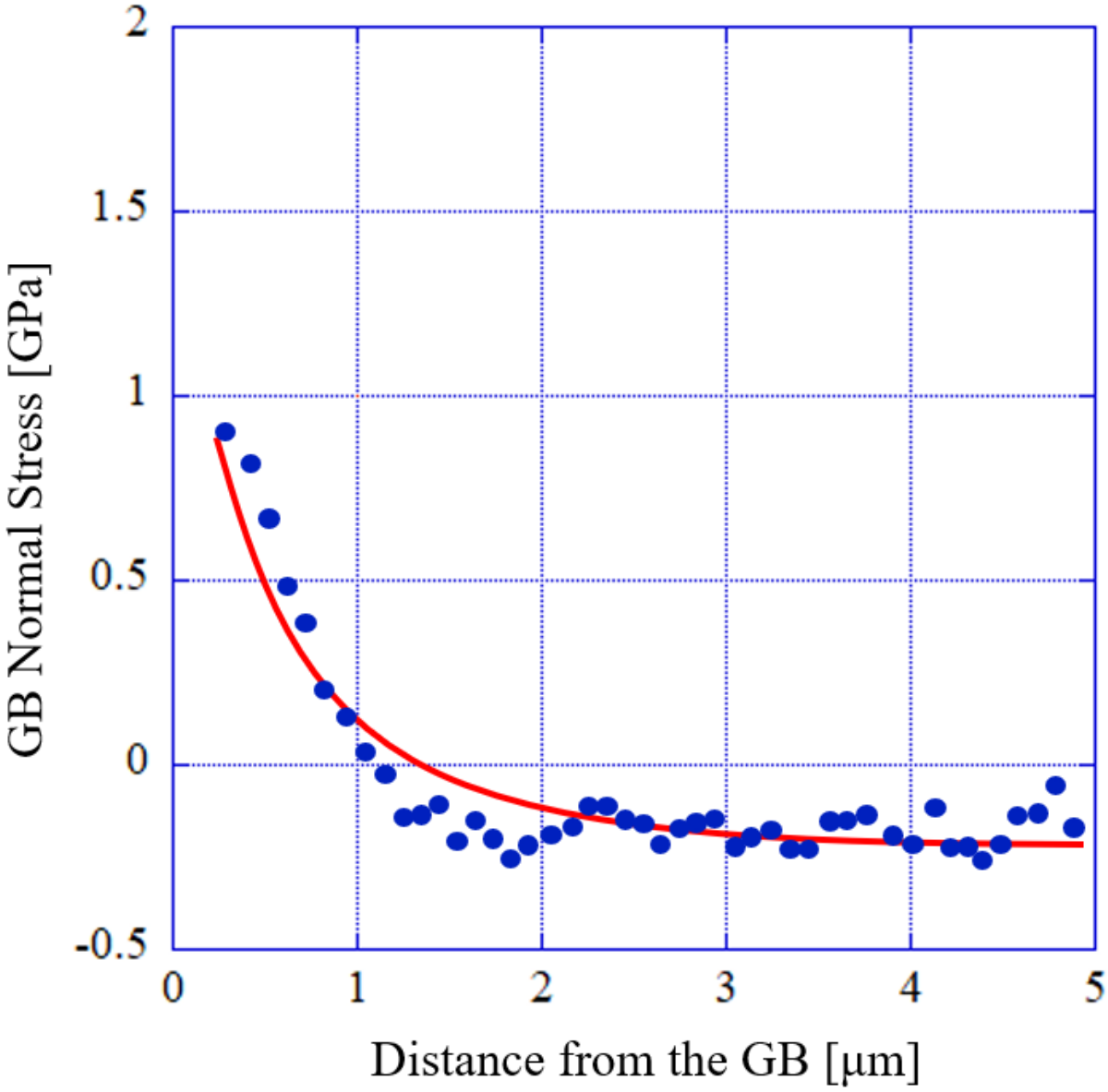

Figure D.56: Tensile stress normal to the grain boundary as a function of distance from the grain boundary in ASCC2 Fe13Cr15Ni 5 dpa tensile bar sample at site ASCC2-56

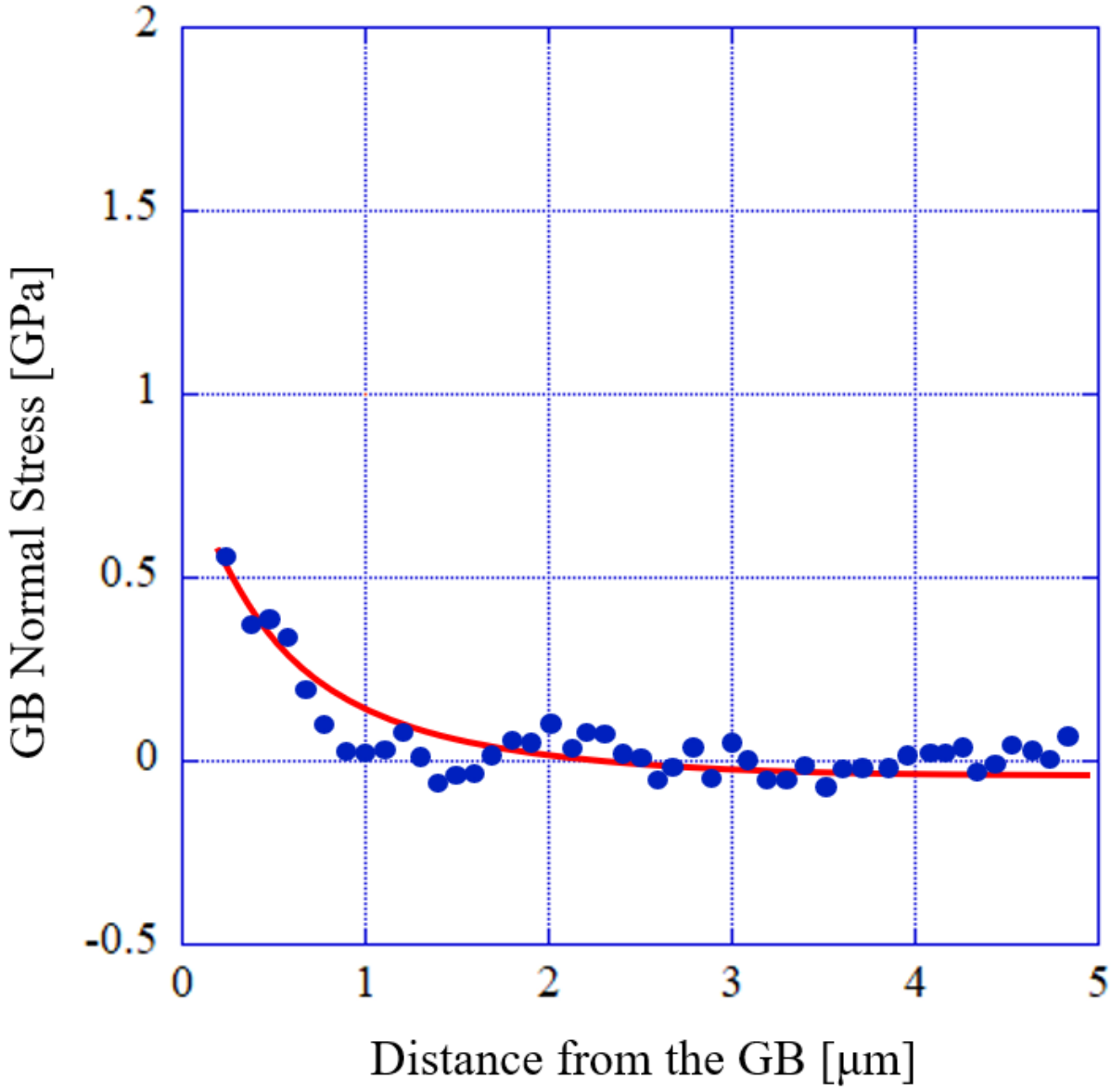

Figure D.57: Tensile stress normal to the grain boundary as a function of distance from the grain boundary in ASCC2 Fe13Cr15Ni 5 dpa tensile bar sample at site ASCC2-57

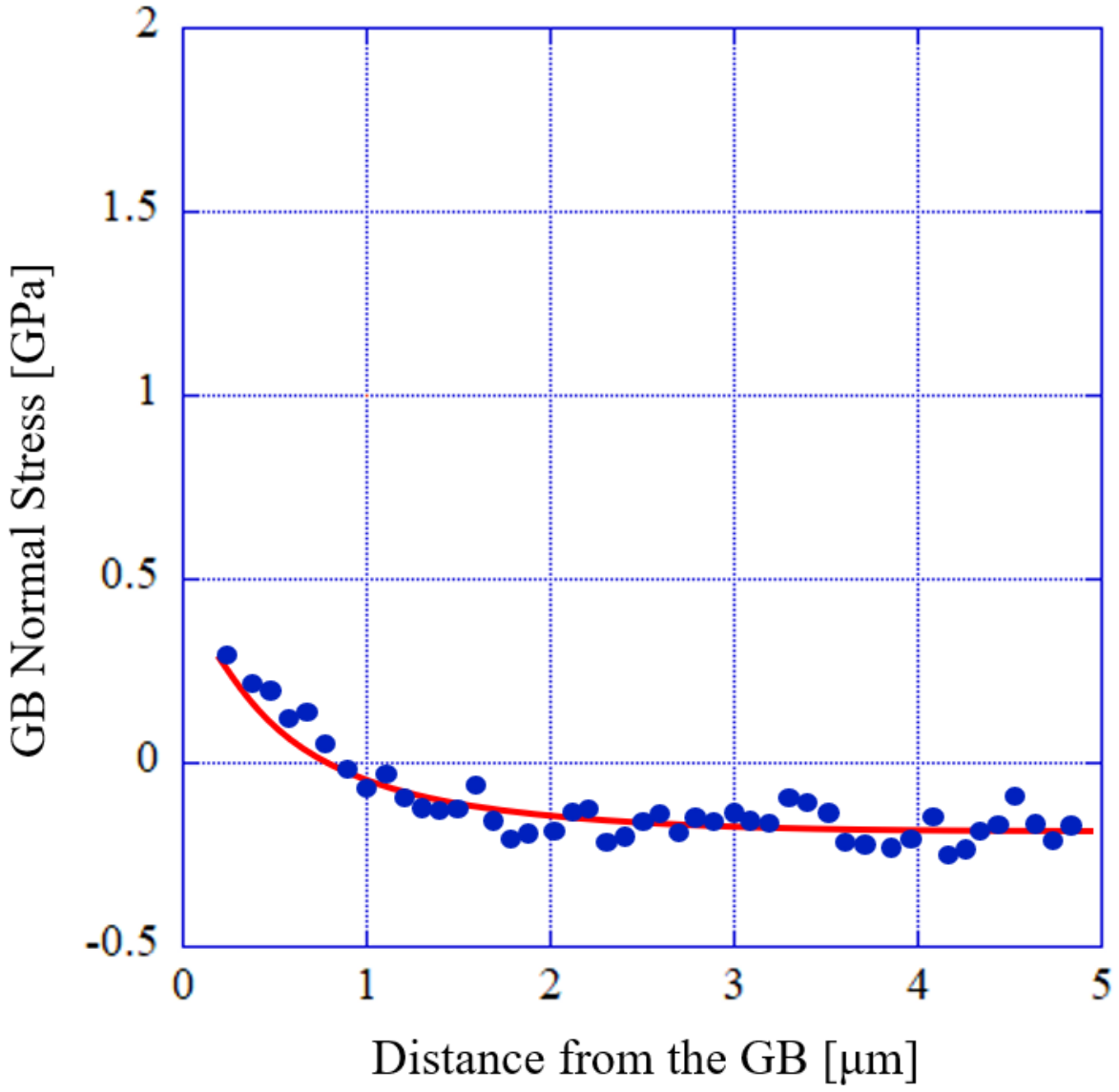

Figure D.58: Tensile stress normal to the grain boundary as a function of distance from the grain boundary in ASCC2 Fe13Cr15Ni 5 dpa tensile bar sample at site ASCC2-58

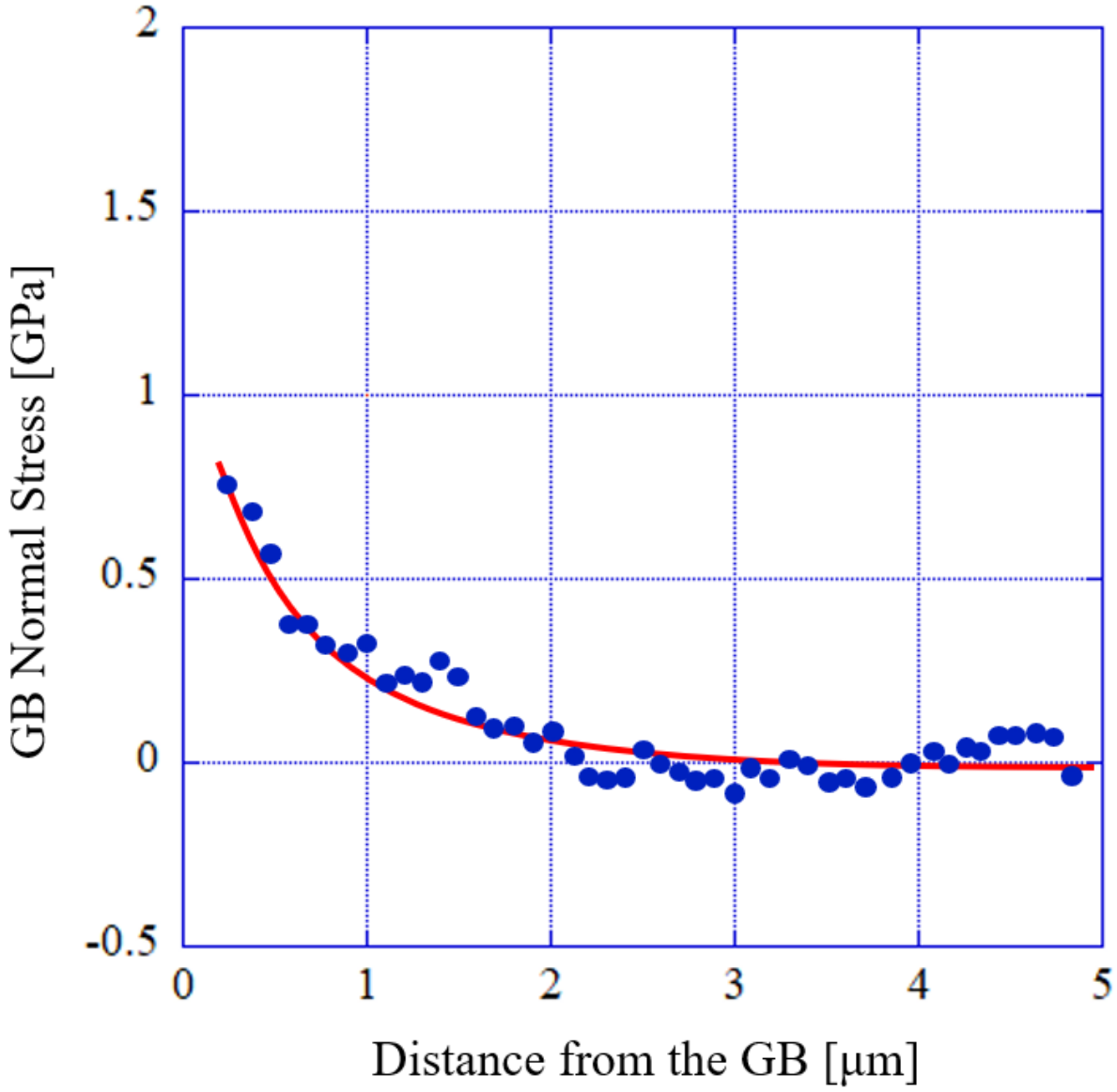

Figure D.59: Tensile stress normal to the grain boundary as a function of distance from the grain boundary in ASCC2 Fe13Cr15Ni 5 dpa tensile bar sample at site ASCC2-59

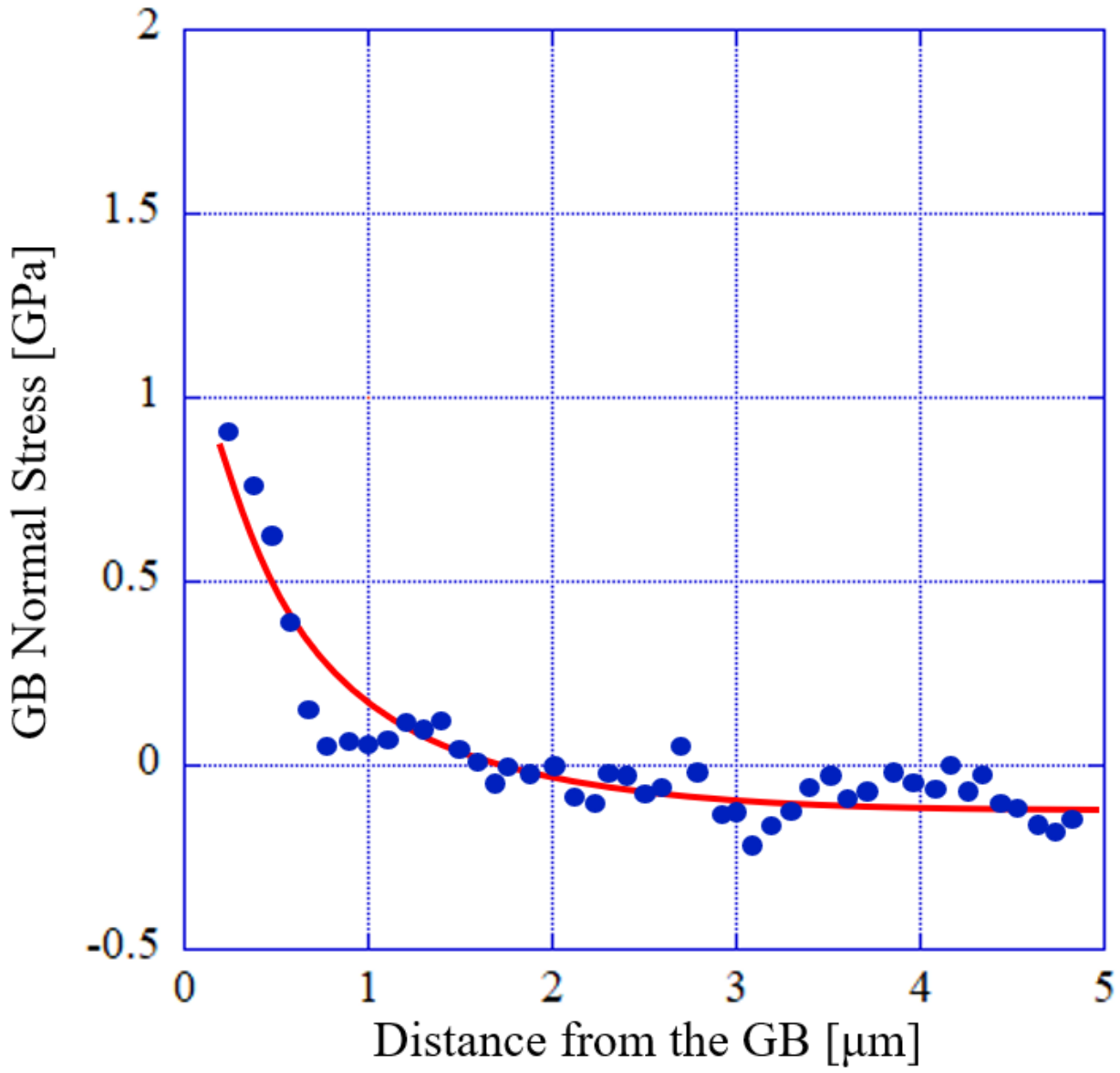

Figure D.60: Tensile stress normal to the grain boundary as a function of distance from the grain boundary in ASCC2 Fe13Cr15Ni 5 dpa tensile bar sample at site ASCC2-60

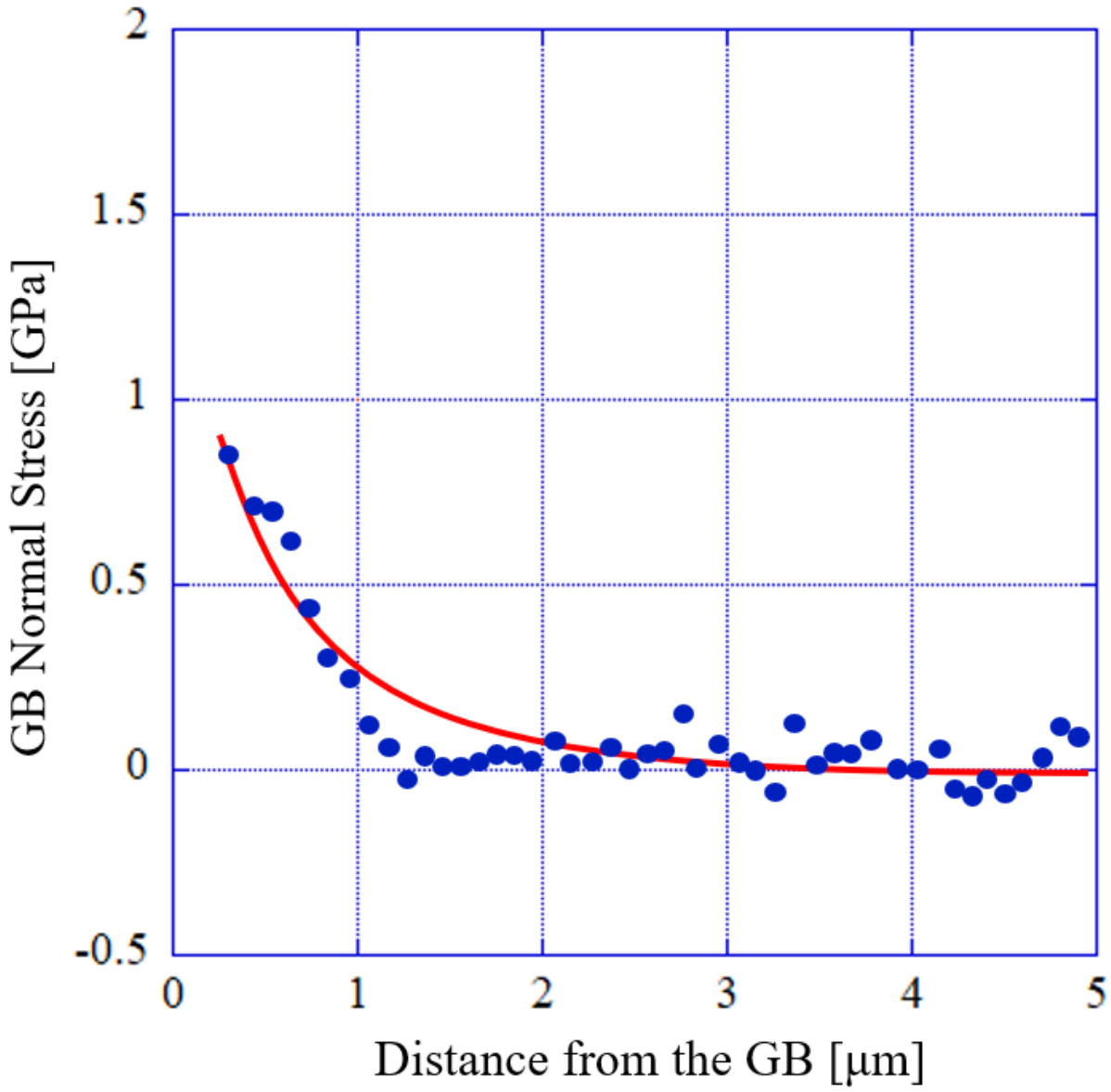

Figure D.61: Tensile stress normal to the grain boundary as a function of distance from the grain boundary in ASCC2 Fe13Cr15Ni 5 dpa tensile bar sample at site ASCC2-61

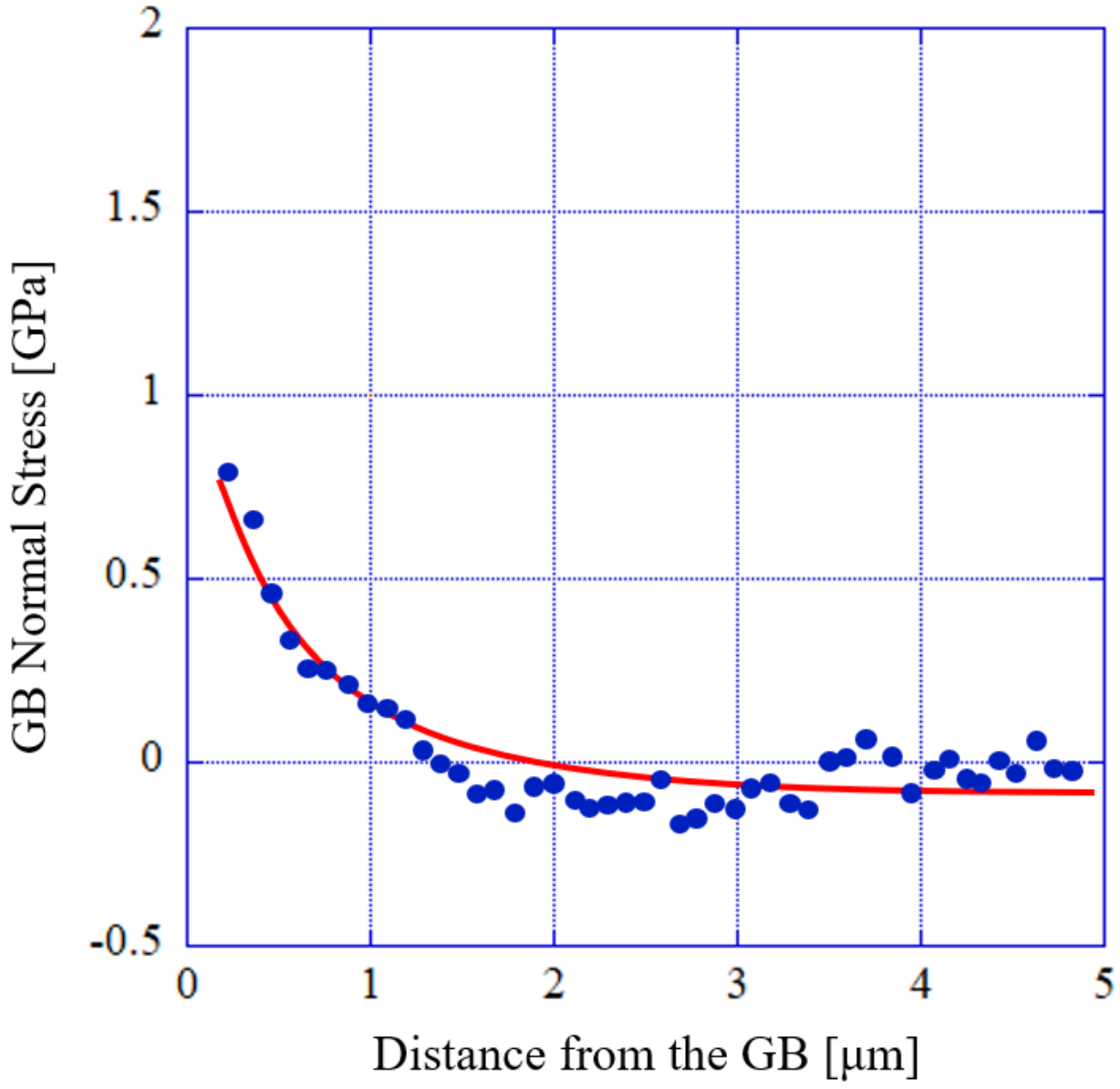

Figure D.62: Tensile stress normal to the grain boundary as a function of distance from the grain boundary in ASCC2 Fe13Cr15Ni 5 dpa tensile bar sample at site ASCC2-62

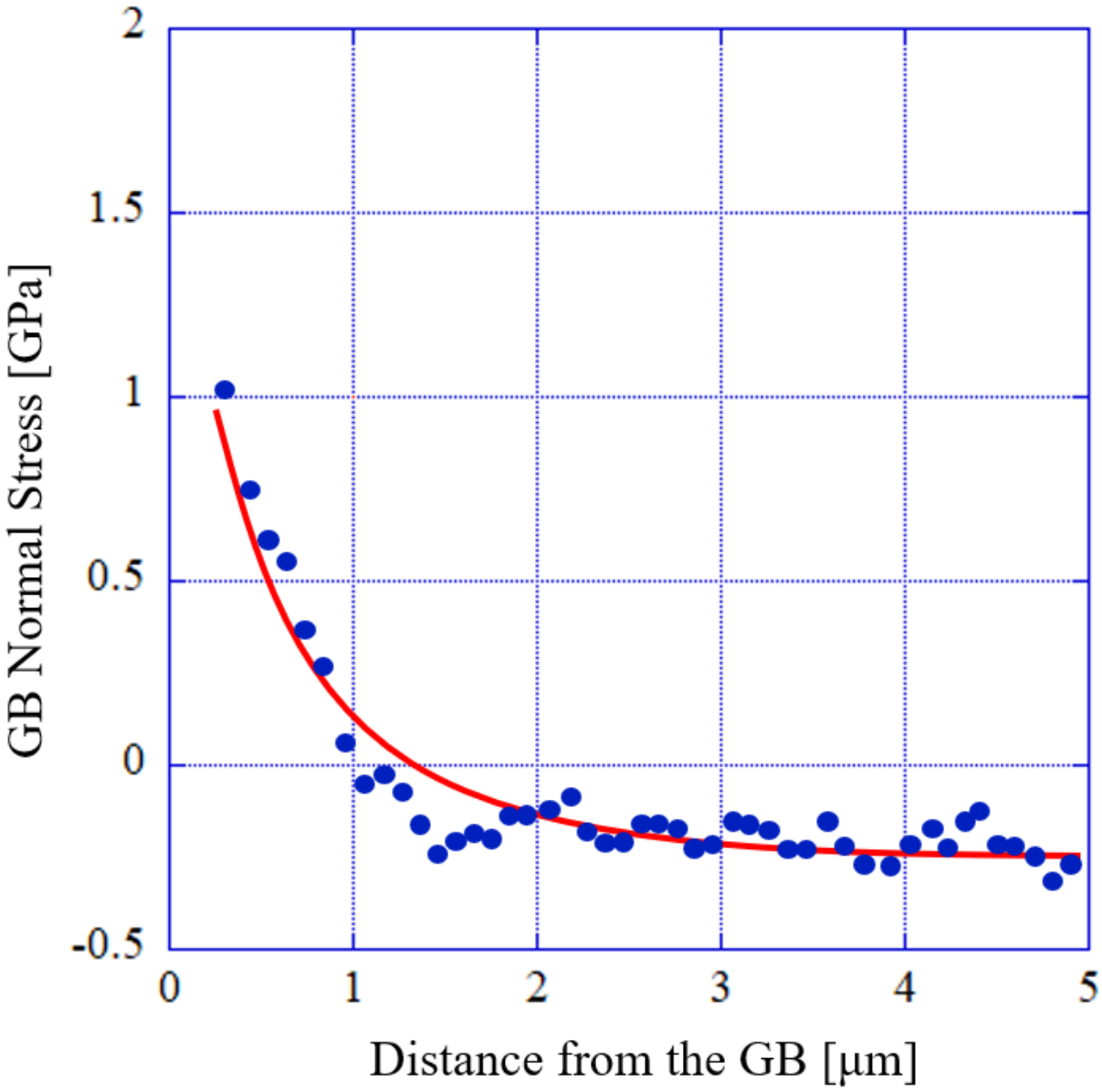

Figure D.63: Tensile stress normal to the grain boundary as a function of distance from the grain boundary in ASCC2 Fe13Cr15Ni 5 dpa tensile bar sample at site ASCC2-63

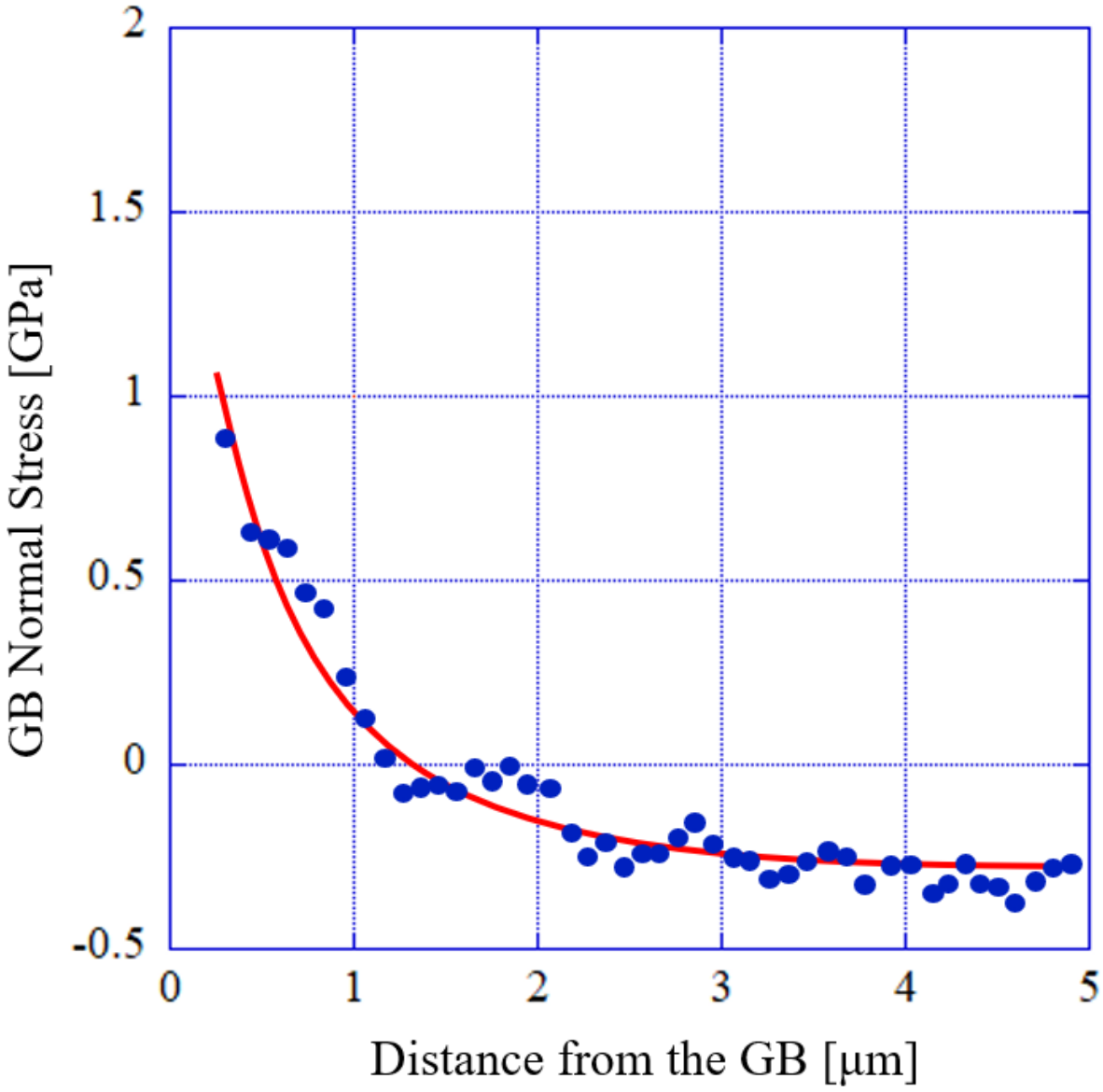

Figure D.64: Tensile stress normal to the grain boundary as a function of distance from the grain boundary in ASCC2 Fe13Cr15Ni 5 dpa tensile bar sample at site ASCC2-64

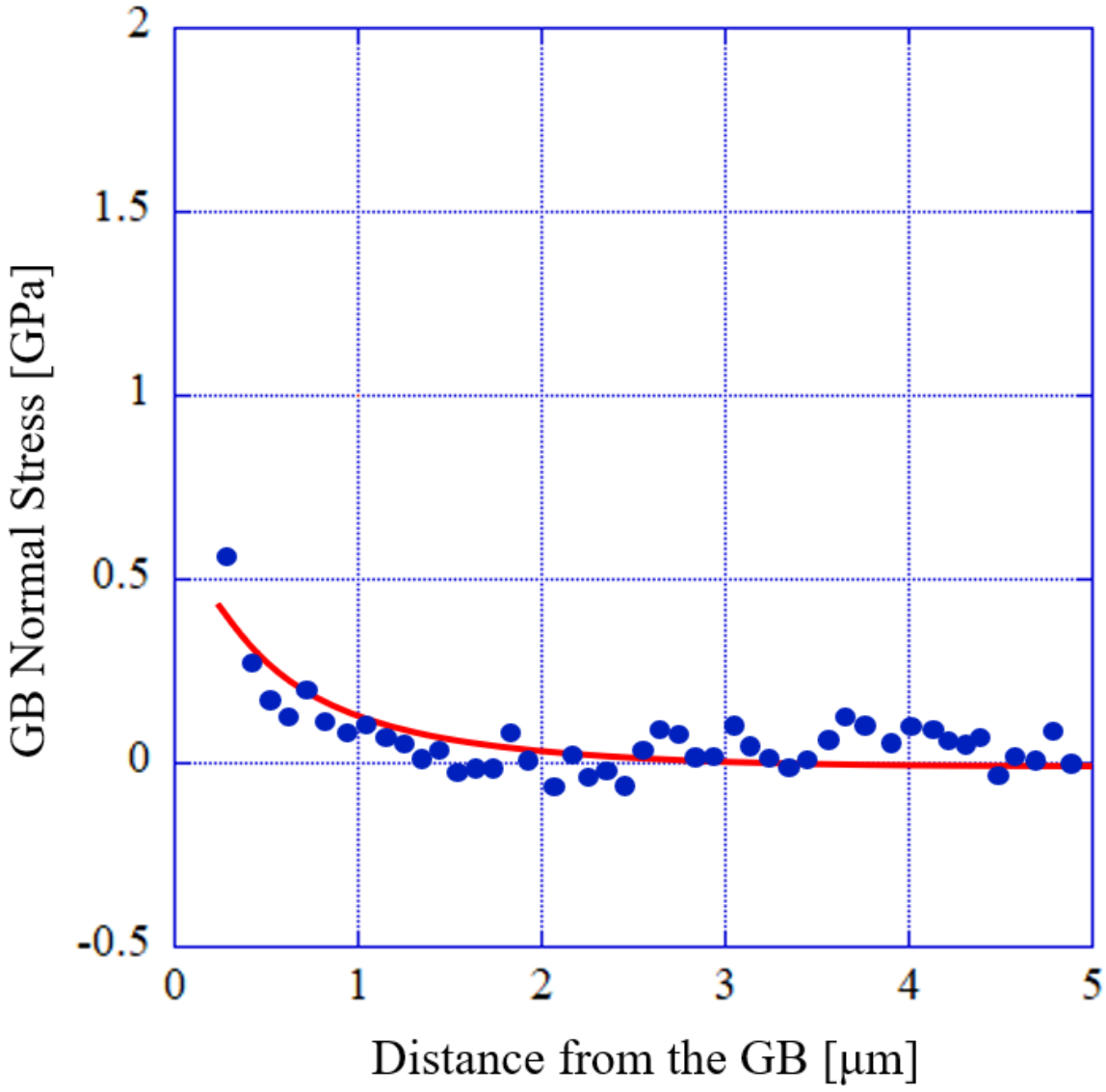

Figure D.65: Tensile stress normal to the grain boundary as a function of distance from the grain boundary in ASCC2 Fe13Cr15Ni 5 dpa tensile bar sample at site ASCC2-65

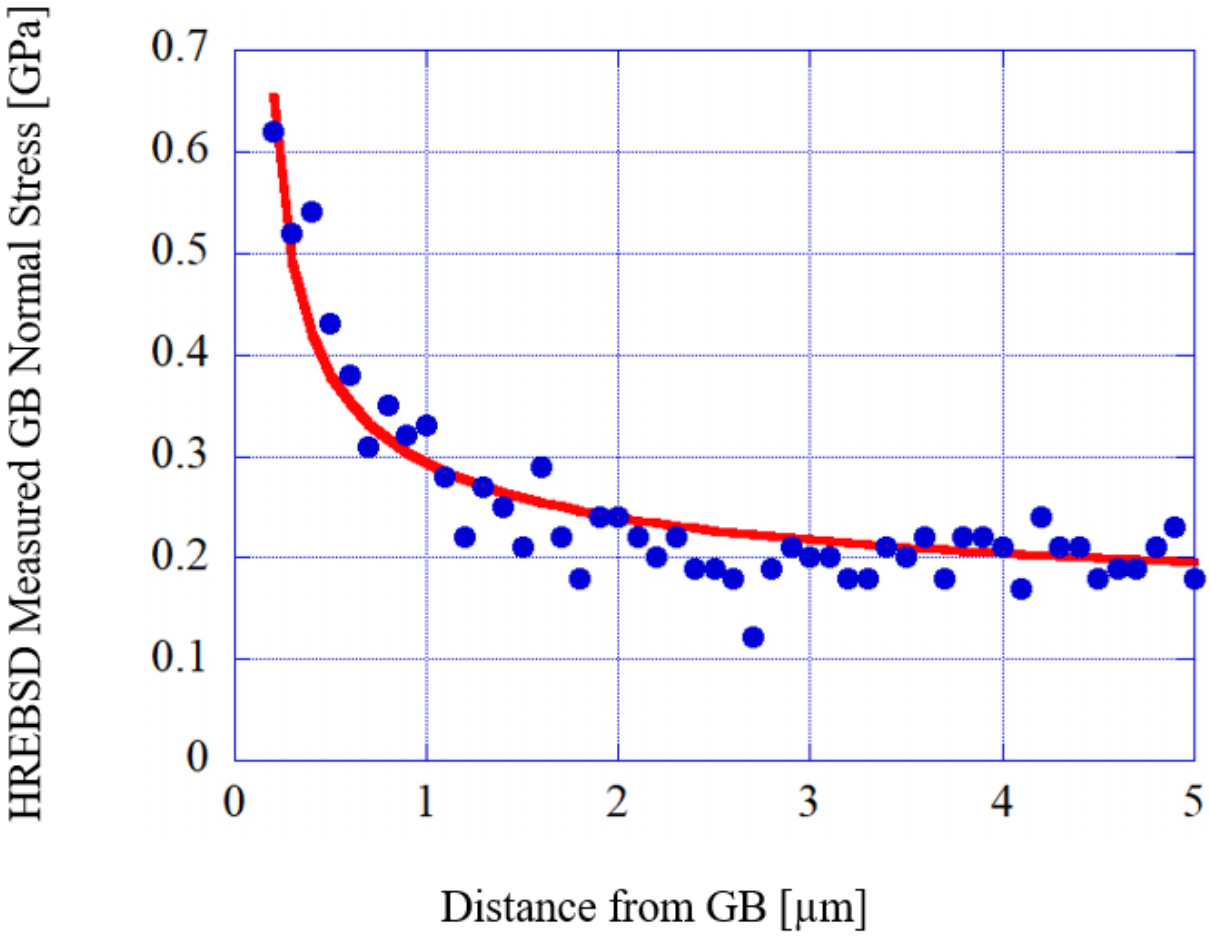

Figure D.66: Tensile stress normal to the grain boundary as a function of distance from the grain boundary in BSCC2 Fe21Cr32Ni 5 dpa tensile bar sample at site BSCC2-1

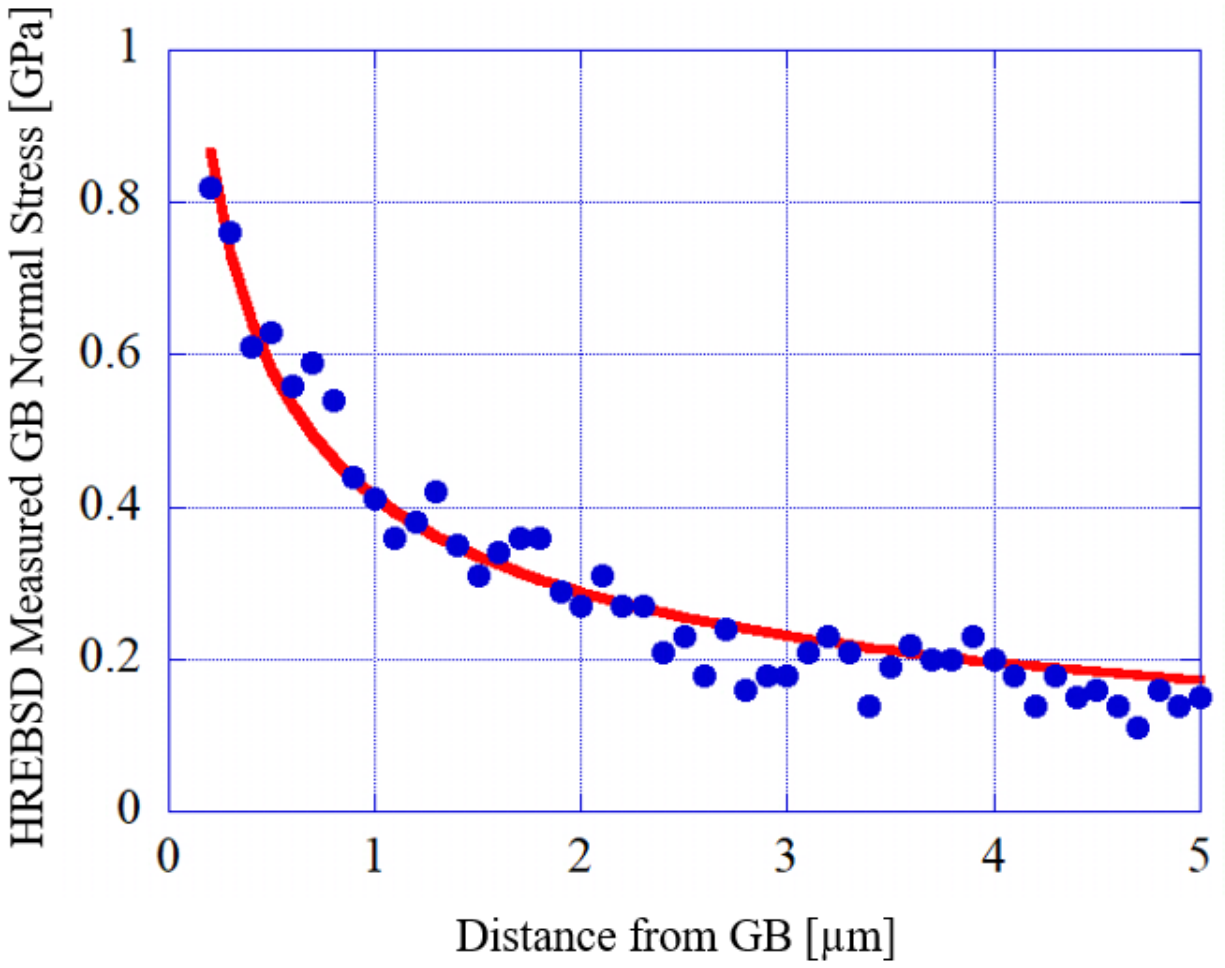

Figure D.67: Tensile stress normal to the grain boundary as a function of distance from the grain boundary in BSCC2 Fe21Cr32Ni 5 dpa tensile bar sample at site BSCC2-2

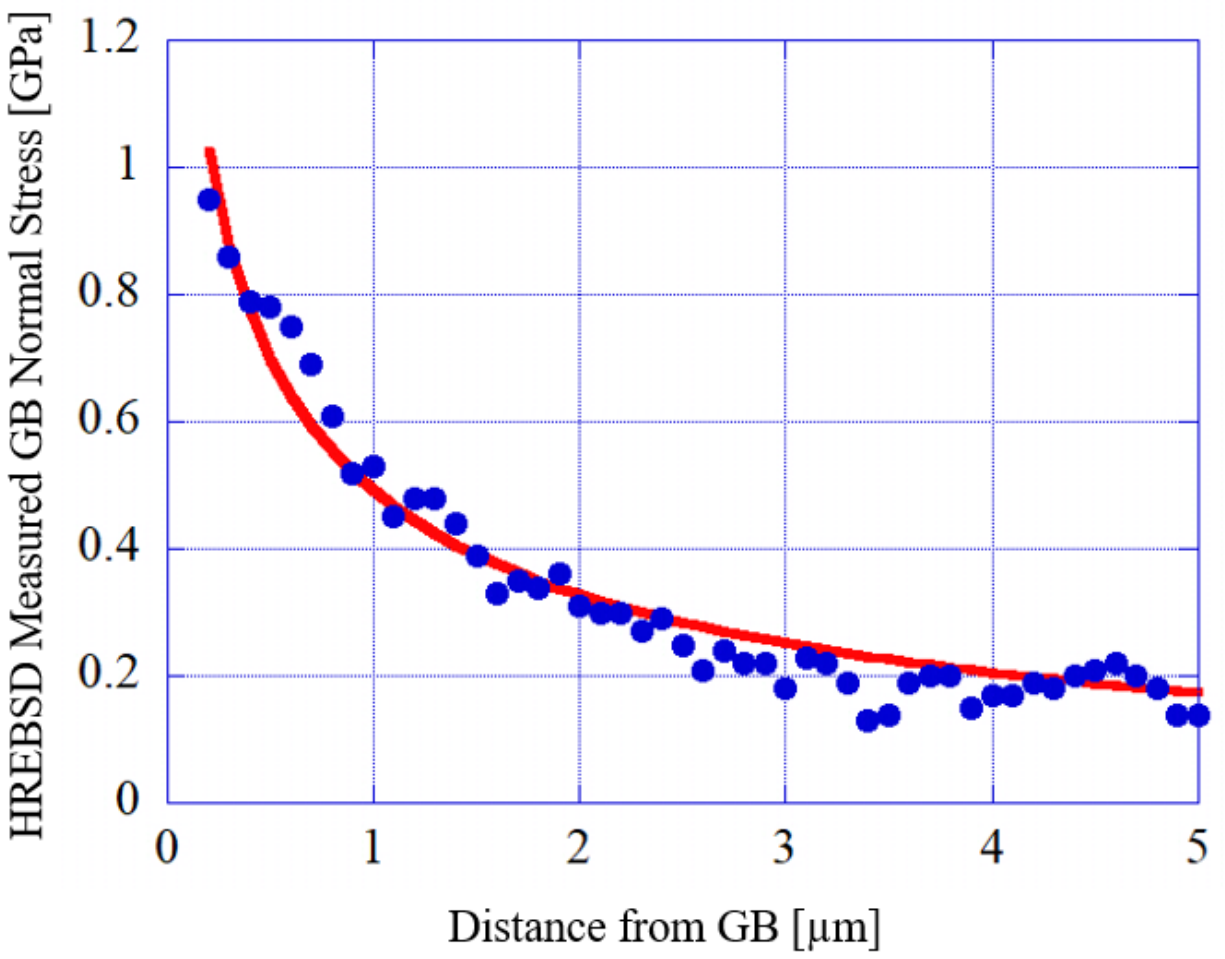

Figure D.68: Tensile stress normal to the grain boundary as a function of distance from the grain boundary in BSCC2 Fe21Cr32Ni 5 dpa tensile bar sample at site BSCC2-3

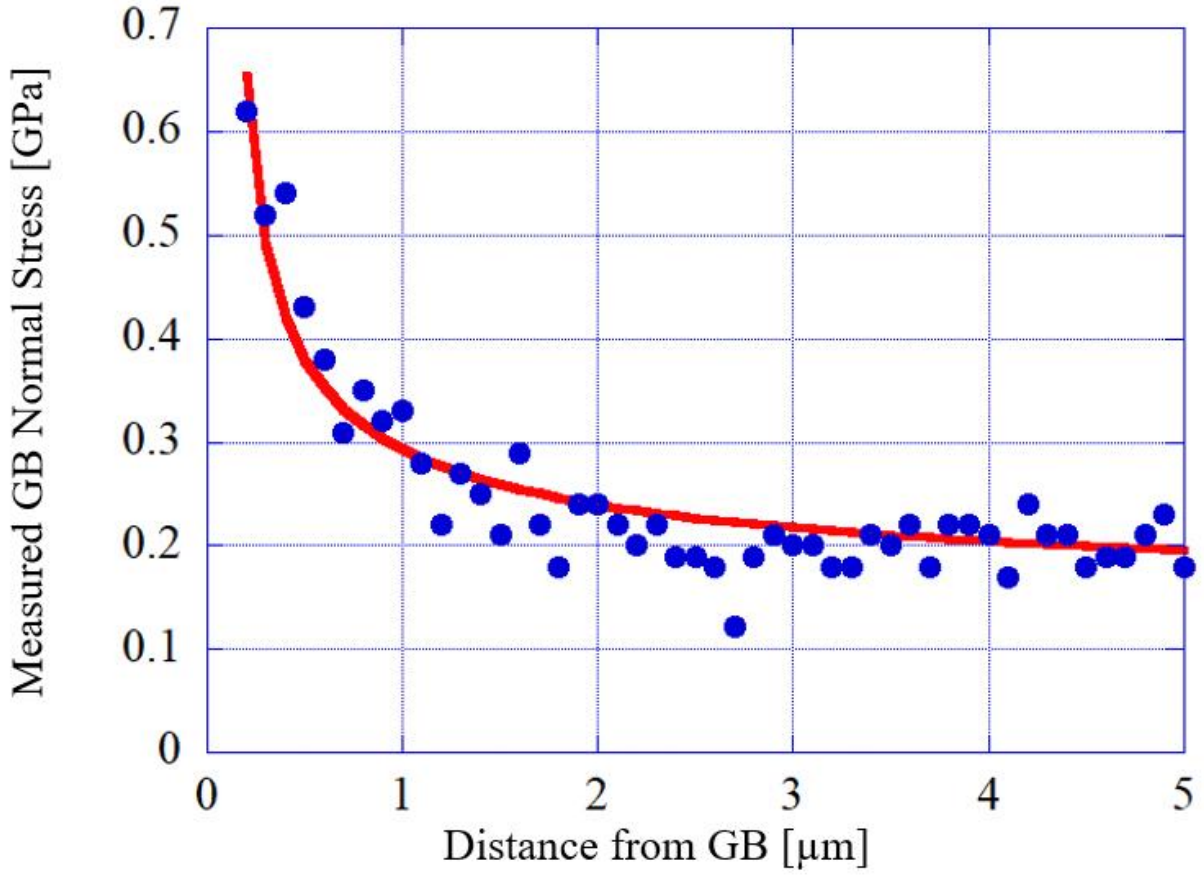

Figure D.69: Tensile stress normal to the grain boundary as a function of distance from the grain boundary in BSCC2 Fe21Cr32Ni 5 dpa tensile bar sample at site BSCC2-4

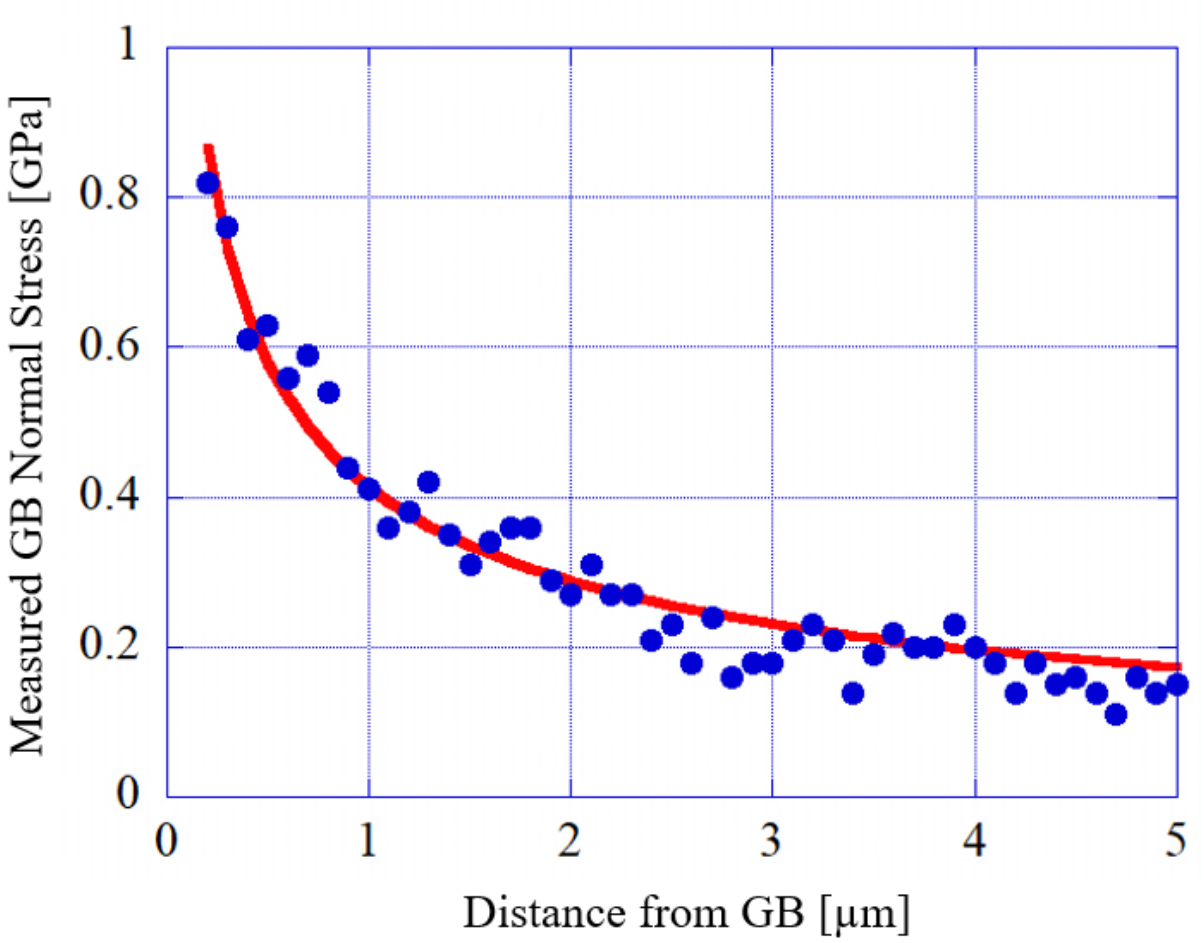

Figure D.70: Tensile stress normal to the grain boundary as a function of distance from the grain boundary in BSCC2 Fe21Cr32Ni 5 dpa tensile bar sample at site BSCC2-5

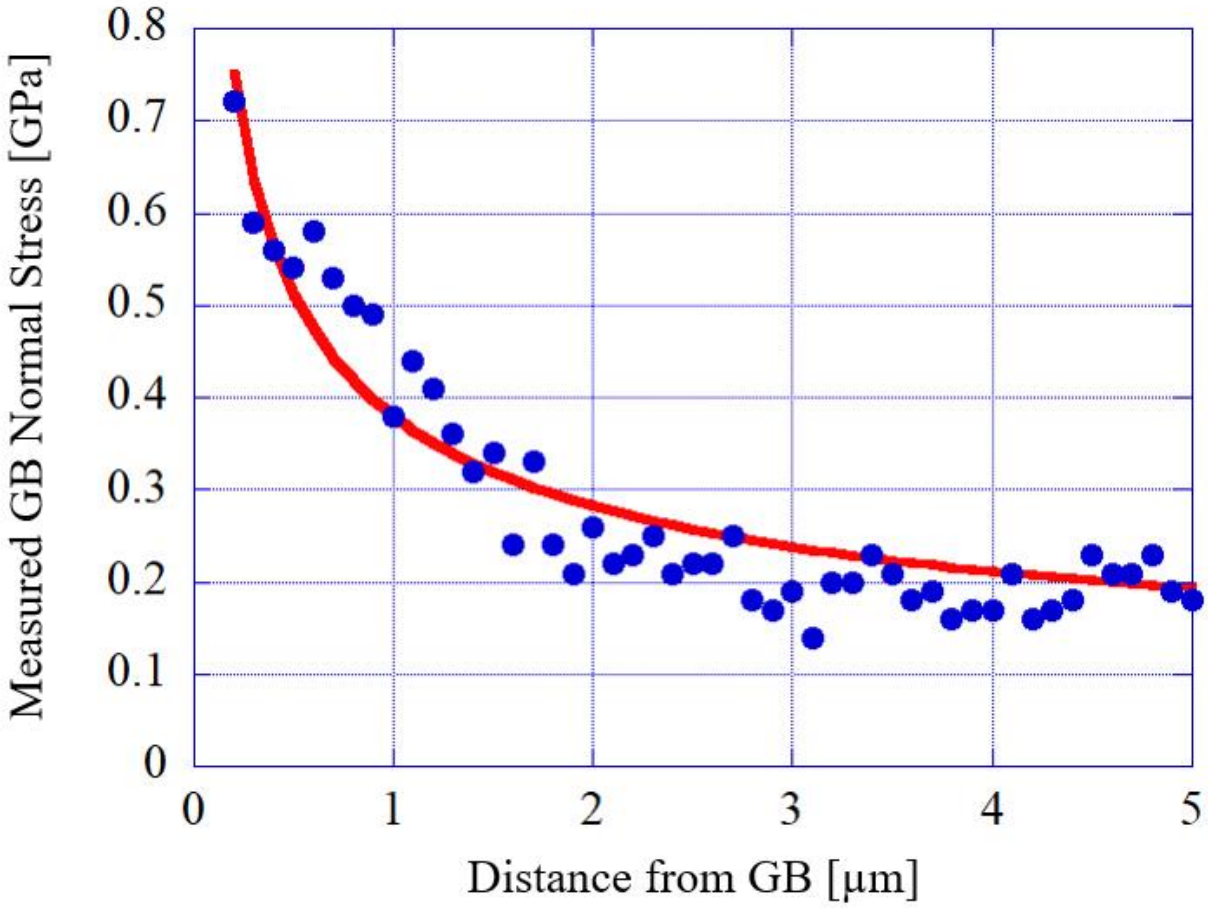

Figure D.71: Tensile stress normal to the grain boundary as a function of distance from the grain boundary in BSCC2 Fe21Cr32Ni 5 dpa tensile bar sample at site BSCC2-6

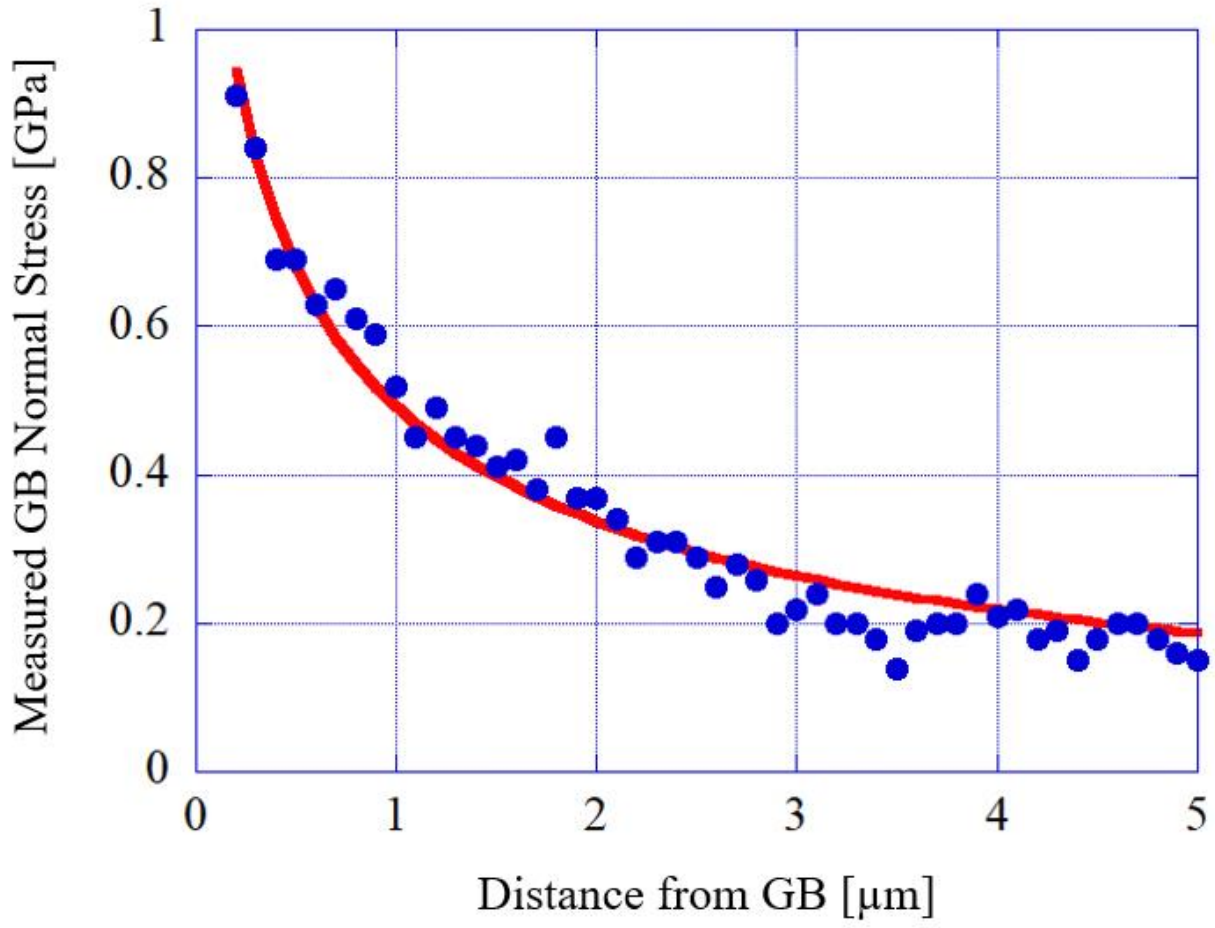

Figure D.72: Tensile stress normal to the grain boundary as a function of distance from the grain boundary in BSCC2 Fe21Cr32Ni 5 dpa tensile bar sample at site BSCC2-7

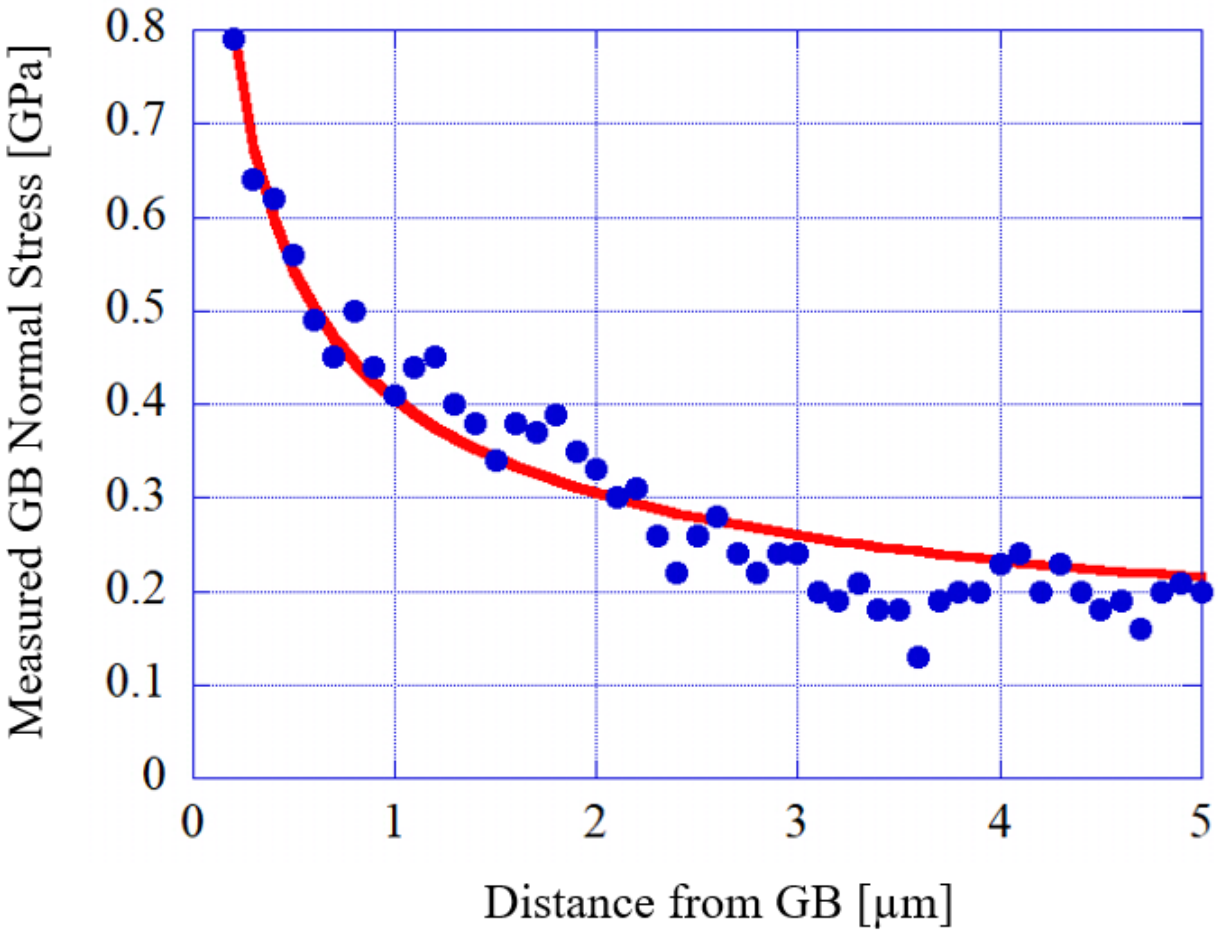

Figure D.73: Tensile stress normal to the grain boundary as a function of distance from the grain boundary in BSCC2 Fe21Cr32Ni 5 dpa tensile bar sample at site BSCC2-8

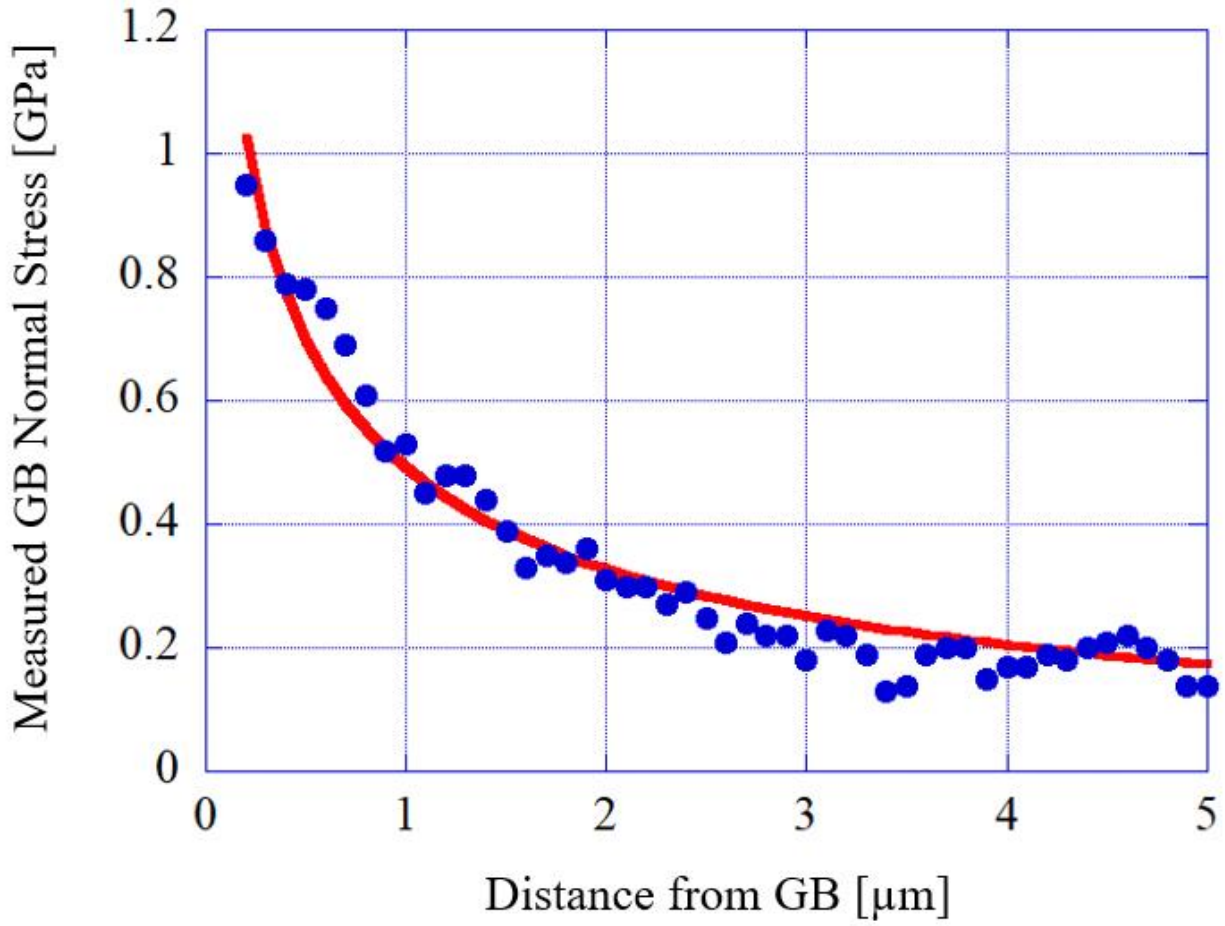

Figure D.74: Tensile stress normal to the grain boundary as a function of distance from the grain boundary in BSCC2 Fe21Cr32Ni 5 dpa tensile bar sample at site BSCC2-9

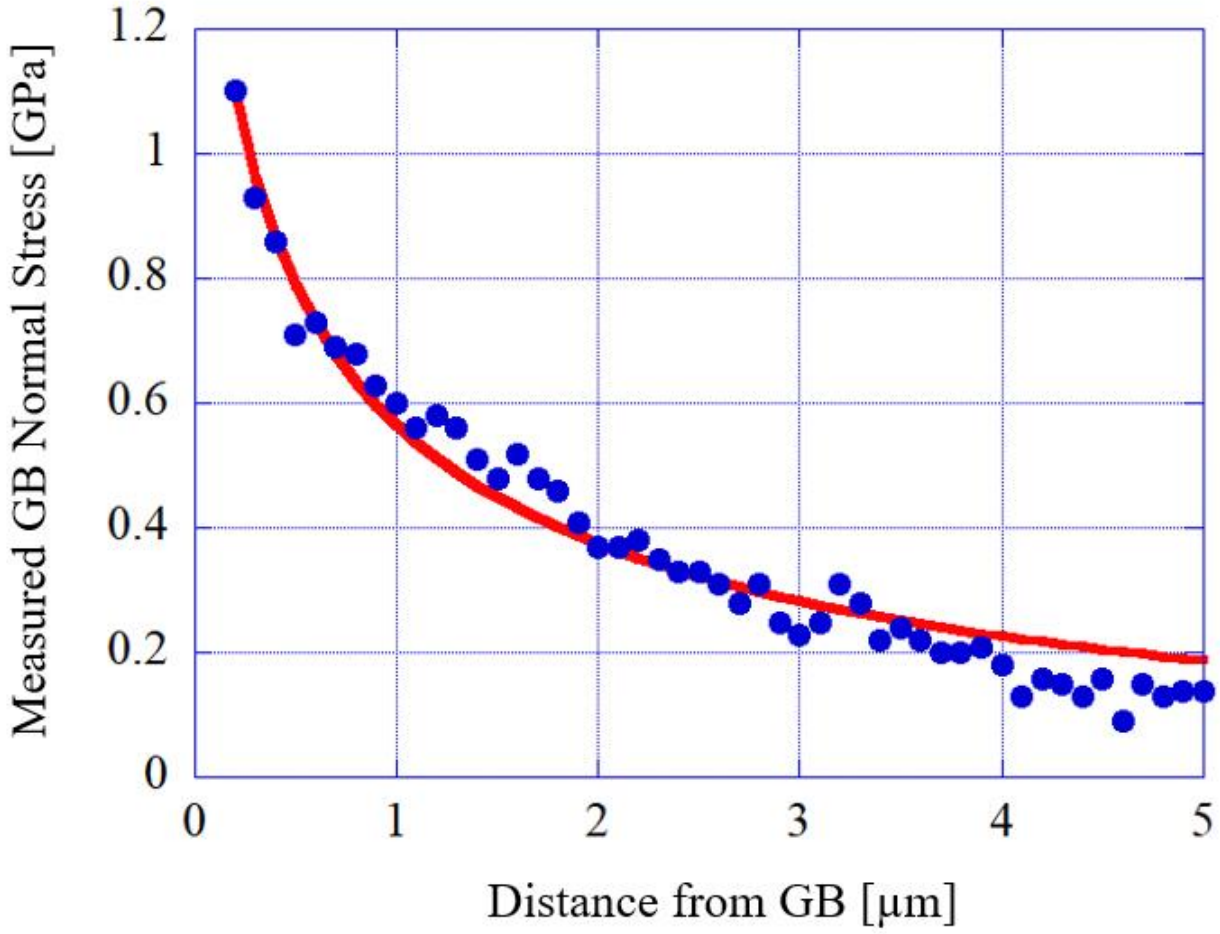

Figure D.75: Tensile stress normal to the grain boundary as a function of distance from the grain boundary in BSCC2 Fe21Cr32Ni 5 dpa tensile bar sample at site BSCC2-10

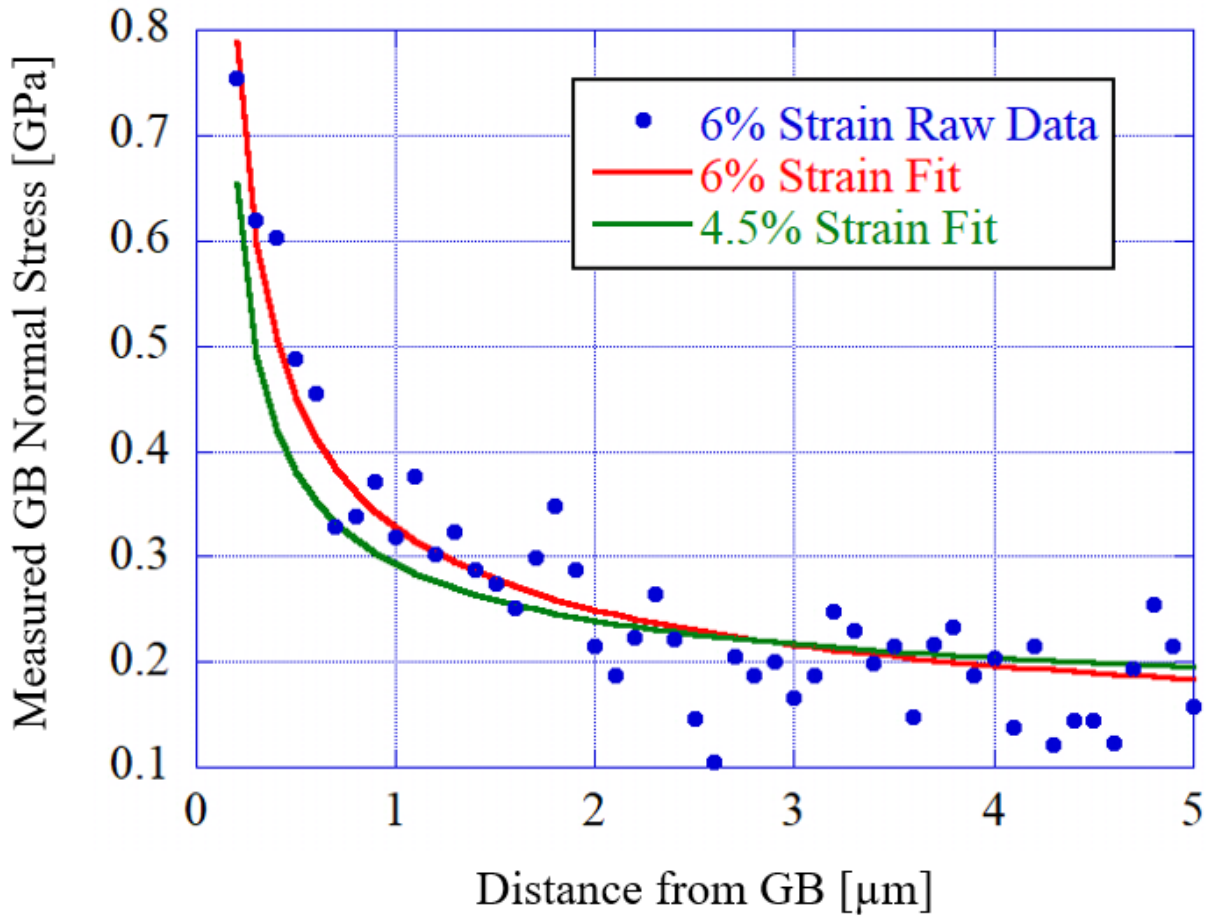

Figure D.76: Tensile stress normal to the grain boundary as a function of distance from the grain boundary in BSCC2 Fe21Cr32Ni 5 dpa tensile bar sample at site BSCC2-21 at 6% total plastic strain (blue data and red fit) and the Eshelby fit for data at the same location after 4.5% plastic strain (green)

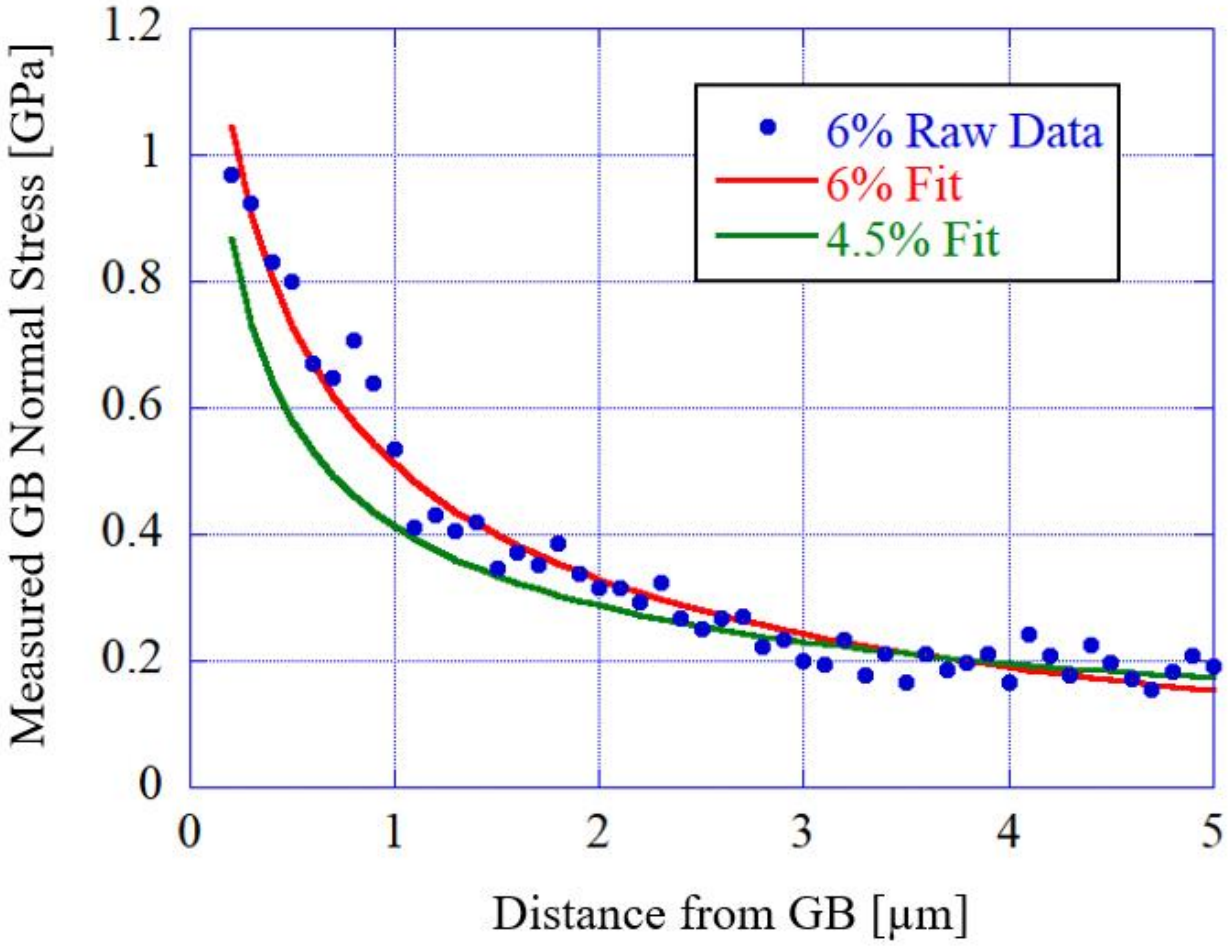

Figure D.77: Tensile stress normal to the grain boundary as a function of distance from the grain boundary in BSCC2 Fe21Cr32Ni 5 dpa tensile bar sample at site BSCC2-22 at 6% total plastic strain (blue data and red fit) and the Eshelby fit for data at the same location after 4.5% plastic strain (green)

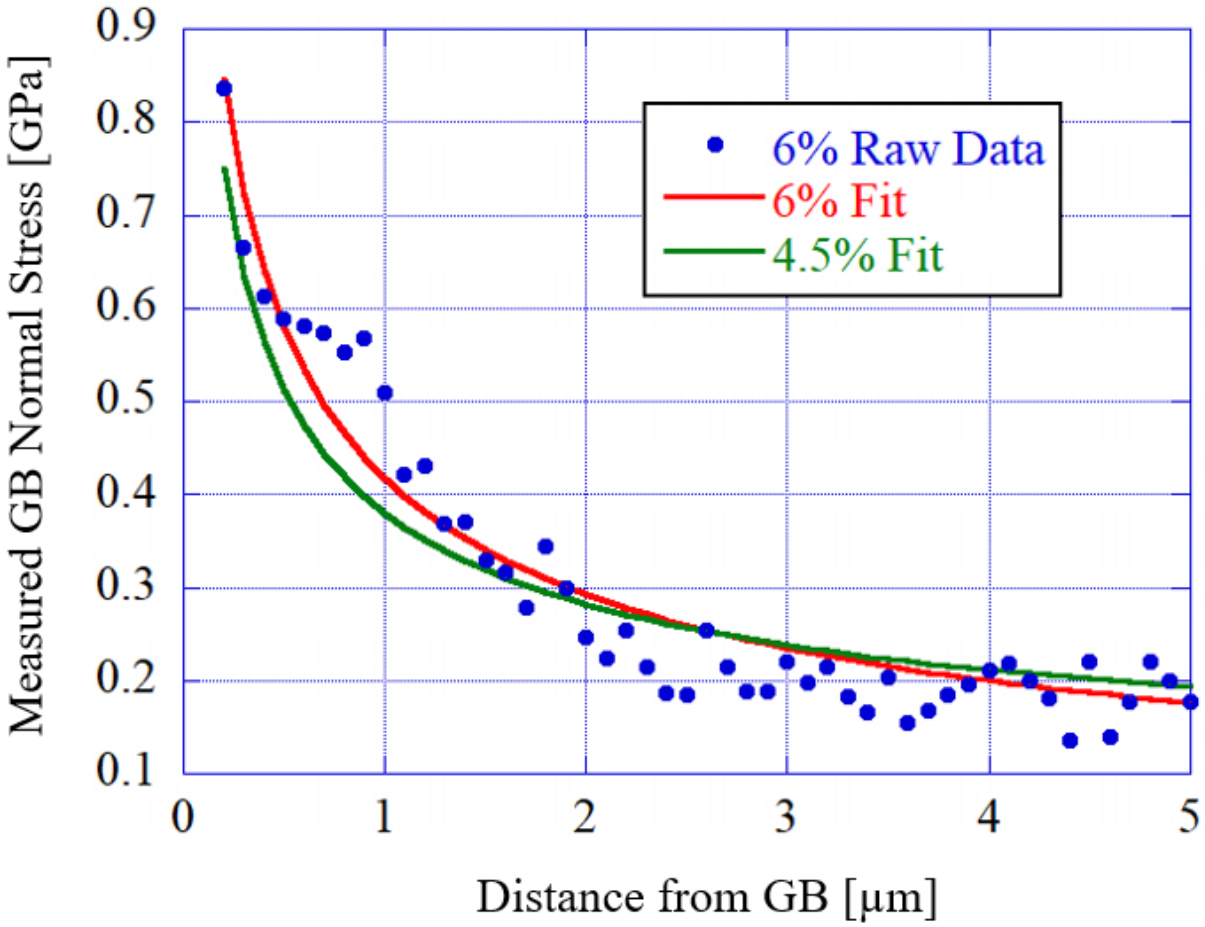

Figure D.78: Tensile stress normal to the grain boundary as a function of distance from the grain boundary in BSCC2 Fe21Cr32Ni 5 dpa tensile bar sample at site BSCC2-23 at 6% total plastic strain (blue data and red fit) and the Eshelby fit for data at the same location after 4.5% plastic strain (green)

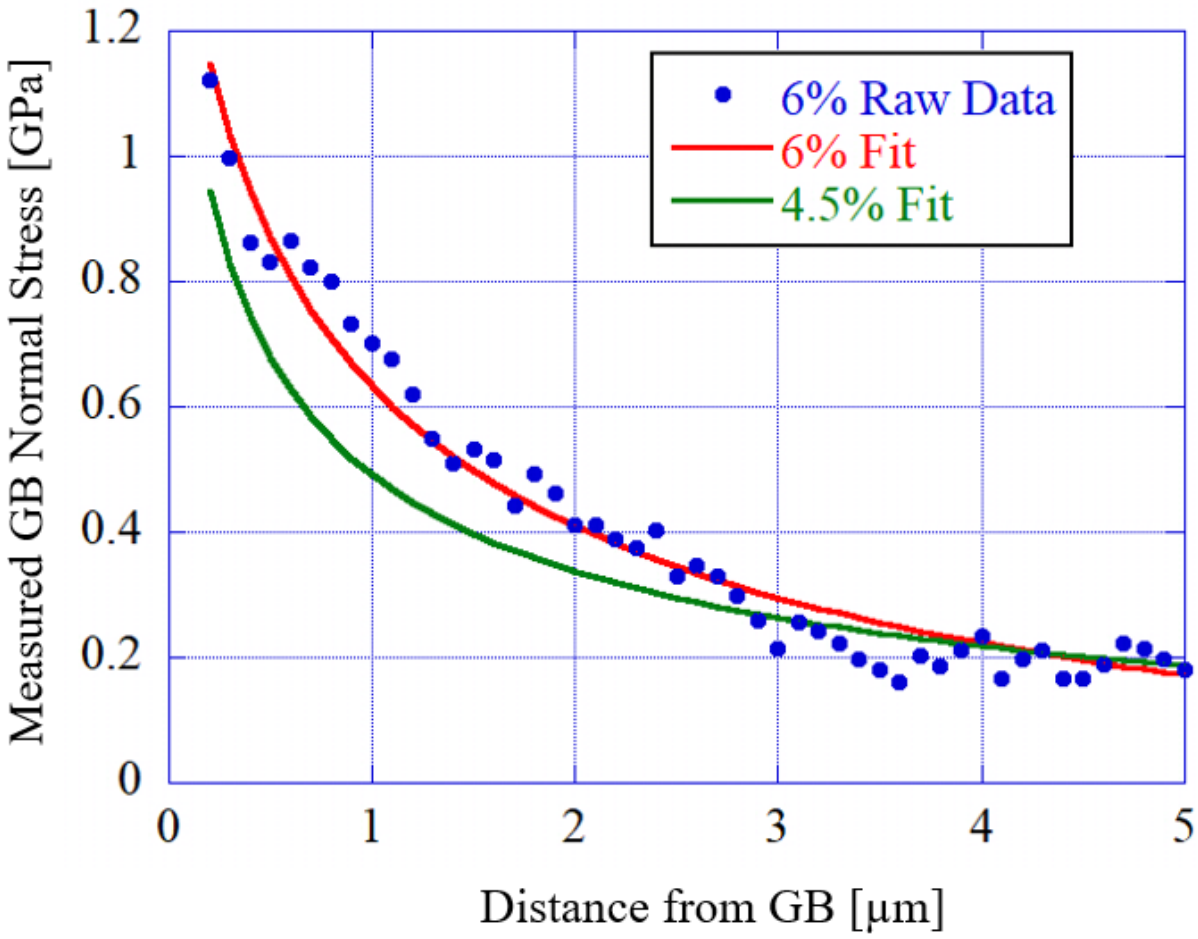

Figure D.79: Tensile stress normal to the grain boundary as a function of distance from the grain boundary in BSCC2 Fe21Cr32Ni 5 dpa tensile bar sample at site BSCC2-24 at 6% total plastic strain (blue data and red fit) and the Eshelby fit for data at the same location after 4.5% plastic strain (green)

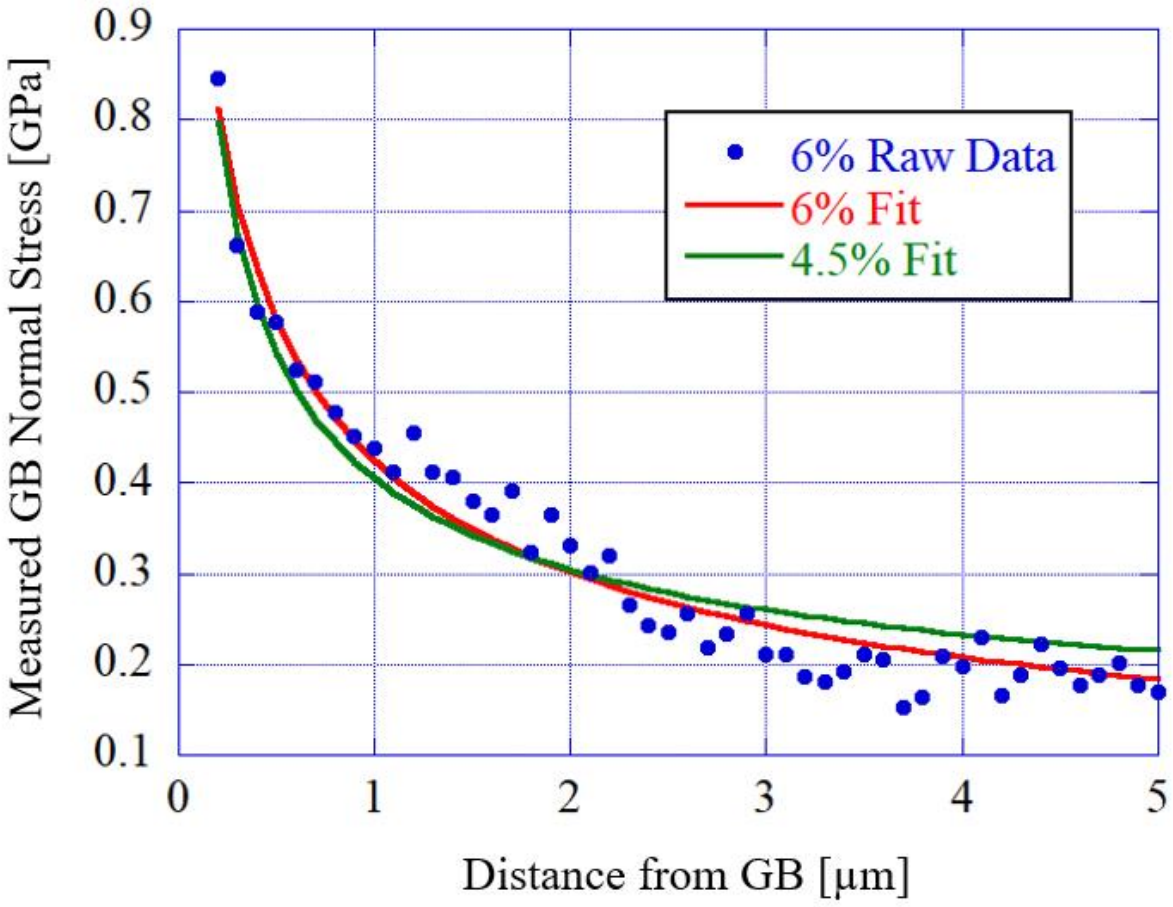

Figure D.80: Tensile stress normal to the grain boundary as a function of distance from the grain boundary in BSCC2 Fe21Cr32Ni 5 dpa tensile bar sample at site BSCC2-25 at 6% total plastic strain (blue data and red fit) and the Eshelby fit for data at the same location after 4.5% plastic strain (green)

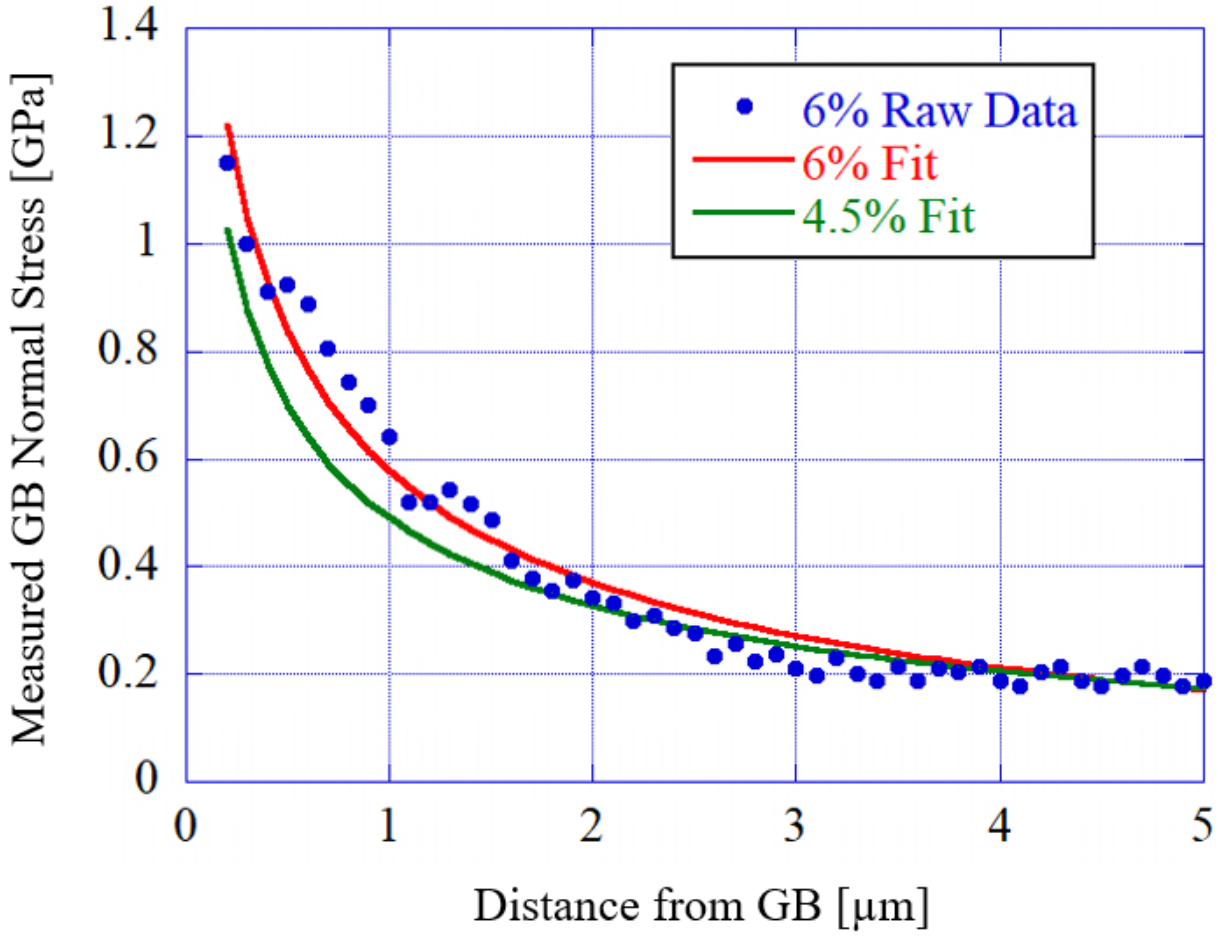

Figure D.81: Tensile stress normal to the grain boundary as a function of distance from the grain boundary in BSCC2 Fe21Cr32Ni 5 dpa tensile bar sample at site BSCC2-26 at 6% total plastic strain (blue data and red fit) and the Eshelby fit for data at the same location after 4.5% plastic strain (green)

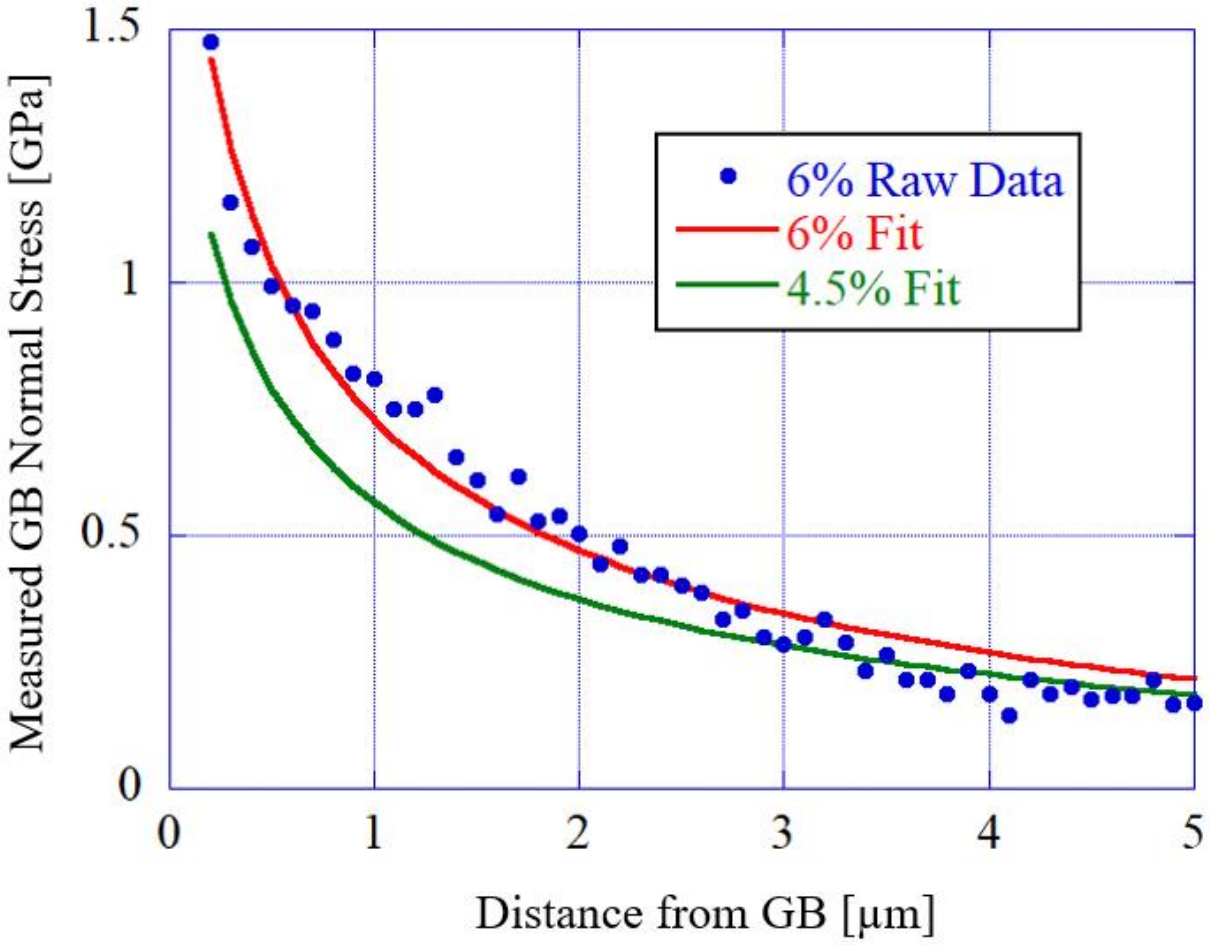

Figure D.82: Tensile stress normal to the grain boundary as a function of distance from the grain boundary in BSCC2 Fe21Cr32Ni 5 dpa tensile bar sample at site BSCC2-27 at 6% total plastic strain (blue data and red fit) and the Eshelby fit for data at the same location after 4.5% plastic strain (green)

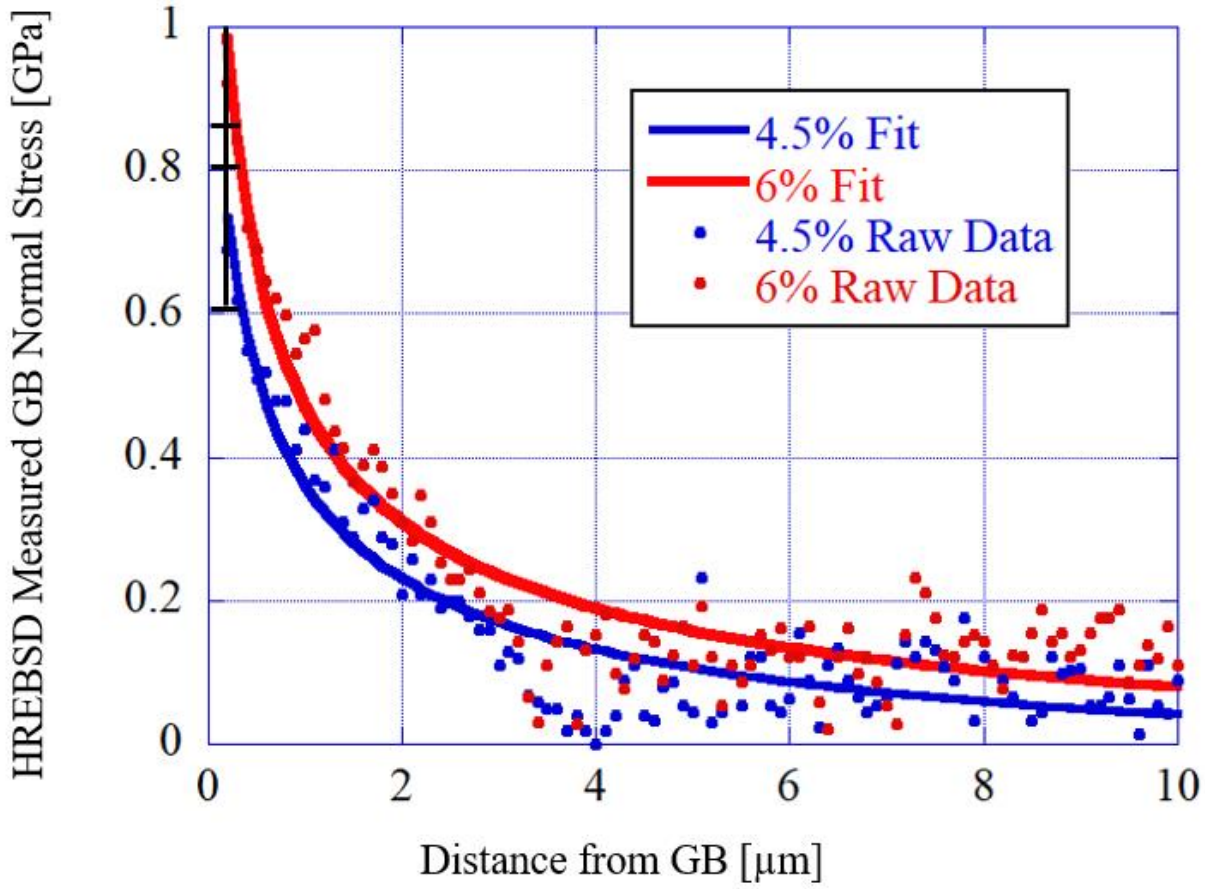

Figure D.83: Tensile stress normal to the grain boundary as a function of distance from the grain boundary in BSCC2 Fe21Cr32Ni 5 dpa tensile bar sample at site BSCC2-28 at 6% total plastic strain (blue data and blue fit) and after 4.5% total plastic strain (blue data and blue fit)

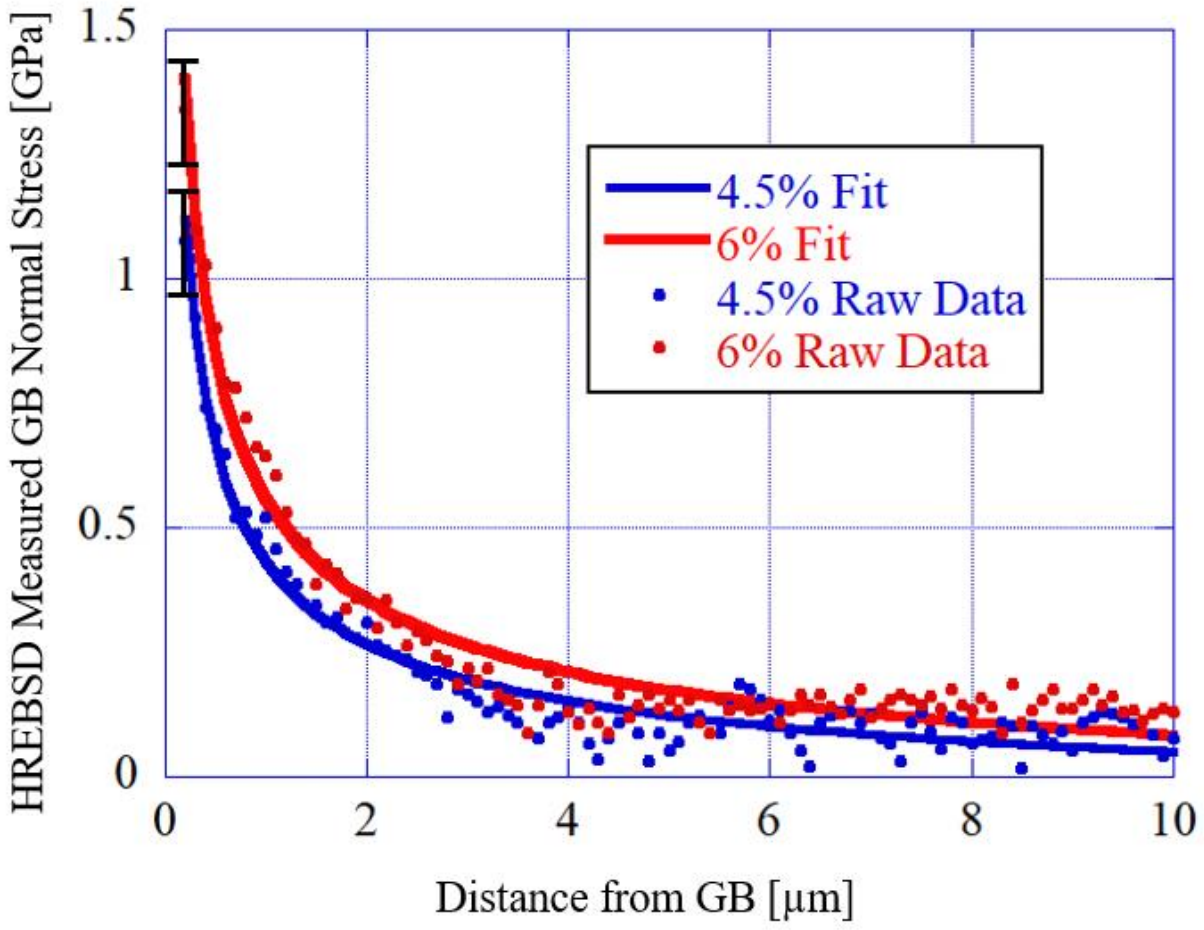

Figure D.84: Tensile stress normal to the grain boundary as a function of distance from the grain boundary in BSCC2 Fe21Cr32Ni 5 dpa tensile bar sample at site BSCC2-29 at 6% total plastic strain (blue data and blue fit) and after 4.5% total plastic strain (blue data and blue fit)

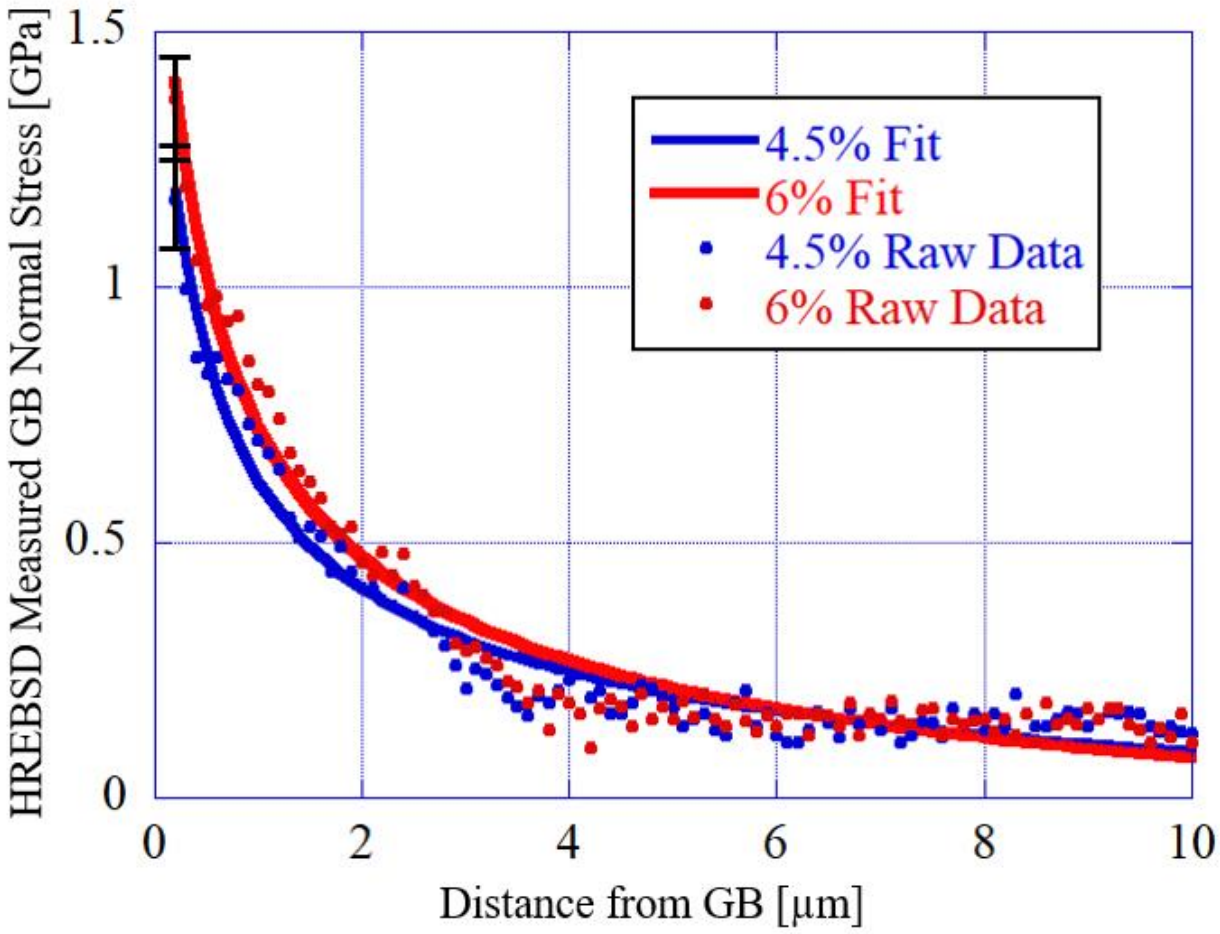

Figure D.85: Tensile stress normal to the grain boundary as a function of distance from the grain boundary in BSCC2 Fe21Cr32Ni 5 dpa tensile bar sample at site BSCC2-30 at 6% total plastic strain (blue data and blue fit) and after 4.5% total plastic strain (blue data and blue fit)

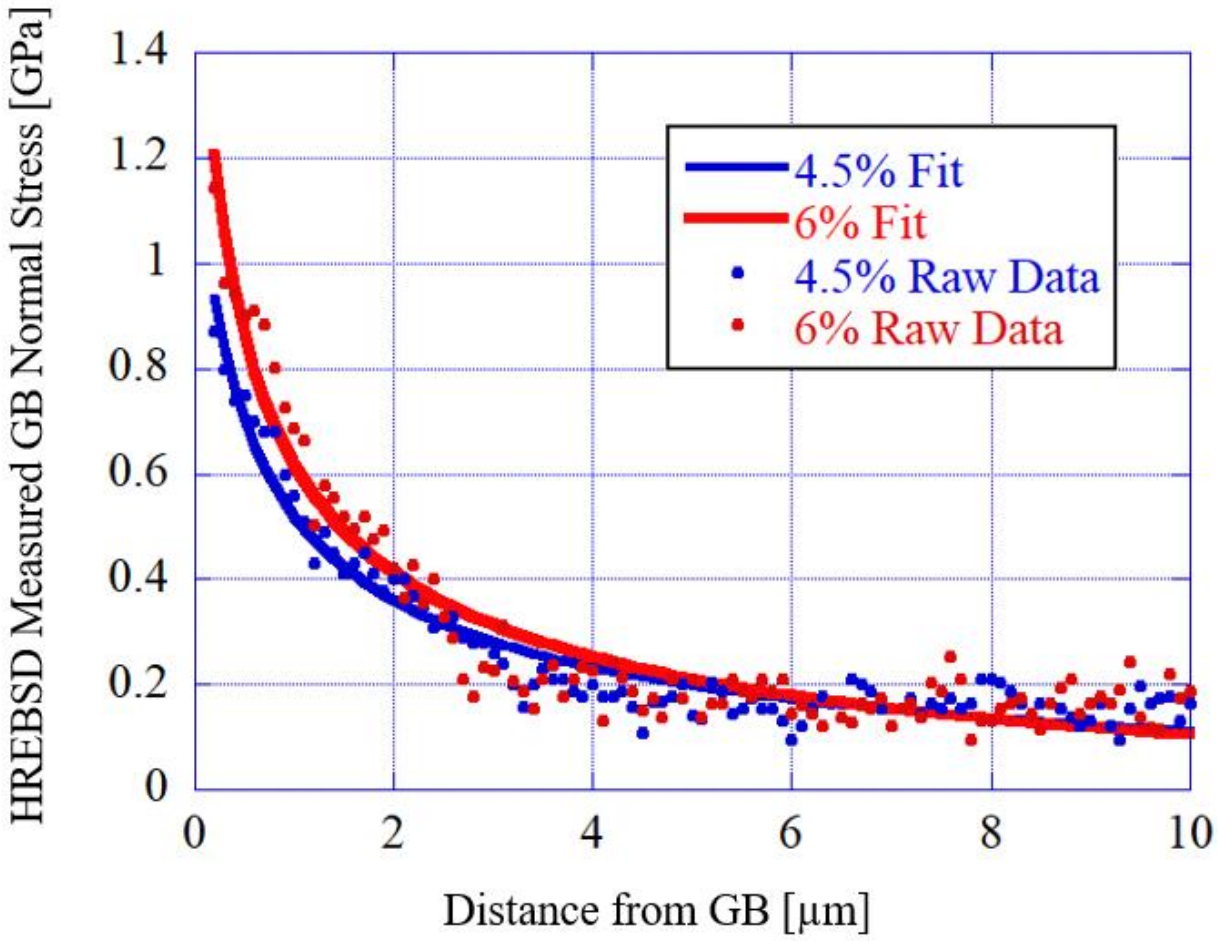

Figure D.86: Tensile stress normal to the grain boundary as a function of distance from the grain boundary in BSCC2 Fe21Cr32Ni 5 dpa tensile bar sample at site BSCC2-31 at 6% total plastic strain (blue data and blue fit) and after 4.5% total plastic strain (blue data and blue fit)

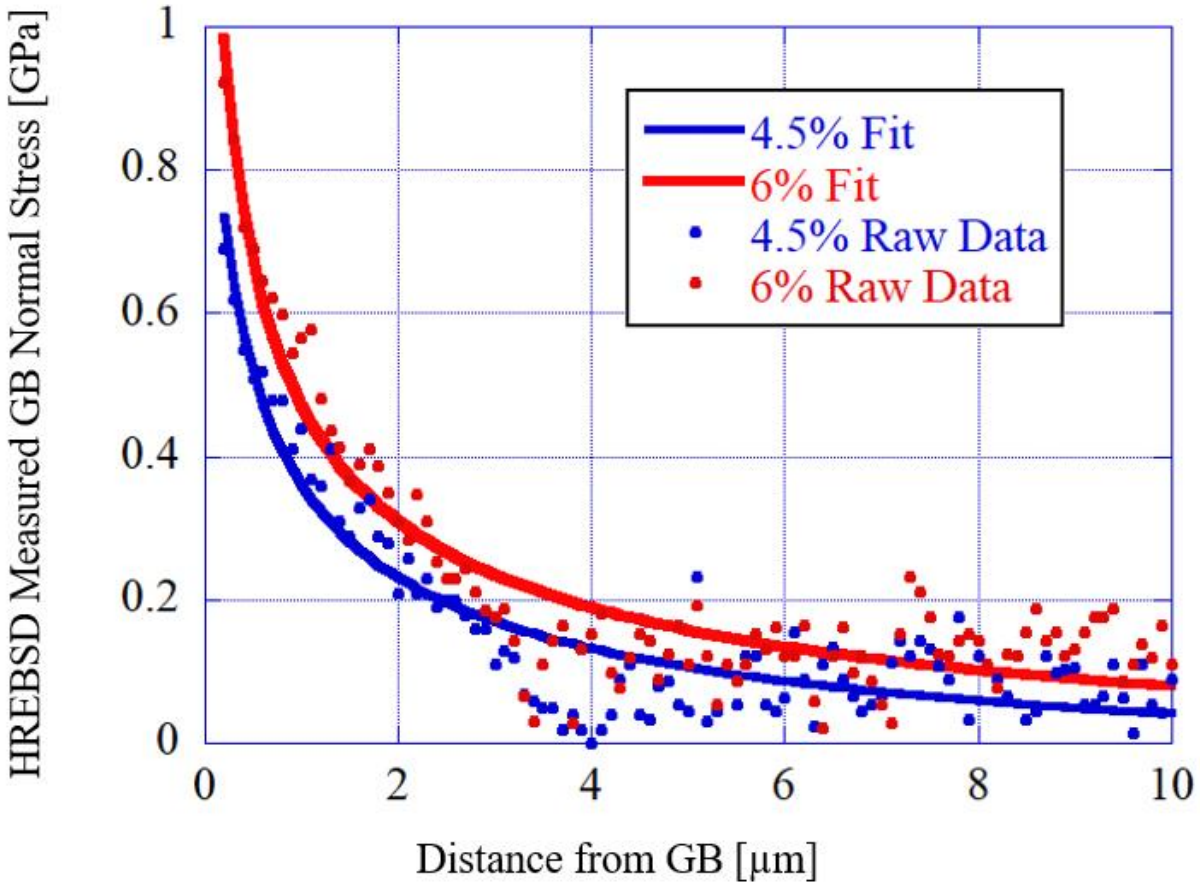

Figure D.87: Tensile stress normal to the grain boundary as a function of distance from the grain boundary in BSCC2 Fe21Cr32Ni 5 dpa tensile bar sample at site BSCC2-32 at 6% total plastic strain (blue data and blue fit) and after 4.5% total plastic strain (blue data and blue fit)

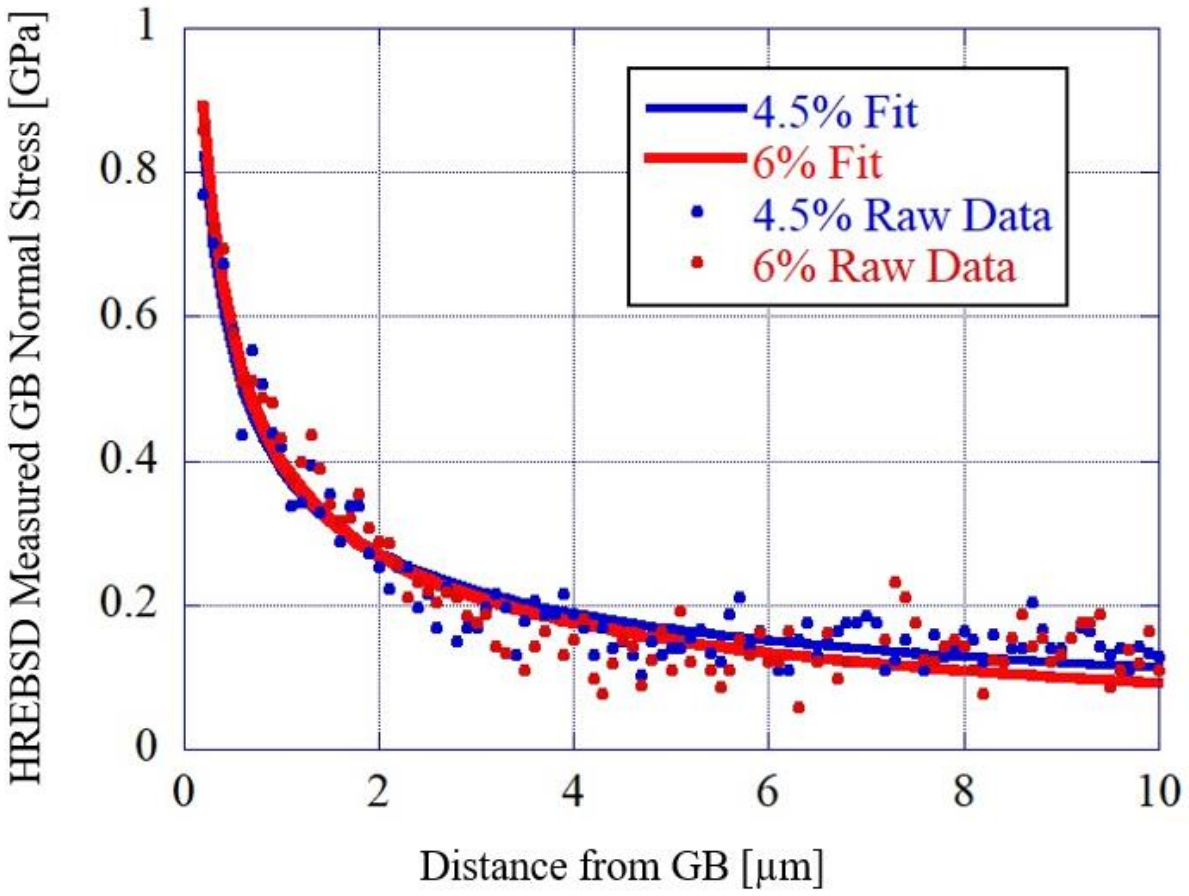

Figure D.88: Tensile stress normal to the grain boundary as a function of distance from the grain boundary in BSCC2 Fe21Cr32Ni 5 dpa tensile bar sample at site BSCC2-33 at 6% total plastic strain (blue data and blue fit) and after 4.5% total plastic strain (blue data and blue fit)

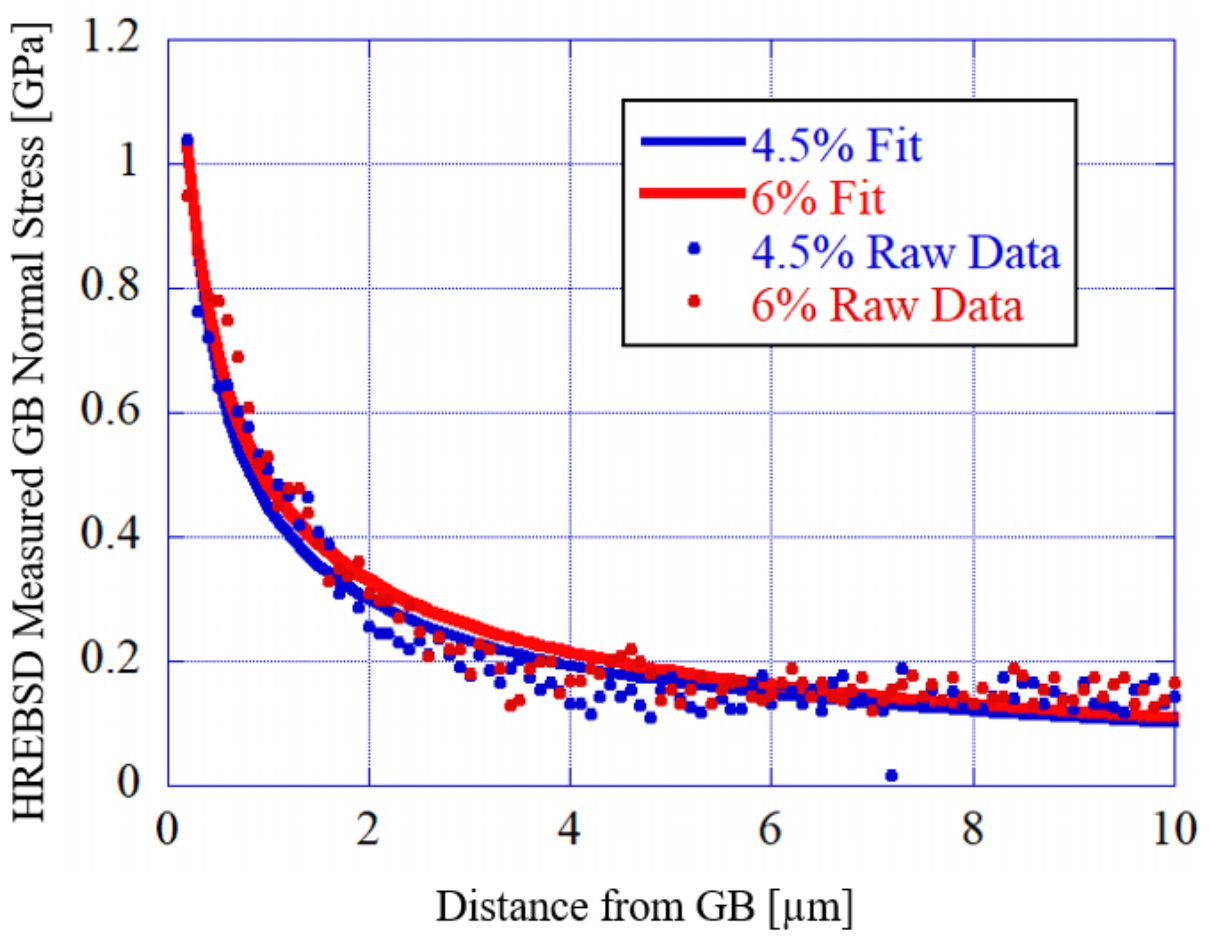

Figure D.89: Tensile stress normal to the grain boundary as a function of distance from the grain boundary in BSCC2 Fe21Cr32Ni 5 dpa tensile bar sample at site BSCC2-34 at 6% total plastic strain (blue data and blue fit) and after 4.5% total plastic strain (blue data and blue fit)

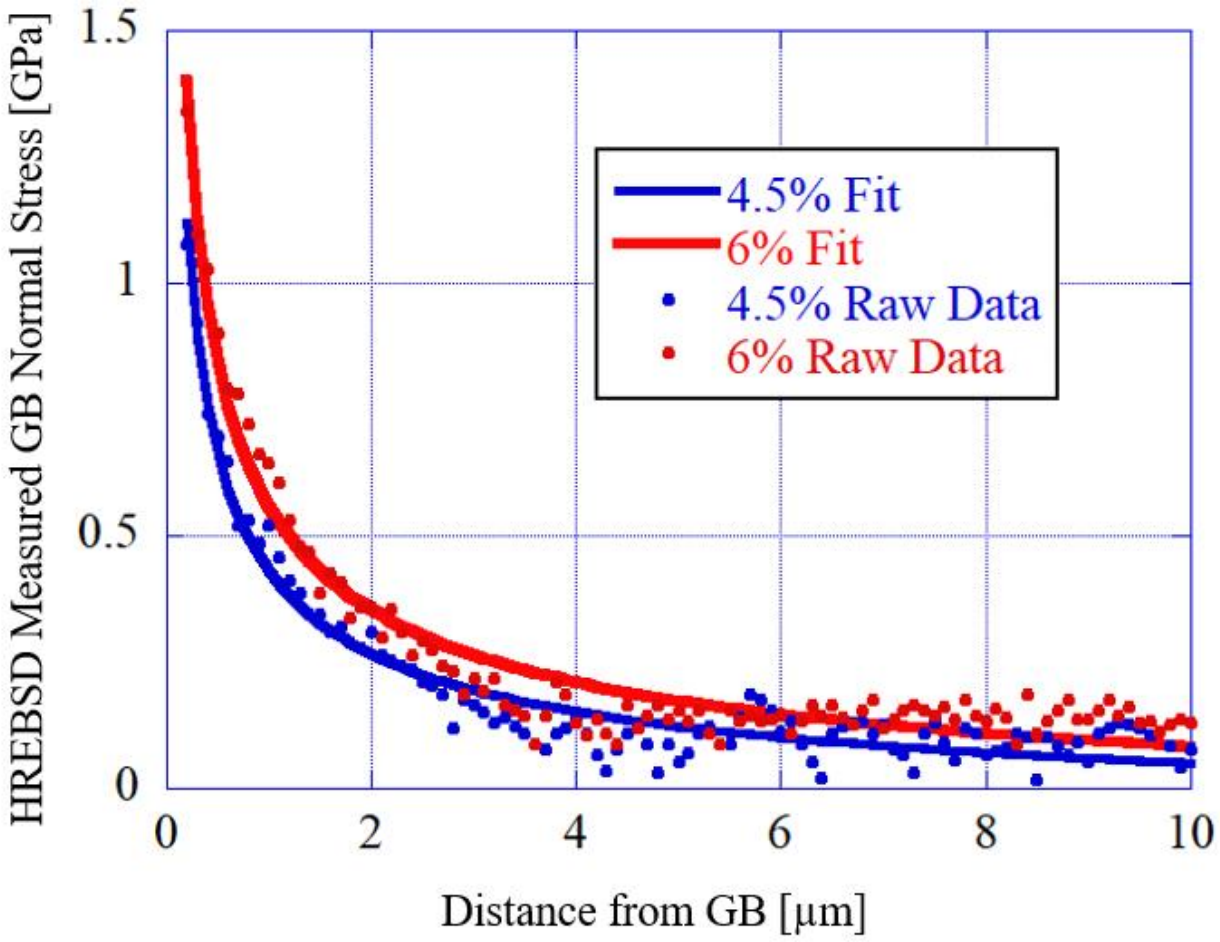

Figure D.90: Tensile stress normal to the grain boundary as a function of distance from the grain boundary in BSCC2 Fe21Cr32Ni 5 dpa tensile bar sample at site BSCC2-35 at 6% total plastic strain (blue data and blue fit) and after 4.5% total plastic strain (blue data and blue fit)

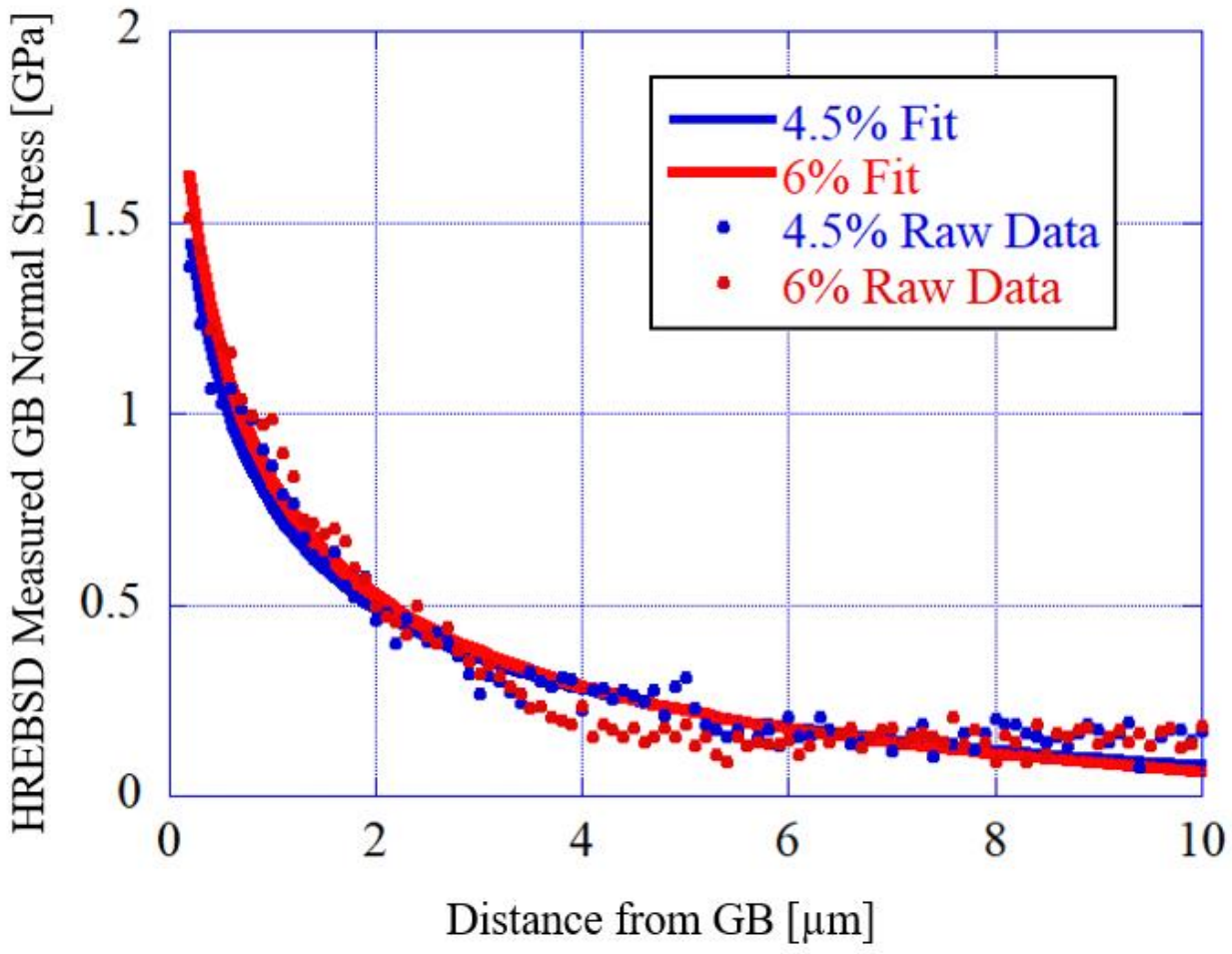

Figure D.91: Tensile stress normal to the grain boundary as a function of distance from the grain boundary in BSCC2 Fe21Cr32Ni 5 dpa tensile bar sample at site BSCC2-36 at 6% total plastic strain (blue data and blue fit) and after 4.5% total plastic strain (blue data and blue fit)

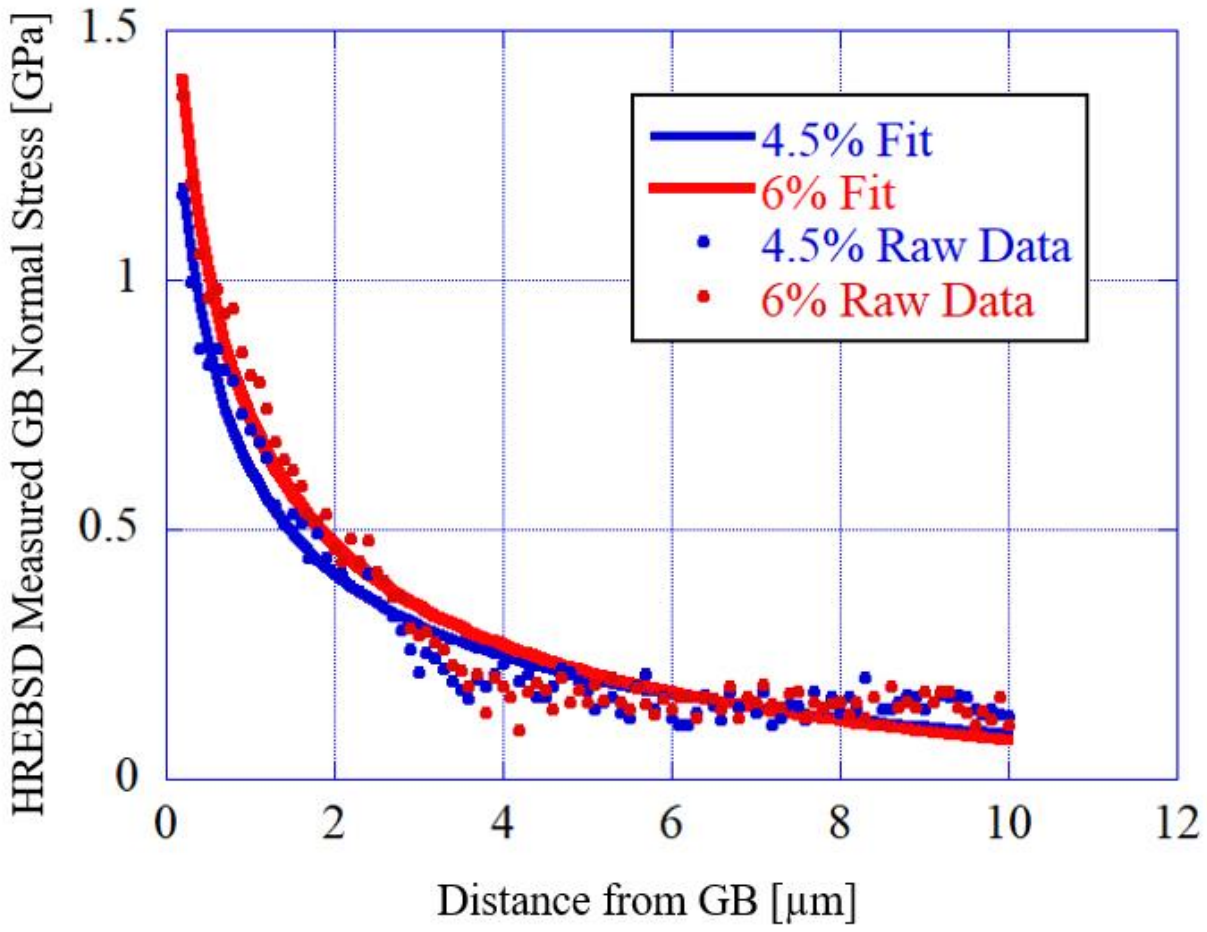

Figure D.92: Tensile stress normal to the grain boundary as a function of distance from the grain boundary in BSCC2 Fe21Cr32Ni 5 dpa tensile bar sample at site BSCC2-37 at 6% total plastic strain (blue data and blue fit) and after 4.5% total plastic strain (blue data and blue fit)

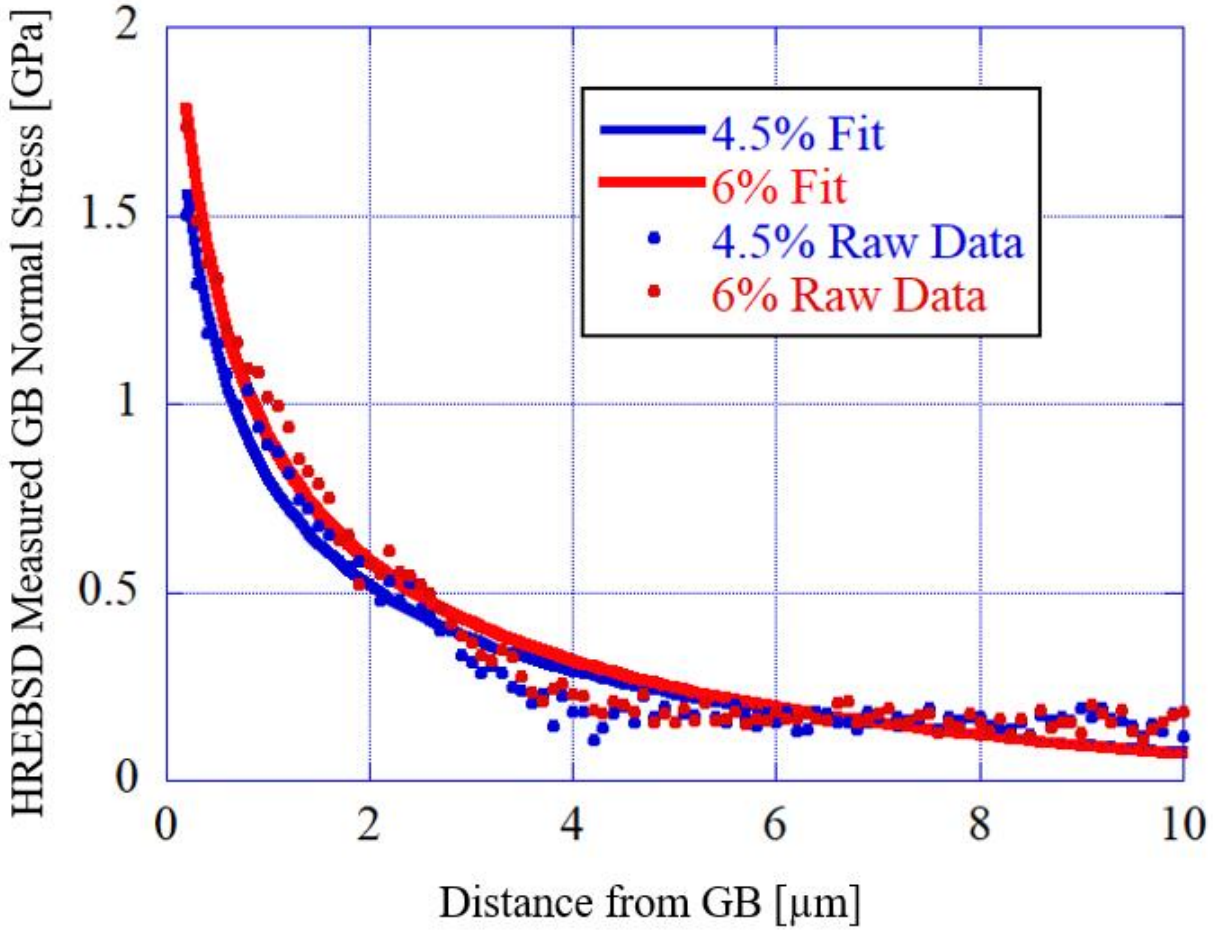

Figure D.93: Tensile stress normal to the grain boundary as a function of distance from the grain boundary in BSCC2 Fe21Cr32Ni 5 dpa tensile bar sample at site BSCC2-38 at 6% total plastic strain (blue data and blue fit) and after 4.5% total plastic strain (blue data and blue fit)

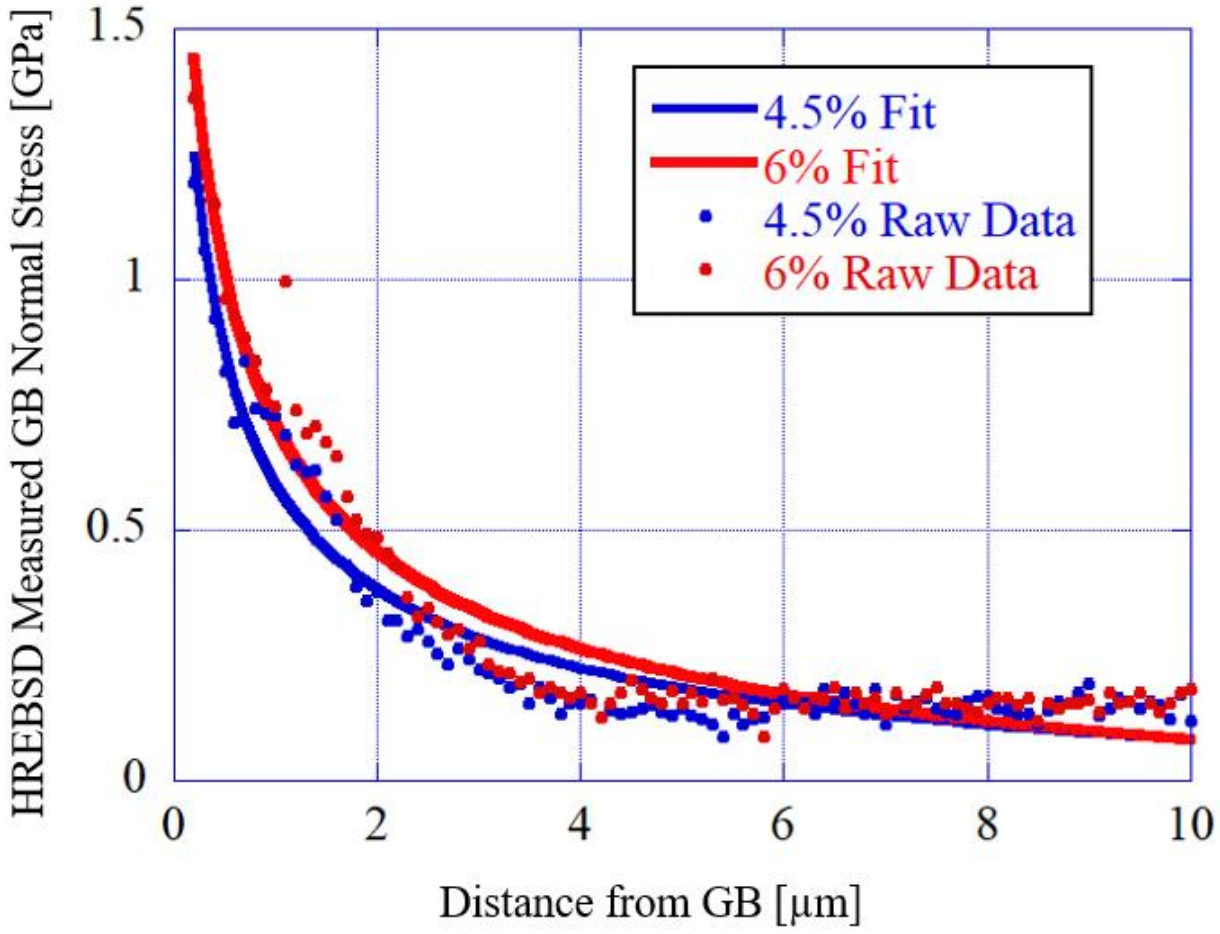

Figure D.94: Tensile stress normal to the grain boundary as a function of distance from the grain boundary in BSCC2 Fe21Cr32Ni 5 dpa tensile bar sample at site BSCC2-39 at 6% total plastic strain (blue data and blue fit) and after 4.5% total plastic strain (blue data and blue fit)

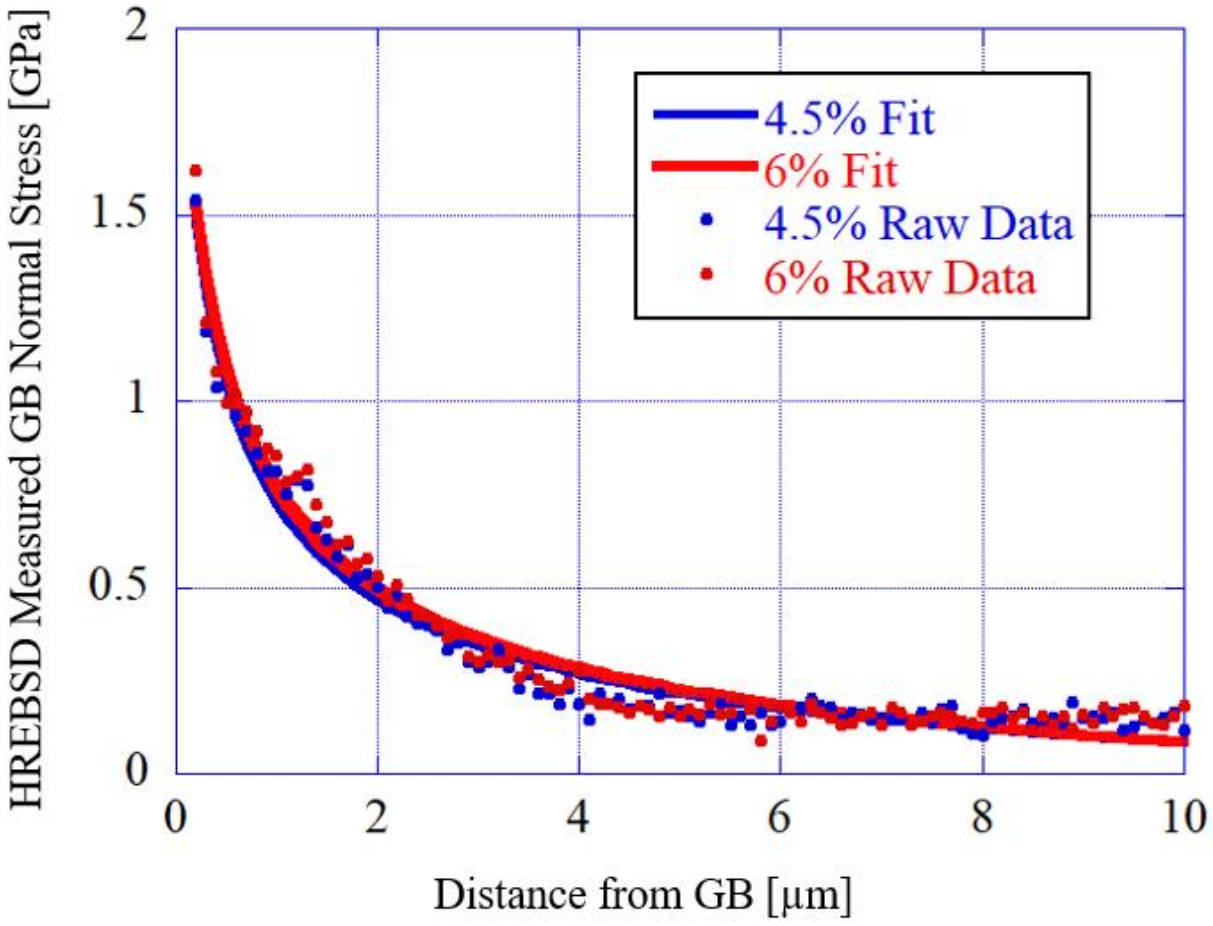

Figure D.95: Tensile stress normal to the grain boundary as a function of distance from the grain boundary in BSCC2 Fe21Cr32Ni 5 dpa tensile bar sample at site BSCC2-40 at 6% total plastic strain (blue data and blue fit) and after 4.5% total plastic strain (blue data and blue fit)

APPENDIX E

Intergranular Cracks at Discontinuous Channel – Grain Boundary Interaction Sites Analyzed by HREBSD in ASCC2 Fe13Cr15Ni 5 dpa Tensile Bar Sample

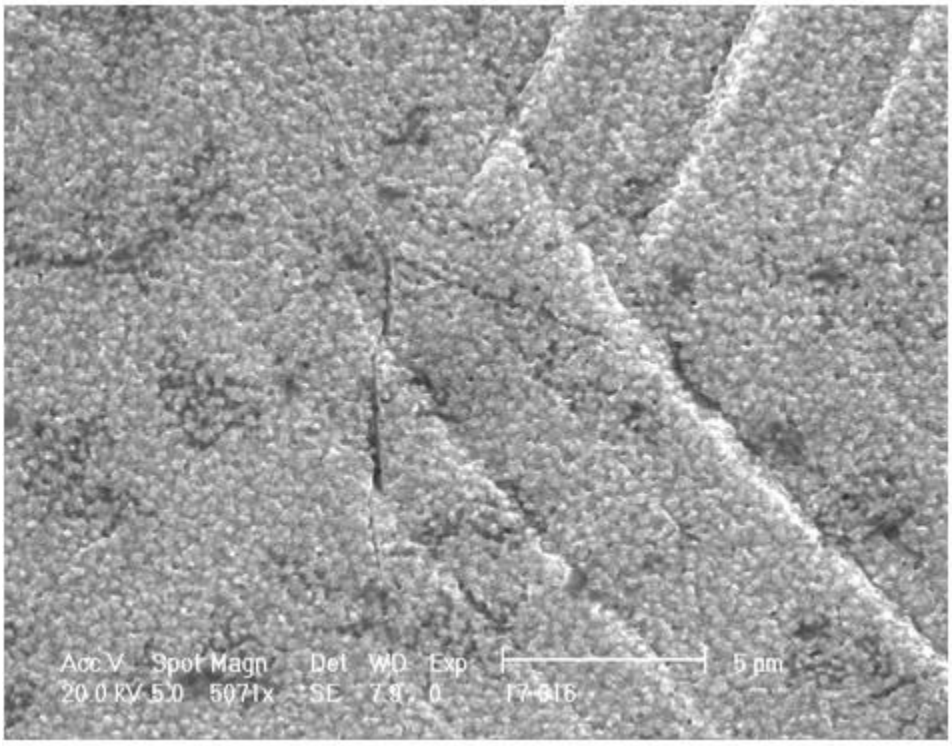

Figure E.1: Intergranular crack initiated in ASCC2 Fe13Cr15Ni 5 dpa tensile bar sample at GB site ASCC2-3

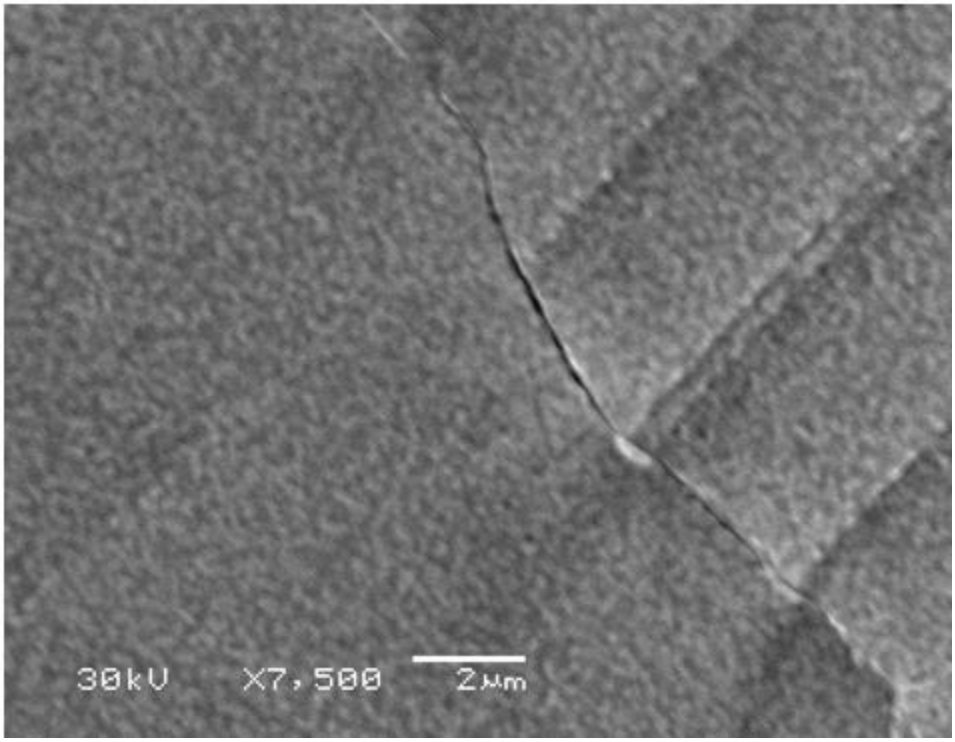

Figure E.2: Intergranular crack initiated in ASCC2 Fe13Cr15Ni 5 dpa tensile bar sample at GB site ASCC2-4

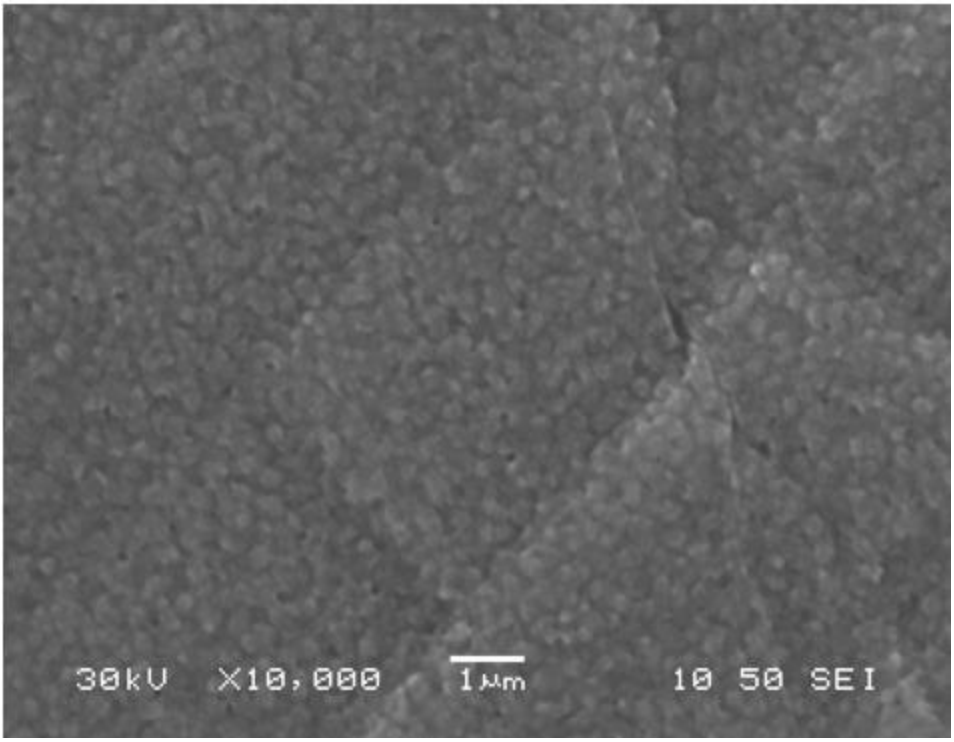

Figure E.3: Intergranular crack initiated in ASCC2 Fe13Cr15Ni 5 dpa tensile bar sample at GB site ASCC2-5

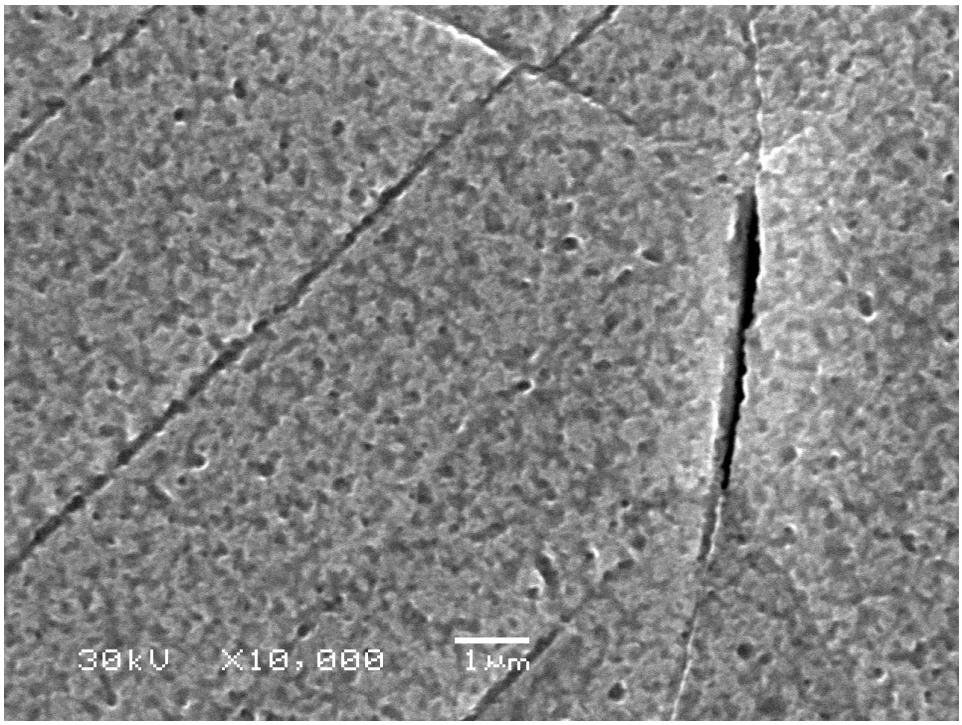

Figure E.4: Intergranular crack initiated in ASCC2 Fe13Cr15Ni 5 dpa tensile bar sample at GB site ASCC2-7

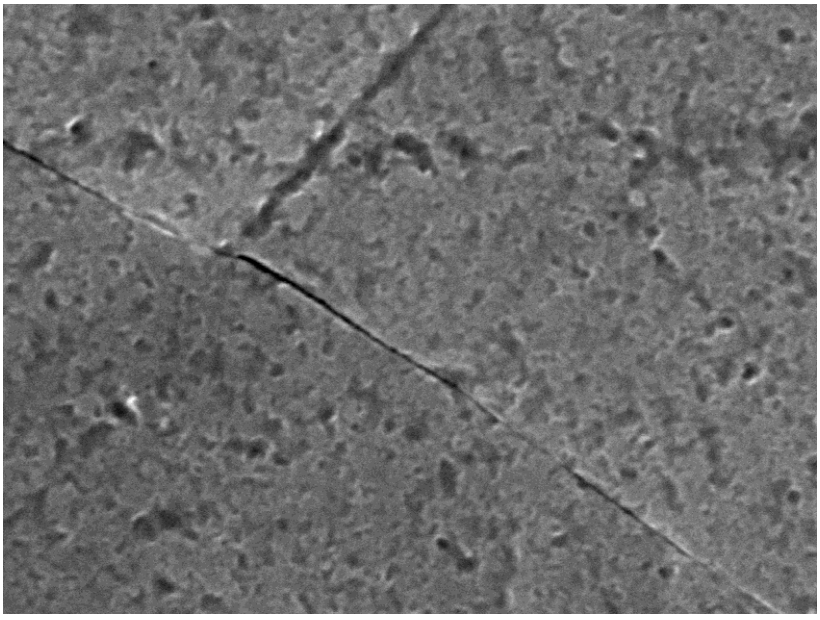

Figure E.5: Intergranular crack initiated in ASCC2 Fe13Cr15Ni 5 dpa tensile bar sample at GB site ASCC2-11

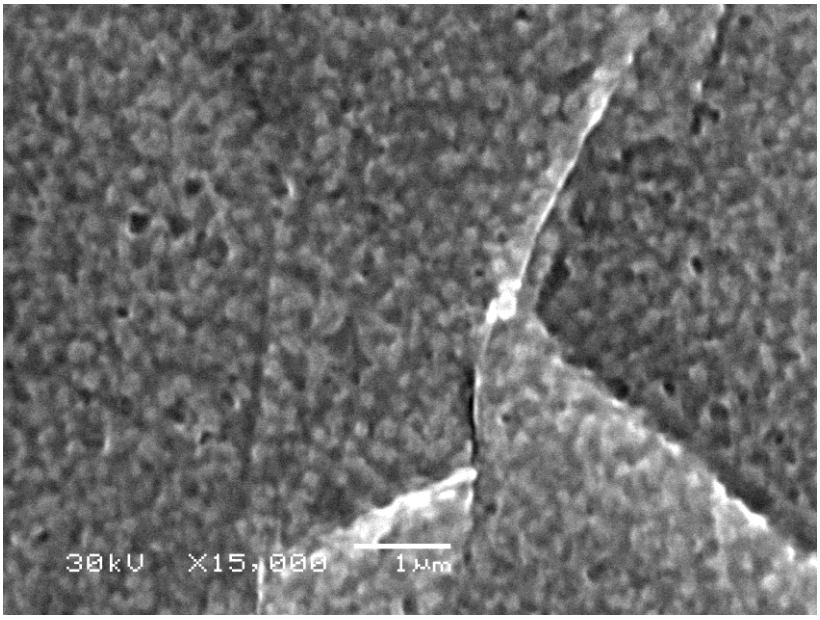

Figure E.6: Intergranular crack initiated in ASCC2 Fe13Cr15Ni 5 dpa tensile bar sample at GB site ASCC2-15

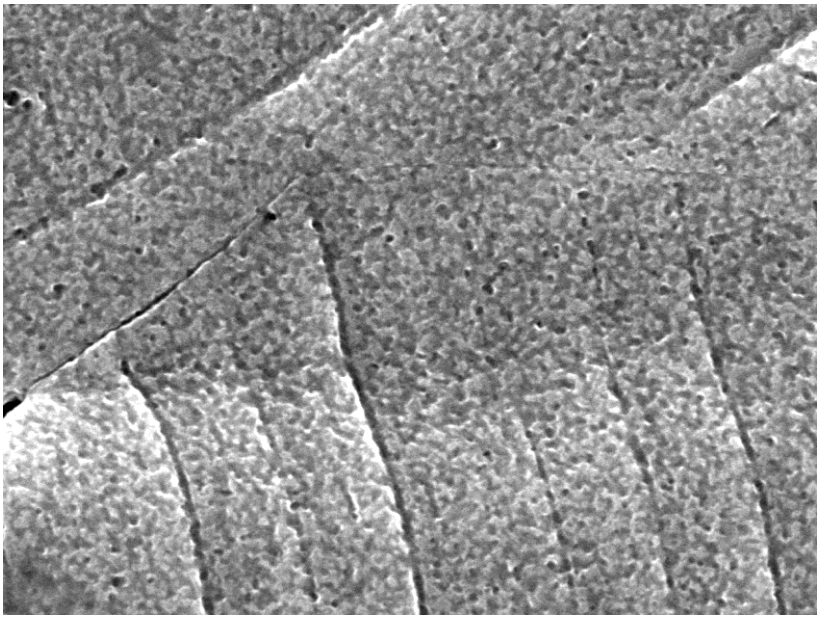

Figure E.7: Intergranular crack initiated in ASCC2 Fe13Cr15Ni 5 dpa tensile bar sample at GB site ASCC2-16

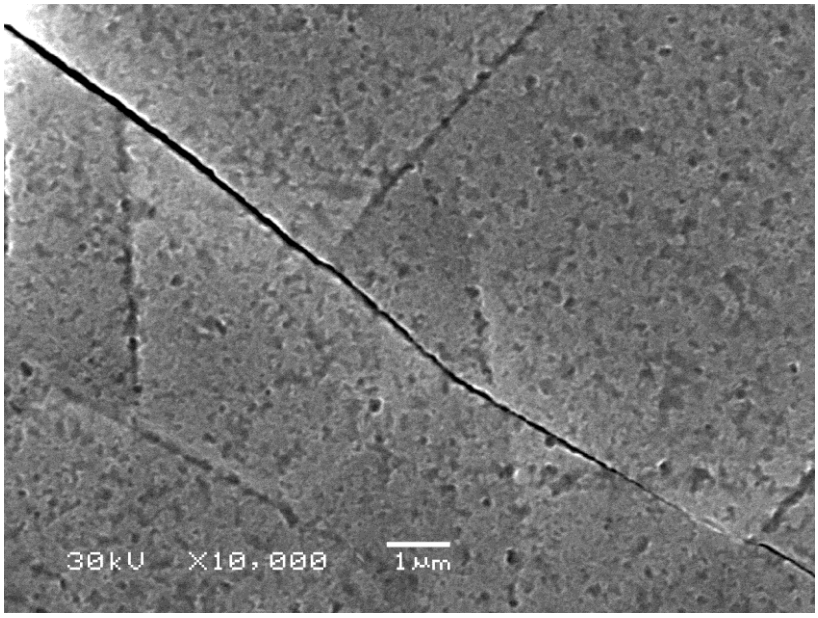

Figure E.8: Intergranular crack initiated in ASCC2 Fe13Cr15Ni 5 dpa tensile bar sample at GB site ASCC2-18

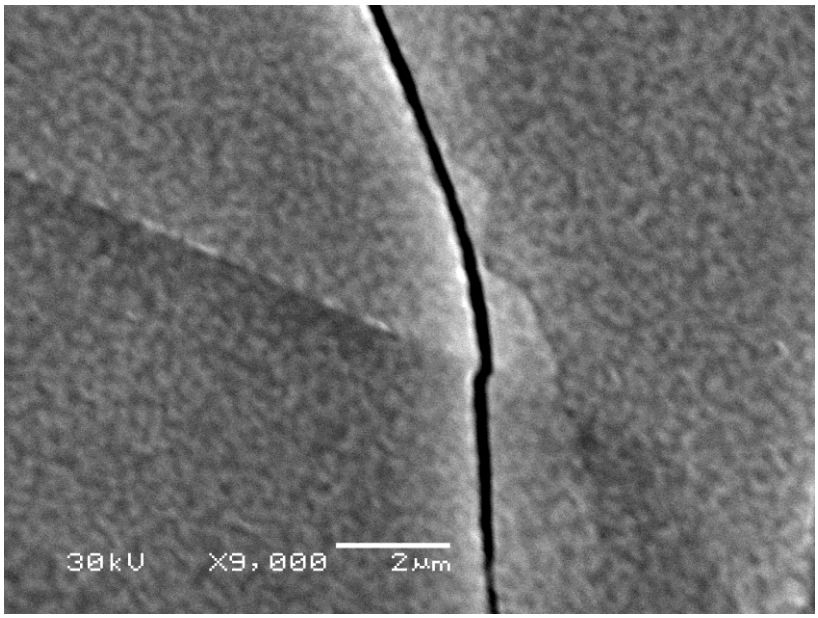

Figure E.9: Intergranular crack initiated in ASCC2 Fe13Cr15Ni 5 dpa tensile bar sample at GB site ASCC2-19

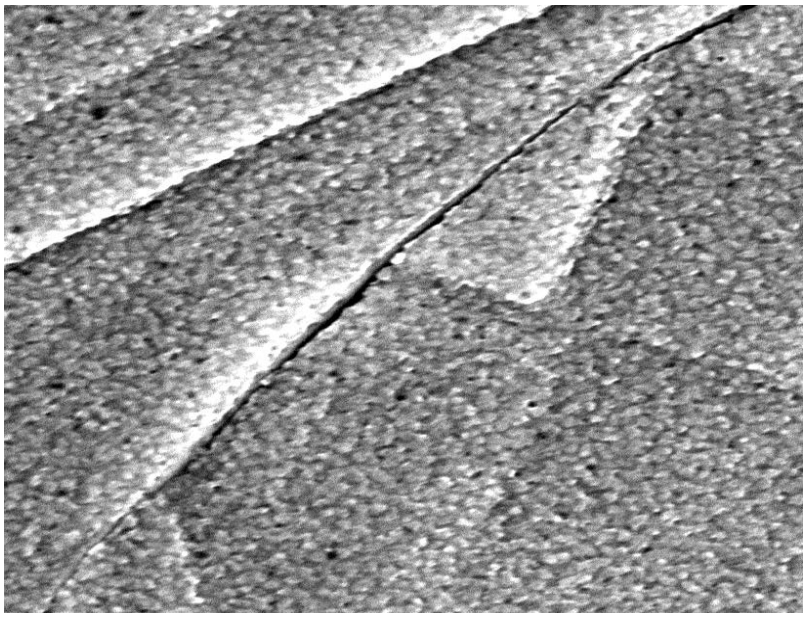

Figure E.10: Intergranular crack initiated in ASCC2 Fe13Cr15Ni 5 dpa tensile bar sample at GB site ASCC2-20

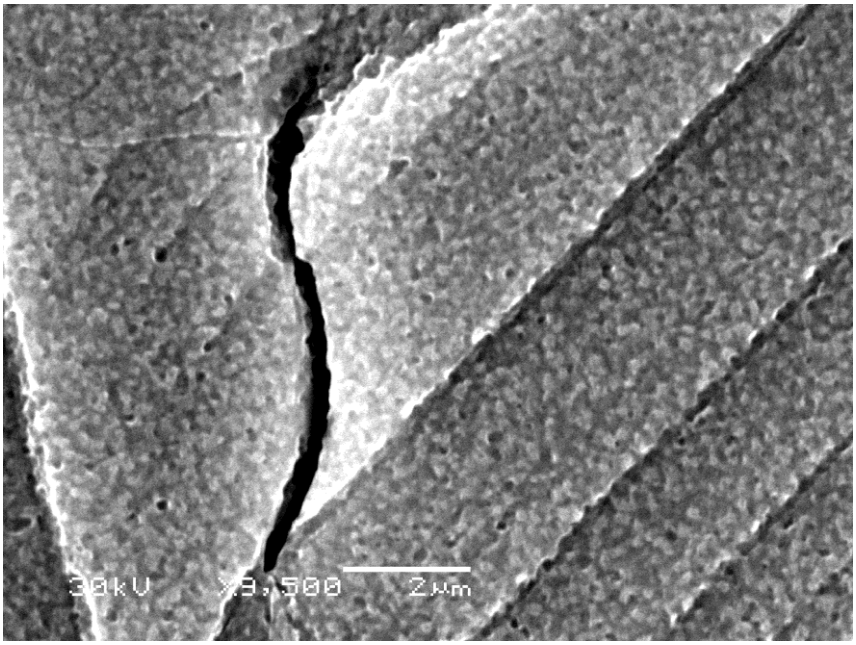

Figure E.11: Intergranular crack initiated in ASCC2 Fe13Cr15Ni 5 dpa tensile bar sample at GB site ASCC21

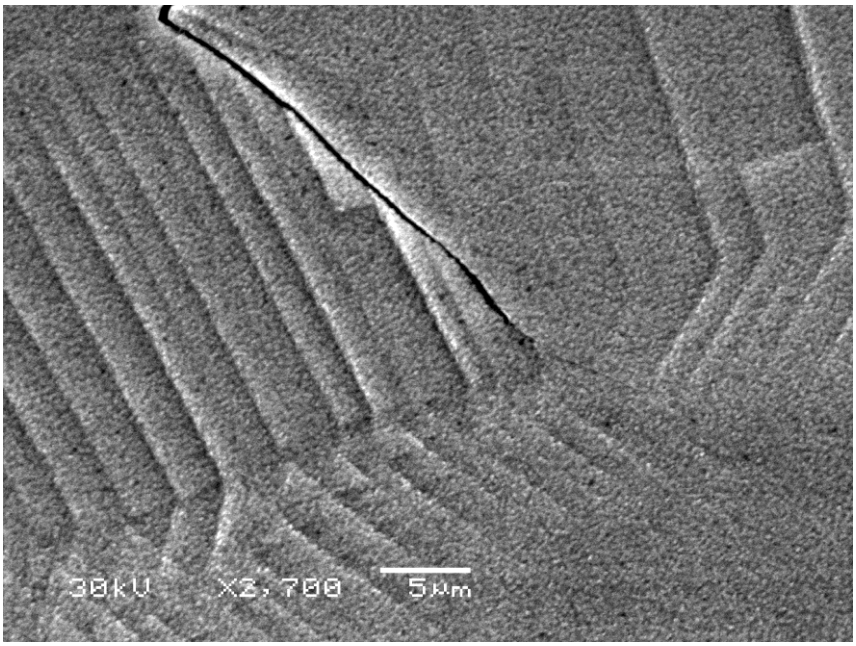

Figure E.12: Intergranular crack initiated in ASCC2 Fe13Cr15Ni 5 dpa tensile bar sample at GB site ASCC2-24

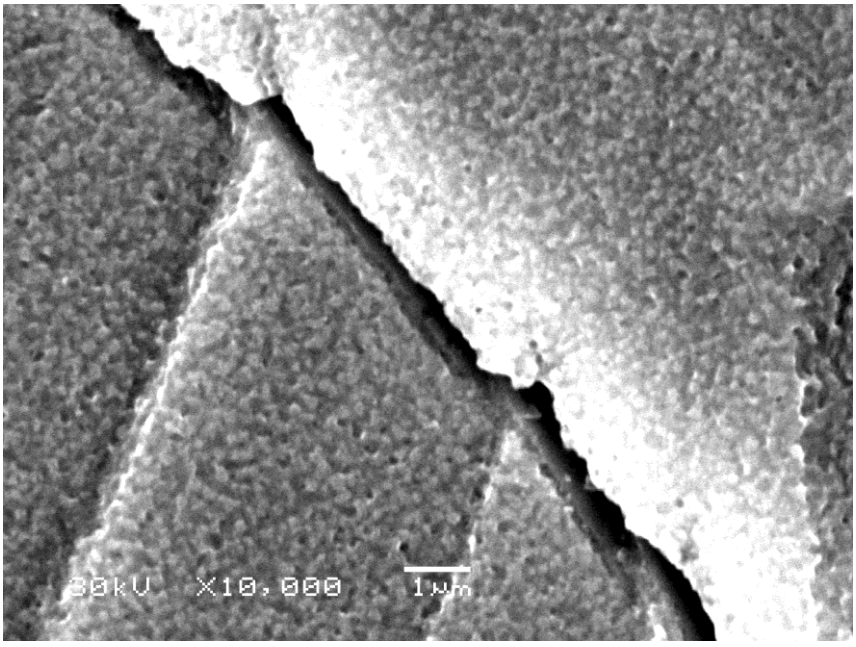

Figure E.13: Intergranular crack initiated in ASCC2 Fe13Cr15Ni 5 dpa tensile bar sample at GB site ASCC2-25

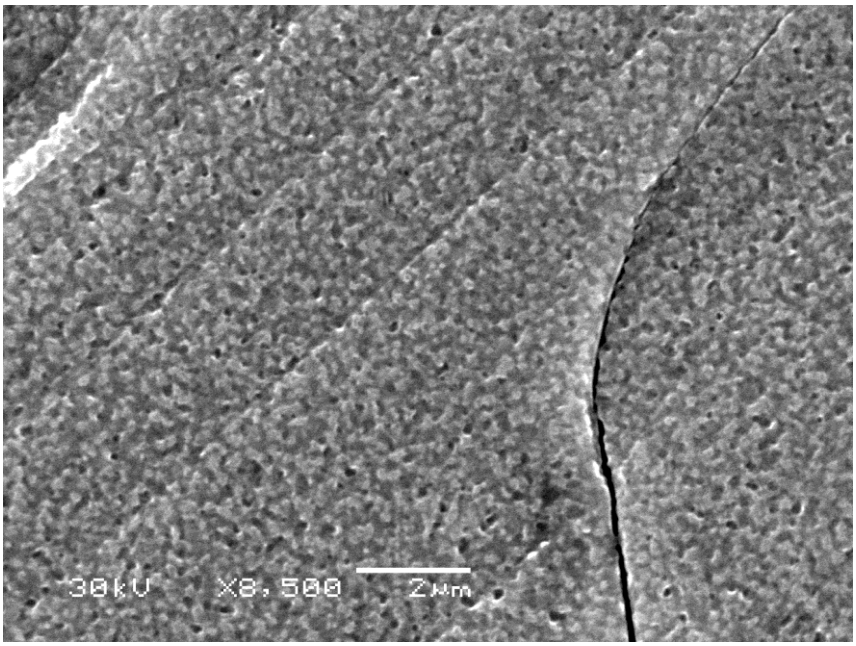

Figure E.14: Intergranular crack initiated in ASCC2 Fe13Cr15Ni 5 dpa tensile bar sample at GB site ASCC2-30

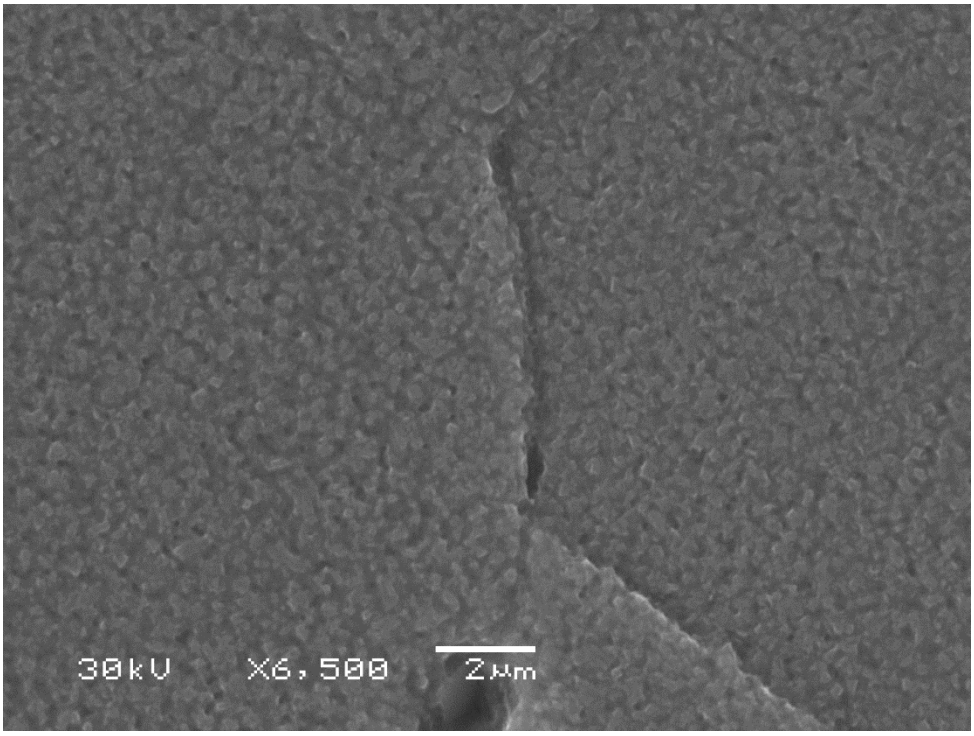

Figure E.15: Intergranular crack initiated in ASCC2 Fe13Cr15Ni 5 dpa tensile bar sample at GB site ASCC2-31

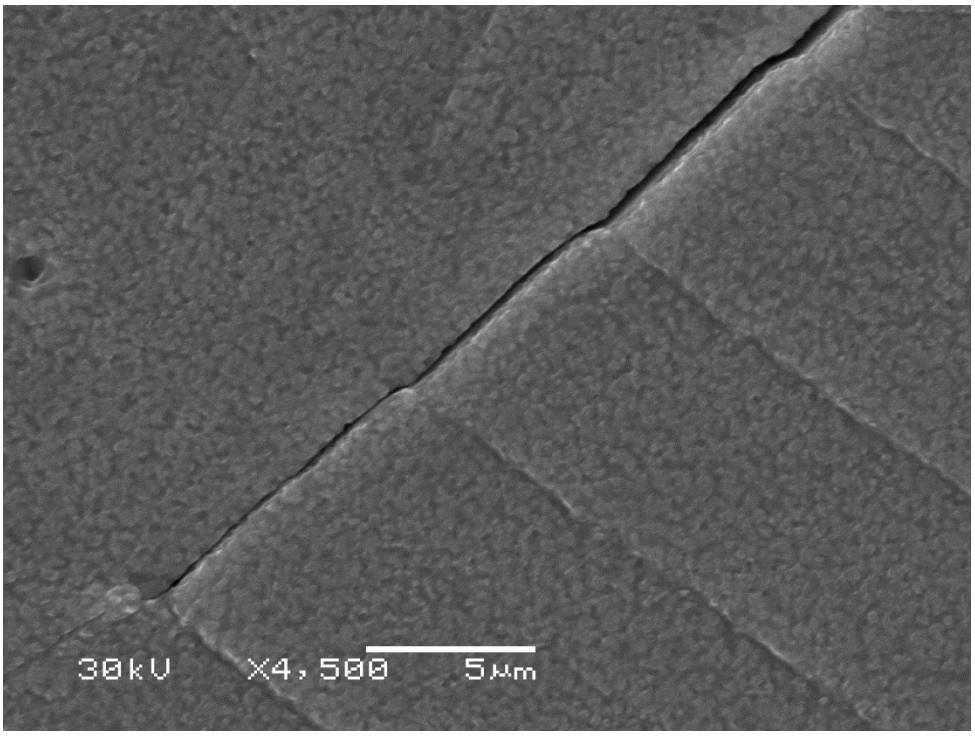

Figure E.16: Intergranular crack initiated in ASCC2 Fe13Cr15Ni 5 dpa tensile bar sample at GB site ASCC2-32

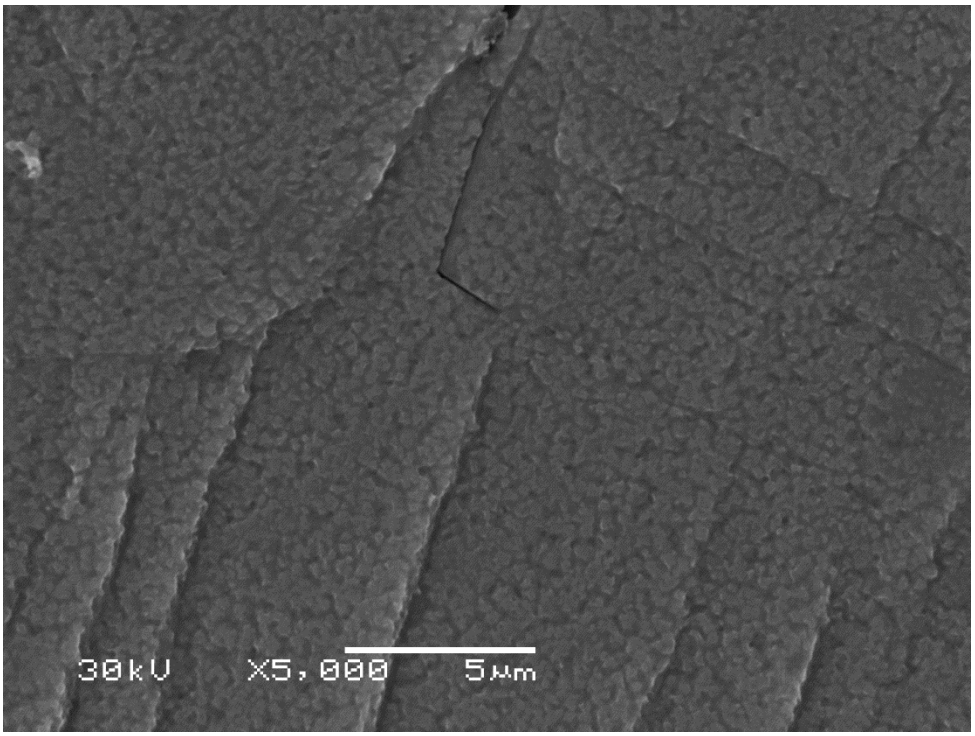

Figure E.17: Intergranular crack initiated in ASCC2 Fe13Cr15Ni 5 dpa tensile bar sample at GB site ASCC2-37

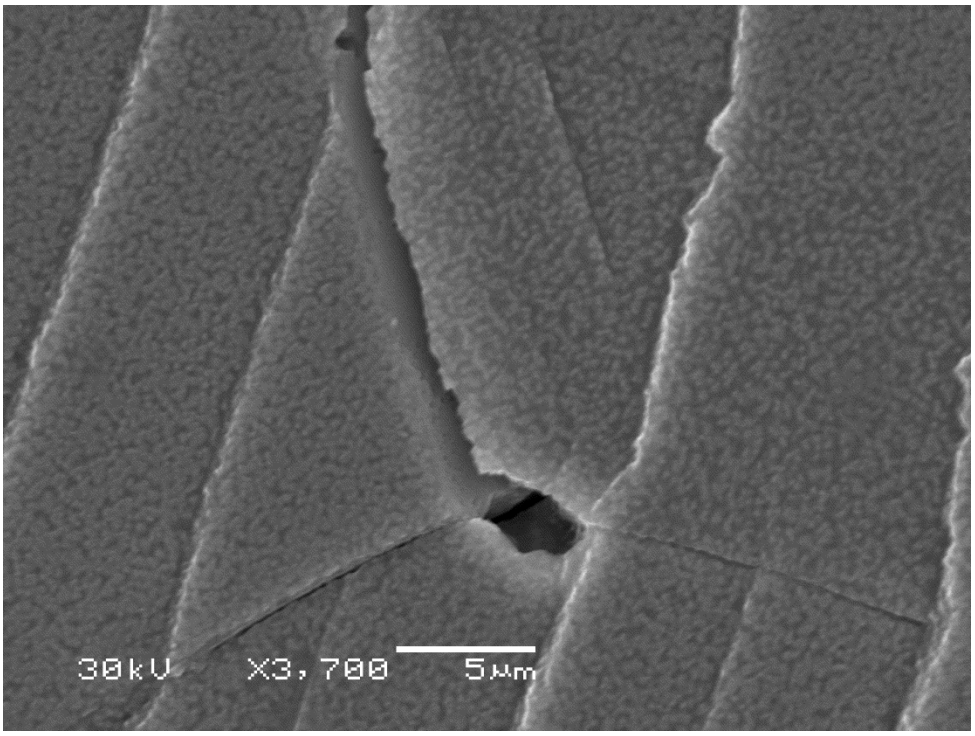

Figure E.18: Intergranular crack initiated in ASCC2 Fe13Cr15Ni 5 dpa tensile bar sample at GB site ASCC2-38

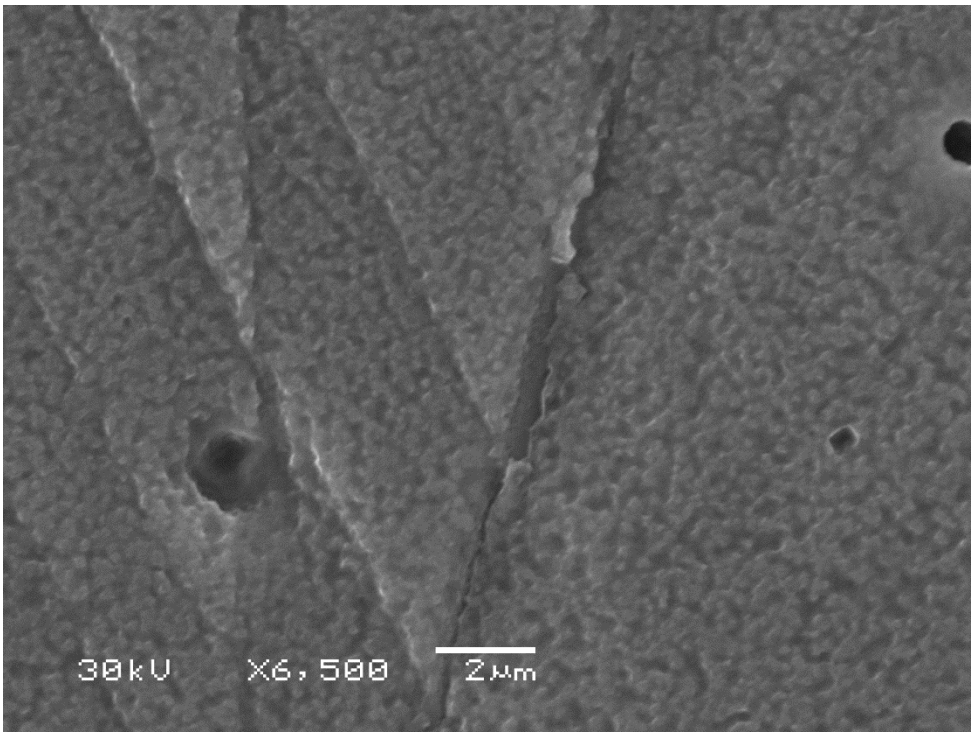

Figure E.19: Intergranular crack initiated in ASCC2 Fe13Cr15Ni 5 dpa tensile bar sample at GB site ASCC2-41

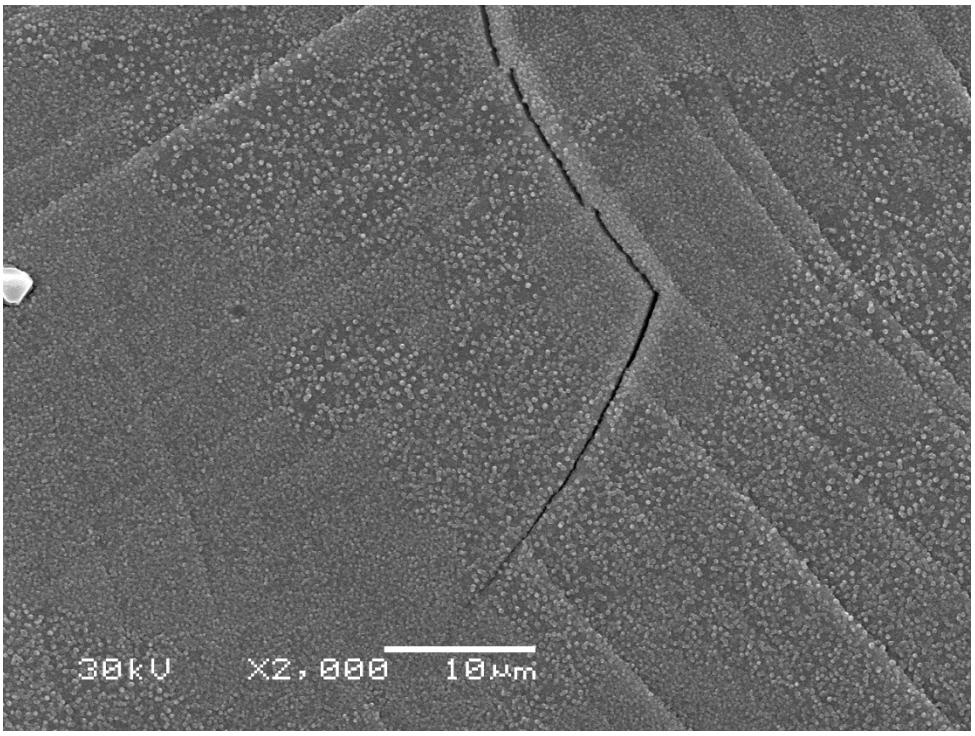

Figure E.20: Intergranular crack initiated in ASCC2 Fe13Cr15Ni 5 dpa tensile bar sample at GB site ASCC2-42

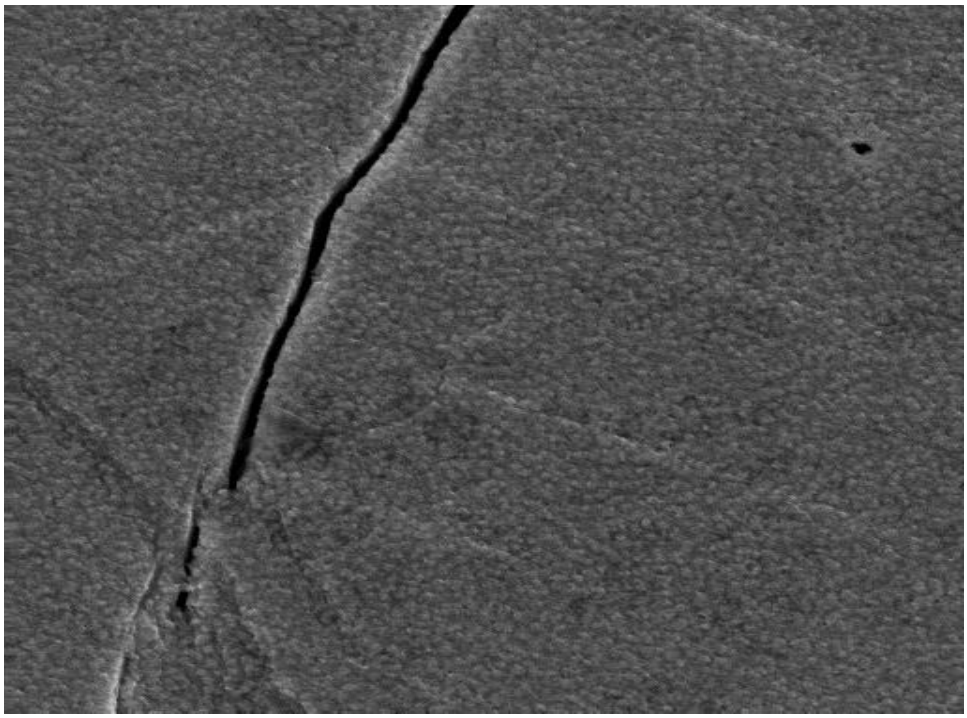

Figure E.21: Intergranular crack initiated in ASCC2 Fe13Cr15Ni 5 dpa tensile bar sample at GB site ASCC2-45

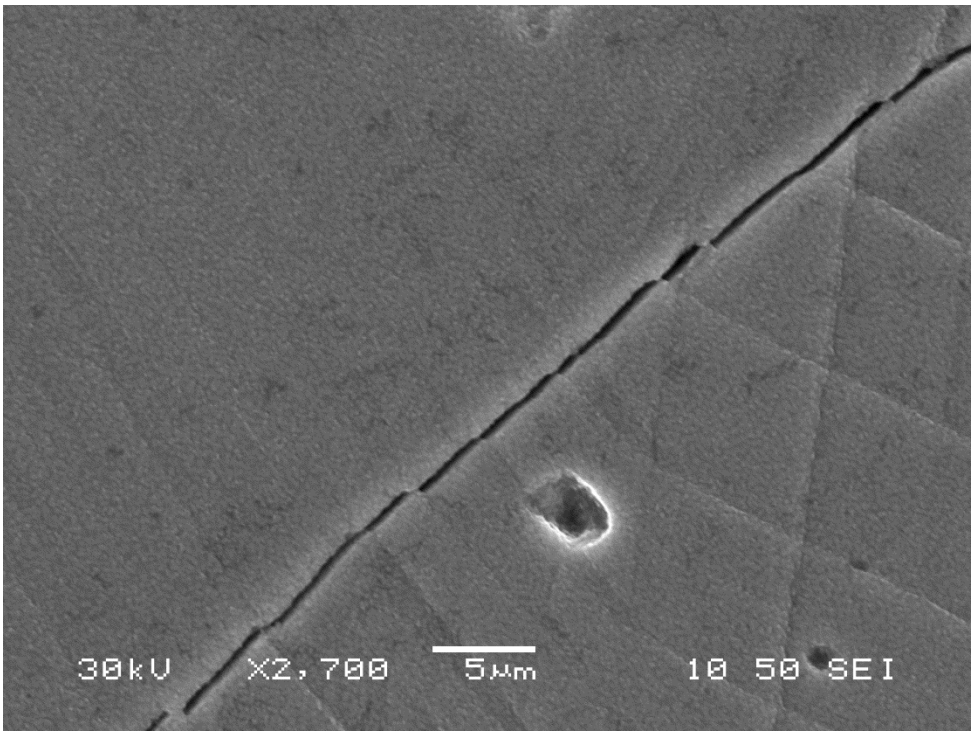

Figure E.22: Intergranular crack initiated in ASCC2 Fe13Cr15Ni 5 dpa tensile bar sample at GB site ASCC2-49

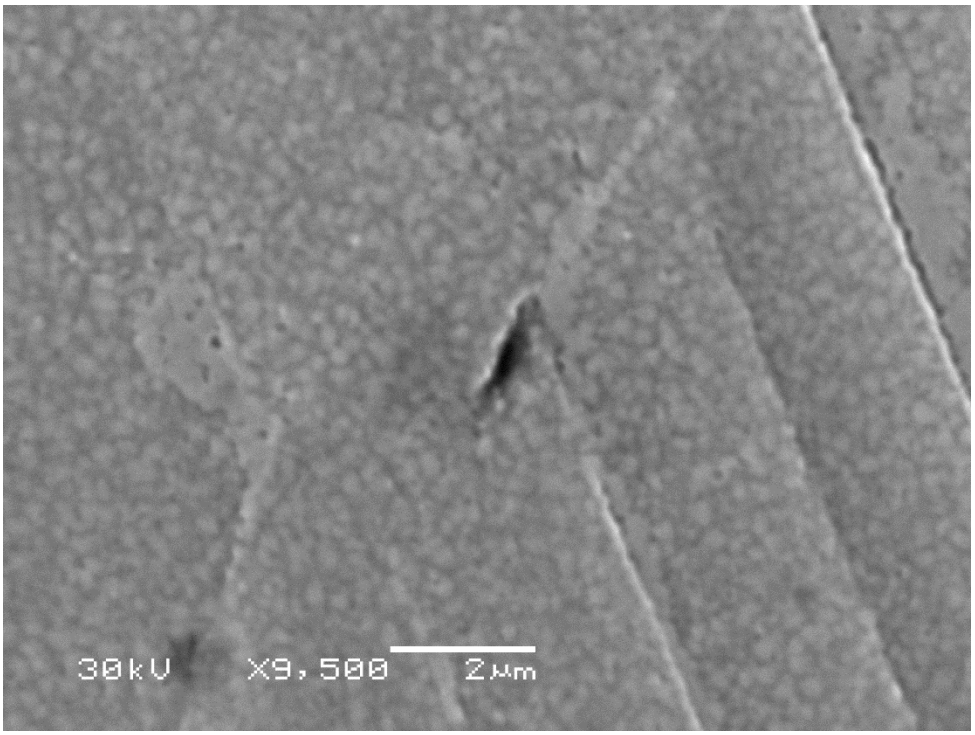

Figure E.23: Intergranular crack initiated in ASCC2 Fe13Cr15Ni 5 dpa tensile bar sample at GB site ASCC2-56

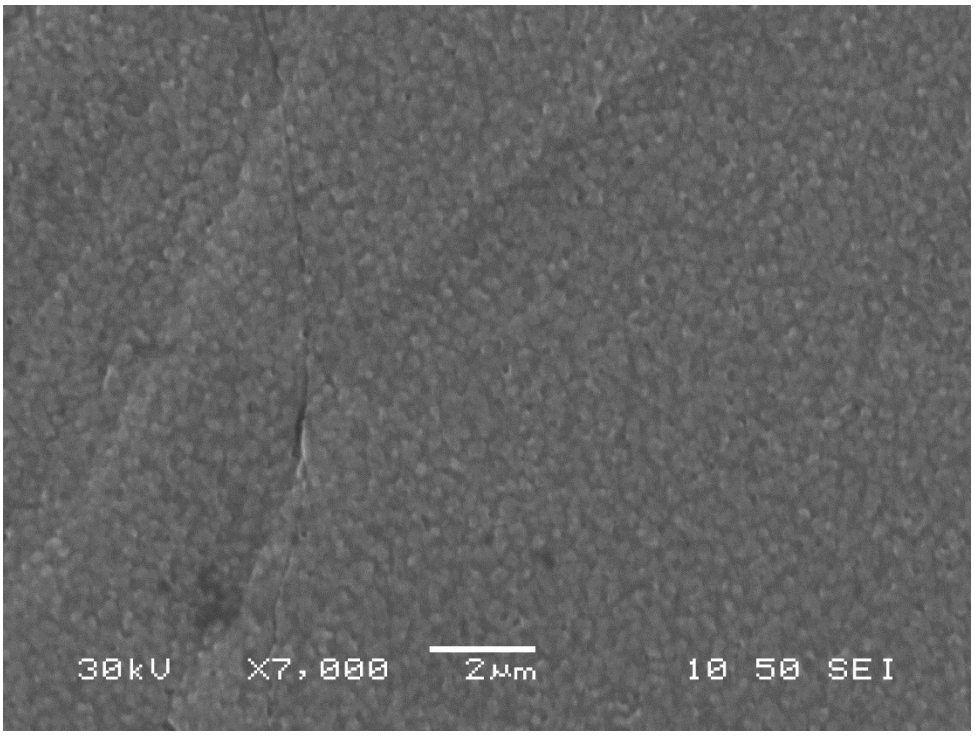

Figure E.24: Intergranular crack initiated in ASCC2 Fe13Cr15Ni 5 dpa tensile bar sample at GB site ASCC2-61

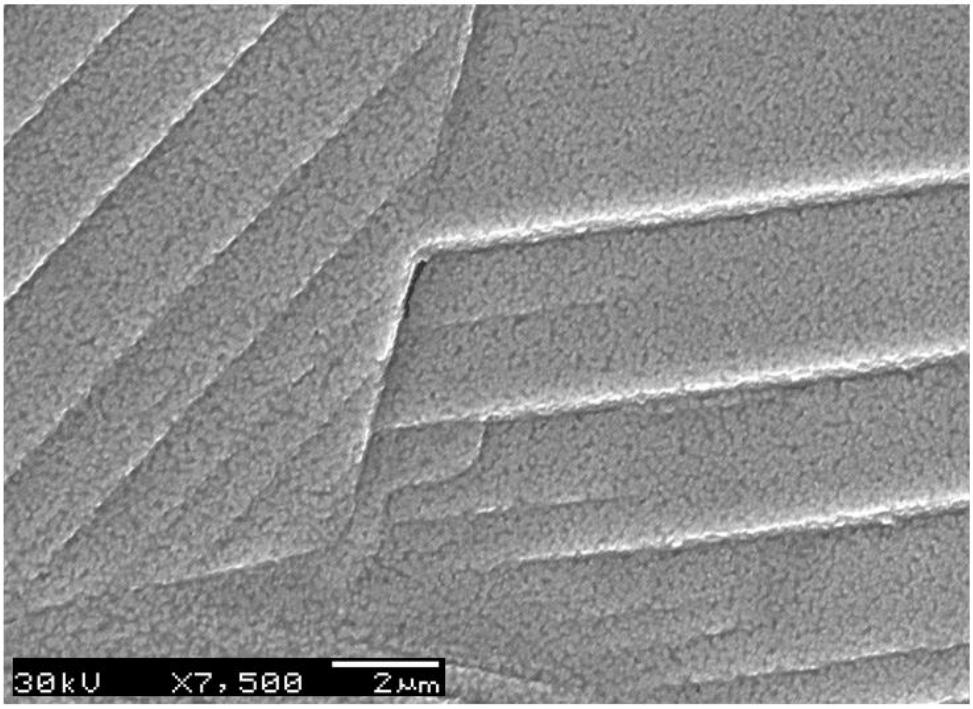

Figure E.25: Intergranular crack initiated in ASCC2 Fe13Cr15Ni 5 dpa tensile bar sample at GB site ASCC2-63

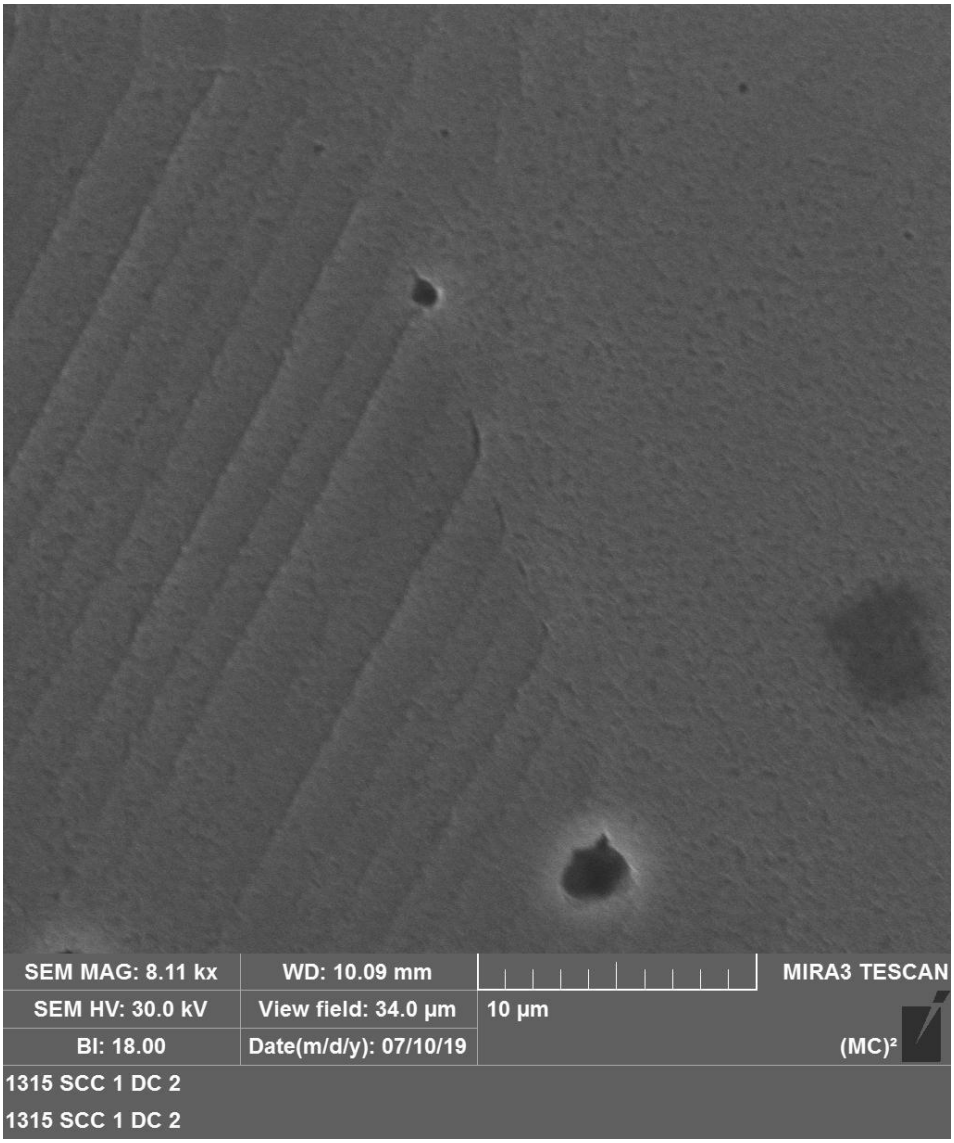

Figure E.26: Intergranular crack initiated in ASCC2 Fe13Cr15Ni 5 dpa tensile bar sample at GB site ASCC2-75

References

[1] E.A. Kenik, IASCC, JNM 212-215, 1994

[2] H.M. Chung JNM 239 1996

[3] P.A. Scott JNM 211 1994

[4] C. F. Cheng JNM 56 1975 11-33

[5] V. N. Shah Nuclear Engineering and Design 134 1992 199-215

[6] L.C. Shao Nuclear Engineering and Design 57 1980 133-140

[7] A. Jenssen *Proc 6 Int Symp Environ Degrad Mat Nucl Power Syst Water React*, 1993 547-554

[8] M. J. Mankin Acta Metallurgica 7 361-366

[9] M. Victoria International Workshop on Basic Aspects of Differences in Irradiation Effects Between FCC, BCC, and HCP Metals and Alloys 1998

[10] M. Kirk Structural Mechanics in Reactor Technology 2003

[11] A. Almazouzi JNM 276 2000 295-296

[12] T. Diaz de la Rubia Nature 406 2000 871-874

[13] B. N. Singh JNM 299 2001 205-218

[14] B.N. Singh JNM 307-311 2002 159-170

[15] P. R. Swann Corrosion 1963

[16] Z. Jiao JNM 361 2007 218-227

[17] J.V. Sharp Philosophical Magazine 16 77-96

[18] D.J. Edwards JNM 342 2005 164-178

[19] E.H. Lee JNM 296 2001 183

[20] M. Briceno JNM 409 18-26

[21] J.S. Robach Philosophical Magazin 83 955-967

[22] M. Suzuki Philosophical Magazine A 64 395-411

[23] I.M. Robertson Acta Materialia 54 2006 1679-1690

[24] T. Onchi JNM 340 2005 219-236

[25] D.J. Edwards JNM 329-333 2004 1072

[26] X. LiJNM 385 2009 329-333

[27] K. Fukuya JNM 378 2008 211-219

[28] K. Fukuya JNM 417 2011 958-962

[29] E.H. Lee Acta Materialia 49 2001 3277

[30] H. Nishioki JNST 45 2008 274-287

[31] M. Sauzay JNM 406 2010 152-165

[32] Z. Jiao JNM 408 2011 246-256

[33] E. Kaxiras Sci Model Simulation 15 2008 59-65

[34] L. Lymperakis Eur Physics Journal 177 2009 41-57

[35] M.F. Horstemeyer Acta Materialia 49 2001 4363-4374

[36] P. Arnoux Corrosion Science 52 2010 1247-1257

[37] E.A. West PhD Thesis University of Michigan 2010

[38] E.A. West JNM 408 2011 142-152

[39] M.D. McMurtrey Material Science Engineering A 528 2011 3730-3740

[40] M.D. McMurtrey International conference on environmental degradation of materials in nuclear power systems

[41] L. Fournier JNM 366 2007 187-197

[42] W. Karlsen JNM 406 2010 138-151

[43] G.S. Was MRS Spring Meeting 2004 87-100

[44] M. Shimada Symposium on Computational Thermodynamics and Materials Design 2001 2331-2341

[45] S.M. Bruemmer MRS Spring Meeting 2004 101-110

[46] E.A. West JNM 2010

[47] Acta Materialia 65

[48] A.W. Thompson Advanced Corrosion Science Technology vol. 7 1980 53

[49] V.N. Shah Nuclear Engineering and Design 134 1992

[50] J. Kacher Micron 43 2012 1099-1107

[51] G.S. Was Current Opinion in Solid State and Materials Science 16 2012 134-142

[52] G.S. Was Fracture and Failure Prevention vol. 261-263 2004 885-901

[53] T. Onchi JNM 340 2005 219-236

[54] Y. Matsukawa Material Science Engineering A 400-401 2005 366-369

[55] Y. Matsukawa Philosophical Magazine 88 2008 581-597

[56] Y. Matsukawa JNM 351 2006 285-294

[57] D. Farkas Philosophical Magazine 80 2000 229-237

[58] D. Farkas Philosophical Magazine 89 2009 3435-3450

[59] T. Nogaret Philosophical Magazine 87 2007 945

[60] T. Onchi JNM 320 2003 194

[61] S.I. Wright Microscopy and Microanalysis 17 2011 316-329

[62] B.L. Adams Metall Trans 24A 1993 819-831

[63] L.N. Brewer Microscopy and Microanalysis 2002 684-685

[64] D.P Field Ultramicroscopy 67 1997 1-9

[65] G. Miyamoto Acta Materialia 57 2009 1120-1131

[66] J.F. Nye Physical Properties of Crystals 1957

[67] X. Tao PhD Thesis Lehigh University 2003

[68] S. Villert Journal of Microscopy 233 2009 290-301

[69] S.T. Wardle Microscopy Society of America 52 680-681

[70] A.J. Wilkinson Material Science Technology 13 1997 79-84

[71] A.J. Wilkinson Ultrmicroscopy 106 2006 307-313

[72] A.J. Wilkinson Material Science Technology 22 2006 1271-1278

[73] T.B. Britton Acta Materialia 60 2012 5773-5782

[74] A.W. Reynolds,Phys. Rev. 98 1955 418

[75] M. Kiritani JNM 216 1994 220-264

[76] C. Cawthorne E.J. Fulton Nature 216 1967 15

[77] G.H. Kinchin R.S. Pease Rep. Progr. Phys. 18 1955 1

[78] M.J. Norgett M.T. Robinson I.M. Torrens Nuclear Engineering Design 33 1975 50

[79] B.N. Singh S.J. Zinkle JNM 206 1993 212

[80] S.J. Zinkle B.N. Singh JNM 199 1993 173

[81] R.E. Stoller, G.R. Odette JNM 251 1997 49

[82] T. Diaz de la Rubia N. Soneda JNM 251 1997 13

[83] T. Diaz de la Rubia Rev. Mater. Sci. 26 1996 213

[84] D.J. Bacon F. Gao JNM 251 1997 1

[85] H.L. Heinisch Philos. Mag. A 67 1993 407

[86] Yu. Osetsky V. Priego submitted Philos. Mag

[87] B.N. Singh S.J. Zinkle M. Eldrup S.I. Golubov

[88] A. Almazouzi JNM< 276 2000 295-296

[89] Y. Nagai Phys. Rev. B 63 2001

[90] M. Eldrup JNM 251 1997 132

[91] M.J. Puska Rev. Mod. Phys. 66 1994 841

[92] E. Meslin JNM 406 2010 73-83

[93] T. Iwata Radiat. Eff. Def. Solids 144 1998 27

[94] A. Iwase JNM 276 2000 178-185

[95] S.I. Golubov JNM 276 2000 78-89

[96] B.N. Singh C.H. Woo Radiat. Eff. Def. Solids 144 1998 119

[97] A. Risbet JNM 50 1974 116

[98] A. Horsewell Radiat. Eff. 102 1987

[99] M. Kiritani JNM 251 1997 237-251

[100] M. Kiritani Mater. Chem. Phys. 50 1997 133

[101] S.J. Zinkle JNM 225 1995 123

[102] M. Vitoria N. Baluc JNM 276 2000 114

[103] N. Ajita Phys. Stat. Sol. 87 1985 235

[104] Yu. Osetsky D.J. Bacon JNM 307-311 2002 852

[105] Venables JA, Harland CJ, 1973, Philosophical Magazine 27, 1193-1200

[106] Dingley DJ 1984 Proc. Royal Microsc. Soc 19, 74-75

[107] Adams BL, Wright SI, Kunze K, 1993 Metall. Trans. 24A, 819-831

[108] Dingley DJ, 2004 Journal of Microscopy 21, 214-224

[109] Wright SI, Nowell MM, Field DP, 2011 Microstructure and Microanalysis 17, 316-329

[110] Troost KZ, Vandersluis P, 1993 Appl Phys Lett 62 1110-1112

[111] Wilkinson AJ 1997 Mater Sci Tech 13 79-84

[112] Tao X, 2003 PhD Thesis Bethlehem, PA Leigh University

[113] Bertness KA, Geiss RH, Keller RR, Quinn TP, 2004 Microelectron Engineering 75 96-102

[114] Wilkinson AJ, Meaden G, Dingley DJ, 2006 Ultramicroscopy 106, 307-313

[115] Nye JF 1957 London: Oxford

[116] Wilkinson AJ, Meaden G, Dingley DJ 2006 Mater Sci Tech 22 1271-1278

[117] Bowen DK, Tanner BK, 1995 J. Appl. Cryst. 28, 753-760

[118] Stone HJ, Withers PJ, Holden TM 1999 Metall. Trans 30 1797-1808

[119] Tamura N, Celetre RS, MAcDowell AA, 2002 Rev Sci Instr 73 1369-1372

[120] Clement L, Pantel R, Kwakman LFT, 2004 Appl Phys Lett 85 651

[121] Villert S, Maurice C, Wyon C, 2009 Microscopy Oxford 233-290

[122] Vaudin MD, Gerbig YB, 2009 Appl Phys Lett 93

[123] Wilkinson AJ, Randman D, 2010 Philosophical Magazine 90 1159

[124] Britton TB, Liang H, Proceedings of the Royal Society 466

[125] Britton TB, Randman D, Wilkinson AJ, 2009 J Mater Res 24

[126] Miyamoto G, Shibata A, Maki T, 2009 Acta Mater 57

[127] Wilkinson AJ, Clarke EE, Britton TB, 2010 J Strain Anal Eng Des 45

[128] Dingley DJ, Randle V, 1992 JMS 27 4545-4566

[129] Baba-kishi KZ, Dingley DJ 1989 Scanning 11, 305-312

[130] Michael JR, Goehner RP, 1993 MSA Bull. 23 168

[131] Russell, K. Prog. Mater. Sci. 1984, 28, 229–434

[132] Holland, J. R.; Mansur, L. K.; Potter, D. I. Phase Stability During Radiation; TMS-AIME: Warrendale, PA, 1981

[133] Nolfi, F. V. Phase Transformations During Irradiation; Applied Science: London and New York, 1983

[134] Ardell, A. J. In Materials Issues for Generation IV Systems; Ghetta, V., et al., Eds.; Springer, 2008; pp 285–310

[135] Was, G. Fundamentals of Radiation Materials Science; Springer-Verlag: Berlin, 2007

[136] Anthony, T. R. Acta. Metall. 1969, 17, 603–609

[137] Anthony, T. R. J. Appl. Phys. 1970, 41, 3969–3976

[138] Anthony, T. R. Phys. Rev. B 1970, 2, 264

[139] Anthony, T. R. Acta Metall. 1970, 18, 307–314

[140] Anthony, T. R.; Hanneman, R. E. Scr. Metall. 1968, 2, 611–614

[141] Anthony, T. R. In Radiation-Induced Voids in Metals; Corbett, J. W., Ianniello, L. C., Eds.; US Atomic Energy Commission: Albany, NY, 1972; pp 630–645

[142] Smigelskas, A. D.; Kirkendall, E. O. Trans. AIME 1947, 171, 130–142

[143] Marwick, A. J. Phys. F Met. Phys. 1978, 8, 1849–1861

[144] Okamoto, P. R.; Harkness, S. D.; Laidler, J. J. Trans. Am. Nucl. Soc. 1973, 16, 70–70

[145] Y. Guo, D.M. Collins, E. Tarleton, F. Hofman, A.J. Wilkinson, B. Britton Acta Materialia vol 182 (2020) pg 172-183

[146] B. Kuhr, D. Farkas, I.M. Robertson, D.C. Johnson, G.S. Was, Metallurgical and Materials Transactions A: Physical Mettallurgy and Materials Science vol 51 2020 pg 667-683

[147] B. Kuhr, D. Farkas, Modelling and Simulation in Materials Science and Engineering vol 27 2019

[148] J. Kacher, B.P. Eftink, B. Cui, I.M. Robertson Current Opinionin Solid State and Materials Science Vol 18 2014, pg 227-243